Anodic and Cathodic Limitations on Localized Corrosion and Stress Corrosion Cracking Propagation of Stainless Steel 304L in Atmospheric Environments

---

A
Dissertation
Presented to
the faculty of the School of Engineering and Applied Science
University of Virginia

---

in partial fulfillment
of the requirements for the degree

Doctor of Philosophy

by

Ryan Katona

December 2021

APPROVAL SHEET

This

Dissertation

is submitted in partial fulfillment of the requirements
for the degree of

Doctor of Philosophy

Author: Ryan Katona

This Dissertation has been read and approved by the examing committee:

Advisor: Robert Kelly

Advisor:

Committee Member: James Burns

Committee Member: John Scully

Committee Member: Giovanni Zangari

Committee Member: Andres Clarens

Committee Member: Eric Schindelholz

Committee Member: Rebecca Schaller

Accepted for the School of Engineering and Applied Science:

Jennifer L. West, School of Engineering and Applied Science

December 2021

Executive Summary

The formation of localized corrosion, characterized by the highly focused metallic dissolution of an otherwise passive alloy, is likely in marine environments. Localized dissolution is characterized as an autocatalytic process and requires a minimum concentration of metal chlorides, that undergo hydrolysis, destroying localized passivity. If these conditions are not met, repassivation will commence and corrosion will stifle. Anodic processes must be supported by cathodic reduction reactions on the external environment. In atmospheric scenarios, a finite water layer thickness combined with solution properties can provide significant ohmic drop in solution creating a finite cathode. At some point, localized corrosion features grow to a size that requires a cathode current that cannot be obtained by the surrounding material, creating a maximum pit size. Both anodic and cathodic processes are influenced by solution concentration, solution composition, and temperature, therefore, influencing the extent of corrosion on the surface of an alloy. Finally, solution properties are dictated by the exposure relative humidity. As the relative humidity changes both diurnally and seasonally, a wide range of solutions are possible in marine environments. This dissertation addresses environmental changes (relative humidity and temperature) on anodic and cathodic properties. These properties are combined in order to inform upon localized corrosion through analytical and Finite Element Modeling.

The main goals of this dissertation are to (i) develop a robust understanding of reaction mechanisms as a function of environmental parameters, (ii) utilize and enhance analytical predictive capabilities to understand governing factors and more accurately predict pitting corrosion damage, and (iii) utilize FEM modeling approach, electrochemical techniques, and pertinent instrumental characterization tools to systematically investigate the effect of electrolyte layer thickness, solution chemistry, materials surface properties, and geometry on localized corrosion and SCC damage distributions.

The goal of this dissertation was fulfilled by combining experimental and modeling techniques to inform upon the underlying corrosion mechanisms, and governing factors (including environmental factors) for localized corrosion of stainless steel 304L as a candidate system. First, cathodic reduction reaction mechanisms were determined in simulated atmospheric environments utilizing a rotating disk electrode and identified that the relative humidity dictates the reaction mechanism. It was also noted that corrosion can cause for a pH increase in the cathodic region which can further change the reaction mechanism and stifle cathodic currents. Additionally, a novel technique was introduced in order to visually inspect the surface of an alloy with *in-situ* Raman spectroscopy under cathodic control in thin film conditions. Second, anodic properties were assessed in similar environments in which critical parameters, namely the pit stability product and repassivation potential, were determined. Third, the water layer thickness was determined in common exposure environments and the boundary between thin film and bulk corrosion scenarios was identified as a function of relative humidity. These water layer thicknesses were compared to the boundary layer present in accelerated corrosion testing which was determine through the creation of a resistance-based sensor. Fourth, cathodic and anodic properties were combined with water layer thicknesses to predict localized corrosion. Various trends in cathodic kinetics were identified as a function of environment. Additionally, governing parameters for maximum pit sizes were identified for multiple scenarios. Localized corrosion predictions were validated based on long term exposure data in controlled environments. Finally, environmental influences on the electrochemical conditions were assessed for stress corrosion cracking in a Laplace-Equation based FEM modeling approach and highlighted the importance of considering the external environment on crack tip conditions.

Overall, this dissertation developed a fundamental understanding of the effect of environmental parameters on localized, pitting corrosion and stress corrosion cracking. The work provides for a complete means of predicting localized pitting corrosion of SS304L in marine environments as a function of relative humidity which can be used for diagnostic measures. Electrochemical characterization in this dissertation provides meaningful information for better understanding of corrosion processes and identifies governing factors (both experimental and modeling techniques) of corrosion processes.

Acknowledgments

First, I would like to thank my advisor Dr. Rob Kelly for the incredible opportunity to work with him for the past few years. I cannot begin to thank you enough for your support, guidance, and encouragement throughout this PhD. The skills that you have taught me about the many aspects of research are invaluable and I will carry them with me the rest of my life. You are an incredible role model and I will indebted to you for the support you have given. I would also like to thank my committee members, Dr. John Scully, Dr. Andres Clarens, Dr. Giovanni Zangari, Dr. James Burns, Dr. Eric Schindelholz, and Dr. Rebecca Schaller.

I would like to acknowledge current and former CESE members for their welcoming arms into the program and for their help in beginning my journey into the corrosion field. A special thanks to Ms. Lyndsey Blohm, Dr. Katie Lutton, Dr. Veronica Rafla, Mrs. Kate Quiambao-Tomko, Dr. Gilbert Liu, Dr. Piyush Khullar, Dr. Marybeth Parker, Dr. Jayendran Srinivasan, Dr. Patrick Steiner, Dr. Zach Harris, Dr. Greg Kubacki, Dr. Mathew McMahon, and Dr. Noelle Co. I would also like to thank the entire Kelly group (Pedro Atz Dick, Carolina Moraes, Rebecca Marshall, Duane Macatangay, Utibe-Eno Charles-Granville, Danyil Kovalov, and Liat Bell) and the rest of the students in Materials Science and Engineering department. A special thanks to the staff of the materials science department as much of the work would not have been possible without their support. Additionally, I would like to thank undergrad researchers Jacob Carpenter, Timothy Montoya, and Jay Perry who helped with experiments and data collection.

I would also like to thank the many colleagues and support staff at Sandia National Laboratories. I could not have imagined performing a lot of the research in this dissertation more than halfway across the country when I started at UVA. I would specifically like to thank Dr. Eric Schindelholz for bringing me aboard at SNL, countless guidance through the PhD research, incredible professional opportunities, and the many food recommendations in Albuquerque. Additionally, I would like to thank Dr. Schindelholz and Dr. Michael Melia for their supervision while I beavered away in the lab when I did not have my clearance. I would like to thank Dr. Rebecca Schaller for the continued guidance at SNL and for providing many opportunities for professional and personal growth. Finally, I would also like to thank Dr. Charles Bryan, Dr. Andrew Knight, Ms. Sylvia Saltzstein, Dr. Erin Karasz, and Dr. Dave Enos.

I would like to acknowledge my family, especially my mom and dad for their endless support. They continued to push me towards my goals, even if that included a move across the country, and have been a constant source of encouragement. They helped me believe that a PhD is something that I am capable of achieving. I am incredibly thankful for my brother Branden. I do not think I would have even considered graduate school if had not been for you. It started back in the summer of 2015 when we got to spend the summer together at Penn State where you were in graduate school and I got a research position for the summer. I will forever cherish that summer due to the many memories that were created, and it started my interested in the field of materials science. You are one of the most influential people in my life and I can't begin to thank you enough.

I am very grateful for the loving support of my future wife Molly. Being by my side throughout the entire process made it much easier to go to work each morning. Her encouragement during the pandemic was a blessing and the many memories that we have created in New Mexico will forever be with me. I will be forever grateful for everything that you do, and I am incredibly lucky to have you in my life. I look forward to the next chapters in our lives together.

Bibliography

R. M. Katona, J. C. Carpenter, A. W. Knight, R. S. Marshall, B. L. Nation, C. R. Bryan, E. J. Schindelholz, R. F. Schaller, and R. G. Kelly, Natural convection boundary layer thickness at elevated chloride concentrations and temperatures and the effects on a galvanic couple. J. Electrochem. Soc. 168 (2021) 031512. https://doi.org/10.1149/1945-7111/abeb29. **Editor's Choice.**

R. S. Marshall, **R. M. Katona**, M. A. Melia, R. G. Kelly. Pit Stability Predictions of Additively Manufactured SS316 Surfaces Using Finite Element Analysis. In Preparation. 2021

R. M. Katona, J. Carpenter, E. J. Schindelholz, R. G. Kelly, R. F. Schaller. Cathodic Kinetics on Platinum and Stainless Steel in NaOH Environments. Journal of the Electrochemical Society. 2021. https://doi.org/10.1149/1945-7111/ac1318

R.M. Katona, A.W. Knight, E.J. Schindelholz, C.R. Bryan, R.F. Schaller, R.G. Kelly, Quantitative assessment of environmental phenomena on maximum pit size predictions in marine environments, Electrochim. Acta. 370 (2021) 137696. https://doi.org/10.1016/j.electacta.2020.137696.

R.M. Katona, J.C. Carpenter, A.W. Knight, C.R. Bryan, R.F. Schaller, R.G. Kelly, E.J. Schindelholz, Importance of the hydrogen evolution reaction in magnesium chloride solutions on stainless steel, Corros. Sci. 177 (2020) 108935. https://doi.org/10.1016/j.corsci.2020.108935.

R.M. Katona, R.G. Kelly, C.R. Bryan, R.F. Schaller, A.W. Knight, Use of in situ Raman spectroelectrochemical technique to explore atmospheric corrosion in marine-relevant environments, Electrochem. Commun. 118 (2020) 106768. https://doi.org/10.1016/j.elecom.2020.106768.

R.M. Katona, S. Tokuda, J. Perry, R.G. Kelly, Design, Construction, and Validation for in-situ Water Layer Thickness Determination during Accelerated Corrosion Testing, Corros. Sci. 175 (2020) 108849. https://doi.org/10.1016/j.corsci.2020.108849.

R.M. Katona, J. Carpenter, E.J. Schindelholz, R.G. Kelly, Prediction of Maximum Pit Sizes in Elevated Chloride Concentrations and Temperatures, J. Electrochem. Soc. 166. 2019 C3364–C3375. https://doi.org/10.1149/2.0451911jes.

R.G. Kelly, **R.M. Katona**, E.J. Schindelholz, "Pitting," in Corrosion Tests and Standards: Application and Interpretation-Third Edition, (West Conshohocken, PA: ASTM International). Accepted.

C. L. Alexander, C. Liu, A. Alshanoon, **R. M. Katona**, R. G. Kelly, J. Carpenter, C. Bryan, and E. Schindelholz Oxygen Reduction on Stainless Steel in Concentrated Chloride Media. J. Electrochem. Soc. 2018 165: 869-877. https://doi.org/10.1149/2.0181813jes.

Contents

List of Figures

List of Tables

List of Symbols

Table 1: List of Symbols

C_j	Concentration of species j
C_{eq}	Equilibrium concentration
D_j	Diffusivity of species j
DRH	Deliquescence relative humidity
E_{corr}	Corrosion potential
E_{mouth}	Potential at crack mouth
E_{OCP}	Open circuit potential
E_{pit}	Pitting Potential
E_{rp}	Repassivation potential
E_{tip}	Crack tip potential
e_{SS}^{-}	Electrons transferred per mol SS corroded
f	Fraction of saturation
i	Current density
I_{cath}	Cathodic current
I_c/W	Current per width
I_{LC}	Anodic current demand
i_{eq}	Equivalent current density
i_{lim}	Limiting current density
$(i \cdot x)_{crit}$	Critical pit stability product
$(i \cdot x)_{sf}$	Pit stability product under a salt film
I/r	Pit stability for hemisphere
K	Stress intensity
LD	Salt loading density
Me^{n+}	Metal ion with charge
M_{OH^-}	Hydroxyl molarity (mol/L) in cathode region
MW	Molecular weight

MW_{precip}	Precipitate molecular weight
MW_{SS}	Stainless Steel 304 molecular weight
n_{precip}	Stochiometric number for precipitate
Pt	Platinum alloy
Q	Flow rate
r_a	Anode radius
R_{cath}	Cathode radius
RH	Relative humidity
V_{cath}	Cathode volume
V_{precip}	Precipitate volume
WL	Water layer
x	Pit depth
Greek Symbols	
δ	Boundary layer thickness
δ_{nc}	Natural convection boundary layer thickness
κ	Conductivity
κ_{eff}	Effective conductivity
κ_o	Initial solution conductivity
ρ	Density
ρ_{sp}	Specific solution density
ρ_{SS}	Stainless Steel 304 density
ρ_{precip}	Precipitate density
ν	Kinematic viscosity
η	Viscosity
Abbreviations	
BWR	Boiling water reactors
CGR	Crack growth rate
CMOD	Crack mouth opening displacement
CTOD	Crack tip opening displacement

FEM	Finite Element Model
HER	Hydrogen Evolution Reaction
ORR	Oxygen reduction reaction
RDE	Rotating disk electrode
SCC	Stress corrosion cracking
SNF	Spent Nuclear Fuel
SS	Stainless Steel

1. Introduction

1.1. Overview

Alloys are commonly exposed to atmospheric, marine environments, which are characterized by an aggressive thin layer of brine or droplets on the surface. The brine properties (in terms of solution concentration, composition, and temperature) vary both spatially and temporally. If an otherwise passive alloy is exposed to such conditions, a localized corrosion environment can be established on the material leading to materials degradation, the potential for pit-to crack transition and growth, and eventual failure of a structure. While localized materials degradation is highly likely in marine environments, the extent of the damage is dependent upon the material and chemical and electrochemical conditions present in the environment.

There are two main, interconnected research topics that are explored in this dissertation: localized corrosion (pitting and stress corrosion cracking) and transient environments present in exposure settings. There have been numerous research studies focused on each of these respective areas; however, research efforts towards a synergistic approach to the wide range of the material and environmental interactions possible have not been addressed especially with multiple forms of localized corrosion. Additionally, localized corrosion can be decoupled into anodic and cathodic processes, both of which have been studied individually but rarely together. By utilizing experimental and modeling techniques, the underlying corrosion mechanisms, and governing factors (including environmental factors) for localized corrosion can be identified. While this work can generally be applied to atmospheric, marine corrosion, the model system that will be explored in this dissertation will be that of a stainless steel (SS) alloy due to their frequent use in the storage of spent nuclear fuel (SNF).

1.2. Background

1.2.1. Localized corrosion

Localized corrosion is characterized by the highly focused metallic dissolution of an otherwise passive alloy. Pitting corrosion occurs when discrete areas of a material undergo rapid attack, although the vast majority of the surface remains virtually unaffected [1,2]. The presence of some anions like chloride permits attack of the passive layer and assists in the maintenance of high dissolution rates due to their participation in the stabilization of low pH in the pit via cation hydrolysis [2,3]. The stabilization of an aggressive pit chemistry, significantly different in composition from the bulk electrolyte, enables physical separation of the dominant cathode from dominant anode (pit) because of the need to minimize OH^- production locally, and the ability to have metal ions created in the pit to hydrolyze and draw in chloride [1,3,4].

Chemistry Development – There are often considered three stages of pitting: (i) initiation (passive film breakdown), (ii) metastable growth, and (iii) stable growth [3]. Independent of initiation cause and location, the stable propagation of pitting requires maintenance of a sufficient concentrated solution of metal ions (Me^{n+}) whose hydrolysis (Equation 1) results in acidification of the pit base [1,3,4] as presented in Figure 1(b).

$$Me^{n+} + H_2O \leftrightarrow Me(OH)^{(n-1)+} + H^+ \qquad 1$$

Failure to maintain this aggressive, acidic environment will result in the repassivation, or regrowth of the passive oxide, on the surface. There are many factors that impact the ability to maintain the aggressive environment such as potential, alloy composition, electrolyte concentration and composition, and temperature [3], all of which will be explored further.

Pitting is considered to be autocatalytic in nature; once a pitting initiates, the aggressive conditions developed are such that pit growth is promoted [3]. One interpretation of the influence of pit chemistry changes on pit growth and stability was provided by Galvele [5,6] who described the chemistry in terms of electrochemical parameters. The Galvele framework determined the current density (i) required to maintain a critical chemistry at the base of a pit of depth x for a 1-D geometry based on dissolution, outward diffusion, and thermodynamic equilibria of various species. The quantitative model exploited Fick's first law to describe dissolution fluxes required to produce a sufficiently low pH. That is, relationships between concentrations specified by the dissolution i, composition of the material, hydrolysis equilibrium constants, and diffusivities were combined to yield the parameter (xi). This parameter, which became known as the pit stability product, describes the current density (i) at any given pit depth (x) to maintain steady-state dissolution [5,6]. This parameter can be measured experimentally [7], however, the method used generally results in the formation of a salt film (sf) on the surface of the alloy as it leads to the precipitation of a metal chloride salt film (Figure 1(c)). The sf can be described by the saturation concentration of metal salts (C_{sat}) and the corresponding pit stability is denoted as $(i \cdot x)_{sf}$.

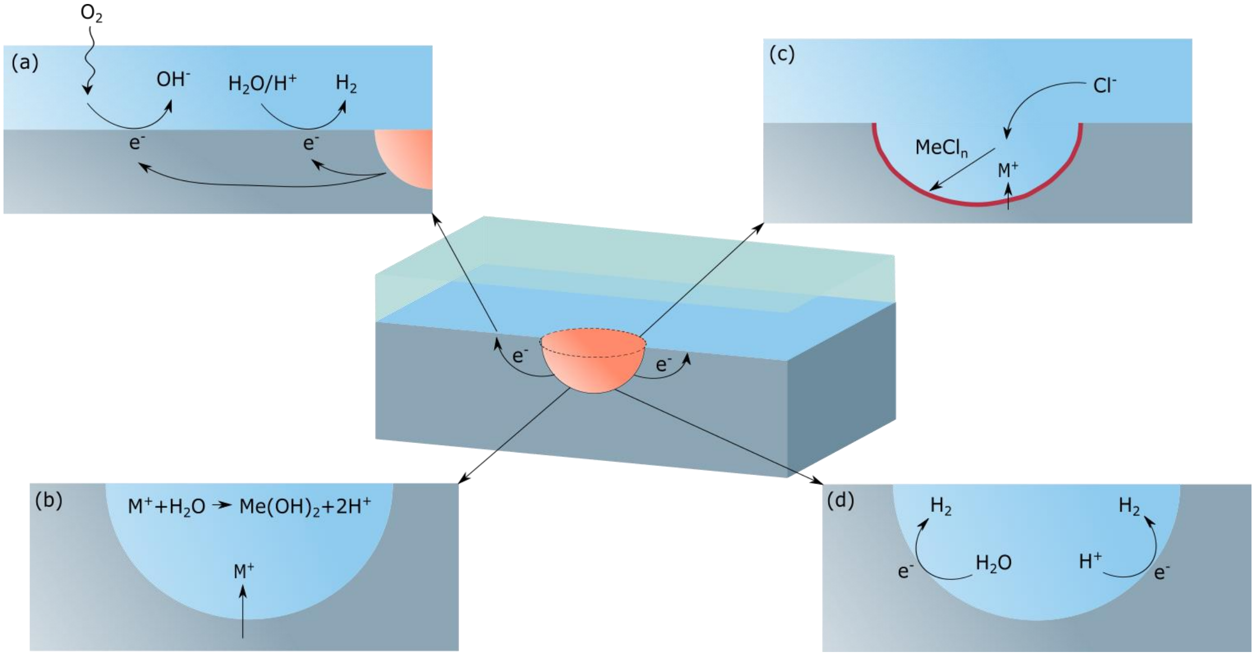

Figure 1: Schematic of various pitting phenomena including: (a) surface cathodic reactions, (b) metal ion hydrolysis, (c) formation of metal chloride salts, and (d) internal cathodic reactions on the pit walls.

Critical Potentials – The stability of pitting corrosion can also be described by characteristic potentials. Traditional thinking states that stable pits will form at potentials greater (more noble) than the pitting potential, E_{pit}, and will grow at potentials above (i.e., more noble than) the repassivation potential, E_{rp}, which is lower than E_{pit}. Thus, E_{rp} describes the critical potential below with new pits cannot initiate and new pits cannot grow [3,8]. The determination of E_{pit} and E_{rp} is dependent upon experimental parameters and has been historically measured by cyclic potentiodynamic polarization (CPP) experiments [9]. A representative CPP experiment is depicted in Figure 2 during which a positive scan from the corrosion potential (E_{corr}) is taken and a substantial increase in i is experienced at E_{pit}, signifying pit growth. At a certain i, the scan direction is reversed and localized corrosion stops when E_{rp} is reached [9]. However, there is abundant experimental evidence suggesting variations in these characteristic potentials with seemingly small differences in experimental parameters, and therefore the use of CPP curves alone is insufficient for the development of a fundamental understanding of the mechanism of pitting corrosion [3,10–12]. Sridhar and coworkers noted that the main issue in using E_{rp} as a predictive parameter is its dependence on prior pit growth [13–15]. Utilizing CPP scans, E_{rp} decreased with the extent of prior pit growth, therefore it cannot be used as a conservative, lower-bound parameter [13–15]. However, it has been shown that for deep pits (i.e., large total charge passed), the value of E_{rp} converges to a single value [8,13–18], and can be utilized as a lower bound to describe pitting corrosion. Sridhar and coworkers introduced a new method of measure E_{rp} by propagating a pit at elevated current densities and utilizing a stepwise scan to low current densities. The convergence of E_{rp} with increased charge was evident as presented in Figure 3 [13–15] and this was further adapted as an ASTM Standard [19].

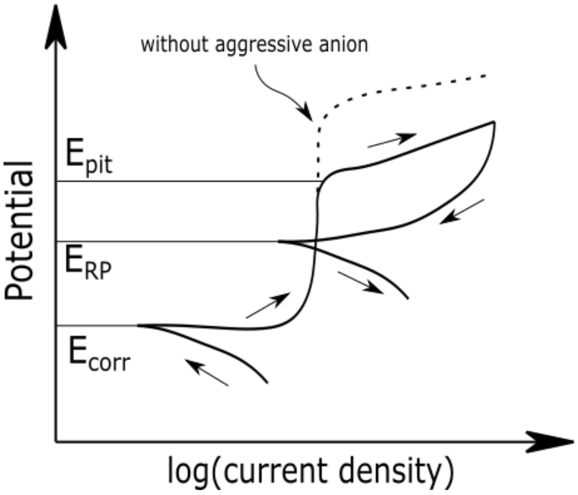

Figure 2: Cyclic potentiodynamic polarization scan. Depiction of governing potentials for pitting corrosion: E_{pit}, E_{rp}, and E_{corr}. The arrows depict the direction of scanning.

Srinivasan and coworkers furthered this formulism of E_{rp} and created unified framework that describes pitting stability in terms of both $(i \cdot x)_{sf}$ and E_{rp} [7,8,16–18,20]. It was noted that mass transport modeling of the 1D pit could provide an estimate of the critical concentration of metal ions at the corroding surface of the pit as it transitioned from stability to repassivation [8]. This helped support the notion that pitting does not need to occur under *sf* conditions and that a fraction of the salt film concentration, denoted f will allow for propagation. The pit stability product under such conditions is described by $(i \cdot x)_{crit}$ and is equal to $f \cdot (i \cdot x)_{sf}$ [7]. Values for f have ranged from 0.43 [21] and 0.50 [8] to 0.75 [22,23].

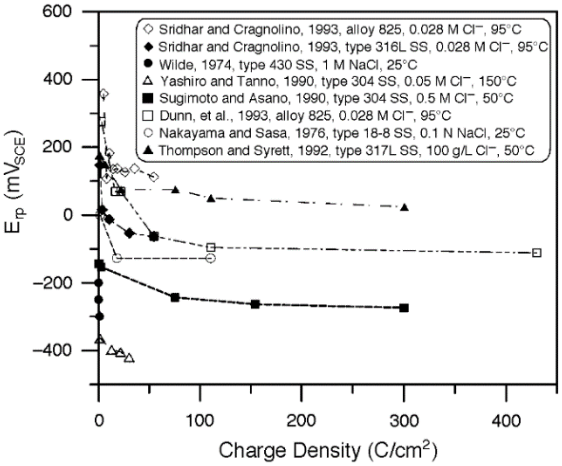

Figure 3: Variation of E_{rp} with increase passed charge density [13].

The framework set forth by Srinivasan and coworkers was also extended to include the critical pH associated with the transition from active corrosion to repassivation. When anodic dissolution occurs at high potentials, the local hydrogen evolution reaction (HER) is suppressed. However, once potentials close to E_{rp} are approached, the local HER reaction rate increases as the anodic dissolution rates decrease. This increase in the local cathodic reaction rate also indicates that its contribution toward the total cathodic current (which balances the total current from anodic dissolution) increases (Figure 1(d)). This relationship is schematically shown in Figure 4 [17] and furthered the understanding of repassivation for localized corrosion environments.

Coupling with external surface – Galvele described the anodic current density required to maintain a critical environment [5,6], and Srinivasan and coworkers connected the critical environment to the repassivation of a 1-D pit [7,8,16–18,20]; however, the conservation of charge requires that the anodic dissolution *must* be balanced by a cathodic current. That is, under freely corroding conditions, the localized corrosion site can only grow as long as its anodic current is matched by the cathodic current from the metal [3,24] as presented in Figure 1(a). The coupling with the external surface creates a natural galvanic couple as the anode and cathode are physically separated. If a substantial amount of the cathodic current that produces OH^- is occurring internally to the corrosion pit, the aggressive, low pH environment cannot be maintained (Figure 4) [17]. There are multiple cathodic reduction reactions, including the oxygen reduction reaction (ORR) and HER that can occur on the external surface or internal to a localized corrosion site. It is generally thought that in atmospheric solutions, ORR is the dominant reaction on the external surface and the efficiency of this reaction (number of electrons transferred) is influenced by solution pH and composition [25].

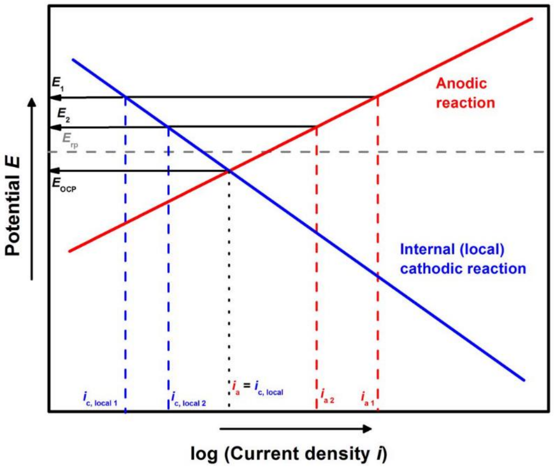

Figure 4: Schematic representation of the increasing influence of the local cathodic reaction toward balancing the current from anodic dissolution, as potentials close to repassivation are reached. Figure from Srinivasen et al. [17].

Modeling of localized corrosion phenomena – Modeling localized corrosion is useful in both understanding fundamentals as well as a tool for structural integrity of metallic components exposed to corrosive environments [26]. There are various models that can be utilized in order to do so including: (i) empirical models [27], (ii) analytical models [24,28,29], (iii) finite difference model [30,31], (iv) boundary element method [32,33], (v) finite volume method [34,35], (vi) Peridynamics [36,37], (vii) phase field models [38,39], and (viii) Finite Element Method (FEM) [26]. Among those, FEM has been the most widely used to investigate transport phenomena in the corrosion systems due to its advantages of dealing with arbitrary shapes, and accessible solution evaluation at any point within the domain without losing much accuracy. Additionally, FEM provides for a good means to predict localized corrosion and can account for the spatial and/or temporal distributions of chemical species, potentials, and currents [26]. Although many models exist in literature, they typically do not relate the pitting processes to the critical values for pitting propagation ($(i \cdot x)_{sf}$ and E_{rp}).

One such model of interest that connects localized corrosion processes to critical values, is an analytical model set forth by Chen and Kelly who were able to numerical account for stability criteria of the anode and the cathode based on charge conservation and predicted maximum pit sizes that would be possible on the surface of passive alloys [24]. As previously discussed, the stability of the anode is determined by $(i \cdot x)_{crit}$ while the stability of the cathode is bounded by E_{rp} and the open circuit potential (E_{ocp}). In thin film environments, ohmic drop will occur in the cathode, providing for a finite area which can be utilized to support anodic dissolution indicating that a finite anode exists [24]. While the model will be described in detail later (Section 5.3.1), all critical values can be determined in the environment of interest and combined to inform upon the maximum extent of pitting corrosion without the computational expense of many numerical methods such as FEM.

As a byproduct of the dissolution process, the coupled cathodic reaction (ORR/HER) will cause the pH in the cathode to rise and cause for precipitation of metal species or constituents in the solution [40]. Typically, models considering brine evolution only account for precipitation from anodic species. Notably, Yin et al. explored the effects of metal ions from dissolution precipitating in the brine on the corrosion of aluminum alloys leading to a decrease in the overall corrosion rate which can stifle the growth of localized corrosion sites [38]. Further work showed steric hindrance leads to reduced current densities and oxygen flux to the surface [39]. Another recent model of interest modeled protection mechanisms of various coatings while accounting for changing cathodic conditions [41]. Additionally, models are also normally restricted to dilute chloride systems [39,42–45] which are only representative of high RH atmospheric conditions [46] and may not be realistic for many atmospheric scenarios of interest as will be described in subsequent section. Furthermore, the bulk of the models in literature focus on the precipitation of metal hydroxides from dissolution and do not consider precipitation of solution species. Finally, most models do not consider ORR to be a limiting reaction or consider atmospheric scenarios.

Alloying effects – In general, the composition and microstructure of an alloy will influence both pitting initiation and propagation. One class of alloys, namely austenitic stainless steels (AuSS), is used widely because of their general corrosion resistance due to the formation of a passive oxide on the surface of the alloy. AuSS are an iron- (Fe) based, passive alloy, with typical additions of nickel (Ni), chromium (Cr) and molybdenum (Mo). Passivity is described as the reduction of a metal due to the reaction of the metal with its environment so as to form a protective film on the metal surface [47]. Specifically in AuSS, Cr is utilized as it forms a Cr_2O_3 oxide which has a lower solubility and higher stability causing a reduction in the passive current density [48,49] and extends the region of passivity [3,49]. Nickel has been thought to stabilize austenitic phases and moderately improve corrosion resistance when added to Fe-Cr alloys [50]. Another common addition to iron-based alloys is Mo and is typically included in SS316 alloys. Mo has been shown to hinder the breakdown of the passive film and slow down the growth of pitting corrosion [49]. Despite the benefits of these alloying elements, the mechanisms for incorporation into a passive film, breakdown, and repassivation are not well understood in literature and are highly transient process [3,47,51].

It is generally accepted that increasing chloride content serves to decrease the stability of the native oxide on a SS surface [1,3,47,49]. When the passive oxide breaks down, corrosion is severely localized and can result in crevice, pitting, and stress corrosion cracking (SCC). Canisters used in SNF applications are commonly stored in welded AuSS canisters [52]. A common SS is the 304 grade and a majority of the composition contains a mixture of Fe-Cr-Ni. Due to the fact that SS304L does not have the addition of Mo, it is typically thought to be more susceptible to localized corrosion damage [53,54] and will be the primary focus of this study.

Overall, the autocatalytic nature of pitting corrosion can be described by critical parameters ($(i \cdot x)_{crit}$ and E_{rp}) and must be supported by a corresponding cathodic current creating an internal or external galvanic couple. Pitting corrosion has been modeled by various methods; however, generally lack a connection to the critical parameters describing the stability. Finally, while many alloying elements have been shown to have an impact on the initiation and propagation of localized corrosion, the stable propagation (described by critical parameters) in marine environments is lacking in literature for austenitic SS alloys and will serve as a foundation for this research.

1.2.2. Characteristics of marine atmospheric solutions

In near-marine settings, chloride-rich sea-salts are likely present on the surface of an exposed alloy surface. Through wave action or evaporation and precipitation, the amount of deposited salt (denoted as the loading density, LD, in g/m^2) on the surface can change over time. At a sufficiently high relative humidity (RH), the salts will deliquesce (absorb water from the atmosphere) to form brine on the storage container surface. Once a brine is present on an alloy, corrosion can begin [55]. However, during regular atmospheric conditions, the brine volume, composition, concentration, and other properties evolve, as deposited salt loads increase and RH on the surface change [46]. As the deliquesced brine on the surface changes, so does the "corrosivity" of the brine and can influence the overall corrosion damage and lifetime of an exposed alloy.

One of the most important factors in determining the brine composition is the RH on the surface of the alloy and is a function of ambient RH, ambient temperature, and surface temperature. Under equilibrium conditions, the surface RH is equal to the activity of water based on the brine composition. As the RH decreases, the concentration of chloride species in solution increases because the lower RH represents lower activities of water in the gas phase, and at equilibrium, the activity of water in the liquid phase must match it. To achieve this equilibrium, some of the water evaporates. As such, the surface RH dictates the brine concentration given a certain composition.

Bryan and Schindelholz showed the controlling nature of the RH by computationally exploring the composition of an ASTM sea-salt brine [56] and is presented in Figure 5. Starting out at high RH, the solution is mainly NaCl, close to 0.6 molal. As the RH decreases (the solution evaporates) the salt concentration increases, until halite (NaCl) precipitates at a concentration equivalent to about 73 % RH. Upon further evaporation, the solution becomes dominant in Mg^{2+} with equilibrium concentrations (C_{eq}) close to 6 molal and 10 molal in Cl^- at a RH of ~ 36 % [46]. At this point the brine is almost entirely $MgCl_2$. As the brine dries out, it is important to note that salts are precipitated, and salts, or a mixture of salts and brine, may be deposited on the alloy surface. If the RH rises over time, as would occur in a diurnal cycle, the salts re-dissolve and the composition of the deliquescent brine follows the path of evaporation in reverse order [46]. It is important to note that Figure 5 represents an ASTM sea-water solution. In reality, the composition will vary by physical location, whether it is inland or coastal [57]. Thus, not only will the concentration of the chloride in solution change with RH, but the composition will also vary widely and will impact various corrosion processes.

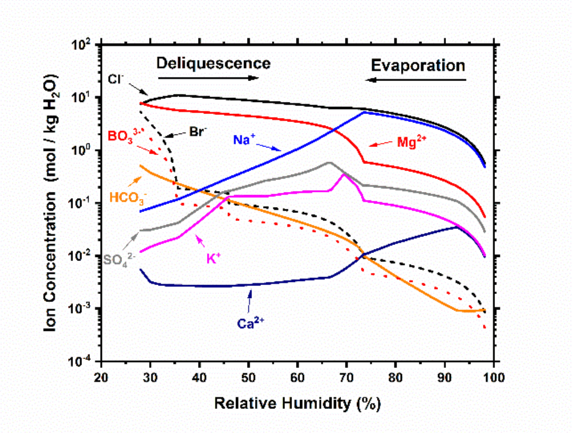

Figure 5: Ion concentration as a function of relative humidity for evaporated ASTM seawater solutions [56] *at 25 ˚C. Figure adapted from* [46].

Another important characteristic about brines that has long been identified [58] to influence potential corrosion in atmospheric condition is the water layer (*WL*) thickness. The *WL* thickness is dependent on C_{eq} which indicates that RH controls the *WL* thickness. In combination with *LD*, the *WL* can be determined given the surface RH and it has been shown that the *WL* thickness can severely impact the corrosion rate [24,28,29].

Generally, corrosion is thought to have an inverse dependence on *WL* thickness. That is, decreasing the *WL* thickness increases the corrosion rate. More specifically, Tomashov initially recognized a corrosion rate dependence with *WL* thickness and qualitatively described four different reaction control mechanisms. Under bulk, full immersion conditions, a plateau in corrosion rate is seen and a constant diffusion layer is achieved (Figure 6). Decreasing the *WL* causes an increased corrosion rate which is due to more rapid diffusion of oxygen across the thinner *WL*. Further decreasing the *WL* thickness reduced dissolution due to anodic control (owing to lower corrosion product solubility in a smaller solution volume). Finally, once a continuous film is lacking, the final regime is reached and is characterized by a very low corrosion rate of dry chemical oxidation [58]. While useful conceptually, the outline presented by Tomashov lacked a demonstrated quantitative description between electrochemical kinetics and the film thickness.

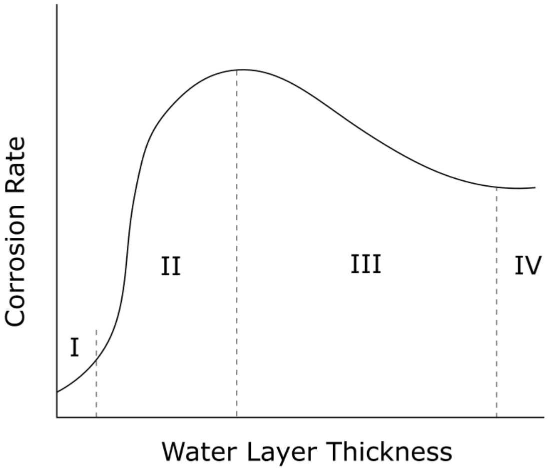

Figure 6: Qualitative representation of the corrosion rate with water layer thickness. This figure is adapted from [58]

Although the general relationship of corrosion rate with *WL* thickness is accepted, there is typically an upper limit to the *WL* thickness effect and it delineates the regime between full immersion and thin film corrosion (boundary between region three and four in Figure 6). This boundary is called the natural convection boundary thickness (δ_{nc}) and is caused by spatially inhomogeneous density due to cathodic reduction reaction byproducts as presented in Figure 7. In a bulk solution, this convection prevents a concentration gradient from extending to infinity and will provide for a limiting drive force for corrosion processes. Below δ_{nc}, an increase in the concentration gradient of reducing species will cause for an increase in the corrosion rate [59]. Thus, the convection creating δ_{nc} serves as a boundary between thin film corrosion and bulk corrosion scenarios. It is interesting to note atmospheric *WL* can either be considered thin film or full immersion depending on the *LD* present on the surface of the alloy. For 0.6 M NaCl solutions, a common atmospheric simulant, δ_{nc} has been determined to be roughly 800 µm [60]. While this is the case for dilute NaCl, representative of high RH environments, δ_{nc} has not been explored in other chloride containing solutions, and the dependence of this value on chloride concentration (*i.e.*, RH) and temperature has not been investigated.

As the RH is such a controlling factor for brine properties, it is of interest to investigate what may actually occur in service conditions. An example of the yearly variation in temperature, ambient humidity, and RH for a near marine location is presented in Figure 8 and shows the wide variability in environmental parameters both diurnally and seasonally. The fluctuations in RH ranges from roughly 100 to 10 % indicating that over one year, an exposed sample will experience a wide range of surface RH and therefore brine compositions and concentrations.

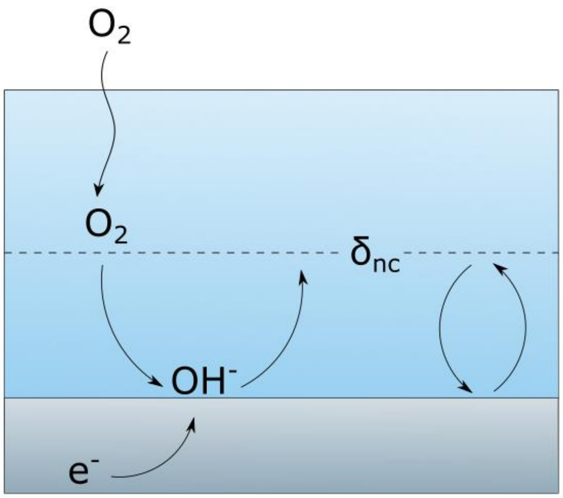

Figure 7: Schematic of the natural convection boundary layer thickness (δ_{nc}) when the oxygen reduction reaction is dominant.

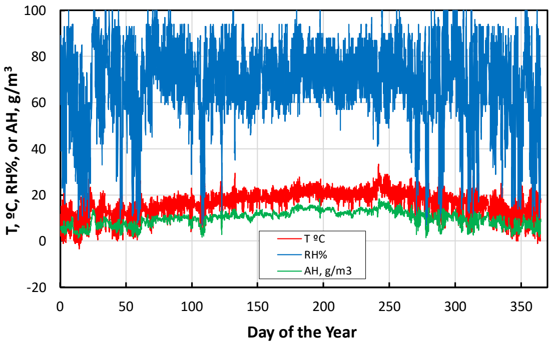

Figure 8: Fluctuations in ambient temperature, relative humidity, and ambient humidity for a near marine site over a one year period [52].

Another influencing factor on localized corrosion and brine properties is the temperature in which an alloy is exposed. As such, the surface temperature plays an important role in determining the surface RH and resultant brine chemistry. One such specific example of an alloy exposed at elevated surface temperatures relative to the ambient temperatures is the storage of SNF in canisters made of SS304L. The material inside of these canisters is physically hot, and during the interim storage period, the canisters will cool, changing the surface RH over time [52]. Additionally, spatial variations of temperature over the surface of the canisters will also differ widely depending on the age and position of the SNF inside the canister. Therefore, irrespective of the ambient conditions, the surface conditions will vary on the canister due to thermal gradients. An example of the calculated surface RH overtime for a canister surface is presented in Figure 9. Examining, Figure 9, each of the lines represent a different location on a canister surface and shows the potential variation an alloy can experience in service. Along with the spatial variation, it is interesting to note that the surface RH will not reach the deliquescence RH (DRH) for NaCl for the 300 years that this simulation covers indicating that the concentrated brine on the surface will be $MgCl_2$ dominant (Figure 5) during these time periods.

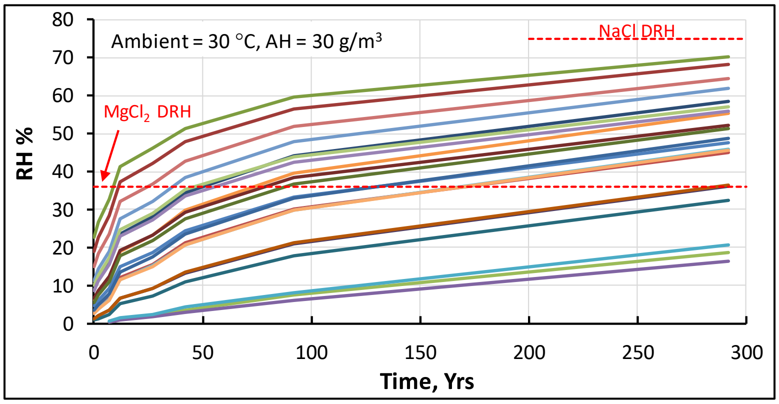

Figure 9: Surface relative humidity on a canister surface at various locations at an ambient humidity of 30 g/m^2 and an ambient temperature of 30 ˚C. Values are compared to the deliquescence relative humidities for $MgCl_2$ and NaCl [52].

Overall, atmospheric environments are characterized by changing electrolyte compositions, orders of magnitude of difference in concentration, and widely different *WL* thicknesses; all of which are governed by the physical location (salt type), temperature, and RH at the surface of exposed alloy. In the event one is considering the elevated temperatures on the surface of an SNF canister, the temperature evolution on the canister will be such that a concentrated chloride brine, containing mainly $MgCl_2$, will be primarily present on the surface. Anodic and cathodic mechanisms have yet to be explored in such environments and therefore have not been incorporated into models highlighting an important need in the community.

1.2.3. *Stress corrosion cracking*

In the presence of a stress, localized corrosion features, such as pits, can serve as a stress concentrator and facilitate the initiation of stress corrosion cracking (SCC). As shown visually in Figure 10, the distribution of stress is concentrated close to the pitting surface, and, for this geometry, is highest near the bottom of the pit [61].

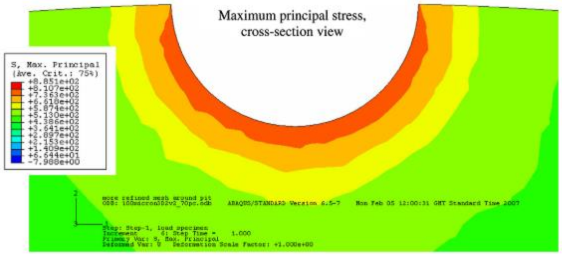

Figure 10: Maximum principal stress distribution for a 100 µm hemispherical pit loaded to 70 % of σ_{ys} [61].

While pits are known to concentrate stresses, an exact metric for the transition to pitting to cracking is elusive. An interpretation of this problem was proposed by Kondo, in which a stress intensity (K) was calculated from a corrosion pit and the transition to a crack happened at a critical value of K. Although correlations between this metric and pit-to-crack transitions were presented in the original paper [62], the overall criteria fails to capture the true physics of the problem due to the fact that microscopic phenomena at the crack tip (K) is applied to a macroscopic feature (pit). Additionally, recent work on crack initiation from corrosion features on aluminum alloys has shown that no single macro- or microscopic feature of the pit initiated a crack [63,64]. Finally, SS alloys are often exposed to high stress in service, such as those of SNF storage [52]. Given a corrosion defect is on the surface of the canister, it is highly probably that SCC will initiate. Therefore, electrochemical conditions in a stable SCC will be the main focus.

Electrochemical conditions in SCC – Chemical and electrochemical properties down the crack are not representative of bulk conditions, and the solutions present are similar to those of pits [65].

Elevated metal cation concentrations have been measured in Al alloys crack tips (~3 M Al^{3+} [66] which is near saturation of $AlCl_3$ at room temperature) which further undergo hydrolysis (Equation 1) decreasing the pH (Figure 11(a)). Due to the occluded environment of the crack tip, acidic stable pH's have been measured in crack tips and range from 1-3.9 under open circuit conditions [66–71]. Furthermore, it has been shown that crack tip conditions are independent of the bulk solution pH [68]. Polarizations away from E_{OCP} also influence crack tip chemistry. Anodic polarization of the bulk surface tend to increase the crack tip anodic dissolution, decreasing the pH and increasing crack growth rate [65,70] whereas cathodic polarizations on the bulk surface increase the cathodic reduction in the crack tip decrease the anodic dissolution rates thus increases crack tip pH [65].

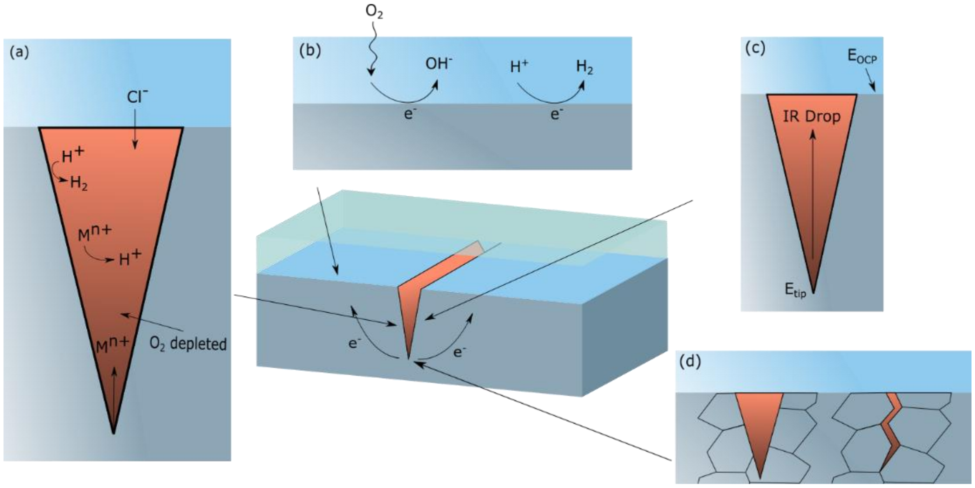

Figure 11: Depiction of various phenomena related to stress corrosion cracking (SCC): (a) crack tip reactions, (b) cathodic reduction reactions occurring on the surface of the alloy, (c) IR drop seen between the crack tip and the surface of the alloy, and (d) transgranular (left) and intergranular (right) modes of SCC.

Similarly to pitting corrosion, crack tips quickly become anoxic as a result of initial ORR reactions and limited transport of oxygen [65,72–74]. As a result, anode and cathode separation is present and, combined with IR drop, the crack tip potential (E_{tip}) is often less noble than the bulk surface [65] as depicted in Figure 11(c). A visualization of the crack tip potential as a function of distance from the crack tip can be seen in work done by Cooper and Kelly [70]. Experimental measurements show a potential gradient of ~1 V/cm as a distance from the crack tip is increased indicating that a majority of the potential drop is local to the crack tip [70]. Turnbull et al. have shown E_{tip} is relatively unpolarizable however does create differences in the overall potential drop experienced by the crack tip. Along with this, E_{tip} is relatively independent of bulk oxygen concentration [75].

As high metal cation concentrations exist at the crack tip due to anodic dissolution, electroneutrality must be maintained and is accomplished through anion migration (generally Cl^-) to the crack tip. Anions will migrate into the crack tip until balanced by transport out of the crack or most commonly until limited by the solubility of species in the crack tip [74]. In comparison to corrosion fatigue (CF), ion migration in SCC can be particularly potent as static loads do not impose advection and convection on the crack tip solution [65]. Turnbull pointed out that no significant effects will occur for deep cracks even in CF environments. However, in fracture mechanics specimens, the openly accessible crack sides of the specimen allow for through thickness ion transport [74]. Overall, the aggressive conditions present in the crack tip highly influence the crack growth rates and all aspects of the crack tip reactions must be accounted for when modeling SCC [65,74].

Modeling SCC systems – Many models describing SCC phenomena date back to the 1980s with a focus on boiling water reactors (BWR). Of particular note, Ford and coworkers [76], Macdonald and coworkers [77,78], and Turnbull and coworkers [74,79,80] have created models to describe intergranular stress corrosion cracking (IGSCC) for sensitized SS304L under BWR conditions. These models have been applied to a multitude of environments, however one note of particular interest from MacDonald his declaration of the need to uphold the natural law of charge neutrality. It is stated that the internal and external environments must be strongly coupled, and this coupling is most likely responsible for the influence of solution conductivity on crack velocity [77]. This point was furthered by Turnbull who noted the importance of all cathodic reactions that must occur on both the internal and external surfaces to consume the current required for cracking [81]. Although many of the electrochemical features of SCC were understood through these various models, the applicability of these models to laboratory or atmospheric conditions is limited for various reasons including: (i) the geometry of the crack is 2-D in most cases and ignores the sides of typical laboratory specimens, (ii) the low conductivity of the solution in many BWR reactor solutions is not applicable to many solutions experienced in atmospheric environments, (iii) full immersion is generally considered in which there is a constant external current density, (iv) models typically don’t have concentration boundary conditions, and (v) the influence of internal and external cathodic reduction reactions on chemical and electrochemical phenomena are not considered. Additionally, Turnbull points out that fracture mechanics specimens should be sealed along the sides in order for the models to be applicable to materials highlighting the importance of modeling the correct geometry [74].

Recent advances in various models have investigated higher chloride concentrations (5 M NaCl) [82,83] and have explored the influence of *WL* thickness [84]; however, they have not been explored together. Additionally, based on the aforementioned assumptions in the models, the application to the atmospheric scenarios of interest (Section 1.2.2) are severely limited and warrant investigation. Therefore, the creation of a new model that accounts for these important limitation is necessary.

1.3. Critical research questions

The overarching research questions from this dissertation work are: (i) what mechanisms control how external (solution composition, solution concentration, geometry, temperature, *WL* thickness) and internal (geometry) factors affect electrochemical and localized corrosion (pitting and stress corrosion)? and (ii) to what extent can we predict damage from localized corrosion and stress corrosion cracking and what are the governing factors in these predictions?

1.4. Scope of dissertation

1.4.1. Objectives

The main goal of this dissertation is to understand atmospheric, environmental influences across a wide range of RH, temperature, and composition combinations on localized corrosion and SCC. Such an objective necessitates that the field of survey be restricted to some extent in order to preserve focus. In this regard, the study employs as its candidate system SS304L in most cases, a common material used in the storage of SNF. The goal is fulfilled by the following tasks:

- Develop a robust understanding of reaction mechanisms as a function of environmental parameters

- Utilize and enhance analytical predictive capabilities to understand governing factors and more accurately predict pitting corrosion damage
- Utilize FEM modeling approach, electrochemical techniques, and pertinent instrumental characterization tools to systematically investigate the effect of electrolyte layer thickness, solution chemistry, and geometry on localized corrosion and SCC damage distributions

1.4.2. Topics outside the scope of dissertation

Literature has focused on passive film breakdown and initiation as well as the metastability of pitting corrosion [1,3]. While initiation is a very important phenomena, conditions for initiation of localized corrosion are stochastic and highly dependent upon the alloy surface [3] and it has been shown that even in the same samples exposed to the same environment, that the initiation time for corrosion will vary widely [1,3]. Second, metastability of pits has been explored and it has been hypothesized that pits transition to stable pits when they attain favorable, aggressive conditions for growth. However, determining the maximum extent of corrosion (i.e., maximum obtainable sizes) is more useful in designing strategies for pit repassivation in industrially-relevant cases where prior pit growth may take place. Finally, in more aggressive environments (which are likely in the environments of interest, Figure 5), it has recently been hypothesized that pit growth is the rate controlling step [85] and therefore is of greater interest to study.

Both pitting corrosion and SCC are explored during this dissertation. It has been shown that pits can lead to the formation of cracks [61], and has been a recent topic of exploration for aluminum alloys [63,64]. No macro or micro feature on the surface of a pit lead to the formation of a crack in the testing and it has been suggested that it could be a combination of these features and potentially related to nature of the grain size [63,64]. Despite significant efforts in determining pit-to-crack transitions, many relationships related to the process are unknown and given high stresses and a large enough corrosion defect, it is likely a crack will be initiated. Studying crack tip electrochemical conditions can help understand critical, environment conditions that will influence the resultant crack growth and potential stifling after initiation. Such a modeling effort not only has implications for field relevant conditions but can also help explain trends in experimental efforts.

The focus of this dissertation is on AuSS, specifically SS304L. The use of SS304L as a candidate alloy is justified by its use in SNF canisters. With no permanent disposal pathway present, it is possible the canisters could be exposed to atmospheric environments for much longer time periods (100's to 1000's of years) than originally anticipated (20 – 40 years). Given the large range of materials (both in terms of composition and surface finish), time frames of exposure, and surface area exposed, pitting will likely occur at some point in the materials lifetime. Additionally, high stresses from the formation of the canisters are present and it is likely that interaction with corrosion defects can initiate a SCC. Therefore, this dissertation is focused on determining the extent of pitting corrosion and SCC of SS304L and how that can be impacted by the exposure environment to identify potential areas of concern as a function of environment.

Nonetheless, much of what is presented can be extended, either directly or indirectly, to address these aspects excluded from the dissertation. Many of the developed models and techniques can be used in other solutions or other alloy systems in order to determine degradation in various environments.

1.5. Organization of dissertation

The background and preceding discussion have identified key areas for investigation which will be explored in this dissertation. Key gaps in knowledge related to environmental impacts on pitting corrosion and SCC have been identified. These knowledge gaps include a common need to understand the controlling role of anodic and cathodic kinetics in both processes. In order to resolve the key dissertation questions, the work is divided into 7 technical chapters. Following these chapters is additional acknowledgements, references, and various appendices incorporating all publications during this work. The structure of the dissertation is such that previous and current papers will be compared and contrasted in the different chapters. Therefore, the chapters are currently not stand-alone papers.

The first chapter provided a literature review which helped identify key areas of research necessary for investigation. The second chapter provides cathodic kinetics as a function of environmental parameters which were identified in Chapter 1. Chapter 2 is a combination of five publications and incorporates main conclusions from each paper while placing atmospheric cathodic reduction reaction mechanisms into perspective.

In the third chapter, the calculation and measurement of WL thickness and solution properties are identified in the wide range of environmental parameters possible in an exposed setting. In addition to the environmental setting, a sensor was created in order to measure WL thicknesses in salt spray environments allowing for the identification of differences between accelerated and environmental exposures. Chapter 4 identifies key anodic parameters, namely $(i \cdot x)_{sf}$ and E_{rp}, in similar environments to Chapter 2. Trends are identified in the kay parameters and reasons for these trends are postulated.

Chapter 5 combines data from Chapters 2-4 in order to make maximum pit size predictions and FEM predictions for a galvanic couple as a function of environmental parameters. This section compares and contrasts the various trends environmental parameters have on the cathodic kinetics. Additionally, governing factors for maximum pit size predictions are identified and separated into broad categories. Finally, validation of the maximum pit size predictions are presented.

SCC electrochemical modeling is presented in Chapter 6. The combined experimental and modeling work creates a model to explore various phenomena related to SCC experiments and the influence of atmospheric variables. The results are compared to existing SCC models and put into perspective in terms of testing as well as exposure results.

Chapter 7 provides a summary of all work presented in this thesis and recommends future works. Following the seventh chapter are references and an appendix encompassing all of the publications accepted or pending acceptance during this dissertation.

2. Evaluation of cathodic kinetics as a function of environment

2.1. Summary

Cathodic kinetics and reaction mechanisms are determined for a wide range of concentrations and temperatures for NaCl, NaOH and $MgCl_2$ brines using a rotating disk electrode. It was determined that for all NaCl solutions and temperatures explored, a near four electron transfer ORR is dominant. In NaOH solutions above a calculated pH of 16.5, ORR is the dominant reaction but a reaction mechanism including a below two electron transfer due to the formation of a superoxide ion is present. At a calculated pH of 16.5, the cathodic reduction reaction is influenced by the dissolution of the native oxide. Finally, in $MgCl_2$ solutions, the hydrogen evolution reaction was the dominant cathodic reduction reaction due to ORR suppression and precipitate formation. The precipitates were directly observed via *in-situ* spectroelectrochemistry. The implications of the cathodic reduction mechanisms will further be discussed in terms of atmospheric corrosion.

The work presented in this chapter has been reported in the following publications:

- **R. M. Katona**, J. C. Carpenter, A. W. Knight, R. S. Marshall, B. L. Nation, C. R. Bryan, E. J. Schindelholz, R. F. Schaller, and R. G. Kelly, *Natural convection boundary layer thickness at elevated chloride concentrations and temperatures and the effects on a galvanic couple*. Journal of the Electrochemistry Society. 2021. Editors Choice. https://doi.org/10.1149/1945-7111/abeb29
- **R. M. Katona**, J. Carpenter, E. J. Schindelholz, R. G. Kelly, R. F. Schaller. *Cathodic kinetics on stainless steel in high pH environments*. Accepted in the Journal of the Electrochemical Society. 2021. https://doi.org/10.1149/1945-7111/ac1318
- **R.M. Katona**, J.C. Carpenter, A.W. Knight, C.R. Bryan, R.F. Schaller, R.G. Kelly, E.J. Schindelholz, *Importance of the hydrogen evolution reaction in magnesium chloride solutions on stainless steel,* Corros. Sci. 177 (2020) 108935. https://doi.org/10.1016/j.corsci.2020.108935.
- **R.M. Katona**, R.G. Kelly, C.R. Bryan, R.F. Schaller, A.W. Knight, *Use of in situ Raman spectroelectrochemical technique to explore atmospheric corrosion in marine-relevant environments,* Electrochem. Commun. 118 (2020) 106768. https://doi.org/10.1016/j.elecom.2020.106768.

- C. L. Alexander, C. Liu, A. Alshanoon, **R. M. Katona**, R. G. Kelly, J. Carpenter, C. Bryan, and E. Schindelholz. *Oxygen Reduction on Stainless Steel in Concentrated Chloride Media*. J. Electrochem. Soc. 2018 165: 869-877. https://doi.org/10.1149/2.0181813jes

2.2. Introduction

Reduction reaction processes on SS and platinum (Pt) alloys are important across a broad range of science and technology areas [86–88]. The reduction mechanism will influence cathodic current density at a given potential further influencing a corrosion couple and the overall current and potential damage state on the surface [25]. On the other hand, passivation of many metals and alloys requires a cathodic process, i.e., oxygen reduction, to reach the passive state and ensure repassivation [25]. Finally, understanding the cathodic reduction reactions and resulting current density has direct influences on predicting localized corrosion [24] or the behavior of galvanic couples [60]. Thus, understanding the operating cathodic reduction mechanisms for SS304L in the many environments that are possible in atmospheric conditions is of importance.

Typically, alloys exposed to atmospheric conditions are assumed to undergo ORR. While this may be the case, there are many material and electrolyte properties that influence the mechanisms and kinetics of an alloy [25]. Most commonly, ORR follows the “direct” four electron transfer as displayed in Equation 2 and 3 for acidic and basic brines respectively.

$$O_2 + 2H^+ + 4e^- \rightarrow H_2O \qquad 2$$

$$O_2 + 2H^+ + 4e^- \rightarrow 4OH^- \qquad 3$$

In addition to the direct transfer, there are multiple various rate limiting steps that cause for a decrease in the number of electrons transferred in ORR. In an acidic solution, a rate limiting step exists such that ORR produces a peroxide (H_2O_2) intermediate via

$$O_2 + 2H^+ + 2e^- \rightarrow H_2O_2 \qquad 4$$

which then gets further reduced to

$$H_2O_2 + 2H^+ + 2e^- \rightarrow 2H_2O \qquad 5$$

In basic media,

$$O_2 + 2H_2O + 2e^- \rightarrow HO_2^- + OH^- \qquad 6$$

$$HO_2^- + H_2O + 2e^- \rightarrow 3OH^- \qquad 7$$

In this case, Equations 4 and 6 are the rate limiting step and a two-electron transfer for ORR is observed. Another series pathway exists for ORR which involves oxygen being reduced to a superoxide anion (O_2^-, Equation 8). In acidic media, O_2^- is further reduced to hydrogen peroxide (H_2O_2) and then to water (Equation 9 and 10).

$$O_2 + e^- \leftrightarrow O_2^- \qquad 8$$

$$O_2^- + 2H^+ + e^- \leftrightarrow H_2O_2 \qquad 9$$

$$H_2O_2 + 2H^+ + 2e^- \leftrightarrow 2H_2O \qquad 10$$

In basic media, O_2^- is reduced to a hydrogen peroxide anion as the intermediate and produces a hydroxyl ion as the final product (Equation 11 and 12).

$$O_2^- + H_2O + e^- \leftrightarrow HO_2^- + OH^- \qquad 11$$

$$HO_2^- + H_2O + 2e^- \leftrightarrow 3OH^- \qquad 12$$

Another potential reduction reaction is HER. In acidic environments HER is given by

$$2H^+ + 2e^- \rightarrow H_2 \qquad 13$$

while in basic environments the HER reaction is given by

$$2H_2O + 2e^- \rightarrow H_2 + 2OH^- \qquad 14$$

As there are many different potential reaction mechanisms (Equations 2 – 14) and the electrolyte/alloy interactions influence the cathodic reduction mechanisms [25], many reaction mechanisms for electrolyte solutions present in atmospheric conditions have not been determined, especially at elevated chloride concentrations or temperatures. Understanding the number of electrons transferred and overall kinetics of ORR and will help determine the degree to which the anodic reaction is polarized as well as the total amount of current available to support dissolution.

There are multiple methods that can be used to determine reaction mechanisms including but not limited to: rotating disk electrodes (RDE) [60,88–93], rotating ring disk electrodes (RRDE) [94–96], cyclic voltammetry [86,93], ultramicroelectrodes [97,98], and electrochemical noise [25]. One of the most popular and readily accessible methods is using the RDE to measure i_{lim} as a function of rotation rate which will in turn give the number of electrons transferred. i_{lim} can be calculated by Fick's first law and assuming one-dimensional diffusion via

$$i_{lim} = \frac{nFD(C_{bulk} - C_{surface})}{\delta} \qquad 15$$

where n is the number of electrons transferred, F is Faraday's constant ($96485\ C/mol$), D is the diffusivity of the reacting species (cm^2/s), C_{bulk} and $C_{surface}$ (assumed to be zero when the reaction is diffusion limited) are the concentrations of the reacting species in the bulk solution and at the electrode surface respectively (mol/cm^3), and δ is the hydrodynamic boundary layer thickness (cm). When using an RDE, δ is the hydrodynamic boundary layer thickness and is given as a function of rotation speed (ω in $rad/\sec = \frac{2\pi}{60} * rpm$) through:

$$\delta = 1.61D^{1/3}\omega^{-1/2}\nu^{1/6} \qquad 16$$

where ν is the kinematic viscosity ($\nu = \eta/\rho$) [99]. Substituting Equation 2 into 1 yields the Levich equation [90,100]:

$$i_{lim} = 0.62nFD_{O_2}^{2/3}\nu^{-1/6}\,C_{O_2,bulk}\omega^{1/2} \qquad 17$$

Thus, by plotting i_{lim} vs. $\omega^{1/2}$ and with knowledge of D_{O_2}, ν, and C_{O_2}, the number of electrons transferred can be determined by the slope of the Levich plot and can help determine the cathodic reduction reaction occurring in the solution of interest. The Levich equation only applies at non-zero rotation rates, as at $\omega = 0$, i_{lim} would be predicted to be zero and the boundary layer thickness infinite.

Although it is important to determine the cathodic reduction reaction in solutions of interest, all of the cathodic reduction reactions that are likely in atmospheric conditions will cause a rise in the pH of the cathode due to the consumption of H^+ or the production of OH^- (Equations 2 – 12). Therefore, on top of fluctuations in solution composition with RH, at one given RH, active corrosion will cause a gradient of pH from the anode to the far field cathode. A pH rise of the cathode has been directly observed by Azmat et al. on zinc under marine solutions [101] and Schindelholz et al. on copper under NaCl electrolytes [40]. *Ex-situ* analysis of electrolyte pools after SS coupon exposures to atmospheric conditions are consistent with the formation of an alkaline electrolyte at cathodic sites due to the ORR reaction [102]. The production of hydroxyl ions from ORR will not only cause a rise in pH but also will cause electro-migration to maintain electroneutrality. As such, a chloride-poor, alkaline solution can be present in the cathode [102–105]. This effect becomes particularly important in atmospheric scenarios where finite electrolyte volumes are present. A schematic of this phenomenon for a droplet is presented in Figure 12. For NaCl solutions, a common component of seawater brines at elevated relative humidities [46], an NaOH-rich brine would be present near the edge of the cathode or in micro-droplets around the original cathode (droplet) [102,104,105] and could potentially change cathodic reduction behavior.

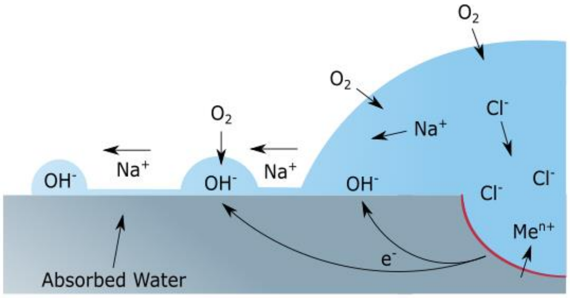

Figure 12: Schematic displaying the creation of a chloride-poor, alkaline solution in the cathode under a droplet. Presented diagram is adapted from [102–105].

In atmospheric conditions, a wide range of environmental conditions exist and can impact cathodic reduction reactions and predictions for atmospheric corrosion. Therefore, cathodic kinetics and the resultant reaction mechanisms as a function of environment (composition, concentration, temperature, *WL* thickness, and cathode evolution) were determined for SS304L and Pt. In order to determine the reaction mechanisms, solution properties (those present in Equation 17) were determined for each solution of interest.

2.3. Experimental

2.3.1. Determination of solution properties

The density (ρ), dissolved oxygen concentration (C_{O_2}), and viscosity (η) were measured for various brines listed in Table 2. Hydrometers were used to measure ρ. The hydrometers were calibrated for specific gravity ranges from 1.000 to 1.220, and 1.20 to 1.420 [106]. C_{O_2} measurements were taken using the Chesapeake Bay Institute modified Winkler iodometric titration method [107,108]. A further description is presented in Appendix A and B. A Brookfield AMETEK LDTV2T Viscometer with an ultra-low η adaptor was used to measure η was measured at 25°C.

2.3.2. Materials

High-speed RDEs with a diameter of 5 mm comprised of SS304L and 99.99% Pt were acquired from Pine Research Instrumentation, Inc. (USA). For experiments using deaerated solutions, an electrode with a surface diameter of 5.5 mm was used in order to form an airtight seal in the gas purge bearing assembly for the cell. Prior to each use, the electrodes were polished using a 1 μm Dialube Diamond Suspension®, then rinsed with ultrapure (18.2 MΩ-cm) water and dried with nitrogen (N_2).

2.3.3. Electrochemical tests

For RDE experiments, a three-electrode cell was used with the alloy specimen as the working electrode (WE) with an exposed area of 0.196 cm^2 (except in deaerated experiments where the electrode area was 0.238 cm^2). The reference electrode utilized in experimentation was either a saturated calomel reference electrode (SCE) or a silver/silver chloride reference electrode (Ag/AgCl). It is noted that $V_{Ag/AgCl} = V_{SCE} + 0.045$ V. A Pt-coated niobium mesh was used as a counter electrode. RDE samples were immersed in the solution of interest in a 150 mL jacketed cell and sparged with lab air to maintain a solution saturated in O_2. RDE samples were rotated using a Pine instruments MSR rotator with an accuracy of ± 1 % of the display reading. Rotation speeds ranged from 100 to 6000 rpm. A schematic of this is shown in Figure 13. The solution temperature was controlled to the desired temperature (± 1 °C) using a water circulator and thermostat. Typically, repetitions were conducted for 500 rpm. Quiescent polarizations were taken both with the RDE set-up without rotation or in a typical ~350 mL flat cell with a WE area of 1 cm^2.

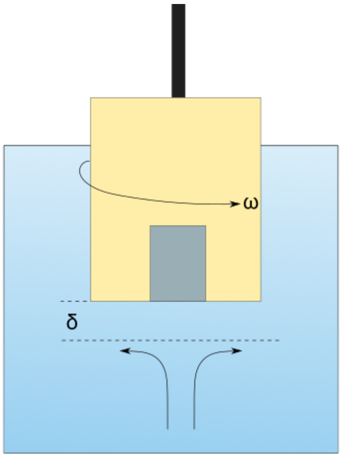

Figure 13: Schematic of rotating disk electrode. δ represents the hydrodynamic boundary layer and ω represents the rotation rate and are related through Equation 16.

Cathodic polarization measurements were performed on SS304L and Pt at scan rates of 0.167 and 1 mV/s respectively after 1 hour of OCP equilibration and stabilization. The scans were performed from OCP to -1.2 V_{SCE}. Potentiodynamic measurements were made various solutions (made from ACS Grade salts) and ultrapure (18.2 MΩ-cm) water and temperatures as presented in Table 2. It is noted that the highest concentration of NaOH (pH = 16.5) may not be present in atmospheric conditions; however, the cathodic reduction behavior is of scientific interest as the high pH may cause the oxide to become unstable.

Table 2: Solutions utilized in cathodic polarization experiments

Solution	**Concentration (M)**	**Temperature (˚C)**	**RH (%)**
$MgCl_2$	0.189	25	99
$MgCl_2$	1.28	25	92
$MgCl_2$	4.98	25, 35, 45	37
NaCl	0.6	25	98
NaCl	1	25, 35, 45	97
NaCl	3	25, 35, 45	88
NaCl	5.3	25, 35, 45	76
NaOH	0.6	25	98
NaOH	3.6	25	86
NaOH	5.4	25	77
NaOH	12.8	25	31
ASW	10.28 M Cl^-, 0.17 M Na^+, 5.31 M Mg^{2+}	25, 35	40

Additional experiments were performed with a CO_2 absorber obtaining a concentration of < 1 ppm of CO_2 in the sparged air. The solution was sparged with the CO_2-free air for eight hours and transferred to the reaction cell via pressure through a system always closed to ambient air. The reaction cell was continuously bubbled with the same CO_2-free air. De-aerated tests were conducted with N_2 sparging gas following the same procedure.

2.3.4. Determination of precipitates present in MgCl$_2$ solutions

A three-electrode flow through cell (Redox.me) was used with a SS304L coupon (ground to 1200 grit, exposed area of 3 cm^2) as the working electrode having a silver/silver chloride (Ag/AgCl) reference electrode, and Pt wire counter electrode. The flow cell solution volume was 4.5 mL with an electrolyte thickness of 2.25 mm above the sample. A schematic of the cell can be seen in Figure 14. Electrolyte solutions, 0.6 M NaCl and 0.189 M MgCl$_{2,}$ were pumped through the cell using a peristaltic pump allowing for variable flow rate (Q) from 0.5 to 50 mL/min (with a sensitivity of 0.25% of the rotation speed of the pump). The solutions were at ambient lab temperatures (22 ± 2˚C). Electrochemical procedures involved a 1-hour open circuit potential (OCP) period followed by a cathodic scan from OCP to -1.4 V$_{Ag/AgCl}$ at a scan rate of 0.167 mV/sec. The solution was flowing continuously through the cell during all experimentation. Polarization scans were also taken in standard flat cell configurations under quiescent conditions and a solution volume of roughly 350 mL, to prevent bulk solution oxygen depletion.

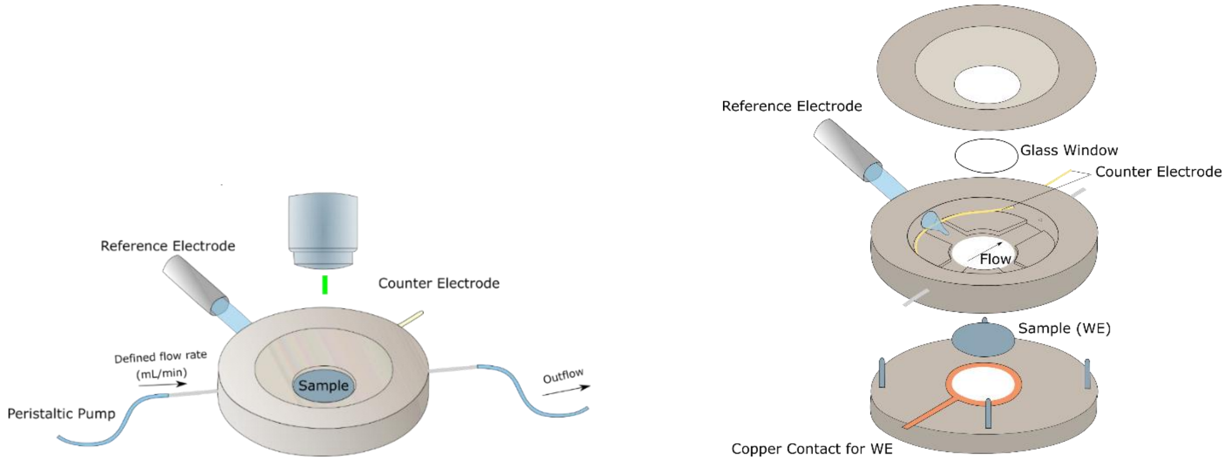

(a) **(b)**

Figure 14:Experimental set up for in-situ Raman analysis: (a) overall set-up and (b) inside configuration of flow cell.

In-situ Raman measurements were obtained using a confocal XploRA Plus Raman microscope (HORIBA Scientific) with a laser wavelength of 532 nm, power of 100 mW (spectra were collected using a 50% reduction in laser power), and a long-distance objective (magnification 10x and a numerical aperture of 0.25). Calibration was performed on a Si wafer. During *in-situ* testing, the laser was focused on the surface of the alloy with a beam diameter of 2.6 µm. Spectra were collected with 3 s exposures and averaged over 10 scans from 2800 to 4000 cm $^{-1}$. Scans were taken approximately every 5 min until the first detection of $Mg(OH)_2$, indicated by a peak at 3654 cm^{-1} [109,110]; then, the collection period increased to roughly every 2 min. The laser was turned off in between scans to reduce surface heating effects.

2.4. Results

First, measured or calculated solution properties are presented for most electrolytes in Table 2. Next, cathodic kinetics were determined in all solutions presented in Table 2 and will be presented starting first with high RH scenarios in which a sodium chloride electrolyte is dominant on the surface of the alloy. These were performed as a function of both concentration (ranging in RH from 98 to ~ 75 % RH) and temperature (25 – 45 ˚C). Third, NaOH cathodic kinetics are explored representing an evolving cathode in atmospheric scenarios at high relative humidities. Fourth, low RH atmospheric cathodic kinetics will be explored by utilizing magnesium chloride and seawater solutions at various temperatures. Finally, cathode evolution in magnesium chloride solutions is explored by the creation of a novel set-up to perform *in-situ* Raman as a function of boundary layer thickness.

2.4.1. Solution properties

Measured solution properties, C_{O_2}, ν, and ρ, are presented in Figure 15(a), (b), and (c) respectively, as a function of chloride concentration and temperature for NaCl and $MgCl_2$ electrolytes. Calculated D_{O_2} (OLI studio) are presented in Figure 15(d) as a function of chloride concentration and temperature for NaCl and $MgCl_2$ electrolytes. With increasing chloride concentration, C_{O_2} and D_{O_2} decrease while ν and ρ increase. With increasing temperature, C_{O_2}, ν, and ρ decrease while D_{O_2} increases.

Calculated solution properties (OLI Studio) are presented in Table 3 for NaOH Solutions at 25 ˚C. Similar to chloride containing solutions, with increasing NaOH concentration, C_{O_2} and D_{O_2} decrease while ν and ρ increase.

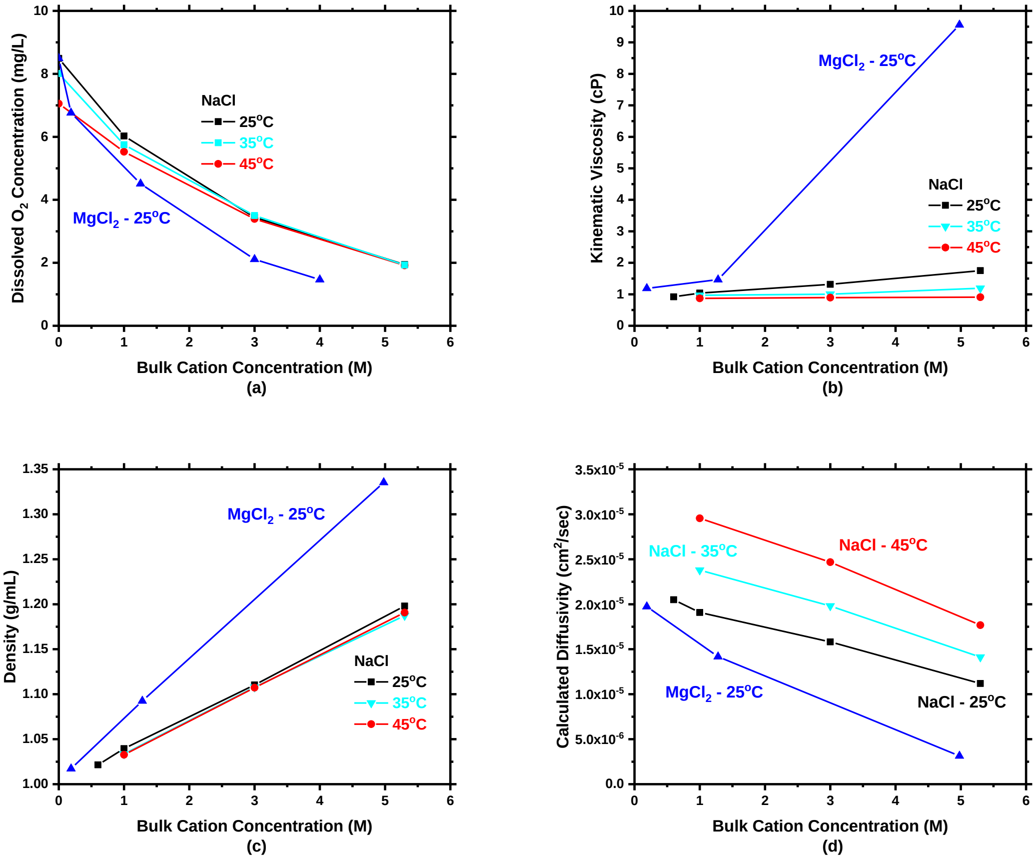

Figure 15: Experimentally measured (a) dissolved oxygen, (b) kinetic viscosity, and (c) density for NaCl and $MgCl_2$ solutions as a function of chloride concentration and temperature. (d) Calculated (modeled) oxygen diffusivity using OLI for NaCl and $MgCl_2$ solutions as a function of chloride concentration and temperature. It is noted that the lines present are not fits but are present to help the reader connect points.

Table 3: Solution properties for NaOH solutions of interest

NaOH Concentration (C_{NaOH})	pH	Saturated Oxygen Concentration (C_{O_2})	Oxygen Diffusivity (D_{O_2})	Density (ρ)	Viscosity (μ)
mol/L		mg/L	cm^2/s	g/L	cP
0.6	13.6	6.72	1.91×10^{-5}	1.023	1.01
3.6	14.5	2.27	1.00×10^{-5}	1.134	1.94
5.4	14.9	1.26	5.20×10^{-6}	1.188	3.08
12.8	16.5	0.26	2.14×10^{-7}	1.354	14.8

2.4.2. NaCl electrolytes

Representative RDE polarization scans for 1 and 5.3 M NaCl at 25 and 45 ˚C solutions are presented in Figure 16 for both Pt and SS304L as a function of rotation rate. Corresponding calculated δ using Equation 16 and solution properties in Figure 15 are given alongside the rotation rates. For Pt (Figure 16(a) and (b)), the polarization measurements are characterized by an activation-controlled region from OCP to approximately -0.1 V_{SCE}, followed by mass transfer (M-T) controlled ORR from -0.1 V_{SCE} to -0.8 V_{SCE} and finally HER below -0.8 V_{SCE}. The potential of the transition to M-T kinetics is dependent upon rotation rate. With increasing solution concentration, i_{lim} decreases whereas with increasing temperature, i_{lim} increases. Similar patterns are seen across the entire range of NaCl solutions that were explored in Table 2 and are presented in Appendix B [91].

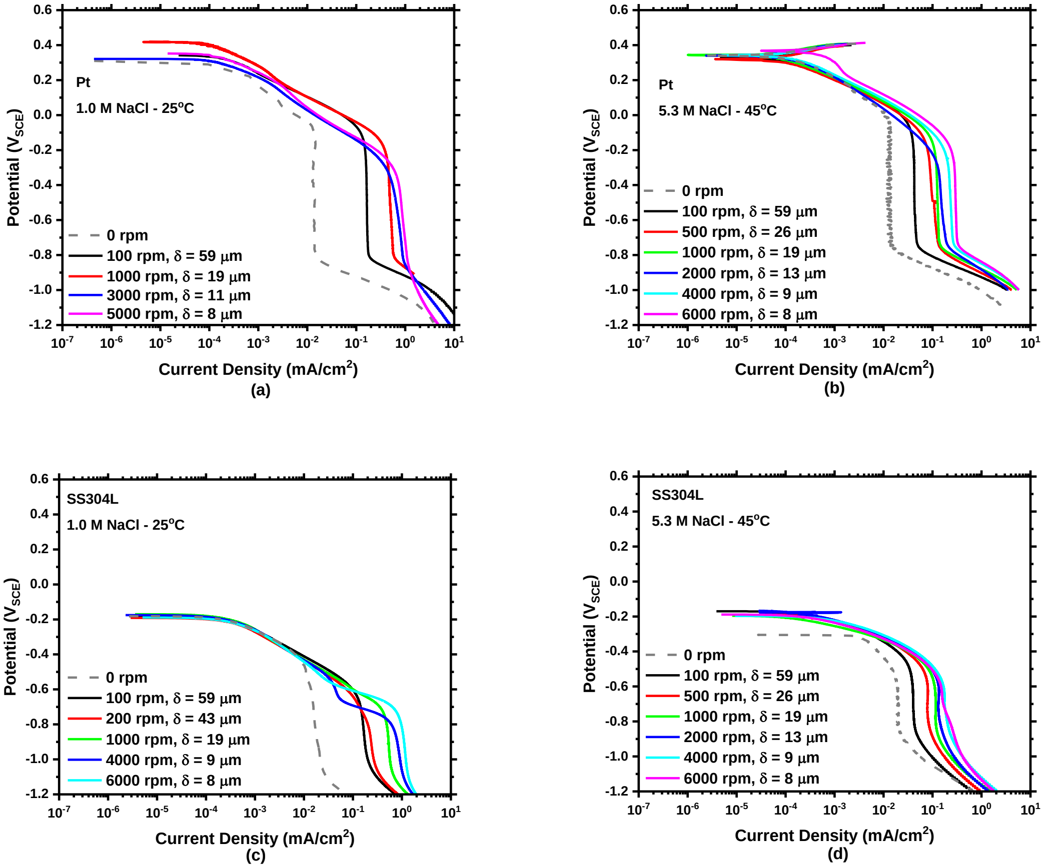

(a) (b) (c) (d)

Figure 16: Experimentally measured cathodic polarization scans for platinum ((a) and (b)) and SS304L ((c) and (d)) in 1 M NaCl at 25 ˚C ((a) and (c)) and 5.3 M NaCl at 45 ˚C ((b) and (d)).

Cathodic polarizations measured on SS304L are shown in (Figure 16(c) and (d)) for the same solution concentrations and temperatures as Pt. The polarization measurements are characterized by an ORR activation-controlled region from OCP to approximately -0.6 V_{SCE} followed by M-T controlled ORR from -0.8 V_{SCE} to -1 V_{SCE} and finally HER below -1 V_{SCE}. As with Pt, the transition to M-T kinetics is dependent upon rotation rate. It is noted that as δ decreases, there is an unusual transition behavior between the activation-controlled regime and the M-T controlled region in the potential range of -0.6 to -0.8 V_{SCE}. With smaller δ the transition becomes more pronounced. The same concentration and temperature trends that were present in Pt are present for SS304L and the entire range of NaCl solutions that were explored in Table 2 and are presented in Appendix B [91].

2.4.3. *NaOH electrolytes*

Cathodic polarization curves for Pt and SS304L in various concentrations of NaOH at 500 rpm are shown in Figure 17(a) and (b) respectively. For polarizations on Pt in NaOH solutions with pH values ≤ 14.9, an ORR activation-controlled region is present from OCP to -0.2 V_{SCE}; below that, the reduction becomes diffusion limited from -0.2 V_{SCE} to roughly -1.0 V_{SCE}. Below -1.0 V_{SCE} the hydrogen evolution reaction (HER) is dominant. For a pH of 16.5, a very small activation-controlled region is present from roughly -0.2 to -0.3 V_{SCE}, which transition to a semi-diffusion-limited region down to to -1.2 V_{SCE}. Below -1.2 V_{SCE}, HER is dominant. Although it may appear that diffusion-limited i_{lim} is present in a pH of 16.5, the current increases between -0.4 V_{SCE} and -1.1 V_{SCE} increases from 6.4×10^{-4} to 3.4×10^{-3} mA/cm^2.

For polarizations on SS304L in NaOH solutions with pH's ≤ 14.9, an ORR activation-controlled region is present from OCP to -0.9 V_{SCE} below which the reduction becomes diffusion limited from -0.9 V_{SCE} to roughly -1.2 V_{SCE}. Below -1.2 V_{SCE}, HER is dominant. For a pH of 16.5, a very small activation-controlled region is present from roughly -0.9 to -1 V_{SCE}, but no diffusion-limited i_{lim} is present. Below -1.2 V_{SCE}, HER is dominant. It is further noted that there is a drastic decrease in OCP (nearly 250 mV) at pH of 16.5, relative to pH's of 13.6, 14.5 and 14.9.

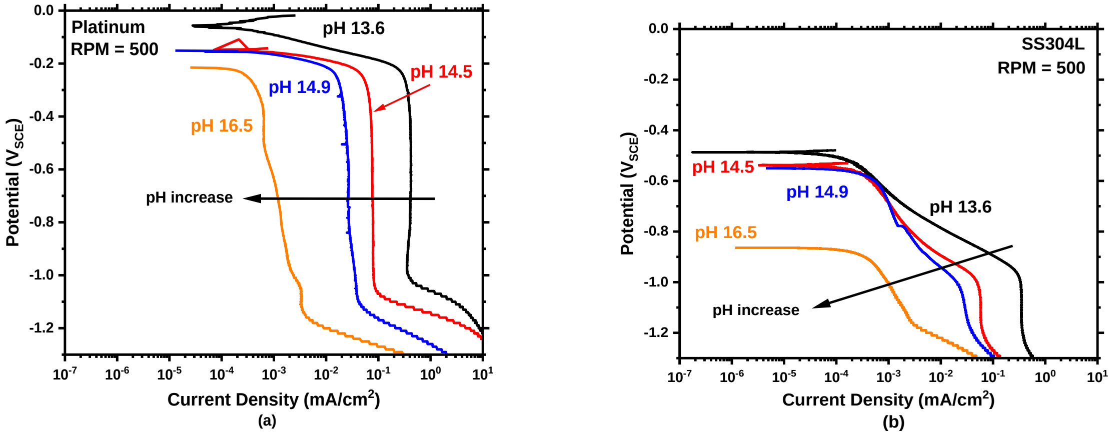

(a)

(b)

Figure 17: Representative cathodic polarization behavior of (a) Pt and (b) SS304L in aerated NaOH solutions at 25 ℃, 500 rpm, and various pH values. Duplicates of each polarizations were performed

Polarization scans were performed after polarization of the surface of SS304L at -1.5 V for one hour and are presented in Figure 18. The cathodic polarization scans for SS304L with a pH value of 13.6 shows little overall difference between the reduced and non-reduced scans with a slight increase in i_{lim} when reduced. In contrast, the change to polarization behavior after reducing the SS304L in pH 16.5 solutions is significant. After reduction of the surface, the OCP in pH 16.5 is near the HER reversible potential (-1.21 V$_{SCE}$) indicative of HER being the only cathodic reduction reaction on the surface.

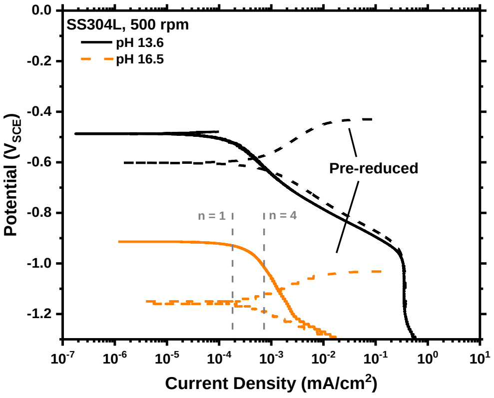

Figure 18:Comparison of cathodic polarization scans of SS304L RDE at 500 rpm in aerated NaOH solutions at 25 ℃. Solid curves represent polished surfaces from Figure 17(b), whereas dashed curves have been reduced for 1 hour at -1.5 VSCE, followed by a cathodic scan.

2.4.4. $MgCl_2$ electrolytes

Measured cathodic polarization scans on Pt in 0.189 and 4.98 M $MgCl_2$ solutions are presented in Figure 19(a) and (b) respectively. Corresponding δ are labeled alongside the rotation speeds. Theoretical i_{lim} for ORR for n = 2 (Equation 17) are indicated by vertical grey dashed lines corresponding to 100 rpm and 6000 rpm. The polarization measurements for Pt are characterized by an ORR activation-controlled region from OCP to approximately -0.1 V_{SCE} followed by mass transfer-controlled ORR from -0.1 V_{SCE} to -0.7 V_{SCE} and finally HER below -0.7 V_{SCE}. Overall, the experimentally measured i_{lim} for ORR matched, on average, within 15% of predicted behavior for rotation speeds above 100 rpm.

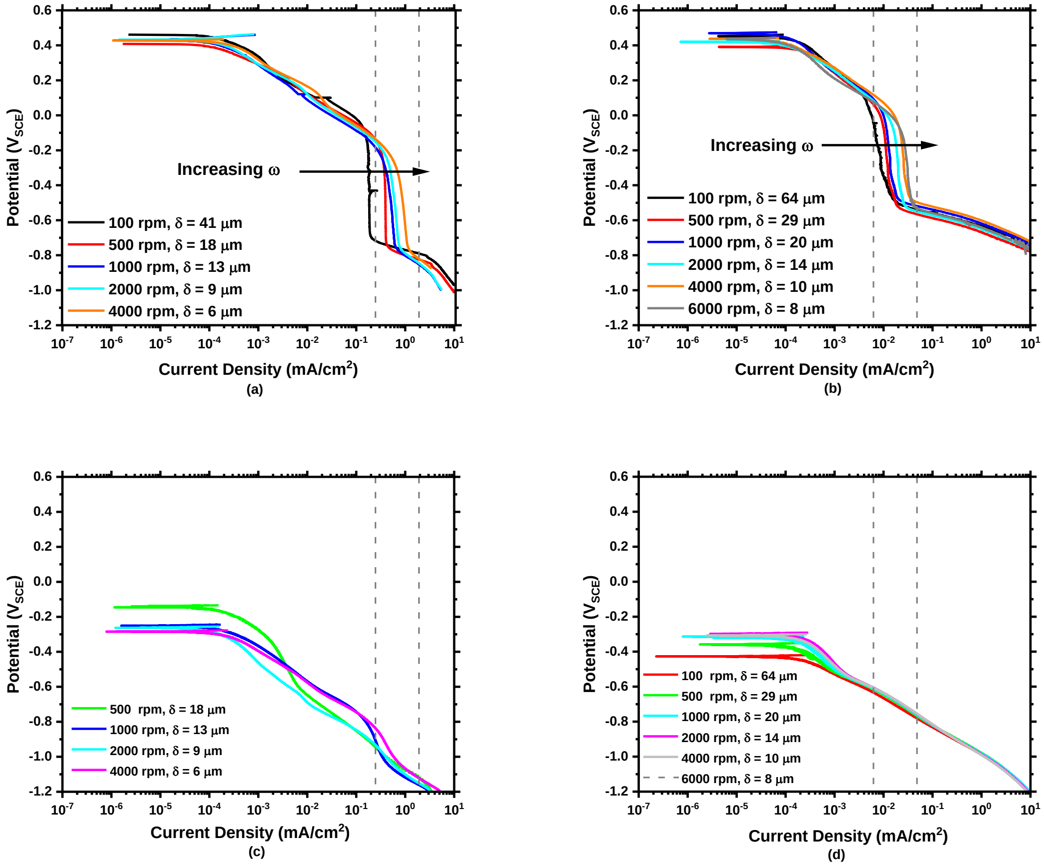

Figure 19: Cathodic polarization scans on platinum ((a) and (b)) and SS304L ((c) and (d)) in 0.189 M $MgCl_2$ ((a) and (c)) and 4.98 M MgCl2 ((b) and (d)) solutions at 25 C as a function of electrode rotation speed. Vertical dashed lines correspond to theoretical i_{lim} (n = 2) calculated from Equation 17 and data from Figure 15 corresponding to rotation speeds of 100 (left) and 6000 (right) rpm.

Cathodic polarization curves as a function of rotation speed for SS304L are presented in Figure 19(c) and (d). In all cases, there is no apparent trend with rotation speed. For ORR reactions, it is expected that with increasing rotation rate an increase in i_{lim} should be seen as for Pt in Figure 19(a) and (b) or for SS304L and Pt in NaCl solutions (Figure 16). In contrast, there is no evident potential region where activation control for solely ORR is dominant on SS304L. Furthermore, the scans are lacking a clear i_{lim} ORR region. In the case of 0.189 (Figure 19(c)), the HER reaction is dominant below -1.1 V_{SCE} as indicated by all rotations converging. In the case of 4.98 M $MgCl_2$ (Figure 19(d)), all rotation speeds converge below a potential of -0.6 V_{SCE}. At all concentrations (Figure 19(c) and (d)), a large spread in OCP is present and it is possible localized corrosion was occurring at the surface of electrodes. An optical microscope was utilized to inspect the surface of the alloy after polarization and pitting was found after some of the scans; however, there was no trend with the number of pits or size of pits with OCP variation.

The same lack of rotational rate dependence present for SS304L in saturated $MgCl_2$ is also present for 500 and 6000 rpm RDE cathodic scans in 40% sea salt brine at 25 ˚C as seen in Figure 20. While other cations and anions are present in solution for the 40 % RH sea salt brine, the concentration of Mg^{2+} in solution is much greater than these constituents. For example, examining Figure 5, the concentration of Mg^{2+} is over two orders of magnitude greater than the concentration of SO_4^{2-} and over three orders of magnitude greater than the concentration of Ca^{2+} (Figure 5). Finally, the lack of i_{lim} is not only present at 25 ˚C, but also at 35 and 45 ˚C for 4.98 M $MgCl_2$ and 35 ˚C for 40 % RH sea salt brine as presented in Figure 21(a) and (b) respectively for 500 rpm.

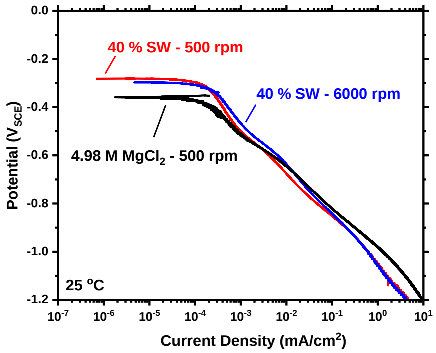

Figure 20: Comparison of 4.98 M $MgCl_2$ (500 rpm) and 40 % RH (500 and 6000 rpm) seawater brine at 25 ˚C.

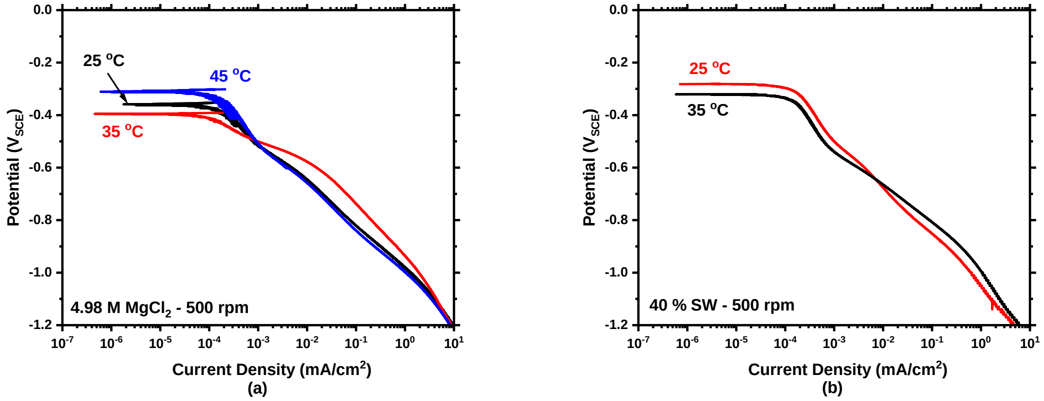

Figure 21: Cathodic polarizations at (a) 25, 35, and 45 ˚C for 4.98 M $MgCl_2$ and (b) 25 and 35 ˚C for 40 % RH sea salt brine. It is noted that all polarizations are at 500 rpm. It is noted that the potential on the ordinate axis is not corrected for potential temperature effects; however, variations are expected to be small.

2.4.5. In-situ spectro-electrochemistry

For NaCl solutions, cathodic polarization scans in the Raman flow cell on SS304L have similar behavior to RDE polarization scans (Figure 16(c) and (d)). Polarization scans are presented in Appendix 0. Overall, as Q increases, i_{lim} increases as presented in Figure 22(a). At low Q (0.0 and 0.5 mL/min), the i_{lim} is less than the i_{lim} for a quiescent, flat cell cathodic polarization. When Q increases to 1.5 mL/min, the i_{lim} yields the same i_{lim} as the quiescent polarization scan. Finally, when $Q > 1.5$ mL/min, the i_{lim} surpasses the i_{lim} for the quiescent polarization, representing a decrease in δ. For 0.189 M $MgCl_2$, there is little-to-no dependence on Q in contrast to NaCl solutions which showed an increase in i_{lim} with increased Q. Additionally, in $MgCl_2$ no value of Q reaches the i_{lim} for expected quiescent ORR (displayed on Pt [90]).

A measured polarization scan for 0.189 M $MgCl_2$ is presented in Figure 23(a), during which, *in-situ* Raman spectra were collected between 2800 – 4000 cm^{-1}, as seen in Figure 23(b). Scans were background-subtracted and normalized to the maximum water peak at 3415 cm^{-1} [109]. As the potential was driven in the cathodic direction from OCP, a strong, sharp Raman peak formed at 3654 cm^{-1} (Figure 23(c)). This peak, at 3654 cm^{-1}, corresponds to the A_{1g} O-H stretching mode of microcrystalline $Mg(OH)_2$ (brucite) [109,110]. Below a potential of -1.1 $V_{Ag/AgCl}$ the normalized intensities show an influence from bubbles on the surface of the alloy (not shown here), likely due to significant H_2 production from HER.

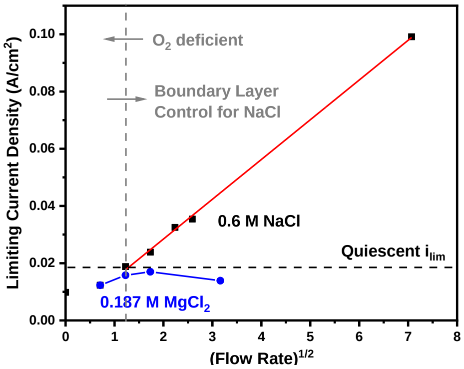

Figure 22: Influence of solution flow rate on the limiting current density for 0.6 M NaCl and 0.189 M MgCl2 solutions. It is noted that all polarizations were performed at lab temperature.

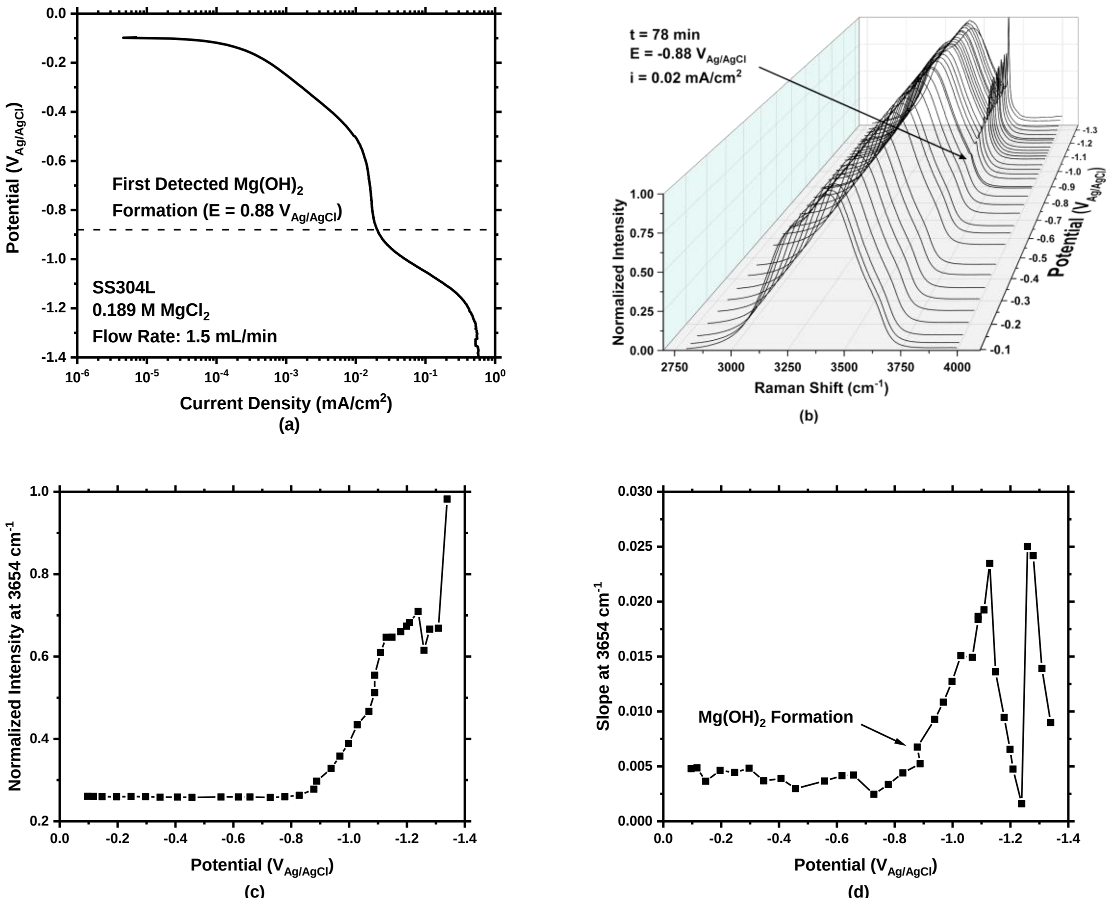

Figure 23: (a) Polarization scan of SS304L in 0.189 M $MgCl_2$. (b) In-situ Raman characterization of SS304L surface as a function of potential in (a). (c) Normalized intensities at a wave number of 3654 cm^{-1}. (d) Slope of (c), indicative of $Mg(OH)_2$ formation.

2.5. Discussion

2.5.1. The oxide film on SS304L reduces the limiting current density for oxygen reduction reactions in sodium-containing solutions in comparison to theoretical predictions

The Fe- and Cr-containing oxide film on SS304L decreases the measured i_{lim} in comparison to Pt and theoretical calculations in Na salt solutions. SS304L exhibits a reduced i_{lim} in comparison to both theoretical predictions and Pt alloys for 0.6 M NaCl and 0.6 M NaOH at nearly all rotation rates as displayed in the Levich plots in Figure 24(a) and (b) respectively. This trend is also present for all NaCl concentrations and temperatures (Appendix B) and all NaOH concentrations 5.4 M and below (Appendix D). The discrepancy between theoretical calculations and measured becomes greater at higher rotation rates (smaller δ) for all solution concentrations.

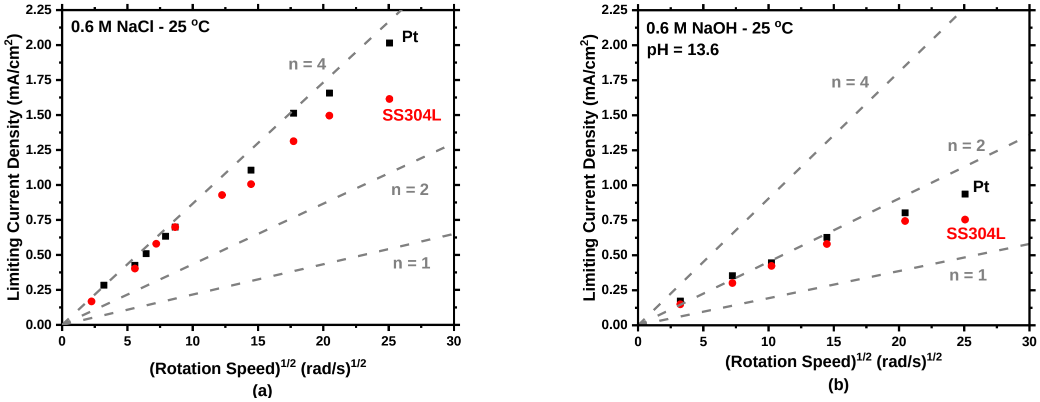

(a) (b)

Figure 24: Levich behavior for Platinum and Stainless Steel 304L exposed to (a) 0.6 M NaCl and (b) 0.6 NaOH at 25 °C.

Upon reducing the oxide prior to polarization, an increase in i_{lim} is measured in sodium solutions. It is known that the iron oxides within the outer film of SS304L are reduced from Fe^{3+} to Fe^{2+} upon cathodic polarization between −0.6 and −0.8 VSCE, leaving behind a defective, non-reducible chromium rich oxide [111–114]. In order to investigate the effects of this remnant oxide, polarization scans were performed after reduction of the SS304L surface at -1.5 V for one hour in 0.6 M NaOH and a slight increase in measured i_{lim} was observed on the reduced in comparison to the non-reduced surface (Appendix D). Additionally, Alexander et al. performed cathodic polarization scans in the negative direction (from OCP to -1.2 V_{SCE}) and in the positive direction (from -1.2 V_{SCE} to OCP) in 1 M NaCl. An increase in i_{lim} was observed on the positive-going scan in comparison to the negative scan with no transitory reduction peaks in the positive scan [88]. Additionally, the oxide is thought to have contributed to the transitory response of the cathodic scan (Figure 17(c) and (d)) as there was no transitory response in the positive scan [88]. Bozec et al. also showed cathodic i_{lim} were increased on pre-reduced surfaces of SS904L and SS316L in seawater solutions in comparison to polished and passivated surfaces [112]. In all cases, an increase in i_{lim} is measured when the iron portion of the oxide is reduced from Fe^{3+} to Fe^{2+} due to the fact that there is no longer a diffusion barrier on the pre-reduced surface despite the surface being partly covered in in a non-reducible chromium layer [112–114].

As the oxide on the SS304L has shown to play an important role in the cathodic reduction behavior it is important to take this into account when determining reaction mechanisms, other electrochemical phenomena such as the natural convection boundary layer, or when modeling corrosion scenarios. Additionally, it has been shown that performing polarizations on Pt provides for results on an oxide free surface to serve as an important baseline and can help identify potential changes that are due to oxide effects and not solution effects. When modeling atmospheric scenarios, one must consider a decrease in the cathodic current due to the oxide as this may play a significant role especially at thin *WL* thicknesses.

2.5.2. Change in reduction mechanism for high pH sodium-containing solutions due to superoxide formation and oxide reduction

The cathodic reduction reaction for sodium-containing solutions is ORR; however, the dominant reaction mechanism is influenced by the anion in solution and resultant pH. As displayed by Alexander et al. [88] and Katona et al. [91] (Appendix B) through Levich behavior, ORR is dominant for Pt and SS304L in NaCl solutions as a function of chloride concentration (0.6 - 5.3 M NaCl) and temperature (25 – 45 ˚C). In NaCl solutions, the number of electrons transferred is near four and there is no observed pattern present with solution concentration or temperature. An example of typical Levich behavior is presented for Pt and SS304L in 0.6 M NaCl at 25 ˚C in Figure 24(a) and is indicative of a near four electron transfer. As such, Equation 3 is the operating mechanism for NaCl solutions. In NaOH solutions, ORR is the operating reduction mechanism; however, the number of electrons transferred ranges from 1.75 at a pH of 13.6 and decreases to 1.30 at a pH of 14.9. This is presented for Pt and SS304L in 0.6 M NaCl at 25 ˚C in Figure 24(b) and is indicative of a less than two electron transfer indicating superoxide formation (Equation 8) is the rate limiting step to the ORR reaction [92].

As presented in Figure 12, cathodic regions on the surface of a corroding alloy, such as SS304L, can become chloride-poor and alkaline-rich in atmospheric scenarios. For an NaCl electrolyte, this region will become rich in NaOH [102–105]. A comparison of the cathodic behavior between 0.6 M NaOH and 0.6 M NaCl at 500 rpm is presented in Figure 25(a). At any given potential, the cathodic current density is lower for 0.6 M NaOH in comparison to 0.6 M NaCl. The same trend holds for 5.4 M NaOH and 5.3 M NaCl (Figure 25(b)). As such, the compositional and pH gradient in the cathode will give rise to a variable potential, current density, and reaction mechanism and it is important to take these changes into consideration when modeling corrosion scenarios.

A change in cathodic reduction mechanisms is present at high pH NaOH solutions due to dissolution of the oxide film. No i_{lim} was measured on SS304L in NaOH solutions at a pH of 16.5, and the measured current exceeds the predicted i_{lim} (Equation 17) for electron transfer numbers of both one and four (Appendix D). As the cathodic current is not consistent with predicted ORR, it is of interest to determine the source of the increased current. First, the OCP for pH 16.5 is in a region of the Pourbaix diagram that predicts active corrosion, producing $Fe(OH)_4^{2-}$. Second, after reduction of the oxide on the surface of the alloy at -1.5 V_{SCE}, the OCP is agreement with predictions for HER at a pH of 16.5 (-1.21 V_{SCE}) indicating HER is the only cathodic reaction and neither the surface oxide (which is a partially covered, non-reducible chromium layer [112–114]) nor dissolved oxygen have an influence on the cathodic behavior (Figure 18). Finally, when cathodic polarization scans are conducted in a de-aerated environment (Appendix D), there is minimal change in the overall cathodic behavior indicating that the oxygen concentration has no effect on the cathodic reduction behavior of SS304L in NaOH solutions with a pH of 16.5. Thus, the cathodic reaction in concentrated NaOH solutions (pH = 16.5) is not ORR and the increased current is due to the reduction of the oxide film (Fe_2O_3) on the surface creating $Fe(OH)_4^{2-}$ before transitioning to HER as the cathodic reduction reaction at significant overpotentials.

To the knowledge of the authors, the cathodic behavior of SS304L has not been investigated at such high pH values. Typically, an increase in cathodic current density on SS alloys is measured in the potential window of -0.6 to -0.8 V_{SCE} and is attributed to the Fe(III) to Fe(II) transition in the oxide film [88,111,115,116]. In NaOH solutions with a pH of 16.5, the OCP is below -0.8 V_{SCE} and the Fe(III) to Fe(II) transition is not responsible for the increase in current density. Instead, reduction of the oxide film to form $Fe(OH)_4^{2-}$ is responsible for the current density increase.

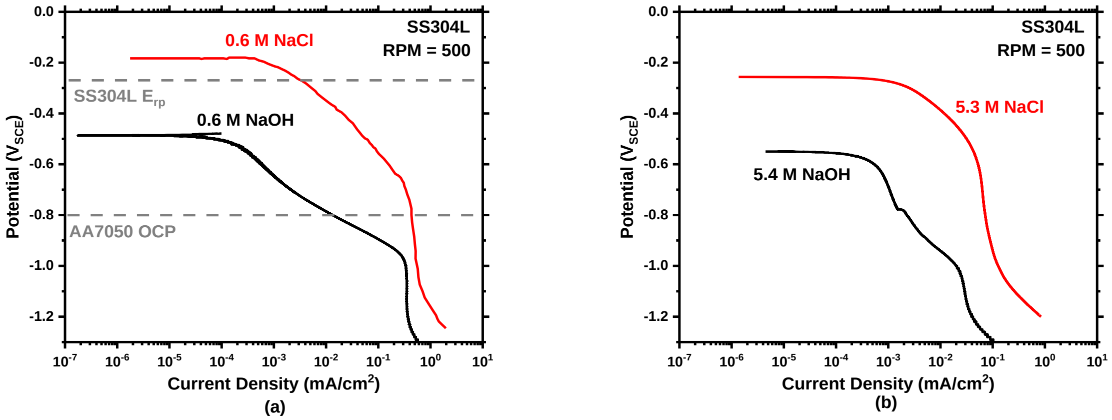

Figure 25: Comparison of cathodic kinetics of SS304L exposed to (a) 0.6 M NaOH and 0.6 M NaCl and (b) 5.4 M NaOH and 5.3 M NaCl [88]. *It is noted that all polarization scans are at a rotation rate of 500 rpm.*

Overall, sodium chloride solutions exhibit ORR when the pH in solution is less than 16.5. The four electron ORR reaction is dominant across a wide range of NaCl solutions (1 – 5.3 M NaCl and 25 - 45 ˚C). In pure NaOH solutions (pH < 16.5), the dominant ORR reaction involves the creation of a superoxide intermediate and a perceived number of electrons transferred of two. Finally, at high pH NaOH solutions (pH = 16.5), the cathodic reduction becomes the reduction of the oxide film and, once completely reduced, becomes HER. As such, it is important to account for changing cathodic reduction mechanisms when an evolving cathode is considered. While informing upon cathodic kinetics is important in Na-containing solutions, there are many constituents to seawater solutions (Figure 5), such as Mg^{2+} at lower RH's, that could influence the cathodic reduction reaction.

2.5.3. $MgCl_2$ and 40 % sea salt brines result in ORR suppression and HER promotion

The cathodic reduction reaction in NaCl solutions is ORR while in $MgCl_2$–dominant solutions the cathodic reduction reaction is HER. A comparison of cathodic polarization scans between 5.3 M NaCl and 4.98 M $MgCl_2$ is presented in Figure 26(a) and (b) for quiescent and 500 rpm scenarios respectively. Exploring the cathodic polarization scans at 500 rpm (Figure 26(b)), it can be seen that the predicted limiting current behavior (Equation 17) is measured for SS304L in 5.3 M NaCl. In contrast, an i_{lim} is not presented for 4.98 M $MgCl_2$ and the polarization scan appears to be under activation-controlled kinetics over the entire potential range explored. The lack of i_{lim} is also measured under quiescent polarization scans for 4.98 M $MgCl_2$ solutions while an i_{lim} is measured for 5.3 M NaCl (Figure 26(a)). The lack of rotational dependence in SS304L in $MgCl_2$ solutions will be explained.

During experimentation, it is noted that $Mg(OH)_2$ and $Mg_2(OH)_3Cl \cdot 4H_2O$ were observed on the electrode surface after polarization in solutions ≤ 1.28 M and ≥ 3 M $MgCl_2$ respectively. These phases were also observed when small amounts of NaOH were titrated in $MgCl_2$ concentrations of various concentrations (Appendix A). This observation is inconsistent with thermodynamic predictions in which $MgCO_3$ is stable at all solution concentrations. However, the remarkably slow kinetics of $MgCO_3$ formation [117–122] prevent appreciable $MgCO_3$ growth before a stability region is reached for $Mg(OH)_2$. This effect is further discussed in Appendix A and will be a key factor will be utilized in explaining the lack of rotation rate dependence on SS304L.

The hypothetical Evans diagram, presented in Figure 27, summarizes the effects of Mg-precipitation influencing the dominance of HER during cathodic polarization. The unusual cathodic polarization behavior of SS304L is attributed to a decrease in overpotential for HER, suppression of ORR, and stochastic, active corrosion driving down OCP. Figure 27 depicts the influences from the following half-cell reactions: ORR, HER, and metal oxidation on the overall cathodic behavior. Each reaction has a corresponding Nernst potential (E_O) and exchange current density (i_o): $E_{O,HER}$, $i_{O,HER}$, $E_{O,ORR}$, $i_{O,HER}$, $E_{O,M}$, $i_{O,HER}$ where "M" denotes anodic metal oxidation reaction. Overall, the major contributors to measured cathodic kinetics are the cathodic shifts of $E_{O,M}$ and $E_{O,ORR}$ and anodic shift of $E_{O,HER}$ with increasing $MgCl_2$ concentration.

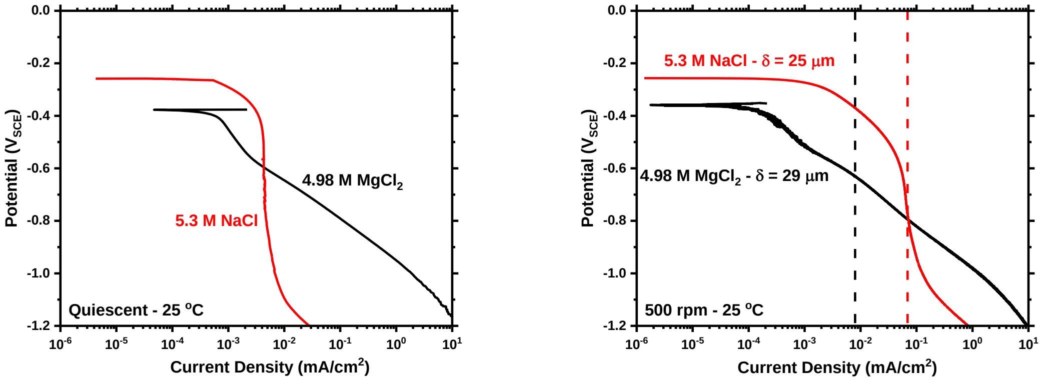

(a) (b)

Figure 26: Comparison of cathodic polarizations in $MgCl_2$ and NaCl brines at 25 ˚C under (a) quiescent conditions and (b) under a rotation rate of 500 rpm. Dashed vertical lines in (b) are calculated i_{lim} for each solution respectively.

First, in Figure 27, localized corrosion is also characterized by decrease in $E_{O,M}$ [123,124] when the bare metal alloy is exposed below a passive film. Pitting is more likely to occur at elevated chloride concentrations along with localized corrosion seen on the surface of the alloy. Therefore $E_{O,M}$ will decrease with increasing $MgCl_2$ concentration as is shown in Figure 27(b) and is denoted by $E_{O,M,active}$. Second, $E_{O,ORR}$ is likely to be suppressed through precipitate formation and decreases in Figure 27(c). Finally, $E_{O,HER}$ is shown to increase with increasing Mg^{2+} concentration. It is known that $E_{O,HER}$ will increase with a decrease in pH as given by [55].

$$E_{HER} = E^{o}_{HER} - m * pH \qquad 18$$

assuming that $[H_2] = p_{H_2} = 1$ [55]. Under standard conditions, $E^{o}_{HER} = 0\ V_{SHE} = -0.244\ V_{SCE}$ and $m = -0.059\ V$. Thus, as the pH for Mg-precipitation increases with decreasing chloride concentration, $E_{O,HER}$ will increase as displayed in Figure 27(d). All three of these fluctuations are summarized in Figure 27(e) with the transition to higher concentrations of $MgCl_2$ being denoted by dashed lines. ORR and metal dissolution have shifted the respective Nernst potential in the negative direction whereas HER has shifted in the positive direction with increasing chloride concentration.

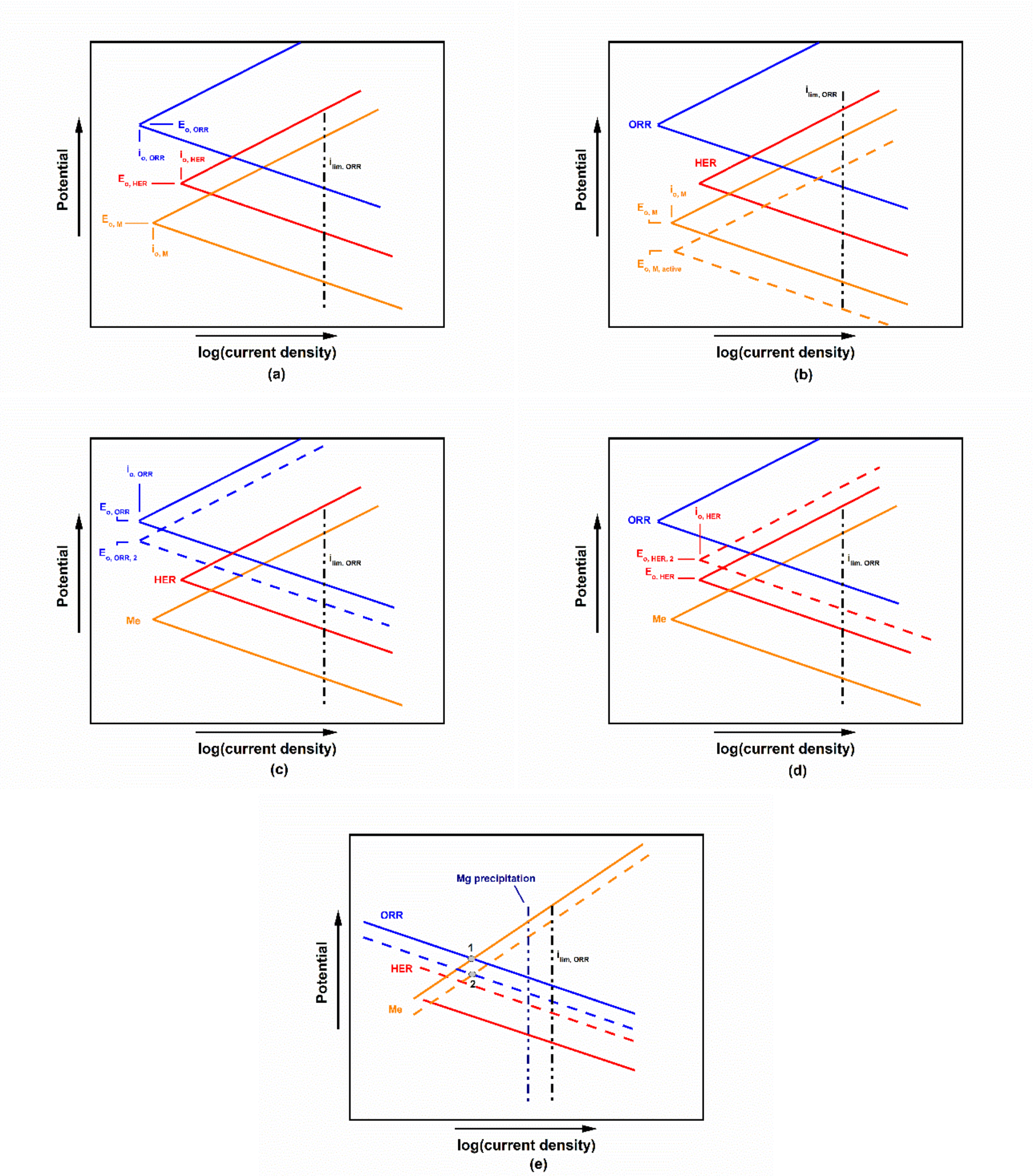

Figure 27: (a) Evans diagram explaining the unexpected cathodic behavior in $MgCl_2$ containing solutions. Influences from (b) anodic dissolution, (c) ORR, and (d) HER were considered in creation of this diagram along with the current for Mg species precipitation. Solid lines are dilute concentrations of $MgCl_2$ and transition to dashed lines with increasing concentration. The resultant Evan's diagram is displayed in (e).

In the Evans diagram in Figure 27(e), there are no depicted variations of i_o. In terms of $i_{O,ORR}$, there is little information about trends associated with chloride concentration. The value of $i_{O,ORR}$

is often convoluted with $i_{O,M}$ and is manifested as i_{corr} or the open circuit corrosion current density. It is known that i_O is dependent upon the binding energy of a species on the surface, among other factors, and it is not expected that binding energy is going to be significantly changed by the solutions present in the study [125]. Also, a t-test for statistical significance for i_{corr} shows no significant difference (at an alpha of 0.05) across all rotation speeds and concentrations studied on SS304L (Appendix A). Finally, during HER it is also well known that an increase in pH will decrease $i_{O,HER}$ [126]. However, the change in $i_{O,HER}$ over the range of possible surface pH in this study is less than half an order of magnitude in current density and any manifestation in an Evan's diagram will be minimal. Thus, i_o will not play a major role in the abnormal cathodic behavior of SS304L.

Overall, the major contributors to measured cathodic kinetics are the depression of $E_{O,M}$ and $E_{O,ORR}$ and increase of $E_{O,HER}$ with increasing $MgCl_2$ concentration as displayed in Figure 27(e). Additionally, the thermodynamically stable formation of $Mg(OH)_2$ and $Mg_2(OH)_3Cl \cdot 4H_2O$ occurs at a current density below $i_{lim,ORR}$. Thus, transient behavior before ORR due to influences from pH fluctuations and precipitate formation is not surprising and helps explain the unexpected behavior in dilute $MgCl_2$ solutions. In saturated $MgCl_2$, HER is the main cathodic reaction and there are minimal transient behaviors.

The inhibiting effects of the Mg^{2+} cation are not only seen in $MgCl_2$ solutions but are also seen in sea salt brines that are dominant in $MgCl_2$. The RH targeted for experimentation was 40 % RH (major components: 10.28 M Cl^-, 0.17 M Na^+, 5.31 M Mg^{2+}) [127]. As presented in Figure 20, the behavior between 4.98 M $MgCl_2$ and 40 % RH sea salt brine is nearly identical. In addition, the same lack of rotational dependence that was present in in 4.98 M $MgCl_2$ is present in 40 % RH sea salt brine as indicated by a similar current density at any given potential between the 500 and 6000 rpm speeds. The same mechanism presented for $MgCl_2$ [90] is believed to be active for the 40 % RH sea salt brine. While other phases may be thermodynamically stable (e.g., $CaCO_3$), the concentrations are too low or the precipitation kinetics are too slow to be the dominant, observed phases. Thus, the formation of Mg-dominant precipitates in 40 % RH sea salt brine are expected to be the major contributors to the measured cathodic kinetics (i.e., lack of i_{lim} and dominance of HER) which are influenced by the depression of $E_{O,M}$ and $E_{O,ORR}$ and increase in $E_{O,HER}$.

The mechanism presented for room temperature $MgCl_2$ solutions is also believed to be operating at elevated temperatures. The precipitated phases are going to be the same as there is little variation in precipitation pH and the precipitated phases are going to be of the same composition [128] as the phase change for saturated solutions will occur at 60 ˚C ($Mg_2(OH)_3Cl \cdot 4H_2O$ at 25 ˚C to $Mg_3(OH)_4Cl_2 \cdot 4H_2O$ at 60 ˚C [128]). As the precipitate phase will not change in the range explored, having the similar cathodic reduction behavior between 25 – 45 ˚C for 4.98 M $MgCl_2$ and 25 – 35 ˚C for 40 % RH sea salt brine is not surprising.

A mechanism explaining the ORR suppression and HER promotion in $MgCl_2$ solutions was proposed. As a result of precipitation and HER promotion in $MgCl_2$ environments, a decreased cathode current in comparison to NaCl environments is possible, especially at small *WL* thicknesses. In Figure 26(b), 4.98 M $MgCl_2$ ($\delta = 29\ \mu m$) has a lowered measured current density in comparison to 5.3 M NaCl ($\delta = 25\ \mu m$) at all potentials more noble than ~ -0.8 V_{SCE} due to the change in reaction mechanism from HER to ORR respectively. This change in reaction mechanism is important to capture when informing upon atmospheric scenarios that can range widely in RH as the change in current density is drastic. While the precipitation of Mg-precipitates was observed after cathodic polarization, *in-situ* formation has not been observed in literature and this will subsequently be discussed.

2.5.4. In-situ Raman spectro-electrochemistry under controllable water layer thicknesses identifies Mg-precipitates during cathodic polarizations

Mg precipitates were identified via *ex-situ* methods after cathodic polarization (Appendix A) and via *in-situ* spectro-electrochemistry during cathodic polarizations in dilute $MgCl_2$ solutions with a flow cell (Appendix 0) [129]. As many Raman cells are characterized by small solution volumes (*i.e.* several mL) [109], it is important to understand potential impacts this may have on systems that contain oxygen before identifying potential stable precipitates. During cathodic polarization, it is possible that the oxygen concentrations can be depleted, under rates of interest for atmospheric corrosion, if no flow is utilized and the pH raised, making the chemical composition of the solution under study not representative of the environment of interest. Additionally, many Raman cells may be utilized with various solution flow rates (Q); flow could potentially be used to control δ and thus relate measurements of precipitate chemistry to different WL thicknesses in atmospheric corrosion [60].

By utilizing NaCl polarization measurements, it was shown that a flow rate of roughly 1.5 mL/min is necessary in order to avoid O_2 depletion in the flow through Raman cell. This value was deduced by comparing polarization scans at various flow rates to a quiescent polarization scan with large a large volume (V ~ 350 mL). When no flow rate was utilized in the Raman cell, a decrease in i_{lim} was measured in comparison to the flat cell i_{lim}. However, when a greater flow rate than 1.5 mL/min was utilized, a further increase in i_{lim} was measured indicating that a diffusion boundary layer can be formed and controlled by the flow rate. It was determined that δ is inversely proportional to the square root of the flow rate $\left(\frac{1}{\sqrt{Q}}\right)$ as displayed in Figure 28. Thus, in order to avoid influences from O_2 depletion it is suggested to utilize a flow rate of 1.5 mL/min.

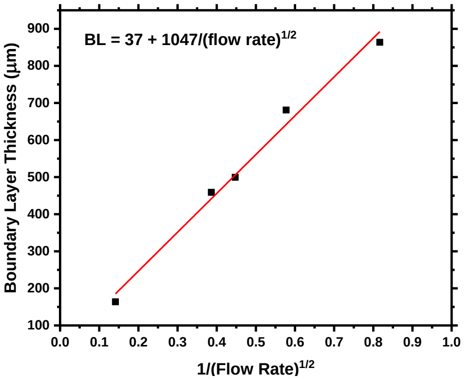

Figure 28: Dependence of the boundary layer thickness vs. the inverse square root of the flow rate (mL/min).

In 0.189 M $MgCl_2$, $Mg(OH)_2$ was identified by a growth in the intensity of the Raman peak at 3654 cm^{-1} on the surface of SS304L during cathodic polarization at a potential of -0.88 $V_{Ag/AgCl}$ (-0.925 V_{SCE}) when utilizing a Q of 1.5 mL/min as seen in Figure 23. While this was the first potential that the precipitate was observed, the $Mg(OH)_2$ precipitate could have been present on another part of the electrode, formed in the boundary layer, or formed and carried away by the flowing solution. Despite these limitations, the observation of the $Mg(OH)_2$ precipitation helps explain dominance of HER in $MgCl_2$ solutions as presented in Katona et al. [90] (Appendix A) and in Section 2.5.3. Additionally, the observation of $Mg(OH)_2$ instead of $MgCO_3$ supports the claim of $MgCO_3$ formation experiencing very sluggish kinetics and that $Mg(OH)_2$ will initially influence corrosion processes (O_2 availability on the surface and solution conductivity) in the cathode region.

2.6. Conclusions

Cathodic kinetics were determined in various solutions and temperatures (Table 2) that span a wide range of environments on the surface of an alloy in atmospheric, marine conditions (Figure 5) and the cathodic reduction reaction mechanisms were shown to change with solution composition and pH. Additionally, cathodic polarizations were performed in conjunction with *in-situ* spectro-electrochemistry to identify precipitation while simulating atmospheric corrosion scenarios with a variable δ. The overall results of this section are displayed in Figure 29.

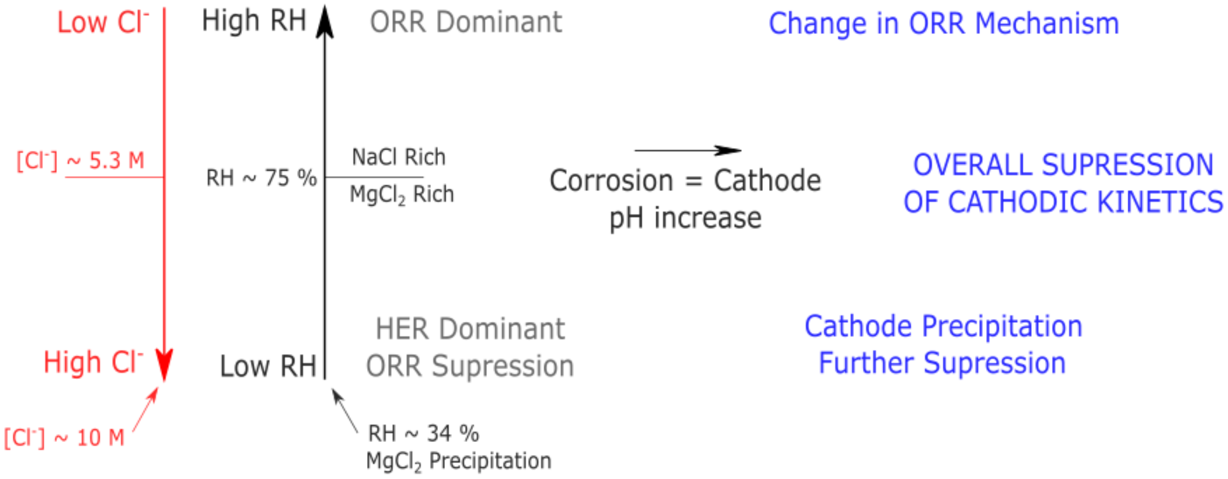

Figure 29: Summary of the solution effects on cathodic kinetics. The ordinate axis represents RH and at high RH the solution is NaCl rich while at lower RH's (< ~ 75 %) the solution is $MgCl_2$ rich. Moving from left to right on the graphic represents corrosion. The solution starts out at its equilibrium pH while corrosion (moving right) causes the cathodic pH to rise.

Examining Figure 29, the ordinate axis represents RH and, therefore, chloride concentration, i.e., decreasing the RH will increase chloride concentration. In marine conditions under high RH (> ~ 75 % RH), the solution is NaCl-rich while at lower RH's (< ~ 75 %) the solution is $MgCl_2$ rich (Figure 5). When corrosion is initiated on the surface of an alloy undergoing localized corrosion, the cathodic kinetics are representative of the solution concentration under equilibrium conditions (equilibrium pH with generally no hydroxide containing precipitates). Under these conditions there are two possibilities for cathodic reduction mechanisms: ORR and HER. ORR is dominate under high RH scenarios (> ~ 75 %) in which NaCl is the dominant salt in solution. Within NaCl stability, decreasing RH will increase NaCl concentration and cause a decrease in O_2 solubility. This solubility decrease will decrease measured current densities and decrease cathodic kinetics. Decreasing further in RH, NaCl precipitates into solution, the brine then becomes dominant in $MgCl_2$. The reaction mechanism now transitions from ORR to HER due to influences from a further decreased O_2 concentration, localized corrosion, and stable precipitation. These trends are not only true for 25 ˚C but also for 35 and 45 ˚C.

When a material is the predominant cathode in a galvanic couple, the cathodic reduction reactions will cause for an increase in pH. Additionally, under OCP conditions, when active corrosion is coupled to the surrounding cathode on the same material, the cathodic reduction reactions will also cause for an increase in cathodic pH. When this occurs, there again are two different scenarios that will occur. Under high RH conditions (NaCl-dominant), it is possible that the brine experiences regions of NaOH dominance (Figure 12). In NaOH-dominant brines, the reaction mechanism changes from a near four-electron transfer to an electron transfer below two, due to the formation of a superoxide intermediate. In this scenario, at any given potential, a decrease in current density is measured in an NaOH solution in comparison to an NaCl solution (0.6 M NaOH vs. 0.6 M NaCl, Figure 25(a)) causing for a suppression in cathodic kinetics. This difference is true for both dilute and concentrated NaCl and NaOH solutions. At low RH solutions ($MgCl_2$-dominant), the coupled cathodic reaction to active corrosion will also cause for a pH rise; however, cathodic precipitation will occur. Deposition on the surface will restrict O_2 diffusion to the surface and decrease the number of active sites for cathodic reduction, causing for a further suppression of cathodic reduction. In either case, when exploring the cathode when active corrosion is occurring, a suppression of cathodic kinetics will be present.

As displayed in Figure 29, across a wide range of RHs that are possible in marine atmospheric environments, the cathodic reduction reaction mechanism can change or be suppressed depending on the RH and corrosion progression. When predicting and modeling atmospheric corrosion damage, it is important to consider the solution properties (concentration and composition) and cathode evolution (changes in pH or cathodic precipitation) as this will influence the cathodic reaction mechanisms, cathodic current, and the overall prediction of corrosion. A certain number of these phenomena will be explored in Section 5.

3. Water Layer

3.1. Summary

The *WL* thickness, often known to control corrosion rate and extent of corrosion damage, is calculated and measured for common exposure environments. First, it was determined that in atmospheric environments, the *WL* thickness is relatively invariant of solution composition above a RH of ~75 %; however, below 75 % RH, $MgCl_2$ solutions do not represent the *WL* for sea-salt brines. Additionally, it was shown that temperature variations do not play a significant role in determining the *WL* thickness. Next, the boundary between thin film and full immersion environments was calculated by determining the natural convection boundary layer. With increased chloride concentration and temperature, the natural convection boundary layer thickness decreases. Third, the *WL* was determined in common salt spray conditions, and it was determined that the *WL* was highly dependent upon the angle of exposure and the thickness increased with a greater angle from vertical. Finally, all of the *WL* thicknesses are put into perspective and the implications on corrosion are discussed.

The work presented in this chapter has been reported in the following publications:

- **R. M. Katona**, J. C. Carpenter, A. W. Knight, R. S. Marshall, B. L. Nation, C. R. Bryan, E. J. Schindelholz, R. F. Schaller, and R. G. Kelly, *Natural convection boundary layer thickness at elevated chloride concentrations and temperatures and the effects on a galvanic couple*. Journal of the Electrochemistry Society. 2021. Editors Choice. https://doi.org/10.1149/1945-7111/abeb29
- **R.M. Katona**, S. Tokuda, J. Perry, R.G. Kelly, Design, Construction, and Validation for in-situ Water Layer Thickness Determination during Accelerated Corrosion Testing, Corros. Sci. 175 (2020) 108849. https://doi.org/10.1016/j.corsci.2020.108849.
- **R.M. Katona**, A.W. Knight, E.J. Schindelholz, C.R. Bryan, R.F. Schaller, R.G. Kelly, Quantitative assessment of environmental phenomena on maximum pit size predictions in marine environments, Electrochim. Acta. 370 (2021) 137696. https://doi.org/10.1016/j.electacta.2020.137696.

3.2. Introduction

Electrolytes formed through salt spray or deliquescence of salt as either droplets or a thin WL on the alloy surface can vary widely in terms of the composition and thickness [46]. As such, the rate and extent of corrosion on the alloy surface can be dictated by the combination of environmental, physicochemical, and geometric variables, which include RH, temperature, electrolyte conductivity, that define the electrolyte film thickness, in addition to the electrochemical kinetics on the alloy surface [58,130–133]. Due to the large likely variation in environmental conditions and WL thicknesses, it is important to quantify these differences and their effects on the expected corrosion.

One of the most important controlling factors for corrosion in atmospheric environments is the *WL* thickness and was identified in Section 1.2.2 and the transition from bulk to thin film kinetics. Numerous authors have attempted to quantitatively determine the transition from bulk, full immersion kinetics to thin film kinetics [58,59,139–148,60,149–157,89,99,134–138] at δ_{nc}. In the absence of natural convection, the diffusional boundary layer would continuously increase with time, lowering the i_{lim} continuously [60]; however, an i_{lim} is observed in all cases. The quantification of δ_{nc} in solutions of various compositions has yielded values from near 250 µm [151,154–158] to between 500 and 1000 µm [60,89,147–150]. Several methods exist to quantify δ_{nc}; however, recently, Liu et al. utilized a RDE and quiescent cathodic polarization scans to quantify δ_{nc} in a dilute chloride-containing brine which could form under atmospheric conditions [60]. It was determined that in 0.6 M NaCl, in which ORR is dominant and the diffusion of oxygen to the metal surface is the rate limiting process [88], δ_{nc} was roughly 800 µm [60]. Below δ_{nc}, the flux of oxygen to the surface of the cathode is determined by the *WL* thickness. While the method presented provides a robust framework, there is still a gap in literature regarding a framework for understanding and predicting δ_{nc} as a function of common environmental parameters such as brine composition, concentration, and temperature and how δ_{nc} compares to both salt spray and deliquesced environments.

As the *WL* thickness is such an important factor in corrosion, this chapter will quantify various *WL* thicknesses and put them into perspective. First, the calculation of atmospheric *WL* thicknesses will be made as a function of RH and composition. Next, δ_{nc} is calculated as a function of solution composition and temperature. Third, the *WL* thickness in accelerated salt spray testing akin to

ASTM B117 will be measured using a designed sensor. Finally, these will be compared, and the implications of the various WL thicknesses will be discussed.

3.3. Experimental

3.3.1. Determination of WL thicknesses in atmospheric environments

The RH and amount of salt(s) present on the surface of the alloy in service determines the thickness of the WL. First, the RH determines the equilibrium salt concentration (C_{eq}) as the RH is equal to the activity of water in air and must match the activity of water in the brine. When the RH decreases, the concentration of chloride species in solution increases because the lower RH represents lower activities of water in the gas phase, and at equilibrium, the activity of water in the liquid phase must match it. Second, the amount of salt (loading density (LD) in units of mass per unit area) can be used to determine the electrolyte layer thickness when combined with the equilibrium concentration through the equation,

$$WL = \frac{LD * \rho_{sp}}{MW * C_{eq}} \tag{19}$$

where MW is the molecular weight of the salt and ρ_{sp} is the specific density. Therefore, the WL thickness can be calculated as a function of salt composition and temperature utilizing Equation 19. It is noted that WL thickness calculations assume a continuous WL.

3.3.2. Determination of the natural convection boundary layer thickness

Experimentally, a finite current density is observed for stagnant electrodes and the finite current density is controlled by δ_{nc} which is determined through the method of Liu et al. [60]. Briefly, i_{lim} from RDE experiments is plotted as a function of $1/\delta$ and a linear fit is achieved (Figure 30(a)). A quiescent polarization scan in full immersion, quiescent conditions (0 rpm) is then obtained and $i_{lim,0\ rpm}$ is extracted. The intersection of $i_{lim,0\ rpm}$ with the linear fit yields δ_{nc} as shown in Figure 30(b).

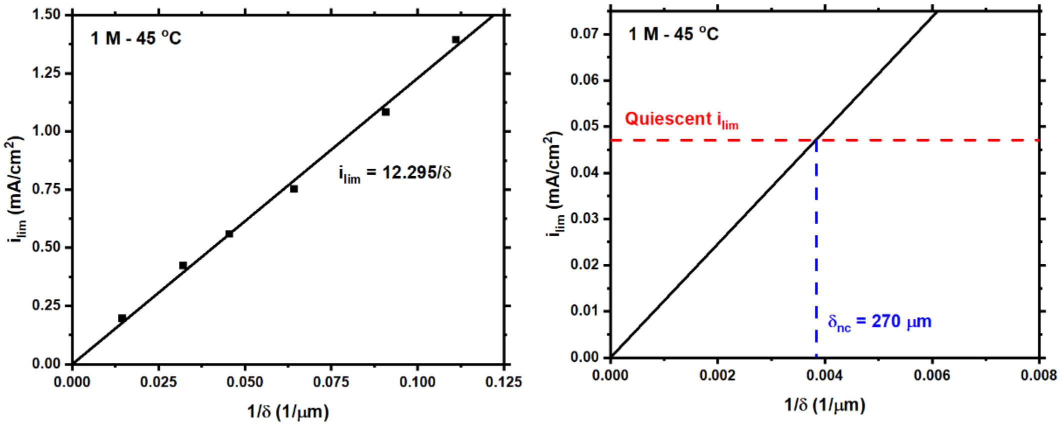

(a) **(b)**

Figure 30: (a) Limiting current density from rotating disk electrode experiments as a function of the inverse of the boundary layer thickness. (b) Intersection of the limiting current density for a quiescent polarization scan and the fit from (a). The difference in scale between (a) and (b) should be noted. This is shown for 1 M NaCl at 45 ˚C.

Further analysis of δ_{nc} was performed by calculating the mass transfer coefficient (K), given by,

$$K = \frac{i_{lim}}{nFC_{bulk}} \qquad 20$$

Finally, the Sherwood number (Sh, also known as the Nusselt number for mass transfer) is calculated, given by

$$Sh = \frac{K}{D/d} \qquad 21$$

Where d is the diameter of the transfer surface (cm) [134,136].

3.3.3. *Sensor creation for determination of WL at various angles*

In order to measure *WL* thickness in salt spray conditions, a sensor was constructed. When sensing electrodes are embedded into an insulating, the equivalent expression for the resistance of the *WL* for the geometry of the sensor shown in Figure 31 is given by:

$$R_s = \frac{\Delta V}{\int I} \tag{22}$$

where ΔV is the potential difference between two points in the electrolyte and $\int I$ is the total current passing between those two points. Equation *22* can be numerically evaluated (in this case using FEM) for a potential difference applied across two points and will serve as the basis for calculating the resistance of various *WL* thicknesses as a function of sensor and experimental parameters.

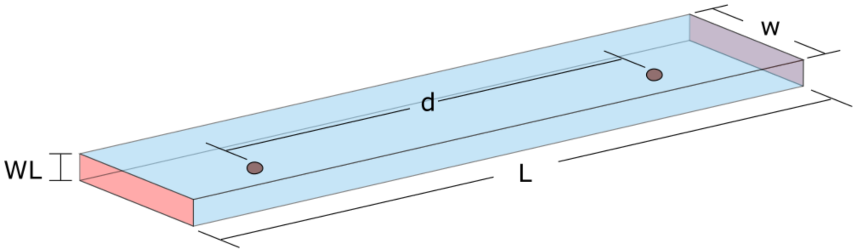

Figure 31: Sensor utilized to determine water layer thicknesses in accelerated corrosion testing.

The modeling framework is based on the Laplace Equation [159] utilizing COMSOL Multiphysics v5.5 (COMSOL, Inc., Burlington, MA) FEM software. A uniform solution layer was created on top of the sensor and was assumed to be rectangular in shape. Various conductivities, widths, and heights were assigned to the *WL* and the width and length of the sensor as well as the radius and spacing of the sensing wires were varied. The measured resistance of the *WL* was then calculated based on Equation 22.

Based upon the FEM results, a sensor was constructed using nickel (99.98%) wire with a radius of 0.5 mm mounted in plexiglass (polymethyl methacrylate). The plexiglass had the following dimensions: w = 10 mm, L = 50 mm, and a variable d. Prior to testing, the sensor was wet ground to 1200 grit silicon carbide paper and placed in a Henniker HPT100 Plasma Cleaner, under 100 Watt and an O_2 only environment for 1 hour to remove hydrocarbon contaminants on the surface of the plexiglass and allowed for a uniform *WL* to form [54], creating an experimental system geometry that is directly comparable to the modeled geometry.

High-frequency electrochemical impedance spectroscopy (EIS) was used to determine *WL* thicknesses. For analysis, a frequency of $3 \cdot 10^5$ Hz was chosen to calculated WL thickness because the phase angle was relatively constant throughout at this frequency. Confirmation of *WL* resistances predicted by FEM was carried out by the use of two methods to create a known *WL* thickness: (i) the use of tape with known thicknesses and a hydrophobic membrane and (ii) placing known volumes of liquid on top of the sensor with a walled structure to contain the *WL*.

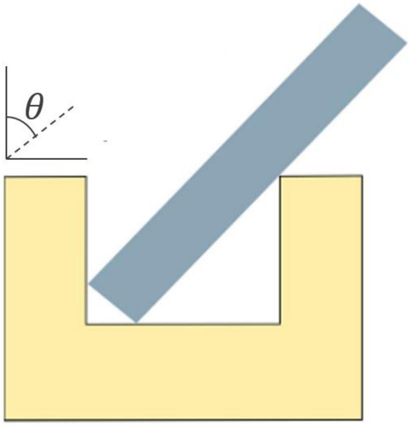

Figure 32: Determination of WL thicknesses in accelerated testing scenarios.

In-situ measurements were made in a commercial salt spray chamber with a continuous salt spray was used in which the solution deposition rate (1 - 2 mL/hr) was determined by ASTM standards [160,161]. The chamber contained heating plates which were kept constant at 25 ˚C. The angle of the sensor was ranged from 0˚ to 47˚ from the vertical as is depicted schematically in Figure 32. The collection rates, as well as angles, cover the range of many other accelerated corrosion standards [162–164]. NaCl solutions were made using both 0.03 M and 0.6 M having measured conductivities of $\kappa = 0.4$ S/m and $\kappa = 8$ S/m, respectively. Equilibrium *WL* thicknesses, measured at a frequency of $3 \cdot 10^5$ Hz, were achieved after roughly 12 hours; therefore, all tests were conducted for at least 24 hours. The measured resistances were converted to *WL* thickness based on the calibration curves constructed from FEM results.

3.4. Results

3.4.1. Water layer thickness in various atmospheric environments

Theoretical WL thicknesses normalized to LD (µm/g/m^2) for NaCl, $MgCl_2$, and sea-salt solutions is displayed in Figure 32. In all cases, with decreasing RH the WL decreases. All solutions have a very similar WL thickness below 75 % RH. For the sea-salt brine, inflections in the curve represent RH conditions at which different salt minerals precipitate. In each case, the WL thickness decreases by roughly a factor of 10 as the RH is reduced from 98% (unevaporated sea-water) to ~75 %, where NaCl precipitates. The brine thickness decreases an additional order of magnitude as the RH drops to about 45 %, where carnallite precipitates. Below roughly 45 %, the brine is nearly pure magnesium chloride.

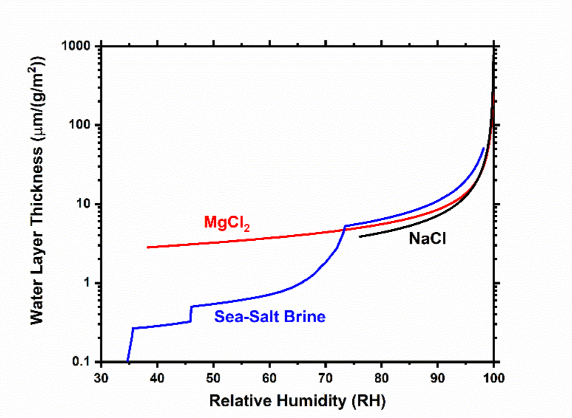

Figure 33: Comparison of water layer thickness in NaCl, $MgCl_2$ and sea-salt brines normalized to loading density. $MgCl_2$ and NaCl are from OLI Studio and sea-salt is from Bryan et al. [46]. *It is noted that 1 g/m^2 = 100 ug/cm^2.*

3.4.2. Natural convection boundary layer thickness in various environments

Calculated δ_{nc} values are presented for NaCl solutions as a function of chloride concentration and temperature in Figure 34(a). Also shown in Figure 34(a) are values obtained for δ_{nc} in 0.6 M at 25 ˚C from Liu et al. [60] and Charles-Granville et al. [89]. Overall, with increasing chloride concentration, δ_{nc} decreases. Additionally, with increasing temperature, δ_{nc} decreases. It is noted that values of δ_{nc} were calculated using i_{lim} for both Pt and SS304L. Generally, SS304L had a higher δ_{nc} due to a lower i_{lim}. Figure 34(b) compares δ_{nc} for NaCl to $MgCl_2$ as a function of chloride concentration at 25 ˚C. Below 5 M chloride, δ_{nc} is similar for both salts.

As seen in Figure 35, δ_{nc} decreases with increased calculated *Sh* (Equation 21). Also included in Figure 35 are values obtained for δ_{nc} in 0.6 M NaCl from Liu et al. [60] and Charles-Granville et al. [89], 0.9 M NaCl from Moraes et al. [41], 0.6 M sodium hydroxide (NaOH) from Katona et al. [92], and 10 mM potassium ferrocyanide ($K_4Fe(CN)_6$) from Amatore et al. [155] all at room temperature. The fit present in Figure 35 utilized data only from this experiment, but values of δ_{nc} from literature [41,60,89,92,155] show good agreement with the fit.

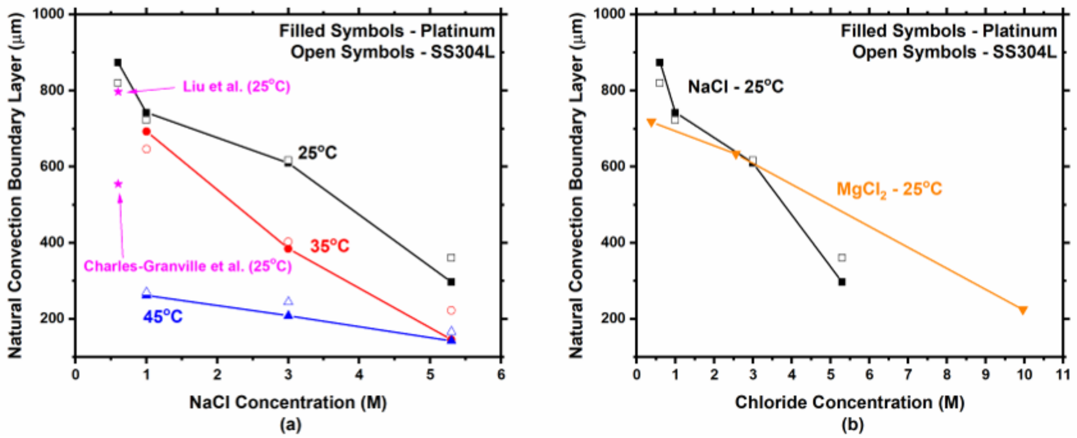

Figure 34: Experimentally calculated natural convection boundary layer thickness as a function of (a) NaCl concentration and temperature and (b) solution composition (NaCl and $MgCl_2$) at 25 °C. It is noted that the x-axis of (b) is total chloride concentration.

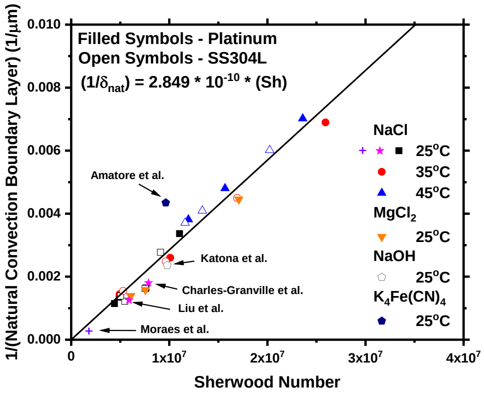

Figure 35: Inverse of natural convection boundary layer as a function of calculated Sherwood number (Sh). Values also plotted were obtained from Liu et al. [60], *Charles-Granville et al.* [89], *Katona et al.* [92], *Amatore et al.* [155], *and Moraes et al.* [41].

3.4.3. Increasing angle in accelerated testing environments increase water layer thicknesses

Confirmation of the calculated resistances for the *WL* sensor is seen in Figure 36, and good agreement is seen in all scenarios explored. When measuring with a known volume of a dilute NaCl electrolyte ($\kappa = 0.4$ S/m), the resistances matched well with predictions with an average percent error of 6.5% (Figure 36(a)). In a more concentrated NaCl solution ($\kappa = 8$ S/m), the resistances matched well again with a lower percent error of 5.1% (Figure 36(b)). The 6.5% error equates to an average difference in calculated *WL* thickness of 0.04 mm and will be taken as the error of the sensor. It is noted that all measured resistances in Figure 36 are slightly below the expected predictions from COMSOL. During the experimentation it was noticed that a small convex meniscus was seen on the top of known volume and which increased the *WL* slightly in the center of the width and would cause the resistance to decrease. Further validation of the sensor was completed using a saturated NaCl ($\kappa = 23$ S/m) electrolyte and measured resistances of the saturated solution matched well with the modeled predictions (Appendix G).

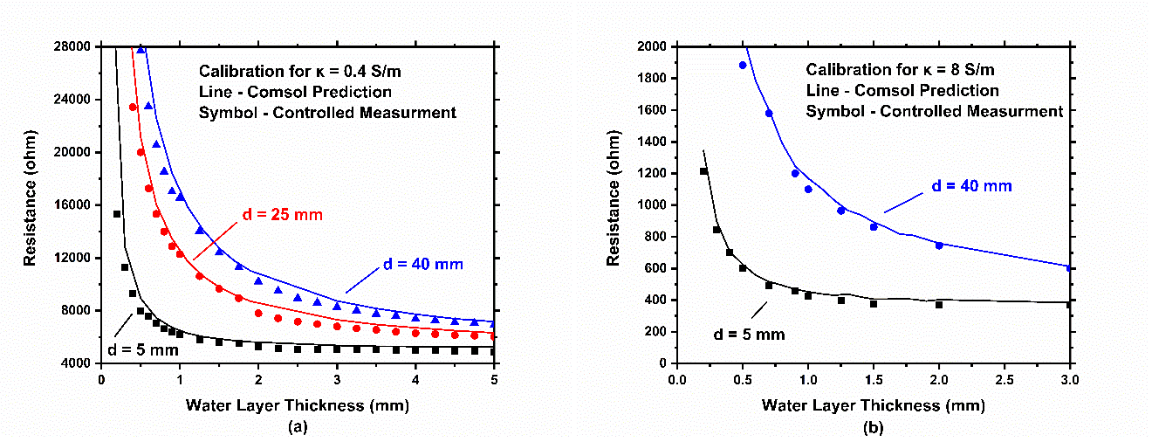

Figure 36: Calibration measurements of the sensor using a known volume of liquid in a controlled environment for an electrolyte with (a) $\kappa = 0.4$ *S/m and (b)* $\kappa = 8$ *S/m.*

The *WL* thickness in accelerated testing is highly dependent on the angle of exposure, and the *WL* thickness increases with increased angle from vertical as seen in Figure 37. *In-situ* tests were performed at various angles ranging from 0° to 47° all using a constant spacing of $d = 5$ mm, covering the range of angles allowed in various accelerated corrosion test standards (ASTM G85 [161], ASTM B117 [161], ASTM B368 [162], ASTM D2247 [163]). These tests showed an increasing *WL* thickness with increasing angle of exposure as seen in Figure 37. When exploring the rate of salt spray deposition, there was not a significant difference between 1.2 mL/hr (Figure

37(b)) and 1.7 mL/hr (Figure 37(a)) when 0.6 M NaCl ($\kappa = 8$ S/m) was used. Replicates were conducted of various tests and the test-to-test variability was ~0.2 mm.

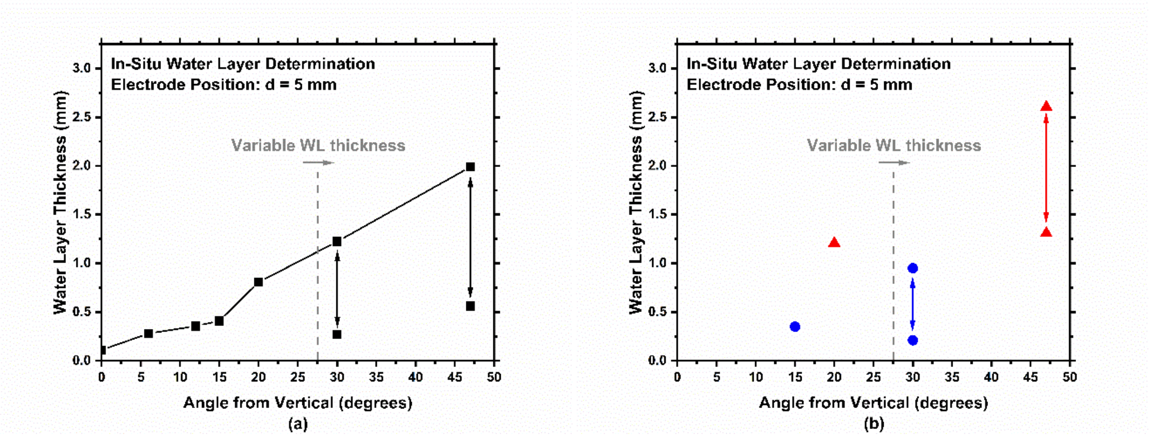

Figure 37: Maximum water layer thickness achieved during continuous salt spray testing as a function of angle, flow rate, and solution conductivity (solution concentration). (a) ■ denotes a conductivity of 8 S/m and a collection rate of 1.7 mL/hr, (b) ▲ denotes a conductivity of 0.4 S/m and a collection rate of 1.7 mL/hr and ● denotes a conductivity of 8 S/m and a collection rate of 1.2 mL/hr, Having double arrows indicates the minimum water layer thickness reached after the water layer slips off.

3.5. Discussion

3.5.1. Single salt solutions do not represent WL thickness of sea-salt brines at low RHs

Single salt solutions (i.e., NaCl and $MgCl_2$) have a similar calculated *WL* thickness above NaCl precipitation (RH > ~ 75 %); however, once NaCl precipitates, the *WL* thickness of sea-salt brines is significantly smaller than $MgCl_2$ solutions as presented in Figure 33. In sea-salt brines, the amount of precipitated salts in solution severely impacts the calculation of the *WL* thickness and causes for a significant decrease in the *WL* thickness [46]. Thus, it is important to understand what may present on an alloy's surface and how this influences the equilibrium *WL* thickness.

Fluctuations in temperature, ranging from 25 to 55 C, do not significantly impact the *WL* thickness in both NaCl electrolytes (Figure 38) and sea salt brines (Figure 4 from Bryan and Schindelholz [46]) over the RH range of 100 to 30 %. As displayed in Figure 38, the *WL* thickness is nearly identical between 25 and 55 ˚C due to the fact that the density, used in Equation 19, does not change significantly across this temperature range (25 to 55 ˚C). The *WL* in sea-salt brines does not change significantly; however, temperature plays a small role in determining where phases precipitate in the seas-salt brines [46]. With increasing temperature, the deliquescent RH of $MgCl_2$ decreases. Although single salts may not represent the *WL* thickness of sea salt brines at low RH and temperature does not influence atmospheric *WL* thickness, it is important to understand how atmospheric *WL* compare to true thin film conditions and what determines this boundary.

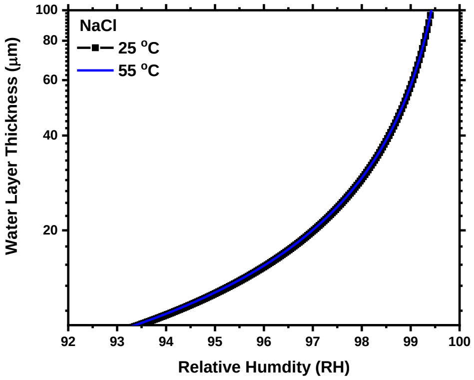

Figure 38: Influence of temperature on WL thickness in NaCl electrolytes. The WL thicknesses were calculated with OLI Studio.

3.5.2. Overall mass transport and diffusive mass transport describe changes in the natural convection layer thickness

Thin film conditions are delineated from bulk conditions by δ_{nc}, and with increasing temperature and chloride concentration, δ_{nc} decreases. Although natural convection in electrochemical systems has been discussed previously in the literature [58,59,139–148,60,149–157,89,99,134–138], there has been a limited amount of experimental work aimed at determining the quantitative thickness of this layer when oxygen is the reactant on the surface of the alloy. Wragg et al. [134,135] and Fenech and Tobias [136] studied free convection under stagnant conditions, producing correlations between dimensionless parameters involving D, density differences between the bulk (ρ_o) and the surface (ρ_i), η, and a characteristic dimension of the electrode (x). In general, the Sh (or Nusselt number for mass transfer) is described in terms of the Schmidt ($Sc = \nu/D$) and Grasshof ($Gr = g * (\rho_o - \rho_i)\rho_{av}^2 x^2/(\rho_i \eta^2)$) numbers. In all cases, a knowledge of the density difference is required to describe the natural convection in the system. In the case of ORR, density differences within the boundary layer are unknown and become complex with the addition of ORR byproducts, such as hydroxyl ions.

Although mass transfer, or *Sh*, could not be described in terms of dimensionless solution variables due to a lack of data in the present case, *Sh* can be calculated per Equation 21 and used to describe δ_{nc} as shown in Figure 35. With increasing *Sh*, δ_{nc} decreases in all cases studied; however, there are differences in governing factors with increased solution concentration or temperature. *Sh* describes mass transport and can be described as the ratio of overall mass transfer coefficient (*K*) to diffusive mass transport (*D/d*) [165] as seen in Equation 21. In order to determine the governing factors of the solution related to mass transport, normalized solution parameters are presented in Figure 39. All variables are normalized with respect to 1 M NaCl at 25 ˚C. With increasing chloride concentration at 25 ˚C (Figure 39(a)), *Sh* and *K* increase, however, D_{O_2} and δ_{nc} decrease. Although *K* increases roughly by a factor of 1.3, D_{O_2} decreases by a factor of 1.7 at 5.3 M NaCl, causing an overall increase in *Sh*. Thus, with increasing chloride concentration, a greater decrease in diffusive mass transport (D_{O_2}) in comparison to overall mass transport coefficient (*K*) causes an increase in *Sh* and a decrease in δ_{nc}. In other words, an increase in chloride concentration decreases δ_{nc} due to an increase in mass transport (*Sh*) with the dominating influence being a decrease in diffusive mass transport (D_{O_2}).

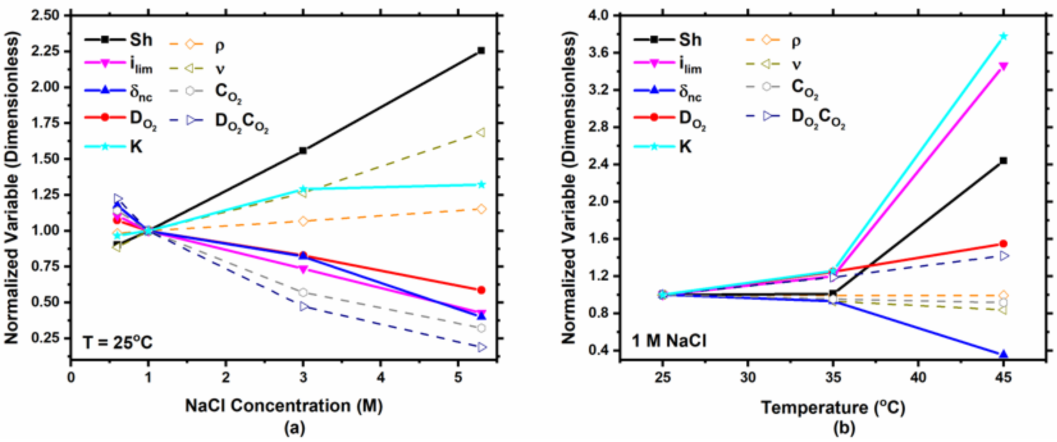

Figure 39: Normalized, measured solution properties for (a) various NaCl concentrations at 25˚C and (b) various temperatures at 1 M NaCl. All values were normalized to 1 M NaCl at 25˚C. It is noted that the ordinate is different between (a) and (b).

Considering the case of 1 M NaCl with increasing temperature, now the governing factor in determining δ_{nc} becomes a significant increase in overall mass transport coefficient (*K*). With increasing temperature at 1 M NaCl (Figure 39(b)), one can see that Sh, K, and D_{O_2} increase, however, δ_{nc} decreases. *K* increases by roughly a factor of 3.8 and D_{O_2} increases by a factor of 1.5 at 45 ˚C in comparison to 25 ˚C causing for an overall increase in *Sh*. Thus, with increasing temperature, a greater increase overall mass transport coefficient (*K*) in comparison in diffusive mass transport (D_{O_2}) causes for an increase in *Sh* and a decrease in δ_{nc}. In other words, an increase in temperature decreases δ_{nc} due to an increase in mass transport (*Sh*) with the dominating influence being a significant increase in overall mass transport coefficient (*K*).

It is important to note that the trend presented agrees with other studies of natural convection boundary layers in literature. Based on the work of Amatore et al. [154], *Sh* was calculated, and both *Sh* and corresponding δ_{nc} (250 µm) are plotted in Figure 35 and very good agreement is observed. Additionally, *Sh* can also describe δ_{nc} when ORR has a two electron transfer (such as in $MgCl_2$) [90] or less than two electron transfer (such as in NaOH) [92]. Thus, with the knowledge of *Sh* for mass transport in an electrochemical system, the unique fit presented in Figure 35 can be used to predict δ_{nc}.

3.5.3. High loading densities needed for atmospheric water layers to reach full immersion conditions

Calculated *WL* thicknesses (*LD* = 1 g/m^2) are at least an order of magnitude less than δ_{nc} and would require astronomically high *LD*s to reach bulk conditions. The *LD* under various conditions has been measured in multiple locations around Japan, as seen in Figure 40. Under external conditions, a *LD* under 1 g/m^2 is seen in most locations and is taken as an upper bound for typical atmospheric conditions. As presented Figure 41(a), the calculated *WL* thickness in atmospheric conditions (*LD* = 1 g/m^2, Figure 40) is much smaller than thin film conditions. Thus, in most atmospheric conditions, if a SS304L sample is polarized into the i_{lim} regime, a dependence of i_{lim} exists according to Equation 15. Above the high, calculated *LD* presented in Figure 41(b), there will be no dependence on i_{lim} and bulk conditions will be present in atmospheric environments.

While it is unlikely that under equilibrium conditions atmospheric conditions experience thin film conditions, it is possible that bulk conditions are present, at least transiently, under conditions such as salt spray or rain fall events. Therefore, for a typical atmospheric exposure, samples are likely to be under thin film, atmospheric conditions.

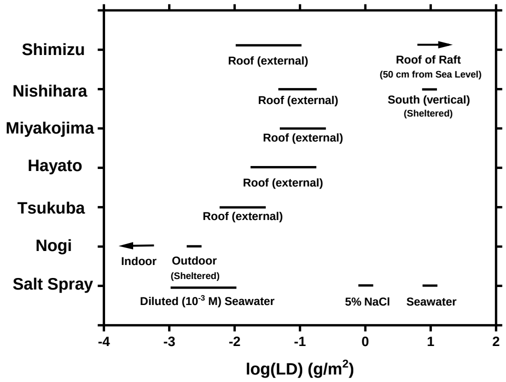

Figure 40:Loading density as a function of location in Japan. The graph is adopted from Shinohara [166].

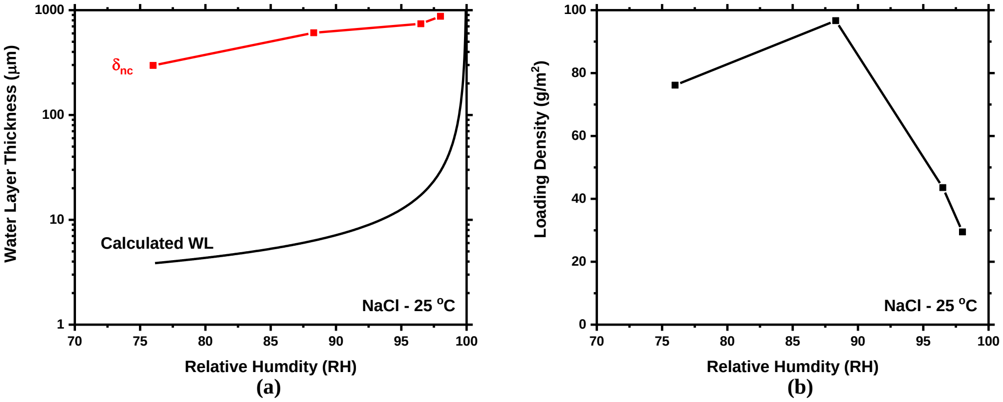

(a) **(b)**

Figure 41: (a) Comparison of natural convection boundary layer thickness and calculated atmospheric water layer thickness (LD = 1 g/m^2) for NaCl electrolytes at 25 ˚C. (b) Calculated loading density needed in atmospheric conditions to reach the natural convection boundary layer.

3.5.4. Bulk conditions are present in simulated, constant salt spray environments at increased sample angles

Samples exposed to ASTM B117 experience thin film environments at low angles (with respect to the vertical) and bulk conditions when exposed at high angles within the standard's specific conditions. A comparison of δ_{nc} and the *WL* thickness measured in accelerated testing is shown in Figure 42. At an exposure angle of 15˚, a sample would experience thin film conditions and a sample at 30˚ would experience both full immersion conditions and thin film conditions due to the transient behavior. Additionally, a stipulation in both ASTM B117 and other accelerated corrosion tests is that the tests may be interrupted on a daily basis [160,161,164] which will affect the *WL* drastically. Within ASTM B117, the test states that interruptions to an exposure can be made for a maximum of 60 min. per 24 hour period [160]. During interruptions, evaporation and run-off can occur and will decrease the *WL* thickness and can decrease the *WL* 18.5% of the original thickness during a 1-hour period. After 112 min of test interruption there was no detectable *WL*. Thus, in addition to the transient behavior causing thin film and full immersion conditions, test interruptions could also cause a sample to experience both regimes of *WL* thickness.

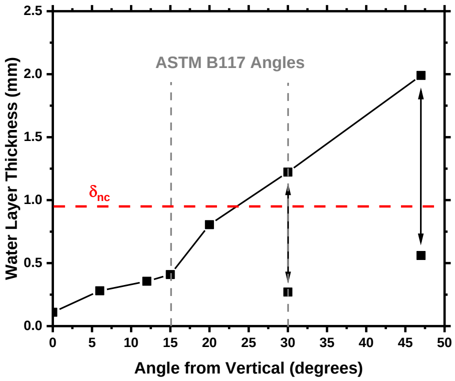

Figure 42: Comparison of the natural convection boundary layer with ASTM B117 accelerated testing WL thicknesses.

The variations that are allowable within ASTM standards can help explain test-to-test and chamber-to-chamber variability. One possible source of the discrepancy between standard chamber test results and service performance is the wide range of *WL* experienced, both thin film and bulk environments, in these tests due to angle of exposure and test interruptions. Additionally, it has been shown that atmospheric conditions are most commonly in thin film conditions (Figure 41) whereas salt spray conditions are in both thin film and bulk conditions (Figure 42). Thus, the applicability of ASTM B117 to atmospheric conditions may be limited due to the differences in *WL* thickness.

3.6. Conclusion

A summary of all *WL* investigated in this dissertation are presented in Figure 43. Starting with the smallest *WL* thickness, atmospheric deliquescence under equilibrium conditions typically ranges from 1 to 300 µm (Figure 33). Spanning roughly the same *WL* thickness is the *WL* induced by a RDE (Section 2.3.2) which ranges from 7 to 200 µm. The lower limit arises due to the fact that at sufficiently high rotation rates turbulent flow is induced and there is no longer a clearly defined boundary layer. The δ_{nc} spans a larger boundary layer thickness (142 to 873 µm) when compared to both atmospheric and RDE *WL* thicknesses. It is noted that the *WL* for δ_{nc}, atmospheric deliquescence, and RDE are dependent upon solution composition and concentration. Finally, the largest *WL* thickness was measured for accelerated corrosion testing scenarios which ranged from 400-1220 µm.

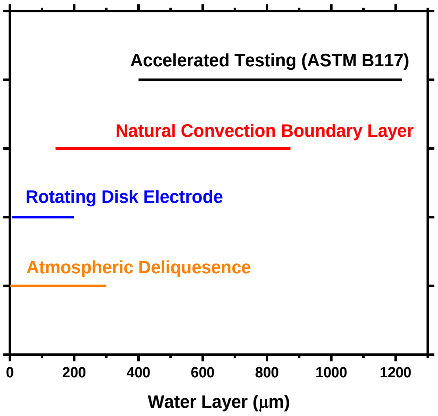

Figure 43: Comparison of water layer thicknesses across accelerated testing scenarios, natural convection boundary layer thicknesses, rotating disk electrode experiments, and atmospheric deliquescence.

The *WL* in various environments plays an important role due to the dependencies on i_{lim} as presented in Equation 15. Below the natural convection boundary layer, i_{lim} decreases and potentially cause an increase in the cathodic current available for dissolution. Therefore, in atmospheric deliquescence and RDE scenarios, an increase in total cathodic current is likely in comparison to bulk, full immersion conditions. In accelerated corrosion testing, the influence of WL on i_{lim} varies within the ASTM standards.

Overall, it is important to consider the influence of WL thickness and how the thickness changes with exposure environment (solution composition, solution concentration, deliquescing, and salt spray) as this is directly related to the cathodic current available for dissolution. It is noted that mixed salt solutions vary significantly than single salt solutions, especially at low RHs. Additionally, it is unlikely that under equilibrium conditions in atmospheric exposures, thin film conditions ($WL < \delta_{nc}$) will be present on the alloy surface. In salt spray conditions, both thin film and bulk conditions exists depending on the angle of exposure. Therefore, it is important to consider all of the variations present in WL thicknesses when modeling corrosion scenarios.

4. Anodic Kinetics: Determination of pit stability product and repassivation potential

4.1. Summary

Key parameters describing stable localized propagation, namely $(i \cdot x)_{sf}$ and E_{rp}, are measured and predicted for solutions commonly present in marine, atmospheric environments. With increased chloride concentration $(i \cdot x)_{sf}$ decreases and with increasing temperature $(i \cdot x)_{sf}$ increases. With increased chloride concentration and temperature, the temperature corrected E_{rp} decreases. Finally, sea-salt brines experienced both elevated values of $(i \cdot x)_{sf}$ and E_{rp} in comparison to both NaCl and $MgCl_2$. The values and trends in $(i \cdot x)_{sf}$ and E_{rp} are explained and are put into context of localized corrosion propagation

The work presented in this chapter has been reported in the following publications:

- **R.M. Katona**, A.W. Knight, E.J. Schindelholz, C.R. Bryan, R.F. Schaller, R.G. Kelly, Quantitative assessment of environmental phenomena on maximum pit size predictions in marine environments, Electrochim. Acta. 370 (2021) 137696. https://doi.org/10.1016/j.electacta.2020.137696.
- **R.M. Katona**, J. Carpenter, E.J. Schindelholz, R.G. Kelly, Prediction of Maximum Pit Sizes in Elevated Chloride Concentrations and Temperatures, J. Electrochem. Soc. 166. 2019 C3364–C3375. https://doi.org/10.1149/2.0451911jes.

4.2. Introduction

Localized corrosion is characterized by rapid penetration in discrete areas in an otherwise resistant surface and is separated into two forms: crevice corrosion and pitting corrosion. In comparison to generalized corrosion, the rate and extent of localized corrosion is often greater in small sheltered volumes, such as a crevice, created by contact with another material. In terms of pitting corrosion, the pit is a self-serving crevice that restricts transport between the bulk solution and the acidified chloride solution in the pit [55]. The electrochemical nature of corrosion processes implies that there are associated critical values for the dissolution flux and the potential characterizing this transition between stable dissolution and repassivation [8]. In order to describe pitting corrosion, there are typical parameters considered, including: $(i \cdot x)_{sf}$ and E_{rp}.

During propagation, the pit provides an occluded volume that hinders mass transport between the pit and the bulk solution. Within the pit, anodic dissolution produces metal cations (Me^{+}) that undergo hydrolysis through Equation 1 and results in an acidic solution destroying local passivity.

Pitting propagation is considered an autocatalytic mechanism and is coupled with Cl^- ion migration into the pit allowing charge neutrality to be maintained within the pit. At high Me^{+} concentrations the formation of a metal-chloride *sf* is possible. As the pit grows, the diffusion of the metal cations out of the pit is based upon the geometry and governs the current required for propagation [6,47]. A detailed analysis of pit chemistry changes on pit growth and stability was provided by Galvele [5,6]. By considering cation dissolution, outward diffusion, and thermodynamic equilibrium of various reactions, a factor known as the pit stability factor, xi where x is the depth and i is the current density, was proposed by Galvele and determines the current density needed for 1-D propagation at a given depth [6]. Thus, a shallow pit requires a high current density to maintain stability, whereas a deeper pit requires lower current density. This value can be determined experimentally; however, the value obtained is generally associated with current needed to maintain a salt film on the solution of the surface of the alloy and is denoted as $(i \cdot x)_{sf}$ [167]. Pitting has been observed to proceed stably at potentials far below those required for salt film formation [7,22,168–171] indicating full saturation of a salt film is not necessary for stable pit propagation. This indicates there is a critical value for the pit stability product, $(i \cdot x)_{crit}$, that is a fraction, f, of $(i \cdot x)_{sf}$.

The highest potential at which repassivation of a pit can occur is E_{rp}, and is defined as the potential below pits will no long propagate. The susceptibility of various alloys to localized corrosion has been examined primarily in terms of two potentials—the breakdown or the pitting potential (E_{pit}) and E_{rp}. The standard framework for pitting is that between the pitting potential E_{pit} and E_{rp}, new pits cannot form but initiated ones can still propagate. Below E_{rp}, pits cannot initiate and existing pits can no longer grow [8]. This experimentally determined value is highly dependent upon experimental conditions [47,55]; however, at high passed charge densities, E_{rp} has been shown to plateau [13–15]. More recently, by exploring the pH necessary for oxide precipitation in the acidic pit environments [172], it was proposed that E_{rp} can be determined through mixed potential theory based on local cathodic reactions occurring on the pit walls [8,172].

Overall, $(i \cdot x)_{crit}$ and E_{rp} represent two critical values for the propagation of a localized corrosion features. A current density is necessary at any given pit depth, as determined by $(i \cdot x)_{crit}$, and if this current density is not achieved the pit will repassivate. Additionally, if the potential of the pit decreases below E_{rp}, the pit can no longer propagate. It is critical that these two parameters are satisfied for stable propagation to occur. As was described in Section 1.2.2, a wide range of environmental conditions exist and can influence these two important parameters. Therefore, $(i \cdot x)_{sf}$ and E_{rp} as a function of environment were determined for SS304L. To aid in the discussion of these parameters, the saturation concentration of metal salt solutions was measured as a function of temperature.

4.3. Experimental

4.3.1. Artificial pit experiments

The $(i \cdot x)_{sf}$ and E_{rp} were determined for SS304L in multiple solution concentrations and temperatures. Solutions were temperature-controlled with an accuracy of $\pm$ 0.1°C. The diameter of the SS304L wire was 50 μm. The wire was embedded in epoxy so that the diameter of the wire was exposed with an area of 7.85×10^{-5} cm^2. The epoxy and wire were wet ground with 320 grit silicon carbide paper. A schematic of the lead-in-pencil configuration used can be seen in Figure 44.

Samples were placed in an electrochemical cell and an anodic potential of + 0.75 V_{SCE} was applied for 5 to 20 minutes to ensure pit initiation. The potential was stepped down to + 0.45 V_{SCE} for different periods of time to allow for pit propagation to different depths. A polarization scan from +0.45 V_{SCE} to -0.6 V_{SCE} at a scan rate of 5 mV/sec was performed. After the polarization scan, the pit was immediately re-initiated by polarization to +0.75 V_{SCE}, and the cycle was repeated. Eight to ten repetitions of the cycle were performed as it has been shown that the pit depth needs to exceed 8-10 times the diameter (~400-500 μm) to prevent measured values from being influenced by the hemispherical diffusion at the pit mouth [20].

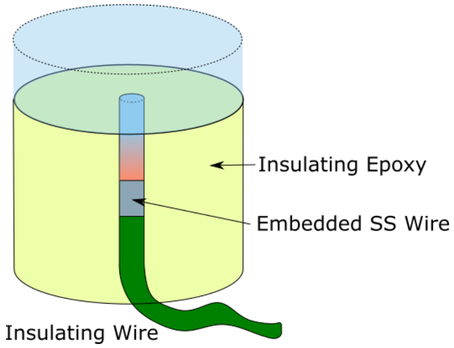

Figure 44: Schematic of lead in pencil configuration.

4.3.2. Determination of the pit stability product

Based on Fick's first law, the diffusion limited current density and pit depth under steady state conditions can be expressed as:

$$i_L d = nFD_{M^+}\Delta C = nFD_{M^+}C_{M^+} = (i \cdot x)_{sf} \qquad 23$$

where n is the number of electrons transferred, F is Faraday's constant $\left(F = 96{,}485\,\frac{C}{mol}\right)$, D_{M^+} is the diffusion coefficient of metal cations, and ΔC is the concentration difference of metal cations at the bottom of the pit and the bulk solution and it is assumed that the concentration at the mouth of the pit is zero at sufficiently deep pits [20]. Based on stoichiometric dissolution of the alloy used in this study, $n_{304} = 2.2$ [173]. It can also be shown that the pit stability product is related to the bulk chloride concentration ($C_{bulk,Cl}$) and the diffusivity of chloride (D_{Cl}) through

$$(i \cdot x)_{saltfilm} = FD_{Cl}nC_{M^+} - FD_{Cl}C_{bulk,Cl} \qquad 24$$

Successive polarization scans allow for the extraction of the limiting current density (i_L) as well as the E_{rp}, as a function of pit depth. Thus, based on Equation 23, plotting the limiting current densities against the reciprocal of the pit depth $(1/d)$ will determine $(i \cdot x)_{sf}$ via the slope of the curve. During the change in potential, the nominal change in current density was small, demonstrating that the reaction was under diffusion-limited conditions.

In order to determine the pit depth, the total anodic charge density during the potentiostatic holds and cathodic polarizations were converted to pit depth. Using Faraday's law for alloys, d can be expressed as:

$$d = \frac{A}{nF\rho} \int_0^t i \, dt \tag{25}$$

Where i is the current density, A is the mean atomic weight ($A_{304} = 55.3\ g/mol$), ρ is the density ($\rho_{304} = 7.8\ g/cm^3$), and dt are infinitesimal time steps [22,173]. These calculations were made assuming stochiometric dissolution of Fe^{2+}, Cr^{3+}, and Ni^{2+}.

4.3.3. Determination of the repassivation potential

The value of E_{rp} was determined by the computer script as the potential during the linear polarization scan at which the values of *Z %* of the next *N* current density data points in the scan were lower than 30 μA/cm^2 as it serves as an unbiased method to calculate E_{rp}. In the present study, *Z* and *N* were set to 70% and 30 points, respectively, in accordance with Srinivasan et al. [16]. The collection rate was 10 points per second. The difference between the measured open circuit potential and E_{rp} under these specified conditions and algorithm parameters was typically less than 2 mV and not greater than 15 mV. This method serves as an unbiased, rational means to determine when the potential has reached a relatively constant value, which is deemed E_{rp}. It is noted that no temperature corrections were made for E_{rp} measurements.

4.3.4. Determination of the metal salt saturation concentration

Saturation concentrations of metal salts ($C_{M^+}^{sat}$) were determined with a procedure similar to that of Chou and Phan [174]. Briefly, metal chloride salt mixtures containing stoichiometric amounts for 304L of Fe^{2+}, Cr^{3+}, and Ni^{2+} were created . $FeCl_2\cdot(4H_2O)$, $CrCl_3\cdot(6H_2O)$, and $NiCl_2$ of analytical grade were weighed and added to a Pyrex® tube. DI-Water ($18.2\ M\Omega.cm$) was added to the tube to an approximate volume of 20 mL. A stir bar was placed in the bottom of the tube. Approximately

5 mL of silicon oil was added to the top of the solution in order to prevent evaporation. The top of the beaker was then sealed with a rubber stopper and filled with a positive pressure of N_2 gas in order to minimize the oxidation of Fe^{2+} ions to Fe^{3+} ions. The solution was then placed in a water bath, heated to above 60°C, and then slowly cooled to room temperature in order to nucleate large salt crystals. The solution was then systematically heated, incrementing first with large differences in temperature and then by ±0.1°C when the solution was close to the saturation point and subsequent dissolution. Time steps of at least 5 min were taken with each temperature increase near saturation. A bright light illuminated the bottom of the test tube in order to help visualize when the last crystal was dissolved. At this point the temperature was recorded. The pH was then measured within 2 minutes corresponding to a maximum measured difference in temperature of 5°C. It is noted that there was no temperature correction for the pH. This process was repeated until a concentration curve was created spanning the temperature range (25-55 °C).

4.4. Results

4.4.1. Increasing chloride concentration decreases pit stability product

For NaCl, MgCl2, and sea-salt brines at 25 ˚C, increasing chloride concentration decreases $(i \cdot x)_{sf}$ as presented in Figure 45. At nearly 10 M Cl^-, $(i \cdot x)_{sf}$ is 0.02 A/m. It is also interesting to note that at equivalent chloride concentrations, $(i \cdot x)_{sf}$ increases from NaCl < $MgCl_2$ < sea-salt brines.

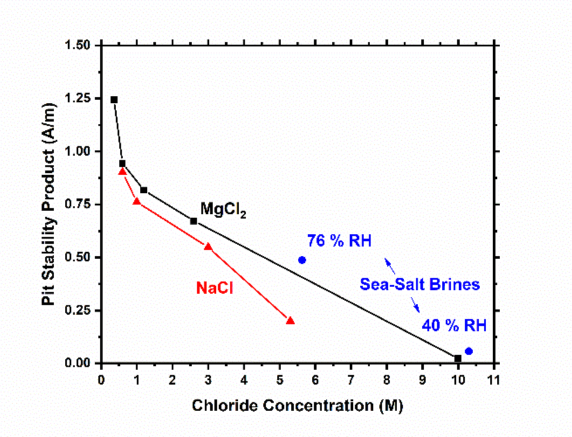

Figure 45: Pit stability product under a salt film as a function of chloride concentration and composition at room temperature. It is noted that the absicca is total chloride concentration.

4.4.2. *Increasing temperature increases pit stability product*

For NaCl solutions, increasing the temperature from 25 to 55 ˚C increases $(i \cdot x)_{sf}$ by roughly a factor of 1.6 at all chloride concentrations as presented in Figure 46. At all temperatures, increasing chloride concentration decreases $(i \cdot x)_{sf}$ with a near linear trend.

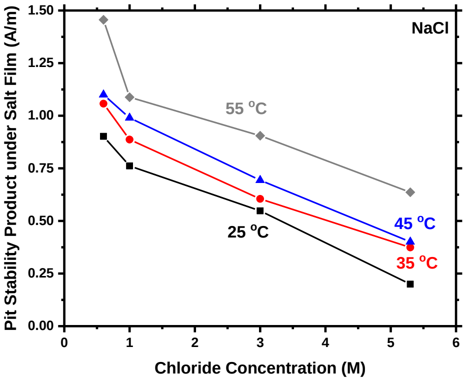

Figure 46: Pit stability under a salt film as a function of chloride concentration and temperature for a sodium chloride electrolyte.

At 35 ˚C, an increase in $(i \cdot x)_{sf}$ is also calculated for $MgCl_2$ and sea-salt brines (Figure 47(a)) in comparison to 25 ˚C (Figure 45). It is also noted that at 35 ˚C, $(i \cdot x)_{sf}$ increases from NaCl < $MgCl_2$ < sea-salt brines at similar chloride concentrations. The same trends exist for $MgCl_2$ at 45 ˚C in that increasing chloride concentration decreases $(i \cdot x)_{sf}$ and that $(i \cdot x)_{sf}$ increases from NaCl < $MgCl_2$.

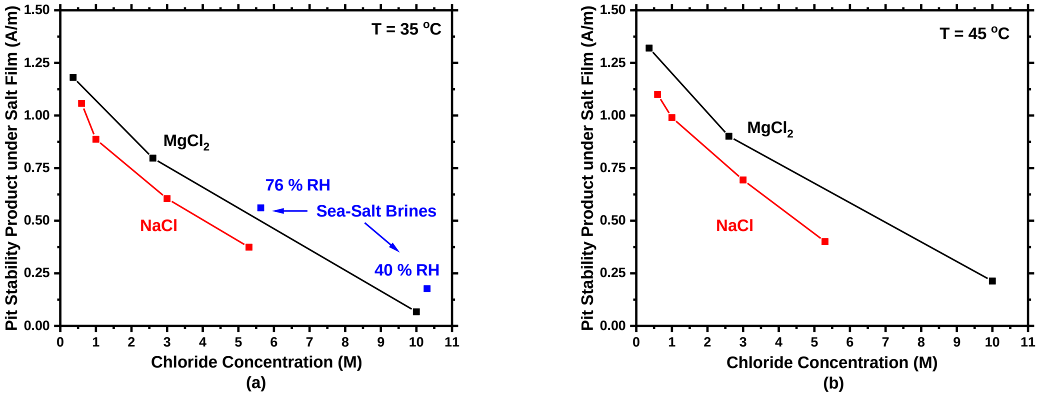

Figure 47: Pit stability product under a salt film as a function of chloride concentration and composition at (a) 35 and (b) 45 ˚C.

4.4.3. Decrease in repassivation potential with increase in chloride concentration and decrease in temperature

With increasing chloride concentration, a decrease in E_{rp} is measured for NaCl (Figure 48), MgCl2, and sea-salt brines (Figure 49) at all temperatures explored (25 – 55 ˚C). Additionally, with increasing temperature, an increase in E_{rp} is measured in all solutions (Figure 48 and Figure 49). It is noted that the reported E_{rp} measurements are at temperature and no corrections were made to the reference electrode potential.

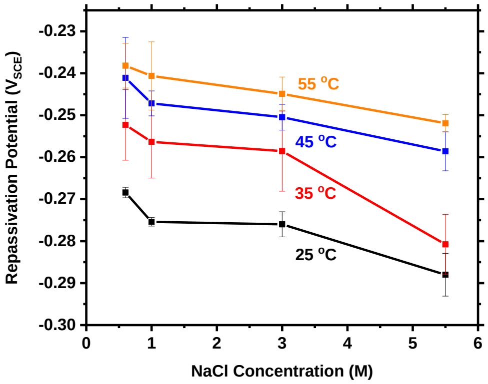

Figure 48: Influence of chloride concentration and temperature on the repassivation potential for sodium chloride solutions. It is noted that there are no temperature corrections for the reference electrode.

It is interesting to note that the E_{rp} for sea-salt brines is elevated at both 25 and 35 ˚C in comparison to both NaCl and $MgCl_2$ solutions as presented in Figure 49(a) and (b) respectively.

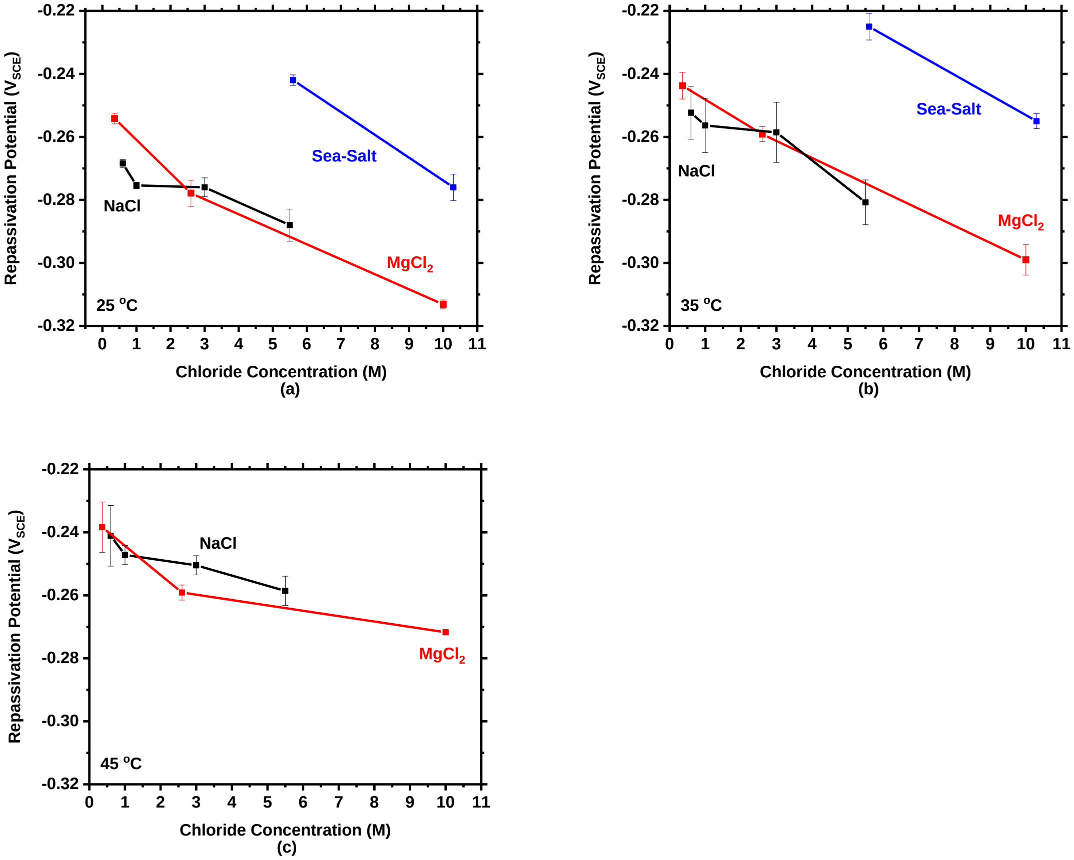

Figure 49: Influence of chloride concentration and solution composition at (a) 25, (b) 35, and (c) 45 ˚C. It is noted that there are no temperature corrections for the reference electrode.

4.4.4. Saturation concentration increases with increasing temperature

In Figure 50(a) an increase in saturation concentration with increased temperature was measured. A saturation molality of 4.81 mol/kg is observed at a temperature of 24.7°C and increases to 6.05 mol/kg at 58.9°C. The molality is reported instead of molarity as the error in volume measurements was too substantial and yielded a molarity with a high corresponding error.

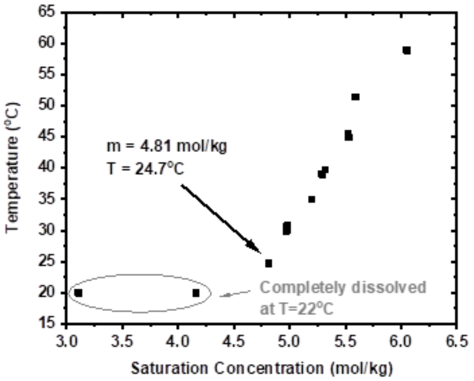

Figure 50: Saturation concentration as a function of temperature for a ternary salt mixture corresponding to the stoichiometric dissolution of SS304L.

4.5. Discussion

4.5.1. Pit stability product decreases with increasing bulk chloride due to a decrease in saturation concentration and metal ion diffusivity

Ernst and Newman [168] have shown that with increasing bulk chloride concentration, the saturation concentration decreases due to the common ion effect. It was shown that the saturation concentration can be calculated with $K_{sp} = [Me^{n+}][Cl^{-}]^{n}$, where K_{sp}, the solubility product, as determined from the saturation concentration in Figure 50 with no bulk NaCl present. Bulk chloride concentrations were converted to molality based on their density at temperature as calculated in OLI Studio. A saturation curve was then created based on both temperature and the impact of bulk chloride concentration. As seen in Figure 51, C_{sat} decreases with increasing bulk chloride concentration due to the common ion effect. Additionally, following the logic set forth by the Stokes-Einstein equation and work done by Ernst and Newman [168] the diffusivity of metal cations is also going to decrease with increasing bulk chloride. Thus, as $(i \cdot x)_{sf}$ is an equivalent expression to $D_{M^+}C_{M^+}^{sat}$ (Equation 23), a decrease in $(i \cdot x)_{sf}$ is expected.

Although K_{sp} is a rather simplified expression for considering the effect of bulk chloride concentration, it is useful in understanding the overall effects of bulk concentration. Along with this, other models have looked at the influence of bulk cations (i.e. Na^{+}) on the $(i \cdot x)_{sf}$ or $D_{M^+}C_{M^+}^{sat}$. Of particular note, Jun et al. calculated effective diffusivities and modified saturation concentrations based on a variable pit viscosity. It was reported that the presence of up to 0.83 M Na^+ at the pit bottom only lowered the solubility by roughly 10 % due of the common ion effect. Additionally, modeling results indicated a low concentration of Na^+ at the bottom of the pit [175,176]. More recently Nguyen and Newman were able to decouple influences on $D_{M^+}C_{M^+}^{sat}$ due to bulk chloride concentrations under dilute conditions. They noted that in moderate to concentrated solutions, the presence of Na^+ at the bottom of the pit is significant, causing a higher potential gradient inside the pit to transport additional chloride for the charge neutrality while maintaining the critical concentration of dissolving metal ions for the pit stability. Therefore, the flux of metal cations is increased, leading to a higher value of $(i \cdot x)_{sf}$ when Na^+ is considered in the mass-transport model [177]. In all cases, increasing the bulk solution composition will decrease both D_{M^+} and $C_{M^+}^{sat}$ to various degrees based on modeling assumptions and will decrease $(i \cdot x)_{sf}$.

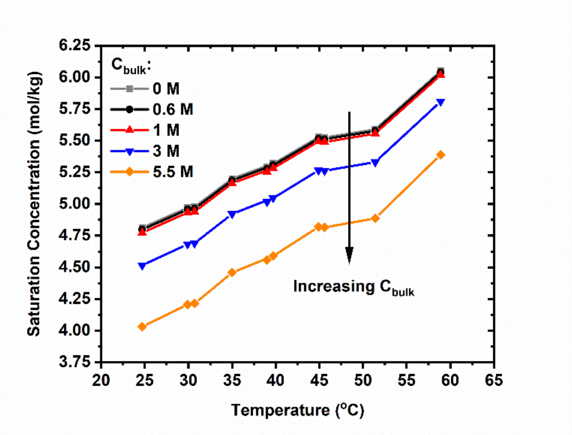

Figure 51: Metal ion saturation concentration corrected for bulk NaCl concentrations by using the common ion effect. It is noted that the bulk chloride concentrations are reported in in molarity, however, were converted to molality based on density calculated in OLI Studio.

Decreasing $(i \cdot x)_{sf}$ with increasing chloride concentration will enhance pitting propagation. While there are many factors that can affect current available for dissolution, if a constant current was assumed, then increasing chloride concentration requires less current at any given depth to maintain the aggressive environment. In other words, it will be harder for the pit to repassivate at higher chloride concentrations.

4.5.2. Pit stability product increases as a function increasing temperature due to an increase in

saturation concentration and metal ion diffusivity

Following the same logic as Section 4.5.1 increases in D_{M^+} and $C_{M^+}^{sat}$ with increasing temperature will cause for an increase in $(i \cdot x)_{sf}$. It has been shown in Figure 50 that with no bulk chloride an increase in temperature increases $C_{M^+}^{sat}$. Additionally, as shown in Figure 51, $C_{M^+}^{sat}$ increases with increasing temperature regardless of bulk chloride concentration. Along with this, based on the Stokes Einstein Equation [176,178,179], the diffusivity of metal cations is expected to increase with temperature. Therefore, increasing temperature will increase both D_{M^+} and $C_{M^+}^{sat}$ at all chloride concentrations and will increase $(i \cdot x)_{sf}$.

When solely considering $(i \cdot x)_{sf}$, increasing temperature will diminish pit propagation. Again, considering a constant current supply, increasing temperature would require an enhanced current density causing repassivation at a smaller pit size. As an increased saturation concentration at increased temperatures is present, the elevated diffusion will serve to dilute the aggressive chemistry and help the pit repassivate.

4.5.3. Influence of bulk cation on pit stability product

In $\mathrm{MgCl_2}$ and sea-salt brines, an increase in $(i \cdot x)_{sf}$ is measured in comparison to NaCl solutions at both 25 ˚C (Figure 45) and at elevated temperatures (Figure 47) at equivalent chloride concentrations. First, considering D_{M^+}, an increase in η is present in $\mathrm{MgCl_2}$ solutions in comparison to NaCl solutions (Figure 15(b)). Based on the Stokes-Einstein relationship [176,178], increasing η would decrease D_{M^+} and cause for a decrease in $(i \cdot x)_{sf}$. Therefore, an increase in η would not be responsible for the increase in $(i \cdot x)_{sf}$. Now considering $C_{M^+}^{sat}$, Nguyen and Newman introduced the idea that a higher potential gradient inside the pit is required to transport additional chloride for charge neutrality increasing the overall flux of metal cations, leading to a higher value of $(i \cdot x)_{sf}$ when $\mathrm{Na^+}$ is considered in the mass-transport model [177]. The increase in flux is proposed to be increased enhanced for salts with higher ionic charges and/or at higher bulk concentration. It is possible that the higher ionic charges cause for an increase in $(i \cdot x)_{sf}$ in MgCl2 and sea-salt solutions in comparison to NaCl solutions; however, further research is necessary and is identified as an area for future research.

While the exact reason for an increase in $(i \cdot x)_{sf}$ is present for $MgCl_2$ and sea-salt brines in comparison to NaCl, it has important implications for modeling localized corrosion. A higher $(i \cdot x)_{sf}$ indicates that at any given pit depth, a higher current density is needed in order to maintain an aggressive environment for pitting. Thus, under a constant current supply, sea-salt solutions will have the lowest pit size followed by $MgCl_2$ and NaCl as the most current density is needed for propagation in sea-salt brines.

4.5.4. Repassivation potential trends explained by competitive process of metal salt or oxide formation

The dependence of E_{rp} with chloride concentration has long been recognized [180]. Anderko and co-workers presented a general model for E_{rp}. The model assumes the status of localized corrosion is determined by competitive processes at the metal–salt film–solution interfaces leading to metal salt or oxide formation and the authors recognized multiple important trends for various alloys. First, with increasing chloride activity (concentration), a decrease in E_{rp} is predicted. Next, with increasing temperature, a decrease in E_{rp} is calculated. Finally, it was noted that increasing amounts of nitrates and sulphates at a given chloride activity (concentration) increase E_{rp} [180]. The formulism for predicting E_{rp} [180] has been incorporated into OLI Studio and predictions of E_{rp} were made for both NaCl solutions at 25 and 55 ˚C and are presented in Figure 52(a). It is noted that measured E_{rp} values at 55 ˚C were corrected for temperature influences. Overall, a similar trend of E_{rp} as a function of chloride concentration exists for both the measured and modeled values at both temperatures. Additionally, the measured E_{rp} for 25 ˚C falls below the modeled E_{rp} while the opposite trend exists for 55 ˚C when corrected for temperature. While E_{rp} was corrected for temperature, it was noticed during experimentation that the reference electrode did not have salt crystals, due to differing solubility of salt with an increase in temperature and could have further influenced the measured E_{rp}.

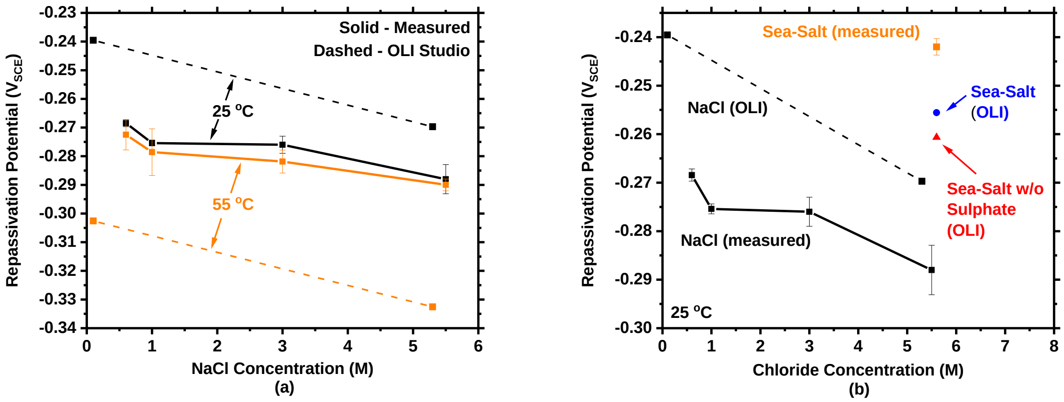

Figure 52: (a) Comparison of measured repassivation potential to calculated repassivation potential (OLI Studio) for NaCl electrolytes. It is noted that the measured repassivation potential at 55 ˚C is temperature corrected. (b) Comparison of the calculated and measured repassivation potential for NaCl and sea-salt solutions at 25 ˚C.

Predicted E_{rp} are also presented in Figure 52(b) for sea-salt solutions at an RH of 75 % and 25 ˚C. In general, an increase in E_{rp} is predicted for sea-salt brines in comparison to pure NaCl solutions which is the same trend for the measured values. An additional prediction of E_{rp} was made with and without sulphate present in the sea-salt brine and an increase in E_{rp} was predicted when sulfate was included in the brine indicating that the addition of inhibitive substances in sea-salt could serve to increase E_{rp}. Overall, similar trends are present between modeled and measured E_{rp} values further supporting Anderko et al.'s model exploiting the competitive processes at the metal–salt film–solution interfaces leading to metal salt or oxide formation [180].

Increasing chloride concentration, decreases E_{rp} facilitating pitting corrosion. This is a similar trend for $(i \cdot x)_{sf}$. With increased temperature, a decrease in correct E_{rp} Figure 52(a) was measured potentially increasing the potential range that pitting can occur. This is opposite the trend of $(i \cdot x)_{sf}$ and could potentially of set corrosion propagation. Finally, both $(i \cdot x)_{sf}$ and E_{rp} are increased for sea-salt solutions in comparison to NaCl and $MgCl_2$ solutions at all temperatures explored indicating that pit propagation may be hindered by inhibiting spectator ions in sea-salt solutions.

4.6. Conclusions

Two critical parameters, namely $(i \cdot x)_{sf}$ and E_{rp}, describing the stable propagation of localized pitting corrosion were determined for multiple environments on the surface of an alloy in atmospheric, marine conditions. With increasing chloride concentration $(i \cdot x)_{sf}$ decreases due to a decrease in $C_{M^+}^{sat}$ (common ion effect) and a decrease in D_{M^+}. With increasing temperature, $(i \cdot x)_{sf}$ increases due to an increase in $C_{M^+}^{sat}$ (common ion effect) and an increase in D_{M^+}. With increased chloride concentration and temperature, the temperature corrected E_{rp} decreases and can be explained by the general repassivation model presented by Anderko et al. [180].

As both $(i \cdot x)_{sf}$ and E_{rp} describe the anodic propagation of pitting corrosion, it is important to consider these two parameters together. As in section 4.5, a constant current will be considered across presented scenarios although this may not be the case for atmospheric scenarios. With increased chloride concentration, both $(i \cdot x)_{sf}$ and E_{rp} decrease and will synergistically provide for larger localized corrosion features. With increased temperature, an increase in $(i \cdot x)_{sf}$ was measured and a decrease in corrected E_{rp} were measured, potentially off-set the two influences. While pitting corrosion would be allowed at a lower potential, a higher current density would be needed to maintain the aggressive environment. The influence of temperature will further be explored for localized corrosion in Section 5. Finally, both $(i \cdot x)_{sf}$ and E_{rp} are increased for sea-salt solutions in comparison to NaCl and $MgCl_2$ solutions at all temperatures explored indicating that pit propagation may be hindered in sea-salt solutions.

5. Cathodic and anodic control of corrosion in atmospheric environments

5.1. Summary

Maximum pit sizes on SS304L and the total current in a AA7050/SS304L galvanic couple were predicted in environments relevant to atmospheric exposures. It is important to note that conclusions made encompass the temperature (25 – 45 ˚C) and chloride concentration ranges (0.189 M to saturated) explored in this dissertation. The controlling factors when increasing temperature and chloride concentration on total cathodic currents were identified. Cathodic kinetics are enhanced with an increase in temperature due to an increase in κ, an increase in D_{O_2}, and an increase in activation controlled kinetics causing for an increase in the current density and a decrease in the overall ohmic drop in the system. With increasing chloride concentration, a decrease in in C_{O_2}, D_{O_2} and equilibrium WL thickness will cause for a decrease in the cathodic kinetics. While κ increases, decreasing overall ohmic drop in the system, the decrease in the overall current density governed by the aforementioned parameters will be greater.

While individual dependencies on the cathodic current can be ascertained, when cathodic currents are combined with the anodic demand, further complex dependencies arose changing dominating parameters. First, when exploring a similar chloride concentration (RH) such as a comparison between $MgCl_2$ and sea-salt brines, the controlling factors decreasing the cathodic current is the WL thickness and is combined with an increase in $(i \cdot x)_{sf}$ to decreasing the maximum pit size. Second, when increasing temperature, an increase in cathodic capacity due to increases in κ and D_{O_2} but is offset in by an increase in $(i \cdot x)_{sf}$ (assuming the fraction of saturation does not change with temperature) and will not significantly change the predicted pit sizes. Next when considering an increase in chloride concentration in different compositions (i.e., saturated NaCl and $MgCl_2$), the suppression of cathodic kinetics due to an overall decrease in i_{eq} and WL thickness outweighs the decreased anodic demand, decreasing predicted max pit sizes. Finally, when increasing chloride concentration when the composition is the same (i.e., 0.6 vs. 5.3 M NaCl), while the cathodic kinetics are suppressed, again due to a decrease in i_{eq} and WL thickness, $(i \cdot x)_{sf}$ decrease much more and causes for an increase in the predicted maximum pit size. Finally, maximum pit size predictions were made when accounting for precipitation of species in the cathode. Predictions were improved when precipitation was incorporated into the model and was confirmed by comparing maximum pit size predictions to two-year exposures.

While there are many different controlling mechanisms for corrosion, the importance of cathodic reactions in atmospheric environments is undeniable. The assumption of an ideal cathode provides a powerful theoretical limit of cathodic current and allows for the calculation of a maximum pit and identification of controlling variables for a given set of environmental conditions. Despite being overconservative by roughly a factor of two, the formulism of the max pit model allows for the identification of governing parameters. The same governing parameters identified using the maximum pit formulism have also been identified as important in FEM simulations again showing the applicability of the maximum pit model and the importance of cathodic reactions in atmospheric environments.

- **R. M. Katona**, J. C. Carpenter, A. W. Knight, R. S. Marshall, B. L. Nation, C. R. Bryan, E. J. Schindelholz, R. F. Schaller, and R. G. Kelly, *Natural convection boundary layer thickness at elevated chloride concentrations and temperatures and the effects on a galvanic couple*. Journal of the Electrochemistry Society. 2021. Editors Choice. https://doi.org/10.1149/1945-7111/abeb29
- **R.M. Katona**, A.W. Knight, E.J. Schindelholz, C.R. Bryan, R.F. Schaller, R.G. Kelly, Quantitative assessment of environmental phenomena on maximum pit size predictions in marine environments, Electrochim. Acta. 370 (2021) 137696. https://doi.org/10.1016/j.electacta.2020.137696.
- **R.M. Katona**, J. Carpenter, E.J. Schindelholz, R.G. Kelly, Prediction of Maximum Pit Sizes in Elevated Chloride Concentrations and Temperatures, J. Electrochem. Soc. 166. 2019 C3364–C3375. https://doi.org/10.1149/2.0451911jes.
- R. S. Marshall, **R. M. Katona**, M. A. Melia, R. G. Kelly, Pit Stability Predictions of Additively Manufactured SS316 Surfaces Using Finite Element Analysis. In Preparation. 2021.

5.2. Introduction

The RH, *LD*, and exposure location control the composition, volume, and other properties of the resultant brine, and will impact anodic and cathodic corrosion kinetics [46,132]. It is necessary to understand the quantitative impacts of the brine properties and evolution on anodic and cathodic kinetics in order to inform upon SS degradation. Additionally, there is an increasing demand for the accurate prediction of localized corrosion damage and computational models can provide a powerful means to simulate the propagation of localized corrosion in multiple exposure environments. Various models have been developed to predict localized corrosion including analytical models [24,28,29,45], Finite Element Models (FEM) [26,38,39,141,181,182], and phase field models [43,44]. Each modeling technique has advantages and disadvantages that are beyond the scope of this dissertation to discuss. However, regardless of the method, the evolution of brine chemistry as corrosion occurs has proven to be difficult to capture. In atmospheric scenarios, ORR is typically assumed to be the cathodic reduction reaction and a by-product of such a reaction is the hydroxyl ion (OH^-) which causes a rise in cathodic pH [40]. In certain solutions, such as sea-salt brines or $MgCl_2$, a pH rise will cause the precipitation of hydroxide-containing species in the cathode [90,129]. Additionally, loss of brine components to solids results in the dehydration of the brine, influencing cathodic properties in thin *WL* thicknesses [183–185]. As such, it is important to account for these precipitates and effects on cathodic and anodic processes in models.

Typically, models considering brine evolution only account for precipitation from anodic species. Notably, Ansari et al. modeled the effects of insoluble corrosion products from pit dissolution and found enhanced iron concentrations and decreased pH in the pit when considering insoluble corrosion products [43]. Yin et al. explored the effects of metal ions from dissolution precipitating in the brine on the corrosion of aluminum alloys leading to a decrease in the overall corrosion rate which can stifle the growth of localized corrosion sites [38]. Further work showed steric hindrance leads to reduced current densities and oxygen flux to the surface [39].

Models are also normally restricted to dilute chloride systems [39,42–45] which are representative of high RH atmospheric conditions [46] and may not be realistic for many (it not most) atmospheric scenarios of interest. Furthermore, the bulk of the models in literature focus on the precipitation of metal hydroxides from dissolution and do not consider precipitation of solution species. Finally, most models do not consider ORR to be a limiting reaction or consider atmospheric scenarios.

Therefore, presented models in literature do not represent the scenario of interest or incorporate all reactions of interest.

One such model that can be modified in order to account for the phenomena of interest is an analytical model proposed by Chen and Kelly for bounding pit sizes [24] and has been utilized by to predict pit sizes in sodium chloride (NaCl) [179] and ferric chloride solutions [54]. The analytical model relies on ohmic drop considerations in the thin electrolyte film to limit the cathodic current supply. Through the inherent coupling of the cathode and anode, a finite cathode implies a finite anode (i.e., a finite pit size). Finding the maximum pit size can be achieved by determining: (i) the maximum cathode current the external surface can generate, and (ii) the minimum dissolution current needed to maintain the critical chemistry in the pit as a function of the pit size. Combining these two relations results in an expression for the maximum pit size obtainable under the given conditions. As such, cathode properties can be updated as a function of metal dissolution and can help determine the influences of cathode evolution on maximum pit sizes.

Finally, when dissimilar alloys are present under an electrolyte and in electrical contact, a galvanic couple forms and, in combination with the *WL* thickness and composition, serves as another controlling factor that can influence corrosion. The *WL* will influence both diffusional kinetics at the cathode and ohmic drop in solution between the anode and cathode, affecting the total amount of cathodic current available to drive dissolution at the anode [60,143,186–189]. However, synergies often exist between the cathode and anode and a majority of the work to date has focused primarily on either one or the other of these two regions. Therefore, FEM will be utilized to investigate environmental influences and identify governing factors for atmospheric corrosion in a galvanic couple.

The goal of this section is as follows: (i) ascertain the effects of solution chemistry, as a function of chloride concentration (from dilute to concentrated), composition, and temperature on maximum pit size predictions, (ii) explore cathode size evolution phenomena and determine significant reactions and defining parameters, (iii) compare maximum pit size predictions to exposure tests, (iv) understand cathodic currents in a galvanic couple between SS304L and an aluminum alloy (AA) 7050-T7451 across varying *WL* thicknesses, chloride concentrations and temperatures, and (v) compare and contrast governing phenomena for maximum pit size predictions and FEM modeling. As a result, improved predictions to inform material degradation in atmospheric environments will be ascertained and important parameters for future investigation will be identified.

5.3. Methods

5.3.1. Max pit model

Pits grow only if the anodic dissolution rate is sufficiently high that it can replace aggressive solution lost by diffusion. One quantitative model for understanding the anodic kinetics required for pitting was set forth by Galvele [6] and yielded $(i \cdot x)_{sf}$. The critical value of this parameter is related to the degree of saturation required to maintain stable propagation. A more in-depth discussion of this critical value is available elsewhere [7,22,168–171]. Given a measurement of $(i \cdot x)_{crit}$ [24], the current, I_{LC}, required for a pit of radius r_a to grow can be calculated:

$$I_{LC} = 3\,(i \cdot x)_{crit} * r_a = \left(\frac{I_{pit}}{r_{pit}}\right)_{crit} r_a \qquad 26$$

This expression represents the *minimum* current required to produce metallic cations for hydrolysis at a rate sufficient to maintain a low pH acting against dilution by diffusion. It is also important to account for the fact that there exists a lower bound of potential below which pits cannot grow, E_{rp}, as demonstrated by Dunn et al. [13]. Both $(i \cdot x)_{sf}$ and E_{rp} were determined in Section 4.

Cathode Kinetics – Under freely corroding conditions, anodic currents must be matched by cathodic currents according to Mixed Potential Theory. Reduction reactions relevant to localized corrosion often have sluggish kinetics, thus requiring increased cathodic polarization to supply higher currents. The bounds for the potential of the cathode for a pitting system are the open circuit potential (E_{ocp}) and E_{rp} which is assumed to exist at the mouth of the pit. The cathodic kinetics within these bounds are the only ones that can provide the current needed to match I_{LC}. When current is passed through an electrolyte, ohmic drop occurs. In atmospheric environments, the electrolyte generally has limited dimensions and, therefore, small currents can lead to substantial ohmic drop along the cathode with the highest current cathodic current density close to the pit mouth (most active potential). As the distance from the pit increases, the potential increases until the position at which the E_{ocp} is reached. Beyond this point, no cathodic current is available to support pit growth as it is consumed by the local passive dissolution.

Calculation of Maximum Cathode Current Available – Calculation of the maximum cathodic current starts with the consideration of the shown schematically in a three-dimensional representation as well as a two-dimensional cross section of this set up can be seen in Figure 53 and Figure 54 respectively. The anode radius is r_a and the radius of the cathode is r_c, where r_c is much larger than r_a, thus $r_c - r_a \cong r_c$. It is noted that the anode radius is the same as the depth of a pit given the assumption that the pit is hemispherical.

Given the cathodic kinetics, the potential bounds, and solution conditions (WL, κ), the total cathodic current that can possibly be drawn by an area of cathode is equal to the mean cathodic current density multiplied by the area of the cathode,

$$I_{cath} = i_{eq} S_{ceq} = i_{eq} \pi r_{eq}^2 \qquad 27$$

where i_{eq} is the equivalent current density, S_{ceq} is the equivalent cathode area, and r_{eq} is the equivalent cathode radius. i_{eq} is equal to the average current density over the potential range from E_{corr} to the potential closest to the pit mouth, E_{rp}, and is given by

$$i_{eq} = \frac{\int_{E_{corr}}^{E_{rp}} \left(i_c - i_p \right) dE}{E_{corr} - E_{rp}} \qquad 28$$

where i_c is the cathodic current density and i_p is the passive current density of the cathode. The radial current path leads to a potential drop (dE) across the differential annular element according to

$$dE = i_{eq}(\pi r_{eq}^2 - \pi r^2)\frac{dr}{\kappa WL 2\pi r} \tag{29}$$

The potential drop (ΔE) is given by integrating Equation 29 from the edge of the cathodic area to the edge of the anodic area,

$$\Delta E = \frac{i_{eq} r_{eq}^2}{2\kappa WL}\left[\ln\left(\frac{r_{eq}}{r_a}\right) - \frac{1}{2}\right] \tag{30}$$

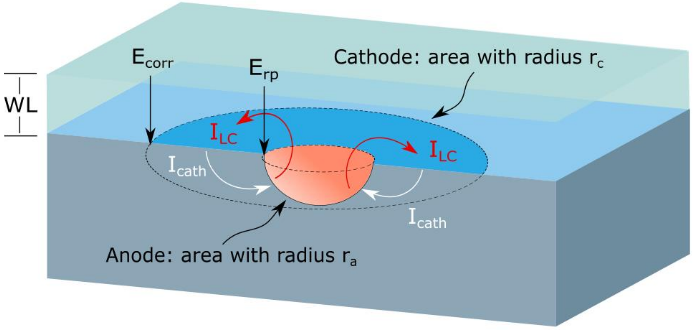

Figure 53: Three-dimensional representation of the anode and cathode galvanic couple under a thin electrolyte layer.

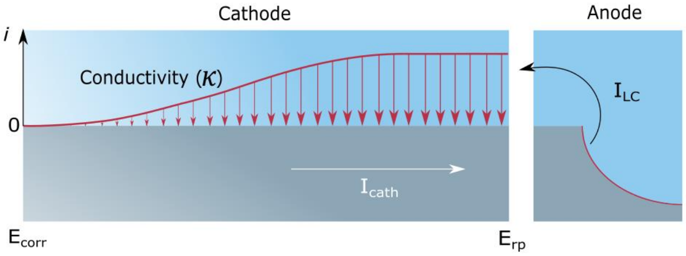

Figure 54: Two-dimensional cross-section of view of galvanic couple. It is noted that the ohmic drop in solution is schematically shown. The highest cathodic current is close to the pit mouth (at E_{rp}) and decreases with increasing radial distance from the pit to a point where no further cathodic current can support anodic growth (at E_{corr}).

By solving Equation 27 for r_{eq} and substituting into Equation 30 one obtains

$$\ln I_{cath} = \frac{4\pi\kappa WL\Delta E}{I_{cath}} + \ln\left[\frac{\left(\pi e r_a^2 \int_{E_{corr}}^{E_{rp}} \left(i_c - i_p\right) dE\right)}{\Delta E}\right] \tag{31}$$

where e is Euler's number. The value of I_{cath} cannot be solved for directly, thus it is solved numerically. In a similar way,[24] an expression for equivalent cathode area can be obtained and one reaches

$$\ln S_{ceq,min} = \frac{\dfrac{4\pi\kappa WL(\Delta E_{max})^2}{\int_{E_{corr}}^{E_{rp}} \left(i_c - i_p\right) dE}}{S_{ceq,min}} + (1 + \ln\pi + 2\ln r_a) \tag{32}$$

Thus, $S_{ceq,min}$ can be solved for numerically and plugged into Equation 27 to get the cathode size.

Coupling of Anode Pit Kinetics, Cathode Kinetics, and Ohmic Drop. Based on the above description of the three parameters, the maximum pit size, r_{max}, is found by the intersection of the anode line as a function of r_a and the cathode line as a function of r_a (Figure 58). Pits less than r_{max} can grow because there is more than enough cathode current available, whereas hemispherical pits of size greater than r_{max} are not possible as there is insufficient cathode current to balance the anodic current needed to maintain the aggressive pit chemistry.

5.3.2. Max pit model with precipitation

In order to account for cathodic precipitation in $MgCl_2$ or sea-salt brines, a mass balance process was utilized. First, the molarity of the hydroxyl ions (M_{OH^-}) accumulated in the solution volume above the cathode was calculated. This calculation can be performed at all r_a through the knowledge of the SS density (ρ_{SS} = 7.8 g/cm^3), molecular weight (MW_{ss} = 55.3 g/mol), and the number of electrons transferred during dissolution ($e_{SS}^- = 2.2$) [179], given by,

$$M_{OH^-} = \frac{\left[\frac{2}{3}(r_a)^3\right]\left[\frac{\rho_{SS} * e_{SS}^-}{MW_{ss}}\right]}{V_{cath}} \quad 33$$

The cathode volume (V_{cath}) can be calculated through the original max pit formulism, as at every r_a, there is a corresponding r_{eq} [24,179]. With the knowledge of the WL and r_{eq}, $V_{cath} = \pi r_{eq}^2 * WL$. Once M_{OH^-} is known, the cathode pH will be calculated and compared to the stability of precipitates in the respective brines [90]. It has been previously determined that non-carbonate precipitates, such as magnesium hydroxides or hydroxychlorides, are kinetically favored in $MgCl_2$ solutions [90,129]. Although carbonate species are often seen in coupon exposures of various alloys in Mg-containing environments, it is hypothesized that hydroxide precipitates are formed first and then back-react with carbon species present in the solution to form the observed phase. Predictions were made considered both carbonate and non-carbonate species and yielded a difference in max pit size of ~ 30 µm. A more detailed discussion on the rates of reactions is present in previous work [90]. For 0.189 M $MgCl_2$ and 76% RH sea-salt brine, the precipitation reaction was assumed to be,

$$Mg_{(aq)}^{2+} + 2OH^- \rightarrow Mg(OH)_{2\,(s)} \quad 34$$

and for 4.98 M $MgCl_2$ and for 40% RH the precipitation reaction was assumed to be[1]

$$2Mg_{(aq)}^{2+} + Cl_{(aq)}^- + 3OH^- + 4H_2O \rightarrow Mg_2(OH)_3Cl \cdot 4H_2O_{\,(s)} \quad 35$$

Once precipitation occurs, the volume of the precipitate (V_{precip}) is calculated through the molecular weight (MW_{precip}) and theoretical density (ρ_{precip}) of the precipitate:

---

[1] The stability of precipitates directly from solution has been shown to be concentration dependent and a more in-depth analysis can be found in work from Katona et al. [90].

$$V_{precip} = \frac{1}{n_{precip}} \frac{M_{OH^-} * V_{cath} * MW_{precip}}{\rho_{precip}} \qquad 36$$

where n_{precip} is the stoichiometric number for hydroxyl ions. The parameters for the precipitates present in each solution are given in Table 4.

Table 4: Precipitate Parameters

Solution	Precipitate	ρ_{precip} (g/cm^3)	MW_{precip} (g/mol)	n_{precip}
0.189 M $MgCl_2$ 76 % RH sea-salt	$Mg(OH)_2$	2.34	58.3	2
4.98 M $MgCl_2$ 40 % RH sea-salt	$Mg_2(OH)_3Cl \cdot 4H_2O$	1.79	182.6	3

Once V_{precip} and V_{cath} are known, the effective conductivity (κ_{eff}) can be calculated through the Bruggeman equation given by,

$$\kappa_{eff} = \kappa_o \left(1 - \frac{V_{precip}}{V_{cath} + V_{precip}}\right)^{\frac{3}{2}} = \kappa_o \left(\frac{V_{cath}}{V_{total}}\right)^{\frac{3}{2}} \qquad 37$$

where $V_{total} = V_{cath} + V_{precip}$ [190]. The calculation for maximum pit sizes with the consideration of precipitation is shown in the flow chart in Figure 55. Increments in anode size were 0.1 µm for all calculations.

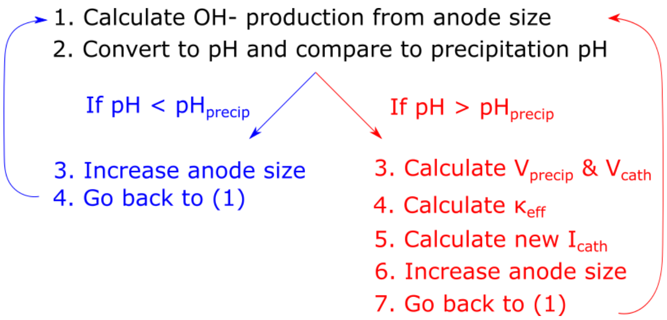

Figure 55: Flow chart for calculation of maximum pit sizes when accounting for cathode precipitation.

5.3.3. Finite Element Modeling

The modeling framework is based on the Laplace Equation to solve for the potential distribution under the assumption of electroneutrality and near-constant electrolyte composition given by [26],

$$\nabla^2 \phi_l = 0 \qquad 38$$

where ϕ_l is the electrolyte potential. COMSOL Multiphysics v5.5 (COMSOL, Inc., Burlington, MA) software was utilized. The potential and current distributions along a SS304L cathode coupled galvanically with AA7050-T7451 anode were modeled using a simplified, two-dimensional geometry which represented the cross-section of a couple under a *WL*, as depicted in Figure 56. The galvanic couple between SS304L cathode and the AA 7050-T7451 anode forms the central focus of this study due to its widespread occurrence in aerospace repairs. Additionally, the controlling behavior of the cathodic kinetics on SS304L in a galvanic couple and the max pit model will be explored. The anode length was fixed at 0.01 m, and the range of cathode lengths considered in this study varied from 0.01 m to 0.5 m, corresponding to an area ratio of 1:1 to 1:50, respectively. The width of both electrodes was considered identical, obviating the necessity for a three-dimensional model. As such, the current per unit width (I_C/W) is calculated by the two-dimensional model. The *WL* thickness was varied across roughly four orders of magnitude from 8 μm to 50,000 μm ($8 \times 10^{-6} – 5 \times 10^{-2}$ m) in order to provide a sufficiently range to capture exposure conditions representative of thin films and full immersion. The lower limit of *WL* was set by the physical limitations of the RDE; above a certain rotation speed (typically above 6000 rpm), the hydrodynamic boundary layer thickness experiences turbulence and Levich behavior no longer exists.

The values used for κ were obtained from OLI Studio Analyzer 10.0. Plots of κ can be seen in Katona et al. for NaCl solutions [179] and Katona et al. for $MgCl_2$ [127]. The anodic boundary conditions (B.C.) were the anodic kinetics of AA7050 (anodic B.C.) obtained from Liu et al. [60] and were assumed to be constant across all chloride concentrations and temperatures. Cathodic B.C. were measured for SS304L cathodic polarizations in NaCl as a function of δ (rpm). When WL thicknesses were greater than δ_{nc}, the cathodic, quiescent polarization scan was utilized. Any WL less than δ_{nc} utilized the cathodic polarization scan corresponding to the WL. Cathodic polarizations for $MgCl_2$ were taken from previous work [90] and it is noted that there was no observed rotational dependence in $MgCl_2$ electrolytes. All calculations were assumed to be steady state and the polarization scans were not dependent upon pH. Both anodic and cathodic currents were measured, and it was ensured currents were identical.

Figure 56: Schematic configuration of a galvanic couple under a thin water layer (SS304L cathode with AA7050 anode). Width of anode/cathode is normal to the x-y plane [91].

5.4. Results

5.4.1. Maximum pit sizes increase slightly with increasing temperature

An increase in maximum pit size is predicted with an increase in temperature (from 25 to 45 ˚C) for both 0.6 and 5.3 M NaCl. The increase in maximum pit size is greater for 5.3 M NaCl (increase of 48.9 µm) in comparison to 0.6 M NaCl (increase of 22 µm). Additionally, an increase in pit size is predicted for an increase in chloride concentration at any given temperature.

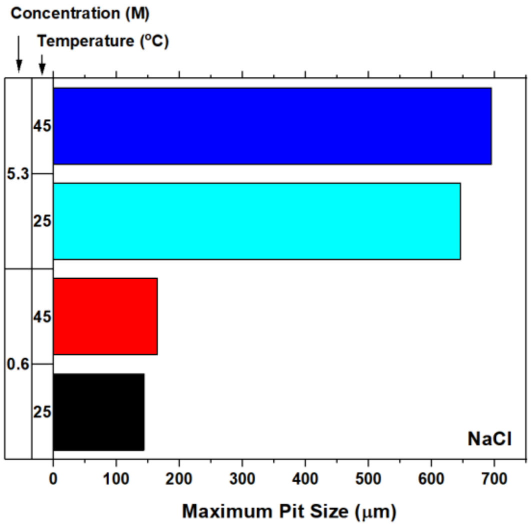

Figure 57: Maximum pit size predictions for an NaCl electrolyte as a function of concentration (0.6 and 5.3 M) and temperature (25 and 45 ˚C). LD = 3 g/m^2 and I_{LC} is for 50% of salt film saturation on the surface of the pit.

5.4.2. Precipitation decreases maximum pit sizes in MgCl$_2$ solutions

Maximum pit size predictions for 50 % of pit saturation, LD = 3 g/m^2, considering both no precipitation and precipitation of cathode solids, are presented in Figure 58(a) and (b) for 4.98 and 0.189 M MgCl$_2$ respectively. Overall, maximum pit sizes and cathode radii (Figure 58(c) and (d)) are larger for 4.98 M MgCl$_2$ in comparison to 0.189 M MgCl$_2$. A maximum pit size of 373.5 μm is predicted for 4.98 M MgCl$_2$ (Figure 58(a)) without precipitation, and the value decreases 20 % when considering the precipitation of $Mg_2(OH)_3Cl \cdot 4H_2O$. For 0.189 M MgCl$_2$ (Figure 58(b)), maximum pit sizes are relatively similar with or without precipitation (160.6 μm without and 155.9 μm with precipitation) decreasing roughly 3 % with precipitation of $Mg(OH)_2$. Furthermore, cathode radii for 4.98 M MgCl$_2$ are roughly 3.4-3.8 times larger than cathode radii for 0.189 M MgCl$_2$ over the range presented in Figure 58, and the ratio of radii decreases with increasing pit size.

Maximum pit size predictions for MgCl$_2$ solutions as a function of MgCl$_2$ concentration, percent anode saturation, and cathode evolution phenomena considered alone and in combination are seen in Figure 59(a). Overall, 4.98 M MgCl$_2$ has a larger pit size in all scenarios when compared to 0.189 M MgCl$_2$. When exploring percent of pit saturation, regardless of solution concentration, 50

% saturation has a larger maximum pit size in comparison to 100 % saturation. Finally, when comparing cathode evolution phenomena, the maximum pit size is highest in the original formulism and decreases in order in the following: precipitation, dehydration (“WL”), and combined precipitation and dehydration. Additionally, for 0.189 M $MgCl_2$ the film and film with precipitation decrease the pit size further than dehydration. Cathode radii are presented for $MgCl_2$ solutions as a function of percent saturation and cathode evolution phenomena that were presented in this paper are seen in Figure 59(b). Overall, cathode radii follow the same trends as maximum pit size predictions, except for when a film is considered for 0.189 M $MgCl_2$ which exhibits a cathode radius roughly 5 times larger than the original formulism.

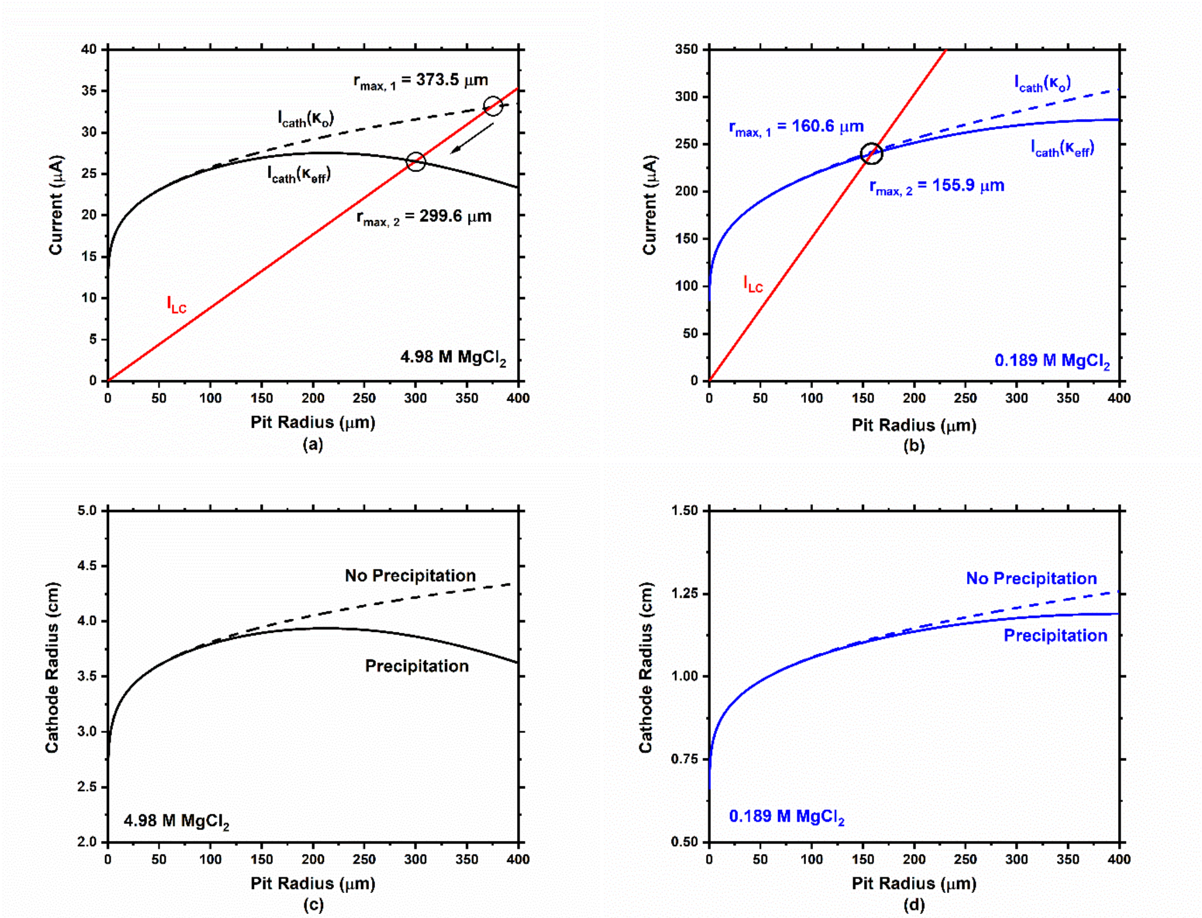

Figure 58: Maximum pit predictions shown both with and without the consideration of precipitation in the cathode for (a) 4.98 and (b) 0.189 M $MgCl_2$. LD = 3 g/m^2 and I_{LC} is for 50% of salt film saturation on the surface of the pit. Cathode radius for (c) 4.98 and (d) 0.189 M $MgCl_2$ with and without precipitation. Note the difference in the ordinate scales between the two solution concentrations in all graphs.

Maximum pit size predictions for NaCl and sea-salt brines are presented in Figure 60(a) for 50 % pit saturation. It was previously shown for $MgCl_2$ electrolytes that pit sizes were larger for 50 % saturation and cathode evolution effects are more severe, thus, predictions for 100 % saturation are not presented. In general, maximum pit sizes are larger in 76 % RH (5.01 M Cl^-) sea-salt in comparison to 40% RH (8.90 M Cl^-) despite having a greater chloride concentration in 40% RH. For 40 % RH sea-salt, maximum pit sizes decrease in the following order: original formulism, precipitation, dehydration, precipitation and dehydration, and salt. The scenario “salt” refers to the fractional volume of precipitated salt of the metal dissolution products in solution [46]. Fractional solution volumes were used in the Bruggeman equation (Equation 20) and the precipitated salt was assumed to be insulating. 76 % RH sea-salt follows the same pattern except for salt, which is nearly identical to the original formulism. For NaCl solutions, 5.3 M NaCl has a greater maximum pit size than 0.6 M NaCl and, when dehydration was considered in both solutions, a decrease in maximum pit size was observed. Cathode radii at maximum pit sizes are presented in Figure 60(b) for sea-salt and NaCl electrolytes at 50 % saturation. The same patterns as maximum pit sizes (Figure 60(a)) are also displayed in cathode radii

It is interesting to note that the predictions for sea-salt brine at 76 % RH and saturated NaCl are significantly different with saturated NaCl having a larger pit size by a factor of roughly 2.5 in the original formulism. This same pattern holds for 40 % RH sea-salt brine and saturated $MgCl_2$, in which saturated $MgCl_2$ has a greater pit size than sea-salt by roughly a factor of 4. Furthermore, despite having a greater chloride concentration in 0.6 M NaCl, maximum pit sizes are nearly identical when comparing with 0.189 M $MgCl_2$ (0.378 M Cl^-). Additionally, saturated NaCl has a greater maximum pit size than saturated $MgCl_2$ by roughly a factor of 1.5 despite $MgCl_2$ having almost double the chloride concentration.

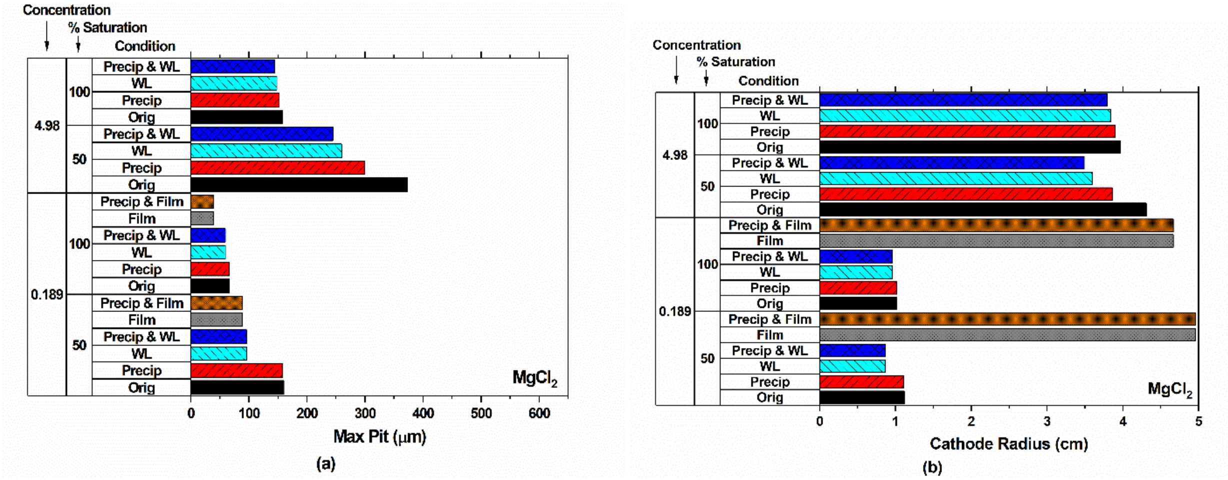

Figure 59: Influence of all cathode evolution scenarios explored for $MgCl_2$ electrolytes on (a) pit size and (b) current. LD = 3g/m^2 in all scenarios. The labels correspond to the following scenarios: Orig – Original maximum pit formulation; Precip – Considering precipitation reactions and the influence on conductivity; WL – considering only dehydration reactions; Precip & WL – considering Precip. and WL together; Film – Original formulism with new cathodic polarization; Precip & Film – New cathodic polarization scan and precipitation reactions.

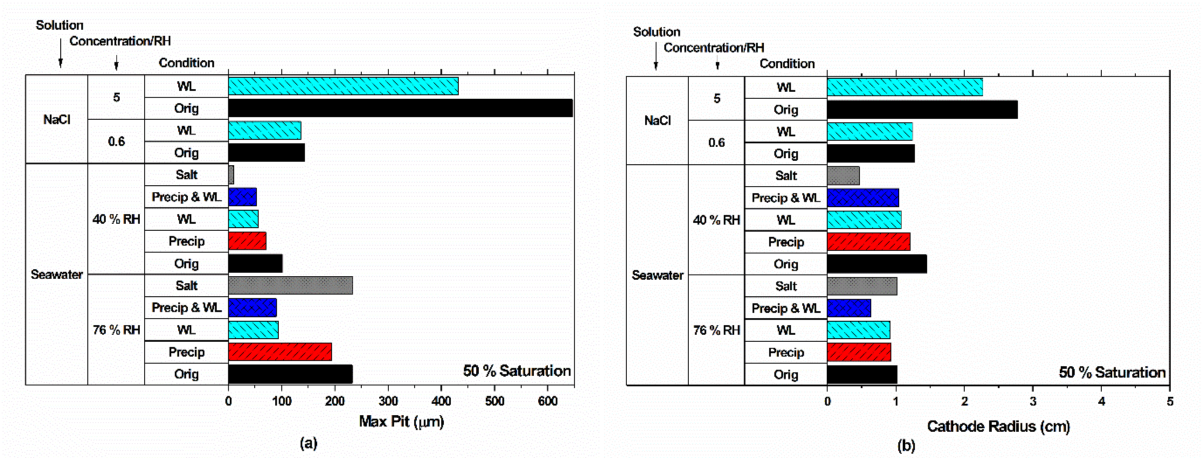

Figure 60: Influence of all scenarios explored for sea-salt and NaCl brines on (a) pit size and (b) current. LD = 3g/m^2 and 50 % saturation is used in all scenarios. The labels correspond to the following scenarios: Orig – Original maximum pit formulation; Precip – considers precipitation reactions and the influence on conductivity; WL – considers only dehydration reactions; Precip & WL – considers precip and WL together; Salt – considerations from the fractional water content due to precipitated salt in solution.

5.4.3. Validation of maximum pit size predictions

Predicted maximum pit sizes are conservative when compared to the maximum pit size in long term-controlled exposures. Recent exposures were performed on SS304 at both 76 and 40 % RH, a temperature of 35 ˚C, under a loading density of 3 g/m^2, and were carried out for two years [27] with periodic evaluation at defined exposure times such as one year [191]. As presented in Figure 61, an increase in maximum pit size up until roughly 26 weeks was measured after which a plateau was measured. After 26 weeks, the 76 % RH exposures have an average measured maximum pit size of 66.5 µm and the 40 % RH exposures have an average measured pit size of 65.3 µm. Predictions of the maximum pit size, at 50 % of salt film saturation, are shown to be larger for 76 % RH in comparison to 40 % RH when the original formulism is utilized. Measured values are less than the predicted maximum pit sizes (66.5 vs. 110 µm for 40 % RH and 65.3 vs. 230 µm for 76 % RH when comparing measured). Additional predictions were made with the precipitation of $Mg(OH)_2$ in solution (Section 5.3.2) and are also presented in Figure 61. A reduction of the predicted maximum pit size with precipitation is calculated. It is interesting to note that the calculation for 40 % RH with precipitation is very close to the measured size of all pits after a time period of 26 weeks and is denoted by a horizontal dashed line in Figure 61.

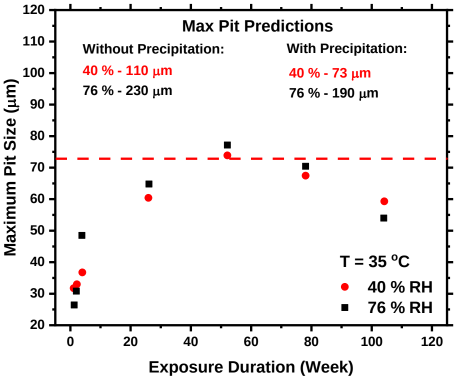

Figure 61: Comparison of exposure testing in sea-salt brines under two relative humidity values (76 and 40 % RH) to maximum pit size predictions. Specifics on the exposure conditions and measured maximum pit sizes can be obtained from Srinivasan et al. [27]. *It is noted that the horizontal, red, dashed line is the predicted maximum pit size for 40 % RH at 35 ˚C.*

5.4.4. Cathodic current per width increases with increase in temperature in galvanic couple

When modeling a AA7050/SS304L galvanic couple, the current per width (I_C/W) is obtained by integrating the current density along the entire L_C and will be the main metric for comparison in the FEM. A greater detailed explanation of the galvanic couple FEM is presented in Appendix B, however, a brief subset of the models will be presented here to compare to the max pit modeling. I_C/W increases with increased temperature (45 ˚C compared to 25 ˚C) for both 1 and 5.3 M NaCl as shown in Figure 56(a) and (b) respectively at the critical cathode length (L_{Crit}). The increase in I_C/W is also shown at very large cathodes (L_C = 0.5 m) by comparing Figure 63(c) and (d).

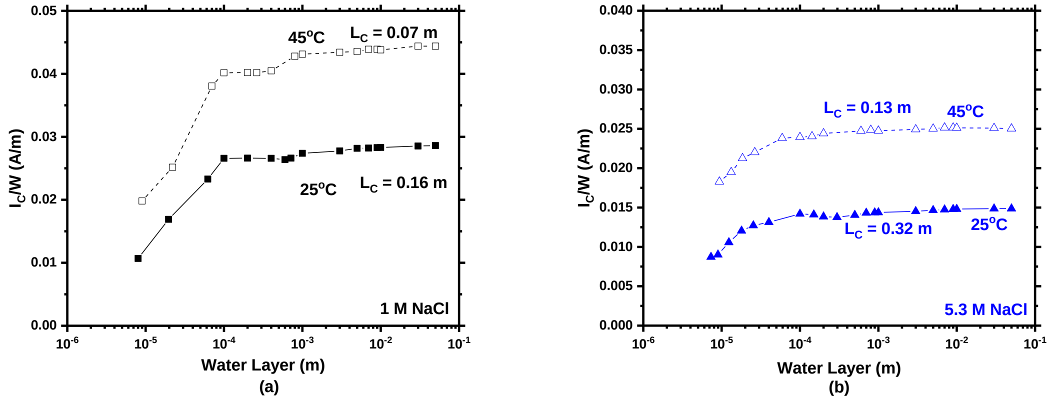

Figure 62: Comparison of the modeled total cathodic current per width (I_C/W) vs. water layer thickness as a function temperature at the respective critical cathode length (L_{Crit}) for (a) 1 and (b) 5.3 M NaCl. It is noted that the ordinate in (a) is different than (b).

5.4.5. Cathodic current per width decrease with increase in chloride concentration

I_C/W decreases with increased chloride concentration for both 25 and 45 ˚C as shown in Figure 63(a) and (b) respectively at L_{Crit}. The decrease in I_C/W is also shown at very large cathodes (L_C = 0.5 m) for 25 and 45 ˚C as shown in Figure 63(c) and (d) respectively.

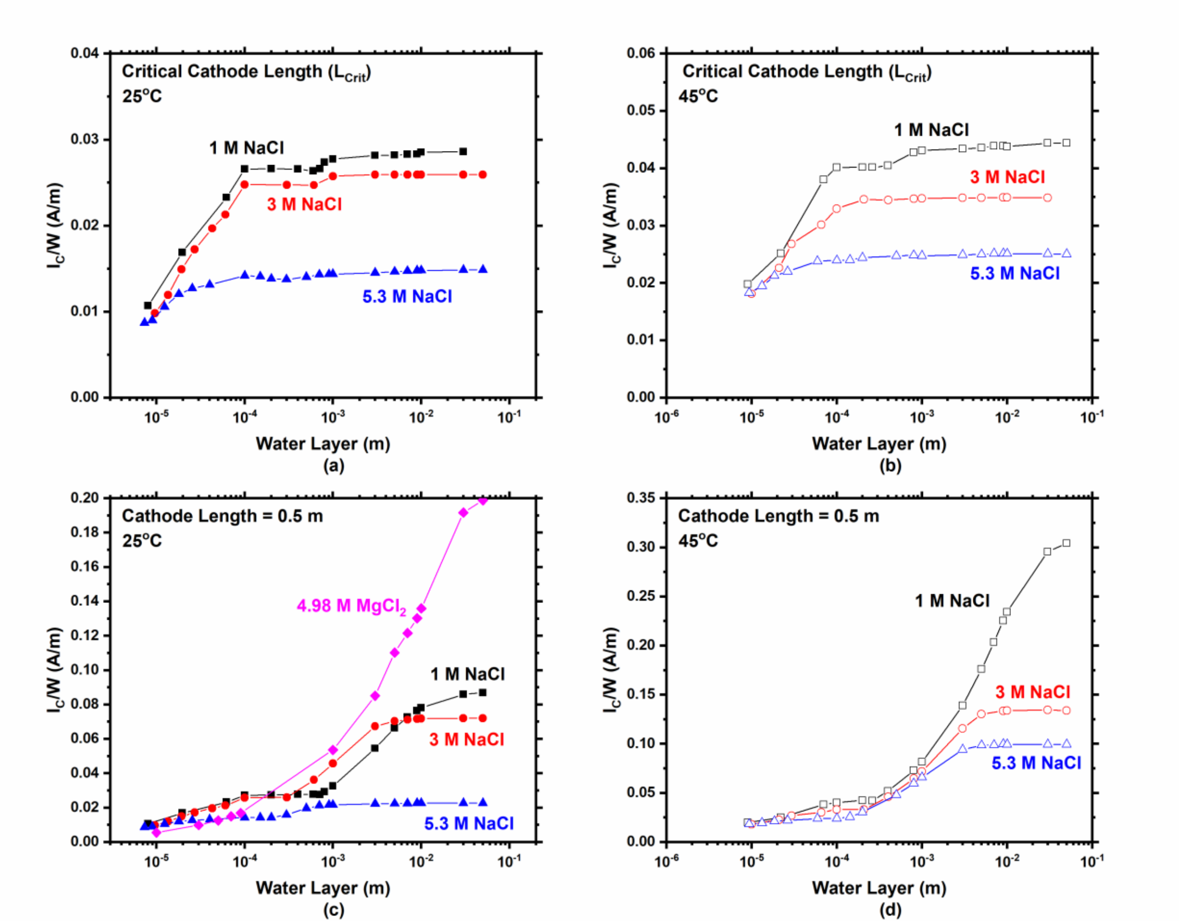

Figure 63: Comparison of the modeled total cathodic current per width (I_C/W) vs. water layer thickness as a function solution concentration at the respective critical cathode length (L_{Crit}) for (a) 25 and (b) 45 ˚C. Comparison of I_c/W vs. water layer thickness as a function solution concentration at a cathode length (L_C) of 0.5 m for (c) 25 and (d) 45 ˚C. It is noted that the ordinate axis is different in each graph.

5.5. Discussion

First, the dependencies of just the cathodic kinetics will be discussed with regard to increasing temperature and chloride concentration for both max pit modeling and a galvanic couple. Next, the interplay of these dependencies with the anodic kinetics will be discussed in terms of predicting the max pit sizes and important parameters will be identified. Fourth, the influence of precipitation and dehydration reactions on max pit predictions will be discussed. Fifth, the consequences of the ideal cathode assumption will be discussed. Finally, overall influences of anodic and cathodic kinetics on a galvanic couple will be explored and important trends will be identified. It is again pointed out that many of the dependencies presented in the AA7050/SS304L galvanic couple are presented in Appendix B.

5.5.1. *Cathodic current enhanced with an increase in temperature*

An increase in cathodic current is predicted for both maximum pit size predictions and galvanic couples with an increase in temperature. First, looking at the maximum pit model, increasing temperature does not change the WL thickness (Figure 38) or C_{O_2} (Appendix B) significantly and will not cause for a significant change in the cathodic current. Next, an increase in temperature will cause for an increase in κ (Appendix E) and D_{O_2} (Appendix B) both which will serve to increase I_{cath}. As seen in Equation 31, κ is a direct input for I_{cath}, thus increasing κ will increase I_{cath}. While D_{O_2} is not a direct input into the max pit model (Equation 31), the change in D_{O_2} will be manifested in i_{eq} which is a result of the integration of the cathodic polarization scan (Equation 28). With increasing temperature, there is an increase in current density at any given potential due to an increase in D_{O_2} (Appendix E). This is manifested in i_{eq} (Equation 31) which will serve to increase the cathodic current. Therefore, with increasing temperature, the main factors increasing I_{cath} are κ and D_{O_2}.

When considering a galvanic couple, the increase in I_C/W is more prominent in comparison to the max pit model under the same temperature increase. While the same increase in κ is prevalent in each system, the coupling potential (through Mixed Potential Theory) for the galvanic couple is much lower than that of the max pit model. In the max pit model, E_{rp} is coupled in the activation-controlled regime (Appendix F) while, in the galvanic couple, the couple potential between the AA7050 and SS304L is in the diffusion limited regime [60]. Therefore, the effects of D_{O_2} cause for a larger increase in the current density when polarized into the diffusion limited regime in contrast to being polarized into the activation-controlled regime and will cause for the greater increase in I_C/W. Overall, with increasing temperature, increases in κ (Appendix E) and D_{O_2} (Appendix B) will be the most dominant factors in determining cathodic currents (I_{cath} and I_C/W).

5.5.2. *Cathodic current decreased with an increase in chloride concentration*

When increasing chloride concentration, for the same salt (i.e., increasing from 0.6 to 5.3 M NaCl), a decrease in the cathodic current, I_{cath} and I_C/W, is calculated. First, when considering the maximum pit size model, increasing chloride concentration will cause for a WL decrease (Figure 33 and Figure 64), a general increase in κ (Appendix E and Figure 64), and a decrease in D_{O_2} and C_{O_2} (Appendix F). First, an increase in κ will increase I_{cath} (Equation 31). Second, a decrease in WL (Figure 64) will cause for a decrease in the I_{cath} as seen in Equation 31. While κ and WL thickness will influence I_{cath} in opposite ways, when considering 0.6 and 5.3 M NaCl, κ will increase by a factor of 4 however the WL will decrease by a factor of 8 (Figure 64) for a constant LD. Thus, changes in WL thickness will play a greater role in determining I_{cath} in comparison to κ. Finally, the decrease in D_{O_2} and C_{O_2} with increased chloride concentration will cause for a significant decrease in i_{eq} as presented in Figure 64(a) and (b) for both $MgCl_2$ and NaCl solutions respectively at 25 ˚C. Therefore, when increasing chloride concentration under the same composition changes in WL, D_{O_2}, and C_{O_2} will cause for a decrease in I_{cath}.

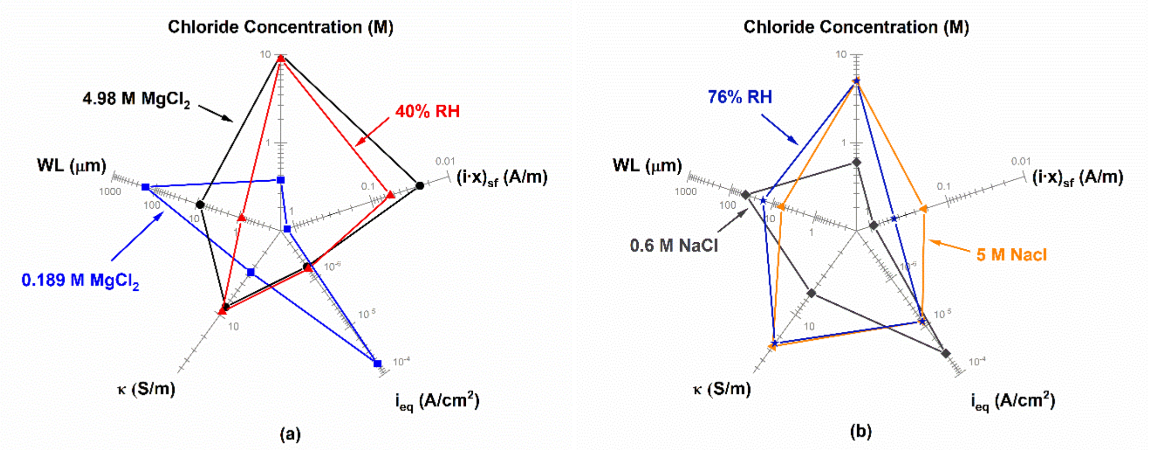

Figure 64: Radar plots comparing properties for (a) $MgCl_2$ solutions and sea-salt at 40 % RH and (b) NaCl solutions and sea-salt at 76 % RH. Examined in the plots are chloride concentration, water layer thickness, pit stability product under a salt film, equivalent current density, and conductivity of the solution.

Similarly to the max pit model, a decrease in I_C/W is present for the AA/SS304L galvanic couple due to a decrease in D_{O_2} and C_{O_2} (Appendix F). As with the max pit model, an increase solely in κ will cause for an increase in I_C/W. However, as the galvanic couple is polarized into the diffusion limited regime and both D_{O_2} and C_{O_2} are decreasing, the decrease in current density will be more severe than the max pit model and shows the dominating role that cathodic kinetics have in determining I_C/W. Additionally, an increase in solution concentration increases the percentage of the cathode that is in the M-T limited kinetics region because an increase in solution κ decreases the ohmic drop and broadens the M-T regime enhancing the influence of D_{O_2} and C_{O_2}. Therefore, with increasing chloride concentration (under the same solution composition), influences from a decreasing WL thickness and D_{O_2} and C_{O_2} will outweigh the influence of an increasing κ causing for an overall decrease in cathodic current (I_{cath} and I_C/W).

5.5.3. Governing factors of maximum pit size predictions are dependent upon equilibrium solution relative humidity

Maximum pit size predictions using solutions with similar chloride concentrations (*i.e.* using $MgCl_2$ instead of sea-salt brine at 40 % RH) produce larger pit sizes than sea-salt and show the importance of having the correct environmental input parameters. As presented in Figure 59(a) and Figure 60(a), sea-salt solutions have lower predicted pit sizes than the analogous single salt system. In order to determine the governing factors, the inputs to the maximum pit size model were compared in radar plots and are presented in the radar diagrams in Figure 64. The radar plots in Figure 64 have five different quantitative axes arranged in a radial fashion. Each axis represents either the chloride concentration or a direct input to the maximum pit model ($(i \cdot x)_{sf}$, i_{eq}, κ_o, or WL). A colored line, representing a single solution, then connects all five axes and describes the quantitative inputs for that solution. It should be noted that all axes are on a logarithmic scale and do not have the same step size. Finally, the axes are oriented such that a value moving toward the center of the radar plot would produce a decrease in the predicted maximum pit size with all else being held equal. Thus, if there are two similar pentagons on the radar plots, the smaller pentagon would have a smaller predicted maximum pit size in comparison to the larger pentagon.

First, surrogate brines will be compared and the importance of having accurate input parameters will be discussed. Considering saturated $MgCl_2$ and 40 % RH sea-salt brine (Figure 64(a)), one can see that the chloride concentration, κ, and i_{eq} are all very similar and likely do not account for the significant differences in pit size predictions. However, saturated $MgCl_2$ has a greater WL and lower $(i \cdot x)_{sf}$ in comparison to 40 % RH sea-salt brine. This combination will lead to increased ohmic drop in 40 % RH sea-salt, decreasing I_{cath} (as discussed in Section 5.5.2 for increasing chloride concentration). Additionally, as an increased anodic current demand (increased $(i \cdot x)_{sf}$) is present for sea-salt brines, the maximum pit sizes are decreased by roughly 275 µm (Figure 59(a) and Figure 60(a)) when combined with the decreased cathodic current. Now looking at the comparison between 76 % RH sea-salt brine and saturated NaCl, the same trends follow with the difference in pit size being nearly 415 µm (Figure 60(a)). Although this result may seem surprising, the available cathodic currents for saturated NaCl and 76 % RH sea-salt brine are much higher than for saturated $MgCl_2$ and 40 % RH. Thus, differences in $(i \cdot x)_{sf}$ will cause a larger change in predicted pit sizes when the cathodic current is higher.

Perhaps against intuition, increasing chloride concentration in atmospheric corrosion scenarios does not always cause an increase in pit sizes and is influenced by solution composition. When exploring concentration increases of $MgCl_2$ and NaCl solutions, an increase in pit size is predicted. However, when comparing concentrated $MgCl_2$ and NaCl, the chloride concentration is almost doubled in $MgCl_2$ solutions, but, a larger pit size is seen in concentrated NaCl (Figure 59 and Figure 60). When looking at the properties of each solution in Figure 64, the WL are similar, however, $MgCl_2$ has an $(i \cdot x)_{sf}$ that is lower by an order of magnitude. Although a lower $(i \cdot x)_{sf}$ would lead to an increased pit size, saturated $MgCl_2$ experiences a large decrease in i_{eq} due to ORR suppression (Appendix A), decreased D_{O_2} and C_{O_2} (Appendix F), and a decreased κ (Figure 64). The combination of these factors causes I_{cath} to be roughly 160 µA less (Appendix F, Figure S2). This decrease in I_{cath} diminishes the effects of $(i \cdot x)_{sf}$. This effect is seen again when comparing 0.6 M NaCl and 0.189 M $MgCl_2$ as 0.189 M $MgCl_2$ has a larger pit size. In this case, a similar $(i \cdot x)_{sf}$ is present for both solutions and the governing factor becomes an increase in WL for 0.189 M $MgCl_2$ in comparison to 0.6 M NaCl.

Overall, the governing factors for maximum pit size are not the same across all solution combinations but can be separated into two broad groups based on the solutions that were explored within: (i) similar chloride concentrations (RH) and (ii) varying chloride concentrations (RH). Under similar chloride concentrations, the WL and $(i \cdot x)_{sf}$ are the most influential factors. When varying chloride concentrations, changes in WL, i_{eq}, and κ are the most influential parameters.

This effect is very similar to that which occurs when the temperature is increased at a single concentration of NaCl [179]. At elevated temperatures, an increase in cathode current was seen with increasing temperature due to an increase in i_{eq} and κ, but a decrease in $(i \cdot x)_{sf}$ caused the pit sizes to be relatively invariant to temperature swings [179].

5.5.4. Dehydration reactions coupled with precipitation will cause the most significant inhibition of corrosion damage

The presence of a $Mg(OH)_2$ film on the surface of the alloy resulted in the smallest predicted pit size (Figure 59(a)), however, it is not the best-case scenario for corrosion inhibition. As shown in Figure 59(a) and Figure 60(a), predicted pit sizes decreased in the following order for all solutions explored: original > precipitation > dehydration > dehydration + precipitation. These effects on maximum pit sizes are summarized schematically in Figure 65. Further decreases in predicted maximum pit sizes are seen when a film is on the surface (for 0.189 M $MgCl_2$) and when salt precipitates are considered for 40 % RH sea-salt.

The presence of a film on the surface of the alloy decreased i_{eq} causing a decrease in pit size. A lower i_{eq} causes a much larger r_{eq} (for which it is less likely to have 1 pit active) in comparison to no film (Figure 59(b)), because the lower current densities lead to lower ohmic drop per unit length. As E_{rp} was assumed to be the same, a larger r_{eq} is needed in order to account for this decrease in ohmic drop. With a larger r_{eq}, the effects of precipitation and dehydration are minimal due to an increased solution volume. In this scenario, nearly the entire *WL* is present on the surface at the predicted maximum pit size, allowing for pits to initiate after the original pit has repassivated. In contrast to the case without a film, dehydration can occur much more rapidly (due to an overall smaller solution volume). In this scenario, the *WL* decreases roughly 42 % in 0.189 M $MgCl_2$ and any pit initiating in the future will experience larger ohmic drop, resulting in a smaller pit size, and further contributing to brine dry out. When only precipitation is considered, a reduction in conductivity would be experienced by any future pit growth, however, the ohmic drop would not be as severe when considering both dehydration and precipitation. Thus, understanding dehydration and precipitation together is crucial to predicting overall material degradation.

For mixed salt solutions at low RH, such as 40 % RH sea-salt, salts precipitating on the surface caused the greatest decrease in predicted pit size (Figure 60(a)) due to the small fractional water content. At such low RH, there is roughly 35 % water with 65 % precipitated salts by volume in solution and, when assumed to be ionically insulating, cause a significant decrease in the predicted pit size. Although this case proved to be the most severe, it is unlikely that a continuous, uniform WL on the order of 1 µm will be present over the entire cathode, thus, droplets may form. Droplets forming on the surface would provide for a different scenario than modeled.

It is important to understand why precipitation and dehydration vary in efficacy based on the solution concentration. For precipitation at a constant pit size, there is a larger volume fraction of a precipitate for the 4.98 M $MgCl_2$ in comparison to 0.189 M $MgCl_2$ due to the smaller overall volume of liquid. Via Bruggeman's equation, this leads to a larger effective resistivity which, when combined with smaller WL, leads to an increased ohmic potential drop, a decreased r_{eq}, and thus a decrease in I_{cath}. Thus, due to greater change in I_{cath} in 4.98 M MgCl2 solutions, a greater change in pit sizes are expected in saturated solutions for precipitation reactions. This trend is opposite to observations for dehydration reactions, *i.e.,* a greater decrease in predicted pit sizes are seen in 0.189 M $MgCl_2$ in comparison to 4.98 M $MgCl_2$ when dehydration is considered. This observation is directly related to the amount of chloride present in the cathode. Considering the same pit size in both solutions, the migration of chloride to the pit is going to be the same in both solutions. Although this may be the case, the overall amount of chloride is much higher in 4.98 M $MgCl_2$ than in 0.189 M $MgCl_2$ due to an increase in both cathode size and chloride concentration. This result would indicate that the activity of water in solution is going to fluctuate much more in dilute solutions and cause the WL decrease to be more severe. Thus, dilute solutions will experience brine dry-out from dehydration reactions at smaller pit sizes compared to saturated solutions. Overall, the maximum pit model is most sensitive to input parameters for concentrated solutions, however, the sensitivity of these parameters is decreased when precipitation and dehydration occur.

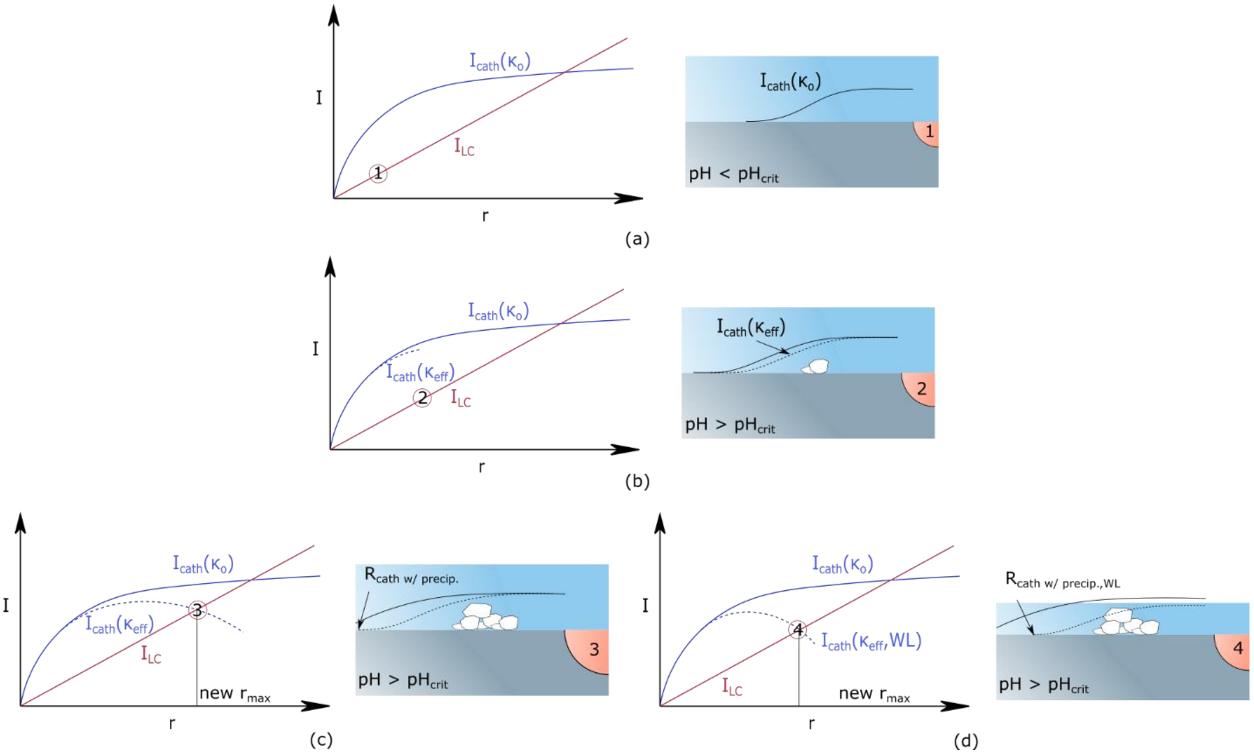

Figure 65: Qualitative representation of governing reactions for atmospheric corrosion and relative severity for solutions containing precipitates. (a) A small pit that has not reached the bounding cathodic current nor the critical pH for precipitation. (b) A medium sized pit that has not reached the bounding cathodic current however has reached a pH in which precipitation is thermodynamically possible. (c) Maximum pit size when only precipitation is considered in the cathode. (d) Maximum pit size when precipitation and dehydration are considered in the cathode

5.5.5. Consequences of an ideal cathode assumption

One of the main assumptions of the maximum pit model is that all positions along the cathode provide an ideal amount of current. This provides a powerful theoretical limit for the cathodic current and allows for the calculation of a maximum pit for a given set of environmental conditions. When comparing between controlled exposure environments and maximum pit size predictions, a conservative pit size is predicted both for sea-salt environments (Figure 61) and for $FeCl_3$ environments [54]. The conservative nature of the ideal cathode assumption shows the utility of the max pit formulism in predicting potential materials degradation due to pitting corrosion. These predictions were further improved to account for allow for a variable cathodic current due to the precipitation of solid species in solution and helped to improve the accuracy of maximum pit size predictions (Figure 61). Despite having conservative predictions, in practice, a perfect cathode is never achievable. Using experimentally determined potentiodynamic scans as boundary conditions for the cathode and the anode, a more realistic pitting scenario can be obtained [192].

Marshall et al. evaluated critical pit sizes at a variety of different cathode diameters via FEM in 3M NaCl for a constant WL thickness of 16 μm (LD = 3 g/m^2) for SS316. It is important to note that a more noble E_{rp} is present for SS316 in comparison to SS304L and will result in a decrease in the maximum pit size predictions [54]. At a cathode diameter of approximately 45 cm, the critical pit radius from FEM calculations plateaus (Figure 66). The maximum pit at 50 % saturation under the same conditions for SS316 is included in the plot. Although the FEM calculated cathode diameters out to 65 cm, nearly 5 times of that needed by an "ideal" cathode, the *critical* radius never reaches the predicted *maximum* radius. This result suggests that the theoretical estimates of the maximum pit radius is conservative by at least a factor of 2 under these conditions. The maximum pit size could further decrease if another pit were to become active or if the WL across the surface was not uniform. Interestingly, a similar comparison between the maximum pit model and outdoor exposure testing on SS316 is seen in literature [24]. Although the experimental exposures of pit depth varied with location and exposure time, a comparison of the averaged values with the predicted maximum pit calculation also shows the maximum pit model overestimating the experimental results by 2 times. A similar overestimation is present for SS304L in sea-salt brines with an increase in predicted maximum pit sizes by a factor of roughly 1.5 for 40 % RH (Figure 61).

Another interesting point is the extreme size required for a realistic cathode to achieve its full current capacity. The maximum pit model predicts that if a cathode was perfectly consuming all of the available current from one singular pit, the cathode diameter of a given scenario with $r = 15\ \mu m$ and $WL = 16\ \mu m$ would only need to be 12.8 cm. However, a 12.8 cm *realistic cathode* does not behave ideally, as evident by the lack of polarization at the edge of the cathode. Not until cathode diameters of nearly 45 cm is the entire current capacity being used, and even at these large dimensions the total current is nearly 50% less than the predicted current from a 12.8 cm idealized cathode as stated above. That is to say, the FEM predicts a cathode diameter of 45 cm is needed to supply the full current capacity *to one pit*. In addition, this prediction assumes that no other pits are present within this diameter as then the cathode current would be shared among all active pits.

Experimentally, however, Budiansky *et al.* have shown that pits interact and form clusters on a realistic SS316 surface [193].

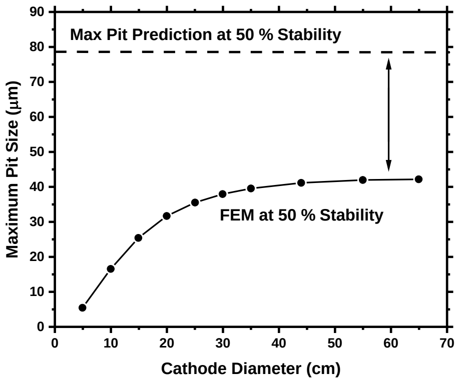

Figure 66: Critical hemispherical pit radius as a function of critical cathode radius, as calculated via FEM using the pit stability product (I/r) at 50% saturation as the stability criterion, in 3M NaCl; the red dashed line represents the maximum pit radius at 50% saturation in the same conditions, as predicted by the maximum pit model [192].

5.5.6. Predicting corrosion under a varying electrolyte

When modeling atmospheric corrosion scenarios, it is important to note that the electrolyte chemistry will change with corrosion damage and time and will influence both the potential, current density, and pH. When considering the maximum pit size formulism, the equivalent cathodic current density of an ideal cathode and can be calculated by integrating the current density from OCP to E_{rp} [24,28,29]. In 0.6 M NaCl, E_{rp} is roughly -0.265 V_{SCE} [179] and is denoted in Figure 25(a). In 0.6 M NaOH (pH = 13.6), the OCP is less than E_{rp} indicating that at a pH of 13.6 the cathode would no longer be able to supply current for localized anodic dissolution. In this scenario, the total cathodic current available would not only be limited by ohmic drop (governed by solution conductivity and *WL* thickness) [24], but would also be limited by a decrease in the pH dropping the OCP below E_{rp}. As an expression for i_{eq} as a function of pH is not available, this cannot be incorporated into the maximum pit size calculations, however, the logic can help explain the discrepancy between maximum pit size predictions for 76 % RH sea-salt brines (Figure 61).

Another form of localized corrosion that experiences chemistry changes in the cathode is a galvanic couple. An applicable modeling study by Liu et al. simulated the cathodic current in a galvanic couple between SS316L and AA7050 [60] and Katona et al. who explored a S304L and AA7050 couple [91]. While SS316L and SS304L contain different elemental compositions, the polarization scans are similar in 0.6 M NaCl [116] and any comparisons made within will be qualitatively the same. The OCP of AA7050 is roughly -0.8 V_{SCE} [60] and would be in the diffusion limited regime of 0.6 M NaCl while the OCP is in the activation-controlled kinetics of 0.6 M NaOH as displayed in Figure 25(a). Therefore, the coupled current density from mixed potential theory between an AA/SS304L couple is lower in NaOH in comparison to NaCl. If one were to account for the changing electrolyte and the influence of pH on the cathodic kinetics, it is likely that a decreased cathodic current would be calculated. The same argument holds for saturated NaCl when comparing to 5.4 M NaOH and 5.3 M NaCl as shown in Figure 25(b). In all cases, comparing between NaCl and NaOH, utilizing NaCl polarization curves will be conservative as a higher cathodic current would be calculated. A higher cathodic current would equate to a higher amount of corrosion damage

The effect of cathodic kinetics on an AA/SS304L is quantitatively shown in Figure 67. In this scenario, AA7050 is galvanically coupled to a SS304L alloy. The Laplace equation was utilized in this study. A conductivity of 5.5 S/m was utilized in the 0.6 M NaCl solution [60] while the 0.6 M NaOH solution utilized a conductivity of 11.6 S/m (OLI Studio). Despite having over double the conductivity, the NaOH solution still experiences an average of 60 % decrease in I_C/W in comparison to the NaCl solution at both L_C = 0.01 and 0.1 m. This trend holds across the 3 orders of magnitude of *WL* thickness that were explored. Thus, as previously mentioned the controlling nature of the cathodic kinetics is displayed. When accounting for a complete reactive transport model (with pH dependent boundary conditions) it is important to account for variation in reversable potentials, changes in the activation-controlled kinetics, changes in O_2 diffusivity, and a change in reaction mechanism. When considered, it is likely that the overall current will be decrease as shown in Figure 67. Thus, modeling with the chloride analogue is conservative in this case.

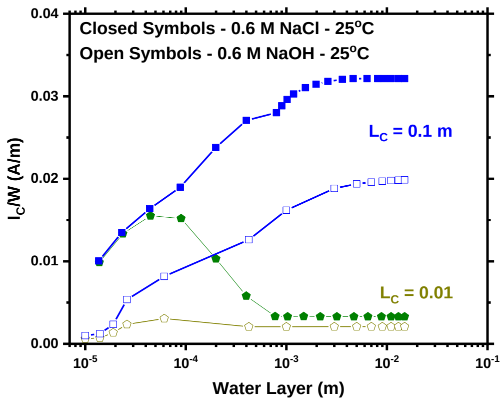

Figure 67: Effect of cathodic kinetic boundary conditions on the current per width (I_C/W) of an AA/SS galvanic couple as a function of cathode size and water layer thickness.

5.6. Conclusions

Predictions were made for maximum pit sizes on SS304L and for the total current in a AA7050/SS304L galvanic couple in environments relevant for atmospheric exposures. The controlling factors when increasing temperature and chloride concentration on total cathodic currents were identified for both the maximum pit model and the galvanic couple are schematically presented in Figure 68. It is important to note that these conclusions encompass the temperature (25 – 45 ˚C) and chloride concentration ranges (0.189 M to saturated) explored in this dissertation. It was identified that cathodic kinetics are enhanced with an increase in temperature due to an increase in κ and an increase in D_{O_2} causing for an increase in the current density and a decrease in the overall ohmic drop in the system. This is schematically shown in Figure 68 by an increase in current density near the cathode/anode interface and a higher current density with increase distance away from the anode. With increasing chloride concentration, a decrease in in C_{O_2}, D_{O_2} and equilibrium *WL* thickness will cause for a decrease in the cathodic kinetics. While κ increases, decreasing overall ohmic drop in the system, the decrease in the overall current density governed by the aforementioned parameters will be greater. This effect is shown in Figure 68 by an overall decrease in current density but persisting further out in the cathode.

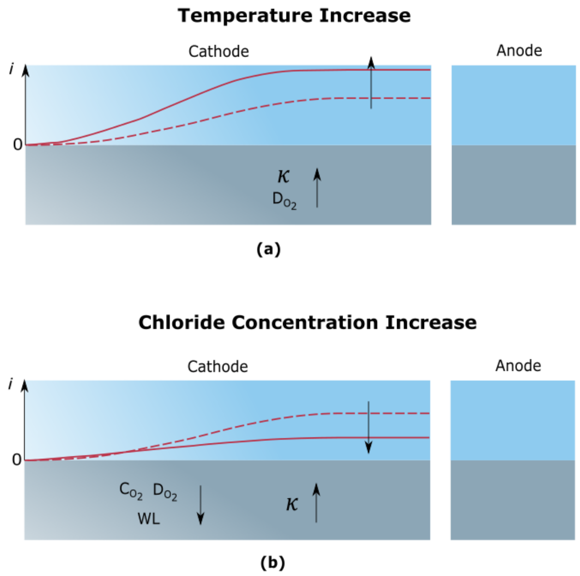

Figure 68: Influence of (a) increasing temperature and (b) chloride concentration on the cathodic kinetics for a generic anode (either for a galvanic couple or for maximum pit calculations). It is noted that these represent changes in temperature or chloride concentration when the same salt is explored (i.e. comparing chloride changes in a single salt).

As previously discussed, the cathode current will show certain dependencies with changing environmental parameters, however, when combined with the anodic demand, further complex dependencies arose. First, when exploring a similar chloride concentration (RH) such as a comparison between $MgCl_2$ and sea-salt brines, the controlling factors decreasing the cathodic current is the *WL* thickness and is combined with an increase in $(i \cdot x)_{sf}$ to decrease the maximum pit size as shown in Figure 69(a). Second, when increasing temperature as seen in Figure 69(b), an increase in cathodic demand due to increases in κ and D_{O_2} is offset in by an increase in $(i \cdot x)_{sf}$ to not significantly change the pit sizes. Next when considering an increase in chloride concentration in different compositions (i.e. saturated NaCl and $MgCl_2$), the suppression of cathodic kinetics due to an overall decrease in i_{eq} and *WL* thickness outweighs the decreased anodic demand. This leads to an overall decrease in the predicted max pit size as depicted in Figure 69(c). Finally, when increasing chloride concentration when the composition is the same (i.e. 0.6 vs. 5.3 M NaCl), while the cathodic kinetics are suppressed, again due to a decrease in i_{eq} and *WL* thickness, $(i \cdot x)_{sf}$ decrease much more and causes for an increase in the predicted maximum pit size (Figure 69(d)). Finally, maximum pit size predictions were improved when a changing electrolyte (precipitation and dehydration) were incorporated into the model for sea-salt solutions.

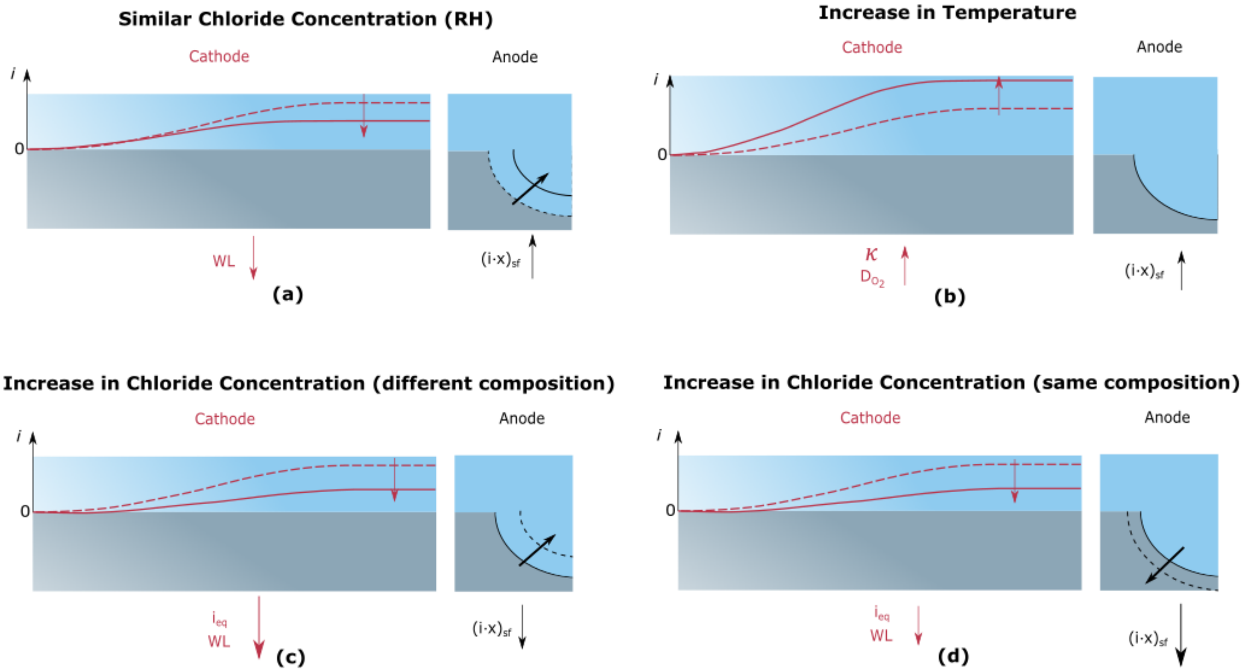

Figure 69: Controlling factors for (a) similar chloride concentrations, (b) increase in temperature, (c) increase in chloride concentration (different composition), and (d) increase in chloride concentration (same composition) on the maximum pit size predictions.

While there are many different controlling mechanisms for corrosion, the importance of cathodic reactions in atmospheric environments is undeniable. The assumption of an ideal cathode provides a powerful theoretical limit of cathodic current and allows for the calculation of a maximum pit and identification of controlling variables for a given set of environmental conditions. Despite being overconservative by roughly a factor of two, the formulism of the max pit model allows for the identification of governing parameters. The same governing parameters in the maximum pit formulism have also been identified as in FEM simulations again showing the applicability of the maximum pit model.

6. Cathodic and anodic control of crack tip chemistries

6.1. Summary

Crack tip electrochemical conditions are explored utilizing a reactive transport FEM. It was determined that an increase in cathode length, decreasing *WL* thickness, and increasing crack length increases total cathodic current per width, increasing metal chloride concentrations, and decreasing the pH. Increasing K decreases the total current per width, decreases the metal chloride concentration, and increases the pH. It is important to remember that crack tip current densities are not specific at a specific level of K (*i.e.,* increasing K does not impose an anodic current density) and that the conclusions are based on equilibrium conditions of the crack tip. Finally, artificially increasing ORR on the external surface 100-fold increases the potential drop of the crack tip while causing for saturated conditions and a decreased pH largely due to an unpolarizable external surface.

It was shown that HER is the dominant cathodic reduction reaction in the crack while ORR in the crack accounts for less than 0.1 % of the total cathodic current in the system at steady state. It was also determined that the concentration of species and potential distribution across the crack was uniform. The importance of coupling the crack tip to the external environment was noted and importance of the external cathode size was investigated and compared to literature experiments. Further, the complex interactions between cathode size and *WL* thickness, similar to that of a galvanic couple, are present for SCC scenarios. The presented model can give insight into the electrochemically short crack phenomena and support the anodic dissolution mechanism at grain boundaries. Finally, the presented results and discussion calls into question whether electrochemical similitude is achieved between different specimens, different crack lengths, and between laboratory specimen and field relevant samples.

6.2. Introduction

As mentioned in Section 1.2.3, chemical and electrochemical properties down the crack are not representative of bulk conditions, especially at the crack tip which is assumed to be the primary site for anodic reactions. Elevated metal cation concentrations have been observed in multiple alloy systems [66,69,194] and due to the occluded environment of the crack tip, acidic stable pH's have been measured in crack tips under open circuit conditions [66–71]. Various models exist in order to investigate crack growth rate (CGR) and crack tip conditions of both CF and SCC and associated environments including: PLEDGE [76], coupled environmental fracture model (CEFM) [77,78], mass transport modeling of crack tip phenomena [74,79,80], and FEM with mass transport modeling [195]. The PLEDGE model does not account for charge conservation and cathodic reductions in the crack. Along with this, it does not account for the external environment which has been shown to have an impact on the CGR and crack tip conditions [76], thus providing a poor model to predict crack tip conditions or CGR. The CEFM was primarily built to predict CGR and was based on the following assumptions: (i) the crack walls are parallel, (ii) the crack walls are inert, (iii) cracking occurs via the film rupture/slip dissolution mechanism, (iv) current generated by crack tip dissolution is consumed by reduction on the external surface and (v) dilute solution theory.

Although CEFM has provided useful points for discussion over the past few decades, the assumptions lead to important limitations. First, it has been shown that when assuming a parallel-sided crack in comparison to a trapezoidal crack, the crack tip potential and pH are impacted with the parallel-sided crack having an increased crack tip pH [81]. Second, Turnbull has further pointed out that taking into account crack wall electrochemical reactions plays a significant role in determining both the crack tip pH and potential [74,81]. When taking into account cathodic reactions in the crack, it is possible that the crack tip experiences a further polarization (creating a larger potential difference between the surface and crack tip) to support anodic dissolution which further impacts local chemistry [81]. Finally, dilute solution theory is used. It has been pointed out that concentrated solutions can arise from crack tip dissolution, thus, dilute solution transport may not be appropriate for these conditions but requires advanced solvers [74].

Another take on crack tip modeling was taken on by Turnbull and coworkers in which the crack tip solutions are predicted rather than crack tip growth rates [74,80,81,84]. Trapezoidal cracks have been used by Turnbull and Feriss [80] whereas Danielson et. Al. [196] adopted a parabolic expression to define a more realistic crack tip shape. The crack tip shape, in this case, has little impact on the crack tip chemistry, however, as previously mentioned, overall crack shape (*i.e.* parallel or trapezoidal) has proven to be important [74]. Turnbull considered mass transport in a crack occurring by diffusion, ion migration and fluid flow. Due to the proximity of the walls of the crack, the concentration and potential profiles between the walls can be reasonably assumed to be flat allowing for the averaging of the two-dimensional transport equations across the crack. Neglecting through-thickness variations in the concentration and potential, leads to one-dimensional mass conservation for dilute solutions. Solving the system of one-dimensional equations can yield the pH and E_{tip} (potential drop) for a crack at various depths [84] and can be compared to the conditions experimentally determined values. While an increase in bulk chloride concentration (increased conductivity) decreases the potential drop seen in the crack tip, the pH of the crack tip is decreased further due to increased hydrolysis and is seen in Figure 70 [84].

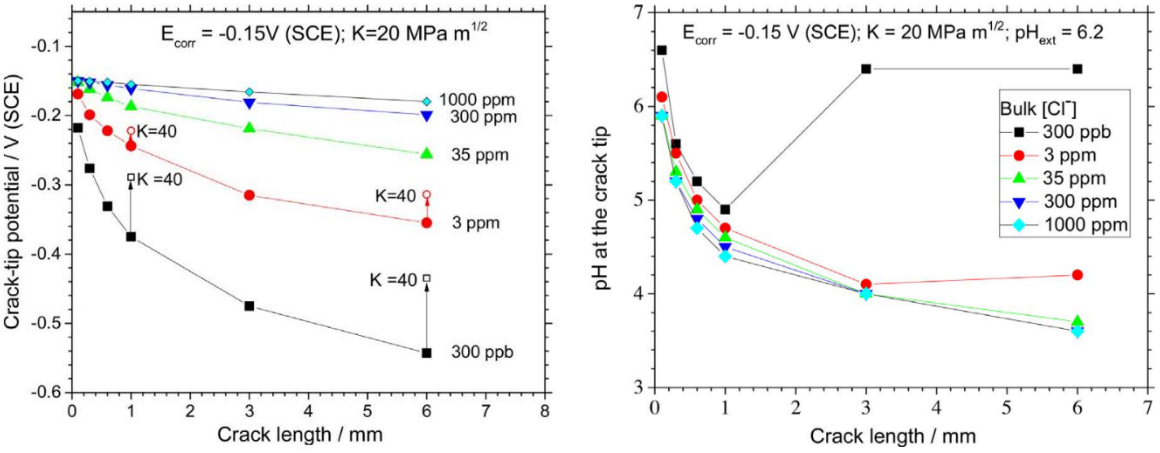

(a)

(b)

Figure 70: Variation in calculated (a) crack tip potential and (b) pH as a function of bulk chloride concentration for FV566 steel at 90˚C [95].

Both Macdonald [197] and Turnbull [84] have attempted to apply their models to thin film boundary conditions either in flowing solutions or actual thin film conditions respectively. Although it is not clear all assumptions that were taken into account in Turnbull and Wright's work, a decrease in crack tip potential was seen with decreasing *WL* thickness [84]. The work of Kwon et al. hypothesized that enhanced CGR were seen with increased solution flow due to an increase in oxygen on the external surface which is predicted by the CEFM [197]. Although both models show an influence of oxygen diffusion on the bulk surface, a full analysis of the effects of thin film electrolytes seen in atmospheric environments has not been completed. Furthermore, many previous models have focused on modeling in dilute solutions (conditions present in boiling water reactor environments) which are not applicable to atmospheric environments.

Finally, a recent model coupled crack chemistry calculations in PHREEQC, electrochemical and transport equations in COMSOL, and trapping-affected hydrogen diffusion in ABAQUS [195]. The modified form of the Nernst–Planck equation for moderately dilute electrolytes was utilized to simulate mass transport inside a crack. Additionally, the formation of hydrogen bubbles in the crack tip was accounted for in changes by changing the local conductivity. It was also assumed that the tip is fully exposed to the environment, because the passive film is broken by plastic deformation and low pH and the crack tip current density was a function of E_{corr}, E_{rp}, i_{rp}, i_{corr} and corresponding Tafel slopes [195]. However, ORR on the external surface and subsequent changes on the external surface due to ORR (pH and L_C) were not incorporated. The only cathodic reaction was HER. Despite this limitation, great agreement between modeled [195] and experimental [70] electrochemical potentials was presented and showed the utility of utilizing FEM to predict crack tip electrochemistry.

It is important to note the computational differences between models in literature. The method utilized by Turnbull is separated out in four steps: (i) solve crack chemistry for a defined E_m and calculated the current at the mouth, (ii) solve the Laplace equation for E_{corr}, (iii) derive the external potential drop on the cathode, and (iv) iterate until values of E_{corr} and the external drop are in agreement (values converge) [74]. This is in contrast to the method used by Macdonald and coworkers which also has four steps: (i) a value for the external surface potential drop is assumed, (ii) the value of E_m is then determined based on the potential drop, (iii) the transport processes in the crack are then determined and a value for the current density at the mouth of the crack is determined, and (iv) the Laplace equation is solved for the external environment and iterated until the external potential drop is converged [198]. A main point of contention between these models includes a disagreement in the determination of E_{corr}. Turnbull and coworkers iterate until the external potential drop converges with an experimentally determined E_{corr} but Macdonald and coworkers calculate E_{corr} from environmental parameters (i.e., temperature, O_2 concentration, etc.) and iterate until convergence upon this value is achieved. While this may be the case, recently Marshall et al. showed that E_{corr} may not be achieved for a pitting scenario unless the cathode size is relatively large with respect to the anode. For example, given a hemispherical pit with a radius of 15 µm exposed to a 3 M NaCl electrolyte with a thickness of 16 µm approaches E_{corr} when the cathode size is roughly 45 cm [192]. This stems from the fact that near OCP, the current densities approach i_{corr} and are generally very small. Under these circumstances, small current densities lead to a small ohmic drop and the inability to physically reach E_{corr}. Thus, forcing the external cathode to be a calculated value of E_{corr} may not be physically achievable in typical CGR specimens.

6.3. Model description

The presented model simulates electrochemical conditions in the center of a crack in a single edge notch tension (SENT) geometry exposed to a 3 M NaCl solution at room temperature (25 ˚C). The concentration of 3 M NaCl was chosen based on recent SCC tests for a custom 465 alloy (Fe-based) in which various atmospheric scenarios were explored [199], available electrochemical data for ORR (Appendix B), as well as a similar bulk solution conductivity $\left(19.7\frac{S}{m}\right)$ in comparison to the conductivity of saturated metal salt solution $\left(21.8\ \frac{S}{m}\right)$ [192]. Calculations are made for an open system considering an oxygen partial pressure of 0.21 atm. Simulations are made in a 2D geometry exploiting symmetries. Passive and active anodic dissolution were considered at the crack tip and crack walls which are balanced by both HER and ORR occurring at the crack tip, crack walls, and external surface. As a byproduct of dissolution, the production rate of ionic species was calculated by Faraday's law using the local current densities from the partial reactions occurring at the alloy surface. Subsequent metal hydrolysis as well as metal salt formation were considered which have influences on the pH and rate (current density) of electrochemical reactions. Additionally, HER and ORR influence the pH (Equations 2-14), therefore all electrochemical reactions are written as a function of solution parameters (*i.e.* chloride concentration, pH, or oxygen concentration) accounting for the changing electrolyte conditions.

6.3.1. Governing Equations

The most complete means of describing the materials balance of charged species in an electrochemical system is the Nernst-Plank Equation. It is given by the summation of the diffusion, migration, convection, and homogeneous reaction terms:

$$\frac{\partial C_i}{\partial t} = -\nabla \cdot N_j + R_j = -\nabla\left(D_j \nabla C_j\right) + \frac{z_j F}{RT} \nabla \cdot \left(D_j C_j \nabla \phi_l\right) - \nabla \cdot \left(C_j v\right) + R_j \qquad 39$$

where N_j is the mass flux, C_j is the concentration, z_j is the number of charges, D_j is the diffusivity, ϕ_l is the electrolyte potential, F is Faraday's constant (96485 C/mol), v is the fluid velocity, and R_j is the homogeneous production of species j. Equation 39 represents a complete transient description of the potential, current density, and concentration distribution, but is computationally expensive in terms of complexity and time [26]. Assuming electroneutrality and near-constant electrolyte composition, the Nernst-Plank Equation can be reduced to the Laplace equation given by Equation 38 and helps greatly reduce the computational time [26,41]. Due to the high conductivity of the 3 M NaCl solution $\left(19.7 \frac{S}{m}\right)$, the compositional changes of the electrolyte as a result of SS304L dissolution, hydrolysis, and metal salt formation were assumed to negligibly affect the conductivity of the solution. This is supported by the fact that a saturated solution of $FeCl_2$, $NiCl_2$, and $CrCl_3$ (roughly 5 M concentration) has a conductivity of $21.8 \frac{S}{m}$ [192]. Therefore, in the realms of possible solution compositions, the change in κ is minimal and was assumed constant at the bulk κ of 3 M NaCl. Additionally, it is also assumed that diffusion adds a negligible contribution to the current, allowing for the Laplace equation to be used. Thus, species transport was decoupled from the current distribution model, Ohm's law (Equation 40) was used to solve for the electrolyte current density, and the Laplace equation (Equation 38) was used to solve for potential distribution. The ionic transport of minor species was solved independently. This approach was used to overcome some of the difficulties associated with solving the Nernst-Planck equations with electroneutrality [26,41].

$$i = -\sigma \nabla \phi_l \qquad 40$$

Overall, the local solution composition was calculated at each time step based upon the products of cathodic and anodic reactions and the hydrolysis and metal salt formation of the metal ions. The transport of ions in solution follows the assumption of dilute species with influences from migration in an electric field. The flux of a species j in solution is presented as

$$J_j = -D_j \nabla C_j - z_j u_j F C_j \nabla V \qquad 41$$

where u_j is the mobility and ∇V is the potential field in to which the ion is subjected. The mobility is given by the Nernst-Einstein relationship defined as

$$u_j = \frac{D_j}{RT} \qquad 42$$

For each species, D_j is assumed to be dependent on the total chloride concentration. There have been multiple sources in literature on how to approach this including a viscosity dependent diffusivity [200] and semi-empirical models [142]. Due to the complexity of modeling diffusivities in solutions with elevated concentrations [201], a new approach is introduced within. Diffusivities are calculated in OLI Studio as a function of chloride concentration and will be presented in 6.3.3.

6.3.2. Crack tip geometries

The geometry of an SENT crack is shown in Figure 71. It is noted that loading of the SENT sample is in the positive and negative x direction with crack growth in the negative z direction. The crack mouth opening displacement ($CMOD$) of an SENT crack (Figure 71) is given by

$$CMOD = \frac{4\sigma a}{E'} V_1\left(\frac{a}{b}\right) \qquad 43$$

where σ is the load, a is the crack length, $V_1\left(\frac{a}{b}\right)$ is a geometric factor, a is the crack length, b is the sample width, and E' is an elastic constant.

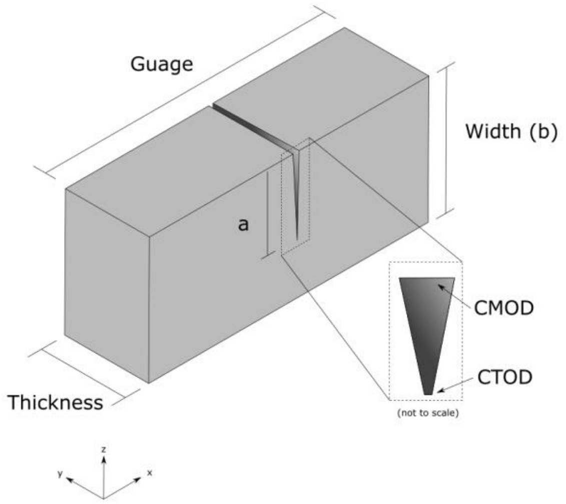

Figure 71: Schematic of an SENT sample. Loading of the SENT sample is in the positive and negative x direction with crack growth in the negative z direction.

For plane strain conditions, E' is given by

$$E' = \frac{E}{1-\nu} \tag{44}$$

where E is Youngs Modulus and ν is Poisson's ratio. $V_1\left(\frac{a}{b}\right)$ is given by [202]

$$V_1\left(\frac{a}{b}\right) = \frac{1.46 + 3.42\left(1 - cos\left(\frac{\pi a}{2b}\right)\right)}{cos\left(\frac{\pi a}{2b}\right)^2} \tag{45}$$

The width of a trapezoidal crack tip, or the crack tip opening displacement ($CTOD$) is defined as

$$CTOD = 0.6(1-\nu^2) * \frac{K^2}{E\sigma_{ys}} \tag{46}$$

where K is the stress intensity factor and σ_{ys} is the yield strength of the material [81]. K is given by

$$K = \sigma\sqrt{\pi a} \cdot f\left(\frac{a}{b}\right) \qquad 47$$

where $f\left(\frac{a}{b}\right)$ is a geometric factor as seen in Equation 48 [202].

$$f\left(\frac{a}{b}\right) = \sqrt{\frac{2b}{\pi a} tan\left(\frac{\pi a}{2b}\right)} * \frac{\left(0.752 + 2.02\left(\frac{a}{b}\right) + 0.37\left(1 - sin\left(\frac{\pi a}{2b}\right)\right)^3\right)}{cos\left(\frac{\pi a}{2b}\right)} \qquad 48$$

Thus, given material and sample properties (E, σ_{ys}, ν, and b), $CMOD$ (Equation 43) and $CTOD$ (Equation 46) can be specified at a given a as long as σ or K are known.

6.3.3. Chemical reactions and solution properties

The hydrolysis and formation of metal salts (Equations 49 - 56) that were considered for Fe, Cr, and Ni species are presented in Table 5. The equilibrium constants (K_{eq}) were obtained primarying from In-Drift Precipitates/Salts Model [203] and supplemented with data from Sun et al. [200]. Solubility constants (K_{sp}) were obtained from In-Drift Precipitates/Salts Model [203] and are presented in Table 6.

Table 5: Reactions and equilibrium constants utilized

Reaction	**K_{eq}**	**Eqn. Number**	**Ref.**
$Fe^{2+} + H_2O \leftrightarrow FeOH^+ + H^+$	$3.090 \cdot 10^{-10}$	49	[203]
$Fe^{2+} + Cl^- \leftrightarrow FeCl^+$	$6.792 \cdot 10^{-1}$	50	[203]
$Cr^{3+} + H_2O \leftrightarrow CrOH^{2+} + H^+$	$2.692 \cdot 10^{-4}$	51	[203]
$Cr^{3+} + 2H_2O \leftrightarrow Cr(OH)_2^+ + 2H^+$	$1.445 \cdot 10^{-10}$	52	[203]
$Cr^{3+} + Cl^- \leftrightarrow CrCl^{2+}$	$7.757 \cdot 10^{-3}$	53	[200]
$Cr^{3+} + 2Cl^- \leftrightarrow CrCl_2^+$	$1.578 \cdot 10^{-2}$	54	[200]
$Ni^{2+} + H_2O \leftrightarrow NiOH^+ + H^+$	$3.162 \cdot 10^{-10}$	55	[203]

$Ni^{2+} + Cl^{-} \leftrightarrow NiCl^{+}$	$1.009 \cdot 10^{-1}$	56	[200]

Table 6: Solubility Constants

Reaction	**K$_{sp}$**	**Eqn. Number**	**Ref.**
$Fe^{2+} + 2OH^{-} \leftrightarrow Fe(OH)_{2,s}$	$6.607 \cdot 10^{-15}$	57	[203]
$Cr^{3+} + 3OH^{-} \leftrightarrow Cr(OH)_{3,s}$	$2.239 \cdot 10^{-33}$	58	[203]
$Ni^{2} + 2OH^{-} \leftrightarrow Ni(OH)_{2,s}$	$3.311 \cdot 10^{-18}$	59	[203]

Reactions in Table 5 were defined kinetically as forward and backward reactions. In the absence of literature reaction rates, the forward reaction rates (k_f) were assumed to be sufficiently fast (10^3 1/sec) with the backward reaction rate constant (k_b) as defined by:

$$k_b = \frac{k_f}{K} \tag{60}$$

The rate of metal hydrolysis precipitation was defined using a step function to ensure the reaction would only occur after the saturation was reached as shown in Equation 61 [41]:

$$r_{Me(OH)_{n,s}} = k\left(c_{Me^{n+}} \cdot c_{OH^{-}}^{n} - K_{sp}\right) * H(x) \tag{61}$$

where $H(x)$ is a Heaviside function given by,

$$H(x) = \begin{cases} 0, x \leq 0 \\ 1, x > 0 \end{cases} \tag{62}$$

and x defines the solubility limit:

$$x = \frac{c_{Me^{n+}} \cdot c_{OH^{-}}^{n}}{K_{sp}} - 1 \tag{63}$$

Finally, the water dissociation reaction was also included in the model and was assumed to be at equilibrium:

$$H_2O \leftrightarrow H^+ + OH^- \tag{64}$$

Diffusivities were calculated as a function metal salt chloride concentration utilizing OLI Studio (Version 10.0). An example of the process is shown in Figure 72 in which the diffusivity of Fe^{2+} is plotted as a function of total chloride concentration and with a cubic function. The general form of the fit presented in Figure 72 is given by

$$D = A_3[Cl^-]^3 + A_2[Cl^-]^2 + A_1[Cl^-] + A_o \tag{65}$$

where A_{1-3} represent fitting coefficients and A_o represents the diffusivity at infinite dilution. The fitting parameters for all species considered are presented in Table 7. Diffusivities for solid compounds (*i.e.* $FeCl_2$) were assumed to be small and roughly 100 times slower than ionic counterparts (*i.e.* $D_{FeCl_2} = D_{FeCl^+}/100$) in a similar manner to Sun et al. [200].

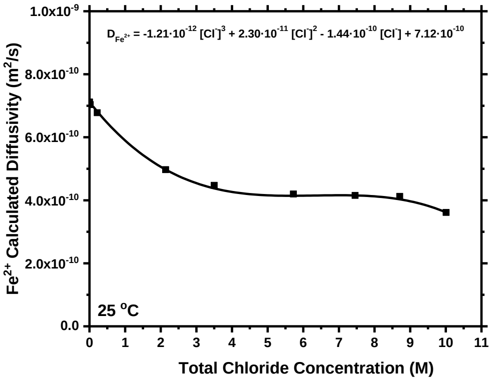

Figure 72: Calculated (OLI Studio) Fe^{2+} diffusivity as a function of total chloride concentration.

Table 7: Calculated diffusivities for all species in model

Species	$\mathbf{A_3 \cdot 10^{12}}$	$\mathbf{A_2 \cdot 10^{11}}$	$\mathbf{A_1 \cdot 10^{10}}$	$\mathbf{A_o \cdot 10^{10}}$

Fe^{2+}	-1.21	2.30	-1.44	7.12
$FeCl^{+}$	-1.57	2.81	-1.63	7.02
$FeOH^{+}$	-1.57	2.80	-1.62	7.11
Cr^{3+}	-1.22	2.16	-1.23	6.03
$CrCl^{2+}$	-1.86	3.35	-1.95	7.98
$CrCl_2^{+}$	-1.33	2.38	-1.39	5.93
$CrOH^{2+}$	-1.32	2.35	-1.36	6.03
$Cr(OH)_2^{+}$	-1.33	2.38	-1.39	6.02
Ni^{2+}	-1.50	2.66	-1.56	7.05
$NiCl^{+}$	-1.55	2.77	-1.62	6.95
$NiOH^{+}$	-1.55	2.77	-1.60	7.04
OH^{-}	-12.0	22.4	-13.4	52.4
H^{+}	-24.2	44.8	-25.5	93.0
Cl^{-}	-4.79	8.72	-5.06	2.03
Na^{+}	-1.51	0.89	-1.09	13.3
O_2	-3.36	6.40	-4.08	20.5

In order to test the validity of programing the reactions presented in Table 5 and Table 6, metal salt solutions ($FeCl_2$, $CrCl_3$, and $NiCl_2$) were created in COMSOL, OLI Studio, and EQ3/6. The equilibrium pH as a function of total chloride concentration was evaluated.

As previously discussed, the solution was assumed to have a constant conductivity of $19.7\frac{S}{m}$ for 3M NaCl calculated through OLI Studio. Various *WL* thickness were utilized ranging from bulk (> 609 µm, Figure 34(a)) to thin film conditions (100 µm).

6.3.4. Electrochemical reactions and creation of boundary conditions

All kinetic reactions are fit to Tafel expressions. ORR kinetics are fit to a cathodic Tafel expression given by,

$$i_{act,ORR} = \frac{C_{O_2}}{C_{O_2,ref}} \cdot i_{o,ORR} \cdot 10^{\frac{\eta_{O_2}}{A_{O_2}}} \tag{66}$$

where C_{O_2} is the O_2 at the surface of the alloy, $C_{O_2,ref}$ is the reference O_2 concentration, η_{O_2} is the overpotential for ORR reactions, A_{O_2} is the cathodic (< 0) Tafel slope, and $i_{o,ORR}$ is the exchange current density for ORR. The total current for ORR is given by,

$$i_{ORR} = \frac{i_{act,ORR}}{1 + \frac{i_{act,ORR}}{i_{lim}}} \tag{67}$$

where i_{lim} is defined based on *WL* thickness and can be obtained from Appendix B. The current density for ORR will consume O_2 and produce OH^- with a four-electron transfer. As the ORR reaction is dependent on the dissolved oxygen concentration, a dissolution rate of oxygen is defined at all air/electrolyte interfaces and is defined as [204],

$$F_{O_2} = \left(1 - \frac{C_{O_2}}{C_{O_2,ref}}\right) \cdot F_{max,O_2} \tag{68}$$

where $C_{O_2,ref}$ is the solubility of oxygen in 3 M NaCl at 25 ˚C and F_{max,O_2} is the limiting value for dissolution of oxygen into the electrolyte ($3.5 \cdot 10^{-5}$ mol/m^2/s) [205].

HER cathodic kinetics have a similar form to ORR kinetics and is given by

$$i_o = i_{o,Cl,HER} \cdot 10^{\frac{\eta_{HER}}{A_{HER}}} \tag{69}$$

where η_{HER} is the overpotential for HER reactions, A_{HER} is the cathodic (< 0) Tafel slope, and $i_{o,Cl,HER}$ is the exchange current density at a given chloride concentration for HER. The current density for HER will produce H_2 and consume H^+ with a number of electrons transferred of two. Anodic kinetics are fit to an anodic Tafel expression given by,

$$i_{act,M} = i_{o,Cl,M} \cdot 10^{\frac{\eta_M}{A_M}} \tag{70}$$

where η_M is the overpotential for anodic dissolution reactions, A_M is the anodic (> 0) Tafel slope, and $i_{o,Cl,M}$ is the exchange current density at a given chloride concentration for ORR. The total current for anodic dissolution is given by,

$$i_M = \frac{i_{act,M}}{1 + \frac{i_{act,M}}{i_{Cl,pass,M}}} \tag{71}$$

where $i_{Cl,pass,M}$ is the passive current density and is a function of the chloride concentration. Finally, i_M will inform the production of metal species with a number of electrons transferred of 2.2 and dissolution according the stoichiometric composition of SS304L.

Electrochemical boundary conditions for both HER and anodic dissolution were created in de-aerated solutions containing $CrCl_3$ and LiCl and NaCl, $CrCl_3$, and LiCl. Ideally, a stoichiometric solution of $FeCl_2$, $CrCl_3$, and $NiCl_2$ would have been utilized to create the boundary conditions. However, as $FeCl_2$ will oxidize rapidly, $CrCl_3$ and LiCl solutions were utilized in order to represent a crack-tip environment and avoid potential oxidation of $FeCl_2$ solutions. For the present case, metal salt solutions were created utilizing 18 % $CrCl_3$ and 46 % LiCl by molarity to create for 100 % Cl in the system. For example, a 10 M metal chloride system contained 1.8 M $CrCl_3$ (5.4 M Cl^-) and 4.6 M LiCl. All reported concentrations will be with regard to total chloride concentrations. In addition, solutions were also created with 3 M NaCl, $CrCl_3$, and LiCl. For example, a 4 M solution in this case corresponds to 3 M NaCl with 0.18 M $CrCl_3$ (0.54 M Cl^-) and 0.46 M LiCl. The distinction between these two solutions will be clear.

Solutions were de-aerated for roughly 2 hours. During the de-aerating period, the OCP was monitored and it was ensured that the it was stable (< 1 mV/min drift) prior to start of the polarization measurement. Scans were taken in the cathodic direction starting 0.05 V noble to the

OCP to a potential of -1.3 $V_{Ag/AgCl}$ at a scan rate of 0.167 mV/sec. Additionally, scans were taken in the anodic direction starting 0.05 V below the OCP to a potential of roughly 1.0 $V_{Ag/AgCl}$ or until the pitting potential was identified at a scan rate of 0.167 mV/sec.

In the present model, the CTOD is assumed to be active and the current density will be dependent upon the solution concentration. The walls of the crack are assumed to be passive, again with a current density dependent upon the solution concentration. HER and ORR were assigned to all electrode surfaces and are dependent upon solution concentration. For ORR, the reaction is also dependent upon the concentration of oxygen in solution.

6.3.5. Summary of model

Overall, the Laplace equation is coupled with the transport of dilute species (with concentration dependent diffusivities) to inform upon equilibrium crack tip conditions under various conditions. The simulation will be performed in a 2D scenario representative of the center line of the crack where the shortest diffusion distance will be through the crack mouth. Such a geometry is representative of a trans granular crack. The surface of the crack and crack walls will be considered homogenous and will not account for influences from chemical or structural differences. Additionally, roughness of the crack walls will not be considered.

For a base comparison study, the following parameters will be utilized. First, the solution utilized will be 3 M NaCl, K will be fixed at 10 $MPa\sqrt{m}$, a will be 2 mm (corresponding to the length of recent pre-cracks [199]), the WL thickness will be 4 mm (4000 µm) and is considered to be full immersion ($WL > \delta_{nc}$, Figure 34), and L_{cath} will be 0.02 m (20 mm). Next, electrochemical boundary conditions are dependent upon the chemistry of the solution and will be evolved over time and the consumption and production of solution species will be dictated by the respective current densities. Third, four other parameters will be varied independently from the base case, including a (increasing to 4 mm), WL thickness (decreasing to 0.1 mm which is considered to be thin film conditions), L_C (increasing to 0.1 m), and K (10 to 20 $MPa\sqrt{m}$). Additionally, a scenario will be presented in which the cathodic kinetics on the external surface are increased by multiplying the exchange current density by 100 ($100 \cdot i_{act,ORR}$). The models are ran for roughly four hours in order to achieve steady state conditions for the crack. Finally, the results will be compared and contrasted between themselves as well as with other models in literature.

6.4. Results

This section will be organized as followed. First, the electrochemical boundary conditions will be presented, and parameters of interest will be fit as a function of chloride concentration. Next, a comparison of modeled pH, comparing COMSOL, OLI Studio, and EQ3/6, under steady state conditions will be presented. Third, a base case for comparison will be presented representing full immersion conditions. Fourth, increasing L_C, decreasing WL thickness, increasing a, and increasing K will be compared to the base case. Finally, a simulation will be presented in which the ORR kinetics on the external surface are increased.

6.4.1. Boundary Conditions

Cathodic polarization scans in de-aerated $CrCl_3$/LiCl solutions and in de-aerated 3 M NaCl + $CrCl_3$/LiCl are presented in Figure 73(a) and (b) respectively. With increasing chloride concentration, an increase in current density is measured.

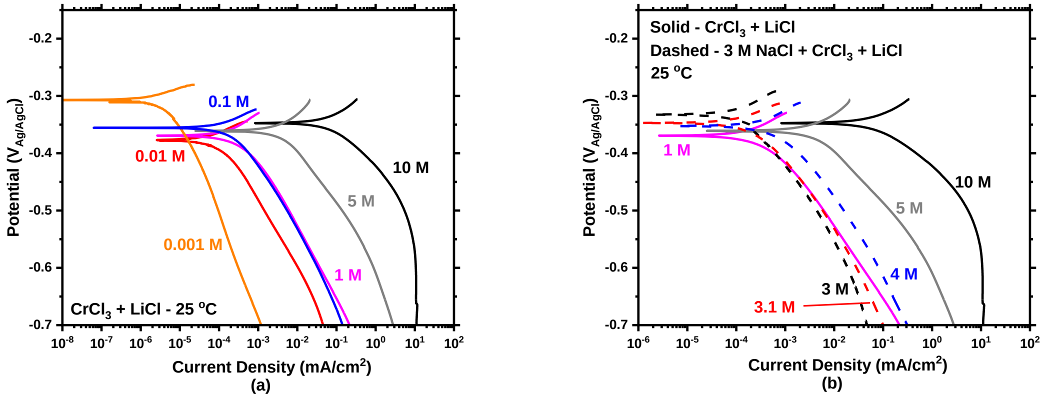

Figure 73: (a) Comparison of cathodic kinetics in $CrCl_3$ and LiCl solutions and (b) with the presence of 3 M NaCl in solution. It is noted that all dashed curves have 3 M NaCl with metal chloride salts added to make up the total chloride molarity.

Anodic polarization scans in de-aerated $CrCl_3$/LiCl solutions and in de-aerated 3 M NaCl + $CrCl_3$/LiCl are presented in Figure 74(a) and (b) respectively. With increasing chloride concentration, an increase in current density and a decrease in the pitting potential is measured.

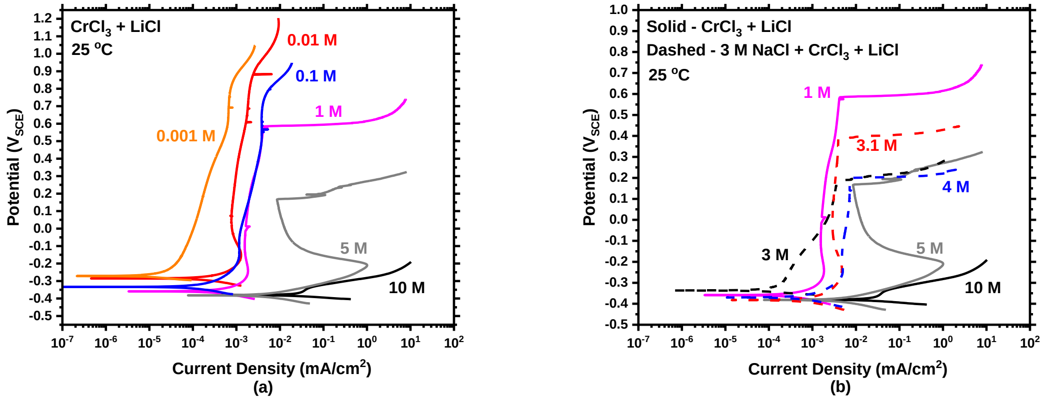

Figure 74: (a) Comparison of anodic kinetics in $CrCl_3$ and LiCl solutions and (b) with the presence of 3 M NaCl in solution. It is noted that all dashed curves have 3 M NaCl with metal chloride salts added to make up the total chloride molarity.

Both cathodic (Figure 73) and anodic (Figure 74) polarization scans were fit according to Equations 69 and 70 – 71 respectively. It is noted that for HER and anodic dissolution, a constant reference potential was utilized when calculating the respective η. All fitted Tafel parameters for HER and anodic dissolution are presented in Table 8 in Equations 72-74 and 75-78 respectively. In addition to these parameters, cathodic parameters for ORR were fitted utilizing Equations 66-67 in the presented polarization scans in Appendix B for 3 M NaCl. In this case, a variable $E_{o,ORR}$ was utilized (Equation 79) due to the fact that pH adjustments were not made to 3 M NaCl brines.

Table 8: Equations for electrochemical boundary conditions

Variable	Equation	Eqn. Number
$E_{o,HER}$	$-0.1\ V_{Ag/AgCl}$	72
$i_{o,Cl,HER}$	$(4.24 \cdot 10^{-5}\ [Cl^-] - 1.30 \cdot 10^{-4})\ [mA/cm^2]$	73
A_{HER}	$-0.12\ \frac{V}{decade}$	74
$E_{o,M}$	$-0.6\ V_{Ag/AgCl}$	75

$i_{o,Cl,M}$	$\left(9.92\cdot10^{-9}+\frac{-4.36\cdot10^{-6}-9.92\cdot10^{-9}}{1+\left(\frac{[Cl^{-}]}{0.49214}\right)^{3.49}}\right)[mA/cm^{2}]$	76
$i_{Cl,pass,M}$	$\left(5.37\cdot10^{-6}*e^{2.16[Cl^{-}]}\right)[mA/cm^{2}]$	77
A_M	$0.04\ \frac{V}{decade}$	78
$E_{o,ORR}$	$\left[1.23+E_{correct}-\frac{RT}{4F}*\log\left(\frac{1}{0.21*10^{-\mathrm{pH}}}\right)\right]\ V_{Ag/AgCl}$	79
$E_{correct}$	$-0.199\ V$	80
$i_{o,ORR}$	$7\cdot10^{-16}\ mA/cm^{2}$	81
A_{O_2}	$-0.118\ \frac{V}{decade}$	82
i_{lim,O_2}	$Bulk: 9.23\cdot10^{-6}\frac{mA}{cm^{2}}; 100\ \mu m: 1.70\cdot10^{-6}\ mA/cm^{2}$	83

6.4.2. pH comparison between COMSOL and various thermodynamic databases

Equilibrium solutions of a stoichiometric salt corresponding to the composition of SS304L were created and a decrease in modeled pH with increase metal salt concentration is presented in Figure 75 for all programs utilized. In general, the pH calculated in EQ3/6 is decreased in comparison to COMSOL and OLI Studio. Despite the slight differences, good agreement is observed between the three programs.

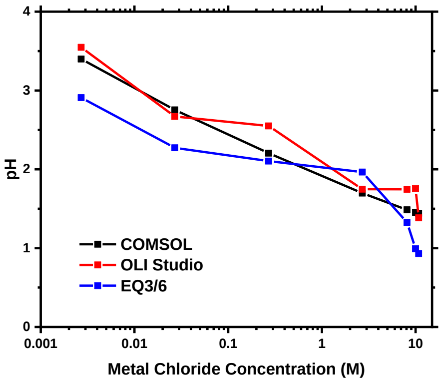

Figure 75: Comparison of modeled pH values between COMSOL, OLI Studio, and EQ3/6 for a ternary metal salt solution.

6.4.3. Full immersion conditions

Total anodic and cathodic I_C/W are presented in Figure 76(a) and (b) respectively. It is noted that cathodic currents are presented on a logarithmic scale and are positive. In reality, the magnitude of the total cathodic current is equal to that of the total anodic current, with its sign indicating its direction. Overall, with increasing time, both anodic and cathodic currents generally increase with time before reaching a steady state value. It is noted that there is a temporary maximum near 1.5 hours in both the anodic and external ORR currents before decreasing to their respective steady state values.

Further analysis was performed on the full immersion conditions in which the total cathodic current was evaluated both internal and external to the crack as displayed in Figure 76(c). A greater portion of the cathodic current is external to the crack at all times. Of the current that is external to the crack, a majority of this current is due to the ORR reaction as displayed in Figure 76(d). Internal to the crack, a majority of the cathodic current is due to HER after roughly 0.75 hours (Figure 76(e)).

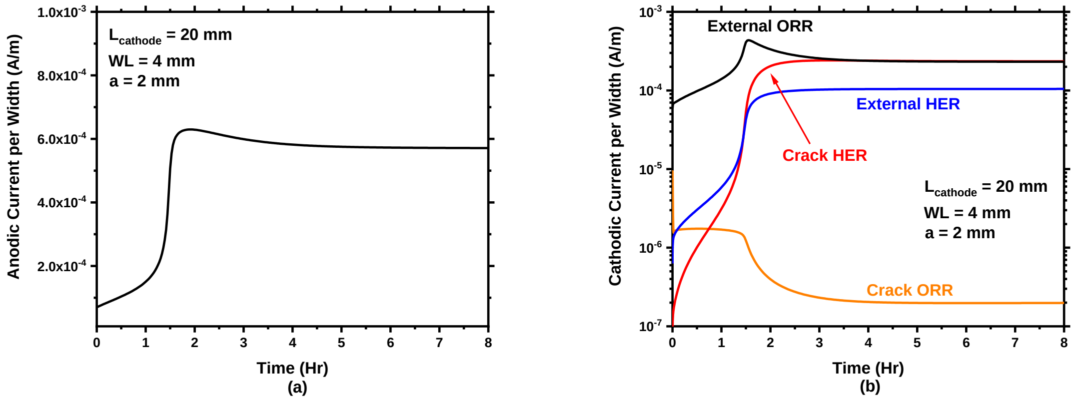

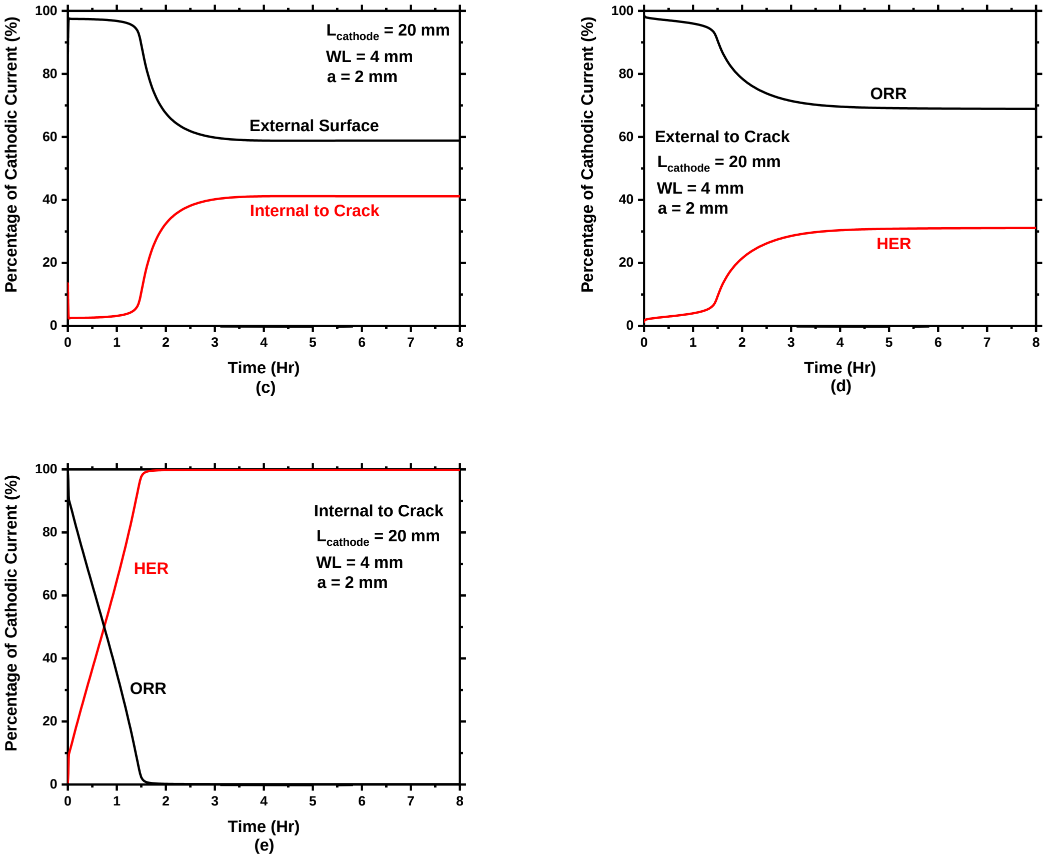

Figure 76: Electrochemical conditions for a crack under full immersion conditions showing (a) total current per width and (b) cathodic currents per width separated into HER and ORR contributions on the internal and external of the crack. It is noted that cathodic currents are opposite signs that of anodic currents; however, in (b) the cathodic currents are presented as positive for easier interpretation. (c) Percentage of cathodic current on the external and internal surface, (d) percentage of cathodic current due to HER and ORR external to the crack, and (e) percentage of cathodic current due to HER and ORR on the internal surfaces.

The potential, presented in Figure 77(a) and (b), is lowest at the crack tip, followed by the crack mouth and cathode edge. The potential drop that exists at steady state between the crack tip and crack mouth is roughly 7 mV and results in a potential drop of 3.5 V/m. Additionally, the highest metal concentration is at the crack tip, followed by the crack mouth and cathode edge as presented in Figure 77(c). The equilibrium concentration of metal at the crack tip is roughly 2.4 M while the cathode edge does not get above 10^{-7} M. Finally, the crack tip experiences the lowest pH (1.9 at steady state) and the cathode edge has the highest pH (Figure 77(d)).

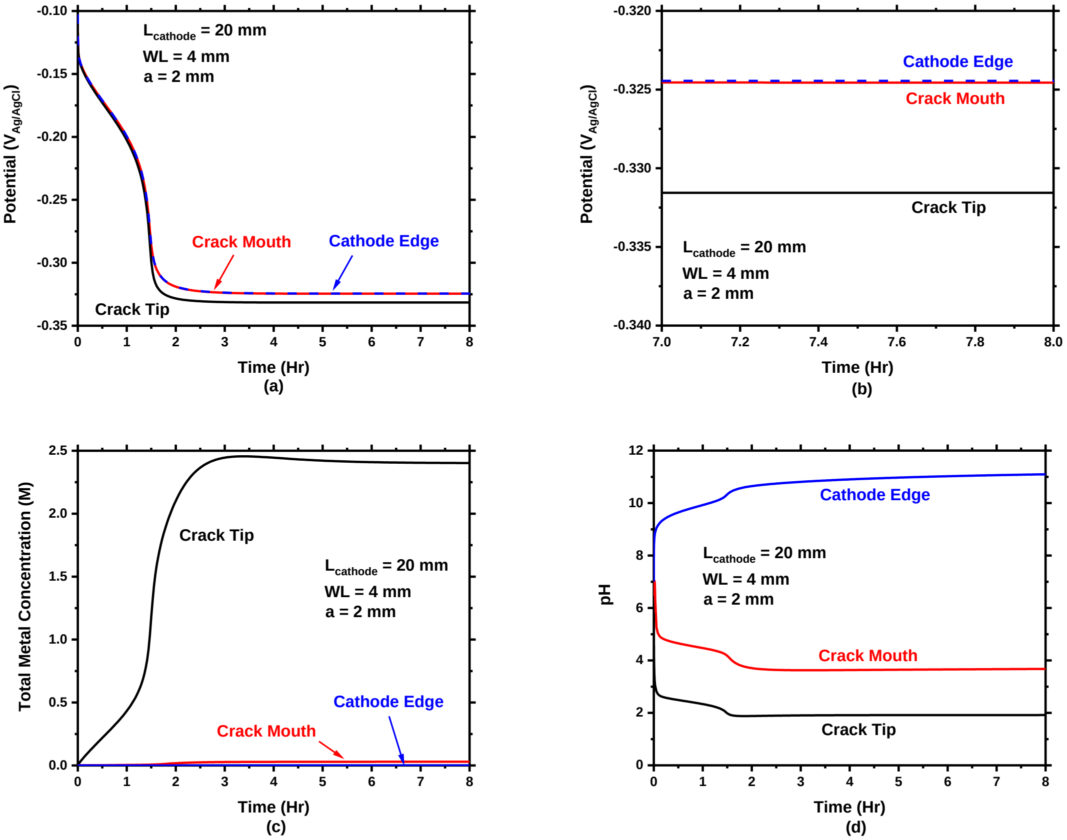

Figure 77: Influence of full immersion on the (a) potential of the crack tip, crack mouth and cathode edge, (b) potential at long time, (c) total metal concentration, and (d) pH.

6.4.4. Increasing cathode length increases dissolution current and percentage of cathode outside of the crack

As presented in Figure 78(a), increasing L_C from 20 mm to 100 mm under full immersion conditions (WL = 4000 µm = 4 mm), increases the I_C/W by roughly a factor of 4 under steady state conditions. Increasing L_C also increased the percentage of the cathodic current that was external to the crack (Figure 78(b)). Of the current on the external surface, the percentage of that current that was due to ORR was increased with an increase in L_C as presented in Figure 78(c). Finally, internal to the crack, HER becomes the dominant reaction as seen in Figure 78(d); however, the transition from ORR dominant to HER dominant occurs at a later time with increased L_C.

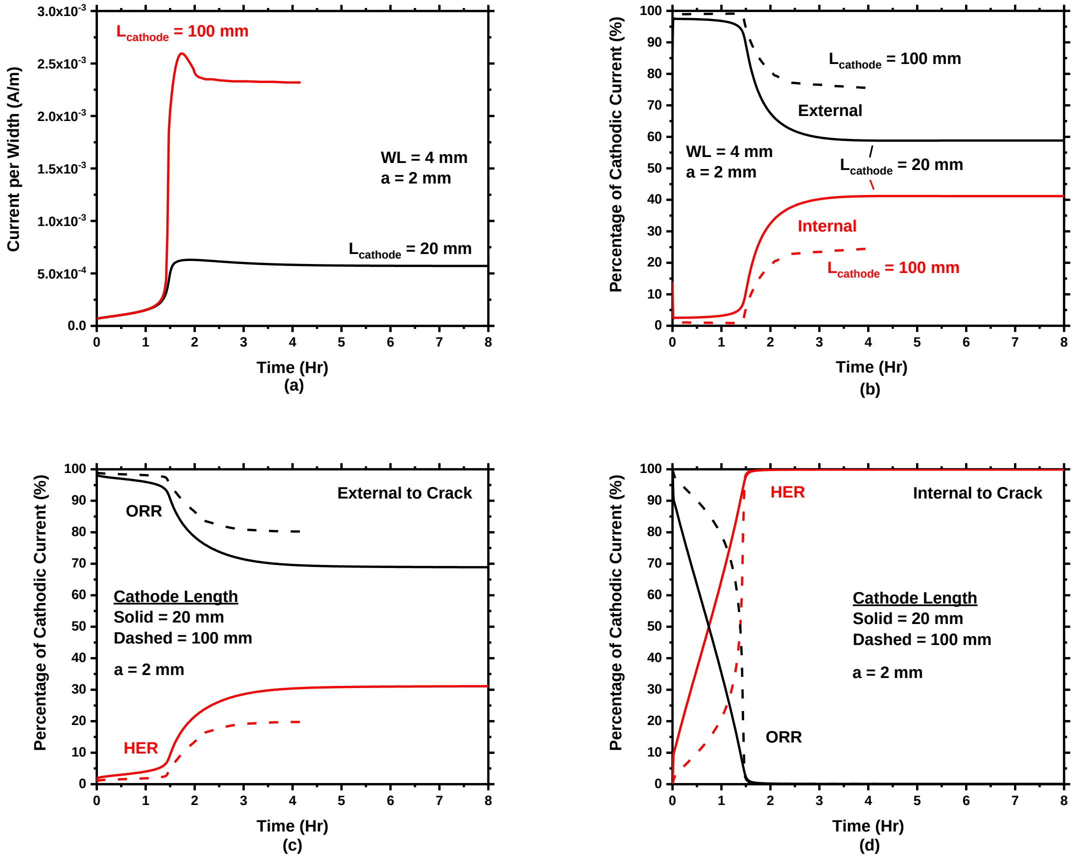

Figure 78: Influence of cathode length on (a) the total current per width, (b) percentage of cathodic current internal and external to the crack, (c) percentage of HER and ORR external to the crack, and (d) percentage of HER and ORR internal to the crack. It is noted that the stress intensity ($10\ MPa\sqrt{m}$), crack length (2 mm), and WL thickness (4 mm) are held constant.

As displayed in Figure 79(a), the potential at the crack tip is increased with increased L_C. Additionally, the crack tip total chloride concentration, Figure 79(b), increases with increasing L_C causing for a decrease in crack tip pH (Figure 79(c)). It is also interesting to note that the cathode pH is decreased with increased L_C.

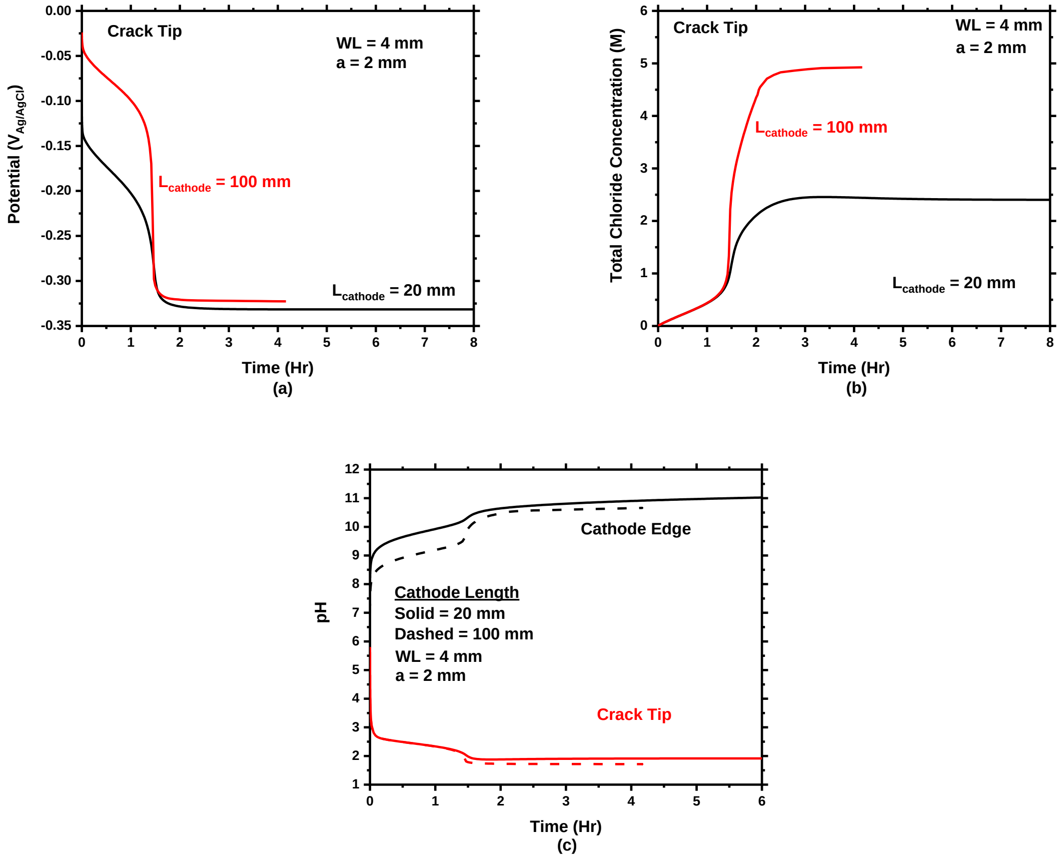

Figure 79: Influence of cathode length on (a) the potential at the crack tip, (b) total metal chloride concentration at the crack tip, (c) pH at the crack tip and cathode edge. It is noted that the stress intensity ($10\ MPa\sqrt{m}$), crack length (2 mm), and WL thickness (4 mm) are held constant.

6.4.5. Decreasing WL thickness increases current per width and percentage of cathode exterior to cathode

Decreasing the *WL* thickness from 4 to 0.1 mm (bulk to thin film respectively) increases the I_C/W by roughly a factor of 2 as shown for steady state conditions in Figure 80(a). More cathodic current is on the external surface for a smaller *WL* thickness and a greater contribution of this current is ORR as shown in Figure 80(b) and (c) respectively. Internally to the crack, the majority of the cathodic current is still HER at steady state; however, with decreased *WL* thickness, there is an increased contribution from ORR internal to the crack as shown in Figure 80(d).

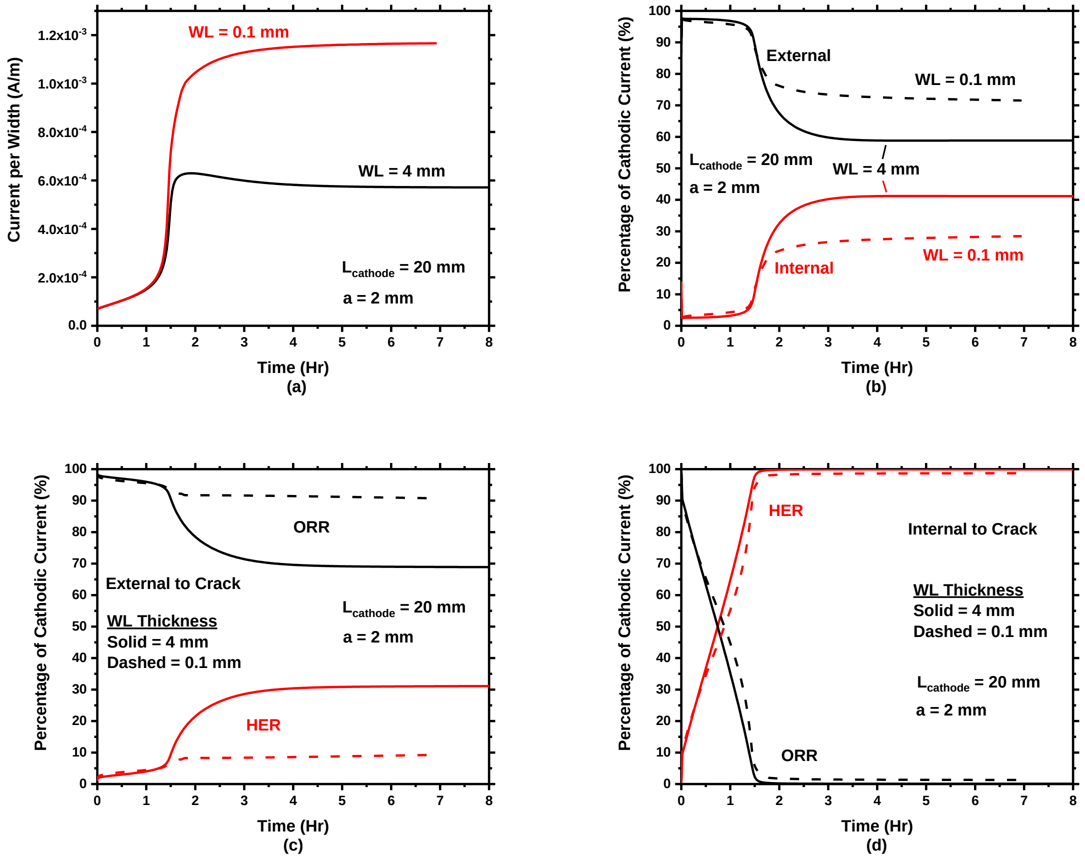

Figure 80: Influence of WL thickness on (a) the total current per width, (b) percentage of cathodic current internal and external to the crack, (c) percentage of HER and ORR external to the crack, and (d) percentage of HER and ORR internal to the crack. It is noted that the stress intensity ($10\ MPa\sqrt{m}$)*, crack length (2 mm), and cathode length (20 mm) are held constant.*

Decreasing the *WL* thickness to 0.1 mm increases the potential at the crack tip (Figure 81(a)) and increases the crack tip chloride concentration (Figure 81(b)) in comparison to a crack exposed to a 4 mm *WL* thickness. Figure 81(c) displays that the pH at the crack tip is decreased and at the cathode edge it is increased for a decrease in the *WL*.

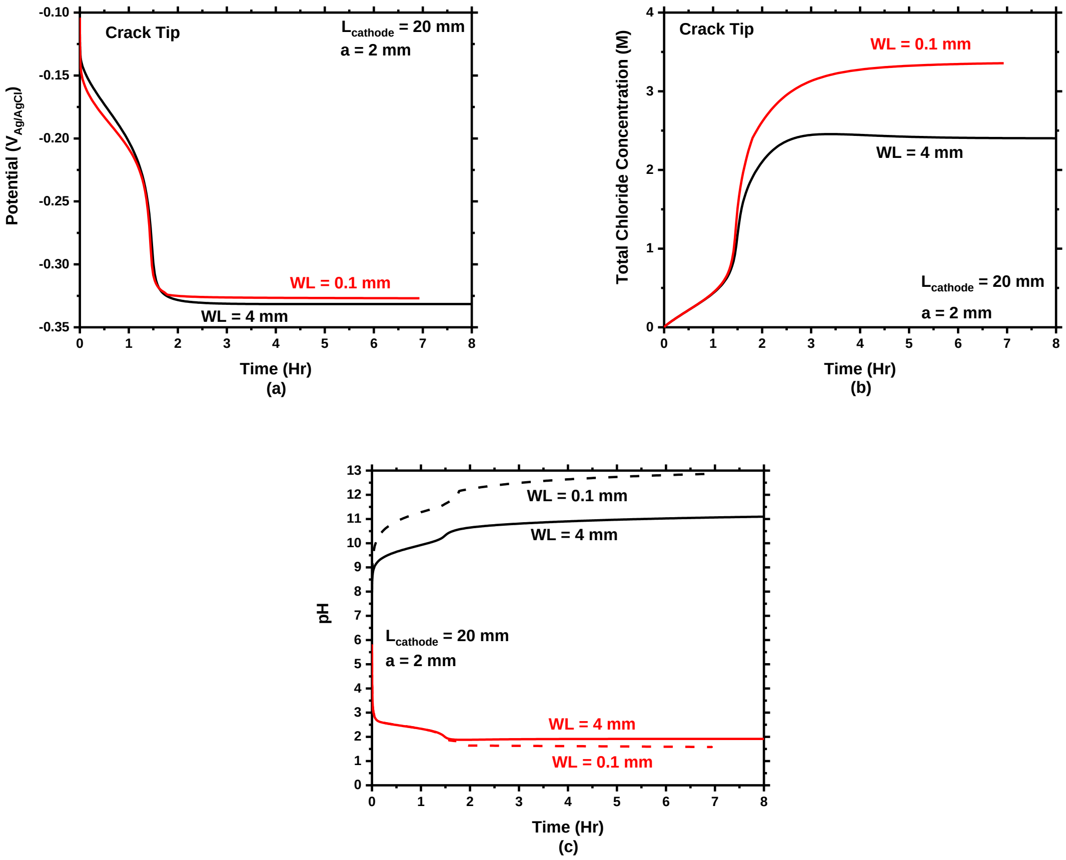

Figure 81: Influence of WL thickness on (a) the potential at the crack tip, (b) total metal chloride concentration at the crack tip, (c) pH at the crack tip and cathode edge. It is noted that the stress intensity ($10\ MPa\sqrt{m}$), crack length (2 mm), and cathode length (20 mm) are held constant.

6.4.6. Increasing crack length increases total current per width

Increasing crack length from 2 to 4 mm, increases I_C/W as presented in Figure 82(a). I_C/W in the case of the 4 mm crack does not reach a plateau due to the fact that the crack tip environment becomes saturated. In contrast to a 2 mm crack, a majority of the cathodic current for a 4 mm crack is supplied from the inside of the crack as presented in Figure 82(b). The transition from the external surface being the dominant cathode to the internal surface being dominant occurs around roughly one hour. While the current on the external surface remains predominantly ORR (Figure 82(c)), the internal current becomes dominant in HER after roughly 15 minutes (Figure 82(d)**).**

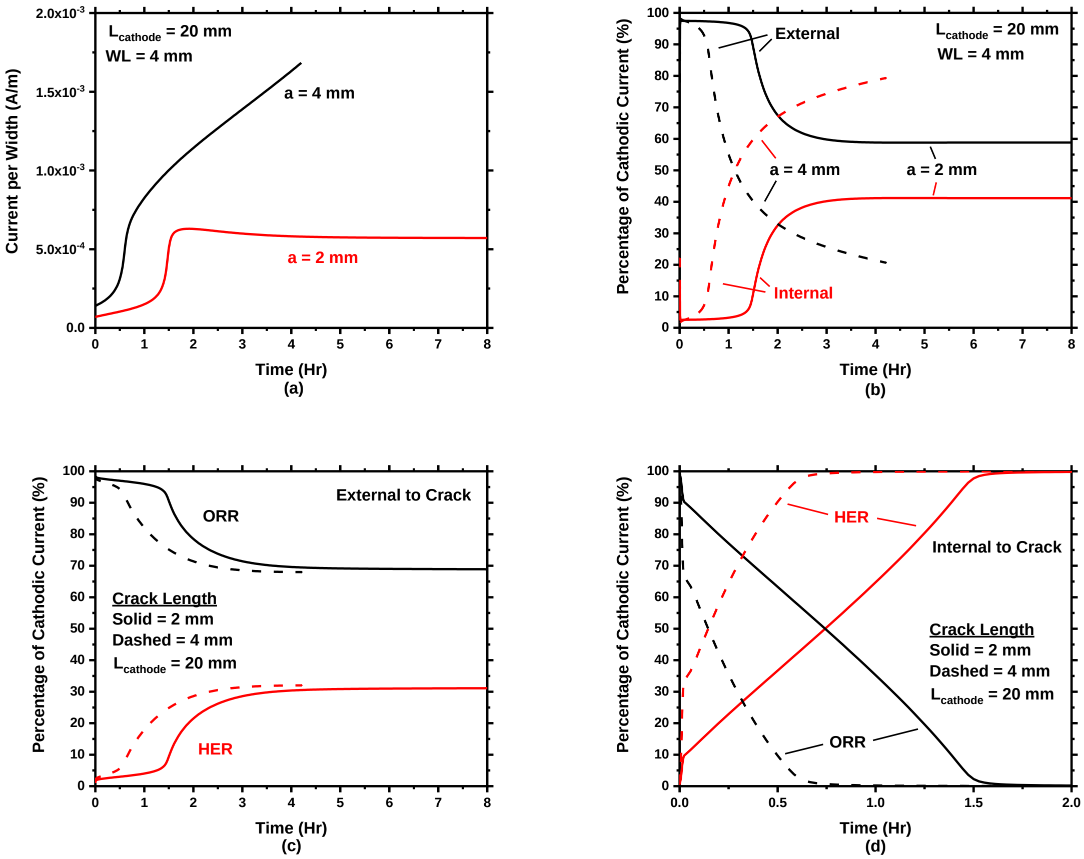

Figure 82: Influence of crack length on (a) the total current per width, (b) percentage of cathodic current internal and external to the crack, (c) percentage of HER and ORR external to the crack, and (d) percentage of HER and ORR internal to the crack. It is noted that the stress intensity ($10\ MPa\sqrt{m}$), cathode length (20 mm), and WL thickness (4 mm) are held constant. Note the time scale in (d)

The crack tip potential also becomes polarized to a more negative potential in a much shorter timer period as seen in Figure 83(a) for the crack length of 4 mm. Additionally, when increasing the crack length, the chloride concentration at the crack tip increases and becomes saturated after roughly 4 hours (Figure 83(b)). Finally, as presented in Figure 83(c), increasing the crack length to 4 mm decreases the crack tip pH and increases the cathode pH in comparison to a 2 mm crack.

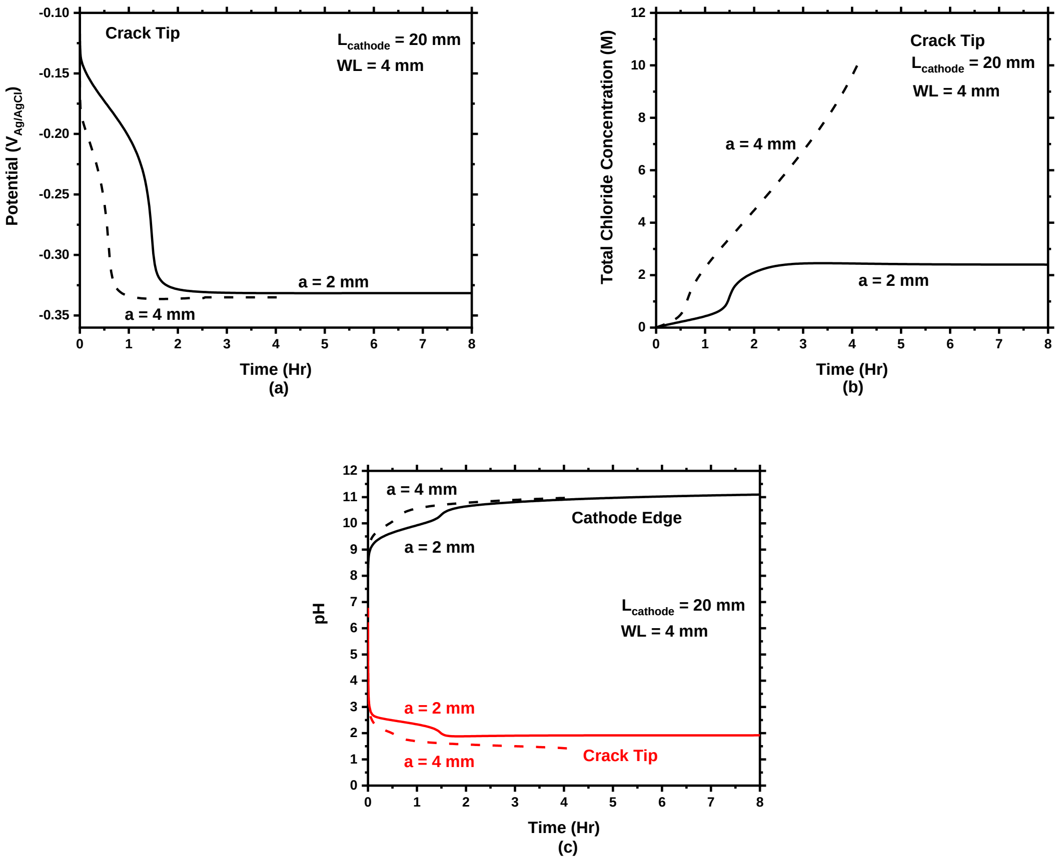

Figure 83: Influence of crack length on (a) the potential at the crack tip, (b) total metal chloride concentration at the crack tip, (c) pH at the crack tip and cathode edge. It is noted that the stress intensity ($10\ MPa\sqrt{m}$), cathode length (20 mm), and WL thickness (4 mm) are held constant.

6.4.7. Increasing stress intensity decreases ohmic drop and increases crack tip pH

Increasing K from 10 to 20 $MPa\sqrt{m}$ decreases I_C/W as seen in Figure 84(a). The current external to the crack is dominant with increasing K (Figure 84(b)) and the majority of the external current is ORR (Figure 84(c)). The current internal to the crack does not become dominant in HER and after the 8 hour simulation when increasing K as the current internal to the crack still had a majority of its current from ORR as presented in Figure 84(d).

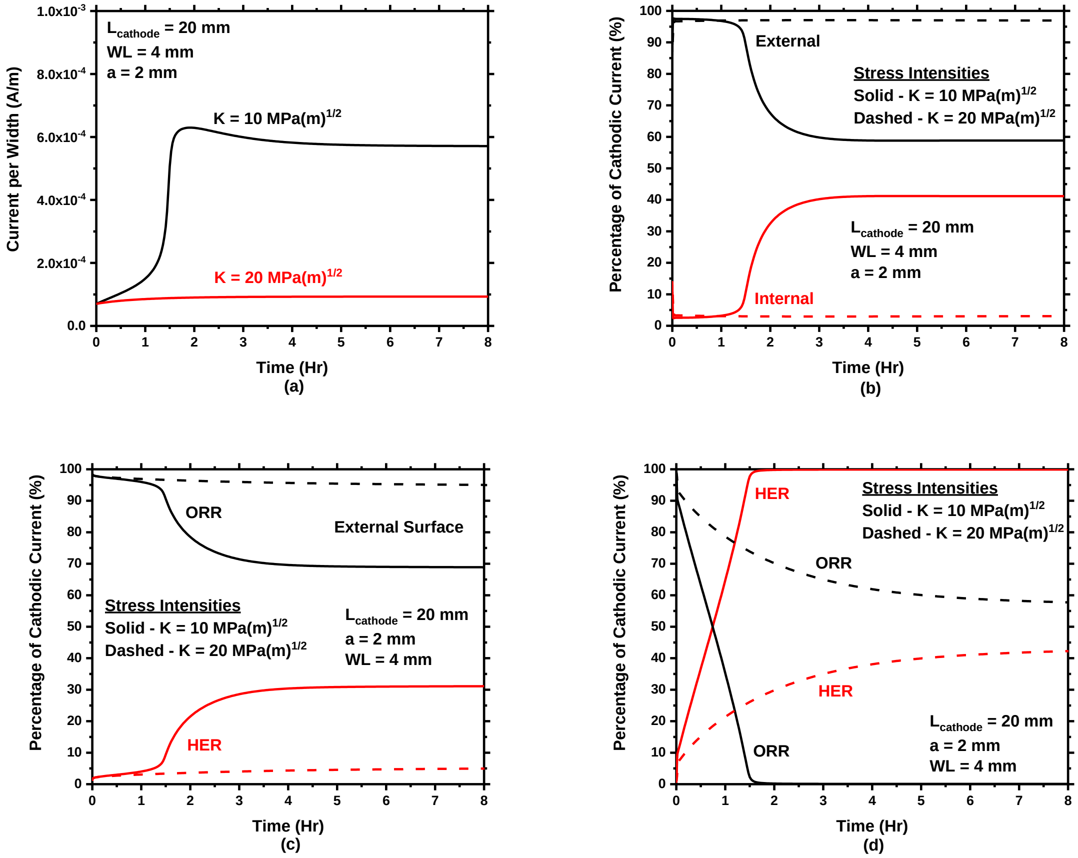

Figure 84: Influence of stress intensity on (a) the total current per width, (b) percentage of cathodic current internal and external to the crack, (c) percentage of HER and ORR external to the crack, and (d) percentage of HER and ORR internal to the crack. It is noted that the cathode length (20 mm), crack length (2 mm), and WL thickness (4 mm) are held constant.

Increasing K increases the potential at the crack tip as presented in Figure 85(a) and decreases the potential drop between the crack tip and mouth (Figure 85(b)). Additionally, the chloride concentration at the crack tip is drastically lower when increasing K and the pH is higher as presented in Figure 85(c) and (d) respectively. It is important to note that there is no K dependence on the anodic kinetics implemented into the model.

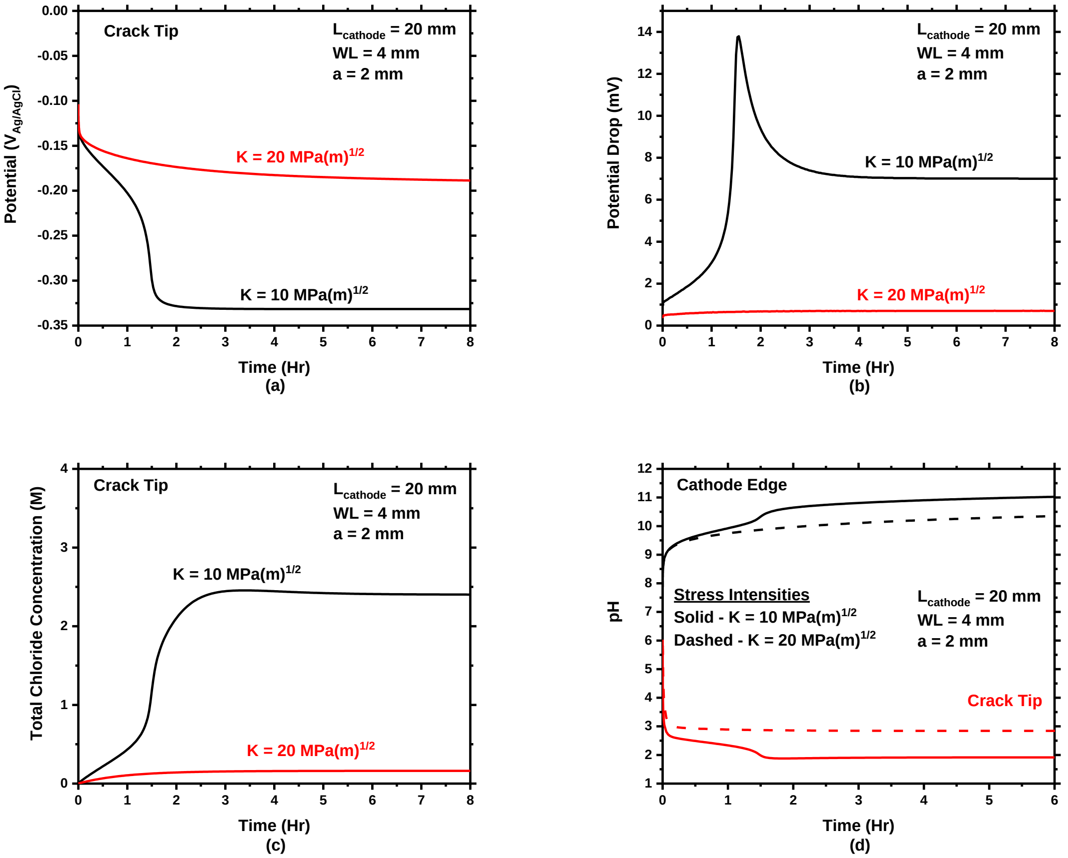

Figure 85: Influence of stress intensity on (a) the potential at the crack tip, (b) total metal chloride concentration at the crack tip, (c) pH at the crack tip and cathode edge. It is noted that the cathode length (20 mm), crack length (2 mm), and WL thickness (4 mm) are held constant.

6.4.8. Artificially increasing ORR increases potential drop between crack tip and external surface

A simulation was conducted in which the ORR cathodic kinetics on the external surface were enhanced. This was carried out by multiplying the exchange current density by 100 ($100 \cdot i_{act,ORR}$) and a comparison to the original ORR reaction is presented in Figure 86. Additionally, hydroxyl production in the cathode was turned off, pH variation in the reversible potential were based on a pH of 7, there was no limiting current density, and ORR was not accounted for in the crack. This largely makes the external cathode resistant to polarization.

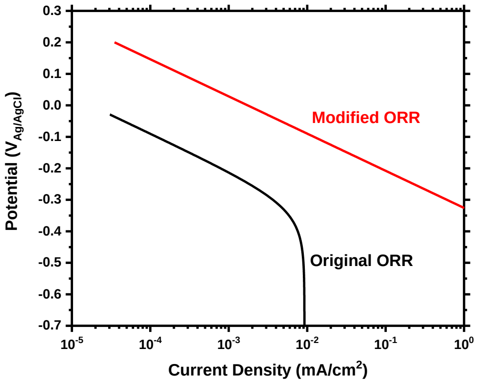

Figure 86: Comparison of original ORR under bulk conditions and modified ORR utilized in COMSOL simulations. The modified ORR does not have a limiting current density and has an exchange current density equal to $100 \cdot i_{act,ORR}$.

As presented in Figure 87(a) and (b), the cathode edge and mouth are at a more noble potential in comparison to the crack tip. The potential drop between the crack tip and the crack mouth is 176 mV in comparison to the potential drop of 7 mV of the regular kinetics as presented in Figure 77. Despite the increased kinetics, the cathode mouth and cathode are still polarized below 0 $V_{Ag/AgCl}$. Additionally, the simulation is ran for roughly 1.75 hours due to the fact that saturation is reached at the crack tip Figure 87(c).

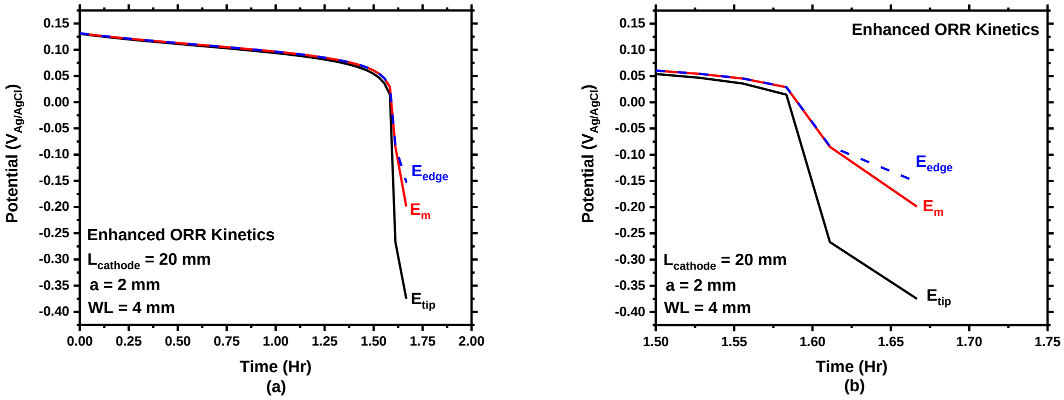

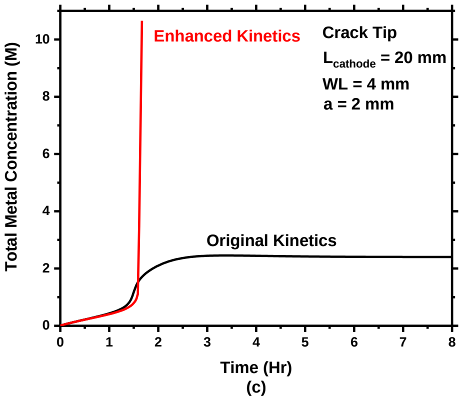

Figure 87: Influence of modified external kinetics on the (a) potential of the crack tip, crack mouth, and cathode edge. (b) Zoom in of (a) during hours 1.5 to 1.75 hours. (c) Influence of enhanced cathodic kinetics on total metal chloride concentration at the crack tip.

6.5. Discussion

To help guide the reader, this section will be organized in the following way. First, the presented model will be compared to other models present in literature. Second, the importance of cathode size will be discussed, and the concept of electrochemical similitude will be introduced. Third, the complex interactions between the WL thickness and L_C will be noted and the effect of crack size will be explored. Finally, it is important to remember that the presented model and assumptions presented in Section 6.3.5 are geared toward understanding trends in crack tip electrochemical properties and will not be utilized to predict CGR.

6.5.1. Comparison of the derived model with existing models in literature

Within this section, the results of the present model will be compared with other models in literature, mainly that of Macdonald and coworkers and Turnbull and coworkers. An assumption made in both models of Macdonald and coworkers and Turnbull and coworkers is that the oxygen concentration in the crack tip is consumed quickly and there are no internal ORR reactions [77,206]. In the current model, the contributions of all reactions can be deconvoluted as a function of time. It is directly shown that under steady state conditions a majority of the cathodic current internal to the crack is due to HER (Figure 76(e)) and the contribution to the total cathodic current from ORR internal to the crack is less than 0.1 %. It is important to note that while the contributions are small, this value is non-zero due to contributions of ORR near the crack mouth as presented in Figure 88. It is also important to note that this is for a condition in which K is held constant. Turnbull notes that under CF conditions O_2 entering the crack may be enhanced [74] and, due to the Multiphysics coupling in COMSOL, this is something that could also be investigated in a future iteration of the model.

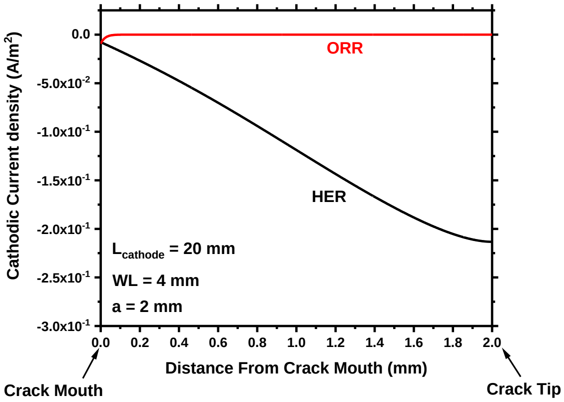

Figure 88: Current density of HER and ORR on the crack flank at t = 6.5 hrs.

Due to the proximity of the walls of the cracks, the concentration and potential profiles are generally assumed to be flat, perpendicular to the crack walls [74]. This can be directly evaluated in COMSOL and is presented in Figure 89. As displayed in Figure 89(a) and (b) the concentration of the total metal cations and pH (measure of the concentration of H^+) is uniform at the crack tip and the middle of the crack length ($a/2$). At the mouth of the crack, the metal concentration decreases slightly, and the pH increases slightly near the crack wall. A similar phenomena is present for the ϕ_l (Figure 89(c)) in which the crack tip and middle of the crack length have uniform profile and the crack mouth has a very slight increase near the crack wall. As the concentration and potential profiles are generally uniform throughout the crack (Figure 89), the assumptions of Macdonald and Turnbull in that the potential and concentrations are constant across the width of the crack are upheld. Additionally, the fact that there are very small changes in the through thickness of the crack, could be utilized in future FEM models of a crack as the mesh size could be modified in the crack tip to account for no through thickness variation and help improve computationally efficiency.

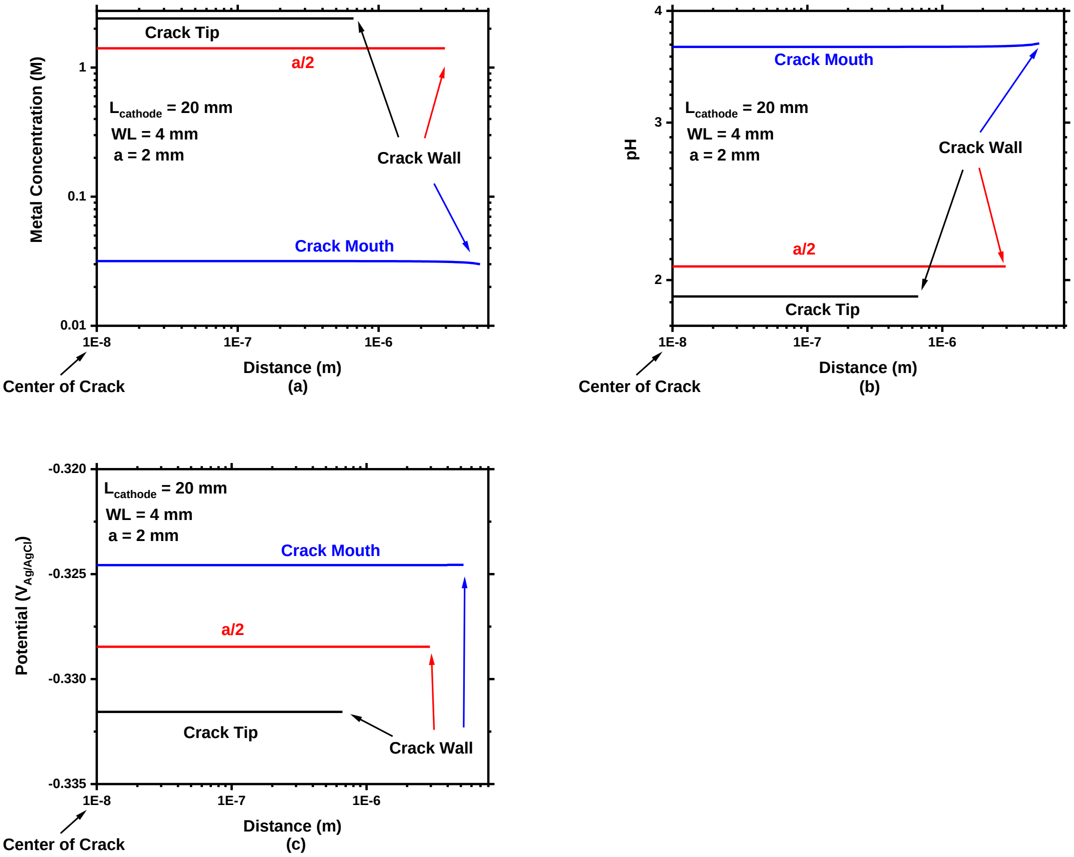

Figure 89: Influence of position in the crack on the (a) total metal concentration, (b) pH, and (c) electrolyte potential. These plots are evaluated at t = 8 hours.

The importance of considering the external environment has been noted historically in previous models. Turnbull mentions that the net imbalance of the total anodic and cathodic currents within the crack will result in an outflow of anodic current which has to be balanced on the external surface by a net cathodic reaction [74]. Macdonald stresses that simple charge conservation considerations show that the internal and external environments must be strongly coupled [77]. The present work further highlights the importance of the external reactions and additionally emphasizes how the external contribution changes with important parameters such as cathode length (*i.e.*, sample size), *WL* thickness, and crack length.

The next comparison that will be made concerns the potential drop in the system. First, with increasing chloride concentration, Turnbull noted a decrease in the potential drop between the mouth and the tip (Figure 70) [84]; however, the model did not account for changes in anodic electrochemical parameters with increasing chloride. Second, Kovalov et al. showed that increasing chloride concentration increased the potential drop at elevated NaCl concentrations and ranged from roughly 0.6 to 1.8 V from the external surface to the crack tip. It was hypothesized that the increased potential drop was caused by an increase in the coupling current due to depassivation of the crack apex and chloride catalysis of the electro-dissolution reaction at the crack tip [82]. However, while the change in anodic parameters with change in bulk chloride concentration were implemented, changes in HER local to the crack tip as well as changes in the passive current density on the crack flank were not including. In the present model, it is important to remember that a very small potential drop is calculated (Figure 77(b)). Additionally, the local HER reactions become the dominant cathodic reduction in the crack tip (Figure 76(e)) as the anodic current at the crack tip increases (Figure 76(a)). As both the anodic and cathodic currents internal to the crack are increasing and as the crack flank provides for an increased contribution to the total cathodic reduction reactions (Figure 76(c)), a large potential drop is not calculated due to the ability of the local cathodic reaction to compensate for an increased anodic reaction. Therefore, the importance of chemistry influences on both anodic and cathodic reactions is noted. Finally, it was shown that artificially increasing the cathodic kinetics ($100 \cdot i_{act,ORR}$), increases the potential drop between the crack tip and the crack mouth. As the external surface is fixed in other models, not allowing the crack tip to polarize the external surface, extreme potential drops may be possible.

As presented in Figure 84 and Figure 85, increasing K increases the percentage of cathodic current on the external surface, decreases the ohmic drop between the crack mouth and the crack tip, and increases the pH. This is similar to Turnbull et al. (Figure 70(a)) who calculated a decrease in the potential drop with an increase in K [84]. It is interesting to note that Macdonald et al. noticed an increase in the potential drop at the crack tip with increasing K. This was attributed to the increased rate of crack propagation (and hence current emanating from the crack) at the higher stress level. However, it is noted that geometrical changes were not taken into consideration (i.e. a wider CMOD with an increased K) [77]. By not accounting for changes in the crack shape, it is likely that conditions at the crack tip were more severe than in reality due to the fact that with increased CMOD, the ohmic drop decreases and diffusion is accelerated. As presented in Figure 85(d), increasing K increases the crack tip pH potentially due to greater diffusion of metal cations away from the crack tip.

Finally, the importance of geometry of the crack tip was explored in a similar method to Turnbull [81]. As presented in Table 9, it is evident that a parallel-sided crack is not a good approximation of a trapezoidal crack. In comparison to a trapezoidal crack, the parallel sided crack is not polarized as negatively, the chloride concentration at the crack it decreased, and the pH is increased.

Table 9: Influence of geometric parameters on crack tip conditions

$\boldsymbol{K}$ $(\boldsymbol{MPa\sqrt{m}})$	**Geometry**	**Crack Width (m)**	$\boldsymbol{E_{tip}}$ $(\boldsymbol{V_{Ag/AgCl}})$	$\boldsymbol{pH_{tip}}$	$\boldsymbol{Cl_{tip}}$ $(\boldsymbol{M})$
10	Parallel-sided	$\frac{CTOD + CMOD}{2}$	-0.219	4.64	0.33
10	Trapezoidal	$CTOD$ to $CMOD$	-0.332	1.92	2.41

6.5.2. Importance of cathode size on electrochemical similitude

The field of fracture mechanics commonly uses K to describe the crack tip driving force for crack extension. This similitude allows transfer of experimentally determined laboratory material properties to engineering-level components helping to predict overall lifetimes of in-service alloys. Additionally, this allows for various experimental samples, such as SENT and compact tension (CT) samples to be utilized. However, exposure to different corrosive environments (such as change in chloride concentration), exposure of various crack lengths, or exposure of different sample sizes at the same mechanical driving force (K) do not provide for the same CGR or the same threshold K for initiation [199,207–212]. An example of two experimental phenomena is presented in Figure 90(a) and (b) highlighting the experimental influence of L_C (area) on AA and WL thickness on custom 465 SS respectively. In both cases, the respective mechanical driving force is the same, but geometrical differences and external environments change CGR, indicating that the crack tip driving force for crack extension is not the same. K does not have the ability to account for changing electrochemical properties (*e.g.*, chloride concentration, pH, potential *etc.*) indicating that electrochemical similitude is not achieved.

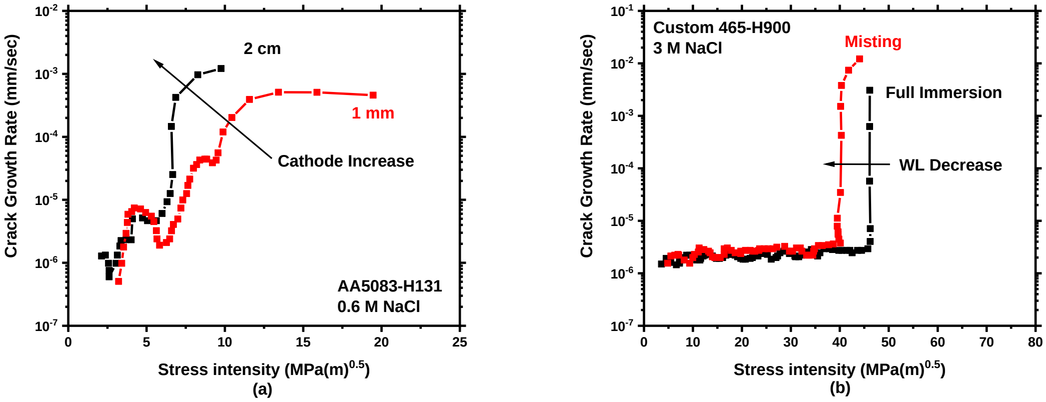

Figure 90: Experimental influence of (a) cathode length (area) on the crack growth rate response for AA5083 adapted from Steiner and Burns [207] *and (b) influence of experimental conditions (WL thickness) on the crack growth of custom 465 adapted from* [199].

The importance of coupling anodic crack tip reactions to cathodic reactions occurring on the surface cannot be ignored as a majority of the crack tip is external to the crack tip for short cracks (Figure 76, Figure 78, Figure 80, and Figure 84). When increasing crack length, the majority of the cathodic current switches to the crack walls (Figure 82); however, the contribution from the external surface is still significant. This further supports the need to account for the conservation of charge and the fact the internal and external environments must be strongly coupled [77]. However, the influence of many external variables, such as the L_C, have not been modeled.

Various experimental studies have explored environmental and geometrical influences on the CGR response. Of particular note, Steiner and Burns performed full immersion SCC experiments for AA5083 in 0.6 M NaCl under different cathodic areas as presented in Figure 90(a). This study was performed by painting the exposed alloy surface area around the crack tip and varying from 1 cm to 0.5 mm above and below the crack path (2 cm and 1 mm total height, respectively). Under these conditions, it was noted that the initiation threshold was increased (higher K) and the stage two CGR (at the same K) was decreased for the 1 mm total exposed area in comparison to the 2 cm exposed area. This indicates that crack growth for AA5083 is hindered with a lower area of exposed cathode [207]. While modeled in a SS system in Section 6.4.4 and experimental results were on AA, a similar trend is achieved. That is, with decreasing L_C, a decrease in the I_C/W is obtained causing for a decrease in metal cations at the crack tip and an increase in pH. This reduces the electrochemical driving force at the crack tip and could serve to decrease CGR kinetics.

Another study of particular interest comes from Richey et al. who investigated the influence of sample size of Ni-based alloys in high temperature de-aerated water. In this study, CGR were compared in CT specimens of different dimensions. It was noted that in smaller samples an enhanced CGR was measured in comparison to larger samples [210]. Similarly, Itow et al. determined CGR for various CT sample sizes in SS304L in simulated BWR environments. It was indicated, again, that the smaller sample size had an increased CGR [211]. While this may indicate that the reduced cathodic area on the external surface increases CGR, it is important to note that crack lengths and thickness of the crack fronts are different when testing in different CT configurations. Testing different cathodic areas with nominally the same crack length (such as in Section 6.4.4 and Steiner and Burns [207]) cannot inform upon the studies where both crack length and cathode area are changing. Additionally, it is important to remember that SCC specimens are 3D while modeled scenarios are 2D. Finally, these aforementioned tests were either de-aerated and/or at elevated temperatures. Despite these differences, the interaction between cathode area (representative of sample geometry) and crack length are identified as an important area for future study.

While considering the external cathodic reactions are important, the reactions internal to the crack cannot be ignored. It is interesting to note that the initial cathodic reductions in the crack are ORR as presented in Figure 76, Figure 78, Figure 80, and Figure 84. This is due to the assumption that the solution in the crack tip is initially aerated. Over time, as the cathodic reduction reactions are occurring in the crack, the oxygen is becoming depleted and the reaction rate is decreasing. Eventually, there will be little to no oxygen in the crack and HER will become the dominate reaction and this occurs around a time of roughly three hours. Despite HER becoming the dominant reaction, the ORR reaction does not dissipate completely to zero. This is due to the fact that the O_2 at the crack mouth is not zero and, therefore, there will be a minimal amount of ORR inside the crack walls as presented in Figure 91 for a simulation time of 6.5 hours. The contribution due to ORR is greater for a decrease in WL thickness due to an increase in O_2 near the surface due to a shorter diffusion distance.

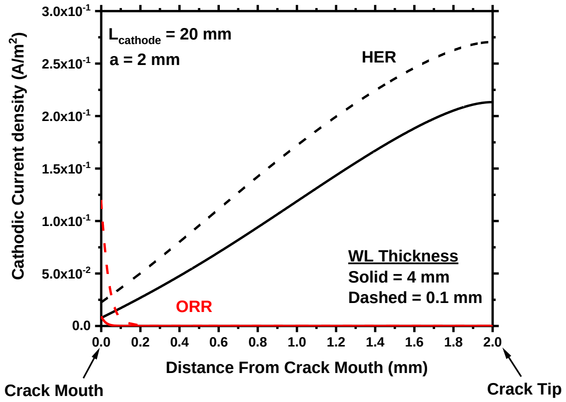

Figure 91: Influence of WL thickness on HER and ORR current densities along the crack wall at 6.5 hours.

Overall, the controlling role of the external surface on electrochemical conditions in the crack is noted. The results and discussion highlight the need to understand the extrapolation of SCC CGR obtained in laboratory scale specimens to field relevant conditions. That is, extrapolating from an SENT or CT specimen geometry with a limited geometry (*i.e.*, cathode size) to a field sample (such as a canister) with a large surface area (*i.e.* large cathode) could be problematic as electrochemical conditions may not be the same and electrochemical similitude may not be achieved at the crack tip.

6.5.3. Understanding the complex interactions between water layer thickness and cathode length

The influence of cathodic reduction reactions and the interplay between geometry of the cathode and *WL* have been recognized for corrosion scenarios [60,91]; however, to the knowledge of the author, has not been explored for SCC scenarios. Originally presented by Liu et al., complex interplays between the *WL* thickness and L_C were identified for a galvanic couple exposed to dilute chloride [60]. This work was furthered in this dissertation (Appendix B, [91]) to identify these complex interactions at elevated chloride concentrations and temperatures. Not only do these relationships exist for galvanic couples, but the presented model also shows the complex interactions between *WL* thickness and L_C exist for SCC scenarios. As presented in Sections 6.4.4

and 6.4.5, an increase in the L_C or a decrease in *WL* thickness increase the total I_C/W in the system. As a result, increasing in total I_C/W increases the chloride concentration and decreases the pH at the crack tip resulting in more aggressive conditions at the crack tip.

To briefly review, for a galvanic corrosion scenario and small L_C, it was shown when decreasing the *WL* from full immersion to thin film conditions, an increase in the I_C/W was calculated as presented in Figure 92. For a large cathode (*i.e.*, greater than L_{Crit}), decreasing the *WL* thickness decreases the I_C/W. Furthermore, increasing the cathode length in bulk conditions (*i.e.*, *WL* > δ_{nc}) increases the I_C/W.

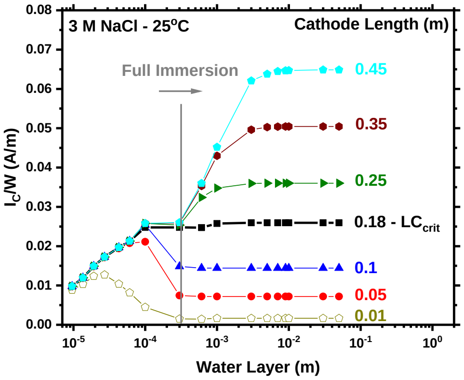

Figure 92: Total cathodic current per cathode width (I_C/W) vs. water layer thickness for a galvanic couple as a function of cathode length at 25˚C for 3 M NaCl.

The scenarios presented for crack tip conditions in Sections 6.4.4 and 6.4.5 are similar to that presented Figure 92 for a galvanic couple. First, increasing the L_C under bulk conditions increases I_C/W as presented in Figure 78. This again is due to the fact that the cathode is under bulk conditions (Appendix B, [91]). Second, decreasing the *WL* thickness (100 µm < δ_{nc}) at a small L_C (20 mm = 0.02 m) increases I_C/W. Therefore, very similar behaviors exist between a galvanic couple [60,91] and SCC scenarios, highlighting the need to account for the complex reactions between *WL* thickness and L_C.

When interpreting SCC results, it is important to remember the complex interplay between *WL* thickness and L_C. While a decrease in *WL* thickness caused for an increase in the total cathodic current in the presented geometries (L_C= 20 mm), it is likely that if this was studied at a much larger L_C (*e.g.* 500 mm) that a decrease in the WL thickness could cause for a decrease in I_C/W similar to that seen in corrosion scenarios. Turnbull and Wright modeled a thin liquid film and postulated that a greater potential drop would reduce crack growth and increase the threshold for initiation [84]. However, the effect of L_C was not accounted for in their model and, instead, the external surface was forced to be the open circuit potential. Forcing the external surface to reach the open circuit potential may be unrealistic as it takes a large surface area for a cathode to reach the open circuit potential and the open circuit potential can change for thin WL [192]. In the present model, when decreasing WL thickness, the crack tip is more noble (Figure 81(a)) and the pH is lower at the crack tip indicating more aggressive conditions. This could serve to decrease the threshold for crack initiation and increase CGR in thin film conditions for small L_C.

A recent study from Harris et al., presented in Figure 90(b), indicated a decrease in the threshold for SCC initiation with a decrease in WL thickness (misting compared to full immersion) for a Custom 465 SS. It was noted that a decrease in WL thickness decreased the threshold for initiation; however, a similar stage two CGR was measured for all WL thicknesses (bulk and misting). It is also noted that while the WL thickness is changing, the cathodic area is also changing due to the fact that in thin film conditions just the sides are being utilized in comparison to all sides for bulk conditions as shown in Figure 93 [199]. As a misting environment exposed under completely vertical conditions is close to a WL thickness of 100 µm [213], the decrease in WL thickness in Section 6.4.5 would be similar to comparing a full immersion to misting conditions. As such, a decrease in WL thickness, decreases pH at the crack tip. Additionally, an increase in HER current density is present near the crack tip with a decrease in WL thickness as presented in Figure 91. The acidification and increase in HER near the crack tip could provide for a larger driving force for SCC initiation in decreased WL thicknesses. While this logic does not explain the similar stage two CGR response [199], it is possible there is an interaction of K and a as pointed out by Turnbull and Wright [84] and that could be influencing the CGR.

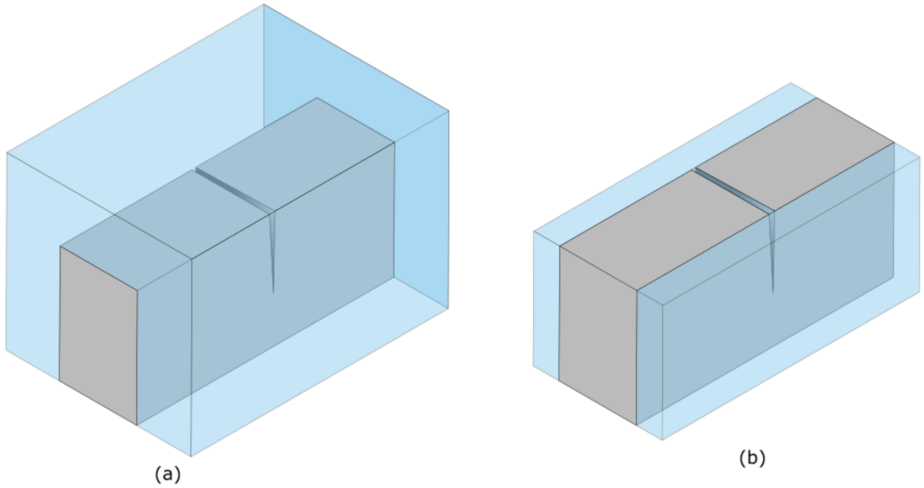

Figure 93: Schematic of stress corrosion cracking experimental set-up for (a) full immersion conditions and (b) thin film conditions.

Another study of interest, comes from Steiner and coworkers [207,214] who investigated SCC of AA in full immersion, thin film, and wicking scenarios. It was noticed that WL thicknesses < 92 µm the CGR behavior was similar to wicking conditions. For a WL thickness of 92 µm, the CGR behavior exhibited both wicking and full immersion characteristics in duplicate testing. It was suggested that this could have been due to crack tip ohmic difference enhanced by H_2 bubbles or corrosion product, crack-front shape change governed by through-thickness potential difference, or microstructural heterogeneity. Additionally, for WL thicknesses of 184 and 229 µm, a noticeably lower stage two CGR was measured in comparison to the 92 and 137 µm WL thicknesses [214]. Despite the variation in CGR response and WL and differing behavior between duplicates, having increases and decreases in CGR with changes in WL thickness is not surprising based on the variation in I_C/W in a galvanic couple for short L_C (Figure 92). Take for instance the 0.1 m cathode for a galvanic couple in Figure 92. Decreasing the WL thickness from bulk to thin film conditions increases the corrosion rate to a maximum I_C/W at roughly at 100 µm before decreasing further, eventually below that of the full immersion scenario. While limited scenarios of WL thickness and L_C were investigated in this dissertation, the complex interplay between WL thickness and L_C could be responsible for the disparity in CGR .

It is interesting to note the potential for bubble formation in the crack suggested by Steiner and coworkers [214]. The formation of bubbles in the crack tip and the influence on predicted electrochemical conditions was recently investigated by Lee and coworkers [195]. By accounting for changes in conductivity due to hydrogen bubble formation through the Bruggeman equation (similar to that utilized in Section 5.3.2), it was shown that the potential at the crack tip can be significantly influenced especially by volume fraction of bubbles inside the electrolyte [195]. With the increased HER near the crack tip as the *WL* is decreased, Figure 91, it is possible that bubble formation could also influence the stochastic nature of the CGR at decreased *WL* thicknesses. Incorporation of this effect into future model iterations is also possible.

6.5.4. Electrochemical effects of short cracks

An important geometric feature of cracks is the length and the electrochemical behavior of short and long cracks. Gangloff has shown that small corrosion fatigue cracks in Custom steel 4130 (0.1 to 2 mm) grow up to 500 times faster than long cracks (15 to 40 mm) under full immersion conditions in aqueous solutions. Experiments were performed under non-potentiostatic and potentiostatic control. The difference in CGR was attributed to enhanced cathodic hydrogen production within the occluded short crack. The increased hydrolytic acidification to form H^+ and decreased oxygen inhibition to consume H^+ within small cracks were probable contributors to the chemical driving force [208]. However, these conclusions were based on a model that did not account for passive dissolution on the wall of the crack [84]. Zhou et al. also observed an increase in crack growth for short cracks in aqueous solutions for FV566 steam turbine blade steel. It was speculated that a hydrogen assisted cracking mechanism was responsible for the increases crack growth. This was rationalized due to the known susceptibility of martensitic stainless steels to hydrogen assisted cracking with the key assumption that acidity might develop preferentially in the short crack; the reduced pH would dominate the kinetics of hydrogen uptake despite a more noble crack-tip potential [209]. However, Zhou et al. did not account for the passive nature of the crack walls and the limited response of the current on the walls to anodic polarization. In further modeling Turnbull and Wright found that for longer cracks, the pH is most acidic and the potential is more negative than short cracks when accounting for the anodic dissolution on the walls [84].

The more recent modeling of Turnbull and Wright [84], is supported by the current research (Figure 82 and Figure 83) indicating that enhanced hydrogen production would be present for longer cracks. Turnbull and Wright suggest that the enhanced crack growth is due to an anodic dissolution mechanism, related to an increased activity of the grain boundary [84]. While the presented model cannot predict grain boundary activity, the model can be updated in further iterations to account for grain boundary interactions and provide more insight into this problem

6.6. Limitations and implications

As with all models, the modeling approach used here has several limitations. First, an assumption is made that a uniform thin layer of electrolyte exists across the entire external surface couple, which is not always the case in practice due to imperfect wetting, especially at the edge of the cathode/anode. This imperfect wetting would lead to a shorter effective length of cathode available. Next, it was assumed that κ was constant and was not influenced by corrosion products or bubbles in solution. Third, only ohmic drop is considered, which is an intrinsic limitation of the use of Laplace Equation-based modeling, with the current being dominated by migration rather than diffusion. Fourth, the transport of minor species in dilute solutions was utilized; however, diffusive transport in concentrated solutions requires complex, compositionally dependent diffusivities which are not available in literature for this system. Fifth, a chloride-concentration-based pH was utilized; however, the general agreement of pH calculated with concentration- and activity-based pHs (Figure 75) is encouraging. Sixth, the sides of the crack were assumed to be smooth. In reality, the crack flanks are rough which can serve to retard diffusion of ions out of the crack. Additionally, a rough surface will have an increased surface area and could influence anodic and cathodic reactions on the walls of the crack. Turnbull mentions roughness may influence passive current density on the walls of the crack [84]. Seventh, inhomogeneities were not considered on the crack walls. Finally, anodic and cathodic boundary conditions were created utilizing solutions of $CrCl_3$ and LiCl to avoid influences from Fe^{2+} oxidation.

Despite these limitations, the implications of this work should be noted. The primary objective in modeling crack tip electrochemistry is to provide the information necessary to predict crack tip reaction rates and draw qualitative inferences regarding the effect of environment on CGR. Utilizing a reactive transport FEM to inform upon crack tip electrochemical conditions, various assumptions of other models were explored. It was indicated that less than 0.1 % of the total cathodic current is due to ORR inside the crack, therefore, not considering ORR internal to the crack is justified. Additionally, due to the proximity of the walls of the cracks, the concentration and potential profiles can be assumed to be flat. Finally, this work indicated that the WL thickness, L_C, and crack length influence the electrochemical conditions at the crack tip. The coupling with the external environment is undeniably important when considered SCC scenarios. In addition to coupling with the external surface, anodic reactions on the crack wall and cathodic reactions due to hydrogen are also deemed to be important especially when considering the concentrated solutions that may arise. Due to the external coupling and the consideration of solution dependent boundary conditions electrochemical similitude may not be achieved between different samples, different sample sizes, and between laboratory specimens and extrapolating to field relevant geometries.

6.7. Conclusions

Crack tip electrochemical conditions were explored utilizing a reactive transport FEM. Electrochemical boundary conditions were determined through polarizations in simulated crack tip environments. Diffusivities and conductivities were determined in OLI studio while equilibrium reaction values were determined from literature. Finally, the crack tip geometry was a trapezoidal shape with CMOD and CTOD determined by fracture mechanics principles and material properties.

It was determined that an increase in L_C, decreasing WL thickness, and increasing CGR increases total cathodic I_C/W, increasing metal chloride concentrations, and decreasing the pH. Of interesting note, increasing K decreases the I_C/W, decreases the metal chloride concentration, and increases the pH. It is important to remember that crack tip current densities are not specific at a specific level of K (*i.e.*, increasing K does not impose an anodic current density) and that the conclusions are based on equilibrium conditions of the crack tip. Additionally, the assumption of a trapezoidal vs. a parallel-sided crack was explored indicating that a parallel-sided crack does not accurately capture the physics of a crack. Finally, artificially increasing ORR on the external surface 100-fold increases the potential drop of the crack tip while causing for saturated conditions and a decreased pH.

These results were compared with existing models in literature and to SCC experiments. First, it was shown that HER is the dominant cathodic reduction reaction in the crack and ORR in the crack accounts for less than 0.1 % of the total cathodic in the system. It was also determined that the concentration and potential distribution across the crack was uniform. Third, the importance of coupling the crack tip to the external environment was noted. The importance of the size of the external cathode was investigated and compared to literature experiments. Additionally, the complex interactions between cathode size and *WL* thickness, similar to that of a galvanic couple, are present for SCC scenarios. The presented model can give insight into the electrochemically short crack phenomena and support the anodic dissolution mechanism at grain boundaries. Finally, the presented results and discussion calls into question whether electrochemical similitude is achieved between different specimens, different crack lengths, and between laboratory specimen and field relevant samples.

7. Summary and recommended future work

7.1. Summary

Experimental and modeling techniques were utilized to inform upon the underlying corrosion mechanisms, and governing factors (including environmental factors) for localized corrosion of SS304L. This was achieved by defining potential environments and highlighting the importance of RH on the concentration, composition, and resulting brine properties that are possible in marine environments. Subsequently, cathodic and anodic properties were assessed in these environments which were combined with determination of *WL* thicknesses to model various corrosion scenarios. Localized corrosion predictions were validated based on long term exposure data in controlled environments. Finally, environmental influences on the electrochemical conditions were assessed in a Laplace-Equation based FEM modeling approach.

In marine conditions under high RH (> ~ 75 % RH), the solution is NaCl-rich while at lower RH's (< ~ 75 %) the solution is $MgCl_2$ rich (Figure 5). ORR is dominate under high RH scenarios (> ~ 75 %) in which NaCl is the dominant salt in solution. Within NaCl stability, decreasing RH decreases measured current densities and decreases cathodic kinetics. Decreasing further in RH, NaCl precipitates into solution, the brine then becomes dominant in $MgCl_2$. The reaction mechanism now transitions from ORR to HER due to influences from a further decreased O_2 concentration, localized corrosion, and stable precipitation. These trends are not only true for 25 ˚C but also for 35 and 45 ˚C. When a material is the predominant cathode in a galvanic couple, the cathodic reduction reactions will cause for an increase in pH. When this occurs, there again are two different scenarios that will occur. Under high RH conditions (NaCl-dominant), it is possible that the brine experiences regions of NaOH dominance, changing the ORR from a near four-electron transfer to an electron transfer below two, due to the formation of a superoxide intermediate. This difference is true for both dilute and concentrated NaCl and NaOH solutions. At low RH solutions ($MgCl_2$-dominant), the coupled cathodic reaction to active corrosion will also cause for a pH rise; however, cathodic precipitation will occur. Deposition on the surface will restrict O_2 diffusion to the surface and decrease the number of active sites for cathodic reduction, causing for a further suppression of cathodic reduction. In either case, when exploring the cathode when active corrosion is occurring, a suppression of cathodic kinetics will be present.

Two critical parameters, namely $(i \cdot x)_{sf}$ and E_{rp}, describing the stable propagation of localized pitting corrosion were determined under marine conditions. With decreasing RH, $(i \cdot x)_{sf}$ decreases due to a decrease in $C_{M^+}^{sat}$ (common ion effect) and a decrease in D_{M^+}. With increasing temperature, $(i \cdot x)_{sf}$ increases due to an increase in $C_{M^+}^{sat}$ (common ion effect) and an increase in D_{M^+}. As both $(i \cdot x)_{sf}$ and E_{rp} describe the anodic propagation of pitting corrosion, it is important to consider these two parameters together. It was also noted that in $MgCl_2$ and sea-salt brines, an increase in $(i \cdot x)_{sf}$ was measured in comparison to NaCl solutions at both 25 ˚C (Figure 45) and at elevated temperatures (Figure 47) at equivalent chloride concentrations.

The thickness of WLs in various atmospheric environments were explored. Starting with the smallest WL thickness, atmospheric deliquescence under equilibrium conditions typically ranges from 1 to 300 µm (Figure 33) and decreases with a decrease in RH. Spanning roughly the same WL thickness is the WL induced by a RDE which ranges from 7 to 200 µm. The lower limit arises due to the fact that at sufficiently high rotation rates turbulent flow is induced and there is no longer a clearly defined boundary layer. The δ_{nc} spans a larger boundary layer thickness (142 to 873 µm) when compared to both atmospheric and RDE WL thicknesses. It is noted that the WL for δ_{nc} decreases with decreasing RH and increases in temperature. Finally, the largest WL thickness was measured for accelerated corrosion testing scenarios which ranged from 400-1220 µm. Overall, it is important to consider the influence of WL thickness and how the thickness changes with exposure environment (solution composition, solution concentration, deliquescing, and salt spray) as this is directly related to the cathodic current available for dissolution. Additionally, it is unlikely that under equilibrium conditions in atmospheric exposures, thin film conditions ($WL < \delta_{nc}$) will be present on the alloy surface. In salt spray conditions, both thin film and bulk conditions exist depending on the angle of exposure. Therefore, it is important to consider all of the variations present in WL thicknesses when modeling corrosion scenarios.

The cathodic kinetics were evaluated in different environments and geometries (pitting and galvanic corrosion). It was identified that cathodic kinetics are enhanced with an increase in temperature due to an increase in κ and an increase in D_{O_2} causing for an increase in the current density and a decrease in the overall ohmic drop in the system. With decreasing RH, a decrease in in C_{O_2}, D_{O_2} and equilibrium WL thickness will cause for a decrease in the cathodic kinetics. While κ increases, decreasing overall ohmic drop in the system, the decrease in the overall current density governed by the aforementioned parameters will be greater.

As previously discussed, the cathode current will show certain dependencies with changing environmental parameters, however, when combined with the anodic demand, further complex dependencies arose. First, when exploring a similar chloride concentration (RH), the controlling factors decreasing the cathodic current is the WL thickness and is combined with an increase in $(i \cdot x)_{sf}$ to decrease the maximum pit size. Second, when increasing temperature, an increase in cathodic demand due to increases in κ and D_{O_2} is offset in by an increase in $(i \cdot x)_{sf}$ to not significantly change the pit sizes. Next when considering a decrease in RH in different solution compositions, the suppression of cathodic kinetics due to an overall decrease in i_{eq} and WL thickness outweighs the decreased anodic demand. This leads to an overall decrease in the predicted max pit size. Finally, when decreasing RH under the same solution composition (i.e. 0.6 vs. 5.3 M NaCl), while the cathodic kinetics are suppressed, again due to a decrease in i_{eq} and WL thickness, $(i \cdot x)_{sf}$ decreases much more and causes for an increase in the predicted maximum pit size. Finally, maximum pit size predictions were improved when a changing cathodic electrolyte (precipitation and dehydration) was incorporated into the model for sea-salt solutions.

Crack tip electrochemical conditions are explored utilizing a reactive transport FEM. It was determined that an increase in L_C, decreasing WL thickness, and increasing CGR increases total cathodic current per width, increasing metal chloride concentrations, and decreasing the pH. Increasing K decreases the total current per width, decreases the metal chloride concentration, and increases the pH. It is important to remember that crack tip current densities are not specific at a specific level of K (*i.e.,* increasing K does not impose an anodic current density) and that the conclusions are based on equilibrium conditions of the crack tip. Finally, artificially increasing ORR on the external surface 100-fold increases the potential drop of the crack tip while causing for saturated conditions and a decreased pH largely due to an unpolarizable external surface.

Additionally, it was shown that HER is the dominant cathodic reduction reaction in the crack and ORR in the crack accounts for less than 0.1 % of the total cathodic current in the system at steady state. It was also determined that the concentration and potential distribution across the crack was uniform. The importance of coupling the crack tip to the external environment was noted and importance of the external cathode size was investigated and compared to literature experiments. Further, the complex interactions between cathode size and WL thickness, similar to that of a galvanic couple, are present for SCC scenarios. The presented model can give insight into the electrochemically short crack phenomena and support the anodic dissolution mechanism at grain boundaries. Finally, the presented results and discussion calls into question whether electrochemical similitude is achieved between different specimens, different crack lengths, and between laboratory specimens and field relevant samples.

7.2. Recommended future work

Cathodic kinetics were explored as a function of RH (composition and concentration). It was indicated that changing RH and active corrosion (pH rise in the cathode) changes the cathodic reduction reaction mechanisms. The cathodic reduction reaction mechanisms need to be investigated as a function of pH and chloride concentration as there could be competing influences between these two variables. The results of this experimental investigation can then be utilized in reactive transport modeling informing upon corrosion.

An assumption in the presented modeling work for maximum pit size predictions assumed that the fraction of saturation was not dependent upon the solution concentration, composition, or temperature. As $(i \cdot x)_{crit}$ was shown to have an important role in pit size predictions, it is important to understand how f may vary with the aforementioned parameters. While there are various methods to determine this in literature [8,21], these methods have not been validated on various concentrations or solutions. Additionally, there is an inherent scan rate dependence on determining f when utilizing 1D electrodes which does not hold true for extreme scenarios. For example, f cannot be determined at slow scan rates (*i.e.*, 0.01 mV/sec) for deep pits (akin to the method of Li et al. [21]) while f cannot be determined for fast scan rates (*i.e.*, 100 mV/sec) utilizing the method of Srinivasan et al. [8]. It is possible that the model developed in Section 6 could be adapted to help inform upon the critical values present in a concentrated pit solution near saturation by the addition of a porosity to account for amorphous corrosion products present near the surface of a corroding holiday. Being able to track species concentration, pH, potentials, and current densities can provide for a unified model to help inform upon repassivation, f, and oxide nucleation.

Modeling scenarios were performed under a thin film (Chapter 5 and 6) utilizing both analytic models and FEM. In reality, it is unlikely that a uniform *WL* thickness will be present on the surface of the alloy. More realistically, a droplet will be present on the surface of a corroding alloy under equilibrium conditions. While this has been modeled in literature [215], there have been limited studies utilizing the model and various phenomena have not been incorporated such as the effects of electrolyte composition/concentration, size of the droplet, location of anode, and cathodic inhabitation from precipitated species. Additionally, working in a confined liquid volume (i.e. thin *WL* or droplet) will cause for electrolyte changes (*i.e.*, chloride migration and pH increase in the cathode). This will cause for the activity of the water to change in solution and, under equilibrium conditions, the activity of water needs to match that of the surrounding atmosphere. Therefore, not only should future models account for changes in RH (*e.g.*, changes in *WL* thickness from RH changes), but it is also suggested that changes due to corrosion processes are implemented.

Presented FEM was performed with the Laplace equation utilizing chemistry dependent electrode boundary conditions. In future models, especially those with large concentration gradients between a confined area and the bulk solution, a variable conductivity may be necessary to completely describe the system. This can be accomplished in combination with the Laplace equation or the full Nernst Plank Equation can be utilized. In practice, to use the Nernst Planck Equation in combination with the electroneutrality condition, at each time step for each spatial element, a “make-up” ion is necessary for electroneutrality. However, there is limited physical basis as which ion should be utilized as the make-up ion and requires additional investigation for complete implementation.

A sensor was constructed in Chapter 3 to inform upon *WL* thickness in salt spray environments. Stemming from this work there are two suggestions. First, utilizing this sensor it was identified that the angle of exposure with the standard limits has a significant influence on the *WL* thickness. A greater exploration of ASTM standards for accelerated corrosion testing is needed and it is possible that tighter restrictions on angle of exposure and sample sizes are needed. Second, atmospheric scenarios and other accelerated corrosion tests are subjected to wetting and drying cycles. As the resistance-based sensor to determine *WL* thickness is dependent on the conductivity of the solution, a need to account for changing conductivity and *WL* thickness is necessary to inform corrosion in these scenarios.

In-situ Raman spectroelectrochemistry was utilized to investigate precipitated species in a dilute $MgCl_2$ electrolyte and introduced a technique to perform this under flowing conditions. First, it is suggested to perform similar experiments in other solutions (*i.e.*, sea-salt brines) and other concentrations of $MgCl_2$ to investigate the cathodic behavior and the potential for cathodic inhibition from precipitated species. Second, this work highlighted that the formation of $MgCO_3$ is inhibited and will likely form on the surface of the alloy from a conversion of $Mg(OH)_2$ or other non-carbonate species. In order to accurately model corrosion scenarios, it is necessary to investigate the kinetics of precipitated species both from anodic and cathodic reactions. Additionally, it is possible that these species can change phases with temperature or RH and could impact corrosion processes.

Modeling work for SCC scenarios (Chapter 6) indicated a significant influence on the total current in the system from the external cathode. A majority of testing on the influence of sample size has been conducted in BWR environments (low κ) where ohmic drop is going to be more severe and potentially not have a large impact on testing. Testing various sample sizes or artificially increasing the cathodic area through a zero-resistance ammeter could provide a valuable means for testing this. Additionally, the modeling research indicated electrochemical similitude may not be achieved in various scenarios and this needs to be verified experimentally. Finally, the presented modeling scenarios were performed in 2D while fracture mechanics specimens are inherently 3D. The developed framework can be extended to 3D scenarios.

8. Further acknowledgements

Sandia National Laboratories is a multi-mission laboratory managed and operated by National Technology and Engineering Solutions of Sandia, LLC., a wholly owned subsidiary of Honeywell International, Inc., for the U.S. Department of Energy's National Nuclear Security Administration under contract DE-NA0003525. This document is SAND2021-10395 T.

9. References

[1] Szklarska-Smialowska, Z., *Pitting and Crevice Corrosion*, NACE International, Houston, TX, 2005

[2] Evans, U. R., "The passivity of metals. Part I. The isolation of the protective film", *J. Chem. Soc.*, 1927, p. 1020–1040

[3] Frankel, G. S., "Pitting Corrosion of Metals. A Review of the Critical Factors", *Journal of The Electrochemical Society*, Vol. 145, 1998, p. 2186–2198

[4] Evans, U. R., "The passivity of metals. Part II. The breakdown of the protective film and the origin of corrosion currents", *J. Chem. Soc.*, 1929, p. 92–110

[5] Galvele, J. R., "Transport Processes in passivity breakdown - II. Full hydrolysis of metal ions", *Corrosion Science*, Vol. 21, 1981, p. 551–579

[6] Galvele, J. R., "Transport Processes and the Mechanism of Pitting of Metals", *Journal of The Electrochemical Society,* Vol. 123, 1976, p. 464–474

[7] Srinivasan, J. and Kelly, R. G., "One-Dimensional Pit Experiments and Modeling to Determine Critical Factors for Pit Stability and Repassivation", *Journal of The Electrochemical Society*, Vol. 163, 2016, p. C759–C767

[8] Srinivasan, J. and Kelly, R. G., "On a recent quantitative framework examining the critical factors for localized corrosion and its impact on the galvele pit stability criterion", *Corrosion*, Vol. 73, 2017, p. 613–633

[9] "ASTM G61-86: Standard Test Method for Conducting Cyclic Potentiodynamic Polarization Measurements for Localized Corrosion Susceptibility of", 2018, p. 1–5

[10] Wilde, B. E. and Williams, E., "The use of current/voltage curves for the study of localized corrosion and passivity breakdown on stainless steels in chloride media", *Electrochimica Acta*, Vol. 16, 1971, p. 1971–1985

[11] Wilde, B. E., *Localized Corrosion* R. W. Staehle, B. F. Brown, J. Kruger, and A. Agarwal, Editors, p. 342, NACE, Houston, TX, 1974

[12] Wilde, B. E., "A Critical Appraisal of Some Popular Laboratory Electrochemical Tests for Predicting the Localized Corrosion Resistance of Stainless Alloys in Sea Water", *Corrosion*, Vol. 28, 1972, p. 283–291

[13] Dunn, D. S., Cragnolino, G. A., and Sridhar, N., "An Electrochemical Approach to Predicting Long- Term Localized Corrosion of Corrosion-Resistant High-Level Waste Container

Materials", *Corrosion Engineering*, Vol. 56, 2000, p. 90–104

[14] Sridhar, N. and Cragnolino, G. A., "Applicability of Repassivation Potential for Long-Term Prediction of Localized Corrosion of Alloy-825 and Type-316L Stainless-Steel", *Corrosion*, Vol. 49, 1993, p. 885–894

[15] Dunn, D. S., Sridhar, N., and Cragnolino, G. A., "Long-Term Prediction of Localized Corrosion of Alloy 825 in High-Level Nuclear Waste Repository Environments", *Corrosion Science*, Vol. 52, 1996, p. 115–124

[16] Srinivasan, J., McGrath, M. J., and Kelly, R. G., "A High-Throughput Artificial Pit Technique to Measure Kinetic Parameters for Pitting Stability", *Journal of The Electrochemical Society*, Vol. 162, 2015, p. C725–C731

[17] Srinivasan, J. and Kelly, R. G., "Evaluating the Critical Chemistry for Repassivation at the Corroding Surface Using Mass Transport Model-Based Artificial Pit Experiments", *Journal of The Electrochemical Society*, Vol. 163, 2016, p. 768–777

[18] Srinivasan, J. and Kelly, R. G., "Evaluating the Critical Chemistry for Repassivation at the Corroding Surface Using Mass Transport Model-Based Artificial Pit Experiments", *Journal of The Electrochemical Society*, Vol. 163, 2016, p. C768–C777

[19] ASTM International, *ASTM G192 - Standard Test Method for Determining the Crevice Repassivation Potential of Corrosion-Resistant Alloys Using a Potentiodynamic-*, 08 ed., p. 1–10, 2014

[20] Srinivasan, J., Liu, C., and Kelly, R. G., "Geometric Evolution of Flux from a Corroding One-Dimensional Pit and Its Implications on the Evaluation of Kinetic Parameters for Pit Stability", *Journal of The Electrochemical Society*, Vol. 163, 2016, p. C694–C703

[21] Li, T., Scully, J. R., and Frankel, G. S., "Localized Corrosion: Passive Film Breakdown vs Pit Growth Stability: Part V. Validation of a New Framework for Pit Growth Stability Using One-Dimensional Artificial Pit Electrodes", *Journal of The Electrochemical Society*, Vol. 166, 2019, p. C3341–C3354

[22] Gaudet, G. T. et al., "Mass transfer and electrochemical kinetic interactions in localized pitting corrosion", *AIChE Journal*, Vol. 32, 1986, p. 949–958

[23] Pistorius, P. C. and Burstein, G. T., "Metastable pitting corrosion of stainless steel and the transition to stability", *Phil. Trans. R. Soc. Lond*, Vol. 1992, 1992, p. 531–559

[24] Chen, Z. Y. and Kelly, R. G., "Computational Modeling of Bounding Conditions for Pit

Size on Stainless Steel in Atmospheric Environments", *Journal of The Electrochemical Society*, Vol. 157, 2010, p. C69–C78

[25] Klapper, H. S. and Goellner, J., "Electrochemical noise from oxygen reduction on stainless steel surfaces", *Corrosion Science,* Vol. 51, 2009, p. 144–150

[26] Liu, C. and Kelly, R. G., "A Review of the Application of Finite Element Method (FEM) to Localized Corrosion Modeling", *Corrosion*, Vol. 75, 2019, p. 1285–1299

[27] Srinivasan, J. et al., "Long-Term Effects of Humidity on Stainless Steel Pitting in Sea Salt Exposures", *Journal of the Electrochemical Society*, Vol. 168, 2021, p. 021501

[28] Chen, Z. Y., Cui, F., and Kelly, R. G., "Calculations of the Cathodic Current Delivery Capacity and Stability of Crevice Corrosion under Atmospheric Environments", *Journal of The Electrochemical Society*, Vol. 155, 2008, p. C360–C368

[29] Chen, Z., Cui, F., and Kelly, R. G., "An Analytical Modeling Method for Calculating the Current Delivery Capacity of a Thin-Film Cathode and the Stability of Localized Corrosion under Atmospheric Environments", *ECS Transactions*, Vol. 3, 2019, p. 443–457

[30] Doig, P. and Flewitt, P. E. J., "A Finite Difference Numerical Analysis of Galvanic Corrosion for Semi-Infinite Linear Coplanar Electrodes", *Journal of The Electrochemical Society*, Vol. 126, 1979, p. 2057–2063

[31] Heppner, K. L., Evitts, R. W., and Postlethwaite, J., "Prediction of the crevice corrosion incubation period of passive metals at elevated temperatures: Part I - Mathematical model", *Canadian Journal of Chemical Engineering*, Vol. 80, 2002, p. 849–856

[32] Aoki, S. and Kishimoto, K., "Prediction of galvanic corrosion rates by the boundary element method", *Mathematical and Computer Modelling,* Vol. 15, 1991, p. 11–22

[33] Varela, F. E., Kurata, Y., and Sanada, N., "The influence of temperature on the galvanic corrosion of a cast iron-stainless steel couple (prediction by boundary element method)", *Corrosion Science,* Vol. 39, 1997, p. 775–788

[34] Scheiner, S. and Hellmich, C., "Finite Volume model for diffusion- and activation-controlled pitting corrosion of stainless steel", *Computer Methods in Applied Mechanics and Engineering*, Vol. 198, 2009, p. 2898–2910

[35] Onishi, Y., Takiyasu, J., Amaya, K., Yakuwa, H., and Hayabusa, K., "Numerical method for time-dependent localized corrosion analysis with moving boundaries by combining the finite volume method and voxel method", *Corrosion Science*, Vol. 63, 2012, p. 210–224

[36] Chen, Z. and Bobaru, F., "Peridynamic modeling of pitting corrosion damage", *Journal of the Mechanics and Physics of Solids*, Vol. 78, 2015, p. 352–381

[37] Chen, Z., Zhang, G., and Bobaru, F., "The Influence of Passive Film Damage on Pitting Corrosion", *Journal of The Electrochemical Society*, Vol. 163, 2016, p. C19–C24

[38] Yin, L., Jin, Y., Leygraf, C., and Pan, J., "A FEM model for investigation of micro-galvanic corrosion of Al alloys and effects of deposition of corrosion products", *Electrochimica Acta*, Vol. 192, 2016, p. 310–318

[39] Wang, Y., Yin, L., Jin, Y., Pan, J., and Leygraf, C., "Numerical Simulation of Micro-Galvanic Corrosion in Al Alloys: Steric Hindrance Effect of Corrosion Product", *Journal of The Electrochemical Society*, Vol. 164, 2017, p. C1035–C1043

[40] Schindelholz, E. J. et al., "Electrochemical aspects of copper atmospheric corrosion in the presence of sodium chloride", *Electrochimica Acta*, Vol. 276, 2018, p. 194–206

[41] Vicente Moraes, C., Santucci, R., Scully, J. R., and Kelly, R., "Finite Element Modeling of Chemical and Electrochemical Protection Mechanisms Offered by Mg-Based Organic Coatings to AA2024-T351", *Journal of The Electrochemical Society*, 2021

[42] Yin, L., Jin, Y., Leygraf, C., and Pan, J., "A FEM model for investigation of micro-galvanic corrosion of Al alloys and effects of deposition of corrosion products", *Electrochimica Acta*, Vol. 192, 2016, p. 310–318

[43] Ansari, T. Q., Luo, J.-L., and Shi, S.-Q., "Modeling the effect of insoluble corrosion products on pitting corrosion kinetics of metals", *npj Materials Degradation*, Vol. 3, 2019, p. 1–12

[44] Ansari, T. Q. et al., "Phase-field model of pitting corrosion kinetics in metallic materials", *npj Computational Materials*, Vol. 4, 2018, p. 38

[45] Agarwal, A. S., Landau, U., and Payer, J. H., "Modeling particulates effects on the cathode current capacity in crevice corrosion", *Journal of the Electrochemical Society*, Vol. 155, 2008, p. C269–C278

[46] Bryan, C. R. and Schindelholz, E. J., in *Corrosion 2018*,, p. Paper 10516, Phoenix

[47] McCafferty, E., *Introduction to Corrosion Science*, 2010

[48] Okamoto, G., "Passive film of 18-8 stainless steel structure and its function", *Corrosion Science*, Vol. 13, 1973, p. 471–489

[49] Sedriks, A. J., "Plenary Lecture—1986: Effects of Alloy Composition and Microstructure

on the Passivity of Stainless Steels", *CORROSION*, Vol. 42, 1986, p. 376–389

[50] Horvath, J. and Uhlig, H. H., "Critical Potentials for Pitting Corrosion of Ni, Cr-Ni, Cr-Fe, and Related Stainless Steels", *Journal of The Electrochemical Society*, Vol. 115, 1968, p. 791

[51] Olsson, C.-O. A. and Landolt, D., "Passive films on stainless steels - Chemistry, structure and growth", *Electrochimica Acta*, Vol. 48, 2003, p. 1093–1104

[52] Schaller, R. F. et al., *FY20 Status Report: SNF Interim Storage Canister Corrosion and Surface Environment Investigations*, p. 1–209, Albuquerque, NM, 2020

[53] Kain, R. M., Tuthill, A. H., and Hoxie, E. C., "The resistance of types 304 and 316 stainless steels to crevice corrosion in natural waters", *Journal of Materials for Energy Systems*, Vol. 5, 1984, p. 205–211

[54] Woldemedhin, M. T., Shedd, M. E., and Kelly, R. G., "Evaluation of the Maximum Pit Size Model on Stainless Steels under Thin Film Electrolyte Conditions", *Journal of The Electrochemical Society*, Vol. 161, 2014, p. E3216–E3224

[55] Jones, D. A., *Principles and Prevention of Corrosion*, 2nd ed., p. 51, Prentice Hall Inc., Upper Saddle River, NJ, 1996

[56] ASTM International, Ed., "Standard Practice for the Preparation of Substitute Ocean Water", *ASTM International*, Vol. 98, 2013, p. 1–3

[57] Bryan, C. R. and Knight, A. W., *Analysis of Dust Samples Collected from an Inland ISFSI Site (" Site A ")*, p. 1–65, Albuquerque, NM, 2020

[58] Tomashov, N. D., "Development of the Electrochemical Theory of Metallic Corrosion", *Corrosion*, Vol. 20, 1964, p. 7t-14t

[59] Novev, J. K. and Compton, R. G., "Natural convection effects in electrochemical systems", *Current Opinion in Electrochemistry*, Vol. 7, 2018, p. 118–129

[60] Liu, C., Srinivasan, J., and Kelly, R. G., "Electrolyte film thickness effects on the cathodic current availability in a galvanic couple", *Journal of The Electrochemical Society*, Vol. 164, 2017, p. C845–C855

[61] Horner, D. A., Connolly, B. J., Zhou, S., Crocker, L., and Turnbull, A., "Novel images of the evolution of stress corrosion cracks from corrosion pits", *Corrosion Science*, Vol. 53, 2011, p. 3466–3485

[62] Kondo, Y., "Prediction of Fatigue Crack Initiation Life Based on Pit Growth", *Corrosion Science*, Vol. 45, 1989, p. 7–11

[63] Co, N. E. C. and Burns, J. T., "Effects of macro-scale corrosion damage feature on fatigue crack initiation and fatigue behavior", *International Journal of Fatigue*, Vol. 103, 2017, p. 234–247

[64] Co, N. E. C. and Burns, J. T., "Effects of micro-scale corrosion damage features and local microstructure on fatigue crack initiation location", *International Journal of Fatigue*, Vol. 150, 2021, p. 106301

[65] Bland, L. G. and Locke, J. S. W., "Chemical and electrochemical conditions within stress corrosion and corrosion fatigue cracks", *npj Materials Degradation*, Vol. 12, 2017, p. 1–8

[66] Cooper, K. R. and Kelly, R. G., "Using capillary electrophoresis to study the chemical conditions within cracks in aluminum alloys", *Journal of Chromatography A*, Vol. 850, 1999, p. 381–389

[67] Nguyen, T. H., Brown, B. F., and Foley, R. T., "On the Nature of the Occluded Cell in the Stress Corrosion Cracking of AA7075-T651 - Effect of potential, composition, morphology", *Corrosion*, Vol. 38, 1982, p. 319–326

[68] Smith, J. A., Peterson, M. H., and Brown, B. F., "Electrochemical Conditions at the Tip of an Advancing Stress Corrosion Crack in AISI 4340 Steel", *Corrosion*, Vol. 26, 1970, p. 539–542

[69] Sandoz, G., FuJii, C. T., and Brown, B. F., "Solution chemistry within stress-corrosion cracks in alloy steels", *Corrosion Science*, Vol. 10, 1970, p. 839–845

[70] Cooper, K. R. and Kelly, R. G., "Crack tip chemistry and electrochemistry of environmental cracks in AA 7050", *Corrosion Science*, Vol. 49, 2007, p. 2636–2662

[71] Brown, B. F., in *Stress Corrosion Cracking and Hydrogen Embrittlement of iron based alloys*,, p. 747–750, NACE, Houston, TX

[72] Turnbull, A., "Theoretical analysis of influence of crack dimensions and geometry on mass transport in corrosion–fatigue cracks", *Materials Science and Technology (United Kingdom)*, Vol. 1, 1985, p. 700–710

[73] Turnbull, A., "Theoretical evaluation of the dissolved oxygen concentration in a crevice or crack in a metal in aqueous solution", *British Corrosion Journal*, Vol. 15, 1980, p. 165–171

[74] Turnbull, A., "Modeling of the Chemistry and Electrochemistry in Cracks — A Review", *Corrosion*, Vol. 57, 2001, p. 175–189

[75] Turnbull, A., Zhou, S., and Hinds, G., "Stress corrosion cracking of steam turbine disc steel-measurement of the crack-tip potential", *Corrosion Science*, Vol. 46, 2004, p. 193–211

[76] Ford, F. P., Taylor, D. F., Andresen, P. L., and Ballinger, R. G., *Corrosion-Assisted Cracking of Stainless and Low-Alloy Steels in LWR Environments*, 1987

[77] MacDonald, D. D. and Urquidi-MacDonald, M., "A coupled environment model for stress corrosion cracking in sensitized type 304 stainless steel in LWR environments", *Corrosion Science*, Vol. 32, 1991, p. 51–81

[78] Macdonald, D. D., Lu, P. C., Urquidi-Macdonald, M., and Yeh, T. K., "Theoretical Estimation of Crack Growth Rates in Type 304 Stainless Steel in Boiling-Water Reactor Coolant Environments", *Corrosion*, Vol. 52, 1996, p. 768–785

[79] Turnbull, A. and Ferriss, D. H., "Mathematical modelling of the electrochemistry in corrosion fatigue cracks in steel corroding in marine environments", *Corrosion Science*, Vol. 27, 1987, p. 1323–1350

[80] Turnbull, A. and Ferriss, D. H., "Mathematical modelling of the electrochemistry in corrosion fatigue cracks in structural steel cathodically protected in sea water", *Corrosion Science*, Vol. 26, 1986, p. 601–628

[81] Turnbull, A., "Modelling of crack chemistry in sensitized stainless steel in boiling water reactor environments", *Corrosion Science*, Vol. 39, 1997, p. 789–805

[82] Kovalov, D., Fekete, B., Engelhardt, G. R., and Macdonald, D. D., "Prediction of corrosion fatigue crack growth rate in alloys. Part II: effect of electrochemical potential, NaCl concentration, and temperature on crack propagation in AA2024-T351", *Corrosion Science*, Vol. 152, 2019, p. 130–139

[83] Kovalov, D., Fekete, B., Engelhardt, G. R., and Macdonald, D. D., "Prediction of corrosion fatigue crack growth rate in alloys. Part I: General corrosion fatigue model for aero-space aluminum alloys", *Corrosion Science*, Vol. 141, 2018, p. 22–29

[84] Turnbull, A. and Wright, L., "Modelling the electrochemical crack size effect on stress corrosion crack growth rate", *Corrosion Science*, Vol. 126, 2017, p. 69–77

[85] Frankel, G. S., Li, T., and Scully, J. R., "Perspective—Localized Corrosion: Passive Film Breakdown vs Pit Growth Stability", *Journal of The Electrochemical Society*, Vol. 164, 2017, p. C180–C181

[86] Jin, W., Du, H., Zheng, S., Xu, H., and Zhang, Y., "Comparison of the oxygen reduction reaction between NaOH and KOH solutions on a Pt electrode: The electrolyte-dependent effect", *Journal of Physical Chemistry B*, Vol. 114, 2010, p. 6542–6548

[87] Zhang, Q., Liu, P., Zhu, Z., Zhang, J., and Cao, F., "The study of the H_2O_2 during oxygen reduction process on typically corroding metal surface using tip generation-substrate collection mode of SECM", *Corrosion Science*, Vol. 164, 2020, p. 108312

[88] Alexander, C. L. et al., "Oxygen reduction on stainless steel in concentrated chloride media", *Journal of The Electrochemical Society*, Vol. 165, 2018, p. C869–C877

[89] Charles-Granville, U.-E., Liu, C., Scully, J. R., and Kelly, R. G., "An RDE Approach to Investigate the Influence of Chromate on the Cathodic Kinetics on 7XXX Series Al Alloys under Simulated Thin Film Electrolytes", *Journal of The Electrochemical Society*, Vol. 167, 2020, p. 111507

[90] Katona, R. M. et al., "Importance of the hydrogen evolution reaction in magnesium chloride solutions on stainless steel", *Corrosion Science*, Vol. 177, 2020, p. 108935

[91] Katona, R. M. et al., "Editors' Choice—Natural Convection Boundary Layer Thickness at Elevated Chloride Concentrations and Temperatures and the Effects on a Galvanic Couple", *Journal of The Electrochemical Society*, Vol. 168, 2021, p. 031512

[92] Katona, R. M., Carpenter, J., Kelly, R. G., Schindelholz, E. J., and Schaller, R. F., "Cathodic kinetics on platinum and stainless steel in NaOH environments", *In Preparation*, 2020

[93] Babić, R. and Metikoš-Huković, M., "Oxygen reduction on stainless steel", *Journal of Applied Electrochemistry*, Vol. 23, 1993, p. 352–357

[94] Geniès, L., Faure, R., and Durand, R., "Electrochemical reduction of oxygen on platinum nanoparticles in alkaline media", *Electrochimica Acta*, Vol. 44, 1998, p. 1317–1327

[95] Marković, N. M., Gasteiger, H. A., Grgur, B. N., and Ross, P. N., "Oxygen reduction reaction on Pt(111): effects of bromide", *Journal of Electroanalytical Chemistry*, Vol. 467, 1999, p. 157–163

[96] Wroblowa, H. S. and Qaderi, S. B., "Mechanism and kinetics of oxygen reduction on steel", *Journal of Electroanalytical Chemistry*, Vol. 279, 1990, p. 231–242

[97] Zhang, C., Fan, F. R. F., and Bard, A. J., "Electrochemistry of oxygen in concentrated NaOH solutions: Solubility, diffusion coefficients, and superoxide formation", *Journal of the American Chemical Society*, Vol. 131, 2009, p. 177–181

[98] Suter, T. and Bohni, H., "Microelectrodes for corrosion studies in microsystems", *Electrochimica Acta*, Vol. 47, 2001, p. 191–199

[99] Levich, V. G., *Physiochemical hydrodynamics*, Prentice Hall Inc., NJ, 1962

[100] Levich, V. G., "No Title", *Acta Physicochimica Urss*, Vol. 17, 1942, p. 257

[101] Azmat, N. S., Ralston, K. D., Muddle, B. C., and Cole, I. S., "Corrosion of Zn under acidified marine droplets", *Corrosion Science*, Vol. 53, 2011, p. 1604–1615

[102] Schindelholz, E., Risteen, B. E., and Kelly, R. G., "Effect of relative humidity on corrosion of steel under sea salt aerosol proxies I. NaCl", *Journal of the Electrochemical Society*, Vol. 161, 2014, p. 450–459

[103] Weissenrieder, J. and Leygraf, C., "In Situ Studies of Filiform Corrosion of Iron", *Journal of The Electrochemical Society*, Vol. 151, 2004, p. B165

[104] Zhang, J., Wang, J., and Wang, Y., "Micro-droplets formation during the deliquescence of salt particles in atmosphere", *Corrosion*, Vol. 61, 2005, p. 1167–1172

[105] Tsuru, T., Tamiya, K., and Nishikata, A., "Formation and growth of micro-droplets during the initial stage of atmospheric corrosion", *Electrochimica Acta*, Vol. 49, 2004, p. 2709–2715

[106] Thurmond, V. L. and Potter, R. W., *The densities of saturated solutions of NaCl and KCl from 10C to 105C*, p. 10, 1984

[107] Clesceri, L. S., Greenberg, A. E., and Eaton, A. D., *Standard Methods for the examination of water and wastewater*, Washington DC, 1998

[108] Carpenter, J. H., "The Chesapeake Bay Institute technique for the Winkler dissolved oxygen method", *Limnology and Oceanography*, Vol. 10, 1965, p. 141–143

[109] Maltseva, A., Shkirskiy, V., Lefèvre, G., and Volovitch, P., "Effect of pH on $Mg(OH)_2$ film evolution on corroding Mg by in situ kinetic Raman mapping (KRM)", *Corrosion Science*, Vol. 153, 2019, p. 272–282

[110] Downs, B., Robinson, S., Yang, H., and Mooney, P., "RRUFF Project", 2015

[111] Kocijan, A., Donik, Č., and Jenko, M., "Electrochemical and XPS studies of the passive film formed on stainless steels in borate buffer and chloride solutions", *Corrosion Science*, Vol. 49, 2007, p. 2083–2098

[112] Le Bozec, N. et al., "Influence of stainless steel surface treatment on the oxygen reduction reaction in seawater", *Corrosion Science*, Vol. 43, 2001, p. 765–786

[113] Ramasubramanian, N., Preocanin, N., and Davidson, R. D., "Analysis of Passive Films on Stainless Steel by Cyclic Voltammetry and Auger Spectroscopy", *Journal of The Electrochemical Society*, Vol. 132, 1985, p. 793–798

[114] König, U. and Schultze, J. W., "Kinetics of passive layer formation on Fe 20 Cr in

comparison with Fe", *Materials and Corrosion*, Vol. 39, 1988, p. 595–602

[115] De Cristofaro, N., Piantini, M., and Zacchetti, N., "The influence of temperature on the passivation behaviour of a super duplex stainless steel in a boric-borate buffer solution", *Corrosion Science*, Vol. 39, 1997, p. 2181–2191

[116] Liu, C. and Kelly, R. G., "Comparison study of the effect of oxide film properties on cathodic kinetics of stainless steel 304L and 316L during ORR potential window in sulfate solution", *Corrosion*, Vol. 75, 2019, p. 1087–1099

[117] Hostetler, P. . and Christ, C. ., "Studies in the system MgO-SiO2-CO2-H2O(I): The activity-product constant of chrysotile", *Geochimica et Cosmochimica Acta*, Vol. 32, 1968, p. 485–497

[118] Sayles, F. L. and Fyfe, W. S., "The crystallization of magnesite from aqueous solution", *Geochimica et Cosmochimica Acta*, Vol. 37, 1973, p. 87–99

[119] Qafoku, O. et al., "Dynamics of Magnesite Formation at Low Temperature and High pCO2 in Aqueous Solution", *Environmental science and technology*, Vol. 49, 2015, p. 10736–10744

[120] Swanson, E. J., Fricker, K. J., and Park, A. A., "Directed precipitation of hydrated and anhydrous magnesium carbonates for carbon storage", *Physical Chemistry Chemical Physics*, Vol. 16, 2014, p. 23440–23450

[121] King, H. E., Satoh, H., Tsukamoto, K., and Putnis, A., "Nanoscale observations of magnesite growth in chloride- and sulfate-rich solutions", *Environmental Science and Technology*, Vol. 47, 2013, p. 8684–8691

[122] Saldi, G. D., Jordan, G., Schott, J., and Oelkers, E. H., "Magnesite growth rates as a function of temperature and saturation state", *Geochimica et Cosmochimica Acta*, Vol. 73, 2009, p. 5646–5657

[123] Berthomé, G., Malki, B., and Baroux, B., "Pitting transients analysis of stainless steels at the open circuit potential", *Corrosion Science*, Vol. 48, 2006, p. 2432–2441

[124] Isaacs, H. S., Scheffey, C., and Huang, R., in *ECS Transactions*,, vol. 11, p. 1–12, ECS

[125] Song, C. and Zhang, J., in *PEM Fuel Cell Electrocatalysts and Catalyst Layers*, J. Zhang, Editor, p. 89–134, Springer, London

[126] Zheng, J., Sheng, W., Zhuang, Z., Xu, B., and Yan, Y., "Universal dependence of hydrogen oxidation and evolution reaction activity of platinum-group metals on pH and hydrogen binding energy", *Science Advances*, Vol. 2, 2016, p. 1–8

[127] Katona, R. M. et al., "Quantitative assessment of environmental phenomena on maximum pit size predictions in marine environments", *Electrochimica Acta*, Vol. 370, 2021, p. 137696

[128] Pannach, M., Bette, S., and Freyer, D., "Solubility Equilibria in the System Mg(OH)2-MgCl2-H2O from 298 to 393 K", *Journal of Chemical and Engineering Data*, Vol. 62, 2017, p. 1384–1396

[129] Katona, R. M., Kelly, R. G., Bryan, C. R., Schaller, R. F., and Knight, A. W., "Use of in situ Raman spectroelectrochemical technique to explore atmospheric corrosion in marine-relevant environments", *Electrochemistry Communications*, Vol. 118, 2020, p. 106768

[130] Stratmann, M., "The Atmospheric Corrosion of Iron - A Discussion of the Physico-Chemical Fundamentals of this Omnipresent Corrosion Process Invited Review", *Berichte der Bunsengesellschaft für physikalische Chemie*, Vol. 94, 1990, p. 626–639

[131] Cole, I. S., Azmat, N. S., Kanta, A., and Venkatraman, M., "What really controls the atmospheric corrosion of zinc? Effect of marine aerosols on atmospheric corrosion of zinc", *International Materials Reviews*, Vol. 54, 2009, p. 117–133

[132] Schindelholz, E. and Kelly, R. G., "Wetting phenomena and time of wetness in atmospheric corrosion: a review", *Corrosion Reviews*, Vol. 30, 2012, p. 135–170

[133] Simillion, H., Dolgikh, O., Terryn, H., and Deconinck, J., "Atmospheric corrosion modeling", *Corrosion Reviews*, Vol. 32, 2014, p. 73–100

[134] Wragg, A. A. and Ross, T. K., "Superposed free and forced convective mass transfer in an electrochemical flow system", *Electrochimica Acta*, Vol. 12, 1967, p. 1421–1428

[135] Wragg, A. A., "Free convection mass transfer at horizontal electrodes", *Electrochimica Acta*, Vol. 13, 1968, p. 2159–2165

[136] Fenech, E. J. and Tobias, C. W., "Mass transfer by free convection at horizontal electrodes", *Electrochimica Acta*, Vol. 2, 1960, p. 311–325

[137] Wilke, C. R., Eisenberg, M., and Tobias, C. W., "Correlation of Limiting Currents under Free Convection Conditions", *Journal of The Electrochemical Society*, Vol. 100, 1953, p. 513

[138] Tobias, C. W., Eisenberg, M., and Wilke, C. R., "Diffusion and Convection in Electrolysis - A Theoretical Review", *Journal of The Electrochemical Society*, Vol. 99, 1952, p. 359C

[139] Ibl, N., "The use of dimensionless groups in electrochemistry", *Electrochimica Acta*, Vol. 1, 1959, p. 117–129

[140] Gileadi, E., *Electrode Kinetics for Chemists, Chemical Engineers, and Materials*

Scientists, VCH Publishers, Inc., 1993

[141] Dolgikh, O., Bastos, A. C., Oliveira, A., Dan, C., and Deconinck, J., "Influence of the electrolyte film thickness and NaCl concentration on the oxygen reduction current on platinum", *Corrosion Science*, Vol. 102, 2016, p. 338–347

[142] Simillion, H., Van den Steen, N., Terryn, H., and Deconinck, J., "Geometry influence on corrosion in dynamic thin film electrolytes", *Electrochimica Acta*, Vol. 209, 2016, p. 149–158

[143] Marshall, R., Kelly, R., Goff, A., and Sprinkle, C., "Galvanic Corrosion Between Coated Al Alloy Plate and Stainless Steel Fasteners, Part 1: FEM Model Development and Validation", *Corrosion*, Vol. 75, 2019, p. 1461–1473

[144] Nishikata, A. et al., "An electrochemical impedance study on atmospheric corrosion of steels in a cyclic wet-dry condition", *Corrosion Science*, Vol. 37, 1995, p. 2059–2069

[145] Nishikata, A., Ichihara, Y., and Tsuru, T., "An application of electrochemical impedance spectroscopy to atmospheric corrosion study", *Corrosion Science*, Vol. 37, 1995, p. 897–911

[146] Nishikata, A., "Influence of Electrolyte Layer Thickness and pH on the Initial Stage of the Atmospheric Corrosion of Iron", *Journal of The Electrochemical Society*, Vol. 144, 1997, p. 1244–1252

[147] Stratmann, M., Streckel, H., Kim, K. T., and Crockett, S., "On the atmospheric corrosion of metals which are covered with thin electrolyte layers-iii. the measurement of polarisation curves on metal surfaces which are covered by thin electrolyte layers", *Corrosion Science*, Vol. 30, 1990, p. 715–734

[148] Stratmann, M. and Streckel, H., "On the atmospheric corrosion of metals which are covered with thin electrolyte layers—I. Verification of the experimental technique", *Corrosion Science*, Vol. 30, 1990, p. 681–696

[149] Stratmann, M. and Streckel, H., "On the atmospheric corrosion of metals which are covered with thin electrolyte layers-II. Experimental results", *Corrosion Science*, Vol. 30, 1990, p. 697–714

[150] Frankel, G. S. et al., "Potential control under thin aqueous layers using a Kelvin Probe", *Corrosion Science*, Vol. 49, 2007, p. 2021–2036

[151] Dolgikh, O. et al., "Simulation of the role of vibration on Scanning Vibrating Electrode Technique measurements close to a disc in plane", *Electrochimica Acta*, Vol. 203, 2016, p. 379–387

[152] Cheng, Y. L. et al., "A study of the corrosion of aluminum alloy 2024-T3 under thin electrolyte layers", *Corrosion Science*, Vol. 46, 2004, p. 1649–1667

[153] Zhang, S. H. and Lyon, S. B., "The electrochemistry of iron, zinc and copper in thin layer electrolytes", *Corrosion Science*, Vol. 35, 1993, p. 713–718

[154] Amatore, C., Szunerits, S., Thouin, L., and Warkocz, J. S., "The real meaning of Nernst's steady diffusion layer concept under non-forced hydrodynamic conditions. A simple model based on Levich's seminal view of convection", *Journal of Electroanalytical Chemistry*, Vol. 500, 2001, p. 62–70

[155] Amatore, C., Pebay, C., Thouin, L., and Wang, A., "Cyclic voltammetry at microelectrodes. Influence of natural convection on diffusion layers as characterized by in situ mapping of concentration profiles", *Electrochemistry Communications*, Vol. 11, 2009, p. 1269–1272

[156] Amatore, C., Szunerits, S., Thouin, L., and Warkocz, J.-S., "Mapping concentration profiles within the diffusion layer of an electrode Part III. Steady-state and time-dependent profiles via amperometric measurements with an ultramicroelectrode probe", *Electrochemistry Communications*, Vol. 2, 2000, p. 353–358

[157] Amatore, C., Szunerits, S., Thouin, L., and Warkocz, J. S., "Monitoring concentration profiles in situ with an ultramicroelectrode probe", *Electroanalysis*, Vol. 13, 2001, p. 646–652

[158] Scarf, P. and Laycock, P., "Applications of extreme-value theory in corrosion engineering", *Journal of Research of the National Institute of Standards and Technology*, Vol. 99, 1994, p. 313

[159] Wagner, C., "Contribution to the Theory of Cathodic Protection", *Journal of the Electrochemical Society*, Vol. 99, 1952, p. 1–12

[160] "ASTM-B117-16 - Standard Practice for Operating Salt Spray (Fog) Apparatus", *ASTM B117-19*, 2017, p. ASTM International, West Conshohocken, PA,1-12

[161] "ASTM G85-11 - Standard Practice for Modified Salt Spray (Fog) Testing 1", *ASTM International*, 2017, p. 1–14

[162] "ASTM B368-09 - Standard Test Method for Copper-Accelerated Acetic Acid-Salt Spray (Fog) Testing (CASS Test)", *ASTM International*, 2014, p. 1–4

[163] "ASTM D2247-15 - Standard Practice for Testing Water Resistance of Coatings in 100% Relative Humidity", *ASTM International*, 2014, p. 1–7

[164] "Corrosion tests in artificial atmospheres - Salt spray tests (ISO 9227:2014)", *International Organization for Standardization*, 2006, p. 1–28

[165] Ghassemi, M. and Shahidian, A., in *Nano and Bio Heat Transfer and Fluid Flow,*, p. 31–56, Elsevier

[166] Shinohara, T., Motoda, S., and Oshikawa, W., "Evaluation of Corrosivity of Atmosphere by ACM Type Corrosion Sensor", *Zairyo-to-Kankyo*, Vol. 54, 2005, p. 375–382

[167] Laycock, N. J. and Newman, R. C., "Localised dissolution kinetics, salt films and pitting potentials", *Corrosion Science*, Vol. 39, 1997, p. 1771–1790

[168] Ernst, P. and Newman, R. C., "Explanation of the effect of high chloride concentration on the critical pitting temperature of stainless steel", *Corrosion Science*, Vol. 49, 2007, p. 3705–3715

[169] Moayed, M. H. and Newman, R. C., "The Relationship Between Pit Chemistry and Pit Geometry Near the Critical Pitting Temperature", *Journal of The Electrochemical Society*, Vol. 153, 2006, p. 330–335

[170] Kuo, H. C. and Landolt, D., "Rotating disc electrode study of anodic dissolution or iron in concentrated chloride media", *Electrochimica Acta*, Vol. 20, 1975, p. 393–399

[171] Ernst, P. and Newman, R. ., "Pit growth studies in stainless steel foils II. Effect of temperature, chloride concentration and sulphate addition", *Corrosion Science*, Vol. 44, 2002, p. 943–954

[172] Okada, T., "Considerations of the stability of pit repassivation during pitting corrosion of passive metals", *Journal of Electrochemical Society*, Vol. 131, 1984, p. 1026–1032

[173] Woldemedhin, M. T., Srinivasan, J., and Kelly, R. G., "Effects of environmental factors on key kinetic parameters relevant to pitting corrosion", *Journal of Solid State Electrochemistry*, Vol. 19, 2015, p. 3449–3461

[174] Chou, I. M. and Phan, L. D., "Solubility Relations in the System Potassium Chloride-Ferrous Chloride-Water between 25 and 70C at 1 atm", *Journal of Chemical and Engineering Data*, Vol. 31, 1986, p. 154–156

[175] Jun, J., Frankel, G. S., and Sridhar, N., "Effect of chloride concentration and temperature on growth of 1D Pit", *Journal of Solid State Electrochemistry*, Vol. 19, 2015, p. 3439–3447

[176] Jun, J., Frankel, G. S., and Sridhar, N., "Further Modeling of Chloride Concentration and Temperature Effects on 1D Pit Growth", *Journal of The Electrochemical Society*, Vol. 163,

2016, p. C823–C829

[177] Nguyen, V. A. and Newman, R. C., "A Comprehensive Modelling and Experimental Approach to Study the Diffusion-Controlled Dissolution in Pitting Corrosion", *Corrosion Science*, Vol. 186, 2021, p. 109461

[178] Einstein, A., "No Title", *Ann Phys*, Vol. 19, 1906, p. 289–306

[179] Katona, R. M., Carpenter, J., Schindelholz, E. J., and Kelly, R. G., "Prediction of Maximum Pit Sizes in Elevated Chloride Concentrations and Temperatures", *Journal of The Electrochemical Society*, Vol. 166, 2019, p. C3364–C3375

[180] Anderko, A., Sridhar, N., and Dunn, D. S., "A general model for the repassivation potential as a function of multiple aqueous solution species", *Corrosion Science*, Vol. 46, 2004, p. 1583–1612

[181] Van Den Steen, N., Simillion, H., Dolgikh, O., Terryn, H., and Deconinck, J., "An integrated modeling approach for atmospheric corrosion in presence of a varying electrolyte film", *Electrochimica Acta*, Vol. 187, 2016, p. 714–723

[182] Lin, C., Ruan, H., and Shi, S.-Q., "Phase field study of mechanico-electrochemical corrosion", *Electrochimica Acta*, Vol. 310, 2019, p. 240–255

[183] Bryan, C., Schindelholz, E., Knight, A., Taylor, J., and Dingreville, R., *Stability of sea-salt deliquescent brines on heated surfaces of SNF dry storage canisters*, p. SAND2019-0324C, 2019

[184] Schaller, R. F., Jove-Colon, C. F., Taylor, J. M., and Schindelholz, E. J., "The controlling role of sodium and carbonate on the atmospheric corrosion rate of aluminum", *npj Materials Degradation*, Vol. 1, 2017, p. 20

[185] Blücher, D. B., Lindström, R., Svensson, J.-E., and Johansson, L.-G., "The Effect of CO[sub 2] on the NaCl-Induced Atmospheric Corrosion of Aluminum", *Journal of The Electrochemical Society*, Vol. 148, 2001, p. B127

[186] Rafla, V. N., Khullar, P., Kelly, R. G., and Scully, J. R., "Coupled Multi-Electrode Array with a Sintered Ag/AgCl Counter/Reference Electrode to Investigate AA7050-T7451 and Type 316 Stainless Steel Galvanic Couple under Atmospheric Conditions", *Journal of The Electrochemical Society*, Vol. 165, 2018, p. C562–C572

[187] Marshall, R. S., Goff, A., Sprinkle, C., Britos, A., and Kelly, R. G., "Estimating the Throwing Power of SS316 when Coupled with AA7075 Through Finite Element Modeling", *Corrosion*, Vol. 76, 2020, p. 476–484

[188] Liu, C., Kubacki, G. W., and Kelly, R. G., "Application of Laplace equation-based modeling into corrosion damage prediction for galvanic coupling between a zinc plate and stainless steel rods under a thin film electrolyte", *Corrosion*, Vol. 75, 2019, p. 465–473

[189] King, A. D., Lee, J. S., and Scully, J. R., "Finite Element Analysis of the Galvanic Couple Current and Potential Distribution between Mg and 2024-T351 in a Mg Rich Primer Configuration", *Journal of The Electrochemical Society*, Vol. 163, 2016, p. C342–C356

[190] Bruggeman, D. A. G., "Berechnung verschiedener physikalischer Konstanten von heterogenen Substanzen. I. Dielektrizitätskonstanten und Leitfähigkeiten der Mischkörper aus isotropen Substanzen", *Annalen der Physik*, Vol. 416, 1935, p. 636–664

[191] Weirich, T. D. et al., "Humidity Effects on Pitting of Ground Stainless Steel Exposed to Sea Salt Particles", *Journal of The Electrochemical Society*, Vol. 166, 2019, p. C3477–C3487

[192] Marshall, R. S., Katona, R. M., Melia, M. A., and Kelly, R. G., "Pit Stability Predictions of Additively Manufactured SS316 Surfaces Using Finite Element Analysis", *In Preparation*, 2021

[193] Budiansky, N. D., Organ, L., Hudson, J. L., and Scully, J. R., "Detection of Interactions among Localized Pitting Sites on Stainless Steel Using Spatial Statistics", *Journal of The Electrochemical Society*, Vol. 152, 2005

[194] Cui, Z. Y. et al., "Crack growth behaviour and crack tip chemistry of X70 pipeline steel in near-neutral pH environment", *Corrosion Engineering Science and Technology*, Vol. 51, 2016, p. 352–357

[195] Lee, D., Huang, Y., and Achenbach, J. D., "A comprehensive analysis of the growth rate of stress corrosion cracks", *Proceedings of the Royal Society A: Mathematical, Physical and Engineering Sciences*, Vol. 471, 2015, p. 20140703

[196] Danielson, M. J., Oster, C. A., and Jones, R. H., "Crack tip chemistry modelling of intergranular stress corrosion cracks in nickel containing segregated phosphorus and sulfur", *Corrosion Science*, Vol. 32, 1991, p. 1–5

[197] Kwon, H. S., Wuensche, A., and Macdonald, D. D., "Effects of flow rate on crack growth in sensitized type 304 stainless steel in high-temperature aqueous solutions", *Corrosion*, Vol. 56, 2000, p. 482–491

[198] Engelhardt, G. R., Macdonald, D. D., and Urquidi-Macdonald, M., "Development of fast algorithms for estimating stress corrosion crack growth rate", *Corrosion Science*, Vol. 41, 1999, p. 2267–2302

[199] Harris, Z. D., Amino, K., Steiner, P. s., and Burns, J. T., in *TMS 2020*,, San Diego, CA

[200] Sun, X., Srinivasan, J., Kelly, R. G., and Duddu, R., "Numerical investigation of critical electrochemical factors for pitting corrosion using a multi-species reactive transport model", *Corrosion Science*, Vol. 179, 2021, p. 109130

[201] Hung, G. W. and Dinius, R. H., "Diffusivity of Oxygen in Electrolyte Solutions", *Journal of Chemical and Engineering Data*, Vol. 17, 1972, p. 449–451

[202] Tada, H., Paris, P. C., and Irwin, G. R., *The Stress Analysis of Cracks Handbook, Third Edition*, ASME Press, St. Louis, Missouri, 2000

[203] *In-Drift Precipitates/Salts Model*, Sandia National Laboratories, Albuquerque, NM, 2007

[204] Thébault, F., Vuillemin, B., Oltra, R., Allely, C., and Ogle, K., "Modeling bimetallic corrosion under thin electrolyte films", *Corrosion Science*, Vol. 53, 2011, p. 201–207

[205] Nishikata, A., Ichihara, Y., Hayashi, Y., and Tsuru, T., "Influence of Electrolyte Layer Thickness and pH on the Initial Stage of the Atmospheric Corrosion of Iron", *Journal of The Electrochemical Society*, Vol. 144, 1997, p. 1244–1252

[206] Turnbull, A. and Thomas, J. G. N., "A Model of Crack Electrochemistry for Steels in the Active State Based on Mass Transport by Diffusion and Ion Migration", *Journal of the Electrochemical Society*, Vol. 129, 1982, p. 1412–1422

[207] Steiner, P. J. and Burns, J. T., "Mechanistic Studies of Intergranular Stress Corrosion Cracking in Al-Mg Alloys under Atmospheric Exposure Conditions", *CORROSION*, Vol. 74, 2018, p. 1117–1131

[208] Gangloff, R. P., "Crack size effects on the chemical driving force for aqueous corrosion fatigue", *Metallurgical Transactions A*, Vol. 16, 1985, p. 953–969

[209] Zhou, S., Lukaszewicz, M., and Turnbull, A., "Small and short crack growth and the solution-conductivity dependent electrochemical crack size effect", *Corrosion Science*, Vol. 97, 2015, p. 25–37

[210] Richey, E., Morton, D. S., and Moshier, W. C., in *Corrosion 2006*,, p. 1–25, San Diego, CA

[211] Itow, M., Kikuchi, M., and Suzuki, S., in *Corrosion 2000*,, p. 1–9, Orlando, FL

[212] Harris, Z. D. and Burns, J. T., "The effect of loading rate on the environment-assisted cracking behavior of AA7075-T651 in aqueous NaCl solution", *Corrosion and Materials Degradation*, 2021, p. in review

[213] Katona, R. M., Tokuda, S., Perry, J., and Kelly, R. G., "Design, Construction, and Validation for in-situ Water Layer Thickness Determination during Accelerated Corrosion Testing", *Corrosion Science*, Vol. 175, 2020, p. 108849

[214] Steiner, P., Harris, Z., Vicente Moraes, C., Kelly, R., and burns, james, "Investigation of IG-SCC growth kinetics in Al-Mg alloys in thin film environments", *Corrosion*, 2021

[215] Venkatraman, M. S., Cole, I. S., Gunasegaram, D. R., and Emmanuel, B., "Modeling Corrosion of a Metal under an Aerosol Droplet", 2010, p. 1650–1653

Appendices

It is noted that the following appendices are the accompanying first author, peer-reviewed publications as given in the biography section of this dissertation. The figures, equations, tables, and citations within the appendices are inclusive to each appendix section and the numbered items do not correspond with those in the previous sections.

A. Importance of the hydrogen evolution reaction in magnesium chloride solutions on stainless steel

Importance of the hydrogen evolution reaction in magnesium chloride solutions on stainless steel

R. M. Katona,[1,2] J. C. Carpenter,[1] A. W. Knight,[1] C. R. Bryan,[1] R. F. Schaller[1], R. G. Kelly,[2] E. J. Schindelholz[3, *]

[1] Sandia National Laboratories, Albuquerque, NM 87123 USA
[2] Materials Science and Engineering, University of Virginia, Charlottesville, VA 22904 USA
[3] Materials Science and Engineering, The Ohio State University, Columbus, OH 43210 USA
[*]Corresponding Author; schindelholz.2@osu.edu

Key Words

cathodic kinetics in marine environments, oxygen reduction reaction, atmospheric corrosion, magnesium chloride electrolyte properties

Abstract

Cathodic kinetics in magnesium chloride ($MgCl_2$) solutions were investigated on platinum (Pt) and stainless steel 304L (SS304L). Density, viscosity, and dissolved oxygen concentration for $MgCl_2$ solutions were also measured. A 2-electron transfer for oxygen reduction reaction (ORR) on Pt was determined using a rotating disk electrode. SS304L displayed non-Levich behavior for ORR and, due to ORR suppression and buffering of near surface pH by Mg-species precipitation, the primary cathodic reaction was the hydrogen evolution reaction (HER) in saturated $MgCl_2$. Furthermore, non-carbonate precipitates were found to be kinetically favored. Implications of HER are discussed through atmospheric corrosion and stress corrosion cracking.

1. Introduction

Stainless steels (SS) are often subjected to marine and near-marine atmospheric environments characterized by hygroscopic sea salt particles which adhere to the alloy surface. Through absorption of moisture from the atmosphere, sea salt particles deliquesce and form a corrosive brine on the surface of the alloy. The chemistry and concentration of the seawater brine varies widely with relative humidity (RH) as seen in Figure 1 at 25 ˚C. At high RH values, particularly above the saturation/deliquescence point of NaCl (74% RH), brines are rich in Na^+ and Cl^-. At lower RH values, because of the precipitation of NaCl, the seawater brines composition becomes dominated by Mg^{2+} and Cl^- down to near the saturation/deliquescence point of $MgCl_2 \cdot 6H_2O$ (36 % RH). Additionally, the volume of the brine decreases with decreasing RH [1]. In this way, RH along with salt load control the composition, volume and other properties of the resultant brine, impacting anodic and cathodic corrosion kinetics [1,2].

Historically, anodic kinetics of SS have been the main subject of studies related to concentrated seawater or chloride environments and have been summarized elsewhere for localized pitting corrosion [3], a common mode of corrosion degradation for SS's. However, research on the effects of concentrated chloride brines on cathodic kinetics has been lacking with the exception of Alexander et al. [4]. As cathodic kinetics control pit initiation and growth in combination with anodic kinetics, it is critical to understand the effects of concentrated solution chemistries on cathodic behavior.

In dilute chloride solutions [4–9], the oxygen reduction reaction (ORR) has been shown to be the dominant cathodic reaction on SS alloys near the open circuit potential (OCP) and the rate of reaction is diffusion-limited at sufficiently negative potentials. As such, cathodic rates can be predicted through Levich analysis [10]. Numerous studies have explored cathodic kinetics in atmospheric environments across multiple ferrous alloys as a function of solution cation composition [5,7,8,11], dilute chloride concentrations [4,9,12] and surface finish [6,9] and have further shown the dominance of ORR. A detailed chart of ORR in various media and surface finishes is given by Klapper and Goellner and shows that regardless of the conditions explored, ORR is always the dominant cathodic reduction reaction on ferrous alloys [6]. To date, cathodic kinetics literature in highly concentrated $MgCl_2$ brines is lacking. Additionally, minimal information exists on the high-fidelity control of boundary layer thicknesses as a function of MgCl2 concentration necessary to understand the overall corrosion process at low RH.

Although it has been assumed that ORR is the dominant reduction reaction in chloride-containing environments, various cations have been shown to change the cathodic reduction reaction in other alloy systems and could hold true in SS systems [13,14]. Limited research on Al alloys has shown that Zn^{2+} and Mg^{2+} cations can suppress cathodic kinetics through the formation of films at OCP [13], and Al^{3+} cations can enhance cathodic kinetics by the promotion of the hydrogen evolution reaction (HER) [14]. Thus, as SS alloys are utilized in marine and near-marine environments, characterized by concentrated chloride brines dominated by $MgCl_2$, ascertaining the mechanisms for cathodic reduction reactions in such environments is crucial to understanding the pitting corrosion process.

The objective of this work is to study the cathodic reduction reaction mechanism on SS304L and Pt in 0.189 M to 4.98 M (saturated) $MgCl_2$ as a function of boundary layer thickness using a rotating disk electrode (RDE). To aid in the interpretation of the results, various solution properties for $MgCl_2$ solutions including viscosity (η), density (ρ) and dissolved O_2 concentration $\left(C_{O_2}\right)$ are also presented along with a literature survey of oxygen diffusivities $\left(D_{O_2}\right)$. The thermodynamic stability of Mg^{2+} species was also explored. Finally, the $NaOH$-$MgCl_2$-H_2O-CO_2-O_2 system helped ascertain the kinetics of Mg^{2+} species formation. The dominance of HER as the cathodic reduction reaction on SS304L with increasing $MgCl_2$ concentration due to ORR suppression and Mg-species precipitation acting as a solution pH buffer once a critical pH is reached will be discussed along with critical implications for atmospheric corrosion and stress corrosion cracking.

2. Experimental

2.1 Materials

High speed rotating disc electrodes (RDE) with a diameter of 5 mm comprised of SS304L and 99.99% Pt were acquired from Pine Research Instrumentation, Inc. (USA). For deaerated experiments, a diameter of 5.5 mm was used in order to form an airtight seal in the gas purge bearing assembly for the cell. Prior to each use, the electrodes were polished using a 1 μm Dialube Diamond Suspension®, then rinsed with ultrapure (18.2 MΩ-cm) water and dried with nitrogen (N_2). $MgCl_2$ solutions were prepared using ultrapure water and reagent grade $MgCl_2$ (≥ 99.0% purity).

2.2 Electrochemical tests

A three-electrode cell was used with the alloy specimen as the working electrode (WE) with an exposed area of 0.196 cm^2 (except in deaerated experiments where the electrode area was 0.238 cm^2), a saturated calomel reference electrode (SCE), and a Pt-coated niobium mesh as the counter electrode. The samples were immersed in the solution of interest in a 150 mL jacketed cell and sparged with lab air to maintain a solution saturated in O_2. The WE was rotated using a Pine instruments MSR rotator with an accuracy of ± 1 % of the display reading. Rotation speeds ranged from 100 to 6000 rpm. The solution temperature was controlled to 25 ± 0.1 °C using a water circulator and thermostat. Gamry Interface 1010E potentiostats (Gamry Instruments Inc., Warminster, PA, USA) were used for all electrochemical measurements. Repetitions were conducted for 500 rpm under all solution concentrations.

Cathodic polarization measurements were performed on SS304L and Pt at scan rates of 0.167 and 1 mV/s respectively after 1 hour of OCP equilibration and stabilization. The scans were performed from OCP to -1.2 V_{SCE}. Potentiodynamic measurements were made in three different solutions of $MgCl_2$: (1) 0.189 M, (2) 1.28 M, and (3) 4.98 M corresponding to equilibrium RH's of 99%, 92%, and 37%, respectively [1]. The measured pH of the as prepared solutions ranged as follows: 4.5 to 5 for 4.98 M, 5.5 to 6.1 for 1.28 M and 6.0 to 7.0 for 0.189 M $MgCl_2$. Additional experiments were performed with a CO_2 absorber obtaining a concentration of < 1 ppm of CO_2 in the sparged air. The solution was sparged with the CO_2-free lab air for eight hours and transferred to the reaction cell via pressure through a system always closed to ambient air. The reaction cell was continuously bubbled with the same CO_2-free air. De-aerated tests were conducted with N_2 sparging gas following the same procedure.

2.3 Determination of precipitates present in MgCl2 solutions

In order to determine the nature of the film formed on the surface of the alloy after cathodic polarization, the sample was removed from the cell and immediately wicked dry with a paper tissue. The sample was then placed in a desiccator for at least 24 hours to ensure the sample was dry. The sample was then analyzed with X-ray diffraction (XRD) in a Bruker D2 PHASER equipped with a Cu Kα-source. Reflections in the 2θ range of 10–65˚ were recorded.

Titration experiments were performed to determine the kinetic stability of $MgCl_2$ precipitates. Four solutions of $MgCl_2$ (0.18, 1.28, 3.3, and 4.98 M) were analyzed for precipitate compositions formed in the presence of OH^-. Approximately 15 mL of each solution was added to a scintillation vial and the pH was increased using 3 M NaOH (~200 µL). A gel was formed immediately. To prevent further reactions of the precipitates, the gel was immediately removed and transferred to a large Whatman filter to dry out and wick away the brine. Once dry, the samples were mounted and analyzed via XRD. To separate the phases, instead of using a Whatman filter to wick away the brine, the gels were vacuum filtered to dryness and rinsed to remove any NaCl that formed.

2.4 Determination of MgCl2 solution properties

The density (ρ), dissolved oxygen concentration (C_{O_2}), and viscosity (η) were measured for $MgCl_2$ brines (0.01 M to saturated) at 25°C. ρ was measured using hydrometers calibrated for specific gravity ranges from 1.000 to 1.220, and 1.20 to 1.420 [15]. C_{O_2} measurements were taken using the Chesapeake Bay Institute modified Winkler iodometric titration method [16,17]. Briefly, samples were heated to 25˚C and equilibrated with the ambient air for a few hours, then transferred to a glass-stopper flask, which was calibrated gravimetrically with DI water to contain a total solution volume of 146 mL. Next, 1 mL of 3 M manganese (II) sulfate ($MnSO_4$) and 1 mL of basic potassium iodide (KI) (4 M KI in 8 M NaOH) were added to the flask and capped to allow for minimal air to exist in the flask. The contents of the flask were thoroughly mixed using a magnetic stir bar for several minutes for the KI to disperse and break apart precipitates that formed. To quench the reaction, 50% sulfuric acid (H_2SO_4) was added along with a starch indicator. C_{O_2} was measured via titration of the acidified solution by sodium thiosulfate ($Na_2S_2O_3$). η was measured at 25°C, using a Brookfield AMETEK LDTV2T Viscometer with an ultra-low η adaptor. Roughly

16 mL of each sample was transferred to the sample cell, and each temperature set point equilibrated for 10 mins. Five spindle speeds were analyzed to achieve a torque between 10% and 95% to verify the Newtonian fluid relationship.

2.5 Cathodic Kinetic Analysis

Theoretical diffusion-limited current density (i_{lim}) can be expressed by the use of Fick's first law and assuming one-dimensional diffusion via

$$i_{lim} = \frac{nFD(C_{bulk} - C_{surface})}{\delta} \qquad \text{Eqn. 1}$$

where n is the number of electrons transferred during the electrochemical reaction, F is Faraday's constant ($96485\ C/mol$), D is the diffusivity of the reacting species, C_{bulk} and $C_{surface}$ (assumed to be zero) are the concentration of the reacting species in the bulk solution and at the electrode surface respectively, and δ is the hydrodynamic boundary layer thickness. When using a RDE, δ is given as a function of rotation speed (ω in rad/sec) through,

$$\delta = 1.61 D^{1/3} \omega^{-1/2} \nu^{1/6} \qquad \text{Eqn. 2}$$

where ν is the kinematic viscosity ($\nu = \eta/\rho$) [18]. Substituting Equation 2 into 1 yields the Levich equation [10]:

$$i_{lim} = 0.62 nF D_{O_2}^{2/3} \nu^{-1/6}\, c_{O_2,bulk} \omega^{1/2} \qquad \text{Eqn. 3}$$

Levich behavior is valid in regions where the electrolyte is under laminar flow characterized by the dimensionless Reynolds number (Re):

$$Re = \frac{r^2 \omega}{\nu} \qquad \text{Eqn. 4}$$

where r is the radius of the RDE assembly. The transition to turbulent flow is marked by a Reynolds number of $2 \cdot 10^5$ [19–22].

2.6 Thermodynamic Analysis of Mg^{2+} Brines

A stability diagram was created for the $MgCl_2$-H_2O-CO_2-O_2 system using the thermodynamic solubility and speciation modeling program EQ3/6 [23]. The Yucca Mountain Program thermodynamic database for concentrated salt solutions [24] which implements the Pitzer formalism [25] for calculating activity coefficients, was utilized. The Yucca Mountain Pitzer database was developed to evaluate the composition of concentrated solutions [1]. Specific Ksp values included in the Yucca Mountain Pitzer database used in the creation of this diagram are presented in Table 1 and were gathered from [26–28]. The fugacity (f) of oxygen was set to $\log(f_{O_2}) = -0.68$ in all calculations. Two conditions were considered for CO_2: $\log(f_{CO_2}) = -3.4$ and $\log(f_{CO_2}) = 0$. These conditions correspond to lab air and lab air that has been scrubbed of CO_2. The temperature was held constant at $25°C$.

3. Results

3.1 $MgCl_2$ solution properties at 25˚C

To aid in the interpretation of the results, various solution properties including ρ, η, and C_{O_2} were measured as a function of $MgCl_2$ concentration at 25˚C and are presented in Figure 2. Also presented in Figure 2 are published results for $MgCl_2$ solutions from the following studies: ρ [29,30], η [29,30], C_{O_2} [31–33], and D_{O_2} [31]. As is demonstrated in Figure 2, the measured values in this study align well with values presented in literature. Along with the direct comparison for various concentrations of $MgCl_2$ solutions, average values for pure water were compiled from the following studies: ρ, η [34], C_{O_2} [33,35–37], and D_{O_2} [38–40]. Unique fits, for the measured values in this experiment, for ρ and η, presented in Figure 2(a) and (b), are valid for the entire range of $MgCl_2$ concentrations (0 to 4.98 M $MgCl_2$) whereas C_{O_2} is valid between 0 and 4 M $MgCl_2$. 4.98 M was determined to be the saturation limit of $MgCl_2$ based on the K_{sp} for magnesium hexahydrate

($MgCl_2 \cdot 6H_2O$) determined from Table 1. All further calculations used in this paper will utilize the fits presented in Figure 2.

Reynolds numbers (Re) were calculated for all RDE experimental conditions presented in this study using Equation 4 along with ρ and η fits from Figure 2(a) and (b) respectively. All Re values were $< 2 \cdot 10^5$, with the exception of 0.189 M $MgCl_2$ at 6000 rpm which was excluded, indicating laminar flow [19–22] and all further analyses are not convoluted with influences from turbulence.

3.2 Cathodic kinetics in MgCl2 solutions

3.2.1 Platinum

Measured cathodic polarization scans on Pt in a range of $MgCl_2$ solutions are presented in Figure 3. The corresponding δ calculated from Equation 2 and fits in Figure 2 are labeled alongside the rotation speeds. Theoretical i_{lim} for ORR are calculated from Equation 3 (n = 2) and solution properties in Figure 2 are indicated by vertical grey dashed lines corresponding to 100 rpm and 6000 rpm. The polarization measurements are characterized by an ORR activation-controlled region from OCP to approximately -0.1 V_{SCE} followed by mass transfer-controlled ORR from -0.1 V_{SCE} to -0.7 V_{SCE} and finally HER below -0.7 V_{SCE}. Overall, the experimentally measured i_{lim} for ORR matched, on average, within 15% of predicted behavior for rotation speeds above 100 rpm.

3.2.2 Stainless Steel 304L

Cathodic polarization curves as a function of rotation speed for SS304L are presented in Figure 4. In all cases, there is no apparent trend with rotation speed. For ORR reactions, it is expected that with increasing rotation rate an increase in i_{lim} should be seen as for Pt in Figure 3. In contrast, there is no evident potential region where activation control for solely ORR is dominant on SS304L. Furthermore, the scans are lacking a clear i_{lim} ORR region. In the case of 0.189 and 1.28 M (Figure 3 (a) and (b)), the HER reaction is dominant below -1.1 V_{SCE} as indicated by all rotations converging. In the case of 4.98 M $MgCl_2$ (Figure 3(c)), all rotation speeds converge below a potential of -0.6 V_{SCE}. At all concentrations (Figure 3), a large spread in OCP is present and it is possible localized corrosion was occurring at the surface of electrodes. An optical microscope was utilized to inspect the surface of the alloy after polarization and pitting was found after some of the scans; however, there was no trend with the number of pits or size of pits with OCP variation. The implications of this will be discussed.

3.2.3 De-aerated and buffered cathodic polarization on SS

In order to help determine the dominant cathodic reduction reaction, cathodic polarizations were performed under de-aerated conditions in which the dominant reduction reaction is HER below the hydrogen Nernst potential [41]. De-aerated cathodic polarization scans were performed at 500 rpm in 0.189 and 4.98 M $MgCl_2$ and are seen in Figure 5 (a) and (b) respectively. The de-aerated scans are characterized by a depression of OCP in comparison to the aerated solution. In both de-aerated solutions, there is no sign of ilim for ORR. The OCP's of both solutions are within 37 mV of the HER Nernst potential indicative of HER being dominant for the majority of the cathodic polarization. It is noted that in 4.98 M $MgCl_2$ (Figure 5(b)), the aerated and de-aerated cathodic reductions follow similar behavior. Quiescent polarization in 4.98 M $MgCl_2$ buffered to pH 4 (0.022 M sodium acetate and 0.078 M acetic acid) is also shown in Figure 5(b). The curve is characterized by a similar OCP to de-aerated conditions; however, a higher current density is seen at most potentials during the cathodic polarization.

3.2.4 Cathodic polarization with CO_2 scrubbed air

Further tests were carried out under lab air which contained a concentration of CO_2 less than 1 ppm to help determine the effects of atmospheric variables on the cathodic polarization of Pt and SS304L. Similar cathodic behavior, specifically in the HER dominant region, was exhibited between aerated and CO_2 scrubbed air conditions on Pt and SS304L seen in Figure 6(a) and (b) respectively.

3.3 Characterization of Mg Precipitates after polarization

As seen in Figure 7(a), a white, opaque film was present on the surface of SS304L after cathodic polarization and removal from solution. The XRD pattern of the film after a polarization scan is shown in Figure 7(b) for 1.28 M and 4.98 M $MgCl_2$. In 1.28 M $MgCl_2$, the film was determined to be $Mg(OH)_2$ while in 4.98 M $MgCl_2$ the only species detectable was determined to be $MgCl_2 \cdot 6H_2O$ based on the reference peaks in Figure 7(c) [42]. Any other peaks (e.g. the two prominent peaks between 40° and 45° 2θ) were due to SS304L. The films were wicked with a Kimwipe; however, it is likely that any film on the surface still contained $MgCl_2 \cdot 6H_2O$. This experiment was replicated, and the results were confirmed. When performing analysis on the films formed in saturated conditions, it was evident that $MgCl_2 \cdot 6H_2O$ was present in the samples and is most likely responsible for the XRD pattern (Figure 7(b)), as the film deliquesced over time and could have reacted with the environment while drying.

3.4 XRD of precipitates formed after NaOH titration in $MgCl_2$ solutions

A series of NaOH titrations in $MgCl_2$ brines were carried out to further understand precipitate formation during cathodic polarization. NaOH was used to simulate hydroxyl production at the cathode during polarization. A gel-like, white precipitate instantaneously formed when drops of 3M NaOH were added to each of the solutions. Figure 8 shows XRD spectra of the precipitates after vacuum filtering and exposure to lab air (<20% RH) for 72 hours. $Mg(OH)_2$ was present at low $MgCl_2$ concentrations and $Mg_2(OH)_3Cl \cdot 4H_2O$ was present at high concentrations as seen in Figure 8. No carbonates were detected.

4. Discussion

The experimental results are combined with thermodynamic analyses in this section to show that the formation of a Mg-hydroxide or hydroxychloride precipitates suppress ORR, while simultaneously promoting HER by buffering the pH. This effect becomes more apparent with higher Mg^{2+} concentrations wherein HER dominates the cathodic kinetics in saturated $MgCl_2$ solutions. The following discussion details the rationale behind this conclusion and addresses critical implications it may have on localized corrosion and SCC.

To orient the reader, the discussion is summarized as follows: First, the expected pH at the cathode surface as a function of cathodic current density and solution boundary layer thickness is estimated. The thermodynamic stability and formation kinetics of Mg-precipitates are then discussed in terms of $MgCl_2$ solution pH and concentration. Next, the relationship between the cathode surface pH and precipitation of Mg phases is discussed in the context of to its influence on HER and ORR; providing an explanation for the observed suppression of ORR and promotion of HER on SS. Finally, implications for localized atmospheric corrosion and stress corrosion cracking (SCC) are explored.

4.1 Surface pH of cathode

The cathodic current density measured during polarization can be used calculate the pH on the surface of an alloy [43–52]. The results of surface pH calculation have been confirmed in experimentation by Albery et al. in sodium perchlorate solutions [52] such as

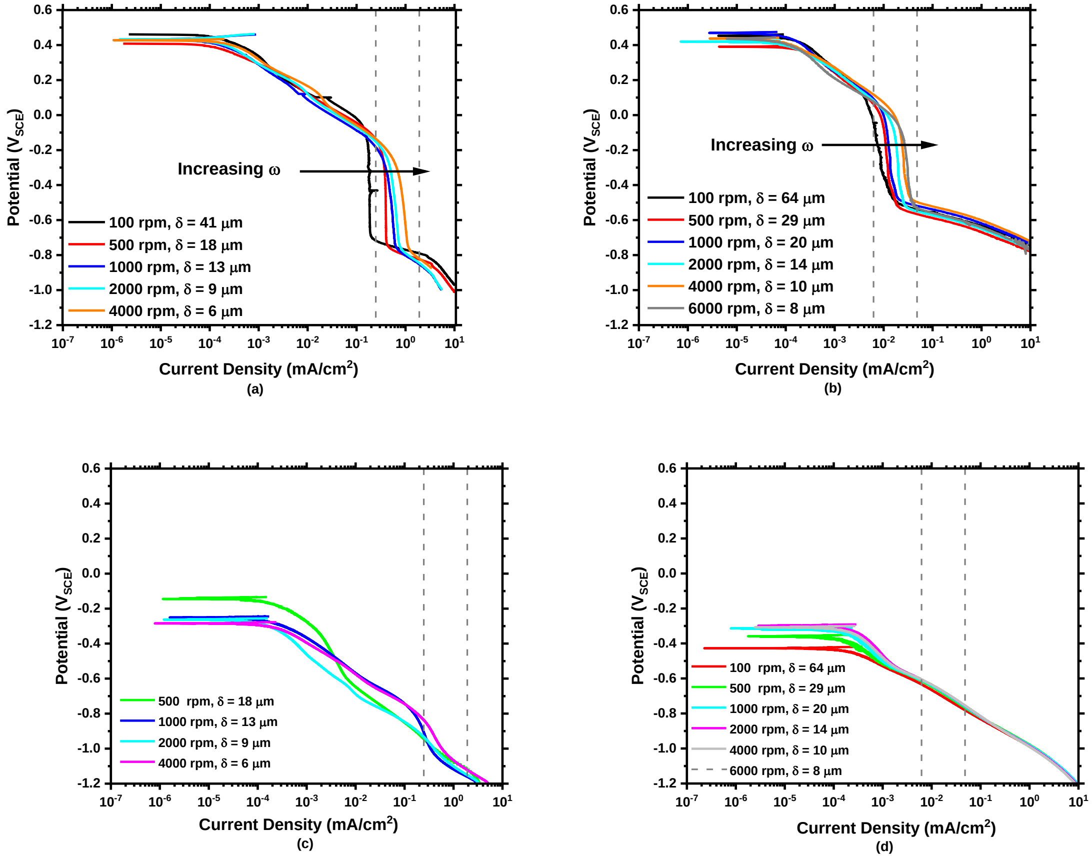

Figure 19, is the current for ORR and/or HER which in turn is the current for OH^{-} production. That is,

$$i_{ORR,HER} = -i_{OH^-} \qquad \text{Eqn. 9}$$

Equation 9 is further combined with Equation 1 and can be solved for the surface concentration of OH^{-} when the reaction is diffusion controlled, thus, the surface pH as a function of the current density for ORR or HER is given in the form of Equation 10:

$$C_{OH^-,surf} = \frac{i_{ORR,HER}\delta}{nFD_{OH^-}} + C_{OH^-,bulk} \qquad \text{Eqn. 10}$$

Surface pH calculations using Equation 10 are seen in Figure 9 for 0.189 M and 4.98 M $MgCl_2$ with the following parameters: $\delta_{0\ 189\ M} = 20\ \mu m$, $\delta_{4.98\ M} = 19\ \mu m$, $D_{OH^-,0.189M} = 4.5 \cdot 10^{-5}\ cm^2/sec$, $D_{OH^-,4.98M} = 7.1 \cdot 10^{-6}\ cm^2/sec$, $n = 1$, and $C_{OH^-,bulk} = 10^{-8}$ $(pH = 6)$ for 0.189 M and $C_{OH^-,bulk} = 10^{-9.5}$ $(pH = 4.5)$ for 4.98 M $MgCl_2$. It is noted that the rotation rates corresponding the δ are different for each solution. The diffusivities were obtained from OLI Studio Analyzer 10 (OLI Systems, Inc., Cedar Knolls, NJ) under bulk conditions at 25˚C. These diffusivities served as an upper bound for surface pH calculations as a concentration gradient of OH^{-} was not considered. Also seen in Figure 9 is i_{lim} corresponding to a boundary layer thickness of 19 or 20 µm calculated using Equation 3.

Examining Figure 9, at low current densities, the pH is close to the bulk pH which is assumed to be 4.5 for 4.98 M 6 for 0.189 M $MgCl_2$. At increased current densities, the surface pH can reach as high as ~12 at a current density of 10 mA/cm^2 in the absence of a buffer or a precipitation reaction. It is critical to point out that the conditions in Figure 9 are for solution chemistries, such as NaCl, that do not buffer pH. If a pH buffer were present in solution, the near surface pH would remain constant once a certain current density is exceeded. Furthermore, if precipitation occurs, the transport of OH^{-} and O_2 are going to be influenced by the precipitates and Equation 10 would no longer be valid. In this case, the Mg^{2+} ions contain a lower diffusivity ($1.3 \cdot 10^{-6}\ cm^2/sec$ at 4.98 M and $6.6 \cdot 10^{-6}\ cm^2/sec$ at 0.189 M (OLI)) than OH$^{-,}$ thus it is likely the buffering reaction is occurring in the diffusion boundary layer and causing a change in pH in the near surface environment. In the next section, it will be shown how precipitation of magnesium hydroxide-bearing phases will buffer the pH and it is possible that the diffusion-limiting current density will not be reached before the buffering reaction occurs.

4.2 pH stability of $MgCl_2$ brines

A speciation diagram for the $MgCl_2$-CO_2-O_2-H_2O system, calculated using the thermodynamic solubility and speciation program EQ3/6 and the Pitzer database, is presented in Figure 10. Note the pH required for Mg-phase precipitation decreases with increasing $MgCl_2$ concentration. The diagram spans the pH range predicted to be possible on the surface (as presented in Figure 9). It is noted that based on thermodynamic calculations, any $Mg(OH)_2$ formed may be metastable and back-react with the $MgCl_2$ brine. If sufficient amounts $MgCl_2$ are present, precipitates can form as amorphous or crystalline Mg-hydroxychloride.

After cathodic polarization (Figure 7) and titration experiments (Figure 8) it was shown that in low $MgCl_2$ concentrations (≤1.28 M $MgCl_2$), $Mg(OH)_2$ is the observed phase and in high $MgCl_2$ concentrations (>3.3 M $MgCl_2$), $Mg_2(OH)_3Cl \cdot 4H_2O$ is observed. Although carbonate phases were not detected in precipitates formed from $MgCl_2$ solutions at short time periods, thermodynamic predictions in Figure 10 indicate that $MgCO_3$ is thermodynamically favored to form over the entire concentration range. When carbonate precipitation is suppressed, the observed phases are indeed predicted, indicating that carbonate phases are likely kinetically inhibited over the time scale of the cathodic polarization experiments. This allows the near surface pH to rise to higher values prior to being buffered by hydroxide precipitation.

The kinetics of formation for $MgCO_3$ and $Mg_5(CO_3)_4(OH)_2 \cdot 4H_2O$ have been shown to be remarkably slow when formed from MgO [53,54] and $Mg(OH)_2$ [55,56] at room temperature and various partial pressures of CO_2 (ranging from $1 \times 10^{-3.5}$ atm to 1 atm). Furthermore, when precipitation was performed directly from a mixture of 10 mM $NaHCO_3$ and 10 mM $MgCl_2 \cdot 6H_2O$ (containing a saturation index (SI) = 1.45 and pH = 8.2), precipitates were not seen for 60 days, however, after 60 days, were determined to be $MgCO_3$ [57]. It has also been noted that the growth rate of $MgCO_3$ is dependent upon the SI [58,59] and at room temperatures and a pH of 8 the growth rate would be 4.1 x 10^{-18} mol/cm^2/s [59].

The NaOH-$MgCl_2$-H_2O-CO_2-O_2 system has not been explored at high pH and short time periods, to the knowledge of the authors and the results (Figure 8) are indicative that non-carbonate phases are kinetically favored in the presence of CO_2. Thermodynamic modeling indicates that in the 0.189 M $MgCl_2$ system, at a pH of 8.01, $MgCO_3$ is supersaturated (SI = 1.57). Precipitation is possible at this given SI [57] but the growth rate is too low [59] to observe appreciable $MgCO_3$ growth before a stability region is reached for $Mg(OH)_2$. Thus, $Mg(OH)_2$ will likely be observed instead of $MgCO_3$. This result is similar to $Mg(OH)_2$ identified primarily in film evolution of Mg alloys through Raman analyses with the presence of CO_2 [60, 61]. Furthermore, it has recently been suggested that hydroxide bearing phases primarily form and later combine to form a carbonate species [62]. Christ and Hostetler have attributed the sluggish kinetics of carbonate species formation to the strong hydration energy of the Mg^{2+} ion [53]. Qafoku *et al*. has further demonstrated that $MgCO_3$ forms from hydrated solids in solution, typically hydromagnesite or nesquehonite [55], and it has been suggested that $Mg(OH)_2$ forms as a precursor to these hydrated states [63]. Thus, it is believed that due to the highly hydrated nature of Mg^{2+} ions, the highly anhydrous $MgCO_3$ is not kinetically favored. Finally, in long-term coupon exposure testing (from 2 days to 1 year) in natural atmospheric $MgCl_2$ environments (ranging in temperatures from 20˚C to 50˚C and RH's from 50%-99%), carbonate-containing Mg species were shown on various alloys [13,62,64–71]. Thus, when considering corrosion surface evolution, it is critical to account of $Mg(OH)_2$ precipitation and any further back reactions or conversions that may occur.

Non-carbonate phases ($Mg(OH)_2$ or $Mg_2(OH)_3Cl \cdot 4H_2O$) are present on the surface of the alloy after cathodic polarization and have been shown to be kinetically favored. It is therefore important to identify the current density and overpotential in which these phases are possible during cathodic polarization. In Figure 9, a pH required for precipitation occurs at a current density lower than i_{lim}. Thus, as more OH^- is produced on the surface from ORR or HER, the pH of the solution will be buffered by the Mg species in solution before i_{lim} is reached. The minimum current densities corresponding to precipitation are $1.2 \cdot 10^{-2}\ mA/cm^2$ and $2.46 \cdot 10^{-4}\ mA/cm^2$ for 0.189 (Figure 4(a)) and 4.98 M $MgCl_2$ (Figure 4(c)) respectively, spanning over 2 orders of magnitude. These current densities correspond to potentials of -0.67 V_{SCE} and -0.39 V_{SCE} for 0.189 M and 4.98 M $MgCl_2$ respectively seen in Figure 4(overpotentials of 0.53 V and 0.10 V respectively). *In-situ* Raman has been performed on polarizations of SS304L in 0.189 M $MgCl_2$, and although the boundary layer is different, $Mg(OH)_2$ was observed at a current density of $2.02 \cdot 10^{-2}\ mA/cm^2$ and a potential of -0.841 V_{SCE} [61]. Overall, precipitation in saturated solutions practically occurs at OCP (0.10 V overpotential) and buffers the near surface pH almost immediately. Upon further polarization below the potential corresponding to precipitation, the near surface pH will be buffered at the equilibrium pH.

4.3 Effects of near surface pH

The pH buffering effect of Mg-hydroxide precipitation will shift the HER reversible potential and in turn the overpotential for HER at a given current density. The Nernst potential dependence of HER at 25 °C is given by,

$$E_{HER} = E_{HER}^{o} - m * pH \qquad \text{Eqn. 11}$$

assuming that $[H_2] = p_{H_2} = 1$ [41]. Under standard conditions, $E_{HER}^{o} = 0\ V_{SHE}\ (-0.244\ V_{SCE})$ and $m = -0.059\ V$. Based on Equation 11, with increased pH at the electrode surface the Nernst potential would decrease. If one were to consider a constant OCP, the overpotential for HER would also increase. That is, to reach the same current density with a higher pH, a more negative potential must be reached.

Trends in measured cathodic potential as a function of solution concentration show evidence of pH buffering of the precipitation of a hydroxide-containing phase on the HER reversible potential (Figure 11). Figure 11(a) shows decreasing average cathodic potentials measured at 1 mA/cm^2 as a function of $MgCl_2$ concentration. 1 mA/cm^2 corresponds to a region dominated by HER (Figures 3,4). Also shown on this plot is the buffer pH corresponding to each solution concentration, assuming precipitation of $Mg(OH)_2$ or $Mg_2(OH)_3Cl \cdot 4H_2O$ is the buffering reaction. Linear fits to potential as function of buffer pH (i.e., pH expected for precipitation) give slopes within 12 mV/pH of the -59 mV/pH given in Equation 11. As the fitted slopes are close to that of the expected

Nernst potential, this further supports that near surface pH is buffered by $Mg(OH)_2$ or $Mg_2(OH)_3Cl \cdot 4H_2O$ precipitation. In contrast, NaCl solutions do not form a stable precipitate within the considered pH range. The overpotential for HER is expected to slightly decrease due to an increase in surface pH (due to a lower diffusivity of OH^-). The potentials at 1 mA/cm^2 are presented for NaCl in Figure 11(b) and were obtained from Alexander et al. [4]. Overall, the potentials are independent of concentration and are lower than the potentials of $MgCl_2$ solutions as expected. Finally, the overpotential for HER ($\eta = E_o - E_{1\ mA/cm^2}$) where E_o is calculated with Equation 11 at the precipitation pH in Figure 10 , is independent of $MgCl_2$ concentration (Figure 11(c)). This is further evidence to support the buffering effect of Mg-precipitation in solution.

To further show the influence of $MgCl_2$ concentration on HER, de-aerated cathodic polarization scans were performed on SS304L in 0.189 M and 4.98 M $MgCl_2$, (Figure 5(a) and (b) respectively). Under de-aerated conditions, the prominent cathodic reaction is HER (Figure 5). It is noted that under $MgCl_2$-saturated conditions in Figure 5(b), the aerated and de-aerated polarization curves are nearly identical, indicating the prominent reaction in both conditions is HER as indicated by the Nernst potential for HER. Furthermore, this indicates that the ORR is suppressed in 4.98 M $MgCl_2$. In 0.189 M $MgCl_2$ (Figure 5(a)), the polarization scan is indicative of the cathodic reaction being under mixed HER and ORR. As both the overpotential and current density (Figure 9) required for Mg-species precipitation are much lower in saturated conditions, it is not surprising that saturated $MgCl_2$ solutions are under HER for almost the entirety of the cathodic scan. In the acetate buffer (pH = 4), HER is further enhanced due to the decrease in pH (increase in proton concentration). This contrasts with solely Mg^{2+} ions, in which precipitates buffer the near surface pH to 7.4. Although the buffered pH is different, the overpotential remains constant (Figure 11(c)). Not only is there a pH dependence on HER, there has also been recent work indicating that ORR proceeds via 2-electron transfer in near neutral solutions [72, 73]. Additionally, it is commonly accepted that in the presence of oxide or hydroxide precipitates, ORR occurs via a 2-electron transfer mechanism [74-77]. It is possible that $Mg(OH)_2$ would have the same effect on both platinum and SS304L; however, further research is necessary. Thus, platinum following 2-electron transfer as predicted from Equation 3 is further indication of a solution buffer from precipitation of hydroxide-containing species. Finally, non-carbonate (hydroxide containing) phases were determined to be kinetically favored in $MgCl_2$ solutions. Irrespective of dissolved CO_2 in solution, the HER region of polarization scans should be the same. As seen in Figure 6, the polarization scans had nearly identical behavior. Thus, evidence is provided for the overpotential of HER being governed by the buffering of the pH by precipitation of $Mg(OH)_2$ or $Mg_2(OH)_3Cl \cdot 4H_2O$.

The precipitation of Mg has been shown to have a clear effect on HER, however precipitates can also impact ORR, including differences in: (i) diffusivity, (ii) diffusion distance, and (iii) concentration of oxidizing species. First, a precipitate, whether on the surface or in the boundary layer, introduces another medium in which the oxidizing species must diffuse through. This likely introduces slower diffusion through the boundary layer suppressing ORR kinetics. Second, introducing a film on the surface could increase the diffusion distance of the oxidizing species. Assuming Fickian diffusion still holds, the hydrodynamic boundary layer in Equation 1 becomes $\delta = \delta_{film} + \delta_{natural}$, increasing the diffusion distance for oxygen, and decreasing i_{lim} [13]. Alternatively, the film could increase surface roughness and drastically change the properties the diffusion boundary layer. However, the current density which a precipitate could form is before i_{lim} and predicated behavior for diffusion limitations are seen on platinum. Thus, increased surface roughness is not believed to have a significant influence. Finally, the electrode surface concentration of oxygen could decrease if diffusion through the precipitate was rate-limiting. That is, the concentration of oxidizing species would no longer be the concentration in the bulk solution, rather it would become the concentration at the precipitate/electrode interface. This concentration is reduced from the bulk solution as this interface will be inside the hydrodynamic boundary layer set by the rotation speed. Additionally, $Mg(OH)_2$ is generally weakly adherent to substrate surfaces [78], potentially resulting in a random distribution either on the surface or in the hydrodynamic boundary layer. This random distribution could be the cause for the stochastic ORR behavior displayed by the cathodic polarization scans on SS304L (Figure 4), and for the discrepancy in measured and theoretical i_{lim} for platinum (Figure 3). In all cases, precipitation would suppress ORR.

4.4 Summary of Mg^{2+} cation effects on cathodic kinetics

The hypothetical Evans diagram, seen in Figure 12, summarizes the effects of Mg-precipitation influencing the dominance of HER during cathodic polarization. The unusual cathodic polarization behavior of SS304L is attributed to a decrease in overpotential for HER, suppression of ORR, and stochastic active corrosion driving down OCP. Figure 12 depicts the influences from the following half-cell reactions: ORR, HER, and metal oxidation on the overall cathodic behavior. Each reaction has a corresponding Nernst potential (E_O) and exchange current density (i_o): $E_{O,HER}$, $i_{O,HER}$, $E_{O,ORR}$, $i_{O,HER}$, $E_{O,M}$, $i_{O,HER}$ where "M" denotes anodic metal oxidation reaction. Overall the major contributors to measured cathodic kinetics are the cathodic shifts of $E_{O,M}$ and $E_{O,ORR}$ and anodic shift of $E_{O,HER}$ with increasing $MgCl_2$ concentration.

Influences from the Nernst potential of each respective half reactions are depicted in Figure 12 with a typical Evans diagram without precipitation shown in Figure 12(a). First, localized corrosion is also characterized by decrease in $E_{O,M}$ [79,80] when the bare metal alloy is exposed below a passive film. Pitting is more likely to occur at elevated chloride concentrations along with localized corrosion seen on the surface of the alloy. Therefore $E_{O,M}$ will decrease with increasing $MgCl_2$ concentration as is shown in Figure 12(b) and is denoted by $E_{O,M,active}$. Second, as previously discussed $E_{O,ORR}$ is likely to be suppressed through precipitate formation and decreases in Figure 12(c). Finally, $E_{O,HER}$ is shown to increase with increasing Mg^{2+} concentration. It is known that $E_{O,HER}$ will increase with a decrease in pH as given by Equation 11 [41]. Thus, as the pH for Mg-precipitation increases with decreasing chloride concentration, $E_{O,HER}$ will increase as displayed in Figure 12(d). All three of these fluctuations are summarized in Figure 12(e) with the transition to higher concentrations of $MgCl_2$ being denoted by dashed lines. ORR and metal dissolution have shifted the respective Nernst potential in the negative direction whereas HER has shifted in the positive direction with increasing chloride concentration.

In the Evans diagram in Figure 12(e), there are no depicted fluctuations of i_o. In terms of $i_{O,ORR}$, there is little information about trends associated with chloride concentration. The value of $i_{O,ORR}$ is often convoluted with $i_{O,M}$ and is manifested as i_{corr} or the open circuit corrosion current density. It is known that i_O is dependent upon the binding energy of a species on the surface, among other factors, and it is not expected that binding energy is going to be significantly changed by the solutions present in the study [81]. Also, a t-test for statistical significance for i_{corr} in Figure 4 shows no significant difference (at an alpha of 0.05) across all rotation speeds and concentrations studied on SS304L. Finally, during HER it is also well known that an increase in pH will decrease $i_{O,HER}$ [82]. However, the change in $i_{O,HER}$ over the range of possible surface pH's in this study is less than half an order of magnitude in current density and any manifestation in an Evan's diagram will be minimal. Thus, i_o will not play a major role in the abnormal cathodic behavior of SS304L.

Regarding the differences between SS304L and Pt, lower catalytic activity is seen in most other alloys besides Pt [83]. These alloys are oxidized more readily than Pt [81] and as such, Pt will have a higher $E_{O,ORR}$ thus a much greater overpotential for HER at the same current density. Therefore, i_{lim} for ORR will be seen on Pt and not on SS304L.

Overall the major contributors to measured cathodic kinetics are the depression of $E_{O,M}$ and $E_{O,ORR}$ and increase $E_{O,HER}$ with increasing $MgCl_2$ concentration as displayed in Figure 12(e). Finally, the thermodynamically stable formation of $Mg(OH)_2$ and $Mg_2(OH)_3Cl \cdot 4H_2O$ occurs at a current density below $i_{lim,ORR}$. Thus, transient behavior before ORR due to influences from pH fluctuations is not surprising and helps explain transient behavior in dilute $MgCl_2$ solutions. In saturated $MgCl_2$, HER is the main cathodic reaction and there are minimal transient behaviors.

5. Implications

5.1 Mg-precipitation solution effects on available cathodic current

During polarization of SS304L, it has been shown that precipitation of insoluble corrosion byproducts in $MgCl_2$ solutions causes ORR suppression. It has also been shown in Figure 9 that the amount of current density required to obtain a surface pH for precipitation is minimal, thus, it is highly likely these various species will be seen on the surface of the alloy during exposure. Phenomena that can occur as a result of exposure to $MgCl_2$ environments in the cathode include (i) decreased cathode efficiency, (ii) brine dry up (decreasing WL thickness), (iii) physical blocking of cathodic reduction sites, and (iv) decreased conductivity due to solid precipitates.

First, the suppression of ORR will reduce the overall current a cathode can supply, which will reduce the extent of pitting corrosion on the surface of a susceptible alloy. For example, when ORR is suppressed, the current at any given potential is going to be smaller and provide lower currents to support dissolution. This has been mathematically described by multiple authors [84–86], however, these models assume that the surface has not been influenced pitting corrosion and it would not be appropriate to directly apply these polarization scans to such models. Next, as discussed by Bryan and Schindelholz [1], when reactions in Table 1 go to completion, the highly deliquescent $MgCl_2$ is replaced with a non-deliquescent solid and the brine dry out can occur. In the severe case, if complete dry out is achieved, corrosion will cease. However, during thinning, it is possible that oxygen diffusion ceases to be the limiting process for ORR, enhancing the oxygen supply for cathodic reduction. Offsetting this, as the brine layer decreases, ohmic drop in solution is increased, further decreasing the cathodic supply for anodic dissolution and decreasing corrosion severity. Third, the physical cathodic sites can be blocked by precipitates [87,88]. When reduction sites are blocked, the current that can be supplied by the cathode will decrease [88]. Having fewer cathodic sites will yield a decreased total cathodic current to support anodic dissolution. Finally, when solid products, such as an insoluble hydroxide or carbonate form, the effective conductivity of the electrolyte layer will decrease as described by Bruggeman [89] and Garnett [90]. A decrease in conductivity will increase solution resistivity and lead to enhanced ohmic drop surrounding a localized corrosion site. In all cases, ORR suppression and precipitation in the cathode with decrease the cathodic current supply and will therefore decrease supply to anodic reactions in localized corrosion sites. These phenomena can be taken into account mathematically by utilizing the Chen and Kelly model who developed an expression for the maximum cathodic current available in atmospheric conditions [82]. It is evident that both a decrease in conductivity and water layer thickness will decrease available cathodic current and decrease maximum attainable pit sizes. Although easy to qualitatively address these phenomena, a full quantitative analysis is outside the scope of this paper. Thus, in order to have accurate representation of atmospheric corrosion, precipitation reactions are an important phenomenon to be considered.

5.2 Potential Effects of $MgCl_2$ solutions on SCC Processes

Our finding that HER is the predominant cathodic reaction in concentrated $MgCl_2$ solutions provides a possible alternative for enhanced cracking of stainless steels in $MgCl_2$ solutions and seawater at low RH. Long term exposures in a low RH seawater solution ($MgCl_2$ rich brine) has shown the presence micro-cracks in comparison to high RH seawater solutions (NaCl rich brine, dilute $MgCl_2$) where no micro-cracks were observed [91]. It was proposed that a possible mechanism for micro-cracking associated with pits via hydrogen environmentally assisted cracking (HEAC) due to the formation of stress-induced martensite. Thus, HER acting as the main cathodic reaction in $MgCl_2$ could lead to an increase HEAC in $MgCl_2$ dominant exposure environments, however, further measurements are needed in order to confirm the hypothesis. Such measurements could be made with scanning electrochemical microscopy (SECM) [92].

6. Conclusions

This study examined cathodic kinetics on Pt and SS304L in $MgCl_2$ solutions at 25˚C. It has been demonstrated that cathodic reduction reactions on SS304L are a mix between ORR and HER becoming dominated by HER in saturated solutions. The work also provided a determination of $MgCl_2$ solution properties and the creation of a stability diagram for Mg-containing solutions. It was determined that enhanced HER was caused by a suppression of ORR and a buffering effect of the Mg-precipitation in the near surface solution via the formation of $Mg(OH)_2$ or $Mg_2(OH)_3Cl \cdot 4H_2O$. Non-carbonate phases were determined to be kinetically favored by studying the NaOH-$MgCl_2$-H_2O-CO_2-O_2 system. When the pH is buffered, the near surface pH remains constant, and decreases the overpotential for HER. HER was also determined to be the primary reaction in saturated $MgCl_2$ solutions. This unique phenomenon has the possibility to decrease the severity of pitting corrosion due to ORR suppression, decreased conductivity, and brine dry up. An increase in SCC via HEAC is a possible concern as hydrogen will be readily available on the cathode surface near localized corrosion sites in $MgCl_2$ solutions.

Acknowledgements

Sandia National Laboratories is a multi-mission laboratory managed and operated by National Technology and Engineering Solutions of Sandia, LLC., a wholly owned subsidiary of Honeywell

International, Inc., for the U.S. Department of Energy's National Nuclear Security Administration under contract DE-NA0003525. Conversions with Dr. David Enos from Sandia National Laboratories is acknowledged and gratefully appreciated. This document is SAND2020-9036 J.

Data Availability

The raw/processed data required to reproduce these findings cannot be shared at this time as the data also forms part of an ongoing study.

References

[1] C.R. Bryan, E.J. Schindelholz, Properties of brines formed by deliquescence of sea salt aerosols, in: Corros. 2018, Phoenix, 2018: p. Paper 10516.

[2] E. Schindelholz, R.G. Kelly, Wetting phenomena and time of wetness in atmospheric corrosion: a review, Corros. Rev. 30 (2012) 135–170. https://doi.org/10.1515/corrrev-2012-0015.

[3] Z. Szklarska-Smialowska, Pitting and Crevice Corrosion, NACE International, Houston, TX, 2005.

[4] C.L. Alexander, C. Liu, A. Alshanoon, R.M. Katona, R.G. Kelly, J. Carpenter, C. Bryan, E. Schindelholz, Oxygen reduction on stainless steel in concentrated chloride media, J. Electrochem. Soc. 165 (2018) C869–C877. https://doi.org/10.1149/2.0181813jes.

[5] S.L.J. Gojković, S.K. Zečević, M.D. Obradović, D.M. Dražić, Oxygen reduction on a duplex stainless steel, Corros. Sci. 40 (1998) 849–860. https://doi.org/10.1016/S0010-938X(98)00004-3.

[6] H.S. Klapper, J. Goellner, Electrochemical noise from oxygen reduction on stainless steel surfaces, Corros. Sci. 51 (2009) 144–150. https://doi.org/10.1016/j.corsci.2008.10.009.

[7] M. Okuyama, S. Haruyama, The cathodic reduction of oxygen on stainless steels in a neutral solution, Corros. Sci. 31 (1990) 521–526. https://doi.org/10.1016/0010-938X(90)90156-Y.

[8] R. Babić, M. Metikoš-Huković, Oxygen reduction on stainless steel, J. Appl. Electrochem. 23 (1993) 352–357. https://doi.org/10.1007/BF00296691.

[9] N. Le Bozec, C. Compère, M. L'Her, A. Laouenan, D. Costa, P. Marcus, Influence of stainless steel surface treatment on the oxygen reduction reaction in seawater, Corros. Sci. 43 (2001) 765–786. https://doi.org/10.1016/S0010-938X(00)00113-X.

[10] V.G. Levich, No Title, Acta Physicochim. Urss. 17 (1942) 257.

[11] S.D. Kapusta, Oxygen reduction on stainless steels in aerated brines, in: Corros. 2004, 2004: pp. 1–18.

[12] C. Liu, J. Srinivasan, R.G. Kelly, Electrolyte film thickness effects on the cathodic current availability in a galvanic couple, J. Electrochem. Soc. 164 (2017) C845–C855. https://doi.org/10.1149/2.1641713jes.

[13] C. Liu, V.A. Yang, R.G. Kelly, Inhibition of Cathodic Kinetics by Zn2+ and Mg2+ on AA7050-T7451, J. Electrochem. Soc. 166 (2019) C134–C146. https://doi.org/10.1149/2.0551906jes.

[14] C. Liu, P. Khullar, R.G. Kelly, Acceleration of the Cathodic Kinetics on Aluminum Alloys by Aluminum Ions, J. Electrochem. Soc. 166 (2019) C153–C161. https://doi.org/10.1149/2.0571906jes.

[15] V.L. Thurmond, R.W. Potter, The densities of saturated solutions of NaCl and KCl from 10C to 105C, 1984. https://doi.org/10.3133/ofr84253.

[16] L.S. Clesceri, A.E. Greenberg, A.D. Eaton, Standard Methods for the examination of water and wastewater, Washington DC, 1998.

[17] J.H. Carpenter, The Chesapeake Bay Institute technique for the Winkler dissolved oxygen method, Limnol. Oceanogr. 10 (1965) 141–143. https://doi.org/10.3758/BF03209628.

[18] V.G. Levich, D.B. Spalding, Physiochemical hydrodynamics, Advance Publications, London, 1977.

[19] D.-T. Chin, M. Litt, An electrochemical study of flow instability on a rotating disk, J. Fluid Mech. 54 (1972) 613–625. https://doi.org/10.1017/S0022112072000904.

[20] Z. Galus, R.N. Adams, The investigation of the kinetics of moderatley rapid electrode reactions using rotating disk electrodes, J. Phys. Chem. 67 (1963) 866–871. https://doi.org/10.1021/j100798a036.

[21] C.M. Mohr, J. Newman, Mass Transfer to a Rotating Disk in Transition Flow, J. Electrochem. Soc. 123 (2006) 1687. https://doi.org/10.1149/1.2132668.

[22] L. Stappers, J. Fransaer, The Effect of Turbulence on the Electrodeposition of Composite Coatings, J. Electrochem. Soc. 152 (2006) C392–C398. https://doi.org/10.1149/1.1914745.

[23] T.J. Wolery, R.L. Jarek, Software User's Manual: EQ3/6 Version 8.0, Sandia National Laboratories, Albuquerque, NM, 2003.

[24] In-Drift Precipitates/Salts Model, Sandia National Laboratories, Albuquerque, NM, 2007.

[25] K.S. Pitzer, Thermodynamics of electrolytes. I. Theoretical basis and general equations, J. Phys. Chem. 77 (1973) 268–277. https://doi.org/10.1021/j100621a026.

[26] M. Altmaier, V. Metz, V. Neck, R. Müller, T. Fanghänel, Solid-liquid equilibria of Mg(OH)2(cr) and Mg2(OH)3Cl·4H2O(cr) in the system Mg-Na-H-OH-Cl-H2O at 25°C, Geochim. Cosmochim. Acta. 67 (2003) 3595–3601. https://doi.org/10.1016/S0016-7037(03)00165-0.

[27] R.T. Pabalan, K.S. Pitzer, Thermodynamics of concentrated electrolyte mixtures and the prediction of mineral solubilities to high temperatures for mixtures in the system Na-K-Mg-Cl-SO4-OH-H2O, Geochim. Cosmochim. Acta. 51 (1987) 2429–2443. https://doi.org/10.1016/0016-7037(87)90295-X.

[28] J.W. Johnson, E.H. Oelkers, H.C. Helgeson, SUPCRT92: A software package for calculating the standard molal thermodynamic properties of minerals, gases, aqueous species, and reactions from 1 to 5000 bar and 0 to 1000°C, Comput. Geosci. 18 (1992) 899–947. https://doi.org/10.1016/0098-3004(92)90029-Q.

[29] S. Phang, R.H. Stokes, Density, viscosity, conductance, and transference number of concentrated aqueous magnesium chloride at 25°C, J. Solution Chem. 9 (1980) 497–505. https://doi.org/10.1007/BF00647738.

[30] T. Isono, Density, viscosity, and electrolytic conductivity of concentrated aqueous electrolyte solutions at several temperatures. Alkaline-earth chlorides, lanthanum chloride, sodium chloride, sodium nitrate, sodium bromide, potassium nitrate, potassium bromide, a, J. Chem. Eng. Data. 29 (1984) 45–52. https://doi.org/10.1021/je00035a016.

[31] H. Ikeuchi, M. Hayafuji, Y. Aketagawa, J. Taki, G.P. Satô, Diffusion coefficients of dioxygen in aqueous electrolyte solutions, J. Electroanal. Chem. 396 (1995) 553–556. https://doi.org/10.1016/0022-0728(95)04011-C.

[32] C.G. MacArthur, Solubility of Oxygen in Salt Solutions and the Hydrates of These Salts, J. Phys. Chem. 20 (1916) 495–502. https://doi.org/10.1021/j150168a003.

[33] F.J. Millero, F. Huang, A.L. Laferiere, The solubility of oxygen in the major sea salts and their mixtures at 25°C, Geochim. Cosmochim. Acta. 66 (2002) 2349–2359. https://doi.org/10.1016/S0016-7037(02)00838-4.

[34] L. Korson, W. Drost-Hansen, F.J. Millero, Viscosity of water at various temperatures, J. Phys. Chem. 73 (1969) 34–39. https://doi.org/10.1021/j100721a006.

[35] B. Case, The diffusivity of oxygen in dilute alkaline solution from 0° to 65°C, Electrochim. Acta. 18 (1973) 292–299. https://doi.org/10.1016/0013-4686(73)80031-3.

[36] R.F. Weiss, The solubility of nitrogen, oxygen and argon in water and seawater, Deep Sea Res. Oceanogr. Abstr. 17 (1970) 721–735. https://doi.org/10.1016/0011-7471(70)90037-9.

[37] C.N. Murray, J.P. Riley, The solubility of gases in distilled water and sea water—II. Oxygen, Deep Sea Res. Oceanogr. Abstr. 16 (1969) 311–320. https://doi.org/10.1016/0011-7471(69)90021-7.

[38] J.E. Vivian, C.J. King, Diffusivities of slightly soluble gases in water, AIChE J. 10 (1964) 220–221. https://doi.org/10.1002/aic.690100217.

[39] G.W. Hung, R.H. Dinius, Diffusivity of Oxygen in Electrolyte Solutions, J. Chem. Eng. Data. 17 (1972) 449–451. https://doi.org/10.1021/je60055a001.

[40] D.M. Himmelblau, Diffusion of dissolved gases in liquids, Chem. Rev. 64 (1964) 527–550. https://doi.org/10.1021/cr60231a002.

[41] D.A. Jones, Principles and Prevention of Corrosion, 2nd ed., Prentice Hall Inc., Upper Saddle River, NJ, 1996.

[42] B. Downs, S. Robinson, H. Yang, P. Mooney, RRUFF Project, (2015). http://rruff.info/.

[43] S.L. Wolfson, W.H. Hartt, An Initial Investigation of Calcareous Deposits upon Cathodic Steel Surfaces in Sea Water, CORROSION. 37 (1981) 70–76. https://doi.org/10.5006/1.3593848.

[44] S.C. Dexter, S.H. Lin, Calculation of Seawater pH at Polarized Metal Surfaces in the Presence of Surface Films, Corros. Sci. January (1992) 50–60. https://doi.org/10.5006/1.3315918.

[45] H.J. Engell, P. Forchhammer, On the change in the pH value of metal surfaces in cathodic protection in seawater, Corros. Sci. 5 (1965) 479–488. https://doi.org/https://doi.org/10.1016/S0010-938X(65)80053-1.

[46] W.J. Albery, Ring-disc electrodes. Part 1.—A new approach to the theory, Trans. Faraday Soc. 62 (1966) 1915–1919. https://doi.org/10.1039/TF9666201915.

[47] W.J. Albery, S. Bruckenstein, Ring-disc electrodes. Part 2.—Theoretical and experimental collection effciencies, Trans. Faraday Soc. 62 (1966) 1920–1931. https://doi.org/10.1039/TF9666201920.

[48] W.J. Albery, S. Bruckenstein, D.C. Johnson, Ring-disc electrodes. Part 4.—Diffusion layer titration curves, Trans. Faraday Soc. 62 (1966) 1938–1945. https://doi.org/10.1039/TF9666201938.

[49] W.J. Albery, M.G. Boutelle, P.J. Colby, A.R. Hillman, Ring–disc electrodes. Part 20.—A general procedure for deducing the faradaic component of a disc-current transient from a ring-current transient, J. Chem. Soc. Faraday Trans. 1 Phys. Chem. Condens. Phases. 78 (1982) 2757–2763. https://doi.org/10.1039/f19827802757.

[50] W.J. Albery, A.R. Mount, Ring–disc electrodes. Part 22.—Theory of the measurement of proton fluxes at the disc, J. Chem. Soc. Faraday Trans. 1 Phys. Chem. Condens. Phases. 85 (1989) 1181–1188. https://doi.org/10.1039/f19898501181.

[51] Z. Lewandowski, W.C. Lee, W.G. Characklis, B. Little, Dissolved Oxygen and pH Microelectrode Measurements at Water-Immersed Metal Surfaces, CORROSION. 45 (1989) 92–98. https://doi.org/10.5006/1.3577838.

[52] W.J. Albery, E.J. Calvo, Ring-Disc Electrodes Part 21: pH measurement with the ring, J. Chem. Soc. Faraday Trans. 1. 79 (1983) 2583–2596.

[53] P.. Hostetler, C.. Christ, Studies in the system MgO-SiO2-CO2-H2O(I): The activity-product constant of chrysotile, Geochim. Cosmochim. Acta. 32 (1968) 485–497. https://doi.org/10.1016/0016-7037(68)90041-0.

[54] F.L. Sayles, W.S. Fyfe, The crystallization of magnesite from aqueous solution, Geochim. Cosmochim. Acta. 37 (1973) 87–99. https://doi.org/10.1016/0016-7037(73)90246-9.

[55] O. Qafoku, D.A. Dixon, K.M. Rosso, H.T. Schaef, M.E. Bowden, B.W. Arey, A.R. Felmy, Dynamics of Magnesite Formation at Low Temperature and High pCO2 in Aqueous Solution, Environ. Sci. Technol. 49 (2015) 10736–10744. https://doi.org/10.1021/acs.est.5b02588.

[56] E.J. Swanson, K.J. Fricker, A.A. Park, Directed precipitation of hydrated and anhydrous magnesium carbonates for carbon storage, Phys. Chem. Chem. Phys. 16 (2014) 23440–23450. https://doi.org/10.1039/c4cp03491k.

[57] I.M. Power, P.A. Kenward, G.M. Dipple, M. Raudsepp, Room Temperature Magnesite Precipitation, Cryst. Growth Des. 17 (2017) 5652–5659. https://doi.org/10.1021/acs.cgd.7b00311.

[58] H.E. King, H. Satoh, K. Tsukamoto, A. Putnis, Nanoscale observations of magnesite growth in chloride- and sulfate-rich solutions, Environ. Sci. Technol. 47 (2013) 8684–8691. https://doi.org/10.1021/es401188j.

[59] G.D. Saldi, G. Jordan, J. Schott, E.H. Oelkers, Magnesite growth rates as a function of temperature and saturation state, Geochim. Cosmochim. Acta. 73 (2009) 5646–5657. https://doi.org/10.1016/j.gca.2009.06.035.

[60] A. Maltseva, V. Shkirskiy, G. Lefèvre, P. Volovitch, Effect of pH on Mg(OH)2 film evolution on corroding Mg by in situ kinetic Raman mapping (KRM), Corros. Sci. 153 (2019) 272–282. https://doi.org/10.1016/j.corsci.2019.03.024.

[61] R.M. Katona, R.G. Kelly, C.R. Bryan, R.F. Schaller, A.W. Knight, Use of in situ Raman spectroelectrochemical technique to explore atmospheric corrosion in marine-relevant environments, Electrochem. Commun. 118 (2020) 106768. https://doi.org/10.1016/j.elecom.2020.106768.

[62] M. Guo, Q. Yin, M. Liu, C. Pan, Z. Wang, Corrosion behavior of 304 stainless steel exposed to a simulated salt lake atmosphere, Acta Metall. Sin. (English Lett. 33 (2020) 857–870. https://doi.org/10.1007/s40195-020-01028-w.

[63] M. Hänchen, V. Prigiobbe, R. Baciocchi, M. Mazzotti, Precipitation in the Mg-carbonate system — effects of temperature and CO2 pressure, Chem. Eng. Sci. 63 (2008) 1012–1028. https://doi.org/10.1016/j.ces.2007.09.052.

[64] P. Volovitch, C. Allely, K. Ogle, Understanding corrosion via corrosion product characterization: I. Case study of the role of Mg alloying in Zn-Mg coating on steel, Corros. Sci. 51 (2009) 1251–1262. https://doi.org/10.1016/j.corsci.2009.03.005.

[65] N.C. Hosking, M.A. Ström, P.H. Shipway, C.D. Rudd, Corrosion resistance of zinc-magnesium coated steel, Corros. Sci. 49 (2007) 3669–3695. https://doi.org/10.1016/j.corsci.2007.03.032.

[66] R. Lindström, L.G. Johansson, G.E. Thompson, P. Skeldon, J.E. Svensson, Corrosion of magnesium in humid air, Corros. Sci. 46 (2004) 1141–1158. https://doi.org/10.1016/j.corsci.2003.09.010.

[67] S.H. Salleh, S. Thomas, J.A. Yuwono, K. Venkatesan, N. Birbilis, Enhanced hydrogen evolution on Mg(OH)2 covered Mg surfaces, Electrochim. Acta. 161 (2015) 144–152. https://doi.org/10.1016/j.electacta.2015.02.079.

[68] D.B. Blücher, J.E. Svensson, L.G. Johansson, The influence of CO2, AlCl3 · 6H2O, MgCl2 · 6H2O, Na2SO4 and NaCl on the atmospheric corrosion of aluminum, Corros. Sci. 48 (2006) 1848–1866. https://doi.org/10.1016/j.corsci.2005.05.027.

[69] C.-F. Lin, K.R. Hebert, Changes Produced by Cathodic Polarization in the Electrical Conduction Behavior of Surface Films on Aluminum, J. Electrochem. Soc. 141 (1994) 104–110. https://doi.org/10.1149/1.2054667.

[70] R. Lindström, J.-E. Svensson, L.G. Johansson, The Influence of Salt Deposits on the Atmospheric Corrosion of Zinc. The Important Role of the Sodium Ion, J. Electrochem. Soc. 149 (2002) B57–B64. https://doi.org/10.1149/1.1432670.

[71] C. Padovani, O.E. Albores-Silva, E.A. Charles, Corrosion control of stainless steels in indoor atmospheres-laboratory measurements under MgCl2 deposits at Constant Relative Humidity (Part 1), Corrosion. 71 (2015) 292–304. https://doi.org/10.5006/1437.

[72] V. Briega-Martos, E. Herrero, J.M. Feliu, Hydrogen peroxide and oxygen reduction studies on Pt stepped surfaces: Surface charge effects and mechanistic consequences, Electrochim. Acta. 334 (2020) 135452. https://doi.org/10.1016/j.electacta.2019.135452.

[73] Q. Zhang, P. Liu, Z. Zhu, J. Zhang, F. Cao, The study of the H2O2 during oxygen reduction process on typically corroding metal surface using tip generation-substrate collection mode of SECM, Corros. Sci. 164 (2020) 108312. https://doi.org/10.1016/j.corsci.2019.108312.

[74] K.G. Boto, L.F.G. Williams, Rotating disc electrode studies of zinc corrosion, J. Electroanal. Chem. 77 (1977) 1–20. https://doi.org/10.1016/S0022-0728(77)80315-X.

[75] C. Deslouis, M. Duprat, C. Tulet-Tournillon, The cathodic mass transport process during zinc corrosion in neutral aerated sodium sulphate solutions, J. Electroanal. Chem. 181 (1984) 119–136. https://doi.org/10.1016/0368-1874(84)83624-2.

[76] P. Delahay, L.J. Stagg, A Polarographic Method for the Indirect Determination of Polarization Curves for Oxygen Reduction on Various Metals, J. Electrochem. Soc. 99 (1952) 546. https://doi.org/10.1149/1.2779649.

[77] Z. Pilbáth, L. Sziráki, The electrochemical reduction of oxygen on zinc corrosion films in alkaline solutions, Electrochim. Acta. 53 (2008) 3218–3230. https://doi.org/10.1016/j.electacta.2007.11.056.

[78] J. Hövelmann, C. Putnis, L. Benning, Metal Sequestration through Coupled Dissolution–Precipitation at the Brucite–Water Interface, Minerals. 8 (2018) 346. https://doi.org/10.3390/min8080346.

[79] G. Berthomé, B. Malki, B. Baroux, Pitting transients analysis of stainless steels at the open circuit potential, Corros. Sci. 48 (2006) 2432–2441. https://doi.org/10.1016/j.corsci.2005.09.012.

[80] H.S. Isaacs, C. Scheffey, R. Huang, The Location of Events Producing Potential Transients During Pitting of Freely Corroding Al and Its Alloys, in: ECS Trans., ECS, 2008: pp. 1–12. https://doi.org/10.1149/1.2925257.

[81] C. Song, J. Zhang, Electrocatalytic oxygen reduction reaction, in: J. Zhang (Ed.), PEM Fuel Cell Electrocatal. Catal. Layers, Springer, London, 2008: pp. 89–134. https://doi.org/10.1007/978-1-84800-936-3_2.

[82] J. Zheng, W. Sheng, Z. Zhuang, B. Xu, Y. Yan, Universal dependence of hydrogen oxidation and evolution reaction activity of platinum-group metals on pH and hydrogen binding energy, Sci. Adv. 2 (2016) 1–8. https://doi.org/10.1126/sciadv.1501602.

[83] S. Trasatti, Work function, electronegativity, and electrochemical behaviour of metals. III. Electrolytic hydrogen evolution in acid solutions, J. Electroanal. Chem. 39 (1972) 163–184. https://doi.org/10.1016/S0022-0728(72)80485-6.

[84] Z.Y. Chen, F. Cui, R.G. Kelly, An analytical modeling method for calculating the current delivery capacity of a thin-film cathode and the stability of localized corrosion under atmospheric environments, ECS Trans. 3 (2007) 443–457. https://doi.org/10.1149/1.2789248.

[85] Z.Y. Chen, R.G. Kelly, Computational Modeling of Bounding Conditions for Pit Size on Stainless Steel in Atmospheric Environments, J. Electrochem. Soc. 157 (2010) C69–C78. https://doi.org/10.1149/1.3261803.

[86] F. Cui, F.J. Presuel-Moreno, R.G. Kelly, Computational modeling of the stability of crevice corrosion of wetted SS316L, ECS Trans. 1 (2006) 17–36. https://doi.org/10.1149/1.2214622.

[87] J.-E. Svensson, L.-G. Johansson, A laboratory study of the initial stages of the atmospheric corrosion of zinc in the presence of NaCl; Influence of SO2 and NO2, Corros. Sci. 34 (1993) 721–740. https://doi.org/10.1016/0010-938X(93)90096-Y.

[88] A.S. Agarwal, U. Landau, J.H. Payer, Modeling particulates effects on the cathode current capacity in crevice corrosion, J. Electrochem. Soc. 155 (2008) C269–C278. https://doi.org/10.1149/1.2890418.

[89] D.A.G. Bruggeman, Berechnung verschiedener physikalischer Konstanten von heterogenen Substanzen. I. Dielektrizitätskonstanten und Leitfähigkeiten der Mischkörper aus isotropen Substanzen, Ann. Phys. 416 (1935) 636–664. https://doi.org/10.1002/andp.19354160705.

[90] J.C.M. Garnett, XII. Colours in metal glasses and in metallic films, Philos. Trans. R. Soc. London. Ser. A, Contain. Pap. a Math. or Phys. Character. 203 (1904) 385–420. https://doi.org/10.1098/rsta.1904.0024.

[91] T.D. Weirich, J. Srinivasan, J.M. Taylor, M.A. Melia, P.J. Noell, C.R. Bryan, G.S. Frankel, J.S. Locke, E.J. Schindelholz, Humidity Effects on Pitting of Ground Stainless Steel Exposed to Sea Salt Particles, J. Electrochem. Soc. 166 (2019) C3477–C3487. https://doi.org/10.1149/2.0551911jes.

[92] C.G. Zoski, Review—Advances in Scanning Electrochemical Microscopy (SECM), J. Electrochem. Soc. 163 (2016) H3088–H3100. https://doi.org/10.1149/2.0141604jes.

[93] ASTM International, ed., Standard Practice for the Preparation of Substitute Ocean Water, ASTM Int. 98 (2013) 1–3. https://doi.org/10.1520/D1141-98R13.2.

Figure Captions:

Figure Captions:

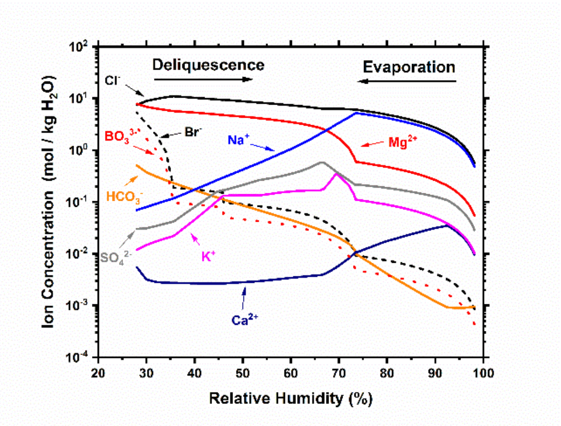

Figure 1: Ion concentration as a function of relative humidity for evaporated ASTM seawater solutions [93] at 25˚C. Figure adapted from [1].

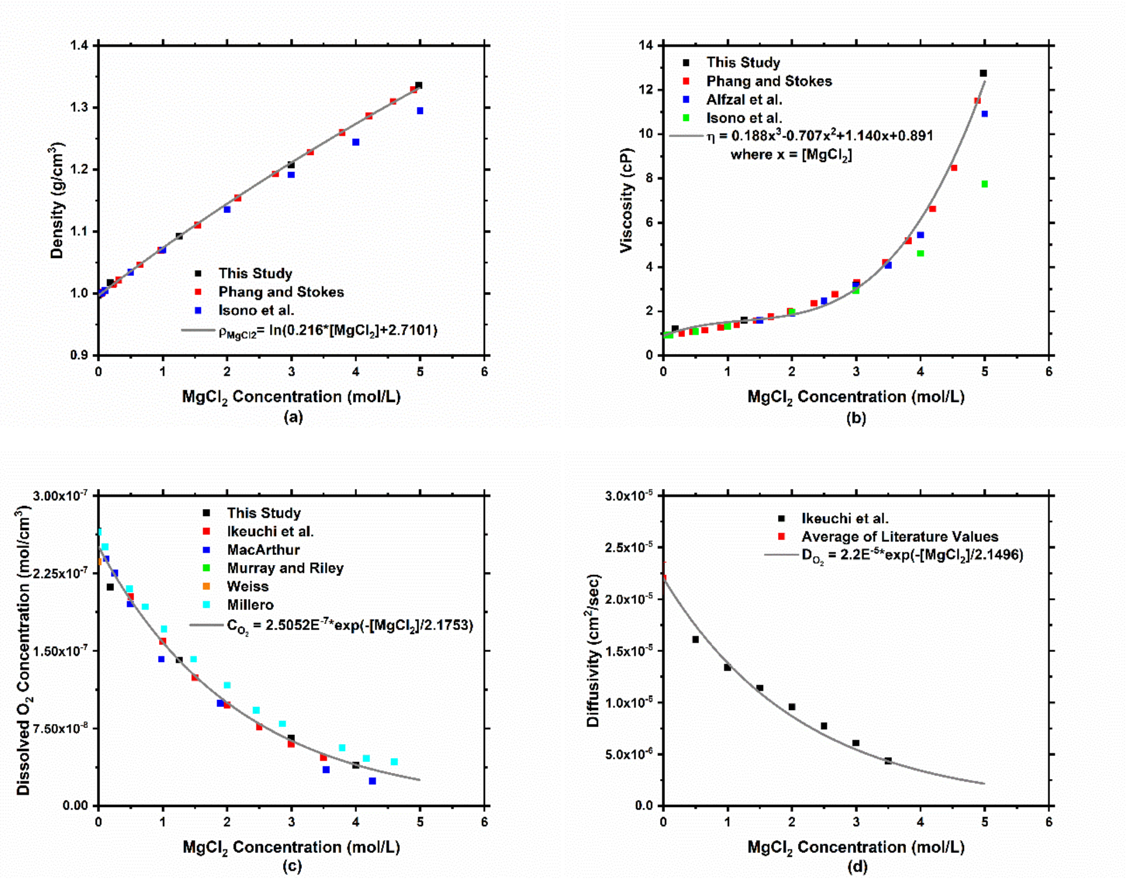

Figure 2: Comparison of measured and reported (a) densities, (b) viscosities, (c) dissolved O_2 concentrations and (d) diffusivities in $MgCl_2$ solution at 25˚C. Values from Phang and Stokes were converted with densities calculated in their study. The fits in (a), (b) and (c) correspond to the measured data in this study. Values in red, at 0 M $MgCl_2$, are literature averages for pure water at 25˚C.

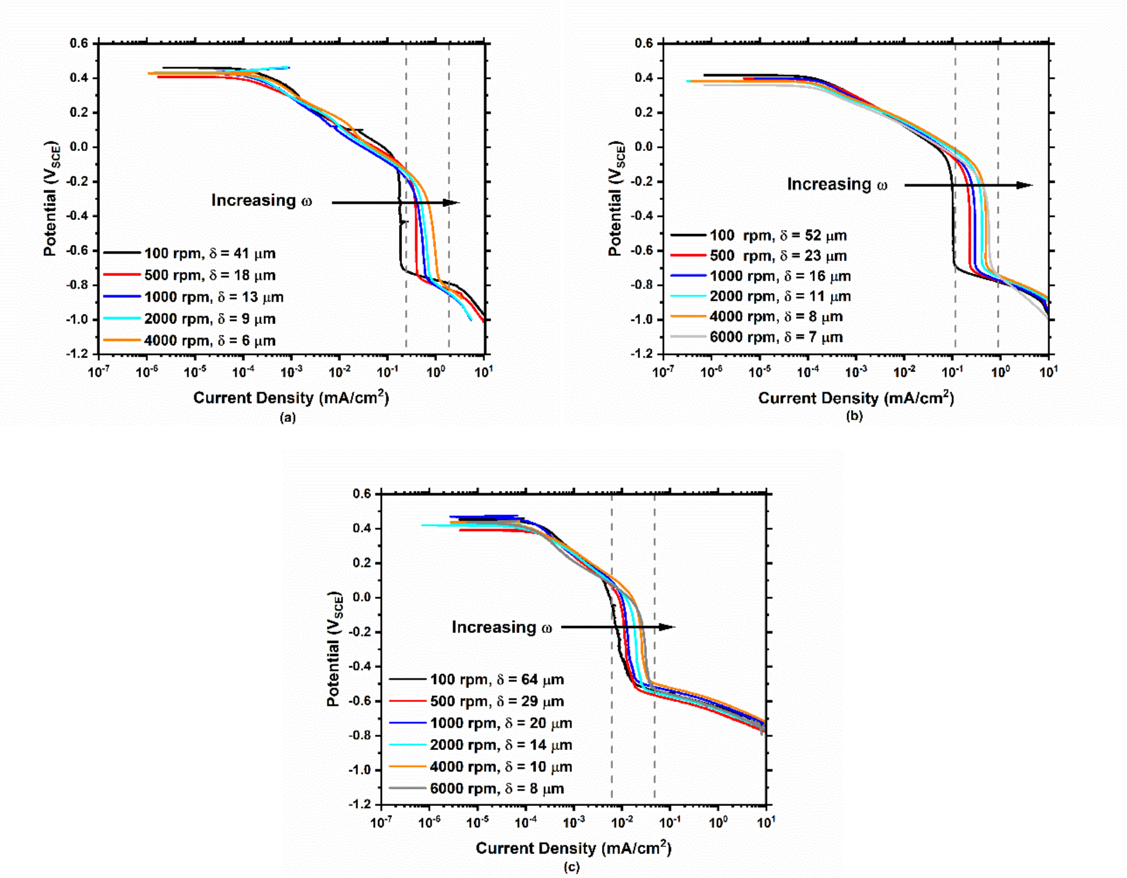

Figure 3: Cathodic polarization scans on Pt in (a) 0.189 M, (b) 1.28 M, and (c) 4.98 M $MgCl_2$ *solutions as a function of electrode rotation speed. Vertical dashed lines correspond to theoretical* i_{lim} *(n = 2) calculated from Equation 3 and data from Figure 2 corresponding to rotation speeds of 100 (left) and 6000 (right) rpm.*

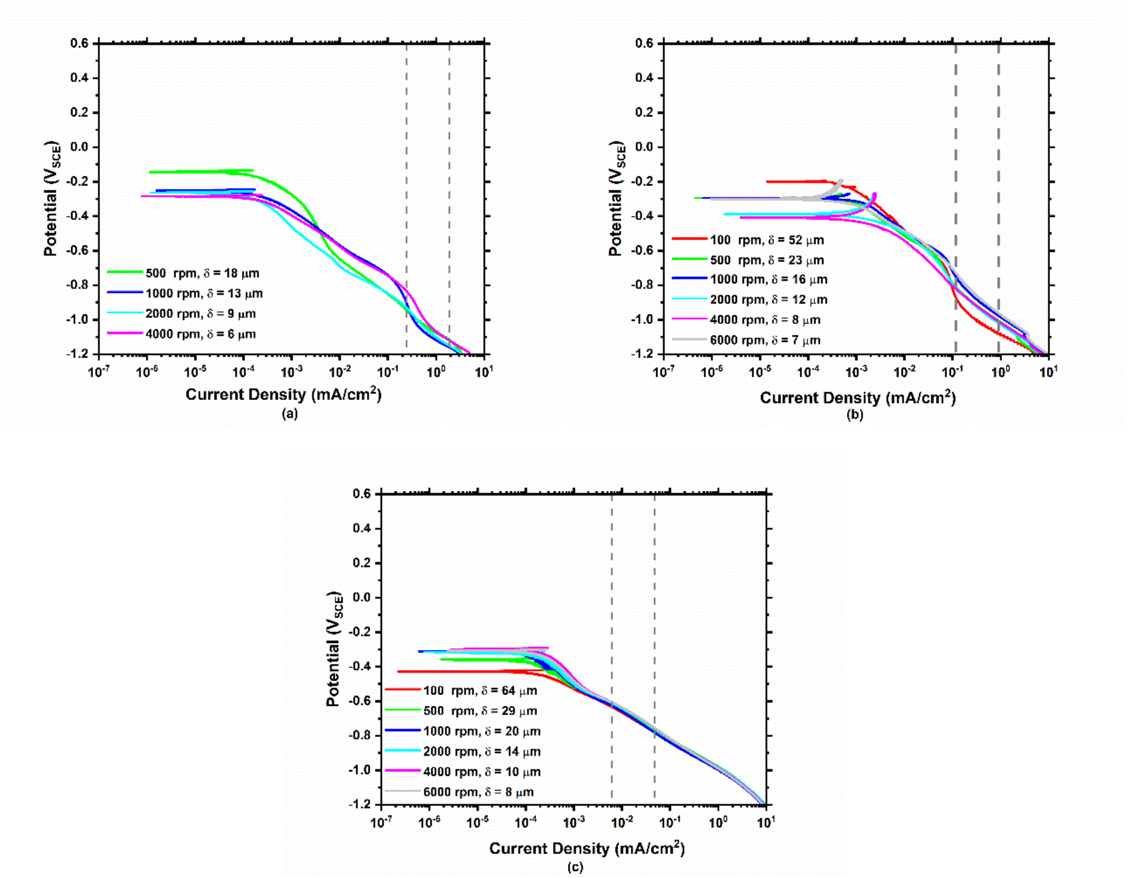

Figure 4: Cathodic polarization scans on SS304L in (a) 0.189, (b) 1.28, and (c) 4.98 M $MgCl_2$ solutions as a function of electrode rotation speed. Vertical dashed lines correspond to theoretical i_{lim} (n = 2) calculated from Equation 3 and data from Figure 2 corresponding to rotation speeds of 100 (left) and 6000 (right) rpm.

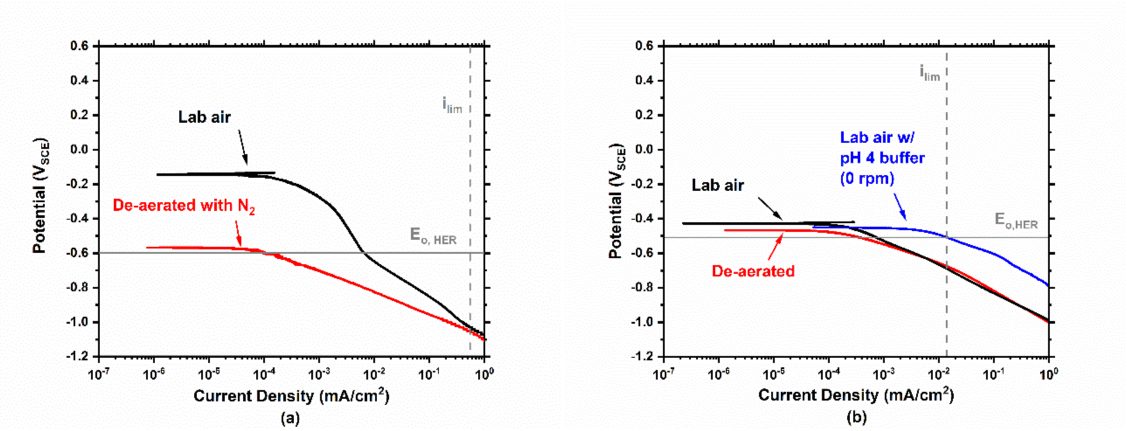

Figure 5: Comparison of cathodic polarization scans on SS304L in aerated and N_2 de-aerated solutions for (a) 0.189 and (b)4.98 M $MgCl_2$ at 25°C and 500 rpm. Also shown in (b) is a

polarization scan with an acetic acid buffer added to solution. Nernst potentials are calculated for a pH of (a) 6 and (b) 4.5 through Equation 11.

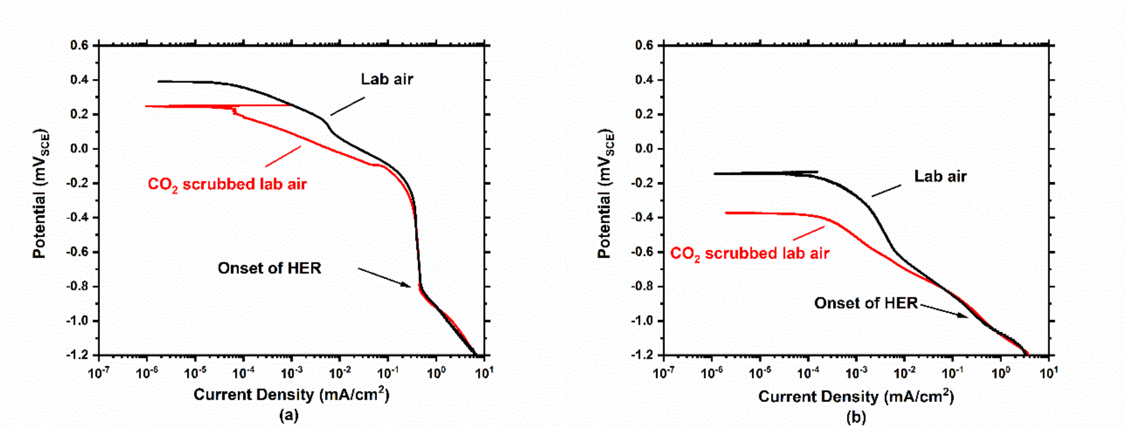

Figure 6: Polarization scans on (a) Pt and (b) SS304L in the presence of atmospheric CO_2 and with the sparged CO_2 concentration < 1 ppm in 0.189 M $MgCl_2$ at a rotation rate of 500 rpm.

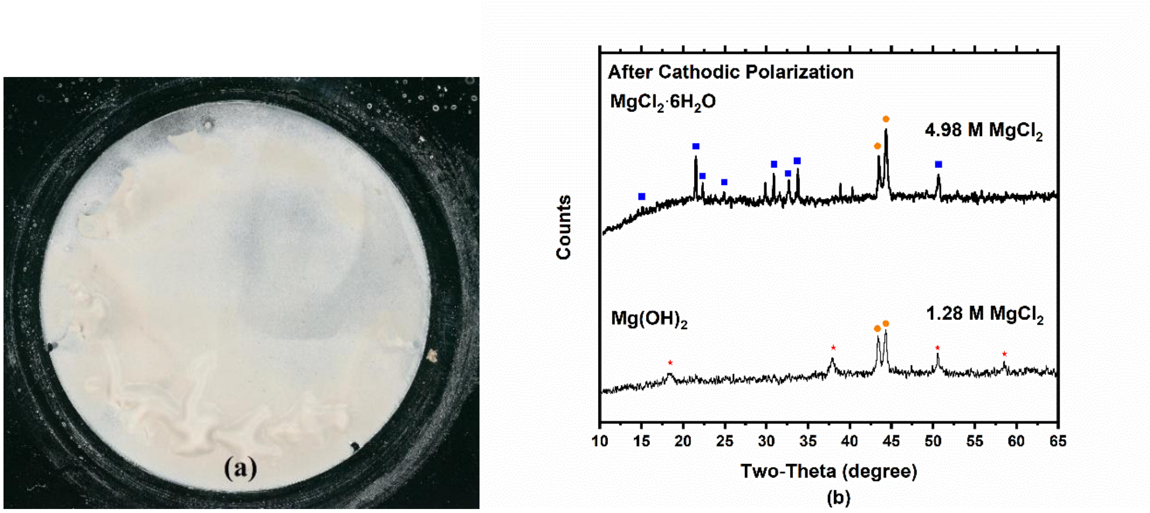

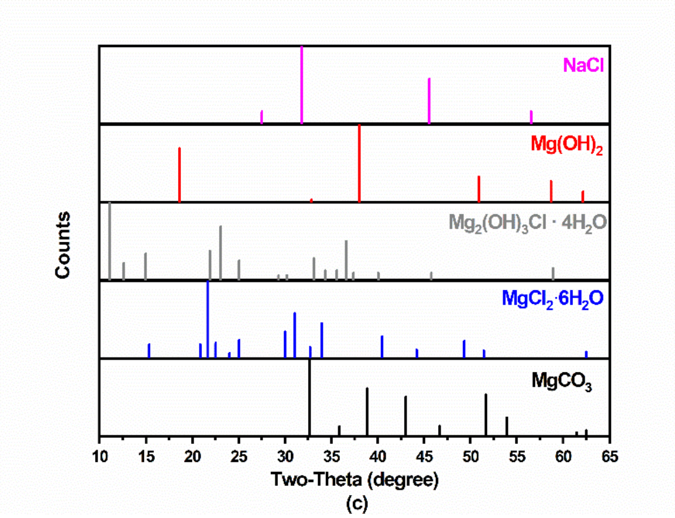

Figure 7: (a) Precipitate film formation on SS304L after cathodic polarization in $MgCl_2$ solution. This representative film was formed in 1.28 M $MgCl_2$ solution after a 1-hour OCP and cathodic polarization from OCP to -1.2 V_{SCE} at a scan rate of 0.167 mV/sec. (b) characterization of film shown to be $Mg(OH)_2$ in 1.28 M $MgCl_2$ and $MgCl_2{\cdot}6H_2O$ in 4.98 M $MgCl_2$.(c) Reference scans for XRD data [42].

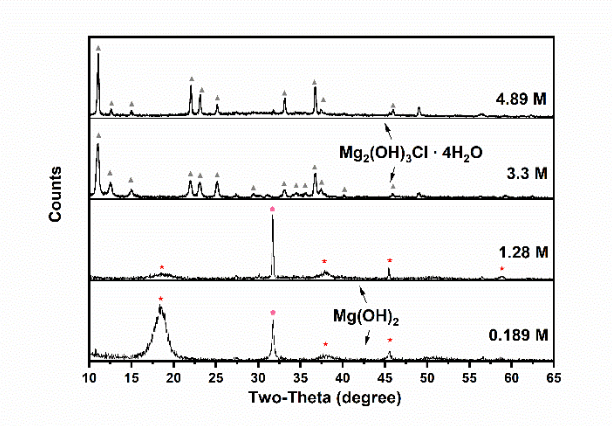

Figure 8: Equilibrium phases detected using XRD after NaOH titration into various $MgCl_2$ concentrations. The samples were vacuum filtered in air for 72 hours before analysis. Reference peaks are seen in Figure 7(c).

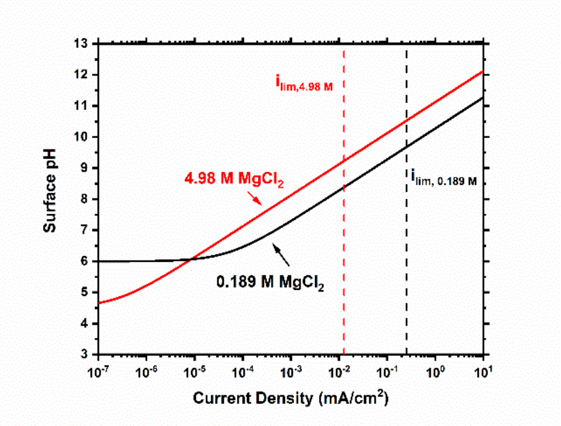

Figure 9: Surface pH for SS304L at δ=20 and 19 µm in 0.189 M and 4.98 M $MgCl_2$ respectively, calculated using Equation 10. The vertical dashed line labeled i_{lim} corresponds each δ calculated from Equation 3 using data from Figure 2.

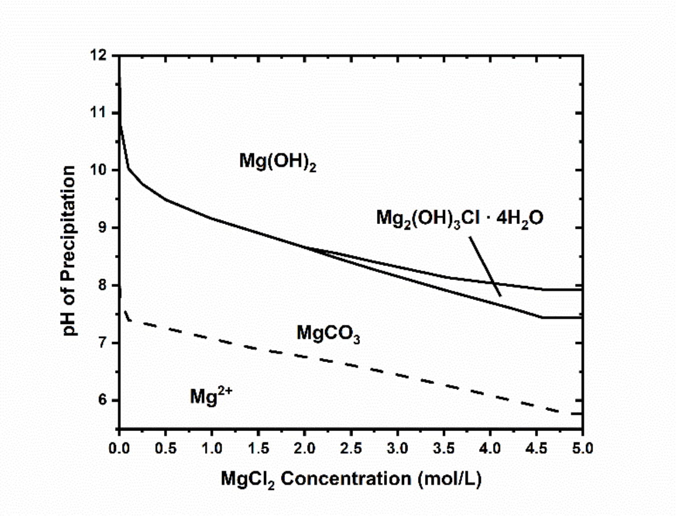

Figure 10: Stability diagram for dissolved H_2O-O_2-CO_2-$MgCl_2$ created in EQ3/6 [23] using the Yucca Mountain Program [24] thermodynamic database containing the K_{sp} values in Table 1 with the utilization of the Pitzer formulism [25]. The temperature was held constant at T = 25˚C,the oxygen content was kept constant at $log(f_{O_2}) = -0.7$, and two cases were considered with regard to the fugacity of CO_2: $log(f_{CO_2}) = -3.4$ (dashed line) and $log(f_{CO_2}) = 0$ (solid lines).

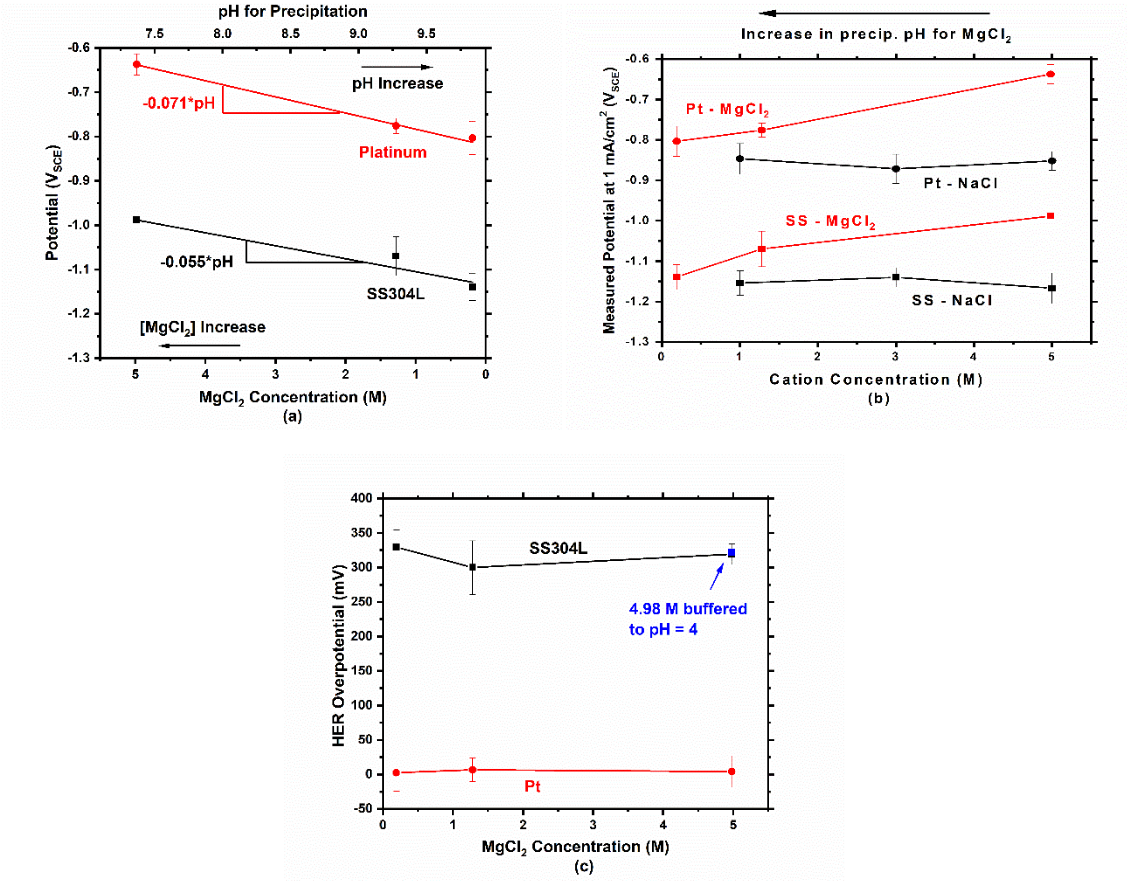

Figure 11: (a) Measured HER potential as a function of MgCl$_2$ concentration and corresponding pH for precipitation of Mg(OH)$_2$ (0.189 and 1.28 M MgCl$_2$) or $Mg_2(OH)_3Cl \cdot 4H_2O$ (4.98 M MgCl$_2$). Potentials were averaged from all rotation speeds in Figure 3 and 4 for Pt and SS304L respectively at a current density of 1 mA/cm^2. Precipitation pHs are gathered from Figure 10. (b) Combined HER potentials for MgCl$_2$ obtained from Figure 3 and 4 and NaCl obtained from Alexander et al. [4]. (c) Overpotential for HER. The Nernst potential was calculated at the precipitation pH given in Figure 10. The overpotential was calculated as $\eta = E_o - E_{1\,mA/cm^2}$. Error bars represent one standard deviation.

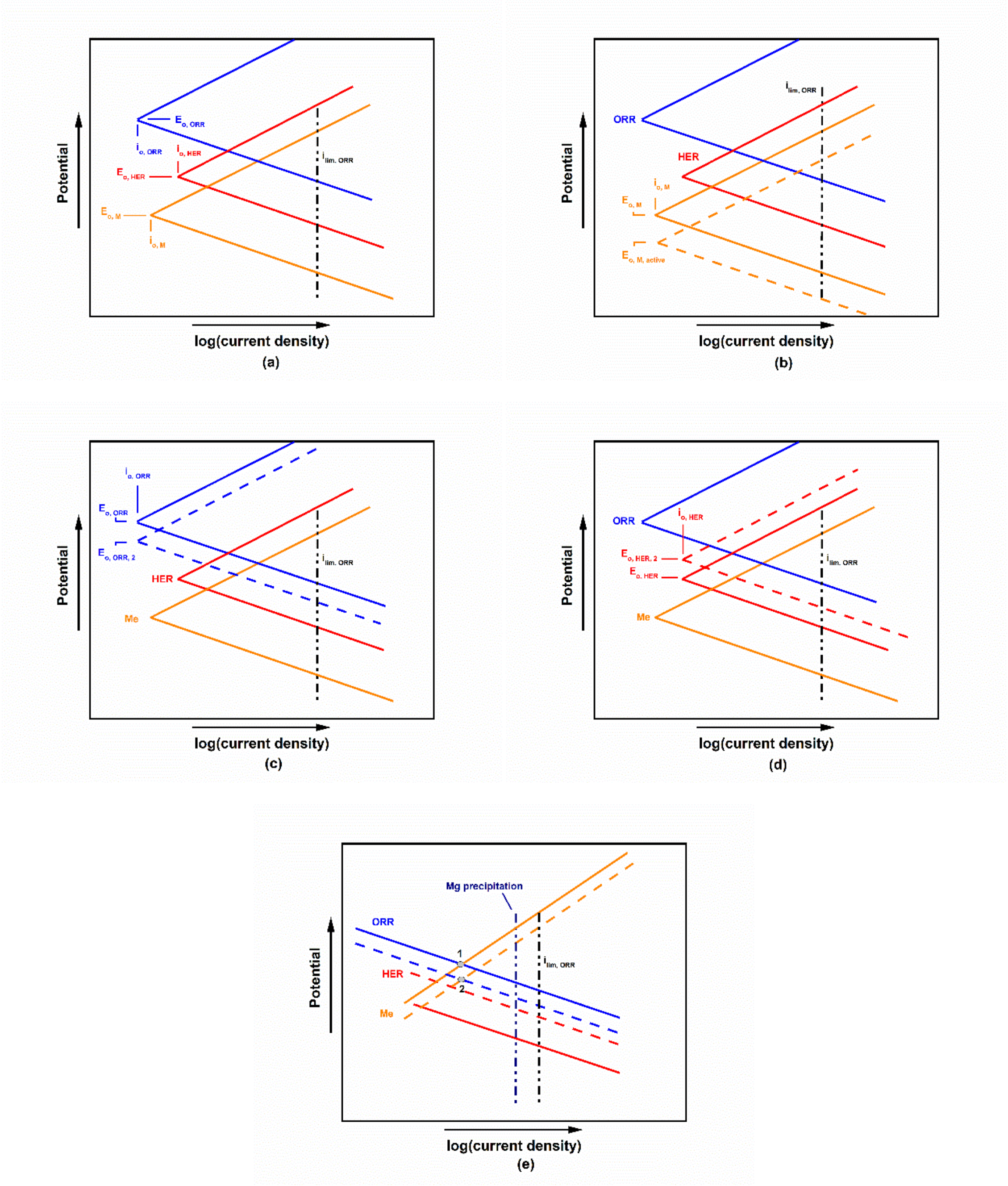

Figure 12: (a) Evans diagram explaining the unexpected cathodic behavior in $MgCl_2$ containing solutions. Influences from (b) anodic dissolution, (c) ORR, and (d) HER were considered in creation of this diagram along with the current for Mg species precipitation from Figure 9. Solid lines are dilute concentrations of $MgCl_2$ and transition to dashed lines with increasing concentration. The resultant Evan's diagram is displayed in (e).

Tables:

Table 1: Reactions for creation of stability diagram

Reaction	**Log K$_{sp}$ at 25 ° C**	**Source**	**Eqn. number**
$Mg(OH)_{2\,(s)} + 2\,H^{+}_{(aq)} \rightarrow Mg^{2+}_{(aq)} + 2H_2O$	17.1± 0.2	[26]	5
$Mg_2(OH)_3Cl \cdot 4H_2O_{(s)} + 3H^{+}_{(aq)} \rightarrow\ 2Mg^{2+}_{(aq)} + Cl^{-}_{(aq)} + 7H_2O$	26.0 ± 0.2	[26]	6
$MgCl_2 \cdot 6H_2O_{(s)} \rightarrow\ Mg^{2+}_{(aq)} + 2Cl^{-}_{(aq)} + 6H_2O$	4.4	[27]	7
$MgCO_{3\,(s)}\ + H^{+}_{(aq)} \rightarrow\ Mg^{2+}_{(aq)} + HCO^{-}_{3\,(aq)}$	2.3	[28]	8

B. Natural Convection Boundary Layer Thickness at Elevated Chloride Concentrations and Temperatures and the Effects on a Galvanic Couple

Natural Convection Boundary Layer Thickness at Elevated Chloride Concentrations and Temperatures and the Effects on a Galvanic Couple

R. M. Katona[1,2,z,*], J. C. Carpenter[1], A. W. Knight[1], R. S. Marshall[2,*], B. L. Nation[1], E. J. Schindelholz[3,**], R. F. Schaller[1,**], and R. G. Kelly[2,***]

[1] Sandia National Laboratories, Albuquerque, NM 87123 USA
[2] Materials Science and Engineering, University of Virginia, Charlottesville, VA 22904 USA
[3]Department of Materials Science and Engineering, The Ohio State University, Columbus, OH 43210 USA

[z]Corresponding Author E-mail Address [rmkaton@sandia.gov]

[*] Electrochemical Society Student Member
[**] Electrochemical Society member
[***] Electrochemical Society Fellow

Key Words

Cathodic kinetics, oxygen reduction reaction, sodium chloride electrolyte properties, Finite Element Modeling

Abstract

The natural convection boundary layer (δ_{nc}) and its influence on cathodic current in a galvanic couple under varying electrolytes as a function of concentration (1 - 5.3 M NaCl) and temperature (25 - 45 ˚C) were understood. Polarization scans were obtained under quiescent conditions and at defined boundary layer thicknesses using a rotating disk electrode on platinum and stainless steel 304L (SS304L); these were combined to determine δ_{nc}. With increasing chloride concentration and temperature, δ_{nc} decreased. Increased mass transport (Sherwood number) results in a decrease in δ_{nc}, providing a means to predict this important boundary. Using Finite Element Modeling, the cathodic current was calculated for an aluminum alloy/SS304L galvanic couple as a function of water layer (WL) thickness and cathode length. Electrolyte domains were delineated, describing (i) dominance of ohmic resistance over mass transport under thin WL, (ii) the transition from thin film to bulk conditions at δ_{nc}, and (iii) dominance of mass transport under thick WL. With increasing chloride concentration, cathodic current decreased due to decreases in mass transport. With increasing temperature, increased cathodic current was related to increases in mass transport and solution conductivity. This study has implications for sample sizing and corrosion prediction under changing environments.

Introduction

Metallic structures are commonly exposed to marine atmospheric conditions, characterized by thin electrolyte layers allowing for the formation an electrochemical or corrosion cell. The electrolyte can be formed through salt spray or deliquescence of salt as either a droplet or a thin water layer (WL) on the alloy surface and the chemical composition and thickness can vary widely [1]. As such, the rate and extent of corrosion on the alloy surface is dictated by the combination of environmental, physicochemical, and geometric variables, which include relative humidity (RH), temperature, electrolyte conductivity, electrolyte film thickness, in addition to the electrochemical kinetics on the alloy surface [2–6]. Due to the large potential variation in environmental conditions and *WL* thicknesses, modeling can serve as an important tool to evaluate environmental effects on the corrosion of alloys and galvanic couples.

One of the most important controlling factors for corrosion in atmospheric environments is the *WL* thickness. Tomashov initially recognized a corrosion rate dependence with *WL* thickness and qualitatively described four different reaction control mechanisms. Under bulk, full immersion conditions, a plateau in corrosion rate is seen and a constant diffusion layer is achieved. Decreasing the *WL* causes an increased corrosion rate which is due to more rapid diffusion of oxygen across the thinner *WL*. Further decreasing the *WL* thickness reduced dissolution due to anodic control (owing to lower corrosion product solubility in a smaller solution volume). Finally, once a continuous film is lacking, the final regime is reached and is characterized by a very low corrosion rate of dry chemical oxidation [4]. While useful conceptually, the outline presented by Tomashov lacked a demonstrated quantitative description between electrochemical kinetics and the film thickness.

Numerous authors have attempted to quantitatively determine the transition from bulk, full immersion kinetics to thin film kinetics [4,7–34]. The transition occurs at the natural convection boundary layer (δ_{nc}) and is formed on surfaces affected by convection or advection in response to thermally or compositionally driven spatially inhomogeneous density distributions [32]. This flow prevents a concentration gradient of the oxidized or reduced species from extending to large distances away from the electrode (i.e. the concentration gradient is finite and close to the surface). In the absence of natural convection, the diffusional boundary layer would continuously increase with time, lowering the diffusion-limited current density (ilim) continuously [9]; however, an ilim is observed in many cases. The quantification of δ_{nc} in solutions of various compositions has yielded values from near 250 µm [21,24–27,35] to between 500 and 1000 µm [9,16,17,19,20,33]. Several methods exist to quantify δ_{nc}; however, recently, Liu et al. utilized a rotating disk electrode (RDE) and quiescent cathodic polarization scans to quantify δ_{nc} in a dilute chloride-containing brine which could form under atmospheric conditions [9]. It was determined that in 0.6 M NaCl, in which the oxygen reduction reaction (ORR) is dominant and the diffusion of oxygen to the metal surface is the rate limiting process [36], δ_{nc} was roughly 800 µm [9]. Below δ_{nc}, the flux of oxygen to the surface of the cathode is determined by the WL thickness. While the method presented provides a robust framework, there is still a gap in literature regarding δ_{nc} as a function of common environmental parameters such as brine composition, concentration, and temperature.

Models have been presented in literature to understand δ_{nc} [21,24]. Of particular note, Amatore et al. [24] described a micro-convection approach in which a diffusion-like term was used to account for natural convection. Dolgikh et al. [21] used this idea and extended it to multi-ion environments. While models exist to investigate natural convection, these models have not been widely applied, and the effects of δ_{nc} on the extent of corrosion in various environments have seldom been explored. Typically, atmospheric, thin film ($< \delta_{nc}$) corrosion modeling scenarios are presented in modeling [6,9–12,37–42]. For example, Palani et al. examined the effect solution concentration on a galvanic couple between AA2024 and a carbon-fiber reinforced polymer (CFRP) as a function of WL thickness. Although they found good agreement between experimental and modeling results, Palani and coworkers only explored dilute concentrations (≤ 0.6 M NaCl), small electrode configurations (0.01 m), and thin WL (< 50 μm) [40]. On the other hand, Liu et al. determined the dependence of the cathodic current delivery capacity on the electrolyte film thickness with relation to δ_{nc} and cathode size in an AA2024/SS316L galvanic couple in 0.6 M NaCl at 25 ˚C. In their study, the total cathodic current was calculated using cathodic boundary conditions obtained through RDE by integrating the current density across the electrode. Various electrolyte layer domains were delineated by WL thicknesses and cathode sizes. For thin films less than δ_{nc}, the total current was generally independent of the size of the cathode and the nature of kinetics at the electrochemical interface, being solely driven by the ohmic resistance in solution. For thick films greater than δ_{nc}, mass transport (M-T) of oxygen to the cathode surface and cathode size dictated the total current. As such, δ_{nc} defined the upper limit of the thin film regime [9], and this needs to be understood as a function of exposure environment in order to inform upon atmospheric corrosion.

When dissimilar alloys are present under an electrolyte and in electrical contact, a galvanic couple forms and, in combination with the *WL* thickness and composition, serves as another controlling factor that can influence corrosion. The *WL* will influence both diffusional kinetics at the cathode and ohmic drop in solution between the anode and cathode, affecting the total amount of cathodic current available to drive dissolution at the anode [9,12,37,39,41,43]. However, synergies often exist between the cathode and anode and a majority of the work to date has focused primarily on either one or the other of these two regions.

Finally, it is important to put the *WL* thicknesses presented in this paper into perspective. In atmospheric conditions, a deliquesced *WL* is dependent upon RH, salt composition, and loading density of the salt (*LD*), and ranges from 1 – 200 µm under typical conditions [1,44]. RDE experiments simulate a *WL* (Equation 2) by imposing a hydrodynamic boundary layer which can range from 7 – 200 µm depending on rotation rate, solution composition/concentration, and temperature [9,36,45]. Third, salt spray accelerated corrosion testing, such as ASTM B117 [46], creates varying WL thickness from 660 – 1210 µm and depends heavily on the angle of exposure [47]. Finally, δ_{nc} determines the transition between thin film and bulk corrosion kinetics and again is dependent upon the solution composition and concentration. For 0.6 M NaCl at 25 ˚C solution δ_{nc} was calculated to be 800 µm [9]. At 25 ˚C and 0.6 M NaCl, an enormous LD of roughly 27 g/m^2 would be needed to reach δ_{nc} via deliquescence of surface salt deposits [44] which is unlikely to be achieved under typical conditions. Thus, the WL thickness (dependent on LD and RH) will likely be controlling the flux of oxygen to the surface and ultimately the cathodic current in atmospheric conditions. However, it should be noted that under either condensation, rain, or salt spray, WLs above 1,000 µm are likely, at least transiently. In addition, the accumulation of corrosion products or inert dust may, through capillary action, create WL that are effectively much larger in terms of the diffusion of oxygen. A wide range of WL thicknesses will be explored in this paper, from thin WL (7 µm or 7×10^{-6} m) to thick WL (50,000 µm or 5×10^{-1} m), encompassing WLs that are present in atmospheric, salt spray, and full immersion conditions.

This paper measures cathodic kinetics on platinum (Pt) and stainless steel 304L (SS304L) under varying electrolyte layers using an RDE, and quantitatively determines δ_{nc} as a function NaCl concentration and temperature. Cathodic kinetics in NaCl and $MgCl_2$ [45] and knowledge of δ_{nc} are combined to inform upon cathodic currents in a galvanic couple between SS304L and an aluminum alloy (AA) 7050-T7451 across thin film to bulk conditions. The results of this study identify not only trends in δ_{nc} that can be described by mass transport phenomena but also discusses controlling mechanisms for galvanic corrosion under varying environmental conditions.

Experimental

Methods utilized within are similar to Alexander et al. [36] and Katona et al. [45] and brief descriptions of these methods are given below.

Brine Properties

The density (ρ), dissolved oxygen concentration (C_{O_2}), and viscosity (η) were measured for NaCl brines (0.6 M to saturated) at 25, 35, and 45 ˚C. Solution ρ were measured using hydrometers calibrated for specific gravity ranges from 1.000 to 1.220, and 1.20 to 1.420. Hydrometer accuracies at temperatures above their calibration temperature was verified by measuring the density of saturated NaCl solutions at the temperatures of interest [48]. C_{O_2} measurements were taken using the Chesapeake Bay Institute-modified Winkler iodometric titration method [49,50]. Briefly, samples were heated to the temperature of interest and equilibrated with the ambient air for a few hours, then transferred to a glass-stopper flask, which was calibrated gravimetrically with DI water to contain a total solution volume of 146 mL. Next, 1 mL of 3 M manganese (II) sulfate ($MnSO_4$) and 1 mL of basic potassium iodide (KI) (4 M KI in 8 M NaOH) were added to the flask and capped to allow for minimal air to exist in the flask. The contents of the flask were thoroughly mixed using a magnetic stir bar for several minutes for the KI to disperse and break apart precipitates that formed. To quench the reaction, 50% sulfuric acid (H_2SO_4) was added along with a starch indicator. C_{O_2} was measured via titration of the acidified solution by sodium thiosulfate ($Na_2S_2O_3$). η was measured at each temperature, using a Brookfield AMETEK LDTV2T Viscometer with an ultra-low η adaptor. Roughly 16 mL of each sample was transferred to the sample cell, and each temperature set point equilibrated for 10 mins. Five spindle speeds were analyzed to achieve a torque between 10% and 95% to verify the Newtonian fluid relationship. Solution properties for $MgCl_2$ were obtained from Katona et al. [45].

Materials

High-speed rotating disc electrodes (RDE) with a diameter of 5 mm comprised of SS304L and 99.99% Pt were acquired from Pine Research Instrumentation, Inc. (USA). Prior to each use, the electrodes were polished using a 1 μm Dialube Diamond Suspension®, then rinsed with ultrapure (18.2 MΩ-cm) water and dried with nitrogen (N_2). Brine solutions were prepared using ultrapure water and reagent grade chemicals (≥ 99.0% purity).

Electrochemical Tests

A three-electrode cell was used with the alloy specimen as the working electrode (WE), a saturated calomel reference electrode (SCE), and a Pt-coated niobium mesh as the counter electrode. The exposed area of the WE during testing was 0.196 cm^2. Samples were immersed in the solution and temperature of interest in a 150 mL water-jacketed cell and sparged with lab air to maintain a solution saturated in O_2. The WE was rotated using a Pine instruments MSR rotator with an accuracy of ± 1 % of the display reading. Rotation speeds ranged from 100 to 6000 rpm, with multiple repetitions carried out at the 500 rpm speed to evaluate method uncertainty. All solutions exhibited laminar flow. The solution temperature was controlled to 25, 35, or 45 ± 1 °C using a water circulator and thermostat. Quiescent polarization scans were performed with the working electrode perpendicular to gravity which permits the assumption of an equivalent diffusional boundary layer thickness for natural convection [33]. Cathodic polarization measurements were performed on SS304L and Pt in 1, 3, and 5.3 M (saturated) NaCl at scan rates of 0.167 and 1 mV/s respectively after 1 hour of open circuit potential (OCP) equilibration and stabilization. The scans were performed from OCP to -1.2 V_{SCE}.

Analysis

The theoretical diffusion-limited current density (i_{lim}) can be calculated by Fick's first law and assuming one-dimensional diffusion via

$$i_{lim} = \frac{nFD\left(C_{bulk} - C_{surface}\right)}{\delta} \qquad 1$$

where n is the number of electrons transferred, F is Faraday's constant ($96485\ C/mol$), D is the diffusivity of the reacting species, C_{bulk} and $C_{surface}$ (assumed to be zero) are the concentrations of the reacting species in the bulk solution and at the electrode surface respectively, and δ is the hydrodynamic boundary layer thickness. When using an RDE, δ is given as a function of rotation speed (ω in rad/sec) through,

$$\delta = 1.61 D^{1/3} \omega^{-1/2} \nu^{1/6} \qquad 2$$

where ν is the kinematic viscosity ($\nu = \eta/\rho$)[8]. Substituting Equation 2 into 1 yields the Levich equation [45,51]:

$$i_{lim} = 0.62nFD_{O_2}^{2/3}\nu^{-1/6}\,C_{O_2,bulk}\omega^{1/2} \tag{3}$$

The Levich equation only applies at non-zero rotation rates, as at ω = 0, i_{lim} would be zero and the boundary layer thickness infinite. Experimentally, a finite current density is observed for stagnant electrodes. The finite current density is controlled by δ_{nc} which can determined through the method of Liu et al.[9]. Briefly, i_{lim} from RDE experiments is plotted as a function of $1/\delta$ and a linear fit is achieved (Figure 3 from Liu et al. [9] and Figure 3 from Charles-Granville et al. [33]). i_{lim} from a quiescent polarization scan in full immersion, under quiescent conditions (0 rpm, referred to as $i_{lim,nc}$) is then obtained. The intersection of $i_{lim,nc}$ with the linear fit yields δ_{nc}.

Further analysis was performed by calculating the overall mass transfer coefficient (K), given by,

$$K = \frac{i_{lim}}{nFC_{bulk}} \tag{4}$$

Finally, the Sherwood number (Sh, also known as the Nusselt number for mass transfer) is calculated, given by

$$Sh = \frac{K}{D/d} \tag{5}$$

Where d is the diameter of the transfer surface (cm) [7,28].

Finite Element Modeling

Modeling described here is an extension of previous work from Liu et al. and the model and initial results are described in more detail in the original publication [9]. It is noted that results from Liu et al. utilized SS316L polarization scans while work here was performed on SS304L [9]. Briefly, the modeling framework is based on the Laplace Equation [52]. COMSOL Multiphysics v5.5 (COMSOL, Inc., Burlington, MA) software was utilized. The potential and current distributions along a SS304L cathode coupled galvanically with AA7050-T7451 were modeled using a simplified, two-dimensional geometry which represented the cross-section of a couple under a *WL*, as depicted in Figure 1. The anode length was fixed at 0.01 m, and the range of cathode lengths considered in this study varied from 0.01 m to 0.5 m, corresponding to an area ratio of 1:1 to 1:50, respectively. The width of both electrodes was considered identical, obviating the necessity for a three-dimensional model. As such, the current per width (I_C/W) is calculated due to the two-dimensional model. The WL thickness was varied across roughly four orders of magnitude from 8 µm to 50,000 µm ($8 \times 10^{-6} - 5 \times 10^{-2}$ m) in order to provide a sufficiently range to capture exposure conditions representative of thin films and full immersion. The lower limit of WL was set by the physical limitations of the RDE; above a certain rotation speed (typically above 6000 rpm), the hydrodynamic boundary layer thickness experiences turbulence and Levich behavior no longer exists.

The values used for solution conductivity (κ) were obtained from OLI Studio Analyzer 9.5 (OLI Systems, Inc., Cedar Knolls, NJ). Plots of κ can be seen in Katona et al. for NaCl solutions [53] and Katona et al. for $MgCl_2$ [54]. The anodic boundary conditions (B.C.) were the anodic kinetics of AA7050 (anodic B.C.) obtained from Liu et al. [9] and were assumed to be constant across all chloride concentrations and temperatures. Cathodic B.C. were measured for SS304L cathodic polarizations in NaCl as a function of δ (rpm). When WL thicknesses were greater than δ_{nc}, the cathodic, quiescent polarization scan was utilized. Any WL less than δ_{nc} utilized the cathodic polarization scan corresponding to the WL. Cathodic polarizations for $MgCl_2$ were taken from previous work [45] and it is noted that there was no observed rotational dependence in $MgCl_2$ electrolytes. All calculations were assumed to be steady state and the polarization scans were not dependent upon pH. Both anodic and cathodic currents were measured, and it was ensured currents were identical.

Results

First, solution properties are presented for NaCl solutions as a function of concentration and temperature. These properties are further utilized to calculated diffusional boundary layers for each rotation rate. Next, cathodic kinetics and Levich behavior for Pt and SS are presented as a function of rpm, solution concentration, and temperature. Third, the calculated boundary layers and limiting current densities are utilized to calculate δ_{nc} under quiescent conditions. The δ_{nc} is then correlated to the *Sh*. Finally, knowledge of δ_{nc} and the obtained cathodic kinetics are utilized to inform upon the cathodic current from an AA/SS galvanic couple as a function of solution composition (NaCl and $MgCl_2$ solutions), solution concentration, temperature, *WL* thickness, and cathode length.

Solution Properties

Measured solution properties, C_{O_2}, ν, and ρ, are presented in Figure 2(a), (b), and (c) respectively, as a function of chloride concentration and temperature for NaCl and $MgCl_2$ electrolytes. Values for $MgCl_2$ are obtained from Katona et al. [45]. Calculated D_{O_2} (from OLI studio) are presented in Figure 2(d) as a function of chloride concentration and temperature for NaCl and $MgCl_2$ electrolytes. With increasing chloride concentration, C_{O_2} and D_{O_2} decrease while ν and ρ increase. With increasing temperature, C_{O_2}, ν, and ρ decrease while D_{O_2} increases.

Cathodic Kinetics

Platinum

Measured cathodic polarization scans on Pt in a range of NaCl solution concentrations (1, 3, 5.3 M NaCl) and temperatures (25, 35, and 45 ˚C) are presented in Figure 3. The corresponding calculated δ using Equation 16 and solution properties presented in Figure 2 are given alongside the rotation speeds. The polarization measurements are characterized by an ORR activation-controlled region from OCP to approximately -0.1 V_{SCE}, followed by mass transfer (M-T) controlled ORR from -0.1 V_{SCE} to -0.8 V_{SCE} and finally HER below -0.8 V_{SCE}. The potential of the transition to M-T kinetics is dependent upon rotation rate. With increasing solution concentration, i_{lim} decreases and with increasing temperature, i_{lim} increases.

Stainless Steel 304L

Cathodic polarizations measured on SS304L are shown in Figure 4 for the same solution concentrations and temperatures as Pt. The polarization measurements are characterized by an ORR activation-controlled region from OCP to approximately -0.6 V_{SCE} followed by M-T controlled ORR from -0.8 V_{SCE} to -1 V_{SCE} and finally HER below -1 V_{SCE}. As with Pt, the transition to M-T kinetics is dependent upon rotation rate. It is noted that as δ decreases, there is an unusual transition behavior between the activation-controlled regime and the M-T controlled region in the potential range of -0.6 to -0.8 V_{SCE}. With smaller δ the transition becomes more pronounced. The same concentration and temperature trends that were present in Pt are present for SS304L.

Levich Analysis

Levich plots for Pt and SS304L are shown in Figure 5 for all chloride concentrations and temperatures. Also plotted in Figure 5 is the predicted Levich behavior (Equation 3) for each NaCl solution for $n = 4$ (ORR reaction producing four hydroxyl ions) using the properties from Figure 2. In general, Pt exhibits linear Levich behavior being slightly below the predicted Levich behavior for a four-electron transfer. It is noted that as the rotation rate is increased, i_{lim} for SS304L decreases with respect to values for Pt. There is no trend in this behavior with concentration or temperature. Additionally, n was calculated for both Pt and SS304L for all chloride concentrations and temperatures and yielded values between 3.8-3.4, and no trend with chloride concentration or temperature was present. It is noted that SS304L had a lower calculated n in comparison to Pt.

Natural Convection Boundary Layer

Calculated δ_{nc} values, based on the formulism of Liu et al. [9], are presented for NaCl solutions as a function of chloride concentration and temperature in Figure 6(a). Also shown in Figure 6(a) are values obtained for δ_{nc} in 0.6 M at 25 ˚C from Liu et al. [9] and Charles-Granville et al. [33]. Overall, with increasing chloride concentration, δ_{nc} decreases. Additionally, with increasing temperature, δ_{nc} decreases. It is noted that values of δ_{nc} were calculated using i_{lim} for both Pt and SS304L. Generally, SS304L had a higher δ_{nc} due to a lower i_{lim}. Figure 6(b) compares δ_{nc} for NaCl to $MgCl_2$ as a function of chloride concentration at 25 ˚C. Polarization scans for $MgCl_2$ on Pt were obtained from Katona et al. [45]. Below 5 M chloride, δ_{nc} is similar for both salts.

As seen in Figure 7, δ_{nc} decreases with increased calculated Sh (Equation 5),. Also included in Figure 7 are values obtained for δ_{nc} in 0.6 M NaCl at 25 ˚C from Liu et al. [9] and Charles-Granville et al. [33], 0.6 M sodium hydroxide (NaOH) from Katona et al. [55], and 10 mM potassium ferrocyanide ($K_4Fe(CN)_6$) from Amatore et al. [25] all at room temperature. The fit present in Figure 7 utilized data only from this experiment, but values of δ_{nc} from literature [9,25,33,55] show good agreement with the fit.

Modeling in a Galvanic Couple

Cathodic current per width as a function of WL thickness and cathode length at 25˚C

The modeled potential and current density as a function of distance away from the AA/SS interface for 1 M NaCl at 25 ˚C and an L_C = 0.3 m are presented in Figure 8. With increasing distance from the AA/SS interface, the potential rises from the coupling potential of AA and SS, nearing the open circuit potential of the SS at far distances. At the same time, the current density of the cathode decreases with increasing distance from the interface. When considering the logarithmic distance from the AA/SS interface (Figure 8(b)), the current density is constant near the interface and decreases rapidly at greater distances. The total cathodic current per width (I_C/W) is obtained by integrating the current density along the entire cathode length.

I_C/W for a SS304L cathode vs. WL thickness as a function of cathode length (L_C) at 25 ˚C are presented in Figure 9(a), (b), and (c) for 1, 3, and 5.3 M NaCl, respectively. For small cathodes (< 0.16, < 0.18, and < 0.32 m for 1, 3, and 5.3 M respectively), I_C/W increases with WL thickness, then decreases to an intermediate minimum at δ_{nc} before reaching a plateau. For intermediate and large cathode lengths (≥ 0.16, ≥ 0.18, and ≥ 0.32 m for 1, 3, and 5.3 M respectively) I_C/W grew before reaching a first plateau at WL thicknesses from roughly 100 μm to δ_{nc} (Figure 6), and then again increased with WL until reaching a second plateau. The second plateau increases with L_C. The L_C denoted as the transition from small to large cathode is considered the critical cathode length (L_{Crit}). At L_{crit}, I_C/W does not decrease with increasing WL thickness above δ_{nc} due to M-T kinetic limitations. Below L_{Crit}, I_C/W decreases with increasing WL thickness as the current has influences from both ohmic control and M-T limitations. At values above L_{Crit}, I_C/W is limited by the cathode size and becomes independent of *WL* thickness due to M-T limitations.

Cathodic current per width as a function of WL thickness and cathode length at 45˚C

I_C/W for a SS304L cathode vs. *WL* thickness as a function of L_C at 45 ˚C are presented in Figure 10(a), (b), and (c) for 1, 3, and 5.3 M NaCl respectively. Although the overall behavior is qualitatively the same as at the lower temperature, the distinction between short and intermediate/long cathode lengths are 0.07, 0.12, and 0.13 m for 1, 3, and 5.3 M respectively.

Critical cathode sizes increase with chloride concentration and decrease with increasing temperature

L_{Crit} is calculated for all scenarios in this study and is presented in Figure 11. With increasing chloride concentration, L_{Crit} increases, while with increasing temperature L_{Crit} decreases.

Increased I_C/W calculated for 4.98 M $MgCl_2$ in comparison to 5.3 M NaCl at large cathode sizes

Figure 12(a) presents I_C/W for a SS304L cathode vs. *WL* thickness as a function of L_C at 25 ˚C in 4.98 M $MgCl_2$. In contrast to 5.3 M NaCl (c), 4.98 M $MgCl_2$ does not have influences from M-T limitations. At all cathode lengths, I_C/W increases with *WL,* eventually plateauing due to the size of L_C. There is no depression in I_C/W with increasing *WL* thickness above δ_{nc} as was present in NaCl at 25 and 45 ˚C, thus, there is no L_{Crit} in 4.98 M $MgCl_2$. A direct comparison of 4.98 M $MgCl_2$ (9.96 M Cl^-) and 5.3 M NaCl is presented in Figure 12(b) and (c). At small *WLs*, a greater I_C/W is calculated in NaCl in comparison to $MgCl_2$ solutions. At large *WLs*, a greater I_C/W is presented in $MgCl_2$ in comparison to NaCl solutions.

Increased I_C/W on SS304L coupled with AA7050 is calculated at elevated temperatures

A comparison of I_C/W at L_{crit} at 25 and 45 ˚C is presented in Figure 13(a), (b), and (c) for 1, 3, and 5.3 M NaCl. At all *WLs* and all NaCl concentrations 45 ˚C has a higher I_C/W in comparison to 25 ˚C despite 45 ˚C having a smaller L_{Crit}.

Increased I_C/W on SS304L coupled with AA7050 is calculated at elevated temperatures

A comparison of I_C/W at L_{Crit} in 1, 3, and 5.3 M NaCl is presented in Figure 13(a) and (b) at 25 and 45 ˚C respectively. Additionally, I_C/W at L_C = 0.5 m in 1, 3, and 5.3 M NaCl is presented in Figure 13(c) and (d), at 25 and 45 ˚C respectively. At L_{Crit} and 25 ˚C (Figure 13(a)), 1 and 3 M NaCl have almost identical behavior, whereas 5.3 M NaCl has lower I_C/W at *WLs* greater than 20 µm. At L_{crit} and 45 ˚C (Figure 13(b)), below a *WL* of 20 µm, all NaCl solutions behave similarly, however, above 20 µm, the I_C/W decreases from 1, 3, to 5.3 M NaCl. At L_C = 0.5 m and 25 ˚C (Figure 13(c)), behavior of all solutions is similar below a *WL* of 100 µm. However, at the thickest *WL* explored (0.05 m), 4.98 M $MgCl_2$ has the highest I_C/W followed by 1, 3, and 5.3 M NaCl in that order. It is interesting to note that between a *WL* of 300 µm and 10,000 µm the data for 3 M NaCl have a higher I_C/W than 1 M NaCl. Finally, at L_C = 0.5 m and 45 ˚C (Figure 13(d)), behavior of all solutions is similar below a *WL* of 10,000 µm above which the highest I_C/W is 1 M NaCl followed by 3 and 5.3 M NaCl.

Discussion

Overall mass transport and diffusive mass transport describe changes in the natural convection layer thickness

The importance of *WL* thickness on the rate of corrosion under atmospheric conditions cannot be understated. One such defining characteristic of a thick *WL* is the presence of natural (or free) convection due to the spontaneous fluid flow created by density gradients. In the present case for NaCl solutions, this flow prevents the oxygen concentration gradient from extending to large distances away from the electrode. In the absence of natural convection, the diffusional boundary layer would continuously increase with time, lowering the diffusion-limited current density continuously [9]. Instead, a well-defined, diffusion-limited current for ORR is found for both Pt and SS304L under all NaCl solutions as presented in Figure 3 and Figure 4 respectively. Calculated δ_{nc} are presented in Figure 6 using the experimental method presented by Liu et al. [9]. In general, i_{lim} for SS in NaCl is slightly below that for Pt (Figure 5) and is attributed to effects of the oxide [36,56]. When the i_{lim} of SS is used to calculate δ_{nc}, this causes an increase in δ_{nc} (Figure 6). Therefore, in order to determine δ_{nc} electrodes that do not have an influence from an oxide, such as Pt, should be utilized.

Although natural convection in electrochemical systems has been discussed previously in the literature [4,7–34], there has been a limited amount of experimental work aimed at determining the quantitative thickness of this layer when oxygen is the reactant on the surface of the alloy; the presented work serves to fill a missing gap. Notably, work has been conducted to describe free convection mass transport [7,18,28–31], specifically when Cu^{2+} ions are reduced in solution [7,18,28,29]; however, the authors do not predict δ_{nc}. Wragg et al. [7,18] and Fenech and Tobias [28] studied free convection under stagnant conditions, producing correlations between dimensionless parameters involving D, density differences between the bulk (ρ_o) and the surface (ρ_i), η, and a characteristic dimension of the electrode (x). In general, the Sh (or Nusselt number for mass transfer) is described in terms of the Schmidt ($Sc = \nu/D$) and Grasshof ($Gr = g * (\rho_o - \rho_i)\rho_{av}^2 x^2/(\rho_i \eta^2)$) numbers. In all cases, a knowledge of the density difference is required to describe the natural convection in the system. In the case of ORR, density differences are unknown and become complex with the addition of ORR byproducts, such as hydroxyl ions.

A further review of natural convection in multiple electrochemistry environments is presented by Novev and Compton [32], however, the quantification of δ_{nc} is seldom presented in literature, especially for atmospheric scenarios, and is highlighted as an important area of study. Of particular note, Amatore and coworkers have determined $\delta_{nc}$for oxidation reactions of multiple solutions [24-27] through the use of a polarized microelectrode. For reactions involving the oxidation $Fe(CN)_6^{4-}$ (10 mM in aqueous 1 M KCl) a δ_{nc} of 230 [24] and 250 µm [25] was measured. For $Fe(CN)_6^{4-}$ (10 mM) and $Fe(CN)_6^{3-}$ (2 mM) in aqueous 1 M KCl a δ_{nc} of 150 µm was measured [26]. For fluorenone (10 mM) and 1-cyanonaphthalene (10 mM) in 0.1 M NBu_4BF_4/DMF a δ_{nc} of 135 µm was measured [27]. The inherent solution and concentration effects on δ_{nc}, as suggested by Liu et al. [9], are apparent not only in one-electron transfer reactions [24-27], but also in ORR reactions, as displayed in Figure 6.

While mass transfer, or Sh, could not be described in terms of dimensionless solution variables due to a lack of data in the present case, Sh can be calculated per Equation 5 and used to describe δ_{nc} as shown in Figure 7. With increasing Sh, δ_{nc} decreases in all cases studied, however, there are differences in governing factors with increased solution concentration or temperature. Sh describes mass transport and can be described as the ratio of overall mass transfer coefficient (K) to diffusive mass transport (D/d) [57] as seen in Equation 5. In order to determine the governing factors of the solution related to mass transport, normalized solution parameters are presented in Figure 15. All variables are normalized with respect to 1 M NaCl at 25 ˚C. With increasing chloride concentration at 25 ˚C (Figure 15(a)), Sh and K increase, however, D_{O_2} and δ_{nc} decrease. Although K increases roughly by a factor of 1.3, D_{O_2} decreases by a factor of 1.7 at 5.3 M NaCl, causing an overall increase in Sh. Thus, with increasing chloride concentration, a greater decrease in diffusive mass transport (D_{O_2}) in comparison to overall mass transport coefficient (K) causes an increase in Sh and a decrease in δ_{nc}. In other words, an increase in chloride concentration decreases δ_{nc} due to an increase in mass transport (Sh) with the dominating influence being a decrease in diffusive mass transport (D_{O_2}).

Considering the case of 1 M NaCl with increasing temperature, now the governing factor in determining δ_{nc} becomes a significant increase in overall mass transport coefficient (K). With increasing temperature at 1 M NaCl (Figure 15(b)), one can see that Sh, K, and D_{O_2} increase, however, δ_{nc} decreases. K increases by roughly a factor of 3.8 and D_{O_2} increases by a factor of 1.5 at 45 ˚C in comparison to 25 ˚C causing for an overall increase in Sh. Thus, with increasing temperature, a greater increase overall mass transport coefficient (K) in comparison in diffusive mass transport (D_{O_2}) causes for an increase in Sh and a decrease in δ_{nc}. In other words, an increase in temperature decreases δ_{nc} due to an increase in mass transport (Sh) with the dominating influence being a significant increase in overall mass transport coefficient (K).

It is important to note that the trend presented agrees with other studies of natural convection boundary layers in literature. Based on the work of Amatore et al. [24], Sh can be calculated for the oxidation of $Fe(CN)_6^{4-}$ to $Fe(CN)_6^{3-}$. Values obtained from their study are as follows: $I = 5\ x\ 10^{-6}\ A$, $d = 1.2\ mm$, $C_{Fe(CN)_6^{4-}} = 0.01\ M$, and $D_{Fe(CN)_6^{4-}} = 5.7\ x\ 10^{-6}\ cm^2/sec$. Based on Equation 5, *Sh* was calculated, and both *Sh* and corresponding δ_{nc} (250 µm) are plotted in Figure 7. While this value lies slightly below the predicted value based on the results presented within, very good agreement is observed. Measurements of δ_{nc} by Amatore et al. were performed in solutions that did not have temperature control and could have influences on convection and δ_{nc} [32,58]. Additionally, *Sh* can also describe δ_{nc} when ORR has a two electron transfer (such as in $MgCl_2$) [45] or less than two electron transfer (such as in NaOH) [55]. Thus, with the knowledge of *Sh* for mass transport in an electrochemical system, the unique fit presented in Figure 7 can be used to predict δ_{nc}.

Regimes of cathodic current are clearly distinguishable and change with chloride concentration and temperature

With changes in L_C, distinct regimes delineate the dependence of cathode current on film thickness for NaCl electrolytes. In general, the potential of the cathode rose from the AA/SS coupling potential at the interface to the OCP of the cathode (SS) as shown in Figure 8. The overall extent and distribution of the potential rise is determined by the ohmic drop and current density in solution. As such, the ohmic drop is determined by the *WL* thickness and temperature, the current/potential relationship, solution conductivity, and the cathode length. A similar treatment to cathodic regimes as was taken by Liu et al. [9] will be presented below.

NaCl Electrolytes

$L_C < L_{Crit}$ – For sufficiently thin *WLs* (< 100 µm), the ohmic drop is dominant, and, generally, less than 20 % of the cathode length was within the M-T limited kinetics (Figure 16(a)). Most of the potentials experienced along the length of the cathode are within activation-controlled kinetics. There are two governing factors for this: (i) an increased ohmic drop due to a thin *WL* and (ii) the potential at which the transition from i_{lim} to activation controlled current densities starts is lower.

For example, under a WL of 8 µm in 1 M NaCl at 25 ˚C, the diffusion limited region starts at a potential of -0.74 V_{SCE} whereas under immersed conditions (δ_{nc} = 714 µm) the diffusion-limited region starts at -0.5 V_{SCE}. With thinner WL (*e.g.*, 8 µm), an increased ohmic drop is present due to the physical geometry and will transition the cathode from M-T kinetics to activation-controlled kinetics at more negative potentials. The current density as a function of distance from the AA/SS interface is shown in Figure 17(a) for L_C = 0.01 m in 1 M NaCl at 25 ˚C and the ohmic drop is signified by the current density decreasing with increased distance from the AA/SS interface. Thus, for small cathode sizes and small WL, the ohmic drop is the controlling mechanism for the galvanic couple. In semi-logarithmic plots such as Figure 9 and Figure 10, the I_C/W region is relatively linear.

For thicker WLs (100 µm to δ_{nc}), there is a combined effect from ohmic and a M-T kinetics. Generally, ohmic resistances dominated when less than 50 % of the cathode was in the region of M-T limited kinetics. When > 50 % of the cathode was within M-T kinetics, the dominant factor controlling the relationship between I_C/W and WL became mass transport with minimal influence from ohmic drop. As a result, for $L_C < L_{Crit}$, the total cathodic current showed a sharp rise with decreasing WL due to the inverse relationship between i_{lim} and the WL thickness and the change in controlling mechanisms. This sharp rise is most evident in 5.3 M NaCl at 25 ˚C for L_C = 0.01 and 0.05 m (Figure 13(c)). The transition between ohmic control and M-T control is illustrated in Figure 12 of Liu et al. [9].

For the large WL thicknesses (> δ_{nc}), the galvanic couple is essentially under full immersion conditions, and ohmic drop across the entire cathode was negligible. The major contribution in this region was the M-T kinetic limitations. The two electrodes were not polarized appreciably from the coupling potential predicted by Mixed Potential Theory. This is shown in Figure 17(a) for WL = 14,000 µm as the cathodic current density moving away from the anode/cathode interface is flat. Generally greater than 50 % of the cathode is in M-T limited kinetics (Figure 16). Thus, the cathodic current density at all points is equal to the coupling current density (for the AA/SS couple, this current density is the mass transport-limited cathodic current density when $WL = \delta_{nc}$) and I_C/W is simply $i_{lim} \cdot L_C$. As shown in Figure 9 and Figure 10, the I_C/W scales linearly with L_C and is generally below I_C/W for a WL of 100 µm. Again, in this regime, the system behaves as if it is fully immersed in the electrolyte.

$L_C = L_{Crit}$ – For sufficiently thin *WLs* (< 100 µm), the behavior is identical to the scenario when $L_C < L_{Crit}$ and ohmic drop is still dominating. A comparison of this behavior is shown for *WL* = 44 µm in 1 M NaCl at 25 ˚C in Figure 17(a). With increased cathode size, the percentage of cathode within M-T limited kinetics decreases (Figure 16(a)), highlighting the importance of ohmic drop in thin *WL*s with increasing cathode size.

For thicker *WLs* (100 µm – δ_{nc}), there again is competition between ohmic drop and M-T limitations. The I_C/W in this regime was constant despite differences in polarization curve behavior with changes in *WL*. With increased *WL* thickness, under the same concentration and temperature, i_{lim} decreases, however, ohmic drop effects will diminish. This unique behavior is illustrated in Figure 17(b) for 1 M NaCl at 25 ˚C. Although Figure 17(b) is for a larger cathode than L_{Crit}, the same trends are present. Directly comparing *WL* thicknesses between 100 µm and δ_{nc} (in this case 714 µm), 100 µm has a greater current density than δ_{nc}. However, the I_C/W also displays the greatest effect from ohmic drop as signified by a sharp decrease in the current density when increasing the distance from the AA/SS interface. Increasing the *WL* from 100 µm to 714 µm, the current density is decreased, but the effects from ohmic drop are also decreased as signified by the current density distribution becoming flatter in Figure 17(b). Thus, when integrating the current along the cathode, I_C/W is roughly the same (Figure 9(a)) between 100 µm and δ_{nc} due to these off-setting phenomena. Another way to approach this effect is to consider the percentage of the cathode that is in the M-T regime. At 100 µm roughly 7 % of the cathode is in M-T limited kinetics, whereas at δ_{nc} (714 µm) roughly 60% of the cathode is in M-T limited kinetics. Thus, under relatively thin *WL*, the effect of the larger ohmic resistance dominated and nulled the effects of enhanced M-T limited kinetics. As a result, I_C/W is constant over this *WL* and L_C range.

For large *WL* thicknesses (> δ_{nc}), the I_C/W displays identical behavior to small cathodes with the caveat that I_C/W is slightly greater than that at δ_{nc}. Again, I_C/W scales directly with cathode size as the couple is essentially under full immersion conditions.

L_C > *L_{Crit}* – For sufficiently thin *WLs* (< 100 µm), the behavior is identical to the two previous scenarios. A comparison of the cathodic current densities for all cathode lengths is shown for *WL* = 44 µm in 1 M NaCl at 25 ˚C in Figure 17(a). With increased cathode size, the cathodic current density decreases and the percentage of cathode within M-T limited kinetics decreases (Figure 16(a)). For thicker *WLs* (100 µm – δ_{nc}), there again is competing factors between ohmic drop and M-T limitations. These trends are identical for when L_C = L_{Crit}. Finally, for large *WL* thicknesses (> δ_{nc}), the trends are the same as the previous groupings with I_C/W increased in comparison to I_C/W at δ_{nc}.

Overall, there is little experimental validation of the presented phenomena as the majority of studies performed are across orders of magnitude of *WL* and do not vary electrode sizes. Of recent note, Tran et al. looked at the coupling current density as a function of *WL* thickness in an aluminum 6061-T6 with a high strength steel (HSS) in 2 M NaCl solutions in thin *WL* [59]. The experimental arrangement contained two (one AA and one HSS) 0.01 × 0.01 m (1 × 1 cm) electrodes mounted 0.005 m apart in an epoxy resin. Various *WL* thicknesses were placed on top of the couple and with decreasing *WL* thickness, an increase in the coupling current density was measured for the AA/HSS couple [59]. This scenario is most similar to the cathode size of 0.01 m presented in Figure 9(a) and (b) for 1 and 3 M NaCl. Calculated I_C/W is 8.7 and 7.7 times higher at a *WL* of 25 µm in comparison to bulk solutions for 1 and 3 M NaCl respectively. This arrangement equates to an average increase in I_C/W of a factor of 8.2 for 25 µm in comparison to bulk solutions and would be comparable to 2 M NaCl. Tran et al. reported a corrosion rate increase of a factor of 8 for a *WL* of 25 µm in comparison to bulk solutions in 2 M NaCl [59] which fits quite well with the modeled currents in Figure 9(a) and (b) and shows the efficacy of this study.

Under all L_C – Thin *WLs* (< 100 um) exhibit the same I_C/W across all L_C greater than 0.05 m despite the larger cathodes having more length to provide current to the anode. When comparing all cathode lengths and thin *WLs* (Figure 17(a)), the current densities are constant at and near the stainless steel/aluminum alloy interface. The constant I_C/W near to the interface is due to the fact that the first few mm of the cathode contribute over 90 % of the total current to I_C/W [9]. Thus, it is not surprising that I_C/W under thin *WL* thicknesses is independent of the cathode length. When cathode lengths are under 0.05 m, the I_C/W is limited by the size of the cathode. On the contrary, the I_C/W at thick water layers (> δ_{nc}) are dependent on the cathode size, because there is limited to no ohmic drop (a constant current density as a function of distance from the interface is shown in Figure 17(a) for the entire cathode length), and the current density is essentially the coupling current density multiplied by the cathode size.

Increasing solution concentration decreases I_C/W due to a significant decrease in C_{O_2} but increases the percentage of the cathode in M-T kinetics due to an increased κ for NaCl solutions. First, when increasing solution concentration, i_{lim} decreases due to a decreased C_{O_2} and D_{O_2} and an increase ν (Equation 3). C_{O_2} has the most severe decrease (Figure 15) and is directly proportional to i_{lim} (Equation 3), thus, will be the most influential parameter when changing solution concentration. Next, a decrease in solution concentration also decreases the current density in the activation-controlled regime. These differences can be seen in Figure 3 and Figure 4 by comparing the individual rows. Finally, with increased solution concentration in NaCl electrolytes, an increase in solution conductivity is present [53]. When directly comparing I_C/W (Figure 14), a decrease in I_C/W is calculated at all L_C values used with an increased solution concentration due to a decrease in i_{lim}. Additionally, an increase in solution concentration increases the percentage of L_C that is in the M-T limited kinetics region because an increase in solution conductivity decreases the ohmic drop and broadens the M-T regime. These two competing phenomena are shown in Figure 17(c) for a large cathode and two WLs (40 and 10,000 µm) in 1 and 5.3 M NaCl at 25 ˚C. Under a WL = 40 µm, an increased current density is calculated in the 1 M NaCl in comparison to 5.3 M NaCl, however, a more rapid decrease in the current density is calculated when moving away from the interface in 1 M NaCl in comparison to 5.3 M NaCl. This effect causes a lower percentage of the cathode to be in M-T kinetics for lower concentrations (Figure 16(b) and (c)).

Increasing the solution temperature increases both I_C/W and percentage of L_C that is within the M-T limited kinetics region. An increase in temperature increases i_{lim} based on Equation 17 due to an exponential increase in D_{O_2} (Figure 2(d) and Figure 15). Additionally, the activation-controlled kinetics are enhanced at elevated temperatures. These two electrochemical trends can be seen when comparing columns in Figure 3 and Figure 4. Finally, an increase in temperature will increase κ [53]. Combining these phenomena will increase I_C/W with increased temperature (Figure 9) as the cathode will experience less ohmic drop (due to increased conductivity), keeping a greater portion of the cathode in the M-T limiting kinetics region (Figure 16(b) and (c)). This can also be seen in Figure 17(d) where, with increased temperature, the calculated cathodic current density is higher and there is less of an ohmic drop effect as signified by a flatter curve.

$MgCl_2$ electrolytes

In saturated $MgCl_2$, distinct regions based on cathode size do not occur (Figure 12) due to a lack of i_{lim} and lack of *WL* dependence on the cathodic kinetics [45]. This indicates that ohmic control is dominating at all L_C and *WL* in 4.98 M $MgCl_2$. As such, there is no decrease in I_C/W with increasing *WL* thickness as there is in NaCl (Figure 12(b)). Under very thin *WLs* (< 30 – 50 µm based on L_C), NaCl has a higher calculated I_C/W (Figure 12(c)). In thin NaCl solutions, an elevated i_{lim} is measured (Equation 1), however, in $MgCl_2$ solutions there is no *WL* dependence and the solution is under activation-controlled HER [45]. Additionally, saturated $MgCl_2$ has a lower conductivity [54] in comparison to saturated NaCl [53]. A lower conductivity in $MgCl_2$ solutions will cause a greater ohmic drop effect in thin *WL* in comparison to saturated NaCl solutions, and because the polarization scan is under activation-controlled kinetics, a greater decrease in the current density is calculated. These competing phenomena are presented in Figure 17(e). Now, in thicker *WL*, saturated NaCl experiences a much smaller i_{lim} in comparison to the activation-controlled $MgCl_2$ kinetics, and, despite ohmic drop still being present at thicker *WL* in $MgCl_2$ as shown in Figure 17(e), a higher I_C/W is calculated.

A similar relationship between NaCl and $MgCl_2$ electrolytes is observed when predicting localized pitting corrosion on a SS using the formulism presented by Chen and Kelly [60]. The model relies on the fact that under freely corroding conditions, pitting can be considered a galvanic couple with the pit (the anode) growing only as long as the anodic current required to maintain the critical solution chemistry is predominantly supported by current from the surrounding material (the cathode). Under the same salt loading density (3 g/m^2), both saturated NaCl and $MgCl_2$ have a *WL* less than 10 µm, and the predicted pit size and predicted cathodic current are larger for saturated NaCl solutions [54]. This is exactly what is predicted in an AA/SS galvanic couple under thin *WL* conditions, as the I_C/W is larger for saturated NaCl solutions (Figure 12(c)).

Implications and Limitations

As with all models, the modeling approach used here has several limitations. First, an assumption is made that a uniform thin layer of electrolyte exists across the entire galvanic couple, which is not always the case in practice due to imperfect wetting, especially at the edge of the cathode/anode. This imperfect wetting would lead to a shorter effective length of cathode available. Next, the assumption of a static and uniform electrolyte layer with constant chemical concentration and conductivity neglects the fact of changes in chemical (solution chemistry, corrosion products), electrochemical (corrosion kinetics) and physical (evaporation, temperature) conditions that can and do occur with time. Third, the current work focused on the contribution from the cathode, using an anode that is largely non-polarizable. Fourth, the assumption of steady-state is made in the study, neglecting the time-evolution of cathodic current available and the evolution of the brine on the surface which can have precipitates or changing boundary conditions. If boundary conditions were dependent upon the pH in solution, it is believed that a decrease in modeled current would occur due to a decrease in the reversable potential for ORR, a decrease in i_{lim}, and a decrease in the number of electrons transferred. Thus, it is believed the presented model is conservative because all of these effects would decrease the predicted current. Fifth, only ohmic drop is considered, which is an intrinsic limitation of the use of Laplace Equation-based modeling, with diffusion effects being captured through the effects on cathodic kinetics. Sixth, the anodic polarization scan of AA was assumed to be constant with changes in temperature and chloride concentration. Finally, quiescent polarization scans were measured with the electrode perpendicular to gravity.

Despite these limitations, the implications of this work, both in terms of natural convection boundary layer thickness determination and galvanic coupling modeling, should be noted. First, the method for determining δ_{nc}, first proposed by Liu et al. [9], was extended to elevated solution compositions and temperatures. The δ_{nc} was determined with the electrode perpendicular to gravity, thus the value determined may not transfer to other configurations. However, one polarization scan was taken with the electrode parallel to gravity (typical flat cell configuration), the i_{lim} was utilized to calculate a new δ_{nc}, and only produced a δ_{nc} that was roughly 40 µm smaller in comparison (~5 % smaller) to the configuration use in Figure 6 at 1 M NaCl at 25 ˚C. This would indicate a minor directional dependence on δ_{nc}, however, further research is necessary. This work further produced a way to predict δ_{nc} in using Sh and was cross-validated with other electrochemical systems, including ORR reactions with two electron transfers ($MgCl_2$ electrolytes) and one electron transfer (NaOH electrolytes), and a one electron transfer of $Fe(CN)_6^{4-}$ to $Fe(CN)_6^{3-}$ [24]. It is noted that in Equation 5, a dependence on the electrode diameter is present. In this study a constant electrode diameter of 0.5 cm was utilized. Fenech and Tobias [28] and Wragg [18] noted that utilizing larger electrode diameters (> 0.5 cm) produced a constant i_{lim} which would indicate a constant δ_{nc}. Thus, extrapolating δ_{nc} values determined in this study to larger electrodes would be valid. Caution should be taken when extrapolating to smaller electrodes sizes due to an increase in i_{lim} with decreasing electrode size. Additionally, when utilizing the fit present in Figure 7 to predict δ_{nc}, the same electrode size should be utilized as further validation is needed to apply the fit to larger electrode diameters.

The importance of knowing δ_{nc} cannot be understated and was shown by exploring an AA/SS galvanic coupling. When considering sample exposures in real-life, atmospheric environments, the value of δ_{nc} and L_C determine if a decrease in total current is experienced with increased *WL*. For example, in saturated NaCl solutions, at 25 ˚C, and *WLs* above δ_{nc} (300 µm), any cathode length shorter than 0.32 m (32 cm) experiences I_C/W decreases in comparison to 100 µm *WL* due to M-T limitations. These limitations should be considered when selecting sample sizes for accelerated chamber testing and atmospheric exposure scenarios. Having a sample that is too small will decrease I_C/W and potentially the corrosion damage experienced. In accelerated testing environments akin the ASTM B117, *WL* thicknesses are highly dependent upon angle of the sample and range from 660 – 1210 µm at exposure angles of 15˚ to 30˚ respectively [47]. In most scenarios, the exposed sample is going to be under full immersion conditions especially at high angles of exposure and the total I_C/W will be dependent upon cathode size. Samples that are too small, will be non-conservative as a decrease in I_C/W will be experienced at thick *WLs*. Therefore, if small samples are utilized in accelerated testing ($L_C < L_{Crit}$), the corrosion damage may be reduced due to M-T limitations in full immersion conditions and will not provide for an accurate representative of thin film, in-service atmospheric environments. Overall, corrosion damage due to the variation in I_C/W in a galvanic couple can vary between accelerated corrosion tests and in-service damage and relies heavily on the sample size.

In atmospheric conditions, WL formation through salt deliquescence is possible and the cathodic current in a galvanic couple can be predicted as a function of environment. The WL is dictated by the loading density (LD, grams of salt per unit surface area, g/m^2), the specific gravity of the solution (ρ_{sp}), the molecular weight (MW), and the equilibrium concentration of the salt (C_{eq}) ($WL = (LD.\rho_{sp})/(MW.C_{eq})$) [61]. C_{eq} is controlled by the relative humidity (RH), because RH is equal to the activity of water based on the brine composition under equilibrium conditions. As the RH decreases, the concentration of chloride species in solution increases [1]. This is due to the fact that the lower RH represents lower activities of water in the gas phase, and at equilibrium, the activity of water in the liquid phase must match it. To achieve this equilibrium, some of the water evaporates. Therefore, I_C/W can be calculated as a function of RH and LD and is presented in Figure 18. With increased RH, LD, and L_C, I_C/W increases. First, increasing RH decreases NaCl concentration. As presented in Figure 14, a decrease in NaCl concentration increases I_C/W. Thus, increasing RH increases I_C/W. Next, increasing LD increases WL thickness. Considering 5.3 M NaCl, at a LD = 0.5 g/m^2, the WL is 1.93 um and at a LD = 3 g/m^2 the WL is 11.59 um. This six-fold increase in WL will increase the I_C/W. Although this may be the case for the presented LD, if a loading density were achieved where full immersion conditions where present, a decrease in I_C/W would occur for a L_C = 0.01 m. As shown in Figure 9, for L_C = 0.01 m and as previously discussed in Section 4.2, a decrease in I_C/W would be observed. This, however, is very unlikely, as an astronomical loading density of 77 g/m^2 is required to reach full immersion conditions ($WL = \delta_{nc} = 297\ \mu m$). Finally, an increase in L_C increases I_C/W at all RH. While small WL typically have an I_C/W that is independent of L_C, an L_C = 0.01 m is limited by physical size and will cause for a decrease in I_C/W. Any $L_C \geq 0.05$ m will behave nearly identical to 0.5 m under the LD presented. Overall, an increase in RH (decrease in NaCl concentration) increases in I_C/W and highlights the important, controlling behavior of cathodic kinetics in atmospheric corrosion.

Conclusions

This study presents cathodic kinetics of platinum and stainless steel 304L in elevated sodium chloride concentrations (1, 3, and 5.3 M NaCl) and elevated temperatures (25, 35, and 45 ˚C) as a function of boundary layer thickness. The natural convection layer was determined for all scenarios presented, and, with increasing temperature and chloride concentration, the natural convection decreases. For the first time, the dependence of the natural convection boundary layer was described by the Sherwood number enabling the prediction of the natural convection boundary layer with a polarization scan and readily available solution parameters. Additionally, the total cathodic current capacity of an aluminum/stainless steel galvanic couple was evaluated as a function of electrolyte film thickness, electrolyte composition, and cathode size. The water layer ranged from full immersion conditions where mass-transport kinetics dominated to the thin film regime where ohmic drop dominated. The natural convection boundary layer defined the upper limit for thin film atmospheric corrosion; for water layers above this limit the total cathodic current scaled with cathode size. A decrease in total cathodic current of the galvanic couple was calculated with increasing chloride concentration due to a decrease in oxygen solubility, decreasing mass transport kinetics. An increase in total cathodic current was calculated with an increase in temperature due to an increase in diffusivity, increasing mass transport kinetics. The results of this study have important implications for sample sizing and corrosion prediction as a function of environment.

Acknowledgements

Sandia National Laboratories is a multi-mission laboratory managed and operated by National Technology and Engineering Solutions of Sandia, LLC., a wholly owned subsidiary of Honeywell International, Inc., for the U.S. Department of Energy's National Nuclear Security Administration under contract DE-NA0003525. Financial assistance from the U.S. Department of Energy's Nuclear Energy University Program under contract DE-NE0008901 is also acknowledged. Helpful discussions with Dr. Charles Bryan (Sandia National Laboratories) and Dr. Chao Liu (Shell) are gratefully acknowledged. This document is SAND2021-2792 J.

Data Availability

The raw/processed data required to reproduce these findings cannot be shared at this time as the data also forms part of an ongoing study.

References

[1] C.R. Bryan, E.J. Schindelholz, in: Corros. 2018, Phoenix, (2018), p. Paper 10516.

[2] M. Stratmann, Berichte Der Bunsengesellschaft Für Phys. Chemie, 94, 626–639 (1990).

[3] I.S. Cole, N.S. Azmat, A. Kanta, M. Venkatraman, Int. Mater. Rev., 54, 117–133 (2009).

[4] N.D. Tomashov, Corrosion, 20, 7t-14t (1964).

[5] E. Schindelholz, R.G. Kelly, Corros. Rev., 30, 135–170 (2012).

[6] H. Simillion, O. Dolgikh, H. Terryn, J. Deconinck, Corros. Rev., 32, 73–100 (2014).

[7] A.A. Wragg, T.K. Ross, Electrochim. Acta, 12, 1421–1428 (1967).

[8] V.G. Levich, Physiochemical Hydrodynamics, Prentice Hall Inc., NJ, (1962).

[9] C. Liu, J. Srinivasan, R.G. Kelly, J. Electrochem. Soc., 164, C845–C855 (2017).

[10] O. Dolgikh, A.C. Bastos, A. Oliveira, C. Dan, J. Deconinck, Corros. Sci., 102, 338–347 (2016).

[11] H. Simillion, N. Van den Steen, H. Terryn, J. Deconinck, Electrochim. Acta, 209, 149–158 (2016).

[12] R. Marshall, R. Kelly, A. Goff, C. Sprinkle, Corrosion, 75, 1461–1473 (2019).

[13] A. Nishikata, Y. Yamashita, H. Katayama, T. Tsuru, A. Usami, K. Tanabe, H. Mabuchi, Corros. Sci., 37, 2059–2069 (1995).

[14] A. Nishikata, Y. Ichihara, T. Tsuru, Corros. Sci., 37, 897–911 (1995).

[15] A. Nishikata, J. Electrochem. Soc., 144, 1244–1252 (1997).

[16] M. Stratmann, H. Streckel, K.T. Kim, S. Crockett, Corros. Sci., 30, 715–734 (1990).

[17] M. Stratmann, H. Streckel, Corros. Sci., 30, 681–696 (1990).

[18] A.A. Wragg, Electrochim. Acta, 13, 2159–2165 (1968).

[19] M. Stratmann, H. Streckel, Corros. Sci., 30, 697–714 (1990).

[20] G.S. Frankel, M. Stratmann, M. Rohwerder, A. Michalik, B. Maier, J. Dora, M. Wicinski, Corros. Sci., 49, 2021–2036 (2007).

[21] O. Dolgikh, A. Demeter, S. V. Lamaka, M. Taryba, A.C. Bastos, M.C. Quevedo, J. Deconinck, Electrochim. Acta, 203, 379–387 (2016).

[22] Y.L. Cheng, Z. Zhang, F.H. Cao, J.F. Li, J.Q. Zhang, J.M. Wang, C.N. Cao, Corros. Sci., 46, 1649–1667 (2004).

[23] S.H. Zhang, S.B. Lyon, Corros. Sci., 35, 713–718 (1993).

[24] C. Amatore, S. Szunerits, L. Thouin, J.S. Warkocz, J. Electroanal. Chem., 500, 62–70 (2001).

[25] C. Amatore, C. Pebay, L. Thouin, A. Wang, Electrochem. Commun., 11, 1269–1272 (2009).

[26] C. Amatore, S. Szunerits, L. Thouin, J.-S. Warkocz, Electrochem. Commun., 2, 353–358 (2000).

[27] C. Amatore, S. Szunerits, L. Thouin, J.S. Warkocz, Electroanalysis, 13, 646–652 (2001).

[28] E.J. Fenech, C.W. Tobias, Electrochim. Acta, 2, 311–325 (1960).

[29] C.R. Wilke, M. Eisenberg, C.W. Tobias, J. Electrochem. Soc., 100, 513 (1953).

[30] C.W. Tobias, M. Eisenberg, C.R. Wilke, J. Electrochem. Soc., 99, 359C (1952).

[31] N. Ibl, Electrochim. Acta, 1, 117–129 (1959).

[32] J.K. Novev, R.G. Compton, Curr. Opin. Electrochem., 7, 118–129 (2018).

[33] U.-E. Charles-Granville, C. Liu, J.R. Scully, R.G. Kelly, J. Electrochem. Soc., 167, 111507 (2020).

[34] E. Gileadi, Electrode Kinetics for Chemists, Chemical Engineers, and Materials Scientists, VCH Publishers, Inc., (1993).

[35] P. Scarf, P. Laycock, J. Res. Natl. Inst. Stand. Technol., 99, 313 (1994).

[36] C.L. Alexander, C. Liu, A. Alshanoon, R.M. Katona, R.G. Kelly, J. Carpenter, C. Bryan, E. Schindelholz, J. Electrochem. Soc., 165, C869–C877 (2018).

[37] R.S. Marshall, A. Goff, C. Sprinkle, A. Britos, R.G. Kelly, Corrosion, 76, 476–484 (2020).

[38] N. Van Den Steen, H. Simillion, O. Dolgikh, H. Terryn, J. Deconinck, Electrochim. Acta, 187, 714–723 (2016).

[39] A.D. King, J.S. Lee, J.R. Scully, J. Electrochem. Soc., 163, C342–C356 (2016).

[40] S. Palani, T. Hack, J. Deconinck, H. Lohner, Corros. Sci., 78, 89–100 (2014).

[41] C. Liu, G.W. Kubacki, R.G. Kelly, Corrosion, 75, 465–473 (2019).

[42] M. Attarchi, A. Brenna, M. Ormellese, Corros. Sci., 179, 109116 (2021).

[43] V.N. Rafla, P. Khullar, R.G. Kelly, J.R. Scully, J. Electrochem. Soc., 165, C562–C572 (2018).

[44] Z.Y. Chen, F. Cui, R.G. Kelly, J. Electrochem. Soc., 155, C360–C368 (2008).

[45] R.M. Katona, J.C. Carpenter, A.W. Knight, C.R. Bryan, R.F. Schaller, R.G. Kelly, E.J. Schindelholz, Corros. Sci., 177, 108935 (2020).

[46] ASTM B117-19, ASTM International, West Conshohocken, PA,1-12 (2017).

[47] R.M. Katona, S. Tokuda, J. Perry, R.G. Kelly, Corros. Sci., 175, 108849 (2020).

[48] V.L. Thurmond, R.W. Potter, The Densities of Saturated Solutions of NaCl and KCl from 10C to 105C, (1984).

[49] L.S. Clesceri, A.E. Greenberg, A.D. Eaton, Standard Methods for the Examination of Water and Wastewater, Washington DC, (1998).

[50] J.H. Carpenter, Limnol. Oceanogr., 10, 141–143 (1965).

[51] V.G. Levich, Acta Physicochim. Urss, 17, 257 (1942).

[52] C. Liu, R.G. Kelly, Corrosion, 75, 1285–1299 (2019).

[53] R.M. Katona, J. Carpenter, E.J. Schindelholz, R.G. Kelly, J. Electrochem. Soc., 166, C3364–C3375 (2019).

[54] R.M. Katona, A.W. Knight, E.J. Schindelholz, C.R. Bryan, R.F. Schaller, R.G. Kelly, Electrochim. Acta, 370, 137696 (2021).

[55] R.M. Katona, J. Carpenter, R.G. Kelly, E.J. Schindelholz, R.F. Schaller, Prep., (2020).

[56] C. Liu, R.G. Kelly, Corrosion, 75, 1087–1099 (2019).

[57] M. Ghassemi, A. Shahidian, in: Nano Bio Heat Transf. Fluid Flow, Elsevier, (2017), pp. 31–56.

[58] C. Amatore, C. Pebay, C. Sella, L. Thouin, ChemPhysChem, 13, 1562–1568 (2012).

[59] V.N. Tran, A. Ooi, E. Tada, A. Nishikata, J. Electrochem. Soc., 167, 131507 (2020).

[60] Z.Y. Chen, R.G. Kelly, J. Electrochem. Soc., 157, C69–C78 (2010).

[61] M.T. Woldemedhin, M.E. Shedd, R.G. Kelly, J. Electrochem. Soc., 161, E3216–E3224 (2014).

Figures and Captions

Figure 1: Schematic configuration of a galvanic couple under a thin water layer (304L cathode with AA7050 anode in this study). Width of anode/cathode is normal to x-y plane. Figure adapted from Liu et al. [9].

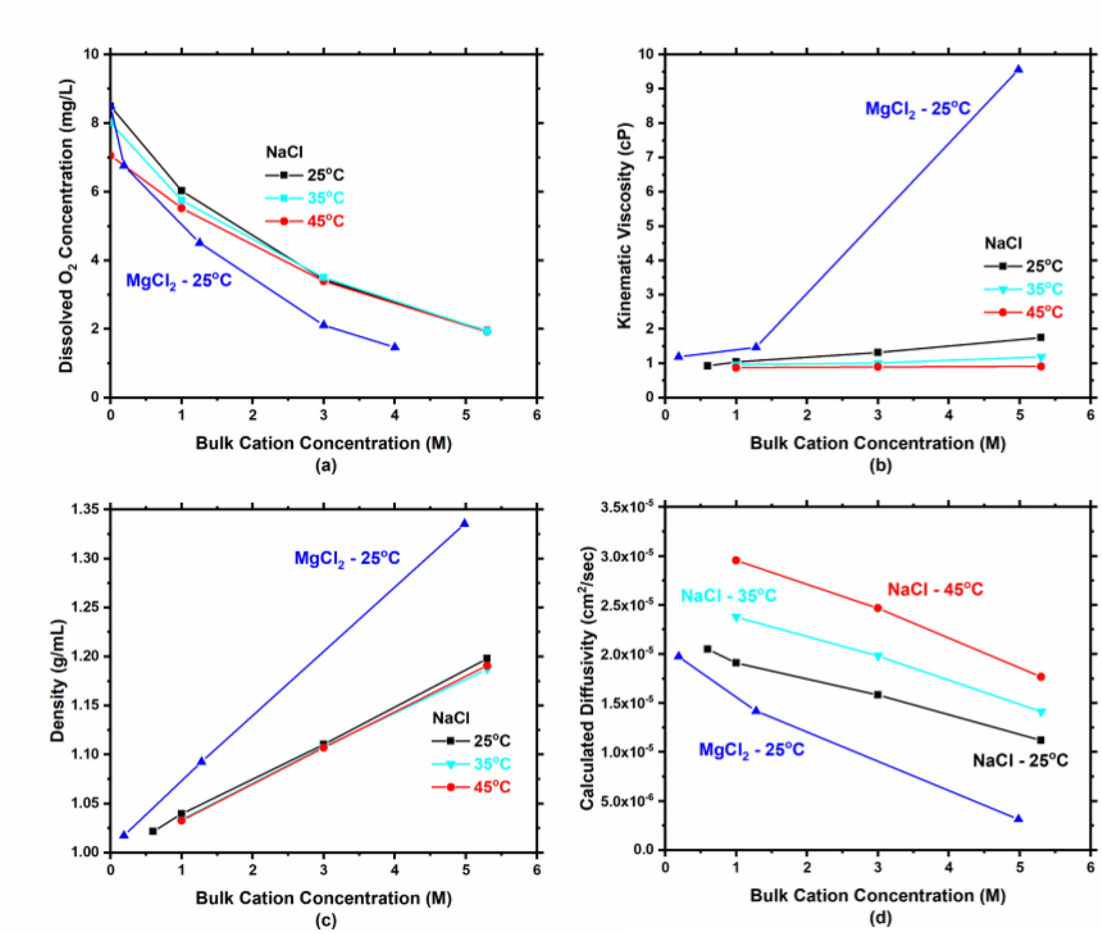

Figure 2: Experimentally measured (a) dissolved oxygen, (b) kinetic viscosity, and (c) density for NaCl and MgCl₂ solutions as a function of chloride concentration and temperature. It is noted that values for MgCl₂ are obtained from Katona et al. [45]. (d) Calculated (modeled) oxygen diffusivity using OLI for NaCl and MgCl₂ solutions as a function of chloride concentration and temperature. It is noted that the lines present are not fits but are present to help the reader connect points.

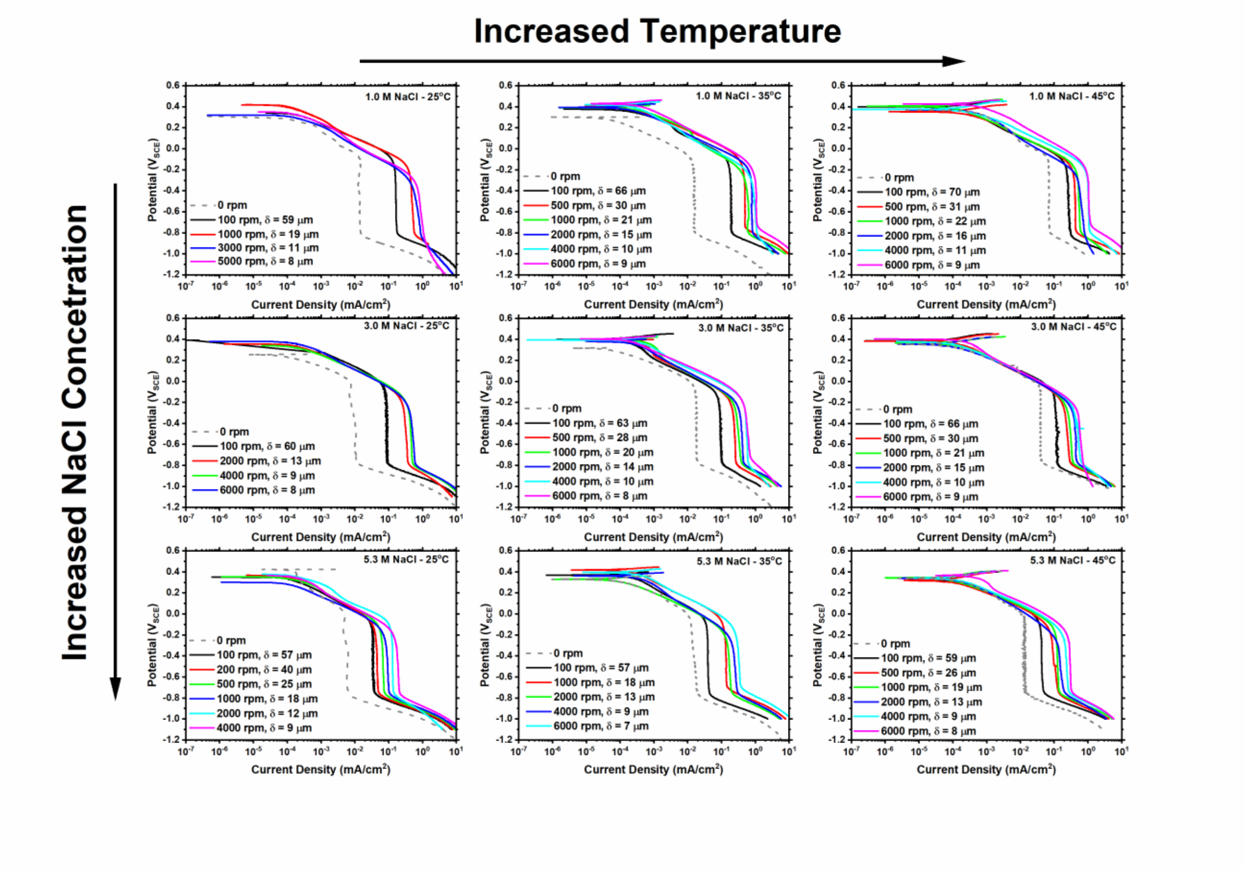

Figure 3: Experimentally measured cathodic polarization scans for platinum in NaCl electrolyte at multiple concentrations (1, 3, 5.3 M) and temperatures (25, 35, and 45 ˚C). It is noted that moving from the top to the bottom increases the concentration and moving from left to right increases temperature.

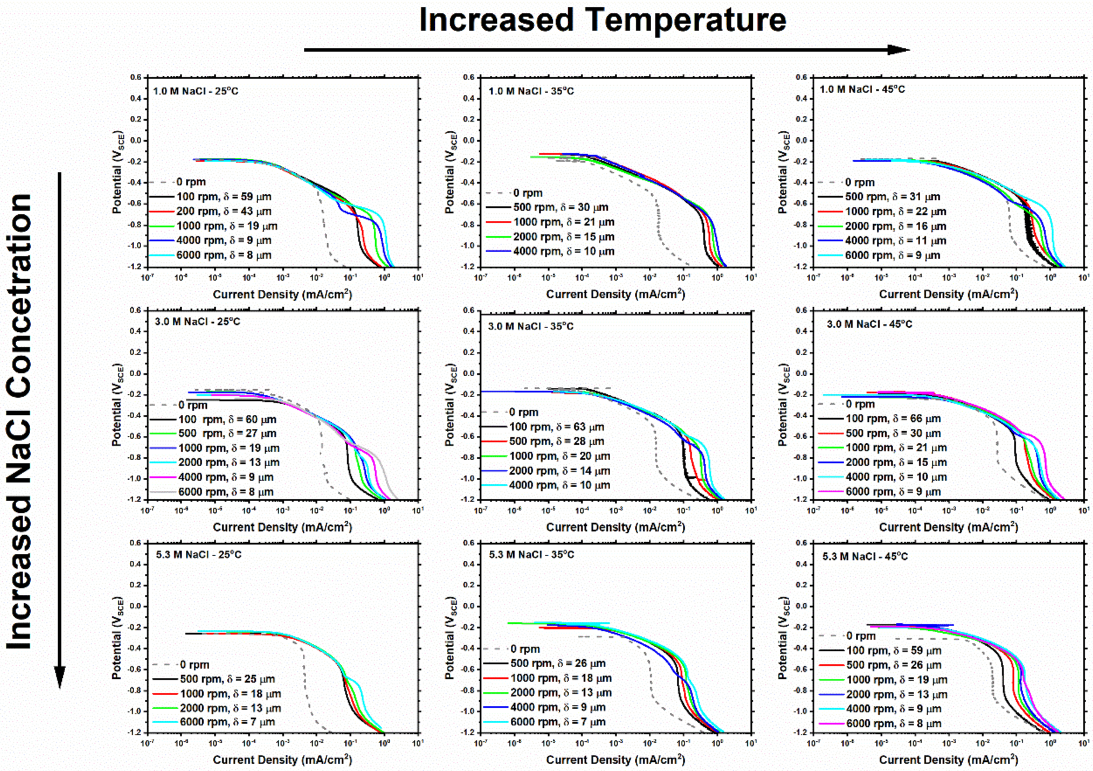

Figure 4: Experimentally measured cathodic polarization scans for SS304L in NaCl electrolyte at multiple concentrations (1, 3, 5.3 M) and temperatures (25, 35, and 45 ˚C). It is noted that moving from the top to the bottom increases the concentration and moving from left to right increases temperature.

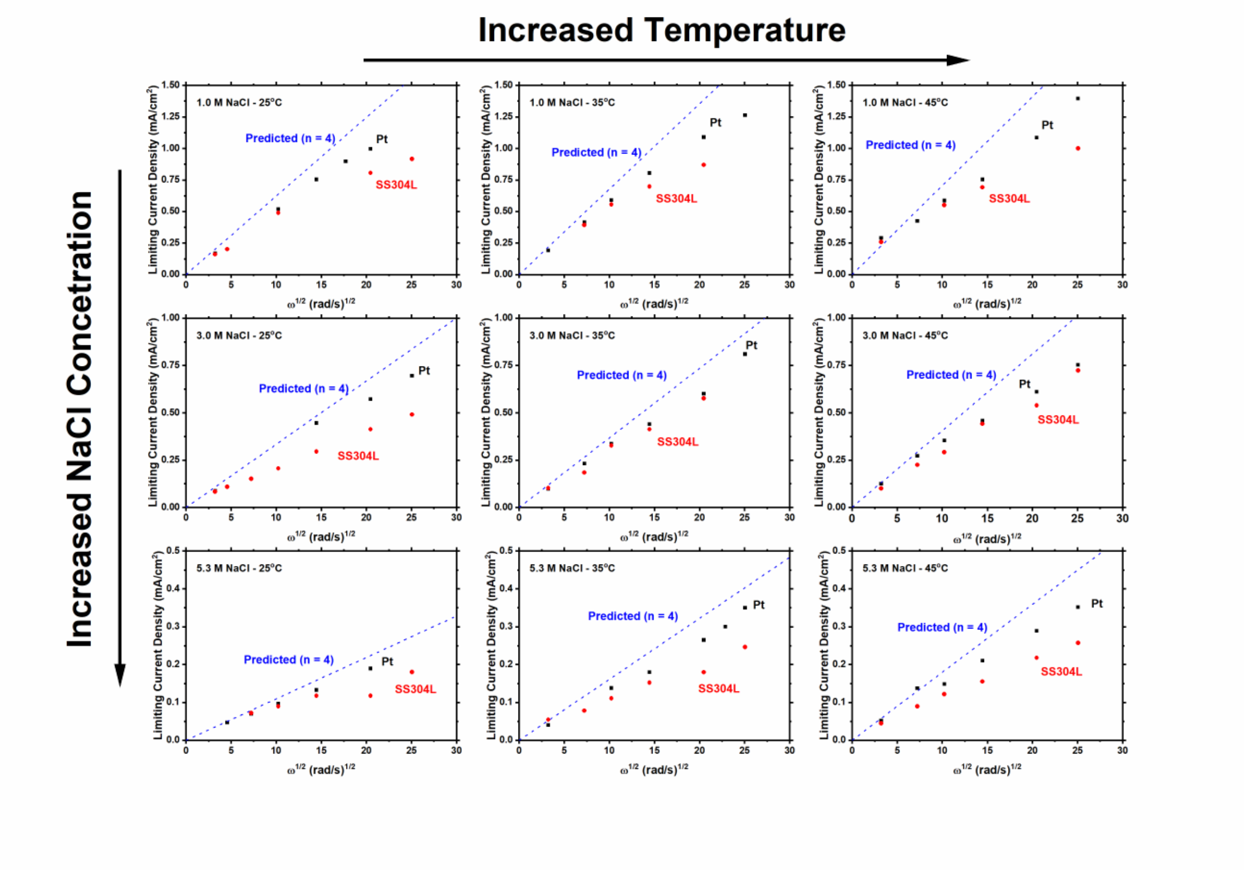

Figure 5: Levich analyses for platinum and SS304L as a function of chloride concentration and temperature. It is noted that moving from the top to the bottom increases the concentration and moving from left to right increases temperature. The dashed line represents theoretical behavior from experimental and modeling results while individual points represent experimentally determined values.

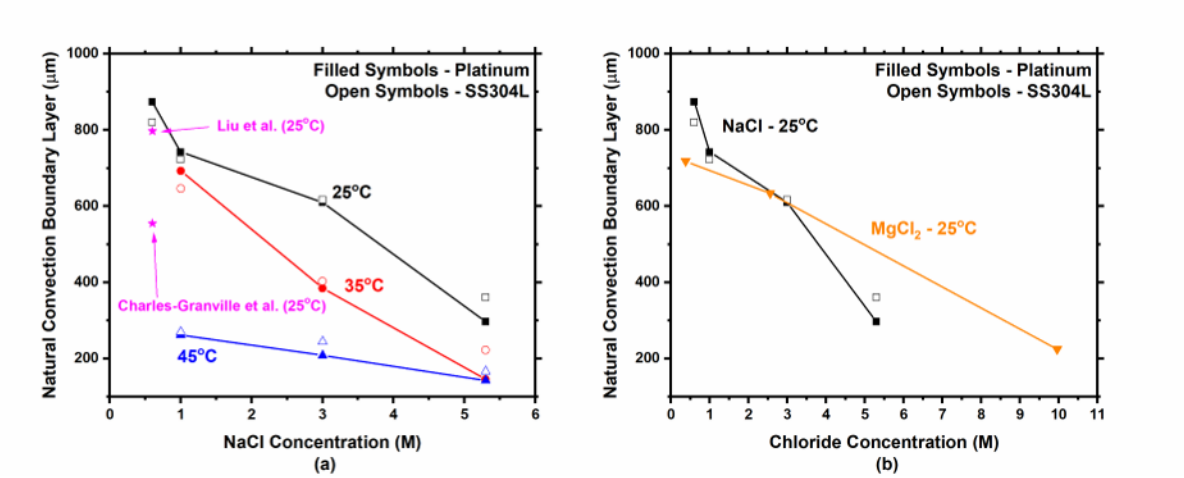

Figure 6: Experimentally calculated natural convection boundary layer thickness as a function of (a) NaCl concentration and temperature and (b) solution composition (NaCl and $MgCl_2$) at 25 ˚C. It is noted that the x-axis of (b) is total chloride concentration.

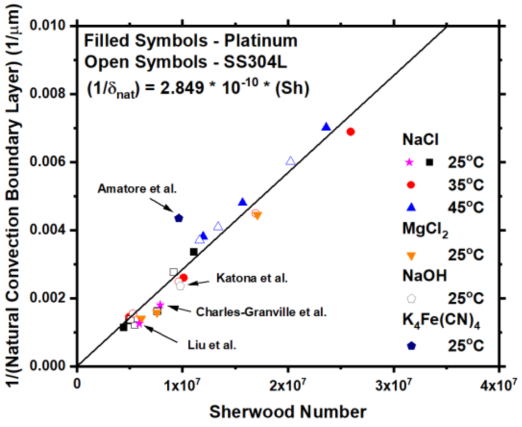

Figure 7: Inverse of natural convection boundary layer as a function of calculated Sherwood number (Sh). Values also plotted were obtained from Liu et al. [9], Charles-Granville et al. [33], Katona et al. [55], and Amatore et al. [25].

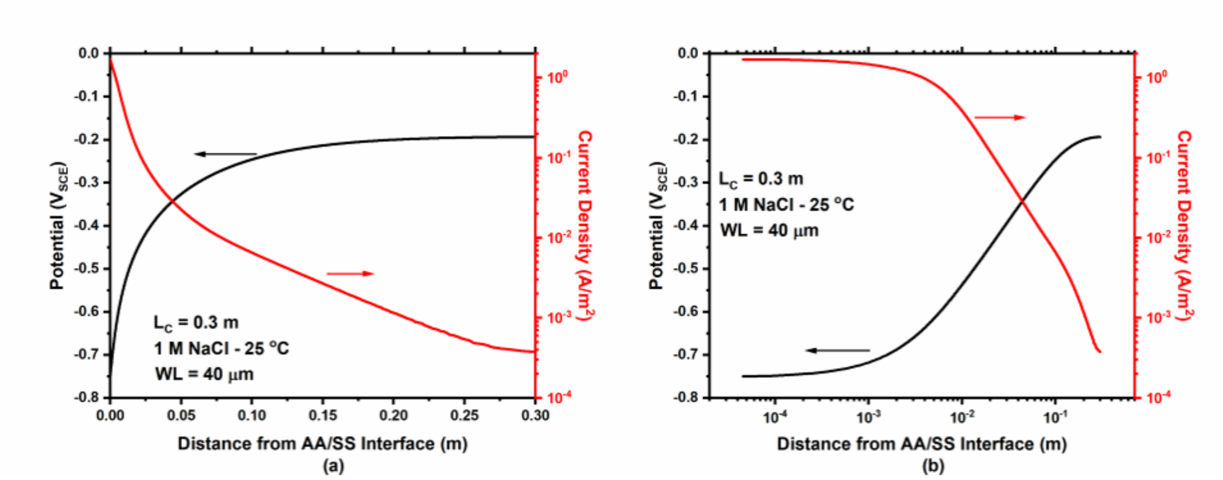

Figure 8: (a) Modeled potential and current density distributions of the cathode as a function of linear distance from the AA/SS interface for 1 M NaCl at 25 ˚C and a cathode length of 0.3 m. (b) Distributions in (a) with a logarithmic distance from the AA/SS interface.

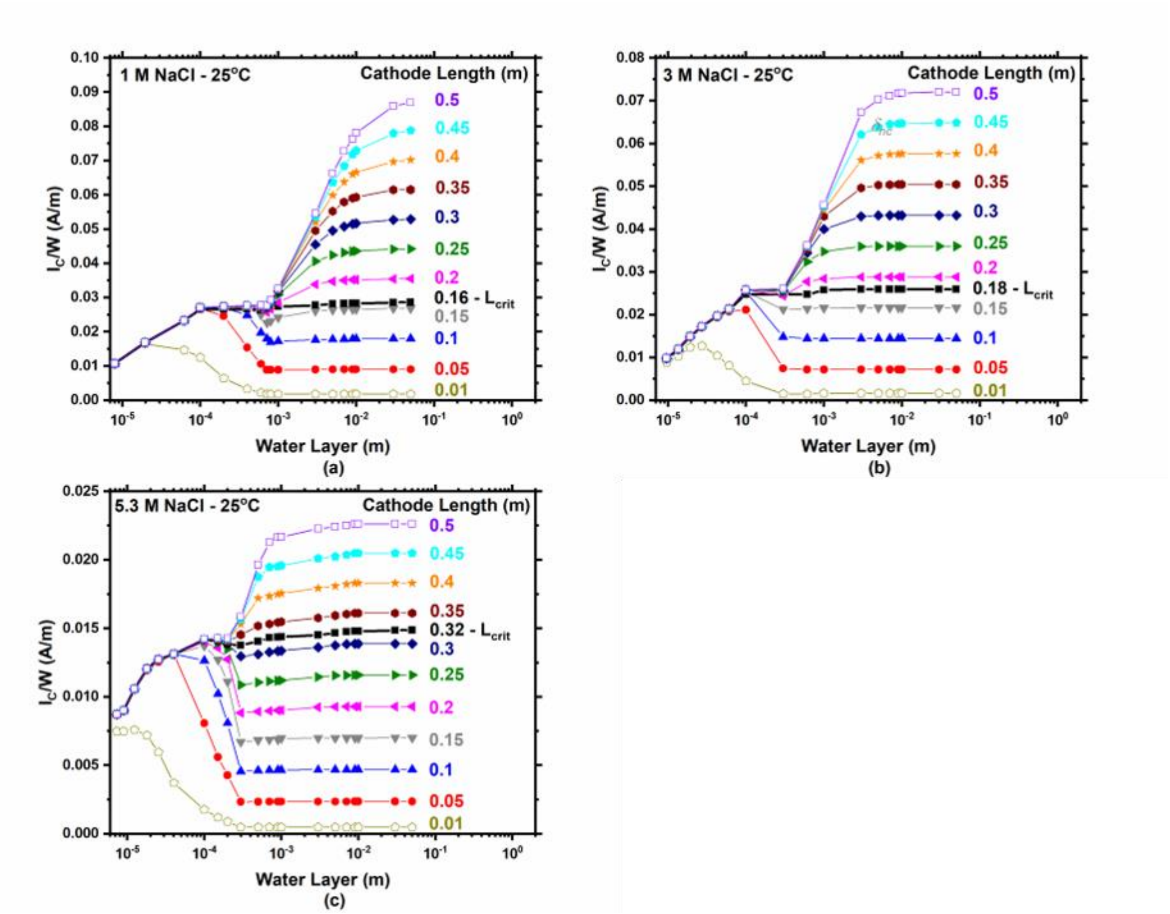

Figure 9: Modeled total cathodic current per cathode width (I_C/W) vs. water layer thickness as a function of cathode length at 25˚C for (a) 1, (b) 3, and (c) 5.3 M NaCl. It is noted that the ordinate in all graphs is different.

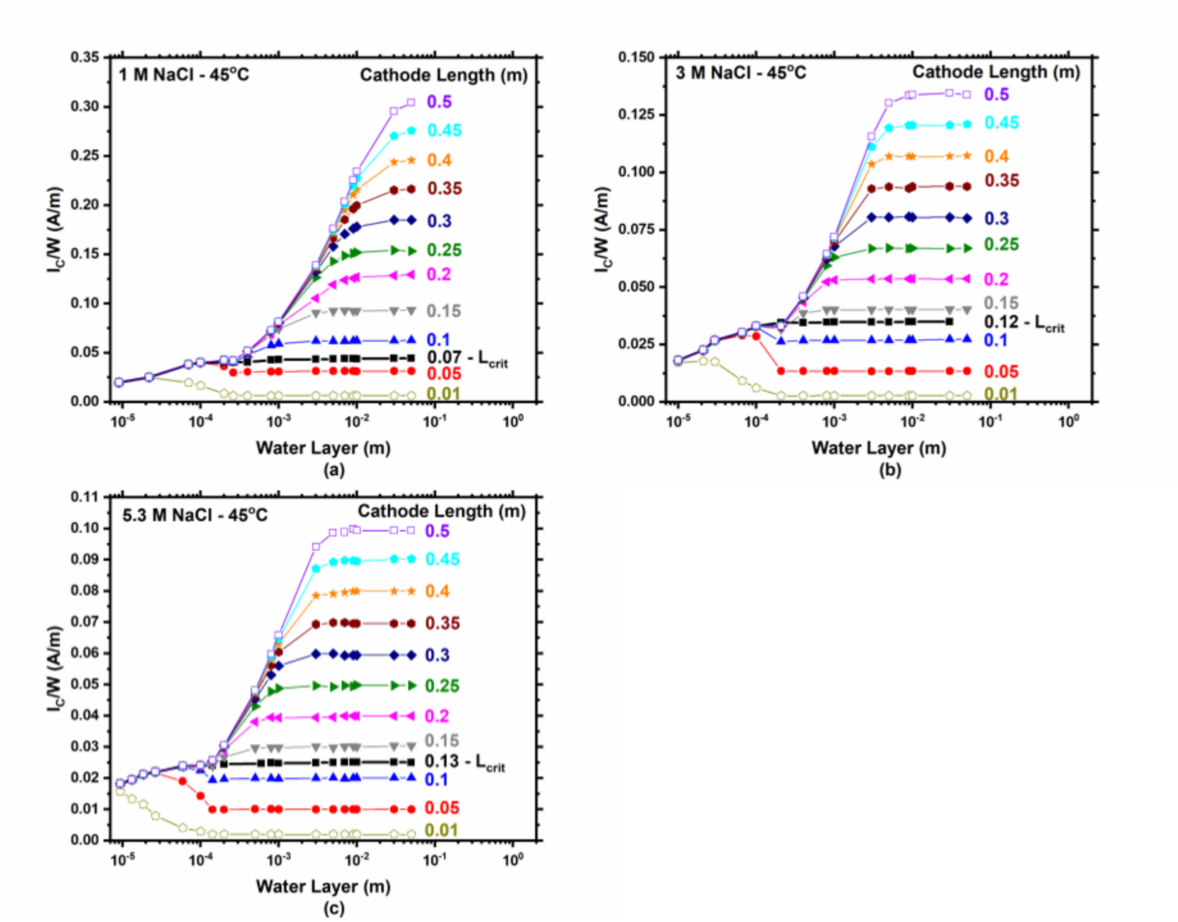

Figure 10: Modeled total cathodic current per width (I_C/W) vs. water layer thickness as a function of cathode length at 45˚C for (a) 1, (b) 3, and (c) 5.3 M NaCl. It is noted that the ordinate is different in all figures.

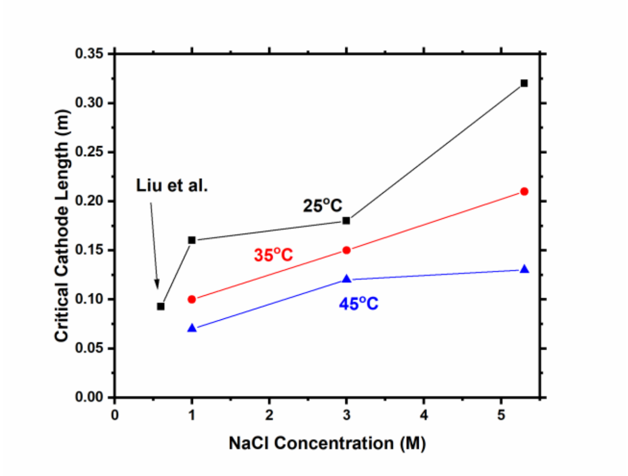

Figure 11: Critical cathode length (L_{Crit}) as a function of chloride concentration and temperature for NaCl brines from modeling results Figure 9 and Figure 10.

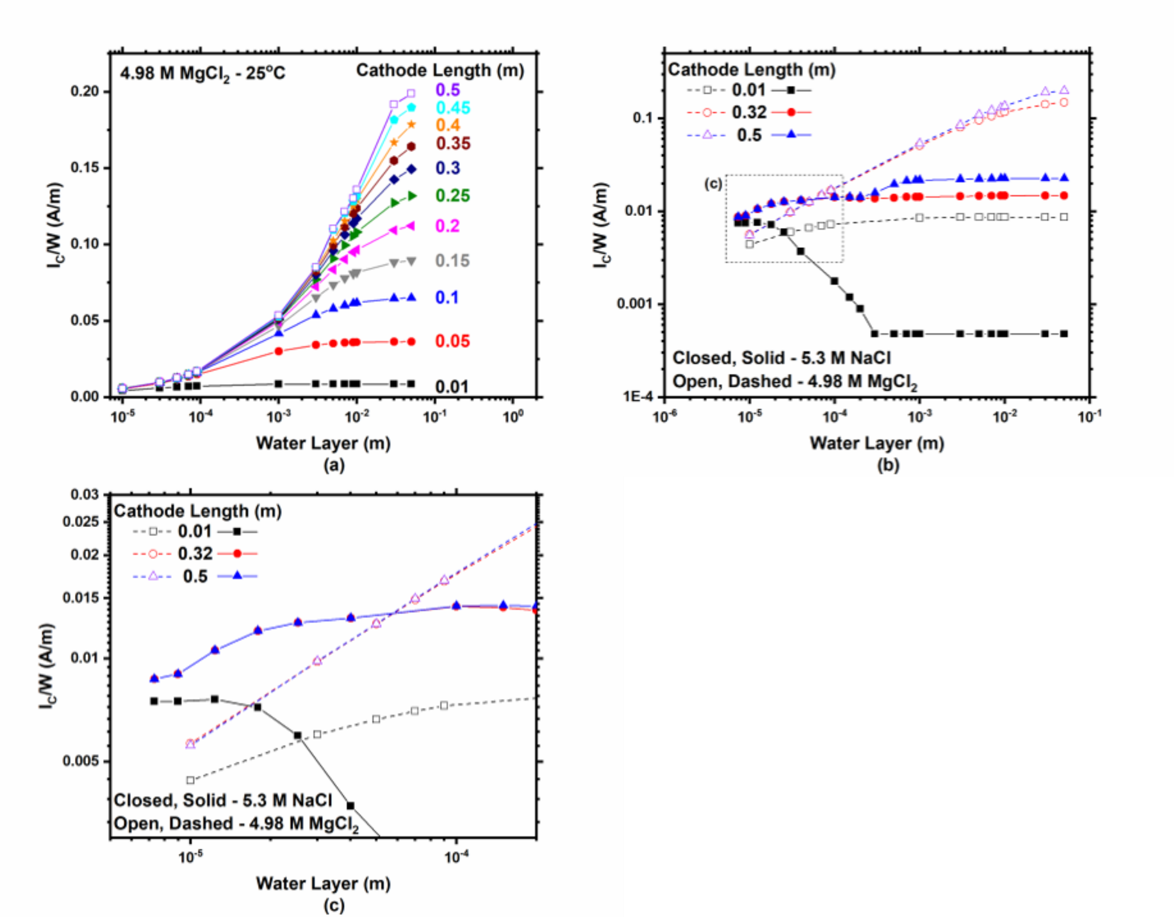

Figure 12: (a) Modeled total cathodic current per width (I_C/W) vs. water layer thickness as a function of cathode length at 25˚C for 4.98 M $MgCl_2$. The cathodic polarization scan for SS304L in $MgCl_2$ was obtained from Katona et al. [45]. (b) Comparison of I_C/W vs. water layer

thickness as a function of cathode length at 25˚C for 4.98 M $MgCl_2$ and 5.3 M NaCl. (c) Zoomed in region as denoted in (b). It is noted that (b) and (c) are log-log plots.

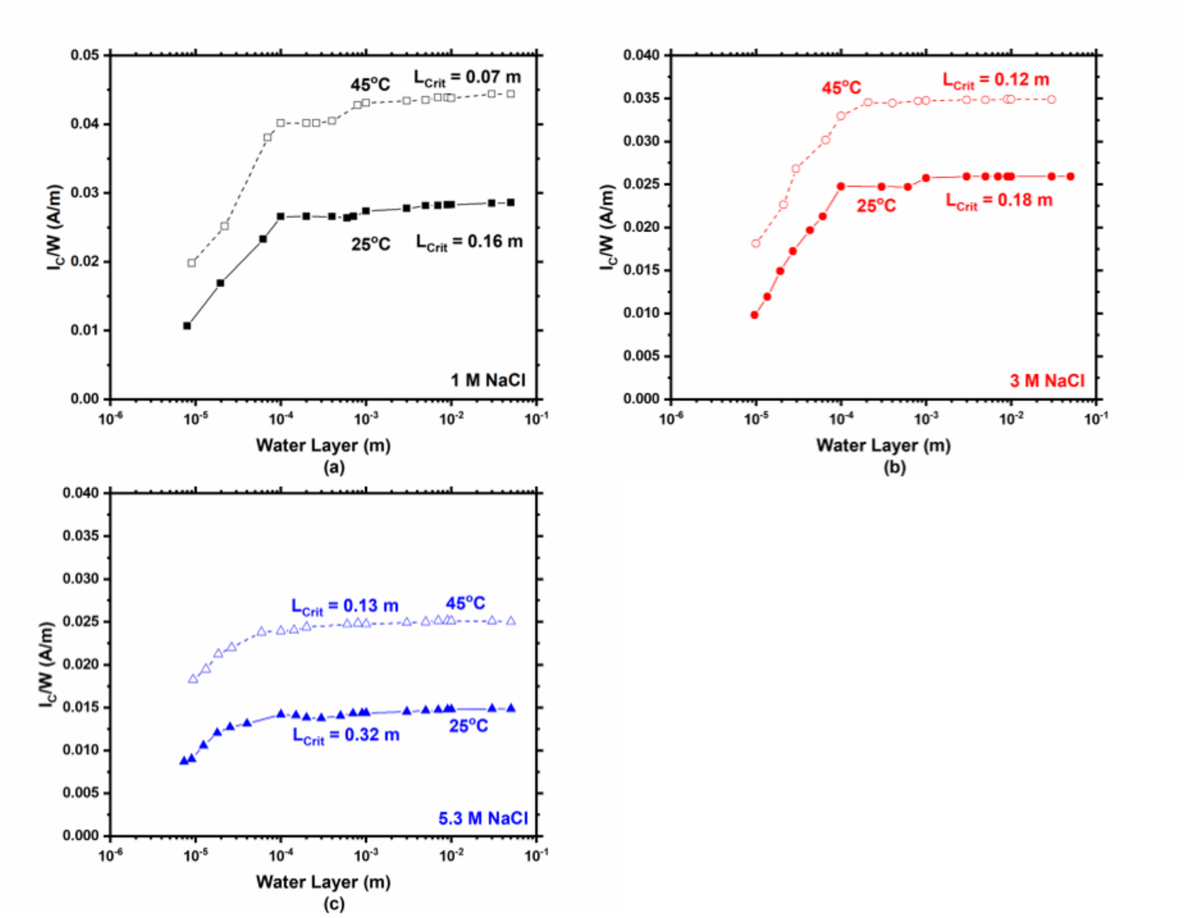

Figure 13: Comparison of the modeled total cathodic current per width (I_C/W) vs. water layer thickness as a function temperature at the respective critical cathode length (L_{Crit}) for (a) 1, (b) 3, and (c) 5.3 M NaCl. It is noted that the ordinate in (a) is different than (b) and (c).

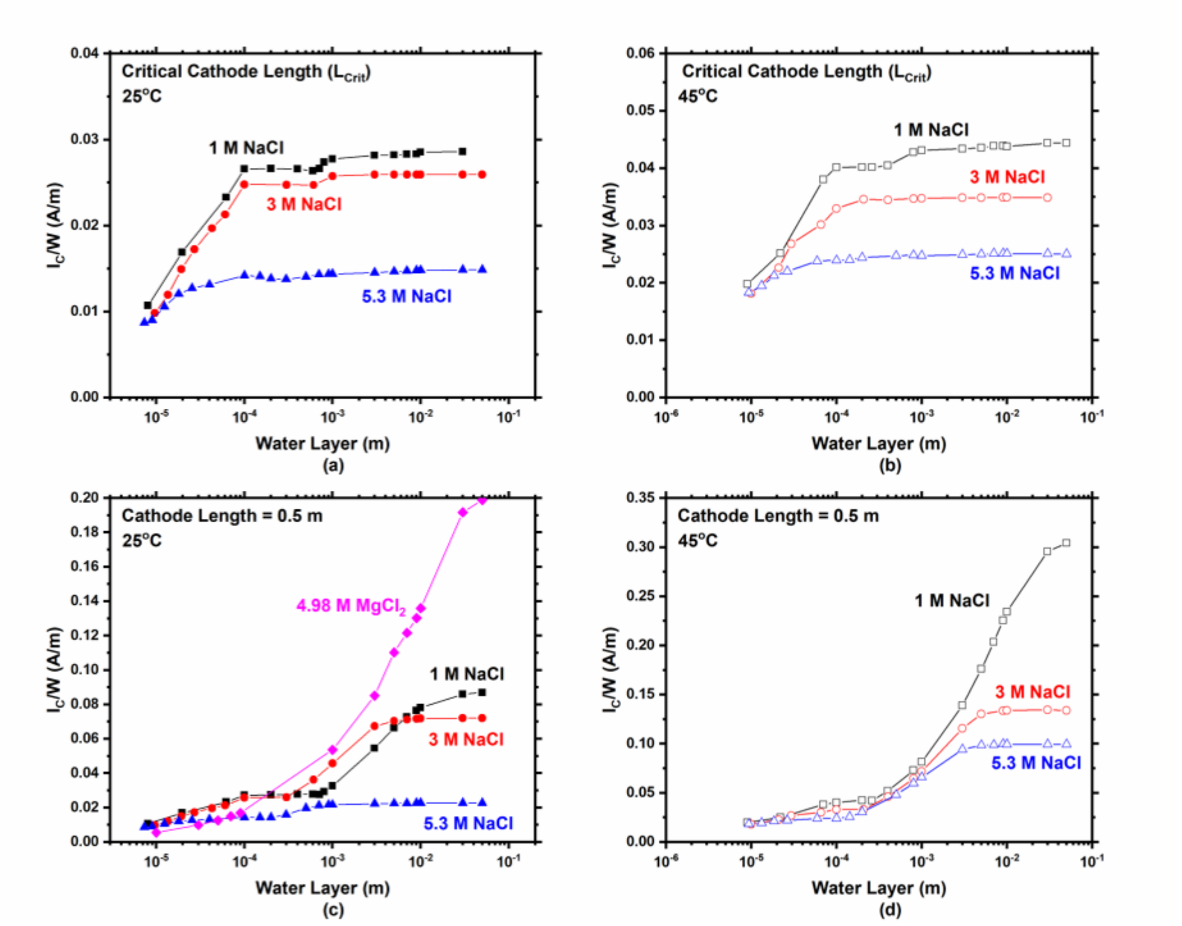

Figure 14: Comparison of the modeled total cathodic current per width (I_C/W) vs. water layer thickness as a function solution concentration at the respective critical cathode length (L_{Crit}) for (a) 25 and (b) 45 ˚C. Comparison of I_c/W vs. water layer thickness as a function solution concentration at a cathode length (L_C) of 0.5 m for (c) 25 and (d) 45 ˚C. It is noted that the ordinate axis is different in each graph.

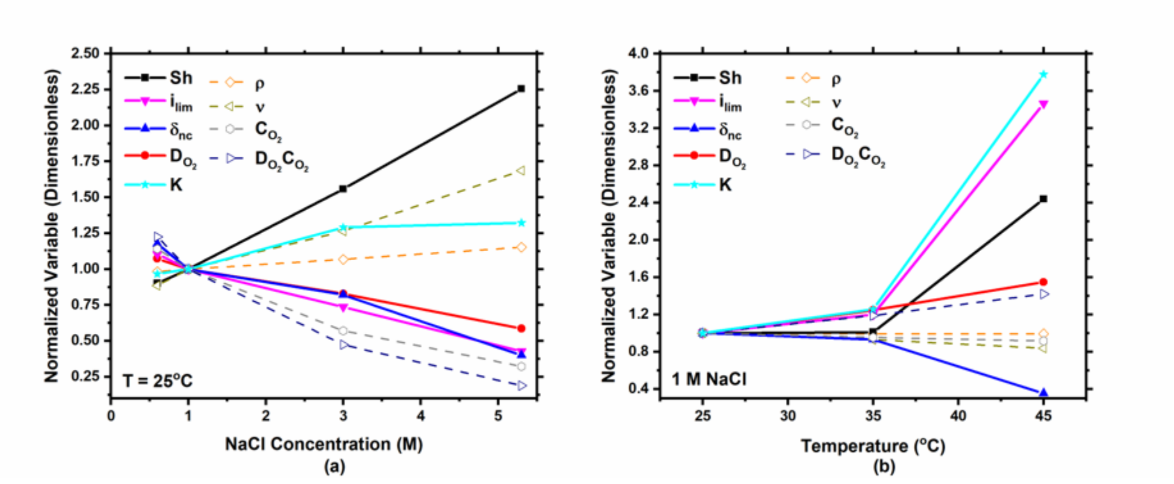

Figure 15: Normalized, measured solution properties for (a) various NaCl concentrations at 25˚C and (b) various temperatures at 1 M NaCl. All values were normalized to 1 M NaCl at 25˚C. It is noted that the ordinate is different between (a) and (b).

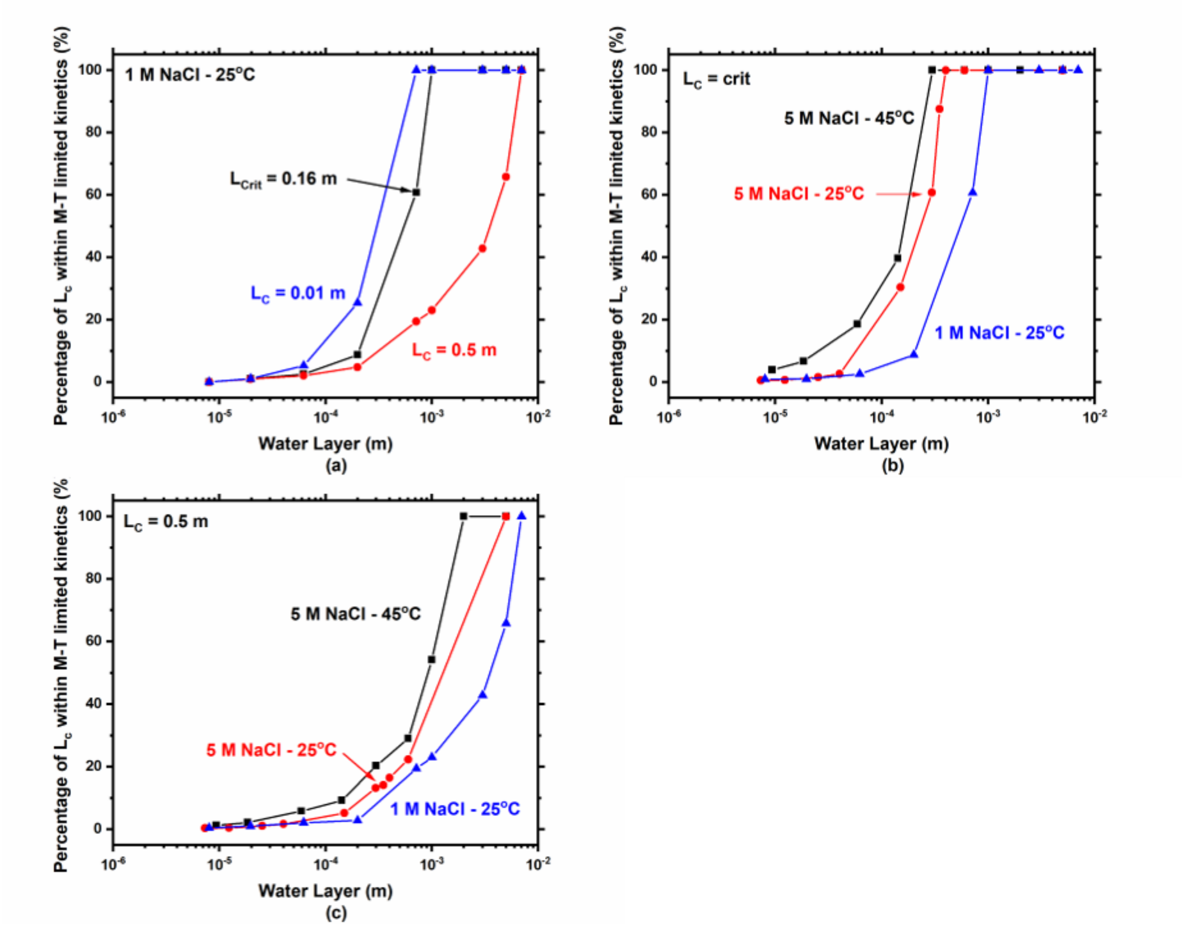

Figure 16: Modeled percentage of the cathode length within mass-transport limited kinetics for (a) 1 M NaCl at 25°C various cathode lengths. (b) Comparison of percentage of the cathode length within mass-transport limited kinetics for 5.3 M NaCl at 25 and 45 °C and 1 M NaCl at 25 °C at (b) the respective critical cathode length and (c) a cathode length of 0.5 m.

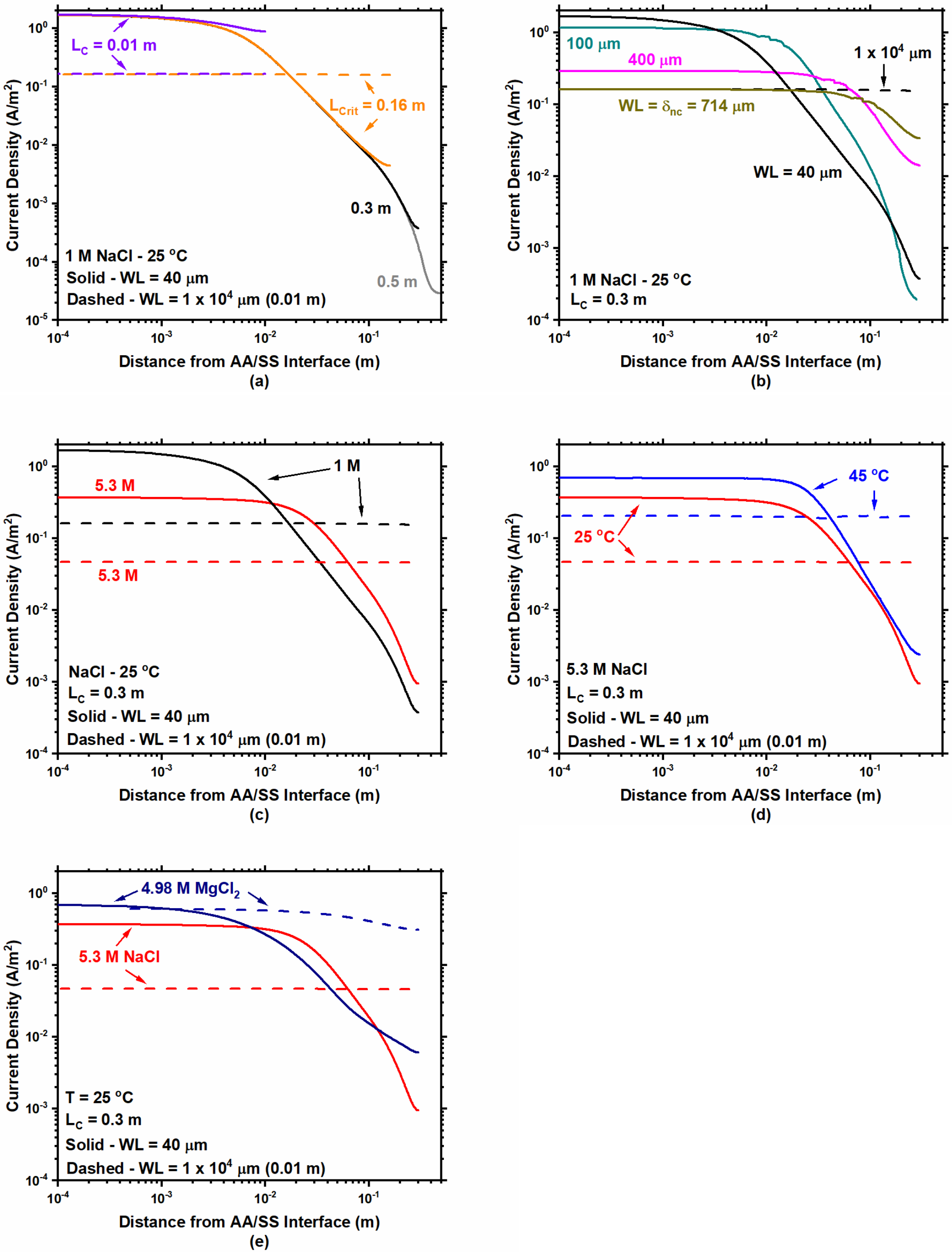

(a) (b) (c) (d) (e)

Figure 17: (a) Modeled current density vs. distance from the AA/SS interface as a function of cathode length and (b) WL at a fixed cathode length. (c) Current density vs. distance from the AA/SS interface as a function of solution concentration and water layer thickness and (d) as a function temperature and cathode length. (e) Comparison of $MgCl_2$ and NaCl current densities from the AA/SS interface at 25 °C as a function of water layer thickness.

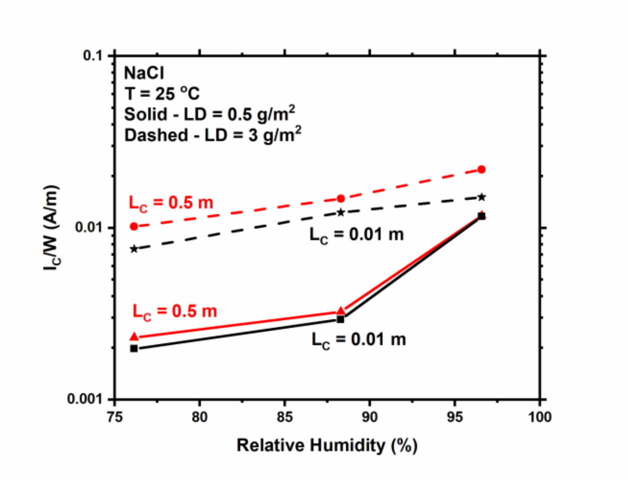

Figure 18: Comparison of the modeled total cathodic current per width (I_C/W) vs. relative humidity as a function loading density (LD) and cathode length (L_C). It is noted that the lines present are not intended as fits rather to guide the eye of the reader.

C. Use of *in-situ* Raman spectroelectrochemical technique to explore atmospheric corrosion in marine relevant environments

Use of *in-situ* Raman Spectroelectrochemical Technique to Explore Atmospheric Corrosion in Marine Relevant Environments

R. M. Katona,[1,2] R. G. Kelly[2], C. R. Bryan[1], R. F. Schaller[1], A. W. Knight[1]

[1] Sandia National Laboratories, Albuquerque, NM 87123 USA
[2] Materials Science and Engineering, University of Virginia, Charlottesville, VA 22904 USA

Key Words

Atmospheric corrosion, diffusion boundary layer, magnesium chloride, magnesium hydroxide (brucite), surface film evolution

Abstract

Here, for the first time, we demonstrate the use of an *in-situ* spectroelectrochemical Raman technique to explore simulated atmospheric corrosion scenarios with a variable boundary layer thickness (δ). The effects of solution flow rate on oxygen concentration and δ were explored. It was found that solution regeneration is necessary to prevent oxygen depletion in the Raman cell. It was further shown that by increasing the solution flow rate, the effective δ decreases and allows for the investigation of atmospheric corrosion scenarios. Finally, the technique developed was utilized to explore the effect of precipitation on the cathodic behavior of SS304L in dilute $MgCl_2$. During cathodic polarization, evidence supports previous observations that magnesium hydroxide species are kinetically favored over the thermodynamically predicted magnesium carbonate.

Introduction

Raman spectroscopy has been used to study the *in-situ* formation of surface precipitates on various alloys and solutions [1-4] as well as intermediates for oxygen reduction reactions (ORR) [5]. Although widely used in analysis of electrochemical reactions, *in-situ* Raman has not been used to probe the evolution of chemical conditions that are representative of common exposure conditions. Precipitation of solids resulting from both anodic and cathodic reactions will impact further corrosion, but the small volumes have made assessment of such environments challenging. Raman's ability to speciate solid products could be powerful in obtaining a better understanding of the factors controlling atmospheric corrosion.

Although the method is attractive, there are barriers to its application. First, many Raman cells are characterized by small solution volumes (*i.e.* several mL) [2]. As ORR is a common cathodic reduction reaction, the oxygen can be depleted, under rates of interest for atmospheric corrosion, and the pH raised, making the chemical composition of the solution under study not representative of the environment of interest. Next, many atmospheric environments are characterized by thin water layers, decreasing the boundary layer thickness (δ) and the diffusion distance for oxygen, which has been proven to be a controlling factor in atmospheric corrosion [6]. As Raman cells may be utilized with various solution flow rates (Q), flow could potentially be used to control δ and thus relate measurements of precipitate chemistry to different water layer thicknesses in atmospheric corrosion [6]. Taking advantage of this capability requires an understanding of the influence of Q on δ and cathodic reduction reactions while performing *in-situ* Raman. To determine these effects, cathodic kinetic reduction kinetics were explored on stainless steel (SS) 304L in an *in-situ* Raman cell over a range of flow rates.

SS is often exposed to marine and near-marine atmospheric environments characterized by deliquesced water layers often containing concentrated sea-salt solutions. This chloride rich deliquesced water layer is highly corrosive and can be detrimental to the overall service lifetime. Various constituents of the sea water brines, such as magnesium (Mg) [7,8], have a strong thermodynamic driving force to form stable precipitates at elevated pH [9]. Such precipitates forming on the surface of the alloy have the propensity to limit the environmental severity for corrosion [10].

During corrosion, any anodic reaction must be balanced by a cathodic reduction reaction. Whether the cathodic reduction reaction is ORR or the hydrogen evolution reaction (HER), a product is the hydroxyl anion (OH^-) which causes a rise in the cathode pH. Elevated cathodic pH values have been observed or measured in various solutions and alloys, and the pH can be significantly higher than the bulk solution [11,12]. As a result, the pH in which stable precipitates form can be achieved during corrosion [9]. In Mg-containing environments, which are dominant in sea water brines at low relative humidities (RH) [7], corrosion products of iron-based alloys have shown the presence of hydroxides, hydroxychlorides, and/or hydroxycarbonates as a result of cathode pH rise [13-15]. The identity and relative amounts of such precipitates depends on many factors, including the solution composition and concentration, however, it has been hypothesized that the formation of carbonate precipitates are kinetically inhibited [9,16]. Thus, it is important to have *in-situ* characterization of the formed precipitates in solutions in order to inform corrosion behaviors as the precipitates can influence water layer thickness, solution conductivity, and the number of cathode sites blocked [10].

The goal of this work is to demonstrate a technique allowing performance of *in-situ* Raman in simulated atmospheric environments with simultaneous electrochemical measurements. The effects of Q on oxygen concentration at the metal surface and δ will be explored and ensure the simulated environments are understood. After development, the technique was used to explore precipitates formed during polarization of SS304L in dilute $MgCl_2$.

Experimental

A three-electrode flow through cell (Redox.me) was used with a SS304L coupon (ground to 1200 grit, exposed area of 3 cm^2) as the working electrode having, a silver/silver chloride (Ag/AgCl) reference electrode with 3 M KCl fill solution, and platinum wire counter electrode. The flow cell solution volume was 4.5 mL with an electrolyte thickness of 2.25 mm above the sample. The cell can be seen in Figure 1. Electrolyte solutions, 0.6 M NaCl and 0.189 M $MgCl_2$, prepared using deionized water (18.2 MΩ-cm) and reagent-grade chemicals (≥ 99.0% purity), were pumped through the cell using a peristaltic pump allowing for variable *Q* from 0.5 to 50 mL/min (with a sensitivity of 0.25% of the rotation speed of the pump). The solutions were at ambient lab temperatures (21.5 ± 2˚C). A Biologic SP200 potentiostat was used for all electrochemical measurements with EC-Lab® V11.3 software. Electrochemical procedures involved a 1-hour open circuit potential (OCP) period followed by a cathodic scan from OCP to -1.4 $V_{Ag/AgCl}$ at a scan rate of 0.167 mV/sec. The solution was flowing continuously through the cell during all experimentation. Polarization scans were also taken in standard flat cell configurations under quiescent conditions and a solution volume of roughly 350 mL, to prevent bulk solution oxygen depletion.

In-situ Raman measurements were obtained using a confocal XploRA Plus Raman microscope (HORIBA Scientific) with a laser wavelength of 532 nm, power of 100 mW (spectra were collected using a 50% reduction in laser power), and a long-distance objective (magnification 10x and a numerical aperture of 0.25). Calibration was performed on a Si wafer. During *in-situ* testing, the laser was focused on the surface of the alloy with a beam diameter of 2.6 µm. Spectra were collected with 3 s. exposures and averaged over 10 scans from 2800 to 4000 cm^{-1}. Scans were taken approximately every 5 min until the first detection of $Mg(OH)_2$, indicated by a peak at 3654 cm^{-1} [2,17]; then, the collection period increased to roughly every 2 min. The laser was turned off in between scans to reduce surface heating effects.

Results

Effect of flow rate on the cathodic behavior of NaCl and $MgCl_2$ solutions

Measured cathodic polarization scans as a function of *Q* on SS304L in 0.6 M NaCl and 0.189 M $MgCl_2$ are seen in Figure 2(a) and (b) respectively. Also presented for 0.189 M $MgCl_2$ is a quiescent polarization scan on platinum from a flat cell configuration in which the i_{lim} for 2-electron transfer ORR is obtained [9].

For NaCl solutions, the measurements on SS304L are characterized by an activation-controlled region from OCP to roughly -0.5 $V_{Ag/AgCl}$ followed by a mass transfer-controlled region, as signified by a constant diffusion limited current density (i_{lim}), from -0.5 to -0.9 $V_{Ag/AgCl}$ below which HER becomes dominant. Overall, as Q increases, i_{lim} increases. At low Q (0.0 and 0.5 mL/min), the i_{lim} is less than the i_{lim} for a quiescent, flat cell cathodic polarization. When Q increases to 1.5 mL/min, the i_{lim} yields the same i_{lim} as the quiescent polarization scan. Finally, when $Q > 1.5$ mL/min, the i_{lim} surpasses the i_{lim} for the quiescent polarization, representing a decrease in δ.

Measurements in $MgCl_2$ solutions, Figure 2(b), are characterized by an activation-controlled region from OCP to approximately -0.5 $V_{Ag/AgCl}$ followed by a transition to a quasi-mass transport-controlled region; however this region is not completely vertical as one would expect for mass transport. Below -0.9 $V_{Ag/AgCl}$ the polarization scan is indicative of HER at all values of Q. The resulting polarization scans in $MgCl_2$ show little-to-no dependence on Q in contrast to NaCl solutions which showed an increase in i_{lim} with increased Q. Additionally, in $MgCl_2$ no value of Q reaches the i_{lim} for expected quiescent ORR (displayed on Pt [9]).

In-situ Raman analysis during electrochemical polarization of $MgCl_2$

A measured polarization scan for 0.189 M $MgCl_2$ is presented in Figure 3(a), during which, *in-situ* Raman spectra were collected between 2800 – 4000 cm^{-1}, as seen in Figure 3(b). Scans were background-subtracted and normalized to the maximum water peak at 3415 cm^{-1} [2]. As the cathodic polarization was driven from OCP, a strong, sharp Raman peak formed at 3654 cm^{-1} (Figure 3(c)). This peak, at 3654 cm^{-1}, corresponds to the A_{1g} O-H stretching mode of microcrystalline $Mg(OH)_2$ (brucite) [2,17]. Below a potential of -1.1 $V_{Ag/AgCl}$ the normalized intensities show an influence from bubbles on the surface of the alloy (not shown here), likely due to significant H_2 production from HER.

Discussion

Solution flow rate dictates oxygen concentration and boundary layer thickness

The mass transport-controlled ORR on SS in NaCl solutions has been thoroughly investigated as a function of both concentration and δ and displays Levich behavior [6,18] for mass transport. i_{lim} under mass transport conditions is given by:

$$i_{lim} = \frac{nFD(C_{bulk} - C_{surface})}{\delta} \qquad \text{Eqn. 1}$$

where n is the number of electrons transferred during the electrochemical reaction, F is Faraday's constant (96485 C/mol), D is the diffusivity of the reacting species (cm^2/sec), C_{bulk} and $C_{surface}$ (assumed to be zero) are the concentration of the reacting species in the bulk solution and at the electrode surface respectively (mol/cm^3).

Through the application of Equation 1, it is shown that quiescent conditions in the flow cell lead to oxygen depletion. Under quiescent conditions in a flat cell, i_{lim} was determined to be 1.86 x 10^{-2} mA/cm^2 which is similar to previously reported results [6]. In the Raman flow cell, when Q = 0 mL/min for 0.6 M NaCl, i_{lim} was 0.98 x 10^{-2} mA/cm^2 as displayed in Figure 2(a). There are multiple factors changing in Equation 1 that could influence i_{lim}, including: D, C_{bulk}, and δ. First, it is likely that C_{bulk} will decrease, as during the initial cathodic reduction, the O_2 concentration in the small sample cell volume will be consumed. Integrating the charge passed from OCP to -0.5 $V_{Ag/AgCl}$ yields a value of 0.74 Coulombs passed. Using Faradays Law and an electron transfer number of 4, it is deduced that 1.9x10^{-6} mols of O_2 would be theoretically consumed. In the 4.5 mL of 0.6 M NaCl, there is a saturated O_2 concentration of 9.4 x 10^{-7} mols [18]. Therefore, the O_2 concentration will be depleted during the polarization, influencing the measured i_{lim}. When this occurs, it is likely that D will also decrease [19,20]. Finally, research has been done to correlate the diffusivity of the reacting species, solution density difference between the bulk and reacting surface and viscosity to δ [21-23]. This relationship has not been established when O_2 is the reducing species as the density difference between the surface and bulk solution is not available in literature. Although the variations in δ are unknown, they are believed to be small as the fluctuations in δ are heavily dependent upon solution density which is unlikely to change significantly with depleted O_2 [24]. Thus, in the cell geometry used, a decrease in D and C_{bulk} is proportional to a decrease in i_{lim}

(Equation 1), and in order to maintain sufficient O_2 concentrations, solution must be regenerated continuously.

Solution Q will not only affect O_2 concentrations but will also determine δ. The influences from variations in the δ are generally studied using a rotating disk electrode (RDE), in which a defined δ is dependent upon the rotation speed of the disk given by

$$\delta = 1.61 D^{1/3} \omega^{-1/2} \nu^{-1/6} \qquad \text{Eqn. 2}$$

where ω is the rotation speed (rad/sec^{-1}) and ν is the kinematic viscosity (cm^2/s). Thus, for RDE experiments, i_{lim} has an inverse dependence on δ and a square root dependence on ω. This dependence was exploited by Liu et al. who determined that $\delta = 16.24\left(\frac{1}{i_{lim}}\right)$ for 0.6 M NaCl [6].

For the flow cell used in these studies, i_{lim} is plotted as a function of $\sqrt{Q}$ (Figure 4(a)) for 0.6 M NaCl. This plot demonstrates a linear dependence of i_{lim} with $\sqrt{Q}$, similar to the dependence of i_{lim} on ω in RDE experiments. Estimates for δ [6] at a given Q > 1.5 mL/min results in a $\frac{1}{\sqrt{Q}}$ dependence with δ as shown in Figure 4(c). Due to the design of the Raman flow cell, it is difficult to ascertain the velocity profile over the surface of the alloy (which would influence δ) as there are multiple inlets and outlets for solution flow (Figure 1(b)). However, if one were to assume that solution velocity is proportional to Q, the velocity (U in cm^2/sec) is:

$$U = \frac{Q}{A} \qquad \text{Eqn. 3}$$

where A is the cross-sectional area (cm^2) of the tube through which the fluid is flowing. Considering solution velocity over a flat plate, as shown in Figure 4(d), the effective diffusion boundary layer thickness ($\bar{\delta}$) as governed by the integration of the Blasius equation (assuming laminar flow) is:

$$\bar{\delta} \sim \frac{1}{L}\int_{L}^{0} 5\sqrt{\frac{\nu x}{U}}\, dx = \frac{10}{3}\sqrt{\frac{\nu}{U}} L^{1/2} \sim \sqrt{\frac{1}{U}} \qquad \text{Eqn. 4}$$

where x is the distance from the edge of the plate to an arbitrary point with total length L. Thus, by combining Equations 1, 3, and 4 the expected dependence on i_{lim} is:

$$i_{lim} \sim \frac{1}{\delta} \sim \sqrt{Q} \qquad \text{Eqn. 5}$$

As i_{lim} displays a linear trend with $\sqrt{Q}$ (Figure 4(a)) and δ displays a linear trend when plotted against $\frac{1}{\sqrt{Q}}$ (Figure 4(c)), it is believed that the fluid velocity over the SS304L sample is proportional to Q and the cell configuration has minimal influence on velocity over the sample surface of interest. Finally, because Q can be varied, and *in-situ* Raman spectra can be collected as a function of δ, the utility of the cell for future work to identify changes to the solution or metal surface chemistry via *in*-situ Raman can aid in understanding the chemical composition in scenarios where δ can vary such as atmospheric corrosion.

It has been shown that i_{lim} is a function of the Q and can control δ for ORR, however it is important to note additional considerations when utilizing this technique. First, as shown in Figure 4(b), there is no Q dependencies for 0.189 M $MgCl_2$. This result is consistent with our previous work, where an RDE study investigating the cathodic reduction behavior of $MgCl_2$ solutions demonstrated that, for dilute to saturated $MgCl_2$ solutions, there was no effect on electrode rotation rate. It was further proposed the cathodic reduction reaction became HER as the surface pH was buffered due to precipitate formation. However, the potential at which the precipitate was formed could not be identified [9]. Second, when investigating surface reactions, it is possible that solution flow could shear precipitates off the alloy surface if solution velocity was sufficiently high. As Raman scans can take a significant amount of time in relation to the solution flow, a precipitate could be missed if Q were too high. Finally, precipitate reactions could be investigated within the formed δ through confocal Raman microscopy.

$Mg(OH)_2$ film formation occurs due to kinetic inhibition of $MgCO_3$

Although Mg-bearing cathodic films have long been known to form on SS during polarization scans [9], the *in-situ* identity of the precipitate during polarization has been elusive. *In-situ* Raman analysis allowed for tracking directly the formation of $Mg(OH)_2$ during polarization by the growth of the intense Raman shift at 3654 cm^{-1}, corresponding to the O-H stretch in microcrystalline brucite [2,17]. Additionally, the formation of $Mg(OH)_2$ at the surface of the alloy supports the hypothesis that the formation of $MgCO_3$ is kinetically inhibited [9,16]. Recent, thermodynamic stabilities for both Mg-species were investigated using Eq3/6 [9] and are displayed in Figure 5. Although, thermodynamic modeling predicts the formation of $MgCO_3$ in the conditions tested in this experiment, no peak was observed ~1095 cm^{-1} (the dominant peak for $MgCO_3$ [17]), when a wider scanning window from 200-4000 cm^{-1} was used (not shown here). Thus, $Mg(OH)_2$ was the only precipitate observed. While this result contradicts the thermodynamic predictions in an open system, it supports previously reported results that the formation of $MgCO_3$ is kinetically inhibited [9,16]. Furthermore, work has shown that the kinetic limitations for the formation of $MgCO_3$ exist to at least a temperature of 150˚C [16], thus, it is unlikely that there are any influences on the formation of $Mg(OH)_2$ from laser heating. The formation of such participates has influences on atmospheric corrosion but have been detailed elsewhere [9].

Conclusions

We present an investigation of *in-situ* spectroelectrochemical Raman techniques to explore the effect of solution flow rate on various atmospheric solution simulants and solution precipitation on cathodic polarization. It was found that solution regeneration is needed to prevent oxygen depletion in the Raman cell used in experimentation. Furthermore, it was shown that by increasing solution flow rate, the effective boundary layer thickness can be controlled allowing the investigation of atmospheric corrosion scenarios. Finally, the utility of the *in-situ* Raman cell was used to explore the effect of solution precipitation on the cathodic behavior of SS304L in dilute $MgCl_2$. During cathodic polarization, evidence was gathered that $Mg(OH)_2$ species are kinetically favored over the thermodynamically predicted $MgCO_3$ in dilute $MgCl_2$ solutions.

Acknowledgements

Sandia National Laboratories is a multi-mission laboratory managed and operated by National Technology and Engineering Solutions of Sandia, LLC., a wholly owned subsidiary of Honeywell International, Inc., for the U.S. Department of Energy's National Nuclear Security Administration under contract DE-NA0003525. This document is SAND 2020-6232 J.

References

[1] S. Li, L.H. Hihara, In situ Raman spectroscopic identification of rust formation in Evans' droplet experiments, Electrochem. Commun. (2012). https://doi.org/10.1016/j.elecom.2012.02.014.

[2] A. Maltseva, V. Shkirskiy, G. Lefèvre, P. Volovitch, Effect of pH on Mg(OH) 2 film evolution on corroding Mg by in situ kinetic Raman mapping (KRM), Corros. Sci. 153 (2019) 272–282. https://doi.org/10.1016/j.corsci.2019.03.024.

[3] C.T. Lee, M.S. Odziemkowski, D.W. Shoesmith, An in situ Raman-electrochemical investigation of carbon steel corrosion in Na2CO3 NaHCO3, Na2SO 4, and NaCl solutions, J. Electrochem. Soc. 153 (2006). https://doi.org/10.1149/1.2140680.

[4] J.E. Maslar, W.S. Hurst, J.J. Bowers, J.H. Hendricks, In situ Raman spectroscopic investigation of stainless steel hydrothermal corrosion, Corrosion. 58 (2002) 739–747. https://doi.org/10.5006/1.3277656.

[5] J.T. Frith, A.E. Russell, N. Garcia-Araez, J.R. Owen, An in-situ Raman study of the oxygen reduction reaction in ionic liquids, Electrochem. Commun. (2014). https://doi.org/10.1016/j.elecom.2014.06.001.

[6] C. Liu, J. Srinivasan, R.G. Kelly, Electrolyte Film Thickness Effects on the Cathodic Current Availability in a Galvanic Couple, J. Electrochem. Soc. 164 (2017) C845–C855. https://doi.org/10.1149/2.1641713jes.

[7] C.R. Bryan, E.J. Schindelholz, Properties of Brines formed by Deliquescence of Sea Salt Aersols, Corros. 2018. (n.d.) Paper 10516.

[8] ASTM International, ed., Standard Practice for the Preparation of Substitute Ocean Water, ASTM Int. 98 (2013) 1–3. https://doi.org/10.1520/D1141-98R13.2.

[9] R.M. Katona, J. Carpenter, A.W. Knight, R.F. Schaller, C.R. Bryan, R.G. Kelly, E.J. Schindelholz, Importance of hydrogen evolution reactions in magnesium chloride solutions on stainless steel, InPreparation. (2020).

[10] A.S. Agarwal, U. Landau, J.H. Payer, Modeling particulates effects on the cathode current capacity in crevice corrosion, J. Electrochem. Soc. 155 (2008) C269–C278. https://doi.org/10.1149/1.2890418.

[11] E.J. Schindelholz, H. Cong, C.F. Jove-Colon, S. Li, J.A. Ohlhausen, H.K. Moffat, Electrochemical aspects of copper atmospheric corrosion in the presence of sodium chloride, Electrochim. Acta. 276 (2018) 2018. https://doi.org/10.1016/j.electacta.2018.04.184.

[12] K. Murase, T. Honda, T. Hirato, Y. Awakura, Measurement of pH in the vicinity of a cathode during the chloride electrowinning of nickel, Metall. Mater. Trans. B Process Metall. Mater. Process. Sci. 29 (1998) 1193–1198. https://doi.org/10.1007/s11663-998-0041-y.

[13] P. Volovitch, C. Allely, K. Ogle, Understanding corrosion via corrosion product characterization: I. Case study of the role of Mg alloying in Zn-Mg coating on steel, Corros. Sci. 51 (2009) 1251–1262. https://doi.org/10.1016/j.corsci.2009.03.005.

[14] N.C. Hosking, M.A. Ström, P.H. Shipway, C.D. Rudd, Corrosion resistance of zinc-magnesium coated steel, Corros. Sci. 49 (2007) 3669–3695. https://doi.org/10.1016/j.corsci.2007.03.032.

[15] M. Guo, Q. Yin, M. Liu, C. Pan, Z. Wang, Corrosion Behavior of 304 Stainless Steel Exposed to a Simulated Salt Lake Atmosphere, Acta Metall. Sin. (English Lett. (2020). https://doi.org/10.1007/s40195-020-01028-w.

[16] E.J. Swanson, K.J. Fricker, A.A. Park, Directed precipitation of hydrated and anhydrous magnesium carbonates for carbon storage, Phys. Chem. Chem. Phys. 16 (2014) 23440–23450. https://doi.org/10.1039/c4cp03491k.

[17] B. Downs, S. Robinson, H. Yang, P. Mooney, RRUFF Project, (2015). http://rruff.info/.

[18] C.L. Alexander, C. Liu, A. Alshanoon, R.M. Katona, R.G. Kelly, J. Carpenter, C. Bryan, E. Schindelholz, Oxygen Reduction on Stainless Steel in Concentrated Chloride Media, J. Electrochem. Soc. 165 (2018) C869–C877. https://doi.org/10.1149/2.0181813jes.

[19] N. Shimizu, I. Kushiro, Diffusivity of oxygen in jadeite and diopside melts at high pressures, Geochim. Cosmochim. Acta. 48 (1984) 1295–1303. https://doi.org/10.1016/0016-7037(84)90063-2.

[20] W. Xing, M. Yin, Q. Lv, Y. Hu, L. Changpeng, J. Zhang, Oxygen solubility, diffusion coefficient and solution viscosity, in: W. Xing, G. Yin, J. Zhang (Eds.), Rotating Electrode Methods Oxyg. Reduct. Electrocatal., Elsevier B.V., 2014: pp. 1–31.

[21] A.A. Wragg, Free convection mass transfer at horizontal electrodes, Electrochim. Acta. 13 (1968) 2159–2165. https://doi.org/10.1016/0013-4686(68)80123-9.

[22] A.A. Wragg, T.K. Ross, Superposed free and forced convective mass transfer in an electrochemical flow system, Electrochim. Acta. 12 (1967) 1421–1428. https://doi.org/10.1016/0013-4686(67)80055-0.

[23] E.J. French, C.W. Tobias, Mass transfer by free convection at horizontal electrodes, Electrochim. Acta. 2 (1968) 311–325. https://doi.org/10.1016/0013-4686(68)80123-9.

[24] H. Watanabe, K. Iizuka, The influence of dissolved gases on the density of water, Metrologia. 21 (1985) 19–26. https://doi.org/10.1088/0026-1394/21/1/005.

Figures

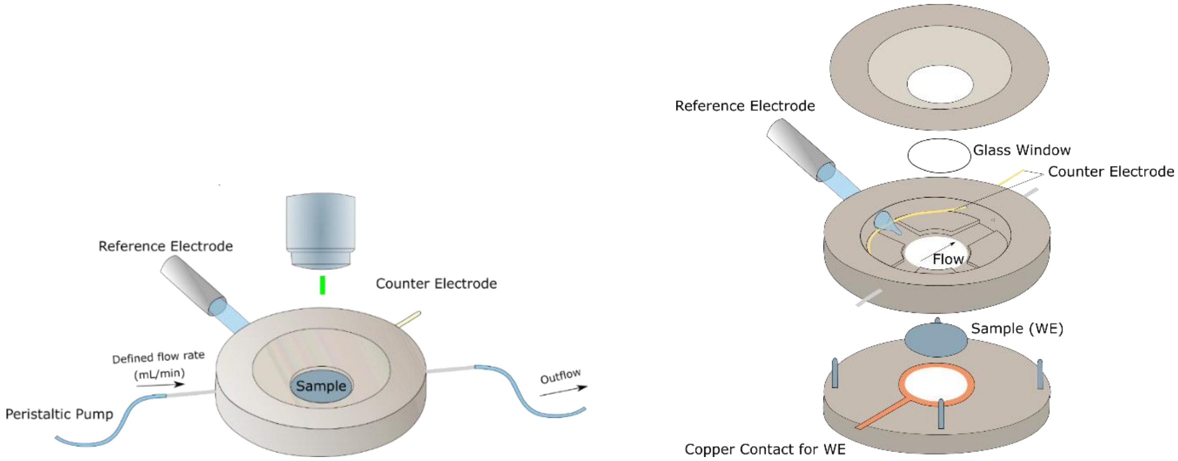

Figure 1:Experimental set up for in-situ Raman analysis: (a) overall set-up and (b) inside configuration of flow cell.

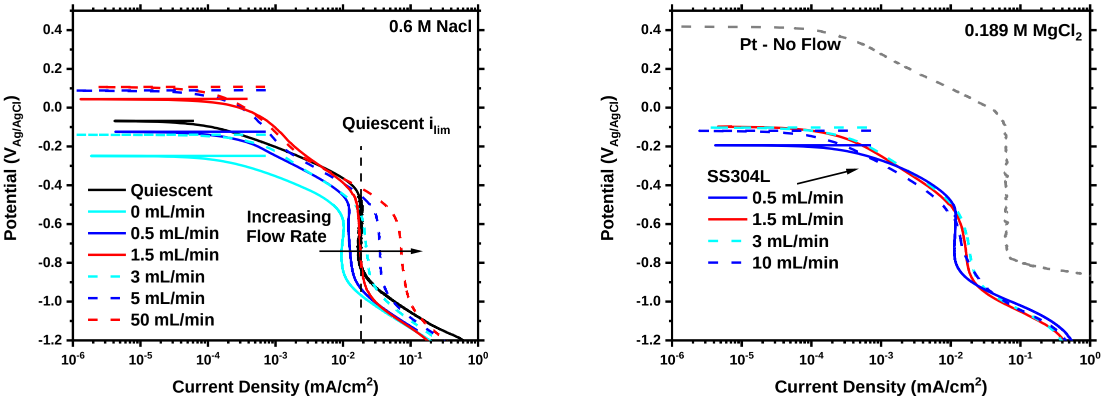

(a)

(b)

Figure 2: Effect of solution flow rate on the cathodic polarization of 304L SS in (a) 0.6 M NaCl and (b) 0.189 M MgCl$_2$ in the flow cell. Also in (b) is a polarization scan for Pt alloy under quiescent conditions [9].

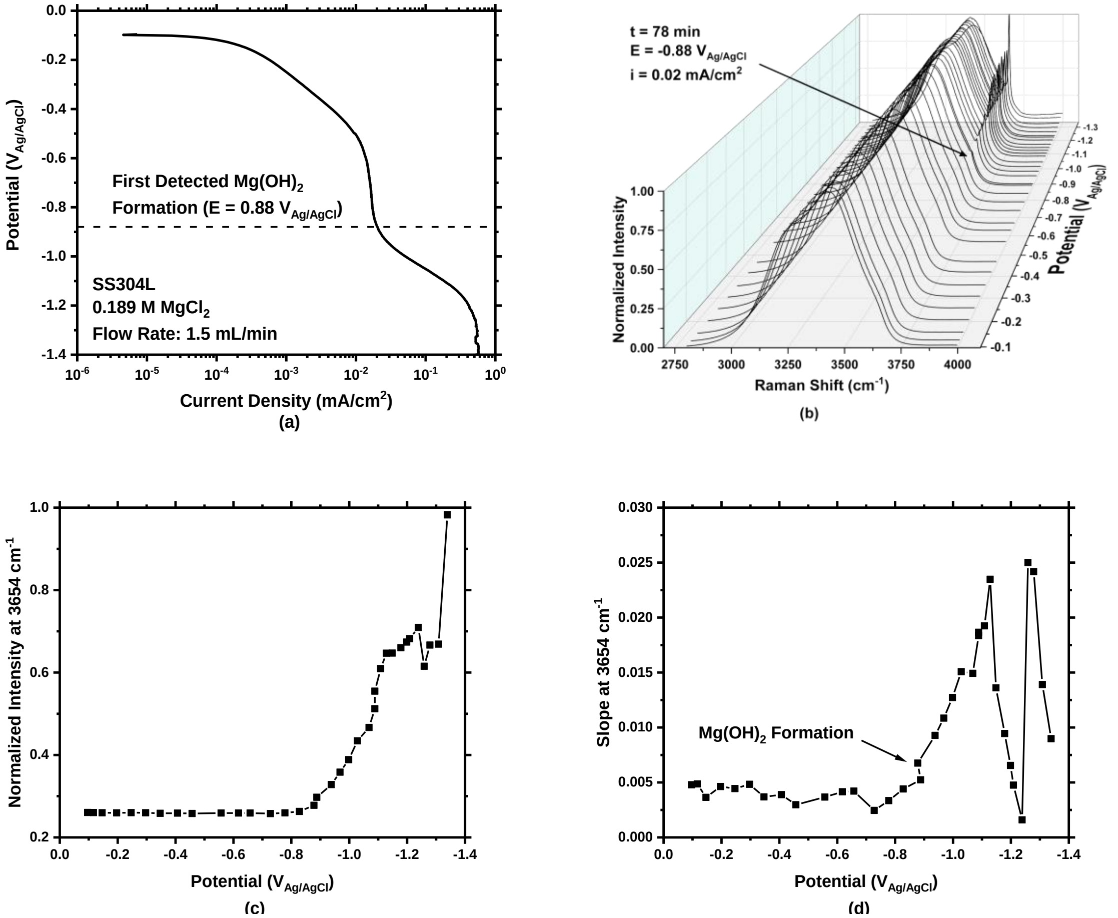

Figure 3: (a) Polarization scan of SS304L in 0.189 M $MgCl_2$. (b) In-situ Raman characterization of SS304L surface as a function of potential in (a). (c) Normalized intensities at a wave number of 3654 cm^{-1}. (d) Slope of (c), indicative of $Mg(OH)_2$ formation.

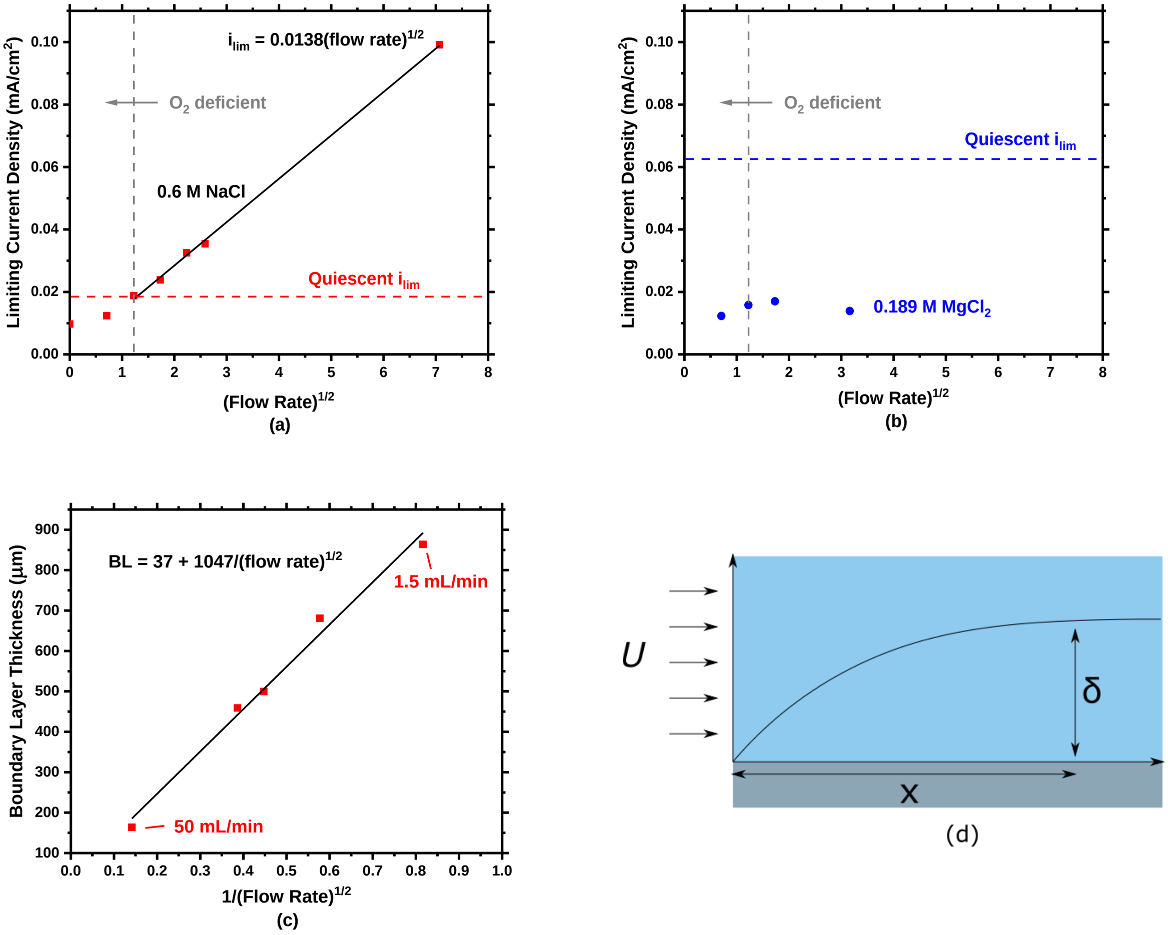

Figure 4: Influence of Q on the limiting current density of SS304L for (a) 0.6 M NaCl and (b) 0.189 M $MgCl_2$. (c) Calculated effective boundary layer thicknesses as a function of flow rate for 0.6 M NaCl solutions. (d) Schematic for boundary layer thicknesses.

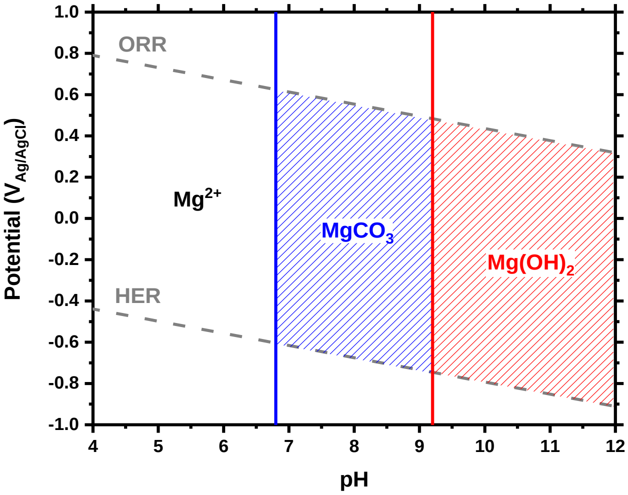

Figure 5: Thermodynamic prediction of species formation for 0.189 M $MgCl_2$.

D. Cathodic kinetics on stainless steel in high pH environments

Cathodic Kinetics on Platinum and Stainless Steel in NaOH Environments

R. M. Katona,[1,2,*,z] J. Carpenter[1], E. J. Schindelholz[3,**], R. F. Schaller[1,**], R. G. Kelly[2,***]

[1] Sandia National Laboratories, Albuquerque, NM 87123 USA
[2] Materials Science and Engineering, University of Virginia, Charlottesville, VA 22904 USA
[3]Department of Materials Science and Engineering, The Ohio State University, Columbus, OH 43210 USA

[z]Corresponding Author E-mail Address [rmkaton@sandia.gov]

[*] Electrochemical Society Student Member
[**] Electrochemical Society member
[***] Electrochemical Society Fellow

Key Words

Sodium hydroxide, oxygen reduction reaction, superoxide formation, atmospheric corrosion

Abstract

During typical atmospheric conditions, cathodic reduction reactions produce hydroxyl ions increasing the pH in the cathodic region. Therefore, cathodic reduction reactions are investigated on platinum and stainless steel 304L (SS304L) in NaOH solutions ranging in pH from 13.6 to 16.5. It was found that in solution pHs less than 16.5 the cathodic reduction reaction on Pt and SS304L was ORR with an electron transfer number less than two due to superoxide formation as an intermediate. Increasing pH decreased the number of electrons transferred. At a pH of 16.5, the cathodic reduction reaction on SS304L is no longer ORR and the cathodic current on the surface of the alloy is due to oxide reduction occurring on the surface as indicated by the creation of multi-

component Pourbaix diagrams. The results of this study have important implications for predicting corrosion in atmospheric environments.

Introduction

Reduction reaction processes on stainless steel (SS) and platinum (Pt) alloys are important across a broad range of science and technology areas [1,2], especially for corrosion processes [3]. Recently, multiple studies have explored cathodic reduction reactions in chloride-containing solutions at their equilibrium pH which could be present in marine and near marine corrosion environments [3-5]. By measuring and understanding these reactions, predictions regarding the extent of corrosion become possible. In NaCl solutions, the oxygen reduction reaction was determined to be dominant following a four electron transfer given by [3]:

$$O_2 + 2H^+ + 4e^- \rightarrow 4OH^- \qquad 1$$

As a result of Equation 1, the pH in the cathode will increase. A pH rise of the cathode has been directly observed by Azmat et al. on zinc under marine solutions [6] and Schindelholz et al. on copper under NaCl electrolytes [7]. Additionally, ex-situ analysis of electrolyte pools after SS coupon exposures are consistent with the formation of an alkaline electrolyte at cathodic sites due to the ORR reaction [8]. The production of hydroxyl ions from ORR will not only cause a rise in pH but will cause electro-migration to maintain electroneutrality. As such, a chloride-poor, alkaline solution can be present in the cathode [8-11]. This becomes particularly important in atmospheric scenarios where finite electrolyte volumes are present. A schematic of this phenomenon is presented in Figure 1 for a droplet. For NaCl solutions, a common component of seawater brines at elevated relative humidities [12], an NaOH rich brine would be present near the edge of the cathode or in micro-droplets around the original cathode (droplet) [8,10,11] and could potentially change cathodic reduction behavior.

Katona et al. made predictions of cathodic pHs (calculated through concentration of the hydrogen ion) under atmospheric conditions for common atmospheric solution chemistries and utilized these pH values to investigate precipitation reactions [13,14]. In order to make such pH predictions, the max pit model formulism presented by Chen and Kelly was utilized [15]. The analytical model relies on ohmic drop considerations in the thin electrolyte film to limit the cathode size and the cathodic current supply. Through the inherent coupling of the cathode and anode, a finite cathode implies a finite anode (i.e., a finite pit size) [15]. As such, Katona et al. calculated total hydroxyl production based on the stoichiometric dissolution of SS304L. This was combined with the finite cathode radius to determine the cathode pH. The pH of SS304L exposed to 5.3 M NaCl under a loading density of 3 g/m^2 (WL = 12 μm) is presented in Figure 2. At the calculated maximum pit size (50 % salt film saturation), the pH is over 14 and illustrates that high pHs that are possible in cathodic regions [13,14].

While determining reaction mechanisms in chloride-containing solutions under natural pH conditions is crucial to understanding corrosion processes, it is also important to understand reaction mechanisms in an evolving cathode solution, specifically at elevated pH's. To date, information regarding the cathodic reduction behavior of SS or iron-based alloys in high pH is focused below a pH of 11. Generally, regardless of the solution composition, all researchers found a four electron transfer (Equation 1) below a pH of 11 [2,16,17]. The cathodic behavior of SSs has not been investigated in solutions of high pH values (nearing 13 and greater) which are possible at the cathode in some atmospheric corrosion scenarios (Figure 2) [7,13]. Additionally, SS cathodic behavior has not been established in pure NaOH solutions which could be possible in the surrounding edge of a cathode. To date, cathodic kinetics in pure NaOH solutions has focused on Pt [1,18]. In general, an increase in pH in pure NaOH solutions produces an electron transfer number nearing one on Pt electrodes. This can be described through the reduction of oxygen forming a superoxide anion as the rate limiting step (O_2^-, Equation 2):

$$O_2 + e^- \leftrightarrow O_2^- \qquad 2$$

In basic media, a hydrogen peroxide anion is the following intermediate and produces a hydroxyl ion as the final product (Equation 3 and 4) [1].

$$O_2^- + H_2O + e^- \leftrightarrow HO_2^- + OH^- \qquad 3$$

$$HO_2^- + H_2O + 2e^- \leftrightarrow 3OH^- \qquad 4$$

As the hydroxyl concentration increases, the ORR reaction rate declines, and the protonation of the superoxide is suppressed; thus, the ORR shifts from a two-electron reduction pathway to a one-electron reduction pathway for Pt in NaOH solutions [1,2]. Although this may be true for Pt, the electrochemical behavior of SS has not been established in pure NaOH solutions or at high pH (> 11).

It is important to note that pH values calculated within are based on activity and not concentration. Specifically, Pitzer activity coefficients are utilized and account for interactions between ions as well as the solvent. Thus, an effective concentration is created through a virial expansion of the excess Gibbs free energy and can vary from solely using a concentration approximation especially at elevated concentrations. For example, a 12.8 M NaOH solution yields a Pitzer pH of 16.5, whereas calculating from the concentration of OH^- gives a pH of 15.1 ($pH = 14 + \log_{10}([OH^-])$). Caution should be taken when applying results and diagrams to systems which do not account for activity coefficients.

The present study investigates the cathodic reduction behavior of SS304L and Pt in NaOH solutions containing elevated pH values (> 13.6) in simulated thin electrolyte film environments utilizing a rotating disk electrode (RDE). The reaction mechanisms on both alloys are determined through Levich behavior, thermodynamic analysis, and additional electrochemical experiments. For SS304L, the presence of an ORR electron transfer between one and two electrons is explained through superoxide formation for pH values < 14.9 whereas for the pH of 16.5 the reduction of the oxide on the surface causes for an increase in cathodic current.

Experimental

Materials and Electrochemical Procedure

The electrochemical procedures presented here utilize the same materials and methods for rotating disk electrodes (RDE) as Alexander et al. [3] and Katona et al. [4]. Briefly, high speed rotating disc electrodes (RDE) with a diameter of 5 mm comprised of SS304L and 99.99% Pt were acquired from Pine Research Instrumentation, Inc. (USA). For deaerated experiments, a diameter of 5.5 mm was used in order to form an airtight seal in the gas purge bearing assembly for the cell. Prior to each use, the electrodes were polished using a 1 μm Dialube Diamond Suspension®, then rinsed with ultrapure (18.2 MΩ-cm) water and dried with nitrogen. NaOH solutions of 0.6, 3.6, 5.4, and 12.8 M at 25 ˚C (corresponding to equilibrium relative humidity values of 98, 86, 77, and 31 % respectively), which correspond to calculated pH values of 13.6, 14.5, 14.9, and 16.5 respectively, were made using reagent grade chemicals (Solution pH's were calculated using EQ3/6 [37] utilizing the Yucca Mountain Program thermodynamic database for concentrated salt solutions using the Pitzer formalism for activity coefficients [38]). Such solutions were chosen as they correspond to the relative humidity of various NaCl solutions. 0.6 M NaOH and NaCl both have a relative humidity of 98 % and therefore would be stable under the same environmental conditions. 3.6 and 5.4 M NaOH correspond to 3 and 5.3 (saturated) M NaCl. Finally, while NaCl is not stable below a relative humidity of ~77 %, it is possible to get NaOH rich regions around precipitated NaCl crystals [8] and it is possible that these regions could be highly concentrated. The deliquescence/saturation point of NaOH is 8.24 ± 2.1 % RH at 25 ºC [19] and is likely a NaOH solution could be viable below the saturation point of NaCl.

Solutions were continuously purged with lab air to maintain oxygen saturation. Rotation rates ranged from 500-6000 rpm and polarizations were measured starting at OCP (after one hour of OCP stabilization) and scanned in the negative direction at a rate of 0.167 mV/sec until -1.3 V_{SCE}. Polarizations were also performed under deaerated conditions akin to the procedure of Katona et al. [4]. For all represented polarization scans shown within, duplicates were performed. Variation between i_{lim} in replicate tests was generally under 6 %.

Analysis

Diffusion-limited electrochemical behavior in RDE systems under laminar flow can be described using the Levich equation [20]:

$$i_{lim} = 0.62nFC_{O_2}D_{O_2}^{\frac{2}{3}}\nu^{-\frac{1}{6}}\omega^{\frac{1}{2}} \qquad 5$$

where i_{lim} is the diffusion limited current, n is the electron transfer number, F is the Faraday constant, C_{O_2} is the concentration of oxygen (or some other reacting species), D_{O_2} is the diffusion coefficient of oxygen, ν is the kinematic viscosity, and ω is the rotation speed of the RDE. Values for the fluid mechanical and mass transfer properties for NaOH used in Equation 5 are shown in Table 1 and are calculated from OLI Studio Analyzer 10 (OLI Systems, Inc., Cedar Knolls, NJ). Calculated values were utilized due to the fact that no source was available in literature that contained the concentration range of interest.

Pourbaix diagrams were generated using the “Hydro-chemical Equilibrium-Constant Database” (HYDRA) and “Make Equilibrium Diagrams Using Sophisticated Algorithms” (MEDUSA) programs from the Swedish Royal Institute of Technology [21,22]. As the passive film on SS340L is primarily composed of a mixture of passive Cr and Fe species [23,24], the relevant ions (in this case Fe and Cr) are input using the HYDRA program and the electrochemical potential, pH, and ion concentrations are varied using the MEDUSA program. A value of 1×10^{-6} M Fe was utilized in all cases as this is a typical value used for construction of Pourbaix diagrams [25]. A value of 0.23×10^{-6} M Cr was utilized as this represents a common ratio of Cr:Fe seen in oxide films [23,24] and the ratio is similar to that of the chemical composition of SS304L. Thus, a Pourbaix diagram can be generated for high pH systems of interest.

Results

Cathodic Polarizations of platinum and SS304L

Cathodic polarization curves for Pt and SS304L in various concentrations of NaOH at 500 rpm are shown in Figure 3(a) and (b) respectively. For polarizations on Pt in NaOH solutions with pH values ≤ 14.9, an ORR activation-controlled region is present from OCP to -0.2 V_{SCE}; below that, the reduction becomes diffusion limited from -0.2 V_{SCE} to roughly -1.0 V_{SCE}. Below -1.0 V_{SCE} the hydrogen evolution reaction (HER) is dominant. For a pH of 16.5, a very small activation-controlled region is present from roughly -0.2 to -0.3 V_{SCE}, which transition to a semi-diffusion-limited region down to to -1.2 V_{SCE}. Below -1.2 V_{SCE}, HER is dominant. Although it may appear that diffusion-limited i_{lim} is present in a pH of 16.5, the current increases between -0.4 V_{SCE} and -1.1 V_{SCE} increases from 6.4×10^{-4} to 3.4×10^{-3} mA/cm^2.

For polarizations on SS304L in NaOH solutions with pH's ≤ 14.9, an ORR activation-controlled region is present from OCP to -0.9 V_{SCE} below which the reduction becomes diffusion limited from -0.9 V_{SCE} to roughly -1.2 V_{SCE}. Below -1.2 V_{SCE}, HER is dominant. For a pH of 16.5, a very small activation-controlled region is present from roughly -0.9 to -1 V_{SCE}, but no diffusion-limited i_{lim} is present. Below -1.2 V_{SCE}, HER is dominant. It is further noted that there is a drastic decrease in OCP (nearly 250 mV) at pH of 16.5, relative to pH's of 13.6, 14.5 and 14.9.

In Figure 4, deaerated polarization scans are shown for solutions with a pH of 13.6 and 16.5 for SS304L. Overall, in all deaerated tests, a depression of OCP is experienced and a decrease in the limiting current density for ORR is seen for NaOH with a pH of 13.6. For NaOH with a pH of 16.5, polarization scans are nearly identical.

Polarization scans were performed after reduction of the SS304L surface at -1.5 V for one hour and are presented in Figure 5. The cathodic polarization scans for SS304L with a pH value of 13.6 shows little overall difference between the reduced and non-reduced scans with a slight increase in i_{lim} when reduced. In contrast, the change to polarization behavior after reducing the SS304L in pH 16.5 solutions is significant. After reduction of the surface, the OCP in pH 16.5 is near the HER reversible potential (-1.21 V_{SCE}) indicative of HER being the only cathodic reduction reaction on the surface.

Levich Analysis

Pt and SS304L in NaOH solutions with pH values ≤ 14.9 exhibited linear Levich behavior as seen in Figure 6(a), (b), and (c) respectively. As an i_{lim} was not exhibited in pH 16.5 for either SS304L or Pt, Levich behavior was not observed. Values of n were calculated using Equation 5 and data in Table 1. The number of electrons transferred for both Pt and SS304L are presented in Table 2 and less than two electrons for all cases presented. It is noted that at high rotation rates in all solutions, i_{lim} is suppressed on SS304L in comparison to Pt.

Pourbaix analysis

In order to investigate solution interactions with the electrode surfaces, Pourbaix diagrams were created. Figure 7(a) and (b) shows the average OCPs of SS304L exposed in NaOH solutions overlaid with binary Fe-Cr Pourbaix diagrams containing no Cr and 0.23 x 10^{-6} M Cr respectively. It is noted that OCP values of SS304L are in a stability field for Fe_2O_3 phase in NaOH solutions with pH values of ≤ 14.9. At a pH of 16.5, the OCP value is in an active corrosion region with the stable species being $Fe(OH)_4^{2-}$ regardless of the Cr content. SS304L OCP values have a variation of -184 ± 43 mV/pH. A Pourbaix diagram and OCP measurements for Pt in the various NaOH solutions is shown in Figure 7(c). Pt OCP values have a variation of -47 ± 21 mV/pH and all lie in the stable region.

Discussion

Superoxide intermediate causes for decreased ORR electron transfer number in pure NaOH solutions

Superoxide formation (Eq. 2) results in a calculated electron transfer of less than two on platinum and SS304L. As previously stated, the electrons transferred range from 1.75 at a pH of 13.6 to 1.30 at a pH of 14.9 as shown in Table 2. A similar decrease in the electron transfer number was also observed by Jin et al. on Pt over the range of 1 to 12 M NaOH (pH of 13.8 to 16.3 respectively) [1]. Additionally, Zhang et al. measured an increase in the superoxide intermediate with increased hydroxyl concentration has been observed with using a scanning electrochemical microscope (SECM) on Pt. This study [18] as well as Wu et al. [26] presented dissolved oxygen concentrations and diffusivities which are closely to those calculated in Table 3 allowing for use in calculating the number of electrons transferred. Despite the heavy dependence on solution properties, the similar values and trends for the number of electrons transferred between the present study and Jin et al. [86] provide for validation in the solution parameters utilized. Overall, the decrease in the electron transfer number is attributed to the suppressed protonation of the superoxide with increased bulk hydroxyl concentration (Equation 11) [86] which has been directly observed with SECM by Zhang et al. [18]. It is interesting to note the calculated *n* are decreased on SS304L in comparison to Pt as shown by a larger negative deviation in slope from the Levich behavior (Figure 6). This deviation has been attributed to effects of the oxide film on SS304L [3,27,28].

Although ORR in pure NaOH solutions has a reaction mechanism involving superoxide formation and an electron transfer below two, alkaline solutions with various supporting anions have a different behavior. Babić et al. explored the ORR behavior of SS304 in 0.5 M NaCl at pH ranges from 4 to 10 (pH adjustments were made with ammonium hydroxide and hydrochloride acid) and found there were no differences in ORR behavior with all solutions, indicative of a four-electron transfer [16]. In sodium perchlorate solutions, Zhang et al. found that iron in near-neutral solutions exhibited electron transfer favoring a two-electron process with H_2O_2 production, yet, when the pH was adjusted to 11.3, a four-electron process was manifested [2]. Additionally, when iron was exposed to NaCl solutions between 0.005 – 1 M at a pH of 10, an electron transfer number of four was observed [17]. Finally, in bromide solutions, Pt experiences an increase in electron number from two to four with increasing pH [29,30]. While the mechanisms in different solutions vary, competitive adsorption [29,30] and influences on protonation [1] likely play a role in determining reaction mechanisms. Thus, the importance of other anions in solution is crucial to determining reaction mechanisms and informing overall corrosion processes. Because elevated pH’s have been directly observed [7] and calculated [13] in atmospheric scenarios, it is important to note that anions ions may influence reaction mechanisms and can influence the overall cathodic current available for dissolution. Therefore, the results presented here may not be directly applicable to atmospheric corrosion scenarios due to the presence of anions ions in the electrolyte solutions.

ORR is not the primary reduction reaction on stainless steel at high concentrations of NaOH

No i_{lim} was measured on SS304L in NaOH solutions at a pH of 16.5, and the measured current exceeds the predicted i_{lim} (Equation 5) for electron transfer numbers of both one and four as seen in Figure 5. As the cathodic current is not consistent with predicted ORR, it is of interest to determine the source of the increased current. First, the OCP for pH 16.5 is in a region of the

Pourbaix diagram that predicts active corrosion as shown in Figure 7(a) and (b), producing $Fe(OH)_4^{2-}$. Second, after reduction of the oxide on the surface of the alloy at -1.5 V_{SCE}, the OCP is in-line with predictions for HER at a pH of 16.5 (-1.21 V_{SCE}) indicating HER is the only cathodic reaction and neither the surface oxide (which has been removed) nor dissolved oxygen have an influence on the cathodic behavior. Finally, when cathodic polarization scans are conducted in a de-aerated environment (Figure 4), there is minimal change in the overall cathodic behavior indicating that the oxygen concentration has no effect on the cathodic reduction behavior of SS304L in NaOH solutions with a pH of 16.5. Thus, the cathodic reaction in concentrated NaOH solutions (pH = 16.5) is not ORR and the increased current is due to the reduction of the oxide film (Fe_2O_3) on the surface creating $Fe(OH)_4^{2-}$ as depicted in Figure 7(a) and (b) before transitioning to HER as the cathodic reduction reaction at significant overpotentials.

To the knowledge of the authors, the cathodic behavior of SS304L has not been investigated at such high pH values. Typically, an increase in cathodic current density on SS alloys is measured in the potential window of -0.6 to -0.8 V_{SCE} and is attributed to the Fe(III) to Fe(II) transition in the oxide film [3,23,27,31]. In NaOH solutions with a pH of 16.5, the OCP is below -0.8 V_{SCE} and the Fe(III) to Fe(II) transition is not responsible for the increase in current density. Instead, reduction of the oxide film to form $Fe(OH)_4^{2-}$ is responsible for the current density increase.

Implications

As presented in Figure 1 and Figure 2, cathodic regions on the surface of a corroding alloy, such as SS304L, can become chloride-poor and alkaline in atmospheric scenarios. For an NaCl electrolyte, this region will become rich in NaOH [8-11]. A comparison of the cathodic behavior between 0.6 M NaOH (Figure 3(b)) and 0.6 M NaCl at 500 rpm is presented in Figure 8(a). At any given potential, the cathodic current density is lower for 0.6 M NaOH in comparison to 0.6 M NaCl. The same trend holds for 5.4 M NaOH and 5.3 M NaCl (Figure 8(b)). As such, the compositional and pH gradient in the cathode will give rise to a variable potential and current density. The following implications compare pure NaCl and pure NaOH solutions and do not account for changes that could occur in a pH adjusted NaCl solution.

When modeling atmospheric corrosion scenarios, it is important to note that the electrolyte chemistry will change with corrosion damage and time and will influence both the potential and the current density. One such example involves the calculation of maximum cathodic currents in atmospheric environments. This involves determining the equivalent cathodic current density of an ideal cathode and can be calculated by integrating the current density from OCP to the repassivation potential [15,32,33]. In 0.6 M NaCl, the repassivation potential is roughly -0.265 V_{SCE} [34] and is denoted in Figure 8(a). In 0.6 M NaOH (pH = 13.6), the OCP is less than E_{RP} indicating that at a pH of 13.6 the cathode would no longer be able to supply current for anodic dissolution. Thus, in the atmospheric corrosion scenario, the total cathodic current available would not only be limited by ohmic drop (governed by solution conductivity, water layer thickness, and cathodic kinetics) [15], but would also be limited by an increase in the pH dropping the OCP below E_{RP}.

Another applicable modeling study by Liu et al. simulated the cathodic current in a galvanic couple between SS316L and AA7050 [35] and was further explored by Katona et al. [36]. While SS316L and SS304L contain different elemental compositions, the polarization scans are similar in 0.6 M NaCl [27] and any comparisons made here will be qualitatively the same. The model investigated by Liu et al. utilized boundary conditions for SS316L in 0.6 M NaCl from RDE experiments for a Finite Element Model which calculated the potential distribution along a metallic surface and the associated cathodic current supplied for electrolyte layers of varying thicknesses. The model utilized a secondary current distribution and did not account for changing electrolytes [35]. The OCP of AA7050 is roughly -0.8 V_{SCE} [35] and would be in the diffusion limited regime of 0.6 M NaCl while the OCP is in the activation-controlled kinetics of 0.6 M NaOH. Therefore, the coupled current density from mixed potential theory between an AA/SS304L couple is lower in NaOH in comparison to NaCl. If one were to account for the changing electrolyte and the influence of pH on the cathodic kinetics, it is likely that a decreased cathodic current would be calculated. The same argument holds for saturated NaCl when comparing to 5.4 M NaOH and 5.3 M NaCl as shown in Figure 8(b). In all cases, utilizing NaCl polarization curves will be conservative as a higher cathodic current would be calculated. A higher cathodic current would equate to a greater amount of corrosion damage.

Conclusions

The cathodic reduction behavior of platinum and stainless steel 304L was investigated in NaOH solutions ranging in pH from 13.6 to 16.5. It was found that in solution pH's less than 16.5 the cathodic reduction reaction on SS304L was the oxygen reduction reaction with an electron transfer number of less than two due to superoxide formation as an intermediate. With increasing pH, the number of electrons transferred decreased. At a pH of 16.5, the cathodic reduction reaction on SS304L is no longer the oxygen reduction reaction and the cathodic current on the surface of the alloy is due to the oxide reduction that is occurring on the surface alloy as indicated by the creation of multi-component Pourbaix diagrams. This has important implications for atmospheric corrosion scenarios.

Acknowledgements

Sandia National Laboratories is a multi-mission laboratory managed and operated by National Technology and Engineering Solutions of Sandia, LLC., a wholly owned subsidiary of Honeywell International, Inc., for the U.S. Department of Energy's National Nuclear Security Administration under contract DE-NA0003525. Financial assistance from the U.S. Department of Energy's Nuclear Energy University Program under contract DE-NE0008901 is also acknowledged. Helpful conversations with Dr. Charles Bryan (Sandia National Laboratories) are gratefully appreciated. This document is SAND####.

References

[1] W. Jin, H. Du, S. Zheng, H. Xu, Y. Zhang, J. Phys. Chem. B, 114, 6542–6548 (2010).

[2] Q. Zhang, P. Liu, Z. Zhu, J. Zhang, F. Cao, Corros. Sci., 164, 108312 (2020).

[3] C.L. Alexander, C. Liu, A. Alshanoon, R.M. Katona, R.G. Kelly, J. Carpenter, C. Bryan, E. Schindelholz, J. Electrochem. Soc., 165, C869–C877 (2018).

[4] R.M. Katona, J.C. Carpenter, A.W. Knight, C.R. Bryan, R.F. Schaller, R.G. Kelly, E.J. Schindelholz, Corros. Sci., 177, 108935 (2020).

[5] H.S. Klapper, J. Goellner, Corros. Sci., 51, 144–150 (2009).

[6] N.S. Azmat, K.D. Ralston, B.C. Muddle, I.S. Cole, Corros. Sci., 53, 1604–1615 (2011).

[7] E.J. Schindelholz, H. Cong, C.F. Jove-Colon, S. Li, J.A. Ohlhausen, H.K. Moffat, Electrochim. Acta, 276, 194–206 (2018).

[8] E. Schindelholz, B.E. Risteen, R.G. Kelly, J. Electrochem. Soc., 161, 450–459 (2014).

[9] J. Weissenrieder, C. Leygraf, J. Electrochem. Soc., 151, B165 (2004).

[10] J. Zhang, J. Wang, Y. Wang, Corrosion, 61, 1167–1172 (2005).

[11] T. Tsuru, K. Tamiya, A. Nishikata, Electrochim. Acta, 49, 2709–2715 (2004).

[12] C.R. Bryan, E.J. Schindelholz, in: Corros. 2018, Phoenix, (2018), p. Paper 10516.

[13] R.M. Katona, A.W. Knight, E.J. Schindelholz, C.R. Bryan, R.F. Schaller, R.G. Kelly, Electrochim. Acta, 370, 137696 (2021).

[14] R.M. Katona, A. Knight, C. Bryan, R.F. Schaller, R.G. Kelly, in: 2020 (ECS, ECSJ, KECS Jt. Meet., Virtual, (2020).

[15] Z.Y. Chen, R.G. Kelly, J. Electrochem. Soc., 157, C69–C78 (2010).

[16] R. Babić, M. Metikoš-Huković, J. Appl. Electrochem., 23, 352–357 (1993).

[17] Y. Miyata, S. Asakura, Corros. Sci., 44, 589–602 (2002).

[18] C. Zhang, F.R.F. Fan, A.J. Bard, J. Am. Chem. Soc., 131, 177–181 (2009).

[19] L. Greenspan, J. Res. Natl. Bur. Stand. - A. Phys. Chem., 81A, 89–96 (1977).

[20] B.Y.B. Levich, (1947).

[21] B. Beverskog, I. Puigdomenech, Corrosion, 55, 1077–1087 (1999).

[22] B. Beverskog, I. Puigdomenech, Corros. Sci., 38, 2121–2135 (1996).

[23] A. Kocijan, Č. Donik, M. Jenko, Corros. Sci., 49, 2083–2098 (2007).

[24] T.L.S.L. Wijesinghe, D.J. Blackwood, Corros. Sci., 49, 1755–1764 (2007).

[25] M. Pourbaix, Atlas of Electrochemical Equilibria in Aqueous Solutions, First Engl, National Association of Corrosion Engineers, Houston, Texas, (1967).

[26] K. Wu, Y. Wang, X. Wang, S. Wang, B. Liu, Y. Zhang, H. Du, J. Clean. Prod., 203, 873–884 (2018).

[27] C. Liu, R.G. Kelly, Corrosion, 75, 1087–1099 (2019).

[28] N. Le Bozec, C. Compère, M. L'Her, A. Laouenan, D. Costa, P. Marcus, Corros. Sci., 43, 765–786 (2001).

[29] V. Briega-Martos, G.A.B. Mello, R.M. Arán-Ais, V. Climent, E. Herrero, J.M. Feliu, J. Electrochem. Soc., 165, J3045–J3051 (2018).

[30] V. Briega-Martos, E. Herrero, J.M. Feliu, Electrochim. Acta, 334, 135452 (2020).

[31] N. De Cristofaro, M. Piantini, N. Zacchetti, Corros. Sci., 39, 2181–2191 (1997).

[32] Z.Y. Chen, F. Cui, R.G. Kelly, ECS Trans., 3, 443–457 (2007).

[33] Z.Y. Chen, F. Cui, R.G. Kelly, J. Electrochem. Soc., 155, C360–C368 (2008).

[34] R.M. Katona, J. Carpenter, E.J. Schindelholz, R.G. Kelly, J. Electrochem. Soc., 166, C3364–C3375 (2019).

[35] C. Liu, J. Srinivasan, R.G. Kelly, J. Electrochem. Soc., 164, C845–C855 (2017).

[36] R.M. Katona, J.C. Carpenter, A.W. Knight, R.S. Marshall, B.L. Nation, E.J. Schindelholz, R.F. Schaller, R.G. Kelly, J. Electrochem. Soc., 168, 031512 (2021).

[37] T.J. Wolery, R.L. Jarek, Software User's Manual: EQ3/6 Version 8.0, Sandia National Laboratories, Albuquerque, NM, (2003).

[38] In-Drift Precipitates/Salts Model, Sandia National Laboratories, Albuquerque, NM, (2007).

Figures

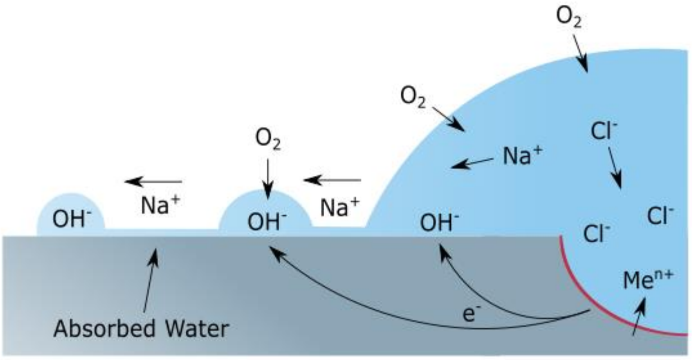

Figure 1: Schematic displaying the creation of a chloride-poor, alkaline solution in the cathode under a droplet. Presented diagram is adapted from [8-11].

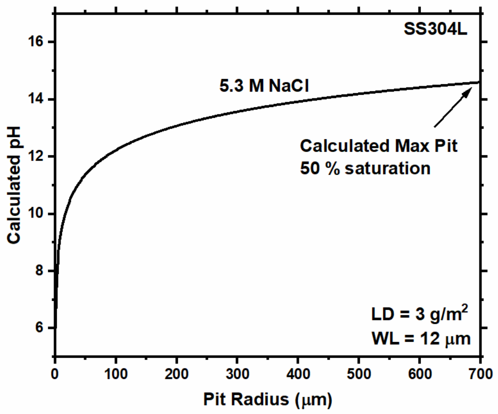

Figure 2: Predicted cathode pH as a function of anode radius for saturated (5.3 M) NaCl. The pH was calculated based on the formulism of Katona et al. [13].

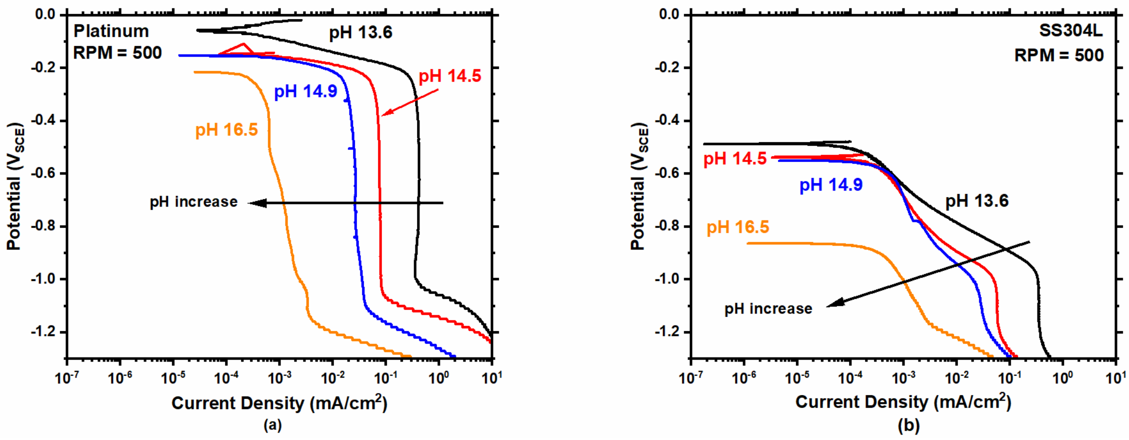

Figure 3: Representative cathodic polarization behavior of (a) Pt and (b) SS304L in aerated NaOH solutions at 25°*C, 500 rpm, and various pH values. Duplicates of each polarizations were performed*

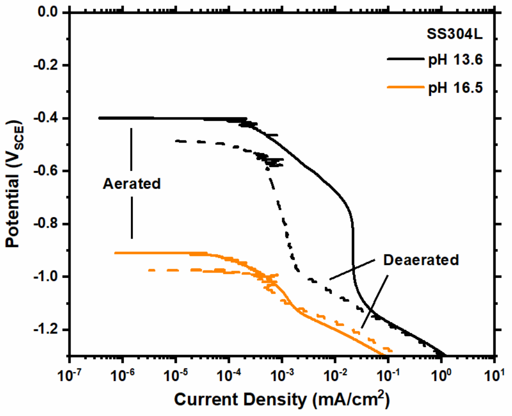

Figure 4: Representative cathodic polarization curves displaying the effect of the oxygen concentration (aerated and deaerated conditions) on SS304L RDEs at 0 rpm in 13.6 and 16.5 pH at 25^{o}C.

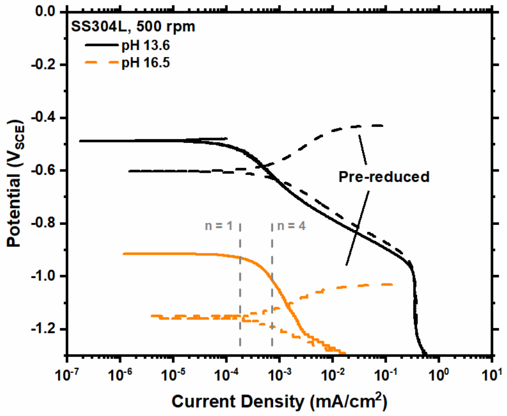

Figure 5:Comparison of cathodic polarization scans of SS304L RDE at 500 rpm in aerated NaOH solutions at 25 ˚C. Solid curves represent polished surfaces from Figure 3(b), whereas dashed curves have been reduced for 1 hour at -1.5 VSCE, followed by a cathodic scan.

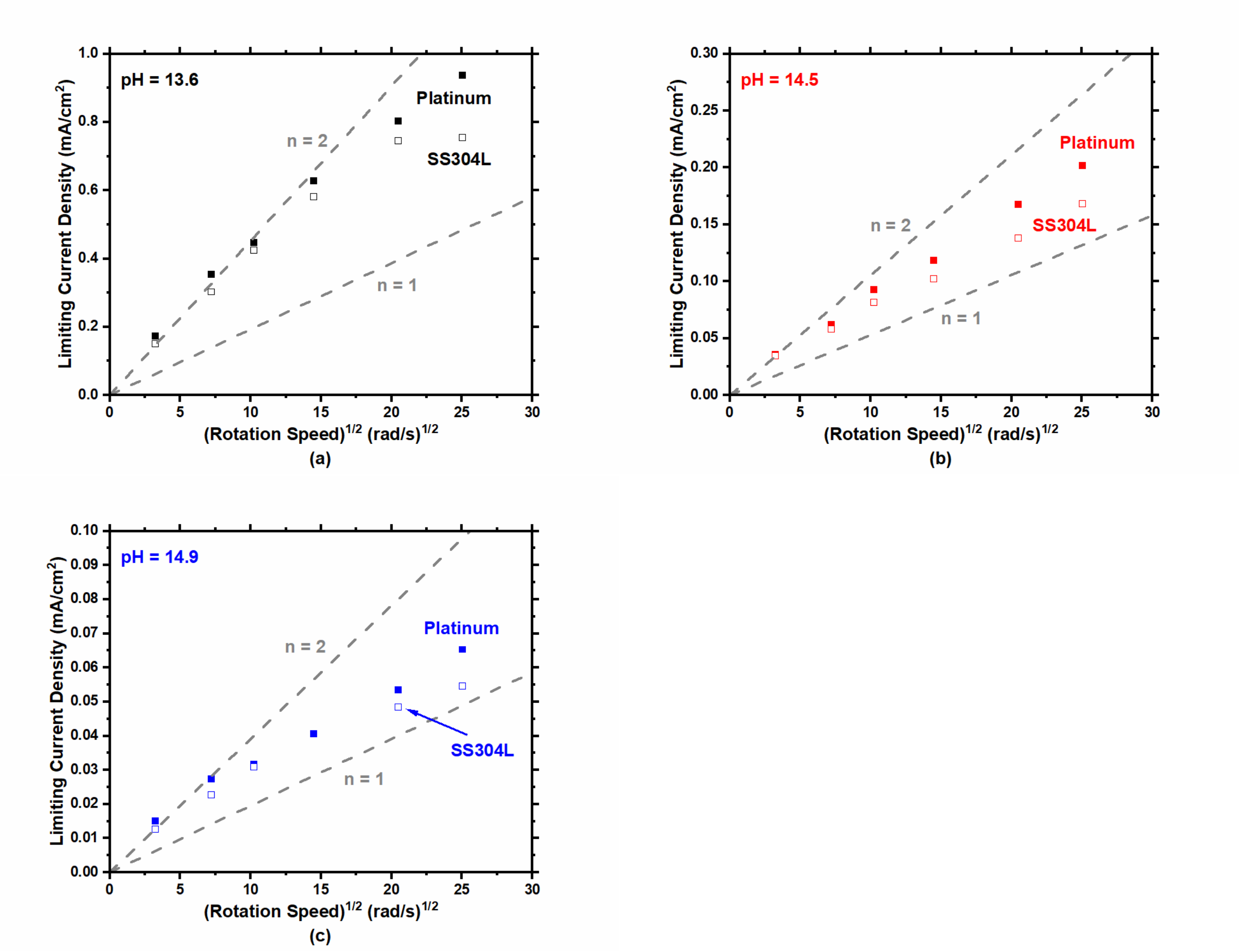

(a)

(b)

(c)

Figure 6: Levich plots displaying the diffusion limited current densities of Platinum (filled squares) and SS304L (open squares) in aerated NaOH solutions with pH values of (a) 13.6, (b) 14.5, and (c) 14.9. Data for rotation rates at 500 rpm are reported as averages of two polarization scans while all other rotation rates are singular experiments.

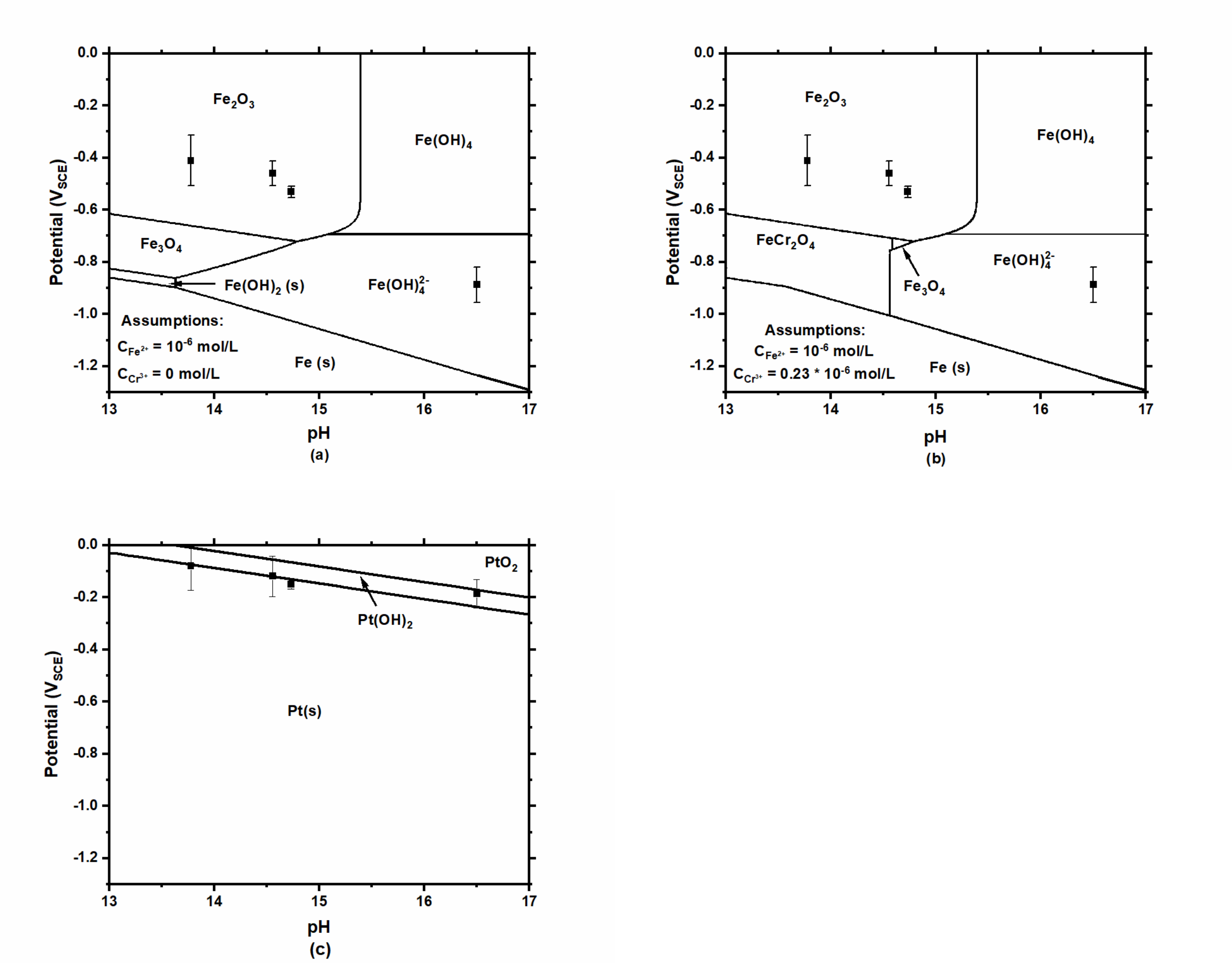

*Figure 7: Overlay of SS304L Pourbaix diagram [21,22] and average OCPs in each NaOH solution. (a) Fe-H_2O system at high pH values. The total concentration of Fe^{2+} is assumed to be 10^{-6} M. (b) Fe-Cr-H_2O system with CrO_4^{2-} concentration of 0.28*10^{-6} M. (c) Trends in average OCP for platinum overlaid with a platinum Pourbaix diagram. Error bars represent one standard deviation.*

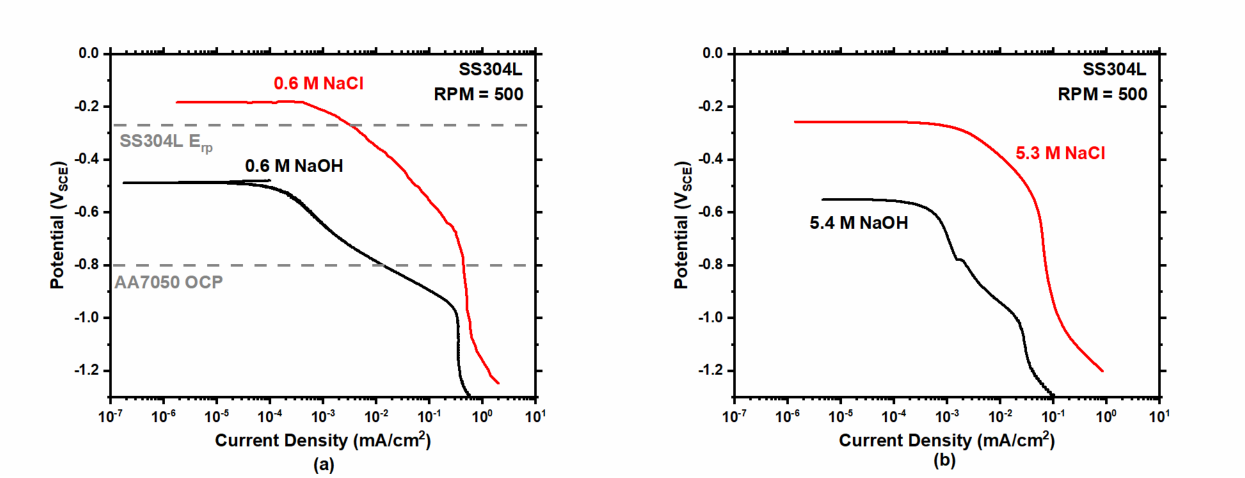

Figure 8: Comparison of cathodic kinetics of SS304L exposed to (a) 0.6 M NaOH (Figure 3(b)) and 0.6 M NaCl and (b) 5.4 M NaOH (Figure 3(b)) and 5.3 M NaCl [3]. It is noted that all polarization scans are at a rotation rate of 500 rpm.

Tables

Table 1: Calculated (OLI Studio) solution properties for NaOH solutions of interest

NaOH Concentration (C_{NaOH})	pH[1]	Saturated Oxygen Concentration (C_{O_2})	Oxygen Diffusivity (D_{O_2})	Density (ρ)	Viscosity (μ)
mol/L		mol/m^3	m^2/s	kg/m^3	$Pa * s$
0.6	13.6	2.10×10^{1}	1.91×10^{-9}	1023	1.01×10^{-3}
3.6	14.5	7.08×10^{-2}	1.00×10^{-9}	1134	1.94×10^{-3}
5.4	14.9	3.95×10^{-2}	5.20×10^{-10}	1188	3.08×10^{-3}
12.8	16.5	8.09×10^{-3}	2.14×10^{-11}	1354	1.48×10^{-2}

Table 2: Calculated electron transfer numbers as a function of NaOH solution pH and electrode material.

NaOH Concentration (M)	**NaOH pH**	**Platinum**	**Stainless Steel 304L**
0.6	13.6	1.8	1.5
3.6	14.5	1.7	1.3
5.4	14.9	1.5	1.3

E. Prediction of Maximum Pit Sizes in Elevated Chloride Concentrations and Temperatures

Prediction of Maximum Pit Sizes in Elevated Chloride Concentrations and Temperatures

R. M. Katona[1,2], J. Carpenter[3], E. Schindelholz[3], R. G. Kelly[1]

[1] Materials Science and Engineering, University of Virginia, Charlottesville, VA 22904 USA

[2] Storage and Transportation Technology, Sandia National Laboratories, Albuquerque, NM 87123 USA

[3] Materials Reliability, Sandia National Laboratories, Albuquerque, NM 87123 USA

Key words: stainless steel, pitting corrosion, 1D artificial pit, maximum pit size, elevated temperature, saturation concentration

Abstract

Calculated maximum pit sizes for stainless steel 304L (SS304L) are presented for atmospheric conditions with elevated chloride concentrations and temperatures. These calculations were carried out by experimentally determining the pit stability product ($(i \cdot x)_{sf}$), repassivation potential (E_{rp}), and cathodic kinetics. These results were aided by determination of a solubility curve as a function of temperature for a stoichiometric metal salt mixture of iron chloride ($FeCl_2$), chromium chloride ($CrCl_3$), and nickel chloride ($NiCl_2$). Based on these newly measured saturation concentrations, metal ion diffusivities were calculated. Overall, it was found that $(i \cdot x)_{sf}$ decreases with increasing chloride concentration and increases with increasing temperature. E_{rp} was determined to decrease with increasing concentration and increase with increasing temperature. When incorporated into the maximum pit size model, these experimental results yielded a small increase in maximum pit size with increasing bulk chloride concentrations and/or increasing temperature.

Introduction

Type 300 stainless steels (SS) are used heavily in marine environments due to their overall excellent corrosion resistance [1,2]. Although characterized as a corrosion resistant alloy, the 300 grade SS are susceptible to localized corrosion in the presence of aggressive anion species, including chloride, which is the dominant anion in marine atmospheres. The stability of localized corrosion propagation is governed by the alloying elements in the sample of interest, the bulk environment (including oxidizing potential) and the critical chemistry within the pit cavity [1].

Pitting corrosion involves localized metal oxidation creating metal cations in the pit cavity which results in low pH, high chloride concentrations due to hydrolysis reactions, electromigration of chloride, and the limited diffusion of these species out of the pit [1,3] Critical conditions for pit stability and further propagation have been described by the repassivation potential (E_{rp}) and the pit stability product ($(i \cdot x)_{sf}$) where i is current density, x is pit depth and the subscript sf indicates the presence of a salt film [2,4]. E_{rp} is a lower bound of electrochemical potential below which propagation will no longer occur, and the pit will repassivate [4] Galvele [5] originally showed that for a one-dimensional pit to sustain dissolution, the quantity $(i \cdot x)$ must exceed a critical value connected to the critical chemistry (pH) required to prevent oxide film formation. It is noted that Galvele's original formulism did not require the presence of a salt film on the surface of the alloy. If at a certain depth (x) the anodic dissolution current density (i) is insufficient to meet the pit stability criterion, the pit will repassivate because the critical chemistry will be lost to the bulk by diffusion. Pit stability is a battle between the production of acidity (via hydrolysis of metal cations produced by the dissolution current density, i) and diffusion of that concentrated solution to the bulk, which is controlled by the diffusion distance, x. Thus, a shallow pit requires a high current density to maintain stability, whereas a deeper pit requires lower current density.

Atmospheric exposure testing of SS in different environmental conditions has shown pit sizes reach a limiting value over time [6-10] The complex process of pitting corrosion under freely corroding conditions has been previously modeled based on the inherent coupling between anodic and cathodic kinetics, and a brief summary of this method is included in the Appendix [11] Simply put, the anodic dissolution at the base of the pit must have an associated cathodic current supply sufficient to meet the anodic current. However, in thin electrolyte conditions, ohmic drop considerations in the thin electrolyte film limit the cathodic current supply. Through the inherent coupling of the cathode and anode, a finite cathode therefore implies a finite anode, *i.e.*, a finite pit size. Finding the maximum pit size can be achieved by determining: (a) the maximum cathode current the external surface can generate, and (b) the minimum dissolution current needed to maintain the critical chemistry in the pit as a function of the pit size. Combining these two relations results in an expression for the maximum pit size obtainable under the given conditions.

Pit sizes in exposure testing have been shown to be dependent upon both electrolyte composition and concentration and temperature in bulk solution [2,12]. In the framework of the maximum pit size model, this dependence implies that anodic and/or cathodic kinetics are dependent on temperature and chloride concentration. Anodic kinetics parameters ($(i \cdot x)_{crit}$, E_{rp}) have been explored as function of electrolyte composition (including chemical species and concentration)[4,12-23] and temperature [14-18,22]. However, as both dilute and concentrated salt solutions can be present on the metal surface when considering a wide range of temperatures and relative humidity in service conditions [24], the parameter space for SS304L material has not been sufficiently explored to inform decisions about anodic kinetics.

Anodic metal dissolution can also lead to saturation in the pit of metal cations $\left(C_{M^+}^{sat}\right)$ and corresponding anion, generally chloride, leading to a diffusion limited current density through metal salt film [22]. The saturation point not only impacts the pit stability product, but also impacts the repassivation characteristics of the pit. Although it is thought that the critical solution composition is substantially less than saturation [14,25,26], much can be understood about pitting by starting by consideration of saturation conditions. Experimental determination of the saturation concentration has been explored by multiple authors [13,19,23,27–33]. As a surrogate for pit chemistries, ferrous chloride ($FeCl_2$) has generally been used as SS alloys are iron-based [13,22]. The saturation point of $FeCl_2$ has been studied extensively as a function of temperature [31-34]. However, SS alloys contain considerable amounts of chromium and nickel which can impact saturation concentrations [23,24]. Assuming stoichiometric dissolution of SS304, iron-, chromium- and nickel-containing metal salts will form. As these metal salts will reach saturation during anodic pit growth at concentrations likely different than that of $FeCl_2$ alone, it is of importance to understand the behavior of the metal salt mixture.

Although equally important to the corrosion process, the impact of environment on cathodic kinetics has been seldom explored [12,35]. Assuming oxygen reduction is the main cathodic reaction happening on the surface of the alloy, this reaction is dependent on both the diffusivity and concentration of oxygen available in solution. With changes in solution concentration and temperatures, consequential changes in these properties will impact the cathodic kinetics and the subsequent cathodic current to support anodic dissolution.

The maximum pit size model framework for atmospheric conditions exploits the requirement of the conservation of charge that controls the coupling of the anode and the cathode reactions on a single surface. Its inputs include anodic kinetic parameters of relevance to the pit ($(i \cdot x)_{sf}$, E_{rp}), cathodic kinetics relevant to the external surface, and information about the solution layer. In this work, anodic and cathodic kinetics across a wide range of chloride concentration and temperature have been explored. The dependence of stoichiometric anodic dissolution on pit chemistry was also determined at elevated temperatures. Coupling of these anodic and cathodic kinetics yields an evaluation of maximum pit sizes across the predicted surface conditions. This approach would allow for more efficient use of resources by determining the conditions of most concern for SS304 materials in marine environments and could serve as an input for inspection and maintenance decisions. This subject is appropriate for an issue of *JES* honoring Hugh Isaacs due to his long-standing interest in pitting, diffusional properties of processes important to pitting, and his establishment of many conditions inside pits using novel, *in-situ* measurement methods [23,30,36–39].

Experimental

Artificial pit experiments: The pit stability product under the presence of a salt film ($(i \cdot x)_{sf}$) and repassivation potential (E_{rp}) were determined for stainless steel 304L (SS304L) in four sodium chloride (NaCl) concentrations (0.6, 1, 3, 5.5 M). Solutions were temperature-controlled with a water bath at four temperatures (25°C, 35°C, 45°C, and 55°C) with an accuracy of ±0.1°C. The composition by certificate of the SS304L wire used can be seen in Table 1. The diameter of the SS304L wire was 50 μm. The wire was embedded in epoxy so that the diameter of the wire was exposed with an area of 7.85×10^{-5} cm^2. The epoxy and wire were wet ground with 320 grit silicon carbide paper. The wires were examined under an optical microscope in order to ensure a cross-section of the wire was fully exposed. Prior to electrochemical testing, the samples were further cleaned with methanol and dried in nitrogen. The lead-in-pencil configuration used in this study can be seen schematically in the work done by Srinivasan et al. [4].

Electrochemical technique: Samples were placed in an electrochemical cell and electrochemical testing was carried out by applying an anodic potential of +750 mV$_{\text{SCE}}$ (versus a saturated calomel electrode (SCE)) for 5 to 20 minutes to ensure pit initiation with a platinum coated niobium mesh as a counter electrode. The potential was stepped down to +450 mV$_{\text{SCE}}$ for different periods of time to allow for pit propagation to different depths. A polarization scan from +450 mV$_{\text{SCE}}$ to -600 mV$_{\text{SCE}}$ at a scan rate of 5 mV/sec was then performed. After the polarization scan, the pit was immediately re-initiated by polarization to +750 mV$_{\text{SCE}}$, and the cycle was repeated. A schematic representation of this sequence can be seen in the work of Srinivasan et al.[4]. Eight to ten repetitions of the cycle were performed as it has been shown that the pit depth needs to exceed 8-10 times the diameter (~400-500 μm) to prevent measured values from being influenced by the hemispherical diffusion at the pit mouth [40]. It is noted that pitting did not always initiate on the first cycle, and a higher potential was sometimes utilized to initiate pitting.

Determination of $(i \cdot x)_{sf}$*:* Based on Fick's first law, the diffusion limited current density and pit depth under steady state conditions can be expressed as:

$$i_L d = nFD_{M^+}\Delta C = nFD_{M^+}C_{M^+}^{sat} = (i \cdot x)_{sf} \qquad (1)$$

where n is the number of electrons transferred, F is Faraday's constant $\left(F = 96{,}485\,\frac{C}{mol}\right)$, D_{M^+} is the diffusion coefficient of metal cations, and ΔC is the concentration difference of metal cations at the bottom of the pit and the bulk solution and it is assumed that the concentration at the mouth of the pit is zero at sufficiently deep pits [40]. Based on stoichiometric dissolution of the alloy used in this study, $n_{304} = 2.2$ [19]. Successive polarization scans allow for the extraction of the limiting current density (i_L) as well as the E_{rp}, as a function of pit depth as shown in Figure 1. Thus, based on Equation 1, plotting the limiting current densities against the reciprocal of the pit depth $(1/d)$ will determine $(i \cdot x)_{sf}$ via the slope of the curve. During the change in potential, the nominal change in current density was small, demonstrating that the reaction was under diffusion-limited conditions.

In order to determine the pit depth, the total anodic charge density during the potentiostatic holds and cathodic polarizations were converted to pit depth. Using Faraday's law for alloys, the depth of the pit can be expressed as:

$$d = \frac{A}{nF\rho} \int_0^t i \, dt \qquad (2)$$

Where i is the current density, A is the mean atomic weight $(A_{304} = 55.3\ g/mol)$, ρ is the density $(\rho_{304} = 7.8\ g/cm^3)$, and dt are infinitesimal time steps [19,38]. These calculations were made assuming stochiometric dissolution of Fe^{2+}, Cr^{3+}, and Ni^{2+}. Automation of these calculations was carried out in Matlab R2017a with a method similar to that set forth by Srinivasan et al.[4].

Determination of E_{rp}: The value of the repassivation potential E_{rp} was determined by the computer script as the potential during the linear polarization scan at which the values of *Z%* of the next *N* current density data points in the scan were lower than 30 μA/cm^2. In the present study, *Z* and *N* were set to 70% and 30 points, respectively, in accordance with Srinivasan et al. [4]. The collection rate was 10 points per second. The difference between the measured open circuit potential and E_{rp} under these specified conditions and algorithm parameters was typically less than 2 mV and not greater than 15 mV. This method serves as an unbiased, rational means to determine when the potential has reached a relatively constant value, which is deemed E_{rp}. It is noted that no temperature corrections were made for E_{rp} measurements.

Determination of $C_{M^+}^{sat}$: Saturation concentrations $(C_{M^+}^{sat})$ were determined with a procedure similar to that of Chou and Phan [32]. A brief summary of this method is provided. Metal chloride salt mixtures containing stoichiometric amounts for 304L of Fe^{2+}, Cr^{3+}, and Ni^{2+} were created in accordance with the composition seen in Table 1. $FeCl_2·(4H_2O)$, $CrCl_3·(6H_2O)$, and $NiCl_2$ of analytical grade were weighed and added to a Pyrex® tube. Water from a Millipore® System with resistivity of $18.2\ M\Omega.cm$ was then added to the tube to an approximate volume of 20 mL. The weight of the solution as well as the liquid volume were recorded. The molality of the solution was calculated based on the total weight of the metal salts. A stir bar was placed in the bottom of the tube. Approximately 5 mL of silicon oil was added to the top of the solution in order to prevent evaporation. The top of the beaker was then sealed with a rubber stopper and filled with a positive pressure of N_2 gas in order to minimize the oxidation of Fe^{2+} ions to Fe^{3+} ions. The solution was then placed in a water bath, heated to above 60°C, and then slowly cooled to room temperature in order to nucleate large salt crystals. The solution was then systematically heated, incrementing first with large differences in temperature and then by ±0.1°C when the solution was close to the saturation point and subsequent dissolution. Time steps of at least 5 min were taken with each temperature increase near saturation. A bright light illuminated the bottom of the test tube in order to help visualize when the last crystal was dissolved. At this point the temperature was recorded. The pH was then measured within 2 minutes corresponding to a maximum measured difference in temperature of 5°C. It is noted that there was no temperature correction for the pH and all reported pH values are at temperature. The solution was not cooled in order to keep the concentration as close to saturation as possible. This process was repeated until a concentration curve was created spanning the temperature range (25-55°C). Duplicates were conducted; however, it was often difficult to make solutions with the exact same molality as once water was added it could not be removed from the system. Therefore, all experiments run are reported and contain an accuracy in temperature of ±0.1°C.

Determination of cathodic kinetics: Cathodic kinetics were determined in solutions less corrosive than NaCl in order to prevent convolution of the cathodic kinetics with anodic dissolution due to open circuit localized corrosion. As cathodic kinetics can be impacted by active corrosion, it is of interest to determine the maximum cathodic kinetics possible on the surface of the alloy in a non-corrosive solution [11]. Sodium bromide (NaBr) was chosen as it was shown to be less corrosive than NaCl as characterized by a transient free OCP values and a post-scan visual inspection of the surface revealing no pitting. Surrogate solutions of NaBr were determined based on the Levich equation concerning the mass transfer diffusion limited current density for oxygen reduction [41].

Thus, based on the Levich equation, the concentration of NaBr which matched the quantity of $i_{lim} \propto D_{O_2}^{2/3}\nu^{-1/6}C_{O_2}^{sat}$ for NaCl solutions at temperature was chosen. In order to determine this quantity, the solution thermodynamics database of the OLI Studio Analyzer 9.5 (OLI Systems, Inc., Cedar Knolls, NJ) software was utilized. The quantity of $D_{O_2}^{2/3}\nu^{-1/6}C_{O_2}^{sat}$ was first calculated for NaCl at a desired concentration and temperature given by experimental parameters. The solution of NaBr at a given temperature that matched the given quantity was then chosen as the surrogate solution.

Determination of maximum pit size: The maximum pit size was determined by the framework set forth by Chen and Kelly, with a brief summary presented in the Appendix [11]. The cathodic current was numerically solved based on Equation A6 as shown in the Appendix. The intersection of the cathodic current from Equation A6 and anodic current from Equation A1 yielded a maximum pit size. Values for conductivity and RH were calculated using the solution thermodynamics database of the OLI Studio and can be seen in Table 2. An areal density of NaCl was assumed in all cases to be 200 μg/cm^2 These calculations were combined with experimental $(i \cdot x)_{sf}$ and E_{rp} results determined in this study. In this study, the $(i \cdot x)_{sf}$ values were converted to that appropriate for a hemispherical geometry given by the expression $(I_{pit}/r_{pit})_{sf}$ as presented in the Appendix.

Results

$(i \cdot x)_{sf}$ and $D_{M^+}C_{M^+}^{sat}$ in NaCl solutions: Figure 1 shows successive polarization scans of SS304L lead-in-pencil experiments which were used to determine the pit stability product $((i \cdot x)_{sf})$ and repassivation potential $\left(E_{rp}\right)$ as shown in Figure 2(a) and (b) respectively. Pit depths on the order of at least 8-10 times the diameter of the wire were used in order to extract $(i \cdot x)_{sf}$. Assumptions of diffusion control during experimentation are validated by the observed linearity between i_{lim} and $(1/d)$. Values from depths less than 400 μm where ignored as there was a deviation from linearity indicating 1-dimensional diffusion control was no longer valid due to hemispherical diffusion in the bulk solution at the pit mouth [40]. Bulk NaCl solutions were used at their natural pH which ranged from 5.5-6.8. The same procedure was repeated across temperatures ranging

from 25°C to 55°C with an accuracy of $\pm 0.1^{o}C$. The dependence of $(i \cdot x)_{sf}$ and $D_{M^+}C_{M^+}^{sat}$ with increased temperature in NaCl solutions can be seen in Figure 3(a) and (b) respectively. It is noted that $(i \cdot x)_{sf}$ and $D_{M^+}C_{M^+}^{sat}$ are directly related based on Equation 1. Both are reported in this instance due to the fact that $(i \cdot x)_{sf}$ is used in the maximum pit calculation, whereas $D_{M^+}C_{M^+}^{sat}$ tends to be more commonly reported in literature. At all concentrations, an increase in $(i \cdot x)_{sf}$ and $D_{M^+}C_{M^+}^{sat}$ is seen with an increase in temperature. At all temperatures tested, $(i \cdot x)_{sf}$ decreased with increasing bulk NaCl concentration. Corresponding $D_{M^+}C_{M^+}^{sat}$ values can be seen in Figure 3(b) and again decrease with increasing bulk chloride concentration.

E_{rp} in NaCl solutions: The high-throughput method used in this study also allowed for the determination of E_{rp} which has been shown to be constant if sufficient charge was passed (*i.e.*, the pit was sufficiently deep) [42,43]. An example of this can be seen in Figure 2(b) where data points with a charge density greater than 1,200 C/cm^2 (corresponding to a pit depth of ~400 µm) were used to generate both an average and standard deviation. It is noted that the approach to a "plateau" E_{rp} was not always via the same pattern. In Figure 2(b), E_{rp} increased with increasing charge density (deeper artificial pits). Other concentrations and temperature followed the opposite trend where increasing the charge density (deeper artificial pits) caused a decrease in E_{rp}. There was no discernable pattern in concentrations or temperatures that lead to an ascension or depression to a plateaued E_{rp} value. This observation is similar to data reported by Woldemedhin *et al.* for lithium chloride (LiCl) solutions [19]. It is also noted that Srinivasan et al.[4] showed no difference in the plateaued value over the scan rate of 5 mv/sec to 100 mv/sec. Overall, E_{rp} as a function of chloride concentration and temperature can be seen in Figure 4. Generally, with increased bulk NaCl concentration, a mild decrease in E_{rp} is seen. Subsequently, with an increase in temperature, E_{rp} increases. It is noted that the reported potentials are at the temperature of the solution. Despite standard deviations being large in comparison to $(i \cdot x)_{sf}$, performing a t-test on all bounding cases confirms the trends. For example, performing a t-test between 0.6 M and 5.5 M solutions at each temperature produces a p-value that is lower than an alpha value of $\alpha = 0.05$ indicating the E_{rp} values are in fact different. However, significant differences were not always seen between 1M and 3M NaCl solutions. In terms of temperature, t-tests were performed between the same NaCl concentrations at temperatures 25°C and 55°C. Values from all concentrations proved to be

significantly different between 25°C and 55°C, however, at 45°C and 55°C not all concentrations were significantly different, suggesting E_{rp} is independent of temperature over the range of elevated temperatures tested in this experimentation.

Cathodic Kinetics in NaBr Solutions: Cathodic kinetics measured on bulk SS304L in NaBr solutions can be seen in Figure 5(a) and (b) corresponding to NaCl solutions of 0.6 M and 5.5 M solutions. The OCP of 0.6 M NaCl surrogate solutions was approximately -100 mV_{SCE}, whereas the OCP for 5.5 M NaCl surrogate solutions was lower and approximately -130 mV_{SCE} for 25°C and -90 mV_{SCE} for 45°C. It is also noted that the OCP increases slightly with increasing temperature at both low and high concentrations. In both Figure 5(a) and (b), two different temperatures are displayed. The elevated temperature (45°C) is characterized by an increase in cathodic currents at all potentials in comparison to those at room temperature (25°C). Note that visual inspection of the SS304L observed a smooth surface after cathodic polarization indicating that no pitting occurred on the surface.

C_{sat}^{M+} *increases with an increase in temperature:* In Figure 6(a) the expected increase in saturation concentration with increased temperature can be seen. The concentration was set by the amount of salt added to the solution. The temperature at which the solution became saturated, C_{sat}, was the measured variable, so the data are plotted as shown in Figure 6(a). A saturation molality of 4.81 mol/kg is observed at a temperature of 24.7°C and increases to 6.05 mol/kg at 58.9°C. The molality is reported instead of molarity as the error in volume measurements was too substantial and yielded a molarity with a high corresponding error. In Figure 6(b), the molality of the individual ions at saturation is reported as a function of temperature and again increases with increasing temperature.

Maximum pit size increases with increasing temperature: Maximum stable hemispherical pits sizes were calculated across a range of 0.6 M to 5.5 M over a range of temperatures from 25°C to 45°C based on the framework of Chen and Kelly [11] and a summary as given in the Appendix. These values were chosen based on the fact that the relative humidity in equilibrium with 0.6 M is ~98% whereas that in equilibrium with saturated NaCl (5.5 M) is ~75%. Values used in the simulation can be found in Table 2 and values for $(ix)_{sf}$ and E_{rp} can be found in Figure 3 and Figure 4 respectively. Cathodic kinetics from Figure 5 were also utilized. Maximum pit size calculations are displayed in Figure 7. An increase in maximum pit size is seen with an increase in chloride concentration regardless of temperature. When comparing the temperature dependence at 0.6 M, there is little difference in the calculated maximum pit size with a difference in pit size of ~1 µm (41.9 vs. 42.5 µm for 25°C vs. 45°C). At 3M (49.9 vs. 58.1 µm for 25°C vs. 45°C) and 5.5M (91.6 vs. 101.7 µm for 25°C vs. 45°C), the difference in calculated maximum pit size was slightly (~10 µm) larger. Thus, maximum pit sizes were generally slightly larger at elevated temperatures, with this trend being more noticeable at elevated chloride concentrations.

Discussion

Anodic and cathodic kinetics of SS304L in chloride-containing solutions were studied both as a function of chloride concentration and temperature. Anodic kinetics were assessed through a high-throughput artificial pit method allowing the extraction of pit stability product under the presence of a salt film ($(i \cdot x)_{sf}$) and the repassivation potential (E_{rp}). Anodic holds were used to grow one-dimensional pits in 50 µm diameter SS304L wire, and pit growth was followed by downward cathodic polarization to obtain these values. Kinetic data were obtained through successive anodic holds and downward cathodic scans. These results are summarized in Figure 3 and Figure 4 for $(i \cdot x)_{sf}$ and E_{rp} respectively. Note that $D_{M^+}C_{M^+}^{sat}$ will be used as a basis for discussion, however, as it is an equivalent expression to $(i \cdot x)_{sf}$ through the use the number of electrons transferred, and Faraday's constant as seen in Equation 1. Cathodic kinetics were assessed in NaBr solutions as they proved to be less corrosive than NaCl solutions. Various concentrations and temperatures were used in order to determine the effects on cathodic kinetics. Anodic and cathodic kinetics are combined and their impact on maximum pit size is explored. A saturation curve for a metal salt containing stoichiometric proportions of alloys to SS304L was also created.

The discussion section is formatted into four main sections. First, the results of the saturation concentration determination are discussed in terms of addition of bulk chloride. Next, although not explicitly used in the maximum pit model, properties of the pit solutions including the pH of the saturated solutions are discussed, as is the diffusivity of the metal cations in saturated solutions. This discussion will allow for the determination of $D_{M^+}C_{M^+}^{sat}$ and will explain trends that are reported in the results. Fourth, the maximum pit sizes will be calculated based on the reported data.

This set of results will be broken down into cathode size and further implications of this study. Finally, limitations of this approach are described and discussed.

C_{sat}^{M+} decreases as a function of increasing bulk chloride concentration at all temperatures due to the common ion effect: Figure 6 provides experimental determination of the saturation concentration for a stoichiometric metal salt mixture of $FeCl_2$, $CrCl_3$, and $NiCl_2$ as a function of temperature. This saturated solution will be referred to as a stoichiometric solution and the molality refers to total molality where the weight of the solute is the total of the weights of the three metal salts. During high-rate metal dissolution in 1-D pitting experiments, a salt film is formed at the surface of the metal and gives rise to a diffusion-limited current density of the metal dissolution at the base of a pit. It is evident that with increasing temperature, the saturation concentration increases. This effect has been extensively shown for $FeCl_2$ solutions by both Chou and Phan [38] and Schimel [34], and a similar trend is seen between both $FeCl_2$ solutions and the stoichiometric solution. A comparison with other reported saturation values can be seen in Figure 8. An increased total molality in the stoichiometric solution was seen in comparison to the solubility of pure $FeCl_2$ solutions. Comparing the $FeCl_2$ molality in the stoichiometric solution seen in Figure 6(b) to the individual solubility of $FeCl_2$ in Figure 8, the solubility of $FeCl_2$ decreases in the stoichiometric solution. This result is consistent with the observation of Isaacs et al. [37] that the addition of $NiCl_2$ and $CrCl_3$ in solution decreases the solubility of $FeCl_2$. It is noted that this method cannot detect the specific salt that would be first to precipitate out of the solution, however, it has been pointed out that $FeCl_2$ is most likely the salt that first precipitates [15,37].

The concentrations presented in both Figure 6 and 8 are the saturation concentration without any effects of additional bulk sodium chloride species in solution. Ernst and Newman [13] have shown that with increasing bulk chloride concentration, the saturation concentration decreases due to the common ion effect. It was shown that the saturation concentration can be calculated with $K_{sp} = [Me^{n+}][Cl^{-}]^{n}$, where K_{sp}, the solubility product, as determined from the saturation concentration in Figure 6with no bulk NaCl present. In order to keep concentrations in the same units, bulk chloride concentrations were converted to molality based on their density at temperature as calculated in OLI Studio. A saturation curve was then created based on both temperature and the impact of bulk chloride concentration. These results can be seen in Figure 9. It is noted that further work has been done in order to investigate the effects of temperature, bulk concentration, and electromigration on effective diffusivity coefficients [15]. Although K_{sp} is a rather simplified expression for taking into account the effect of bulk chloride concentration, it is useful in understanding the overall effects of bulk concentration. Along with this, other models [15,22] assume linear profiles of ion distribution within the pit geometry which may not necessarily be the case. This assumption will be a topic of future research.

As similarly shown by Ernst and Newman [13] and Jun et al. [15,22], an increase in bulk chloride decreases the saturation concentration. It is noted that independent of whether electromigration is taken into account, the same trends of decreasing chloride concentration with increasing bulk chloride concentration are seen [15,22]. As expected, due to the common ion effect, the largest difference at room temperature (T = 24.7°C) is seen between no bulk NaCl and 5.5 M bulk NaCl solutions in which the metal ion saturation concentration is decreased from 4.81 kg/mol (0 M bulk NaCl) to 4.03 kg/mol (5.5 M bulk NaCl).

A further analysis of the literature values of saturation concentration shows that the current calculated values are similar to other reported values. All conversions from molarity and molality used a density of 1.44 g/cm^3 for the density of saturated $FeCl_2$ [37]. Properties of salt films and subsequent mass transport of metallic species through the film have been studied in the past by multiple authors [13,19,22,27–30,37]. Kuo and Landolt [27] determined the ferrous ion saturation concentration at the metal surface to be 4.85 mol/kg based on measurements of the limiting current density for iron in $FeCl_2$ and NaCl. It was noted that in more acidic environments, given by the addition of hydrochloric acid (HCl), the saturation concentration of ferrous ions decreased [27]. Grimm et al. explored the structure and composition of salt films formed in $FeCl_2$ and NaCl solutions and reported ferrous chloride was the first salt precipitated as a salt film and the limiting current density was defined by mass transport limited by this film [28,29]. Isaacs et al. reported *in-situ* X-ray microprobe analysis of a salt film during dissolution of stainless steel 304 in 1 M NaCl to be 5.02 M (6.25 mol/kg). Isaacs et al. used an alloy with a composition of Fe: 66.70, Cr: 17.73, Ni: 12.81, and Mn 1.7% by weight. It was also reported the molar ratio of Fe:Cr:Ni was 3.46:1.08:0.48 respectively for the film [37]. If equimolar dissolution was assumed for the alloy used, one would assume that the same molar ratio would be 3.44:0.92:0.66 which is close to the measured values. Steinsmo and Isaacs also reported the saturation concentration of Fe-17.4Cr alloy in 1M NaCl to be 3.5 M (3.51 mol/kg) and pointed out that $CrCl_3$ could possibly reduce the solubility of $FeCl_2$ [30]. Woldemedhin et al. also equated the steady state fluxes of chloride and metal ions to determine the saturation concentration to be 3.72 M (3.82 mol/kg) [19]. Overall, the metal ion saturation concentration ($C_{M^+}^{sat}$) has been reported for bulk solutions containing 1 M NaCl across a wide range of alloys at room temperatures with various techniques. $C_{M^+}^{sat}$ values range from 3.5M to 5.02M (3.51 mol/kg to 6.25 mol/kg) across these studies. Saturation concentrations have been seldom studied at elevated temperatures with the exception of Jun et al. who evaluated $D_{M^+}C_{M^+}^{sat}$ values for martensitic S13Cr at 85℃ at across various concentrations of NaCl. Calculations for diffusivity accounted for the viscosity and electromigration via OLI Studio. Based on this calculation, the reported saturation concentration at 85℃ was between approximately 4.88 and 4.47 mol/kg based on bulk chloride concentration [15].

Properties of pit solutions

pH of saturated solutions decreases with increased total molality due to metal ion hydrolysis: Although not directly used in the calculation of maximum pit size, the pH of the solution impacts the repassivation behavior of the metal surface and is therefore reported for reference [1]. The pH of saturated solutions was measured within 2 min of saturation and is reported in Figure 10. Solutions were not cooled to room temperature and were within 5°C of the reported saturation concentration. No correction for temperature was made. Little to no precipitation was observed after the pH measurement was allowed to stabilize. Overall, a decrease in pH is seen with increasing molality. This trend is similar to that seen in $FeCl_2$ and $CrCl_3$ solutions [44]. Mankowski et al. reported a pH of ~0.06 with a chloride concentration of 6 N chloride concentration in $CrCl_3$ solutions [44]. This value is very similar to that of Suzuki et al. who determined the pH for artificial pits of 316L to be between 0.06 to 0.17 [45]. The decrease in pH in pits is generally explained as a result of metal ion hydrolysis of dissolved salts [1,3,44]. Thus, increasing the total molality of metal ions in solution would further decrease the pH of the solution. Although this explanation rationalizes the observed decrease in pH with increased molality, it is noted again that the pH measured in the current study was done at the temperature of saturation.

D_{M^+} *increases as a function of temperature and bulk chloride concentrations:* Diffusivity can be approximately modeled with the Stokes-Einstein equation:

$$D_{M^+} = \frac{kT}{6\pi \eta_D r} \qquad (3)$$

where k is the Boltzmann constant ($k = 1.38 \times 10^{-23}\ m^2kg/(s^2K)$), T is the absolute temperature in Kelvin, r is the radius of the diffusing metal ion, η_D is the dynamic viscosity of the solution at temperature T [22,25,46]. Values for the radii of hydrated cations of Fe^{2+}, Cr^{3+}, and Ni^{2+} where taken from Kielland [47]. The radius for hydrated 304L cation was calculated by weighting the radii of the individual cations in stoichiometric proportion of dissolution, which resulted in a value of 3.3Å. The assumption of cations being in the hydrated state serves as a reasonable lower bound for the diffusion coefficient [25]. Dynamic solution viscosities were calculated at temperature based on the saturation concentration seen in Figure 6 in OLI Studio. The following results were calculated based on no bulk chloride concentration, however a similar argument could be made for each bulk chloride concentration. Similarly to the saturation concentration, a more rigorous investigation is needed to inform the concentration and diffusion profiles that are present in the pit in order to get a more accurate effective metal ion diffusivity.

The diffusion coefficient as a function of temperature and solution viscosity can be seen in Figure 11. Although the solubility increases with temperature, the dynamic solution viscosity decreases with increasing temperature, causing an increase in the cation diffusion coefficient (as the radius is assumed to be constant). Although these calculations were carried out for no bulk chloride (*i.e.*, the saturation concentrations from Figure 6 were used and not the corrected values from Figure 9), a similar trend with respect to temperature is expected with an increase in bulk chloride as with increasing temperature the viscosity will still decrease causing an overall increase in the diffusion coefficient. At a single temperature, with increased bulk chloride concentration, a decrease is expected in the cation diffusion coefficient due to an increase in dynamic viscosity. This effect was shown by Jun et al. using electromigration considerations [15].

A summary of reported diffusivities again show that similar results are reported. Multiple authors have explored the diffusion of ions through similar salt films and concentrated solutions [22,27,30,37,38] Kuo and Landolt determined an effective diffusion coefficient of $8.5 \times 10^{-6}\ cm^2/sec$ for ferrous ions created by dissolution of pure iron and reported that others have found ionic diffusion coefficient to be $6 \times 10^{-6}\ cm^2/sec$ [27]. Gaudet et al. found for SS304 a diffusion coefficient of $8.24 \times 10^{-6}\ cm^2/sec$ [38]. Steinsmo and Isaacs reported a diffusion coefficient to be $5.9 \times 10^{-6}\ cm^2/sec$ [30] Isaacs et al. also presented diffusion values calculated through a combination of Fick's and Faraday's law for iron, chromium, and nickel to be $6.4, 5.6, and\ 8.0 \times 10^{-6}\ cm^2/sec$ respectively [37] Jun et al. utilized electromigration to determine the effective diffusion coefficient with varying bulk Na concentrations at $85°C$ and the reported values ranged from $27.3\ to\ 14.4\ \times 10^{-6}\ cm^2/sec$ [15].

$D_{M^+}C_{M^+}^{sat}$ decreases with increasing bulk chloride due to a decrease in saturation concentration and metal ion diffusivity: As shown in Figure 3(b), $D_{M^+}C_{M^+}^{sat}$ decreases with bulk chloride. It has been shown in Figure 9 that C_{sat} decreases with increasing bulk chloride concentration and following the logic set forth by the Stokes-Einstein equation and work done by Ernst and Newman [13] the diffusivity of metal cations is going to decrease with increasing bulk chloride. Thus, a decrease in $D_{M^+}C_{M^+}^{sat}$ might be expected.

$D_{M^+}C_{sat}$ increases as a function increasing temperature due to an increase in saturation concentration and metal ion diffusivity: As shown in Figure 3(b), $D_{M^+}C_{M^+}^{sat}$ increases with temperature. It has been shown in Figure 9 that $C_{M^+}^{sat}$ increases with increasing temperature regardless of bulk chloride concentration. Along with this, the diffusivity of metal cations is expected to increase with temperature as shown in Figure 11. Thus, an increase in $D_{M^+}C_{M^+}^{sat}$ is expected.

Multiple authors have studied both $D_{M^+}C_{M^+}^{sat}$ and $(i \cdot x)_{sf}$ as a function of alloy composition, chloride concentration and temperature [4,13,14,19,22,25,37,48,49] Commonly three different concentrations may be reported: saturation concentration ($C_{M^+}^{sat}$), super saturation concentration (C_{ss}), or the critical pit chemistry (C^*). $C_{M^+}^{sat}$ can be thought of the as the solubility of the metal chloride salt itself. C_{ss} is the supersaturation concentration prior to salt precipitation, whereas C^* can be thought of as the dissolved alloy cation concentration that is needed to sustain pitting [13,14]. C^*, sometimes denoted as C_{crit}, has been reported to range between 60% to 80% [38], as low as 50% to 60% [60], and 66% [50] of $C_{M^+}^{sat}$ indicating complete saturation is not necessary to propagate a pit. Based on the results seen in Figure 6 and taking $C_{crit} = 0.6C_{M^+}^{sat}$, C_{crit} can range from 2.89 mol/kg to 3.63 mol/kg at temperatures of 24.7°C and 58.9°C respectively.

Woldemedhin et al. examined the effects of ferric chloride ($FeCl_3$), acidified LiCl, and NaCl on the anodic kinetic parameters of both SS304L and SS316. They determined that $(i \cdot x)_{sf}$ decreases as a function of the logarithm of the chloride concentration with a slope of -0.11 ± 0.01 for all salts used in the study [19]. Fitting Figure 3(a) at $T = 25℃$ yields a slope of -0.12 ± 0.02 which is in good agreement that work [19]. Both Jun et al.[22] and Ernst and Newman [13] showed a decrease in $D_{M^+}C_{M^+}^{sat}$ with an increase in bulk NaCl concentration at $T = 30℃$ and $T = 85℃$ respectively. All results indicate that with increasing chloride concentration, $(i \cdot x)_{sf}$, and subsequently the product of $D_{M^+}C_{M^+}^{sat}$, will decrease with increasing chloride concentration.

Maximum pit sizes increase with increasing temperature due to increased cathodic capacity: As seen in Figure 7, calculated maximum pit sizes were determined as a function of temperature and NaCl concentration based on the parameters in Table 2 as well as the cathodic polarization scans in Figure 5. The maximum pit size was shown to increase with chloride concentration and temperature, although, the difference due to temperature at 5.5 M NaCl was much larger than 0.6 M. When looking at $(i \cdot x)_{sf}$ presented in Figure 3, an increase in $(i \cdot x)_{sf}$ is seen with increasing temperature. If one were to consider the maximum pit size, in an infinite cathode or for a defined cathode which was independent of temperature and chloride concentration, the maximum pit size would solely be governed by anodic kinetics, *i.e.,* the $(i \cdot x)_{sf}$ value. This result would indicate that at elevated temperatures the maximum pit size would be harder to propagate at a given depth as more current would be needed to support anodic dissolution. For example, at 0.6 M, the pit stability at 25°C is 0.90 A/m while at 45°C it is 1.46 A/m. With a 50 um pit the currents needed for propagation are 45 µA and 73 µA, respectively. Thus, more current is needed for propagation at higher temperatures. For potentiostatic measurements, the potentiostat would simply supply that additional current by increasing the (cathodic) reaction rate on the counter electrode. However, when considering the galvanic coupling of a pit with a surrounding cathode inherent in freely corroding systems, the problem becomes more complex.

Seen in Figure 12(a) and (b) are the constructions used to determine the maximum pit size, by combining the maximum cathode currents based on the anodic radius and the pit stability for a bulk concentration of 0.6 M and 5.5 M NaCl respectively. The cathodic current is decreased at elevated bulk chloride concentrations due to a decrease in calculated current density from the combination of a decreased E_{rp} (Figure 4) and the decreased cathodic currents in polarization scans (Figure 5). In Figure 12(a) the difference between the cathodic current in 0.6 M NaCl at 25°C and 45°C is less than the difference in the cathodic currents at 5.5 M NaCl at those two temperatures. This difference is due to the larger difference in conductivity at elevated NaCl concentrations shown in Figure 12(c). The equivalent cathode radius can also be calculated as seen in Equation A7 [11].

Size of cathode for the maximum pit size increases with increasing chloride concentration: With increasing chloride concentration and temperature, there is an increase in the cathode radius that is seen in Figure 12(d) based on Equation A7. In other words, the areas surrounding the pit that can interact with the pit increases. In all cases, the radius of the effective cathode is approximately one hundred times that of the pit, leading to a cathode to anode area ratio on the order of 10^4. The cathode size depends on the cathodic kinetics and pit size, but also on the characteristics of the water layer. In this manuscript, the water layer was a function of chloride concentration and temperature. Therefore, the increased conductivity associated with higher salt concentrations and/or higher temperatures leads to a decreased solution resistance, and hence a larger cathode size as shown in Figure 12(d).

Implications of maximum pit size at elevated temperatures: Determination of the maximum pit size by coupling cathodic and anodic kinetics provides a bounding value for maximum hemispherical pit depth (radius) in a given material and the environmental exposure parameters\ [11]. The impact of the cathode at elevated temperatures and chloride concentration is more pronounced and plays a large role in determining maximum pit size. Stability of pitting corrosion under freely corroding conditions requires the cathode be able to provide at least the current that the anode demands based on the pit stability product. With changes in environment, both of these parameters change. The results in Figure 12 show that the conductivity of a solution plays a large role in determining the maximum pit size as this will change the available cathodic current to support pit propagation.

This provides an interesting problem when considering other chloride-containing species. Woldemedhin et al. have shown that the pit stability product, at room temperature, is relatively independent of supporting cation in solution and shows a strong dependence on solely chloride concentration [19]. It has been shown that bulk chloride concentration is going to have major impact on the cathodic current available to support anodic dissolution as shown in Figure 12. Now if one were to change the supporting cation, keeping the chloride concentration constant, $(i \cdot x)_{sf}$ is unlikely to change, but the RH at which that chloride concentration is reached will be different, leading to a different WL and conductivity. Together, these parameters will change the IR drop seen in the water layer thickness and influence the cathodic current available to support anodic dissolution. This effect will in turn impact the maximum pit size. When considering pitting in other solutions, such as simulated $MgCl_2$ or sea water, it is of equal importance to determine both anodic kinetics as it is to determine cathodic kinetics.

Limitations: As stated in the original model maximum pit model, the assumptions of the method used should be appreciated, and all assumptions are still made in the current calculations [11]. The pits are assumed to be hemispherical and only one pit is considered to form within the area of the effective cathode. Although not all pits are hemispherical, it is a commonly observed morphology and one that is widely used in pit modeling as a reasonable proxy for actual pits. Of course, if a pit transitions into a smaller localized corrosion site (e.g., an intergranular fissure), the current needed for propagation will be less than for a full hemispherical pit and the damage size could exceed that calculated here. Note that the damage under those circumstances would no longer be a pit, but a pit plus intergranular corrosion. Extension of the modeling framework to other corrosion geometries is a topic of current work. If more than one pit forms within a cathode area, then the pits would share the available cathode current, decreasing the actual maximum size of both pits.

An additional important assumption in the current manuscript is the implicit one that a salt film is required for pit propagation. This assumption is manifested in the use of $(i \cdot x)_{sf}$ rather than a fraction of it corresponding to lower than saturation concentrations at the pit surface. The value of that fraction is a topic of current discussion in the literature [25,26,39] with values ranging from 50 to 80%. The lower the fraction of saturation required, the lower is the slope of the anode line in Figure 12(a) and (b) which would lead to larger maximum pit sizes. A temperature dependence would further modify the slope. Unfortunately, the temperature dependence of that fraction has not been established. Nonetheless, the framework would be able to account for these once the values are unambiguously determined.

Finally, the water layer is assumed to have a constant thickness across the cathode which is exposed to the constant chemistry stated. In practice, the reduction of oxygen or water would lead to alkalinization of the cathode surface which would act to slow the kinetics, so the bounding calculations here would be unaffected. In this work we have not considered the effect of chloride content on the solubility of oxygen in order to allow a focus on the effects of temperature and chloride concentration.

Conclusions

Maximum pit size prediction in atmospheric saline environments on stainless steel 304L were presented. Artificial pit electrodes were utilized to determine $(i \cdot x)_{sf}$, $D_{M^+}C_{M^+}^{sat}$, and E_{rp} in bulk NaCl solutions with concentrations of 0.6, 1, 3, and 5.5 M NaCl in controlled temperature environments of 25, 35, 45, and 55°C. Cathodic kinetics were determined in NaBr solutions corresponding to conditions seen in NaCl solutions again spanning NaCl concentrations of 0.6 to 5.5 M and temperatures of 25 and 45°C. Anodic and cathodic kinetics were combined to determine the maximum pit size [11]. Overall, with increasing bulk chloride concentration and temperature, a modest increase in maximum pit size was seen. Together, these observations and analyses result in the following conclusions:

1. Decreases in $D_{M^+}C_{M^+}^{sat}$ with increasing bulk chloride concentration are due to the common ion effect of metal ions in solution significantly decreasing $C_{M^+}^{sat}$.
2. Increases in $D_{M^+}C_{M^+}^{sat}$ with increasing temperature are due to an increase in the saturation concentration of metal salts formed during anodic dissolution along with an increase in D_{M^+} calculated from the Einstein-Stokes equation
3. An increase in saturation concentration of $FeCl_2$, $CrCl_3$, and $NiCl_2$ and decrease in pH is seen in comparison to $FeCl_2$ solutions at all temperatures.
4. At a constant chloride concentration, the cathodic current available to support sufficient anodic dissolution is increased with temperature due to a substantial increase in solution conductivity.
5. Using the maximum pit size framework, the combination of appropriate anodic and cathodic kinetics yields an increase in pit size and cathode radius with increasing chloride and temperature. In both cases, the effect increasing chloride is larger than that of increasing temperature over the ranges studied.

Acknowledgements

Sandia National Laboratories is a multi-mission laboratory managed and operated by National Technology and Engineering Solutions of Sandia, LLC., a wholly owned subsidiary of Honeywell International, Inc., for the U.S. Department of Energy's National Nuclear Security Administration under contract DE-NA0003525. Financial assistance of the Nuclear Regulatory Commission Fellowship under grant number NRC-HQ-84-16-G-0037 is gratefully acknowledged.

Appendix

The following is a brief description of the derivation set forth by Chen and Kelly for calculation of bounding conditions on pit size on metals in atmospheric environments [11]. Under freely corroding conditions, a galvanic couple is formed with the pit (the anode) growing only as long as the anodic current required to maintain the critical solution chemistry is predominantly supported by current from the surrounding material (the cathode). For atmospheric exposure conditions where a thin electrolyte layer is present [51-53], significant ohmic drop over short distances can lead to a limit on the size of the surrounding cathode area and thus a limit on the cathodic current available to support anodic dissolution. The maximum pit model considers the contributions and coupling of three important processes: (1) anode pit kinetics, (2) cathode kinetics, and (3) ohmic drop. Although a more detailed description and validation of the model can be found elsewhere [11,12], a brief description of the model concept is presented here.

Anode Pit Kinetics. Pitting corrosion is characterized by localized, high-rate anodic dissolution of a metallic alloy. In order for pits to propagate, it has long been recognized that the pit chemistry must highly aggressive, with a low pH and high chloride concentration [1]. This chemistry forms via hydrolysis of metal cations formed by metal dissolution in the pit, compensation of that positive charge by migration of chloride from outside the pit, and limitations on the dilution of the chemistry by diffusion due to geometric considerations. In essence, pits can grow if the anodic dissolution rate is sufficiently high that it can replace aggressive solution lost by diffusion. One quantitative model for understanding the anodic kinetics required for pitting was set forth by Galvele.[6] By exploiting a one-dimensional pit with active metal dissolution occurring at the bottom of a pit with depth, x, surrounded by passive walls, a certain anodic current density, i, is needed for propagation. The parameter, ix, has become known as the pit stability product. For a two-dimensional hemispherical pit, the pit stability is given by I_{pit}/r_{pit}, which can be related by geometry to ix [12]. The critical value of this parameter is related to the degree of saturation required to maintain stable propagation. A more in-depth discussion of this critical value was introduced in the Discussion section of the paper and elsewhere [13,14,25,27,38,50] Given a measurement of $(ix)_{crit}$ [11], the current, I_{LC} required for a pit of radius r_a to grow can be calculated:

$$I_{LC} = \left(\frac{I_{pit}}{r_{pit}}\right)_{crit} r_a \qquad \text{(A1)}$$

This expression represents the minimum current required to produce sufficient metallic cations for hydrolysis to maintain a low pH acting against dilution by diffusion. It is also important to account for the fact that there exists a lower bound of potential below which pits cannot grow, the repassivation potential, E_{rp}, as demonstrated by Dunn et al. [17] In this model, it is assumed that E_{rp} has been determined appropriately. Note that as the pit grows, the minimum dissolution current required for continued growth increases linearly with the radius.

Cathode Kinetics. Under freely corroding conditions, anodic currents must be matched by cathodic currents according to Mixed Potential Theory. Reduction reactions relevant to localized corrosion often have sluggish kinetics, thus requiring increased cathodic polarization to supply higher currents. The bounds for the potential of the cathode for a pitting system are the open circuit potential and E_{rp} which is assumed to exist at the mouth of the pit. The cathodic kinetics within these bounds are the only ones that can provide the current needed to match I_{LC}.

Ohmic Drop. When current is passed through an electrolyte, ohmic drop occurs. In atmospheric environments, the electrolyte generally has limited dimensions and, therefore, small currents can lead to substantial ohmic drop along the cathode with the highest current cathodic current density close to the pit mouth (most active potential). As the distance from the pit increases, the potential increases until the position at which the open circuit potential is reached. Beyond this point, no cathodic current is available to support pit growth as it is consumed by the local passive dissolution. More conductive solutions lead to less ohmic drop, increasing the interaction between the cathode and anode, thus increasing the cathodic current density available to support anodic dissolution.

Calculation of Maximum Cathode Current Available. Calculation of the maximum cathodic current starts with the consideration of the geometry shown in Figure A1. A three-dimensional representation as well as a two-dimensional cross section of this set up can be seen in Figure A2(a) and (b) respectively. The anode radius is r_a and the radius of the cathode is r_c, where r_c is much larger than r_a, thus $r_c - r_a \cong r_c$. It is noted that the anode radius is the same as the depth of a pit given the assumption that the pit is hemispherical. The electrolyte layer has a thickness of WL and a conductivity of κ. Also labeled in Figure A2, are the total cathode current (I_{cath}), the anodic current demand of the pit (I_{LC}), the open circuit potential (E_{corr}), and the repassivation potential (E_{rp}).

Given the cathodic kinetics, the potential bounds, and solution conditions (WL, κ), one could calculate the current distribution of the cathodic numerically, using, for example the Finite Element Method [54]. For the purposes here, the distribution is unnecessary, only the total cathodic current is needed. So, for the geometry given in Figure A1, the total cathodic current is equal to the mean cathodic current density multiplied by the area of the cathode,

$$I_{cath} = i_{eq} S_{ceq} = i_{eq} \pi r_{eq}^2 \qquad \text{(A2)}$$

where i_{eq} is the equivalent current density, S_{ceq} is the equivalent cathode area, and r_{eq} is the equivalent cathode radius. The equivalent current density is equal to the average current density over the potential range from the open circuit potential (E_{corr}) to the potential closest to the pit mouth, E_{rp}, and is given by

$$i_{eq} = \frac{\int_{E_{corr}}^{E_{rp}} (i_c - i_p) dE}{E_{corr} - E_{rp}} \qquad \text{(A3)}$$

where i_c is the cathodic current density and i_p is the passive current density of the cathode. The radial current path leads to a potential drop (dE) across the differential annular element in Figure A1 according to

$$dE = i_{eq} (\pi r_{eq}^2 - \pi r^2) \frac{dr}{\kappa W L 2 \pi r} \qquad \text{(A4)}$$

The potential drop (ΔE) is given by integrating Equation A4 from the edge of the cathodic area to the edge of the anodic area,

$$\Delta E = \frac{i_{eq} r_{eq}^2}{2 \kappa W L} \left[\ln\left(\frac{r_{eq}}{r_a}\right) - \frac{1}{2} \right] \qquad \text{(A5)}$$

By solving Equation A2 for r_{eq} and substituting into Equation A5 one obtains

$$\ln I_{cath} = \frac{4 \pi \kappa W L \Delta E}{I_{cath}} + \ln\left[\frac{\left(\pi e r_a^2 \int_{E_{corr}}^{E_{rp}} (i_c - i_p) dE\right)}{\Delta E} \right] \qquad \text{(A6)}$$

where e is Euler's number. The value of I_{cath} cannot be solved for directly, thus it is solved numerically. Visually this can be thought of by the intersection of two curves, each representing one side of Equation A6, with the righthand side being a function of r_a [11].

In a similar way [11], an expression for equivalent cathode area can be obtained and one reaches

$$\ln S_{ceq,min} = \frac{\frac{4\pi\kappa WL(\Delta E_{max})^2}{\int_{E_{corr}}^{E_{rp}}(i_c - i_p)dE}}{S_{ceq,min}} + (1 + \ln\pi + 2\ln r_a) \qquad \text{(A7)}$$

Thus, $S_{ceq,min}$ can be solved for numerically and plugged into Equation A2 to get a cathode size.

Coupling of Anode Pit Kinetics, Cathode Kinetics, and Ohmic Drop. Based on the above description of the three parameters, the maximum pit size, r_{max}, is found by the intersection of the anode line as a function of r_a (Equation A1) and the cathode line as a function of r_a as shown in the Discussion section in Figures 12(a) and (b). Pits of size less than r_{max} can grow because there is more than enough cathode current available, whereas hemispherical pits of size greater than r_{max} are not possible as there is insufficient cathode current to balance the anodic current needed to maintain the aggressive pit chemistry.

References:

1. E. McCafferty, Introduction to Corrosion Science, Springer Verlag, New York, NY (2010).
2. J. Bhandari, S. Lau, R. Abbassi, V. Garaniya, R. Ojeda, D. Lisson, and F. Khan, J. Loss Prev. Process Ind., 47, 10–21 (2017) http://dx.doi.org/10.1016/j.jlp.2017.02.025.
3. C. F. Baes and R. E. Mesmer, The Hydrolysis of Cations, John Wiley & Sons Inc., New York, (1976).
4. J. Srinivasan, M. J. McGrath, and R. G. Kelly, J. Electrochem. Soc., 162, C725–C731 (2015) http://jes.ecsdl.org/lookup/doi/10.1149/2.0281514jes.
5. J. R. Galvele, J. Electrochem. Soc., 123, 464–474 (1976) http://jes.ecsdl.org/cgi/doi/10.1149/1.2132857.
6. T. Yoshi and M. Nishikawa, Nisshin Seiko Giho, 59, 54 (1988).

7. K. E. Johnson, Corros. Sci., 22, 175 (1982).

8. M. Nakata, N. Ono, and Y. Usada, Corros. Eng., 46, 655 (1997).

9. T. Shibata, H. Kurahashi, S. Kaneko, T. Ohya, and K. Motohasi, Corros. Eng., 33, 335 (1995).

10. Y. Tadokoro and A. Takahashi, Zair. to Kankyo, 48, 34 (1999).

11. Z. Y. Chen and R. G. Kelly, J. Electrochem. Soc., 157, C69–C78 (2010) http://jes.ecsdl.org/cgi/doi/10.1149/1.3261803.

12. M. T. Woldemedhin, M. E. Shedd, and R. G. Kelly, J. Electrochem. Soc., 161, 3216–3224 (2014).

13. P. Ernst and R. C. Newman, Corros. Sci., 49, 3705–3715 (2007).

14. M. H. Moayed and R. C. Newman, J. Electrochem. Soc., 153, 330–335 (2006).

15. J. Jun, G. S. Frankel, and N. Sridhar, J. Electrochem. Soc., 163, C823–C829 (2016).

16. H. Yashiro, K. Tanno, H. Hanayama, and A. Miura, Corrosion, 46, 727–733 (1990).

17. D. S. Dunn, G. A. Cragnolino, and N. Sridhar, Corros. Eng., 56, 90–104 (2000).

18. G. A. Cragnolino and N. Sridhar, Corrosion, 47, 464–472 (1991).

19. M. T. Woldemedhin, J. Srinivasan, and R. G. Kelly, J. Solid State Electrochem., 19, 3449–3461 (2015).

20. A. Anderko, N. Sridhar, and D. S. Dunn, Corros. Sci., 46, 1583–1612 (2004).

21. H. Yashiro and K. Tanno, Corros. Sci., 31, 485–490 (1990).

22. J. Jun, G. S. Frankel, and N. Sridhar, J. Solid State Electrochem., 19, 3439–3447 (2015).

23. L. J. Oblonsky, M. P. Ryan, and H. S. Isaacs, J. Electrochem. Soc., 145, 1922–1932 (1998).

24. C. R. Bryan, D. E. Weirich, and R. P. Dingreville, in Proceedings of the 18th International Symposium on the Packaging and Transportation of Radioactive Materials, (2016).

25. J. Srinivasan and R. G. Kelly, J. Electrochem. Soc., 163, C759–C767 (2016) http://jes.ecsdl.org/lookup/doi/10.1149/2.0651613jes.

26. T. Li, J. R. Scully, and G. S. Frankel, J. Electrochem. Soc., 166, C115–C124 (2019) http://jes.ecsdl.org/lookup/doi/10.1149/2.0211906jes.

27. H. C. Kuo and D. Landolt, Electrochim. Acta, 20, 393–399 (1975).

28. R. D. Grimm, A. C. West, and D. Landolt, J. Electrochem. Soc., 139, 1622–1629 (1992).

29. R. D. Grimm and D. Landolt, Corros. Sci., 36, 1847–1868 (1994).

30. U. Steinsmo and H. S. Isaacs, J. Electrochem. Soc., 140, 643–653 (1993) http://jes.ecsdl.org/cgi/doi/10.1149/1.2056137.

31. Etard, Ann. Chim. Phys., 2, 526–570 (1894).

32. I. M. Chou and L. D. Phan, J. Chem. Eng. Data, 31, 154–156 (1986).

33. H. E. Boeke, N. Jahr. Min., 1, 48 (1911).

34. F. A. Schimmel, J. Am. Chem. Soc., 74, 4689–4691 (1952).

35. C. L. Alexander, C. Liu, A. Alshanoon, R. M. Katona, R. G. Kelly, J. Carpenter, C. Bryan, and E. Schindelholz, J. Electrochem. Soc., 165, 869–877 (2018).

36. J. W. Tester and H. S. Isaacs, J. Electrochem. Soc., 122, 1438 (1975) http://jes.ecsdl.org/cgi/doi/10.1149/1.2134039.

37. H. S. Isaacs, J. H. Cho, M. L. Rivers, and S. R. Sutton, J. Electrochem. Soc., 142, 1111–1118 (1995) http://jes.ecsdl.org/cgi/doi/10.1149/1.2044138.

38. G. T. Gaudet, W. T. Mo, T. A. Hatton, J. W. Tester, J. Tilly, H. S. Isaacs, and R. C. Newman, AIChE J., 32, 949–958 (1986).

39. R. C. Newman and H. S. Isaacs, J. Electrochem. Soc., 130, 1621–1624 (1983).

40. J. Srinivasan, C. Liu, and R. G. Kelly, J. Electrochem. Soc., 163, C694–C703 (2016) http://jes.ecsdl.org/lookup/doi/10.1149/2.1221610jes.

41. V. G. Levich, Acta Physicochim. Urss, 17, 257 (1942).

42. N. Sridhar and G. A. Cragnolino, Corrosion, 49, 885–894 (1993).

43. B. E. Wilde and E. Williams, Electrochim. Acta, 16, 1971–1985 (1971).

44. J. Mankowski and Z. Szklarska-Smialowska, Corros. Sci., 15, 493–501 (1975).

45. T. Suzuki, M. Yamabe, and Y. Kitamura, Corrosion, 29, 18–22 (1973).

46. A. Einstein, Ann Phys, 19, 289–306 (1906).

47. J. Kielland, J. Am. Chem. Soc., 59, 1675–1678 (1937).

48. N. J. Laycock, D. P. Krouse, S. M. Ghahari, A. J. Davenport, T. Rament, and C. Padovani, ECS Trans., 41, 3–16 (2012).

49. R. C. Newman, Corros. Sci., 25, 341–350 (1985).

50. P. Ernst and R. C. Newman, Corros. Sci., 44, 927–941 (2002).

51. Z. Y. Chen, F. Cui, and R. G. Kelly, J. Electrochem. Soc., 155, C360–C368 (2008) http://jes.ecsdl.org/cgi/doi/10.1149/1.2926557.

52. F. Cui, F. Presuel-Moreno, and R. G. Kelly, Corros. Sci., 47, 2987–3005 (2005).

53. F. Cui, F. J. Presuel-Moreno, and R. G. Kelly, Corros. Sci., 62, 251–263 (2006).

54. C. Liu, J. Srinivasan, and R. G. Kelly, J. Electrochem. Soc., 164, C845–C855 (2017).

Tables

Table 1: Composition of Stainless Steel 304L (all values reported in weight percent)

C	Mn	P	S	Si	Cr	Ni	Fe	Co	Nb	Ta	N
0.03	1.59	0.036	0.001	0.27	18.48	9.20	70.26	0.13	0.001	0.001	0.001

Table 2: Parameters used in maximum pit model (Calculated in OLI Studio)

Solution	**Conductivity (S/m)**	**Relative Humidity (%)**	**NaBr Concentration (M)**
0.6 M (25°C)	5.45	98.04	0.73
0.6 M (45°C)	8.91	98.03	0.58
5.5 (25°C)	23.63	78.41	7.34
5.5 (45°C)	41.44	78.39	6.84

Figures

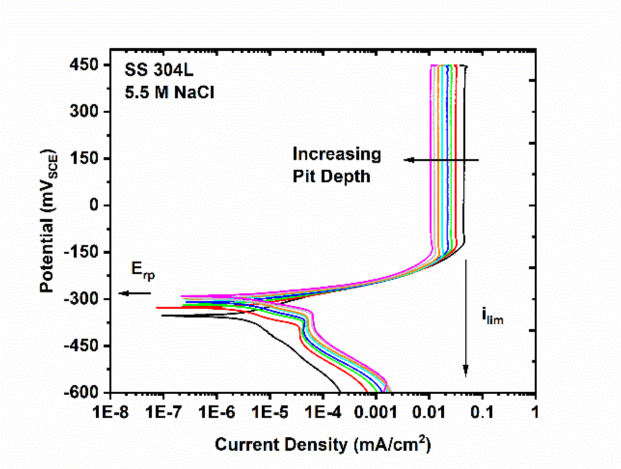

Figure 1: Successive polarization scans of SS304L in 5.5 M NaCl at T = 25°C after pit growth by anodic holds at both +750 mVSCE and +450 mVSCE. Cathodic polarization was initiated at +450 mVSCE and scanned to -600 mVSCE at a scan rate of 5 mV/sec. Extraction of desired parameters, Erp and ilim are labeled. This set of polarization scans is representative of most lead-in-pencil experiments run in this experiment.

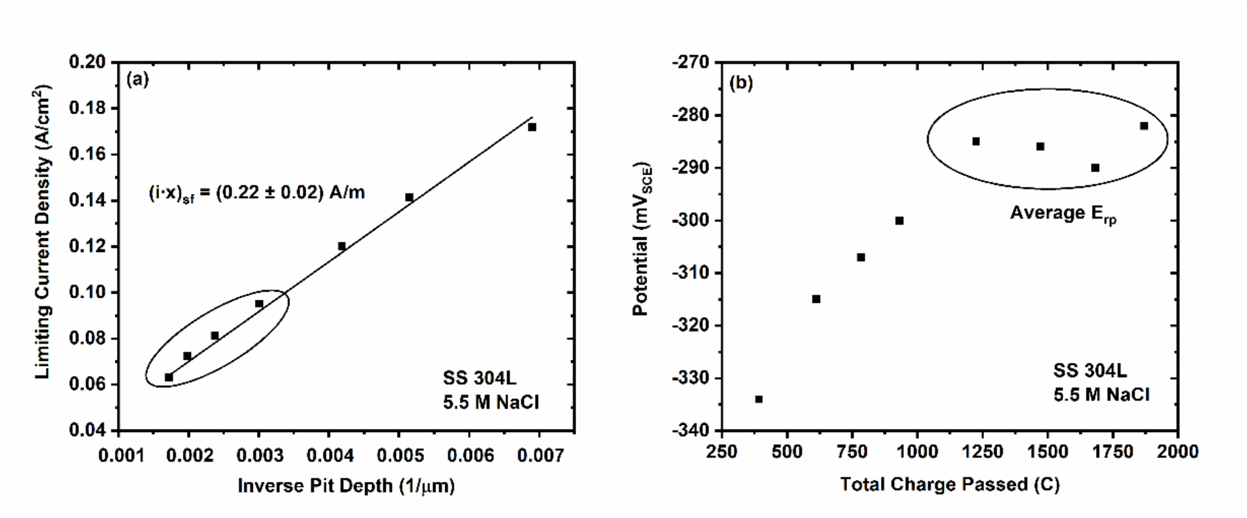

Figure 2: (a) Extraction of pit stability product $(i \cdot x)_{sf}$. It is noted that the x-axis is inverted pit depth in µm. Pits with a depth greater than 8 times the diameter of the pit were considered in the determination of pit stability product. (b) Extraction of the measured repassivation potential data at various pit depths. The Erp value denoted is the plateau which the recorded values approach at deep pit depths/high charge density circled in the plot above. Data refer to 304L in bulk 5.5 M NaCl at T = 25°C.

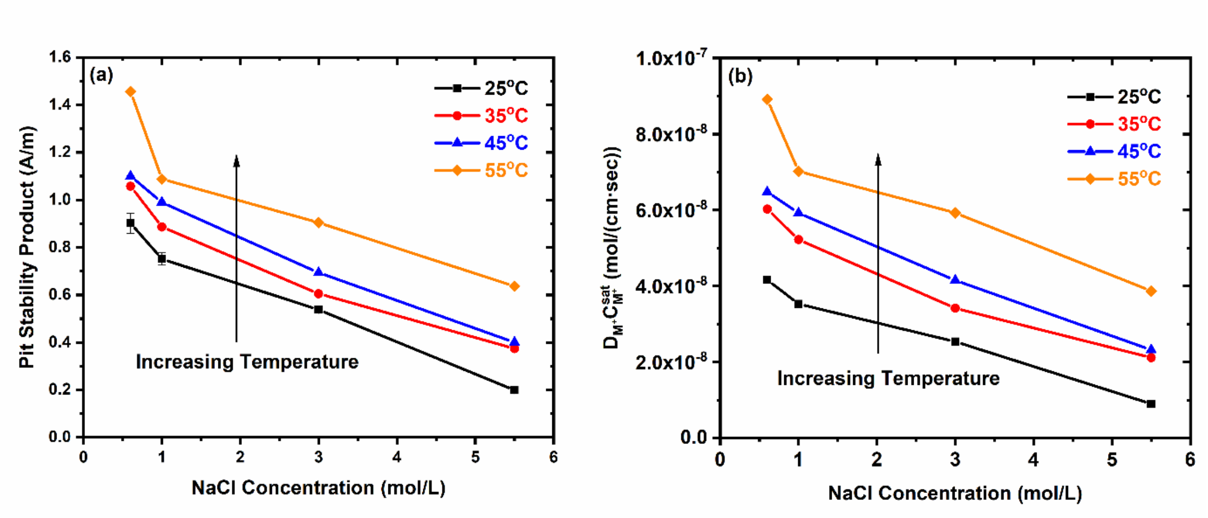

Figure 3: (a) Dependence of the pit stability product ($(i{\cdot}x)_{sf}$) on bulk sodium chloride concentration ([NaCl]) and temperature and (b) corresponding $D_{M+}C^{Sat}_{M+}$ values for stainless steel 304L. It is noted that error bars are included on all measurements, however standard deviation is smaller than the data point in some cases. Standard deviation is representative of at least 4 pit depths.

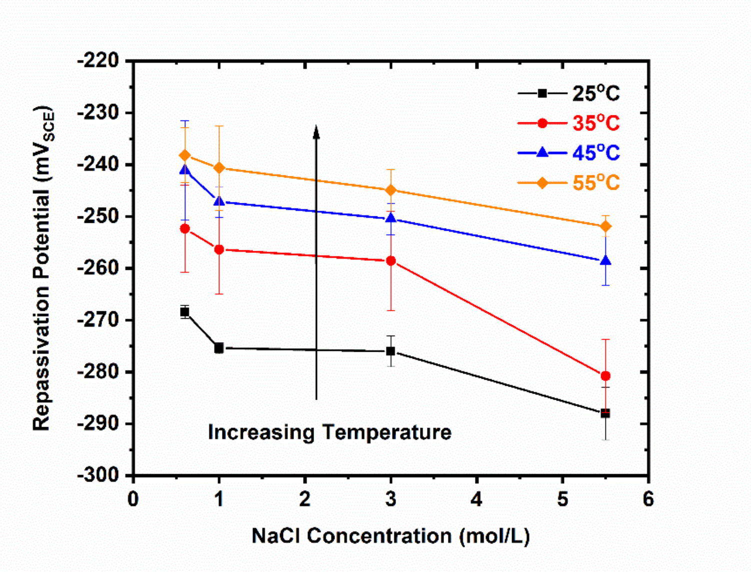

Figure 4: Dependence of repassivation potential on the bulk sodium chloride concentration ([NaCl]) and temperature on the pit stability product for Stainless Steel 304L. Reported temperatures have an accuracy of ±0.1°C and there is no temperature correction for the reference electrode.

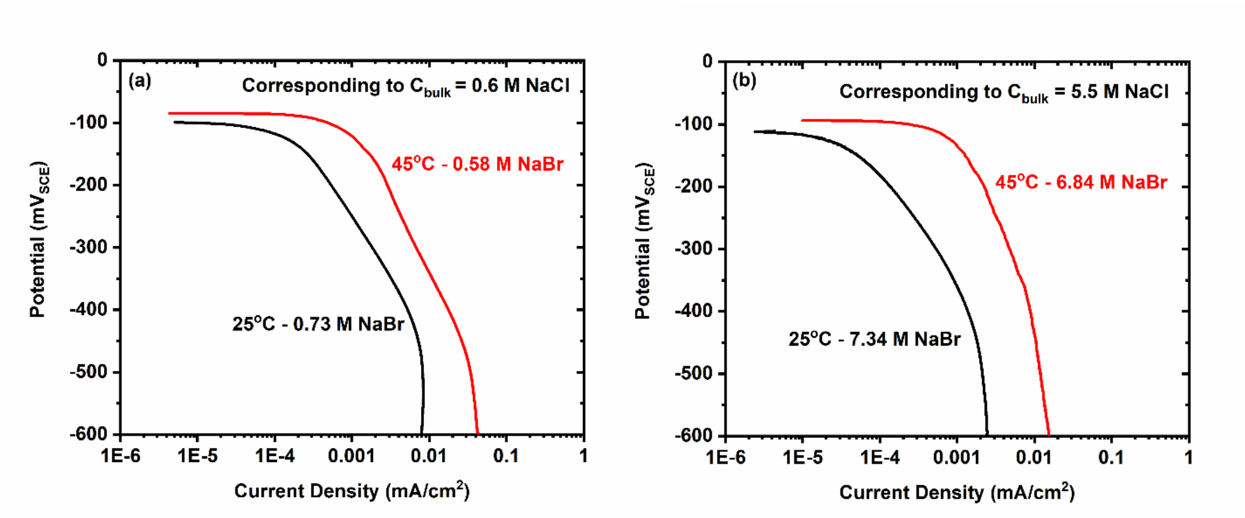

Figure 5: Cathodic polarization scans of stainless steel 304L as a function of temperature and concentration. Samples were held at OCP for 1 hr and where followed by a cathodic scan of 0 mV$_{SCE}$ vs. OCP to -600 mV$_{SCE}$ at a scan rate of 0.167 mV/sec under quiescent conditions. NaBr solutions with concentraions equal to (a) 0.6 M (25°C and 45°C) and (b) 5.5 M (25°C and 45°C) NaCl were used. All reported potentials are at temperature and no temperature correction was made.

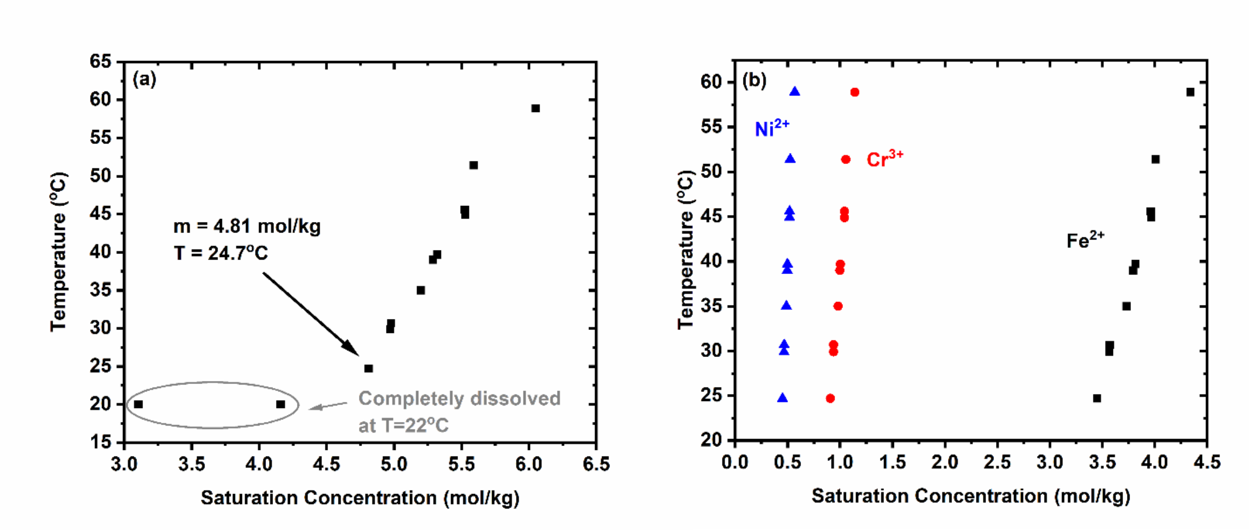

Figure 6: (a) Solubility diagram for stoichiometric mixture of $FeCl_2$, $CrCl_3$, and $NiCl_2$ in stoichiometric proportions with the weight percent in Table 1 as a function of temperature. It is noted that the saturation concentration is the total molality and was calculated by using the total weight of all salts added. (b) Molality of individual metal ions in solution. Reported temperatures have an accuracy of ±0.1°C.

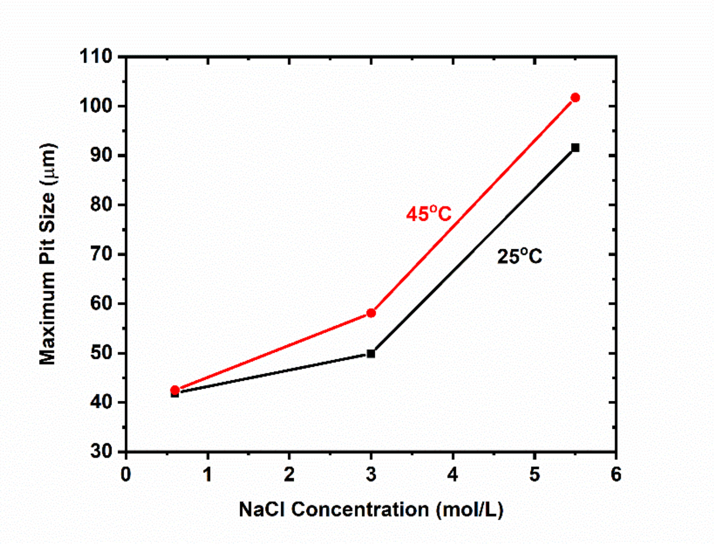

Figure 7: Maximum pit size calculations based on the formulism set forth by Chen and Kelly.[11] It is noted that the reported pit size is the radius and therefore depth of a hemispherical pit. A loading density of 200 μg/cm^2 was used in these calculations. It is noted that a trend between 0.6M and 5.5M is not being interpolated, rather the line connecting the two points is provided to help guide the readers eye. Reported temperatures have an accuracy of ±0.1°C.

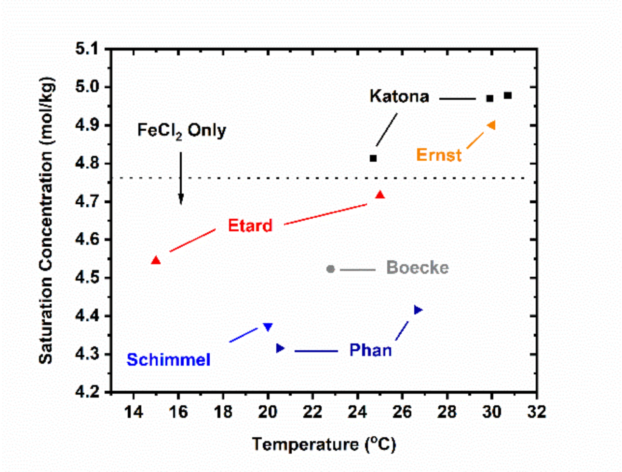

Figure 8: Comparison of saturation concentrations of various solutions. All values below the FeCl$_2$ *line are saturation concentrations determined solely for FeCl*$_2$ *solutions. Values were converted based on a saturation density of FeCl*$_2$ *of 1.44 g/cm*^{3}.[38] *The Ernst value was determined from experimental dissolution pitting experiments and the composition from Ernst was Fe:67.59, Cr:16.89, Ni: 10.75, Mn: 1.5, Mo: 2.74% by weight. Values were taken from [28]-[31] and [46].*

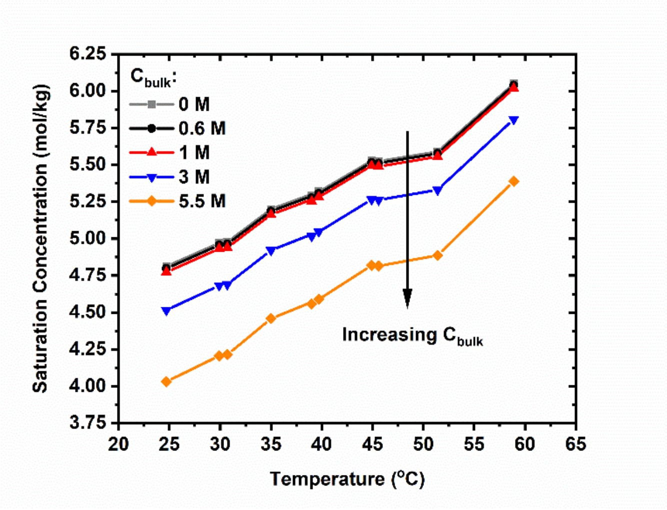

Figure 9: Metal ion saturation concentration corrected for bulk NaCl concentrations by using the common ion effect. It is noted that the bulk chloride concentrations are reported in in molarity, however were converted to molality based on density calculated in OLI Studio.

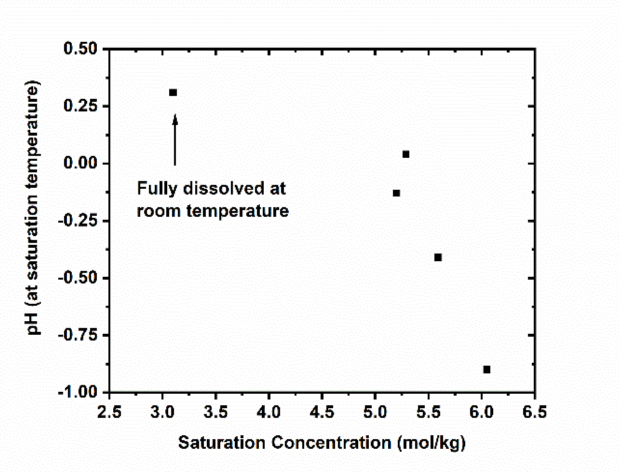

Figure 10: Measured pH as a function of saturation concentration. It is noted that the pH measurements were taken within 2 minutes of saturation. Therefore, the solutions were at elevated temperatures and are within 5°C of the reported saturation temperature and there were no temperature corrections for potential.

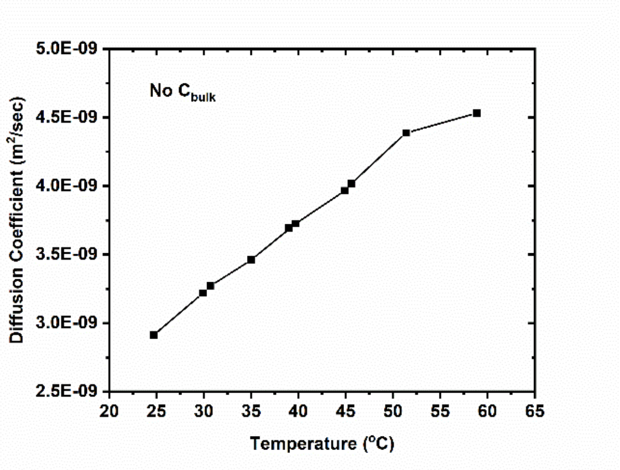

Figure 11: Effective diffusion of metal cations calculated from the Stokes-Einstein equation. The calculated values assume an average ion radius based on stoichiometric dissolution of SS304L. Saturation concentrations from Figure 6 were used in this calculation and no bulk chloride effects were considered. Dynamic viscosities were calculated in OLI Studio and the radius of hydrated cations were used in this calculation, serving as a lower bound for the diffusion coefficient.

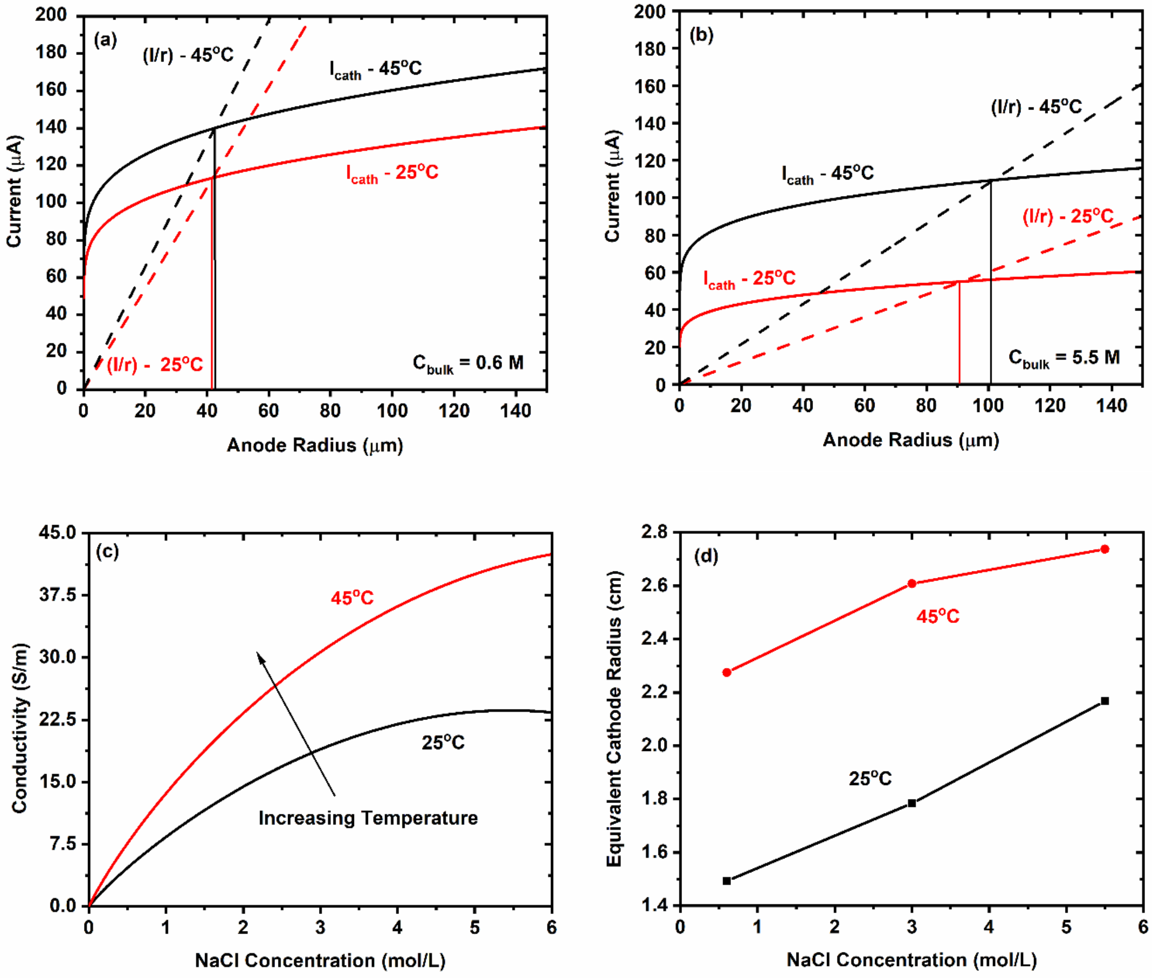

Figure12: Cathode current and anode current for (a) C = 0.6 M and (b) 5.5 M NaCl at both 25°C and 45°C. A loading density of 200 μg/cm^2 was used in these calculations. (c) The calculated conductivity of NaCl solutions as a function of increasing chloride concentration and temperature calculated in OLI Studio. (d) Equivalent cathode radius assuming an anode radius from Figure 7 according to the framework of Chen and Kelly [11]. It is noted that a trend between 0.6M and 5.5M is not being interpolated, rather the line connecting the two points is provided to help guide the readers eye.

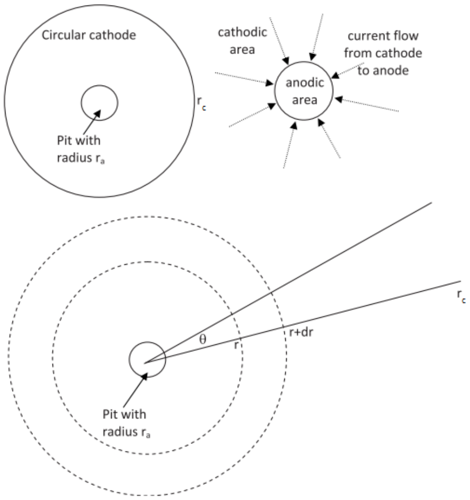

Figure A1: Schematic showing a circular anode with radius, r_a, and the radial current flowing direction. The cathodic current is being supplied by a cathode of radius, r_c, surrounding the anode.

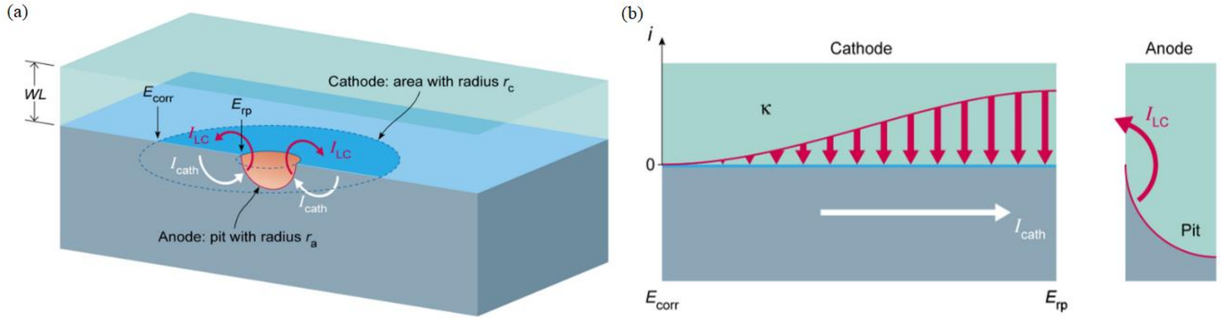

Figure A2: (a) Three-dimensional representation of the anode and cathode galvanic couple under a thin electrolyte of thickness, WL. (b) Two-dimensional cross-section of view of galvanic couple. It is noted that the ohmic drop in solution is schematically shown. The highest current cathodic current is close to the pit mouth (at E_{rp}) and decreases with increasing radial distance from the pit to a point where no further cathodic current can support anodic growth (at E_{corr}).

F. Quantitative assessment of environmental phenomena on maximum pit size predictions in marine environments

Quantitative Assessment of Environmental Phenomena on Maximum Pit Size Predictions in Marine Environments

R. M. Katona,[1,2,*] A. W. Knight[1], E.J Schindelholz[3], C. R. Bryan[1], R. F. Schaller[1], R. G. Kelly[2]

[1] Sandia National Laboratories, Albuquerque, NM 87123 USA
[2] Materials Science and Engineering, University of Virginia, Charlottesville, VA 22904 USA
[3] Materials Science and Engineering, The Ohio State University, Columbus, OH 43210 USA
[*]Corresponding Author; rmkaton@sandia.gov

Key Words

Maximum pit size predictions, magnesium chloride, sea-salt brines, sodium chloride, cathode precipitation, water layer dehydration, pit stability product

Abstract

Maximum pit sizes were predicted for dilute and concentrated NaCl and $MgCl_2$ solutions as well as sea-salt brine solutions corresponding to 40 % relative humidity (RH) ($MgCl_2$-rich) and 76 % RH (NaCl-rich) at 25 ˚C. A quantitative method was developed to capture the effects of various cathode evolution phenomena including precipitation and dehydration reactions. Additionally, the sensitivity of the model to input parameters was explored. Despite one's intuition, the highest chloride concentration (roughly 10.3 M Cl^-) did not produce the largest predicted pit size as the ohmic drop was more severe in concentrated $MgCl_2$ solutions. Therefore, the largest predicted pits were calculated for saturated NaCl (roughly 5 M Cl^-). Next, it was determined that pit size predictions are most sensitive to model input parameters for concentrated brines. However, when

the effects of cathodic reactions on brine chemistry are considered, the sensitivity to input parameters is decreased. Although there was not one main input parameter that influenced pit size predictions, two main categories were identified. Under similar chloride concentrations (similar RH), the water layer thickness (WL), and pit stability product, $(i \cdot x)_{sf}$, are the most influential factors. When varying chloride concentrations (RH), changes in WL, the brine specific cathodic kinetics on the external surface (captured in the equivalent current density (i_{eq})), and conductivity (κ_o) are the most influential parameters. Finally, it was noted that dehydration reactions coupled with precipitation in the cathode will have the largest effect on predicted pit size, and cause the most significant inhibition of corrosion damage.

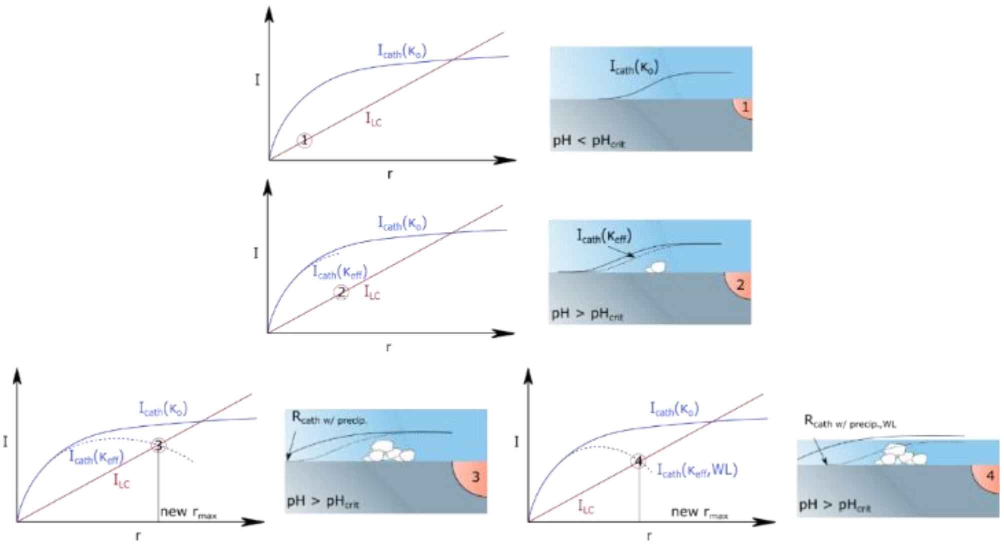

Introduction

Marine and near marine environments are typically characterized by sea-salt aerosols containing high chloride concentrations [1], and they can lead to pitting corrosion of stainless steels (SS) when deposited and deliquesced on the alloy surface. The chemistry and concentration of a marine environments varies widely with relative humidity (RH) [1] and, thus, changes in RH can change the corrosivity of the brine. As such, seawater solutions become sodium chloride (NaCl) rich at high RH values (above 74 % RH) and magnesium chloride ($MgCl_2$) rich at low RH values [1]. In this way, the RH along with salt load control the composition, volume, and other properties of the resultant brine, impacting anodic and cathodic corrosion kinetics [1,2]. It is necessary to understand the quantitative impacts of the brine properties and evolution on anodic and cathodic kinetics in order to inform upon SS degradation.

There is an increasing demand for the accurate prediction of localized corrosion damage and computational models can provide a powerful means to simulate the propagation of localized corrosion in multiple exposure environments. Various models have been developed to predict localized corrosion including analytical models [3–6], Finite Element Models (FEM) [7–12], and phase field models [13,14]. Each modeling technique has advantages and disadvantages that are beyond the scope of this paper to discuss. However, regardless of the method, the evolution of brine chemistry as corrosion occurs has proven to be difficult to capture. In atmospheric scenarios, oxygen reduction reactions (ORR) are typically assumed to be the cathodic reduction reaction and a by-product of such a reaction is the hydroxyl ion (OH-) which causes a rise in cathodic pH [15]. In certain solutions, such as sea-salt brines or $MgCl_2$, a pH rise will cause the precipitation of hydroxide-containing species in the cathode [16,17]. Additionally, loss of brine components to solids results in the dehydration of the brine, influencing cathodic properties in thin water layers [18–20]. As such, it is important to account for these precipitates and effects on cathodic and anodic processes in models.

Typically, models considering brine evolution only account for precipitation from anodic species. Notably, Ansari et al. modeled the effects of insoluble corrosion products from pit dissolution and found enhanced iron concentrations and decreased pH in the pit when considering insoluble corrosion products [13]. Yin et al. explored the effects of metal ions from dissolution precipitating in the brine on the corrosion of aluminum alloys leading to a decrease in the overall corrosion rate which can stifle the growth of localized corrosion sites [11]. Further work showed steric hindrance leads to reduced current densities and oxygen flux to the surface [10].

Models are also normally restricted to dilute chloride systems [4,10,13,14,21] which are representative of high RH atmospheric conditions [1] and may not be realistic for many atmospheric scenarios of interest. Furthermore, the bulk of the models in literature focus on the precipitation of metal hydroxides from dissolution and do not consider precipitation of solution species. Finally, most models do not consider oxygen reduction to be a limiting reaction or consider atmospheric scenarios. Therefore, presented models in literature do not represent the scenario of interest or incorporate all reactions of interest.

One such model that can be modified in order to account for the phenomena of interest is an analytical model proposed by Chen and Kelly for bounding pit sizes [3] and has been utilized by to predict pit sizes in sodium chloride (NaCl) [22] and ferric chloride solutions [23]. The analytical model relies on ohmic drop considerations in the thin electrolyte film to limit the cathodic current supply. Through the inherent coupling of the cathode and anode, a finite cathode implies a finite anode (i.e., a finite pit size). Finding the maximum pit size can be achieved by determining: (i) the maximum cathode current the external surface can generate, and (ii) the minimum dissolution current needed to maintain the critical chemistry in the pit as a function of the pit size. Combining these two relations results in an expression for the maximum pit size obtainable under the given conditions. As such, cathode properties can be updated as a function of metal dissolution and can help determine the influences of cathode evolution on maximum pit sizes.

The goal of this work is three-fold: (i) ascertain the effects of solution chemistry, as a function of chloride concentration (from dilute to concentrated) on maximum pit size predictions, (ii) understand the sensitivity of maximum pit size predictions to all input parameters, and (iii) explore cathode size evolution phenomena and determine significant reactions. As a result, improved predictions to inform material degradation in atmospheric environments will be ascertained. This model will be performed on NaCl, $MgCl_2$, and sea-salt deliquesced brine solutions at various concentrations, representing various RH.

Methods

Calculation of Maximum Pit Size

Maximum pit sizes were calculated using the framework set forth by Chen and Kelly [3]. This framework has been utilized to make predictions in FeCl3 at room temperature [23] and NaCl solutions at various concentrations and temperatures [22]. A full description of this model is presented in the original paper [3] and in the appendix of previous work [22]. Briefly, the model relies on the fact that under freely corroding conditions, pitting can be considered a galvanic couple with the pit (the anode) growing only as long as the anodic current required to maintain the critical solution chemistry is predominantly supported by current from the surrounding material (the cathode). For atmospheric exposure conditions where a thin electrolyte layer is present, significant ohmic drop over short distances limits the size of the surrounding cathode area and thus the cathodic current available to support anodic dissolution. The maximum pit model considers the contributions and coupling of three important processes: (1) anode pit kinetics, (2) cathode kinetics, and (3) ohmic drop. The anode pit kinetics are derived based on measurements of the Galvele pit stability product. The cathode kinetics are derived based on polarization measurements in solutions that mimic the solutions present on the outer, un-pitted surface. Based on these assumptions, an analytical expression for the total cathodic current (I_{cath}) can be derived as follows:

$$\ln I_{cath} = \frac{4\pi\kappa W L \Delta E}{I_{cath}} + \ln\left[\frac{\left(\pi e r_a^2 \int_{E_{corr}}^{E_{rp}} \left(i_c - i_p\right) dE\right)}{\Delta E}\right] \quad 1$$

where κ is the solution conductivity, ΔE is the difference between the open circuit potential (E_{OCP}) and the repassivation potential (E_{RP}), r_a is the anode radius, and i_c and i_p are the cathodic current density and the passive current density of the cathode respectively. The solution characteristics are derived from thermodynamic considerations and the amount and type of salt(s) present on the surface.

Determination of alloy and solution parameters

Maximum pit size predictions were made for SS304L at room temperature (25 ± 2 ˚C) in various solutions representing equilibrium solutions at different RH levels including: $MgCl_2$ (0.189 and 4.98 M), NaCl (0.6 and 5 M), and sea-salt brines corresponding to 76% RH (major components: 5.63 M Cl^-, 4.83 M Na^+, 0.55 M Mg^{2+}) and 40 % RH (major components: 10.28 M Cl^-, 0.17 M Na^+, 5.31 M Mg^{2+}) [1].

Pit stability and repassivation potential

The pit stability product under a salt film ($(i \cdot x)_{sf}$) and E_{RP} were determined through lead-in-pencil measurements based on the procedure of Srinivasan et al. [24-27]. Briefly, 50 µm wires were imbedded in epoxy and wet ground to 320 grit with silicon carbide paper. Samples were placed in an electrochemical cell and electrochemical testing was carried out by applying anodic potentials to grow the 1-D wire to different depths. A polarization scan from 0.45 V_{SCE} to −0.6 V_{SCE} at a scan rate of 5 mV/sec was performed and repeated up to ten times. After experimentation, the limiting current density was plotted vs. the inverse pit depth and the slope was used to determine $(i \cdot x)_{sf}$. E_{RP} was determined as an average of plateaued potentials below a current density of 30 µA/cm^2. A schematic of these two descriptions can be seen for SS304L in Figure 2 of Katona et al. [22]. The composition by certificate of the 304L wire used for measurements can be found in Katona et. al [22]. Values for $(i \cdot x)_{sf}$ and E_{RP} for NaCl solutions were obtained from Katona et al. [22]. For a two-dimensional hemispherical pit, the pit stability is given by I_{pit}/r_{pit}, which can be related by geometry to $(i \cdot x)$ by a factor of three [23,28]. The critical value of this parameter, $(i \cdot x)_{crit}$, is related to the degree of pit saturation required to maintain stable propagation. A more in-depth discussion of this critical value can be found elsewhere[22,25,29–33]. Given a measurement of $(i \cdot x)_{crit}$, the current, I_{LC}, required for a pit of radius r_a to grow stably as a hemisphere can be calculated by $I_{LC} = [3\ (i \cdot x)_{crit}]\ r_a = \left(\frac{I_{pit}}{r_{pit}}\right)_{crit} r_a$. This expression represents the minimum current required to produce sufficient metal cations for hydrolysis to maintain a sufficiently low pH against dilution by diffusion. In most cases the degree of pit saturation was assumed to be 50 % of salt film saturation [34]; however, the sensitivity to this parameter was explored by varying the value from 40 % to 100 % pit saturation, and it is clearly stated when varied.

Cathodic Kinetics

The conductivity (κ_o) and *WL* were determined for the three solutions of interest. *WL* is related to the loading density (*LD*, grams of salt per unit surface area, g/m^2), the specific gravity of the solution (ρ_{sp}), the molecular weight (*MW*), and the equilibrium concentration of the salt (C_{eq}) (*WL*

= ($LD.\rho_{sp}$)/($MW.C_{eq}$)) [23]. For $MgCl_2$ and NaCl solutions, OLI Studio was utilized to determine all parameters of interest. Values of κ_o for $MgCl_2$ as a function of solution composition (RH) can be seen in Figure S1 while NaCl solution κ_o can be seen in Katona et al. [22]. For sea-salt solutions, all solution properties were obtained from Bryan and Schindelholz [1]. Most calculations were made with LD = 3 g/m^2 (300 µg/cm^2). A LD = 3 g/m^2 represents an aggressive salt loading [36] and corresponds with recent laboratory exposure tests of SS304L in sea-salt aerosols [37]. Calculations were also made with an increasing LD in order to simulate salt deposition over time. Variations in LD can also represent different exposure sites and strongly correlate with distance from the coast. An example of this, as well as for accelerated salt spray tests, can be seen in work from Shinohara [36].

Implementing Solution Precipitation and Dehydration

In order to account for cathodic precipitation in $MgCl_2$ or sea-salt solutions, the following process was utilized. First, the molarity of the hydroxyl ions accumulated in the solution volume above the cathode was calculated. This calculation can be performed at all anode radii (r_a) through the knowledge of the SS density (ρ_{SS} = 7.8 g/cm^3), molecular weight (MW_{ss} = 55.3 g/mol), and the number of electrons transferred during dissolution ($e_{SS}^- = 2.2$) [22], given by,

$$M_{OH^-} = \frac{\left[\frac{2}{3}(r_a)^3\right]\left[\frac{\rho_{SS} * e_{SS}^-}{MW_{ss}}\right]}{V_{cath}} \qquad 2$$

The cathode volume (V_{cath}) can be calculated through the original max pit formulism, as at every r_a, there is a corresponding maximum equivalent cathode radius (R_{cath}) [3,22]. With the knowledge of the WL and R_{cath}, $V_{cath} = \pi R_{cath}^2 * WL$. Once M_{OH^-} is known, the cathode pH will be calculated and compared to the stability of precipitates in the respective brines [16]. It has been previously determined that non-carbonate precipitates, such as magnesium hydroxides or hydroxychlorides, are kinetically favored in $MgCl_2$ solutions [16,17]. Although carbonate species are often seen in coupon exposures of various alloys in Mg-containing environments, it is hypothesized that hydroxide precipitates are formed first and then back-react with carbon species present in the solution to form the observed phase. A more detailed discussion on the rates of reactions is present in previous work [16]. For 0.189 M $MgCl_2$ and 76% RH sea-salt brine, the precipitation reaction was assumed to be,

$$Mg^{2+}_{(aq)} + 2OH^- \rightarrow Mg(OH)_{2\,(s)} \qquad 3$$

and for 4.98 M $MgCl_2$ and for 40% RH the precipitation reaction was assumed to be (the stability of precipitates directly from solution has been shown to be concentration dependent and a more in-depth analysis can be found in work from Katona et al.[16])

$$2Mg^{2+}_{(aq)} + Cl^-_{(aq)} + 3OH^- + 4H_2O \rightarrow Mg_2(OH)_3Cl \cdot 4H_2O_{\,(s)} \qquad 4$$

Once precipitation occurs, the volume of the precipitate (V_{precip}) is calculated through the molecular weight (MW_{precip}) and density (ρ_{precip}) of the precipitate:

$$V_{precip} = \frac{1}{n_{precip}} \frac{M_{OH^-} * V_{cath} * MW_{precip}}{\rho_{precip}} \qquad 5$$

where n_{precip} is the stoichiometric number for hydroxyl ions. The parameters for the precipitates present in each solution are given in Table 1.

Once V_{precip} and V_{cath} are known, the effective conductivity (κ_{eff}) can be calculated through the Bruggeman equation given by,

$$\kappa_{eff} = \kappa_o \left(1 - \frac{V_{precip}}{V_{cath} + V_{precip}}\right)^{\frac{3}{2}} = \kappa_o \left(\frac{V_{cath}}{V_{total}}\right)^{\frac{3}{2}} \qquad 6$$

where $V_{total} = V_{cath} + V_{precip}$ [38]. The calculation for maximum pit sizes with the consideration of precipitation is shown in the flow chart in Figure 1. Increments in anode size were 0.1 µm for all calculations.

Two different assumptions were made regarding *WL*: (i) the *WL* was assumed to be constant and the solution concentration did not change and (ii) dehydration reactions were considered based on charge neutrality and a constant ambient RH. Because of *WL* assumption (ii), in order to maintain charge neutrality in the cathode, for every hydroxyl ion that is produced, one chloride ion must be consumed, diluting the cathode chloride concentration. Under a constant ambient RH, the activity of water in the air and the solution must be the same. In order to maintain this equilibrium, the *WL* must decrease to match the activity of water in the brine and air. Metal ion precipitation from dissolution (*i.e.* $Fe(OH)_3$, $Cr(OH)_2$, $Ni(OH)_2$, *etc.*) was ignored and the only stable precipitates were from solution precipitates (*i.e.*, Mg-containing). The composition of the precipitates did not change over time or pit size range. The cathode pH was calculated based on the total OH^- production and total cathode volume. Once a solid precipitates, the solution pH is fixed. For every OH^- produced by the ORR reaction, an equivalent amount of hydroxide-containing precipitate forms. Any variations in the cathode current as a function of distance away from the pit were not considered. Finally, precipitation reactions were assumed to occur instantaneously (*i.e.*, no reaction kinetics were considered). These assumptions are discussed in Section 5.

For clarity in the presented figures, the following notation was used: dashed lines represent original maximum pit predictions without any modifications, solid lines represent the consideration of precipitation reactions on the cathode and dashed-dot lines represent any other phenomenon considered and will be clearly labeled. Pit saturation (*i.e.* the measure of metal chloride saturation within the pit) will always be with respect to the pit surface and precipitation will always refer to the cathode, due to cathodic hydroxide production (*i.e.*, $Mg(OH)_2$ precipitation on the cathode surface).

Results

Alloy and Solution Properties

Anodic Kinetics

The values of $(i \cdot x)_{sf}$ as a function of solution composition and chloride concentration is seen in Figure 2. With increasing chloride concentration, a decrease in $(i \cdot x)_{sf}$ was observed, decreasing to 0.02 A/m at nearly 10 M Cl^-. It is also noted that sea-salt and $MgCl_2$ solutions have a higher measured $(i \cdot x)_{sf}$ at all chloride concentrations when compared to the values measured in NaCl solutions.

Cathodic Kinetics

Cathodic polarization scans for surrogate solutions are displayed in Figure 3(a) and (b) for $MgCl_2$ solutions and sea-salt solutions respectively. In general, with increasing concentration, a suppression of the current at all potentials is seen due to a decrease in $D_{O_2}C_{bulk,O_2}$. Also seen in Figure 3 is E_{RP} for the chloride solution of interest. A depression of E_{RP} is seen with an increase in chloride concentration. Furthermore, when comparing 4.98 M $MgCl_2$ and 40 % RH sea-salt brine, a more noble E_{RP} is seen measured in 40 % RH. When comparing 5 M NaCl (-0.243 $V_{Ag/AgCl}$ [22]) and 76 % RH sea-salt brine, a more noble E_{RP} is seen measured in 76 % RH.

Water Layer Properties

WL normalized to LD (μm/g/m^2) for all solutions is displayed in Figure 4(a). In all cases, with decreasing RH the WL decreases. Although a more detailed explanation is presented elsewhere for the sea-salt data [1], inflections in the curve represent RH conditions at which a salt mineral precipitates. Also obtained from Bryan and Schindelholz [1] is Figure 4(b), which displays the ratio of solution volume to salt volume, which generally decreases with decreasing RH. In both WL and brine to salt ratio, as NaCl precipitates out of solution at roughly 74 % RH, the sea-salt brine volume greatly decreases and, although it becomes a $MgCl_2$-rich brine, the properties of the brine are significantly different from pure $MgCl_2$ due to the precipitation.

Maximum Pit Size Predictions in $MgCl_2$

The calculated pH as a function of anode size in 4.98 M $MgCl_2$ is presented in Figure 5(a). Two pH calculations are presented: (i) not considering precipitate reactions (labeled “No Precipitation”) and (ii) with precipitate reactions included (labeled “Precipitation”). When ignoring precipitation reactions, it is assumed all hydroxyl produced is contained within the equivalent cathode (as defined by R_{cath}) and will neither migrate nor diffuse out of the cathode. Furthermore, the concentration of $MgCl_2$ was assumed to remain constant in the cathode and, as a result, transport of $MgCl_2$ at the cathode edge was assumed to maintain charge neutrality. This assumption is displayed schematically in Figure 5(b). When precipitation reactions are considered, the brine pH will reach a value at which a precipitate is thermodynamically favored and is assumed to precipitate immediately. Upon further cathodic reduction reaction, the OH^- will be immediately consumed in the cathode keeping the pH constant at the pH for thermodynamic stability of the precipitate. The pH for precipitation in the cathode is roughly 7.1 for 4.98 M $MgCl_2$ and is reached when an anode size of 3 µm is exceeded.

Maximum pit size predictions for 50 % of pit saturation, LD = 3 g/m^2, considering both no precipitation and precipitation of cathode solids, are presented in Figure 6(a) and (b) for 4.98 and 0.189 M $MgCl_2$ respectively. Overall, maximum pit sizes and cathode radii (Figure 6(c) and (d)) are larger for 4.98 M $MgCl_2$ in comparison to 0.189 M $MgCl_2$. A maximum pit size of 373.5 µm is predicted for 4.98 M $MgCl_2$ (Figure 6(a)) without precipitation, and the value decreases 20 % when considering the precipitation of $Mg_2(OH)_3Cl \cdot 4H_2O$. For 0.189 M $MgCl_2$ (Figure 6(b)), maximum pit sizes are relatively similar with or without precipitation (160.6 µm without and 155.9 µm with precipitation) decreasing roughly 3 % with precipitation of $Mg(OH)_2$. Furthermore, cathode radii for 4.98 M $MgCl_2$ are roughly 3.4-3.8 times larger than cathode radii for 0.189 M $MgCl_2$ over the range presented in Figure 6, and the ratio of radii decreases with increasing pit size.

The fractional brine content (Equation 37) is displayed in Figure 7 for both saturated and dilute $MgCl_2$ when precipitation is considered. If precipitation is not considered, the fractional brine content would be 1 as $\mathrm{V_{cath}} = \mathrm{V_{tot}}$. With increased anode size, a decrease in the fractional brine content is greater in 4.98 M $MgCl_2$ at any given anode size.

Cathodic precipitation has greater impact on bounding pit sizes at low values of pit solution saturation

Maximum pit size predictions are shown as a function of solution composition, fraction of pit saturation, and with and without the consideration of cathode precipitation (Figure 8(a)). Not surprisingly, with decreased pit saturation a larger maximum pit size is seen. When precipitation is considered, maximum pit size decreases at almost all levels of pit saturations explored and the effect is greater in 4.98 M $MgCl_2$ in comparison to 0.189 M $MgCl_2$ as shown in Figure 8(b).

Finally, with decreasing percent pit saturation, a decrease in the cathode to anode radius ratio is seen in Figure 8(c). This decrease is less severe when precipitation is considered.

Increasing loading density causes increased pit sizes

The influence of LD (WL) on maximum pit size predictions for 4.98 and 0.189 M $MgCl_2$ are presented in Figure 9 and shows an increase in pit size with increasing LD. Additionally, when precipitation is considered, the maximum pit size decreases for both solutions at all LD. The ratio of maximum cathode to maximum pit is seen in Figure 9(b) and displays an exponential decay behavior with increasing LD.

Deviations in the repassivation potential have a greater impact on maximum pit size in saturated solutions in comparison to dilute solutions

Changes of maximum pit size predictions with variations in E_{RP} are shown in Figure 10(a). In general, with a decrease in E_{RP} (more negative), an increase in maximum pit size is seen in both $MgCl_2$ solutions explored. This effect is greater for 4.98 M $MgCl_2$ in comparison to 0.189 M $MgCl_2$ as displayed by normalizing both E_{RP} (normalized $E_{RP} = E_{RP}/E_{RP,true}$ where $E_{RP,true}$ is given in Figure 3) and pit size ($r_{E_{RP}}/r_{E_{RP,true}}$) (Figure 10(b)). Furthermore, the ratio of cathode radius to pit radius, seen in Figure 10(c), decreases with increasing normalized E_{RP} (more negative E_{RP}) and a higher ratio is seen in 4.98 M $MgCl_2$ in comparison to 0.189 M $MgCl_2$. As can be seen in Figure 10(a-c) the maximum pit size and the cathode to anode ratio reach a plateau for 4.98 M $MgCl_2$ with decreased E_{RP} (increased normalized E_{RP}) when precipitation is considered. The overall impact of precipitation on pit size measurements is much greater for saturated solutions and is displayed in Figure 10(d) by taking the ratio of maximum pit size with precipitation to that without precipitation.

Dehydration reactions decrease maximum pit size predictions more than cathode precipitation

Dehydration reactions decrease the electrolyte volume available on the surface of the cathode and limit the cathode current available to support pit growth as shown in Figure 11(a) and (b) for 4.98 and 0.189 M $MgCl_2$ respectively. Overall, a greater decrease is seen in 0.189 M $MgCl_2$ (40 % of original) for dehydration reactions in comparison to 4.98 M $MgCl_2$ (35 % of original). Although the WL is an order of magnitude higher for dilute $MgCl_2$ in comparison to saturated $MgCl_2$ (Figure 4), dehydration reactions cause the WL to decrease much more rapidly for 0.189 M $MgCl_2$ with increased pit size as seen in Figure 11(c). Finally, the impact of LD and E_{RP} on maximum pit size predictions, when dehydration reactions are considered, is seen in Figure 11(d) and (e) respectively. Overall, dehydration reactions (Figure 11(d)) have a larger impact on maximum pit sizes when considering changes in LD in comparison to precipitation reactions (Figure 9(a)). Additionally, when considering variations in E_{RP} and dilute $MgCl_2$, a greater influence is seen with dehydration reactions than precipitation reactions. Conversely, when considering fluctuations in E_{RP} and saturated $MgCl_2$, a greater influence is seen from precipitation reactions (Figure 10(a)) in comparison to dehydration reactions (Figure 11(e)).

Effect of precipitated film on blocking of cathodic reduction sites

In order to assess the effect of precipitation on the overall cathodic kinetics (as expressed in i_{eq}), a film was formed on a SS304L coupon by performing a polarization scan from OCP to -1.2 V that resulted in a visually observable film, similar to our previous observations [16]. A subsequent polarization was performed with the film on the surface. This sequence was performed for two different film conditions: (i) the film was allowed to dry in air for roughly 24 hours and (ii) the film was formed and kept in solution for roughly 24 hours. The two results were very similar and only the polarization scan for the air-dried case is seen in Figure 12.

Cathodic polarization measurements with the presence of an $Mg(OH)_2$ film on the surface are seen in Figure 12 in comparison to polarization measurements without a film. First, a lower OCP is observed when a film is present on the surface of the alloy in comparison to no film. Second, suppression of ORR is seen when a film is present as indicated by a decreased current density at any given potential above ca. -0.25 V. Finally, it is noted that the E_{RP} is roughly at the end of the activation-controlled region when a film is present on the surface.

The presence of a film decreases the predicted maximum pit as can be seen by comparing Figure 13(a) with Figure 6(b). Furthermore, cathode radii are compared with and without a film in Figure 13(b) and indicate that when a film is considered, the cathode radii are roughly 5-6 times larger than without a film. This, in turn, makes precipitation reactions less effective (Figure 13(a)) due to an overall larger solution volume.

Dehydration and film effects on the equivalent current density play the largest role in decreasing pit size predictions in $MgCl_2$ electrolytes

Maximum pit size predictions for $MgCl_2$ solutions as a function of $MgCl_2$ concentration, percent anode saturation, and cathode evolution phenomena considered alone and in combination are seen in Figure 14(a). Overall, 4.98 M $MgCl_2$ has a larger pit size in all scenarios when compared to 0.189 M $MgCl_2$. When exploring percent of pit saturation, regardless of solution concentration, 50 % saturation has a larger maximum pit size in comparison to 100 % saturation. Finally, when comparing cathode evolution phenomena, the maximum pit size is highest in the original formulism and decreases in order in the following: precipitation, dehydration ("WL"), and combined precipitation and dehydration. Additionally, for 0.189 M $MgCl_2$ the film and film with precipitation decrease the pit size further than dehydration. The current at the maximum pit size for $MgCl_2$ solutions is presented in Figure S2(a). Cathode radii are presented for $MgCl_2$ solutions as a function of percent saturation and cathode evolution phenomena that were presented in this paper are seen in Figure 14(b). Overall, cathode radii follow the same trends as maximum pit size predictions, except for when a film is considered for 0.189 M $MgCl_2$ which exhibits a cathode radius roughly 5 times larger than the original formulism.

Maximum Pit Size Predictions in NaCl and Sea-Salt Brines

Maximum pit size predictions for NaCl and sea-salt brines are presented in Figure 15(a) for 50 % pit saturation. It was previously shown for $MgCl_2$ electrolytes that pit sizes were larger for 50 % saturation and cathode evolution effects are more severe, thus, predictions for 100 % saturation are not presented. In general, maximum pit sizes are larger in 76 % RH (5.01 M Cl^-) sea-salt in comparison to 40% RH (8.90 M Cl^-) despite having a greater chloride concentration in 40% RH. For 40 % RH sea-salt, maximum pit sizes decrease in the following order: original formulism, precipitation, dehydration, precipitation and dehydration, and salt. The scenario "salt" refers to the fractional volume of precipitated salt of the metal dissolution products in solution (Figure 4(b)).

Fractional solution volumes were used in the Bruggeman equation (Equation 5) and the precipitated salt was assumed to be insulating. 76 % RH sea-salt follows the same pattern except for salt, which is nearly identical to the original formulism. For NaCl solutions, 5 M NaCl has a greater maximum pit size than 0.6 M NaCl and, when dehydration was considered in both solutions, a decrease in maximum pit size was observed. Cathode radii at maximum pit sizes are presented in Figure 15(b) for sea-salt and NaCl electrolytes at 50 % saturation. The same patterns as maximum pit sizes (Figure 15(a)) are also displayed in cathode radii. The current at the maximum pit sizes for sea-salt brines and NaCl solution are presented in Figure S2(b) at 50 % saturation (see Supplemental Information).

It is interesting to note that the predictions for sea-salt brine at 76 % RH and saturated NaCl are significantly different with saturated NaCl having a larger pit size by a factor of roughly 2.5 in the original formulism. This same pattern holds for 40 % RH sea-salt brine and saturated $MgCl_2$, in which saturated $MgCl_2$ has a greater pit size than sea-salt by roughly a factor of 4. Furthermore, despite having a greater chloride concentration in 0.6 M NaCl, maximum pit sizes are nearly identical when comparing with 0.189 M $MgCl_2$ (0.378 M Cl^-). Additionally, saturated NaCl has a greater maximum pit size than saturated $MgCl_2$ by roughly a factor of 1.5 despite $MgCl_2$ having almost double the chloride concentration.

Discussion

Governing factors of maximum pit size predictions are dependent upon equilibrium solution relative humidity

Maximum pit size predictions using solutions with similar chloride concentrations (*i.e.* using $MgCl_2$ instead of sea-salt brine at 40 % RH) produce larger pit sizes than sea-salt and show the importance of having the correct environmental input parameters. As presented in Figure 14(a) and Figure 15(a), sea-salt solutions have lower predicted pit sizes than the analogous single salt system. In order to determine the governing factors, the inputs to the maximum pit size model were compared in radar plots and are presented in the radar diagrams in Figure 16. The radar plots in Figure 16 have five different quantitative axes arranged in a radial fashion. Each axis represents either the chloride concentration or a direct input to the maximum pit model ($(i \cdot x)_{sf}$, i_{eq}, κ_o, or WL). A colored line, representing a single solution, then connects all five axes and describes the quantitative inputs for that solution. It should be noted that all axes are on a logarithmic scale and do not have the same step size. Finally, the axes are oriented such that a value moving toward the center of the radar plot would produce a decrease in the predicted maximum pit size with all else being held equal. Thus, if there are two similar pentagons on the radar plots, the smaller pentagon would have a smaller predicted maximum pit size in comparison to the larger pentagon.

First, surrogate brines will be compared and the importance of having accurate input parameters will be discussed. Considering saturated $MgCl_2$ and 40 % RH sea-salt brine (Figure 16(a)), one can see that the chloride concentration, κ_o, and i_{eq} are all very similar and likely do not account for the significant differences in pit size predictions. However, saturated $MgCl_2$ has a greater WL and lower $(i \cdot x)_{sf}$ in comparison to 40 % RH sea-salt brine. This combination will lead to an increased ohmic drop in 40 % RH sea-salt, decreasing the total cathodic current supply. As an increased anodic current demand (increased $(i \cdot x)_{sf}$) is present, maximum pit sizes are decreased by roughly 275 µm (Figure 14(a) and Figure 15(a)) when combined with the decreased cathodic current. Now looking at the comparison between 76 % RH sea-salt brine and saturated NaCl, the same trends follow with the difference in pit size being nearly 415 µm (Figure 15(a)). Although this result may seem surprising, it is important to remember the total cathodic currents are presented in Figure S2. The available cathodic currents for saturated NaCl and 76 % RH sea-salt brine are much higher than for saturated $MgCl_2$ and 40 % RH. Thus, differences in $(i \cdot x)_{sf}$ will cause a larger change in predicted pit sizes when the cathodic current is higher.

Perhaps against intuition, increasing chloride concentration in atmospheric corrosion scenarios does not always cause an increase in pit sizes. When exploring concentration increases of $MgCl_2$ and NaCl solutions, an increase in pit size is predicted. However, when comparing concentrated $MgCl_2$ and NaCl, the chloride concentration is almost doubled in $MgCl_2$ solutions, however, a larger pit size is seen in concentrated NaCl (Figure 14 and Figure 15). When looking at the properties of each solution in Figure 16, the WL are similar, however, $MgCl_2$ has an $(i \cdot x)_{sf}$ that is lower by an order of magnitude. Although a lower $(i \cdot x)_{sf}$ would lead to an increased pit size, saturated $MgCl_2$ experiences a large decrease in i_{eq} due to ORR suppression [16], decreased oxygen concentration [16,39], and a decreased κ_o. The combination of these factors causes the total cathodic current to be roughly 160 µA less (Figure S2). This decrease in cathode current diminishes the effects of the disparity in $(i \cdot x)_{sf}$. This effect is seen again when comparing 0.6 M NaCl and 0.189 M $MgCl_2$ as 0.189 M $MgCl_2$ has a larger pit size. In this case, a similar $(i \cdot x)_{sf}$ is present for both solutions and the governing factor becomes an increase in *WL* for 0.189 M $MgCl_2$ in comparison to 0.6 M NaCl.

Overall, the governing factors for maximum pit size are not the same across all solution combinations but can be separated into two broad groups based on the solutions that were explored within: (i) similar chloride concentrations (RH) and (ii) varying chloride concentrations (RH). Under similar chloride concentrations, the WL and $(i \cdot x)_{sf}$ are the most influential factors. When varying chloride concentrations, changes in WL, i_{eq}, and κ_o are the most influential parameters. This effect is very similar to that which occurs when the temperature is increased at a single concentration of NaCl [22]. At elevated temperatures, an increase in cathode current was seen with increasing temperature due to an increase in i_{eq} and κ_o, but a decrease in $(i \cdot x)_{sf}$ caused the pit sizes to be relatively invariant to temperature swings [22].

It is also interesting to note differences in $(i \cdot x)_{sf}$ and E_{RP} between the solutions. A decrease in $(i \cdot x)_{sf}$ with increased bulk chloride has generally been attributed to the common ion effect [22,34]. However, $MgCl_2$ has a higher $(i \cdot x)_{sf}$ in comparison to NaCl solutions at all equivalent chloride concentrations. A similar phenomenon for increased $(i \cdot x)_{sf}$ of $FeCl_3$ in comparison to NaCl was observed by Woldemedhin et al. [40]. Although an in-depth analysis is outside of the scope of this paper, working hypotheses include: (i) changes in metal ion diffusivity due to varying pit solution viscosities and (ii) changes in salt film properties due to complexation effects from bulk ions. Additionally, E_{RP} is generally higher in sea-salt solutions and it is possible that inhibiting spectating ion complexes (*i.e.*, sulfates and carbonates) in solution contribute to a more noble E_{RP}. Finally, E_{RP} falls within the activation-controlled region for the solutions of interest and allows for the use of cathodic kinetics under quiescent conditions.

Precipitation and dehydration decreases the sensitivity of the maximum pit model to all input parameters

In order to assess the sensitivity of maximum pit predictions to input parameters, percent pit saturation (Figure 8), LD (Figure 9 and Figure 11(d)), and E_{RP} (Figure 10 and Figure 11(e)) were varied within $MgCl_2$ solutions. First, considering maximum pit size predictions in $MgCl_2$ solutions, precipitation causes a greater decrease in maximum pit size for 40 % of pit saturation in comparison to 100 % saturation. This effect is due to the cathode radii not changing significantly with increased percent pit saturation (Figure 14(c)). It is important to remember that cathode radii display a logarithmic behavior as a function of anode size (Figure 6(c and d) and Figure 13(b)). With an increase in anode saturation, a smaller maximum pit size is achieved as I/r increases and more current is needed at any given anode size to maintain the critical pit environment. When the pit size decreases, so does the hydroxyl production but more severely than cathode radii. It is again important to remember that hydroxyl production is a cubic function of the anode size (Equation 2). Thus, a pit at 100 % of pit saturation will experience a significant decrease in the anode size, decrease the hydroxyl production, and will diminish any effects from precipitation or dehydration reactions as the cathode radius is relatively independent of pit saturation. This effect is shown schematically in Figure 17. This analysis stresses the importance of ascertaining $(I/r)_{crit}$ as this will have a significant impact on the maximum pit size and hydroxyl production.

Next, with increased LD an increased maximum pit size is predicted as seen in Figure 9 and Figure 11(d). It is interesting to note, that an uncertainty of ± 0.5 g/m^2 causes an uncertainty in pit size of ± 64.4 μm in 4.98 M $MgCl_2$ and ± 27.9 μm in 0.189 M $MgCl_2$ in the original formulism. When precipitation is considered, a decrease in maximum pit size is seen at all LD, and a greater decrease is seen for 4.98 M $MgCl_2$ in comparison to 0.189 M $MgCl_2$. The uncertainty of ± 0.5 g/m^2 results in an uncertainty in pit size of ± 50.5 μm in 4.98 M $MgCl_2$ and ± 27.4 μm in 0.189 M $MgCl_2$. A greater decrease in saturated solutions when precipitation is considered is attributed to a lower cathode volume due to a significantly lower WL (Figure 16(a)).

Finally, fluctuations in E_{RP} (*i.e.*, from ¼ · E_{RP} to 2 · E_{RP}) provided for a larger spread in predicted pit sizes in 4.98 M $MgCl_2$ in comparison to 0.189 M $MgCl_2$. This effect is evident from the polarization scans presented in Figure 3. Decreasing E_{RP} in 4.98 M $MgCl_2$ will cause a greater increase in i_{eq} in comparison to 0.189 M $MgCl_2$ because the polarization scan for 4.98 M $MgCl_2$ has a much lower slope (on an E vs. log(i) plot) and minor fluctuations in potential cause a large fluctuation in current density. Thus, greater increases in i_{eq} will cause a greater total cathodic current and a greater increase in pit size as seen in Figure 10(b). Although this is the case for the original pit formulism, when precipitation is considered, a plateau in pit size is seen with increased, normalized E_{RP} in Figure 10(b). As previously stated, with increased i_{eq} greater pit sizes are predicted and therefore larger hydroxyl production is present in the cathode. This higher hydroxyl concentration will cause greater decreases in the effective conductivity and offset the effects of normalized E_{RP} increases. This phenomenon has greater influences in saturated $MgCl_2$ due to the fact that the WL is orders of magnitude smaller in this solution in comparison to dilute $MgCl_2$ and, based on Equation 6, will have a lower solution volume and greater impact on the effective conductivity.

Dehydration reactions coupled with precipitation will cause the most significant inhibition of corrosion damage

The presence of a film on the surface of the alloy resulted in the smallest predicted pit size (Figure 14 (a)), however, it is not the best-case scenario for corrosion inhibition. As shown in Figure 14(a) and Figure 15(a), predicted pit sizes decreased in the following order for all solutions explored: original > precipitation > dehydration > dehydration + precipitation. These effects on maximum pit sizes are summarized schematically in Figure 18. Further decreases in predicted maximum pit sizes are seen when a film is on the surface (for 0.189 M $MgCl_2$) and when salt precipitates are considered for 40 % RH sea-salt.

The presence of a film on the surface of the alloy decreased i_{eq} causing a decrease in pit size. A lower i_{eq} causes a much larger R_{cath} in comparison to no film (Figure 14(b)), because the lower current densities lead to lower ohmic drop per unit length. As E_{RP} was assumed to be the same, a larger R_{cath} is needed in order to account for this decrease in ohmic drop. With a larger R_{cath}, the effects of precipitation (Figure 13(a)) and dehydration are minimal due to an increased solution volume. In this scenario, nearly the entire WL is present on the surface at the predicted maximum pit size, allowing for pits to initiate after the original pit has repassivated. In contrast to the case without a film, dehydration can occur much more rapidly (due to an overall smaller solution volume). In this scenario, the WL decreases roughly 42 % in 0.189 M $MgCl_2$ and any pit initiating in the future will experience larger ohmic drop, resulting in a smaller pit size, and further contributing to brine dry out. When only precipitation is considered, a reduction in conductivity would be experienced by any future pit growth, however, the ohmic drop would not be as severe when considering both dehydration and precipitation. Thus, understanding dehydration and precipitation together is crucial to predicting overall material degradation.

For mixed salt solutions at low RH, such as 40 % RH sea-salt, salts precipitating on the surface caused the greatest decrease in predicted pit size (Figure 15(a)) due to the small fractional water content (Figure 4(b)). At such low RH, there is roughly 35 % water with 65 % precipitated salts by volume in solution and, when assumed to be ionically insulating, cause a significant decrease in the predicted pit size. Although this case proved to be the most severe, it is unlikely that a continuous, uniform WL on the order of 1 µm will be present over the entire cathode, thus, droplets may form. Droplets forming on the surface would provide for a different scenario than modeled and the effects of droplets on predicted maximum corrosion are the focus of future work.

It is important to understand why precipitation and dehydration vary in efficacy based on the solution concentration. For precipitation at a constant pit size, there is a larger volume fraction of a precipitate for the 4.98 M $MgCl_2$ in comparison to 0.189 M $MgCl_2$ due to the smaller overall volume of liquid. Via Bruggeman's equation, this leads to a larger effective resistivity which, when combined with smaller WL, leads to an increased ohmic potential drop, a decreased R_{cath}, and thus a decrease in I_{cath}. Thus, due to greater change in I_{cath} in 4.98 M MgCl2 solutions, a greater change in pit sizes are expected in saturated solutions for precipitation reactions. This trend is opposite to observations for dehydration reactions, *i.e.* a greater decrease in predicted pit sizes are seen in 0.189 M $MgCl_2$ in comparison to 4.98 M $MgCl_2$ when dehydration is considered. This is directly related to the amount of chloride present in the cathode. Considering the same pit size in both solutions, the migration of chloride to the pit is going to be the same in both solutions. Although this may be the case, the overall amount of chloride is much higher in 4.98 M $MgCl_2$ than in 0.189 M $MgCl_2$ due to an increase in both cathode size and chloride concentration. This result would indicate that the activity of water in solution is going to fluctuate much more in dilute solutions and cause the WL decrease to be more severe. Thus, dilute solutions will experience brine dry-out from dehydration reactions at smaller pit sizes compared to saturated solutions. Overall, the maximum pit model is most sensitive to input parameters for concentrated solutions, however, the sensitivity of these parameters is decreased when precipitation and dehydration occur.

Limitations and Implications

Overall, the role of the calculations performed are to present predictions for various solutions and help identify the controlling reactions present in atmospheric scenarios that could enhance cathodic limitations and decrease the maximum pit size. Exposure testing in sea-salt environments at 35˚C produced a maximum pit depth of approximately 75 µm [37]. This indicates that predictions for sea-salt brines under the original maximum pit formulism (Figure 14 and Figure 15) are indeed an over-estimate and deemed to be conservative. Although predictions made were at room temperature, previous research has shown an increase in predicted pit size with increasing temperature [22]. The presented work attempts to further describe scenarios which could impact cathodic current on the surface of the alloy via various cathode evolution phenomena, however, it is important to understand the assumptions.

In this analysis, it was assumed that non-carbonate species were the initial and only precipitate to form on the surface of the alloy. Although carbonate phases are seen in many analyses of corrosion products, it has been shown that non-carbonate phases are kinetically favored [16,17] and conversion from non-carbonate species to carbonate phases is remarkably slow [41-43]. Although this may be the case, in 4.98 M $MgCl_2$ solutions, a $MgCO_3$ precipitate would cause an increase in predicted pit size of roughly 30 µm. In 0.189 M $MgCl_2$, consideration of $MgCO_3$ decreases predicted maximum pit size by only 0.5 µm. Thus, knowing the composition of the precipitate is more important in saturated solutions where the solution volume is smaller and precipitates are larger. As with the original pit size model, time dependence was not considered, and all reactions were assumed to occur instantaneously. Under in-service conditions, alloys generally go through diurnal and seasonal RH and temperature fluctuations which would increase the complexity of actual time dependencies. For example, increasing equilibrium RH would dilute solution composition, increase WL, and change stable precipitates in solution. In the case of $MgCl_2$ solutions, a pit growing at low RH would have $Mg_2(OH)_3Cl \cdot 4H_2O$ as the stable precipitate and increasing RH would cause a change in stability to $Mg(OH)_2$. Any $Mg_2(OH)_3Cl \cdot 4H_2O$ present in the solution would undergo a back reaction and convert to $Mg(OH)_2$. Additionally, conversion to carbonate species is occurring simultaneously. Information is not available in the literature to provide information on these complex reactions but understanding such reactions is an important area of research for informing on the extent of corrosion. Finally, it was assumed that no metal hydroxides were precipitated at the cathode. Fe/Ni/Cr hydroxides have a lower pH for precipitation in comparison to Mg-containing hydroxides [13,16,44], thus, would have a greater impact on the ohmic drop making the predictions given here conservative (*i.e.* overestimate pit sizes). In addition, the amount of metal species migrating out of the pit is unknown and this would be a kinetically controlled process.

The Bruggeman correction for effective media conductivity was utilized in this study and has been previously used in corrosion modeling studies [4,13,45,46], however, justification for the use of this correction is needed. First, Tjaden et al. explored the Bruggeman equation for use in electrochemical systems and noted that the Bruggeman correlation is only valid in situations where the insulating phase is present in low volume fractions and represented by random isotropic spheres. Additionally, the correction cannot account for directional differences arising from non-spherical particles; however, it is going to fall on the conservative end of corrections (*i.e.* overestimate mixed-media conductivity) [47]. Another area of research that considers effective media conductivity is saturated porous media and Archie's Law is typically used, also utilizing the precipitated volume fraction. In a review of such scenarios, Cai et al. showed that model parameters are highly dependent upon the composition and shape of the precipitates. Although this may be the case, it was shown that having an exponent of 3/2 (as in the Bruggeman equation) is conservative and, in fact, carbonate species have a larger exponent [48]. It is noted that many models produce similar results above a liquid volume fraction of 0.8 [46,48]. Based on Figure 7, $MgCl_2$ solutions have a volume fraction greater than 0.80. Finally, De La Rue and Tobias found that the dependence of effective conductivity was best represented by Bruggeman's approximation when there was a broad range of particle sizes [46]. Thus, the Bruggeman equation is a conservative approximation for effective media conductivity (*i.e.* overestimate effective conductivity) and, in the range of volume fraction expected, variations in effective conductivity approximations are expected to be small.

Next, all calculations were made assuming that precipitates influenced solution properties uniformly (*i.e.* hydroxyl was evenly distributed). In reality, cathodic current, and therefore hydroxyl production, is going to be highest near the edge of the localized corrosion site [3,10]. This distribution would cause for increased precipitation near the edge of the pit, resulting in greater ohmic drop near the pit, and subsequently a smaller I_{cath}. By working with the total cathodic volume, predictions are still bounding.

Pits within this study were assumed to be hemispherical and only one pit is considered to form within the area of the effective cathode. Although not all pits are hemispherical, it is a commonly observed morphology and one that is widely used in pit modeling as a reasonable proxy for actual pits. Of course, if a pit transitions into a smaller localized corrosion site (e.g. an intergranular fissure), the current needed for propagation will be less than for a full hemispherical pit and the damage size could exceed that calculated here. Additionally, the evolution of pit morphology is hypothesized to be a time, material, and stress dependent process and can produce irregular morphologies [37] which could not be captured by the present model. Although it is possible that while under a precipitate or precipitated salt a crevice environment is formed [49], the influences on $(i \cdot x)_{sf}$ are unknown. Furthermore, it was assumed that the conversion from $(i \cdot x)_{crit}$ to $(I/r)_{crit}$ was three. There are multiple values in literature ranging from three [23,28] to four [50,51]. Despite the difference in conversions, a value of three was adopted as this would give a more conservative pit prediction. Finally, if more than one pit forms within a cathode area, then the pits would share the available cathode current, decreasing the actual maximum size of both pits and calculations made within would be bounding.

Despite these limitations, the implications of the work should be noted. SS alloys are used extensively in marine and near marine environments with one such example being the storage of spent nuclear fuel. The predictions made herein can provide insights on the severity of localized corrosion in such environments. This work has shown the importance of ascertaining the exact solution chemistry at an exposure sight and using approximate solutions to inform pit propagation may not represent the extent of corrosion damage. For example, considering sea-salt solutions over single salt equivalents (*i.e.*, comparing saturated NaCl and 76 % RH sea-salt) produces a decreased maximum pit size. Additionally, understanding the exact composition will influence the stable precipitate on the surface of the alloy as well as the dehydration pathway that a cathode would undergo.

Although maximum pit sizes were assumed to be under a continuous thin film, droplets are often observed on the surface of corroding alloys [2,52–54]. An analytical expression for the cathodic current under the droplet is not available, but a qualitative understanding can be obtained from the work presented. In the presence of a droplet, the cathode would be finite and limited by the size of the droplet and subsequent spreading [15,53]. In most cases, the size of droplets, characterized by a diameter on the order of 100's of μm [54,55], is smaller than the size of calculated cathodes, which have a diameter of on the order of 2 cm (2 x 10^4 μm, Figure 14 and Figure 15). Droplet spreading has also been observed on various alloys with diameters up to roughly 2000 μm [15] which is still an order of magnitude lower than calculated cathode sizes. There would be a smaller solution volume than in a continuous layer, and the effects of reduced conductivity due to salts and precipitates would he heightened as the fractional solution volume would be smaller. The precipitation of salts in solution was directly observed in droplets by Guo et al. in a $MgCl_2$ and NaCl mixture during the corrosion of SS304 and a decrease in conductivity was proposed [49]. Additionally, it was noted that the precipitated salts could block oxygen from contacting the surface [49] which would decrease i_{eq}. Having a finite cathode and decreased i_{eq} would decrease the total cathodic current available to support dissolution and would decrease maximum pit sizes. This is unlike thin films where the cathode size can increase beyond the size of a droplet. Finally, dehydration has been directly observed for droplets [15,49] and has been proposed as a possible mechanism for corrosion inhibition on various alloys [19,56,57]. Dehydration has also been shown to reduce maximum pit sizes significantly (Figure 11). Although predictions made herein are not time-dependent, this work quantitatively highlights the importance of considering precipitation and dehydration reactions in corrosion processes and shows the need to incorporate them into predictions.

Predicted maximum cathode radii (Figure 14 and Figure 15) can be as large as 4.5 cm under the original maximum pit model. Considering a pit growing in the center of a sample, that would indicate that the sample width would have to be 9 cm across in order to accommodate the current necessary to achieve the predicted pit size before experiencing cathodic limitations. Specifically, ASTM B117 contains a solution concentration close to 0.6 M NaCl [58] and contains a WL dependent upon angle varying from 660 to 1210 µm [59]. The WL for 0.6 M NaCl under a LD of 3 g/m^2 is 123 µm with a cathode radius of roughly 1.1 cm. With a larger WL, ohmic drop would be diminished, causing for cathodic radii to be larger. Specifically, for 660 and 1210 um WL, cathode radii would be 3.2 and 4.6 cm respectively. This would indicate, that in most accelerated tests akin to B117, pit sizes cathodically limited by the sample size as samples are generally smaller than 9 cm.

Conclusion

Maximum pit sizes were predicted for dilute and concentrated NaCl and $MgCl_2$ solutions as well as sea-salt solutions corresponding to 40 % and 76 % RH at 25 ˚C. Cathode evolution phenomena, including precipitation and dehydration reactions, were also incorporated into predictions in order to ascertain the conservativeness of the model as well as obtain governing factors for pit growth. Despite one's intuition, the highest chloride concentration does not always produce the largest predicted pit size as ohmic drop is often severe in concentrated solutions. The largest pit sizes predicted in this study were found in saturated NaCl. Next, it was determined that pit size predictions are most sensitive to input parameters for concentrated solutions. However, when cathodic evolution is considered, the sensitivity of these parameters is decreased. Although there was not one main input parameter that influenced pit size predictions, two main categories were identified. Under similar chloride conditions (RH), the WL, and $(i \cdot x)_{sf}$ are the most influential factors. When varying chloride concentrations (RH), changes in WL, i_{eq}, and κ_o are the most influential parameters. Finally, it was noted that dehydration reactions coupled with precipitation will cause for the most significant inhibition of corrosion damage.

Acknowledgements

Sandia National Laboratories is a multi-mission laboratory managed and operated by National Technology and Engineering Solutions of Sandia, LLC., a wholly owned subsidiary of Honeywell International, Inc., for the U.S. Department of Energy's National Nuclear Security Administration under contract DE-NA0003525. The financial support of DE-NE0008901 from US DOE National Lab-Idaho and PO 2048607, Sandia National Laboratories, is also acknowledged. Discussions with Rob Sorenson (Sandia National Laboratories) are greatly appreciated. This document is SAND2021-0207 J.

Symbol List

E_{RP}	Repassivation potential
e_{SS}^{-}	Electrons transferred per mol SS corroded
I_{LC}	Anodic current demand
$(i \cdot x)_{sf}$	Pit stability product under a salt film
I/r	Pit stability for hemisphere
LD	Salt loading density
M_{OH^-}	Hydroxyl molarity (mol/L) in cathode region
MW_{precip}	Precipitate molecular weight
MW_{SS}	Stainless Steel 304 molecular weight
n_{precip}	Stochiometric number for precipitate
r_a	Anode radius
R_{cath}	Cathode radius
V_{cath}	Cathode volume
V_{precip}	Precipitate volume
WL	Water layer thickness
Greek Symbols	
κ_{eff}	Effective conductivity
κ_o	Initial solution conductivity
ρ_{SS}	Stainless Steel 304 density
ρ_{precip}	Precipitate density

Data Availability

The raw/processed data required to reproduce these findings cannot be shared at this time as the data also forms part of an ongoing study.

References

[1] C.R. Bryan, E.J. Schindelholz, Properties of brines formed by deliquescence of sea salt aerosols, in: Corros. 2018, Phoenix, 2018: p. Paper 10516.

[2] E. Schindelholz, R.G. Kelly, Wetting phenomena and time of wetness in atmospheric corrosion: a review, Corros. Rev. 30 (2012) 135–170. https://doi.org/10.1515/corrrev-2012-0015.

[3] Z.Y. Chen, R.G. Kelly, Computational Modeling of Bounding Conditions for Pit Size on Stainless Steel in Atmospheric Environments, J. Electrochem. Soc. 157 (2010) C69–C78. https://doi.org/10.1149/1.3261803.

[4] A.S. Agarwal, U. Landau, J.H. Payer, Modeling particulates effects on the cathode current capacity in crevice corrosion, J. Electrochem. Soc. 155 (2008) C269–C278. https://doi.org/10.1149/1.2890418.

[5] Z.Y. Chen, F. Cui, R.G. Kelly, An analytical modeling method for calculating the current delivery capacity of a thin-film cathode and the stability of localized corrosion under atmospheric environments, ECS Trans. 3 (2007) 443–457. https://doi.org/10.1149/1.2789248.

[6] Z.Y. Chen, F. Cui, R.G. Kelly, Calculations of the Cathodic Current Delivery Capacity and Stability of Crevice Corrosion under Atmospheric Environments, J. Electrochem. Soc. 155 (2008) C360–C368. https://doi.org/10.1149/1.2926557.

[7] N. Van Den Steen, H. Simillion, O. Dolgikh, H. Terryn, J. Deconinck, An integrated modeling approach for atmospheric corrosion in presence of a varying electrolyte film, Electrochim. Acta. 187 (2016) 714–723. https://doi.org/10.1016/j.electacta.2015.11.010.

[8] C. Liu, R.G. Kelly, A Review of the Application of Finite Element Method (FEM) to Localized Corrosion Modeling, Corrosion. 75 (2019) 1285–1299. https://doi.org/10.5006/3282.

[9] C. Lin, H. Ruan, S.-Q. Shi, Phase field study of mechanico-electrochemical corrosion, Electrochim. Acta. 310 (2019) 240–255. https://doi.org/10.1016/j.electacta.2019.04.076.

[10] Y. Wang, L. Yin, Y. Jin, J. Pan, C. Leygraf, Numerical Simulation of Micro-Galvanic Corrosion in Al Alloys: Steric Hindrance Effect of Corrosion Product, J. Electrochem. Soc. 164 (2017) C1035–C1043. https://doi.org/10.1149/2.0871714jes.

[11] L. Yin, Y. Jin, C. Leygraf, J. Pan, A FEM model for investigation of micro-galvanic corrosion of Al alloys and effects of deposition of corrosion products, Electrochim. Acta. 192 (2016) 310–318. https://doi.org/10.1016/j.electacta.2016.01.179.

[12] O. Dolgikh, A.C. Bastos, A. Oliveira, C. Dan, J. Deconinck, Influence of the electrolyte film thickness and NaCl concentration on the oxygen reduction current on platinum, Corros. Sci. 102 (2016) 338–347. https://doi.org/10.1016/j.corsci.2015.10.025.

[13] T.Q. Ansari, J.-L. Luo, S.-Q. Shi, Modeling the effect of insoluble corrosion products on pitting corrosion kinetics of metals, Npj Mater. Degrad. 3 (2019) 1–12. https://doi.org/10.1038/s41529-019-0090-5.

[14] T.Q. Ansari, Z. Xiao, S. Hu, Y. Li, J.-L. Luo, S.-Q. Shi, Phase-field model of pitting corrosion kinetics in metallic materials, Npj Comput. Mater. 4 (2018) 38. https://doi.org/10.1038/s41524-018-0089-4.

[15] E.J. Schindelholz, H. Cong, C.F. Jove-Colon, S. Li, J.A. Ohlhausen, H.K. Moffat, Electrochemical aspects of copper atmospheric corrosion in the presence of sodium chloride, Electrochim. Acta. 276 (2018) 194–206. https://doi.org/10.1016/j.electacta.2018.04.184.

[16] R.M. Katona, J.C. Carpenter, A.W. Knight, C.R. Bryan, R.F. Schaller, R.G. Kelly, E.J. Schindelholz, Importance of the hydrogen evolution reaction in magnesium chloride solutions on stainless steel, Corros. Sci. 177 (2020) 108935. https://doi.org/10.1016/j.corsci.2020.108935.

[17] R.M. Katona, R.G. Kelly, C.R. Bryan, R.F. Schaller, A.W. Knight, Use of in situ Raman spectroelectrochemical technique to explore atmospheric corrosion in marine-relevant environments, Electrochem. Commun. 118 (2020) 106768. https://doi.org/10.1016/j.elecom.2020.106768.

[18] C. Bryan, E. Schindelholz, A. Knight, J. Taylor, R. Dingreville, Stability of sea-salt deliquescent brines on heated surfaces of SNF dry storage canisters, 2019.

[19] R.F. Schaller, C.F. Jove-Colon, J.M. Taylor, E.J. Schindelholz, The controlling role of sodium and carbonate on the atmospheric corrosion rate of aluminum, Npj Mater. Degrad. 1 (2017) 20. https://doi.org/10.1038/s41529-017-0020-3.

[20] D.B. Blücher, R. Lindström, J.-E. Svensson, L.-G. Johansson, The Effect of CO[sub 2] on the NaCl-Induced Atmospheric Corrosion of Aluminum, J. Electrochem. Soc. 148 (2001) B127. https://doi.org/10.1149/1.1354614.

[21] L. Yin, Y. Jin, C. Leygraf, J. Pan, A FEM model for investigation of micro-galvanic corrosion of Al alloys and effects of deposition of corrosion products, Electrochim. Acta. 192 (2016) 310–318. https://doi.org/10.1016/j.electacta.2016.01.179.

[22] R.M. Katona, J. Carpenter, E.J. Schindelholz, R.G. Kelly, Prediction of Maximum Pit Sizes in Elevated Chloride Concentrations and Temperatures, J. Electrochem. Soc. 166 (2019) C3364–C3375. https://doi.org/10.1149/2.0451911jes.

[23] M.T. Woldemedhin, M.E. Shedd, R.G. Kelly, Evaluation of the Maximum Pit Size Model on Stainless Steels under Thin Film Electrolyte Conditions, J. Electrochem. Soc. 161 (2014) E3216–E3224. https://doi.org/10.1149/2.023408jes.

[24] J. Srinivasan, M.J. McGrath, R.G. Kelly, A High-Throughput Artificial Pit Technique to Measure Kinetic Parameters for Pitting Stability, J. Electrochem. Soc. 162 (2015) C725–C731. https://doi.org/10.1149/2.0281514jes.

[25] G.T. Gaudet, W.T. Mo, T.A. Hatton, J.W. Tester, J. Tilly, H.S. Isaacs, R.C. Newman, Mass transfer and electrochemical kinetic interactions in localized pitting corrosion, AIChE J. 32 (1986) 949–958. https://doi.org/10.1002/aic.690320605.

[26] N.J. Laycock, R.C. Newman, Localised dissolution kinetics, salt films and pitting potentials, Corros. Sci. 39 (1997) 1771–1790. https://doi.org/10.1016/S0010-938X(97)00049-8.

[27] T.R. Beck, Occurrence of Salt Films during Initiation and Growth of Corrosion Pits, J. Electrochem. Soc. 126 (1979) 1662. https://doi.org/10.1149/1.2128772.

[28] P.C. Pistorius, G.T. Burstein, Metastable pitting corrosion of stainless steel and the transition to stability, Phil. Trans. R. Soc. L. 1992 (1992) 531–559.

[29] J. Srinivasan, R.G. Kelly, One-Dimensional Pit Experiments and Modeling to Determine Critical Factors for Pit Stability and Repassivation, J. Electrochem. Soc. 163 (2016) C759–C767. https://doi.org/10.1149/2.0651613jes.

[30] P. Ernst, R.C. Newman, Explanation of the effect of high chloride concentration on the critical pitting temperature of stainless steel, Corros. Sci. 49 (2007) 3705–3715. https://doi.org/10.1016/j.corsci.2007.03.026.

[31] M.H. Moayed, R.C. Newman, The Relationship Between Pit Chemistry and Pit Geometry Near the Critical Pitting Temperature, J. Electrochem. Soc. 153 (2006) 330–335. https://doi.org/10.1149/1.2210670.

[32] H.C. Kuo, D. Landolt, Rotating disc electrode study of anodic dissolution or iron in concentrated chloride media, Electrochim. Acta. 20 (1975) 393–399. https://doi.org/10.1016/0013-4686(75)90022-5.

[33] P. Ernst, R.. Newman, Pit growth studies in stainless steel foils II. Effect of temperature, chloride concentration and sulphate addition, Corros. Sci. 44 (2002) 943–954. https://doi.org/10.1016/S0010-938X(01)00133-0.

[34] J. Srinivasan, R.G. Kelly, On a recent quantitative framework examining the critical factors for localized corrosion and its impact on the galvele pit stability criterion, Corrosion. 73 (2017) 613–633. https://doi.org/10.5006/2334.

[35] C. Liu, R.G. Kelly, Comparison study of the effect of oxide film properties on cathodic kinetics of stainless steel 304L and 316L during ORR potential window in sulfate solution, Corrosion. 75 (2019) 1087–1099. https://doi.org/10.5006/3134.

[36] T. Shinohara, S. Motoda, W. Oshikawa, Evaluation of Corrosivity of Atmosphere by ACM Type Corrosion Sensor, Zairyo-to-Kankyo. 54 (2005) 375–382. https://doi.org/10.3323/jcorr1991.54.375.

[37] T.D. Weirich, J. Srinivasan, J.M. Taylor, M.A. Melia, P.J. Noell, C.R. Bryan, G.S. Frankel, J.S. Locke, E.J. Schindelholz, Humidity Effects on Pitting of Ground Stainless Steel Exposed to Sea Salt Particles, J. Electrochem. Soc. 166 (2019) C3477–C3487. https://doi.org/10.1149/2.0551911jes.

[38] D.A.G. Bruggeman, Berechnung verschiedener physikalischer Konstanten von heterogenen Substanzen. I. Dielektrizitätskonstanten und Leitfähigkeiten der Mischkörper aus isotropen Substanzen, Ann. Phys. 416 (1935) 636–664. https://doi.org/10.1002/andp.19354160705.

[39] C.L. Alexander, C. Liu, A. Alshanoon, R.M. Katona, R.G. Kelly, J. Carpenter, C. Bryan, E. Schindelholz, Oxygen reduction on stainless steel in concentrated chloride media, J. Electrochem. Soc. 165 (2018) C869–C877. https://doi.org/10.1149/2.0181813jes.

[40] M.T. Woldemedhin, J. Srinivasan, R.G. Kelly, Effects of environmental factors on key kinetic parameters relevant to pitting corrosion, J. Solid State Electrochem. 19 (2015) 3449–3461. https://doi.org/10.1007/s10008-015-2816-9.

[41] I.M. Power, P.A. Kenward, G.M. Dipple, M. Raudsepp, Room Temperature Magnesite Precipitation, Cryst. Growth Des. 17 (2017) 5652–5659. https://doi.org/10.1021/acs.cgd.7b00311.

[42] H.E. King, H. Satoh, K. Tsukamoto, A. Putnis, Nanoscale observations of magnesite growth in chloride- and sulfate-rich solutions, Environ. Sci. Technol. 47 (2013) 8684–8691. https://doi.org/10.1021/es401188j.

[43] G.D. Saldi, G. Jordan, J. Schott, E.H. Oelkers, Magnesite growth rates as a function of temperature and saturation state, Geochim. Cosmochim. Acta. 73 (2009) 5646–5657. https://doi.org/10.1016/j.gca.2009.06.035.

[44] J.R. Galvele, Transport Processes in passivity breakdown - II. Full hydrolysis of metal ions, Corros. Sci. 21 (1981) 551–579.

[45] Y.-C. Chang, R. Woollam, M.E. Orazem, Mathematical Models for Under-Deposit Corrosion, J. Electrochem. Soc. 161 (2014) C321–C329. https://doi.org/10.1149/2.034406jes.

[46] R.E.D. La Rue, C.W. Tobias, On the Conductivity of Dispersions, J. Electrochem. Soc. 106 (1959) 827. https://doi.org/10.1149/1.2427505.

[47] B. Tjaden, S.J. Cooper, D.J. Brett, D. Kramer, P.R. Shearing, On the origin and application of the Bruggeman correlation for analysing transport phenomena in electrochemical systems, Curr. Opin. Chem. Eng. 12 (2016) 44–51. https://doi.org/10.1016/j.coche.2016.02.006.

[48] J. Cai, W. Wei, X. Hu, D.A. Wood, Electrical conductivity models in saturated porous media: A review, Earth-Science Rev. 171 (2017) 419–433. https://doi.org/10.1016/j.earscirev.2017.06.013.

[49] L. Guo, N. Mi, H. Mohammed-Ali, M. Ghahari, A. Du Plessis, A. Cook, S. Street, C. Reinhard, R.C. Atwood, T. Rayment, A.J. Davenport, Effect of mixed salts on atmospheric corrosion of 304 stainless steel, J. Electrochem. Soc. 166 (2019) C3010–C3014. https://doi.org/10.1149/2.0021911jes.

[50] D.E. Williams, J. Stewart, P.H. Balkwill, The nucleation, growth and stability of micropits in stainless steel, Corros. Sci. 36 (1994) 1213–1235. https://doi.org/10.1016/0010-938X(94)90145-7.

[51] J. Newman, Resistance for Flow of Current to a Disk, J. Electrochem. Soc. 113 (1966) 501. https://doi.org/10.1149/1.2424003.

[52] E. Schindelholz, L.K. Tsui, R.G. Kelly, Hygroscopic particle behavior studied by interdigitated array microelectrode impedance sensors, J. Phys. Chem. A. 118 (2014) 167–177. https://doi.org/10.1021/jp4098149.

[53] T. Tsuru, K. Tamiya, A. Nishikata, Formation and growth of micro-droplets during the initial stage of atmospheric corrosion, Electrochim. Acta. 49 (2004) 2709–2715. https://doi.org/10.1016/j.electacta.2004.01.032.

[54] E. Schindelholz, B.E. Risteen, R.G. Kelly, Effect of relative humidity on corrosion of steel under sea salt aerosol proxies I. NaCl, J. Electrochem. Soc. 161 (2014) 450–459. https://doi.org/10.1149/2.0221410jes.

[55] E. Schindelholz, B.E. Risteen, R.G. Kelly, Effect of Relative Humidity on Corrosion of Steel under Sea Salt Aerosol Proxies II. MgCl2, Artificial Seawater, J. Electrochem. Soc. 161 (2014) C460–C470. https://doi.org/10.1149/2.0231410jes.

[56] Z. Dan, I. Muto, N. Hara, Role of Corrosion Products in the Suppression of Atmospheric Corrosion of Aluminum and its Alloys, ECS Trans. 25 (2019) 23–33. https://doi.org/10.1149/1.3407545.

[57] Y. Sato, K. Azumi, Corrosion Inhibition by Zinc Corrosion Products on Zinc-Coated Steel, ECS Trans. 50 (2013) 27–33. https://doi.org/10.1149/05047.0027ecst.

[58] ASTM-B117-16 - Standard Practice for Operating Salt Spray (Fog) Apparatus, ASTM Int. (2017) 1–12. https://doi.org/10.1520/B0117-16.2.

[59] R.M. Katona, S. Tokuda, J. Perry, R.G. Kelly, Design, Construction, and Validation for in-situ Water Layer Thickness Determination during Accelerated Corrosion Testing, Corros. Sci. 175 (2020) 108849. https://doi.org/10.1016/j.corsci.2020.108849.

Figures

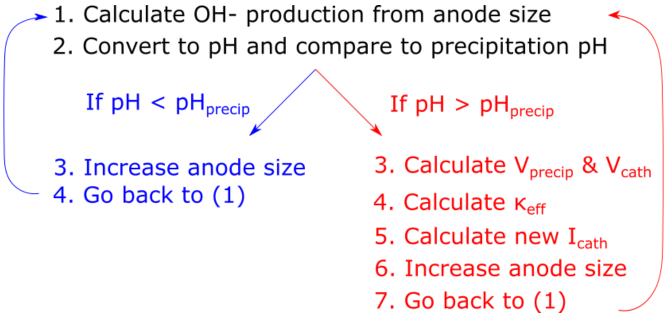

Figure 1: Flow chart for calculation of maximum pit sizes when accounting for cathode precipitation.

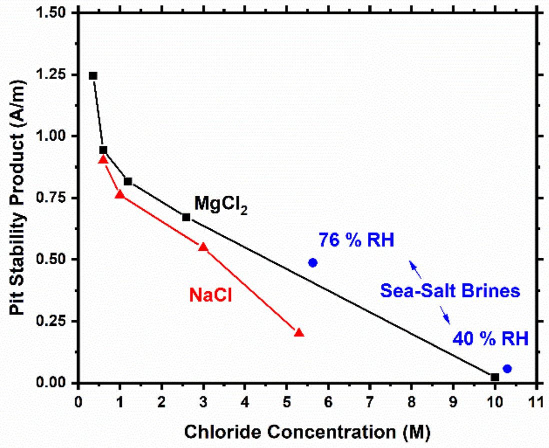

Figure 2: Pit stability product determined through lead-in-pencil experiments as a function of chloride concentration for $MgCl_2$, NaCl, and sea-salt electrolytes at 25°C. Values for NaCl were obtained from Katona et al. [22]. It is noted that the straight line between points is not a fit and is there to guide the eye of the reader.

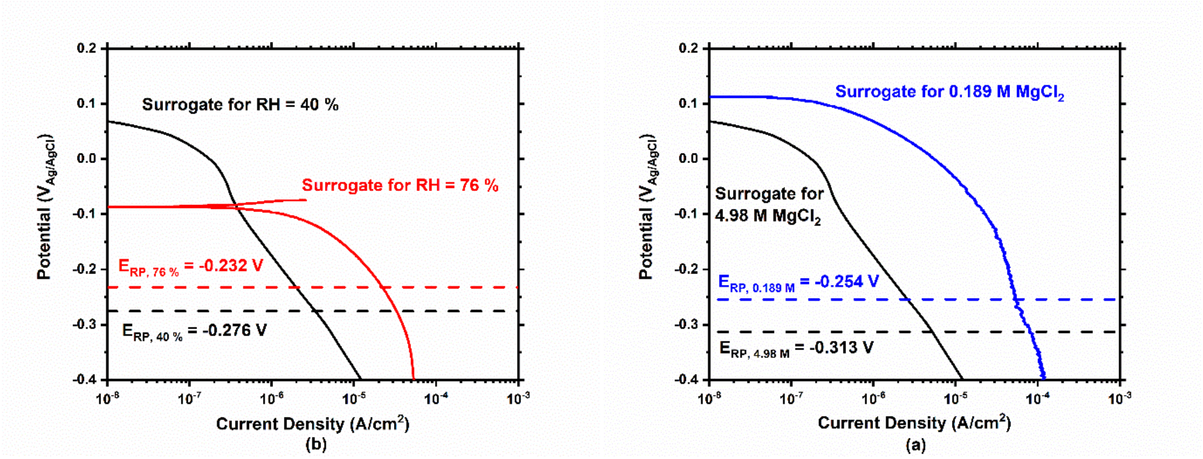

Figure 3: Cathodic polarizations in $MgSO_4$ surrogate solutions for (a) 4.98 and 0.189 M $MgCl_2$. (b) Cathodic polarizations for 76 and 40 % RH sea-salt brine.

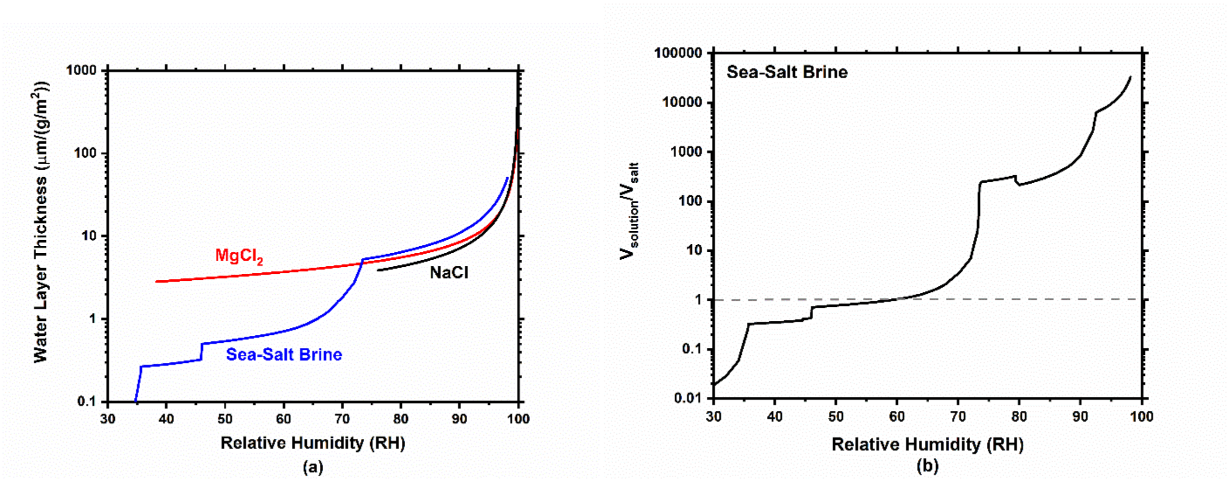

Figure 4: (a) Comparison of water layer thickness in NaCl, $MgCl_2$ and sea-salt brines normalized to loading density. $MgCl_2$ and NaCl are from OLI Studio and sea-salt is from [1]. It is noted that 1 g/m^2 = 100 µg/cm^2 (b) Ratio of solution volume to precipitated salt volume in sea-salt brines obtained from [1].

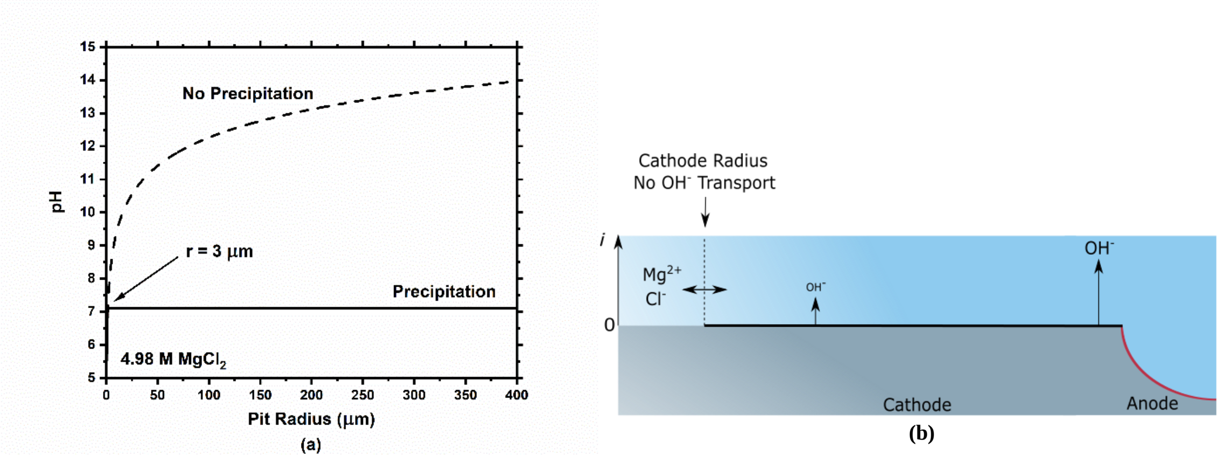

(a)

(b)

Figure 5: (a) Effect of anode radius on the calculated pH for 4.98 M $MgCl_2$. It is noted that once precipitation occurs, a constant pH is reached. (b) pH calculations without precipitation assume OH^- is solely contained in the cathode and $MgCl_2$ concentrations remains constant throughout the cathode.

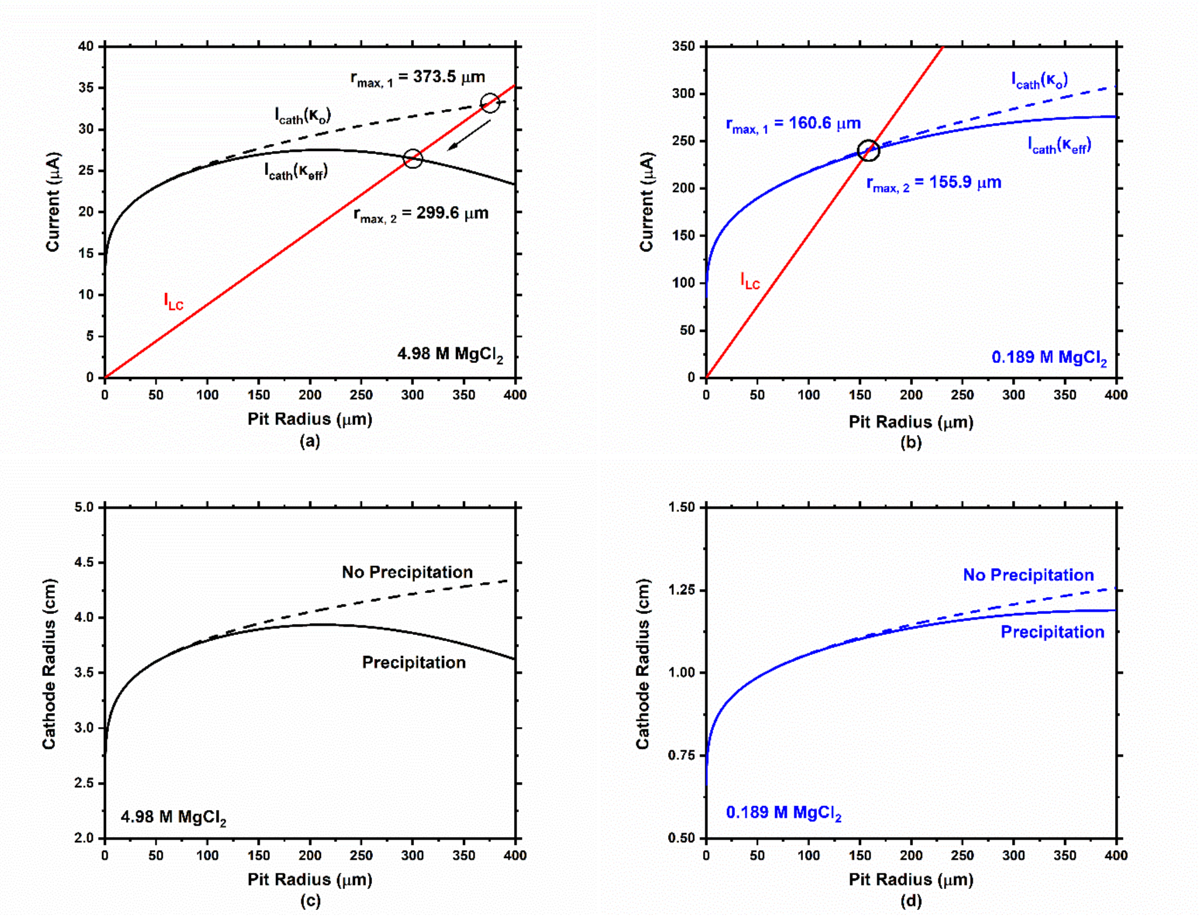

(c)

(d)

Figure 6: Maximum pit predictions shown both with and without the consideration of precipitation in the cathode for (a) 4.98 and (b) 0.189 M $MgCl_2$. LD = 3 g/m^2 and I_{LC} is for 50%

of salt film saturation on the surface of the pit. Cathode radius for (c) 4.98 and (d) 0.189 M $MgCl_2$ with and without precipitation. Note the difference in the ordinate scales between the two solution concentrations in all graphs.

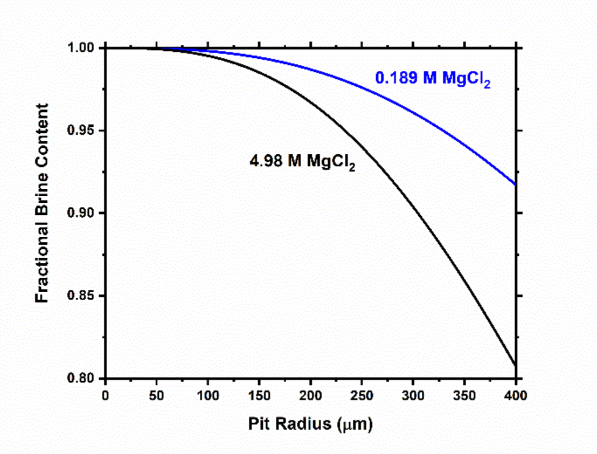

Figure 7: Effect of solution concentration on the fractional brine content (V_{cath}/V_{tot}), given in Equation 6, as a function of anode radius.

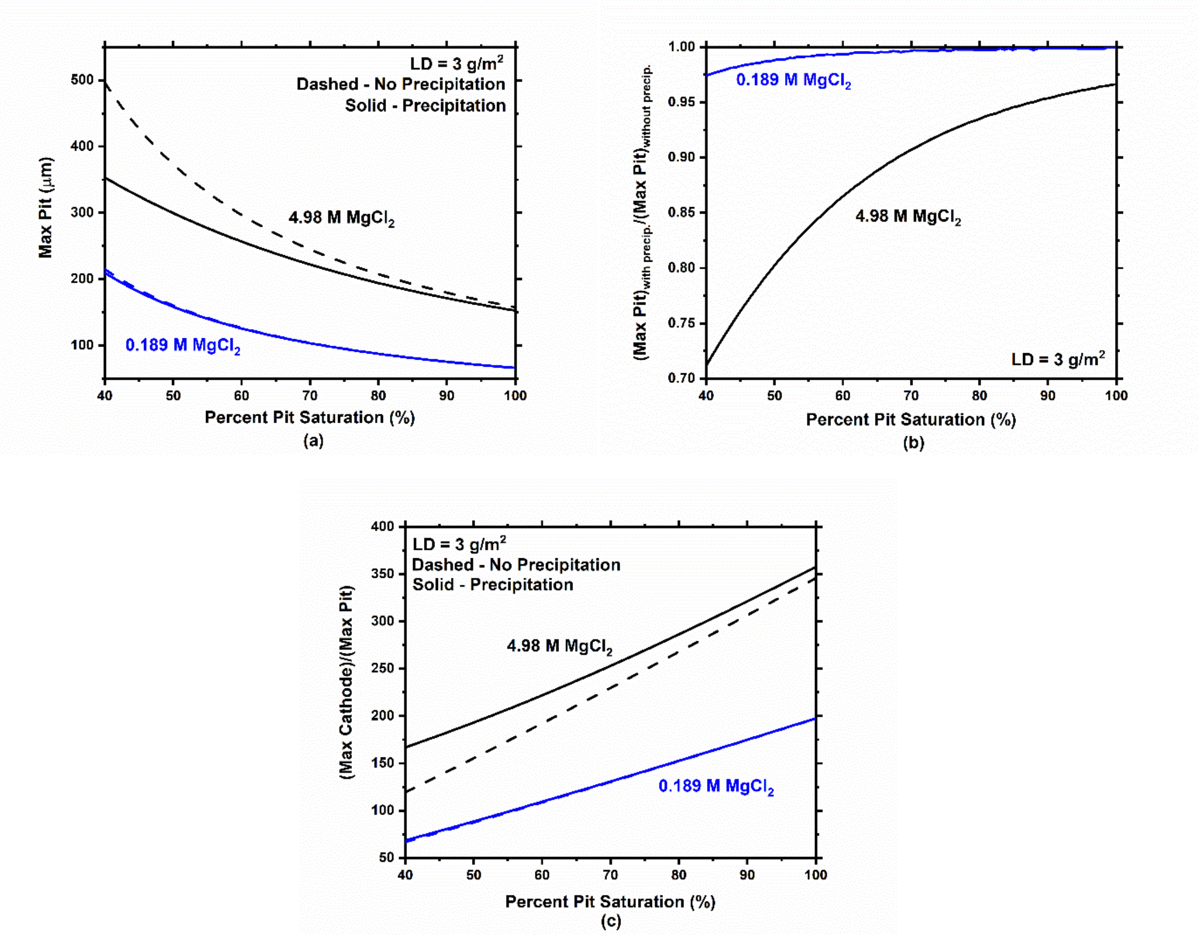

(a)

(b)

(c)

Figure 8: (a) Influence of percent pit saturation on the maximum pit size prediction for 4.98 and 0.189 M $MgCl_2$. (b) Ratio of maximum pit with and without precipitation for 0.189 and 4.98 M $MgCl_2$. (c) Ratio of cathode radius to maximum pit radius for 4.98 and 0.189 M $MgCl_2$.

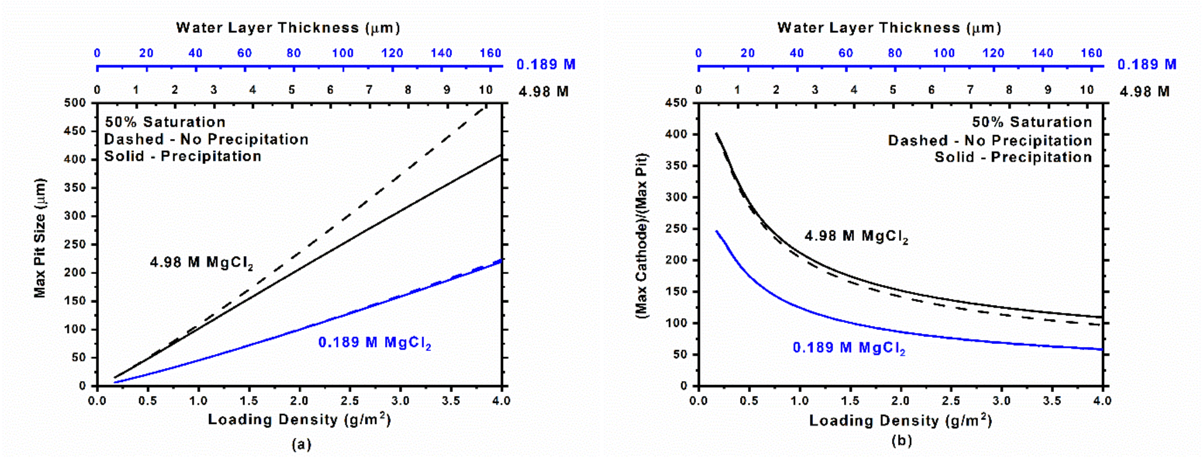

Figure 9: (a) Influence of loading density (water layer thickness) on the calculated maximum pit size with and without precipitation for 4.98 and 0.189 M MgCl₂. (b) Cathode to anode radius ratio as a function of loading density for 4.98 and 0.189 M MgCl₂.

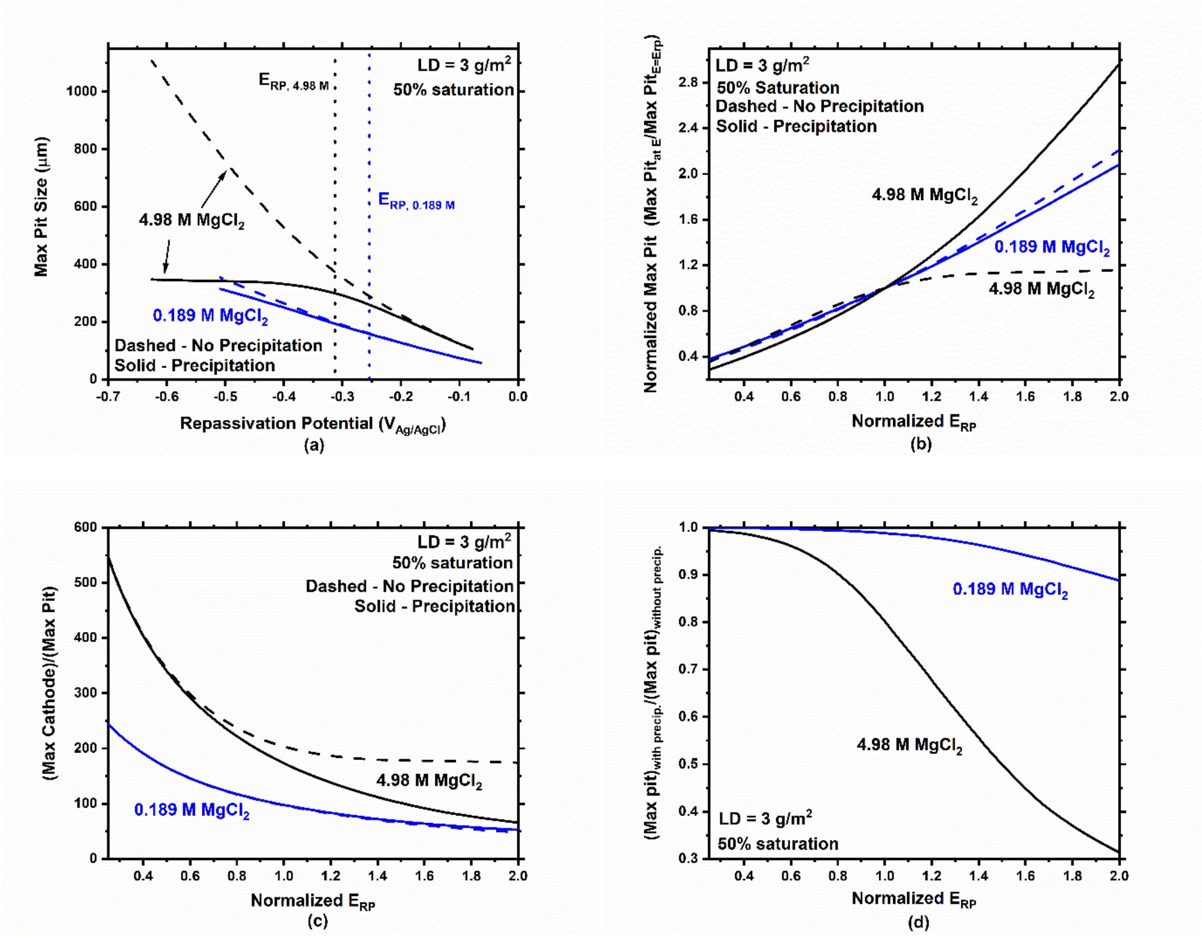

Figure 10: (a) Influence of the repassivation potential on the predicted maximum pit size for 4.98 and 0.189 M $MgCl_2$*. (b) Normalized maximum pit sizes as a function of the normalized repassivation potential. (c) Cathode to anode ratio as a function of the normalized repassivation potential. (d) Ratio of maximum pit with and without precipitation as a function of repassivation potential. All calculations were made under a loading density of 3* g/m^2 *and a percent saturation of 50 %.*

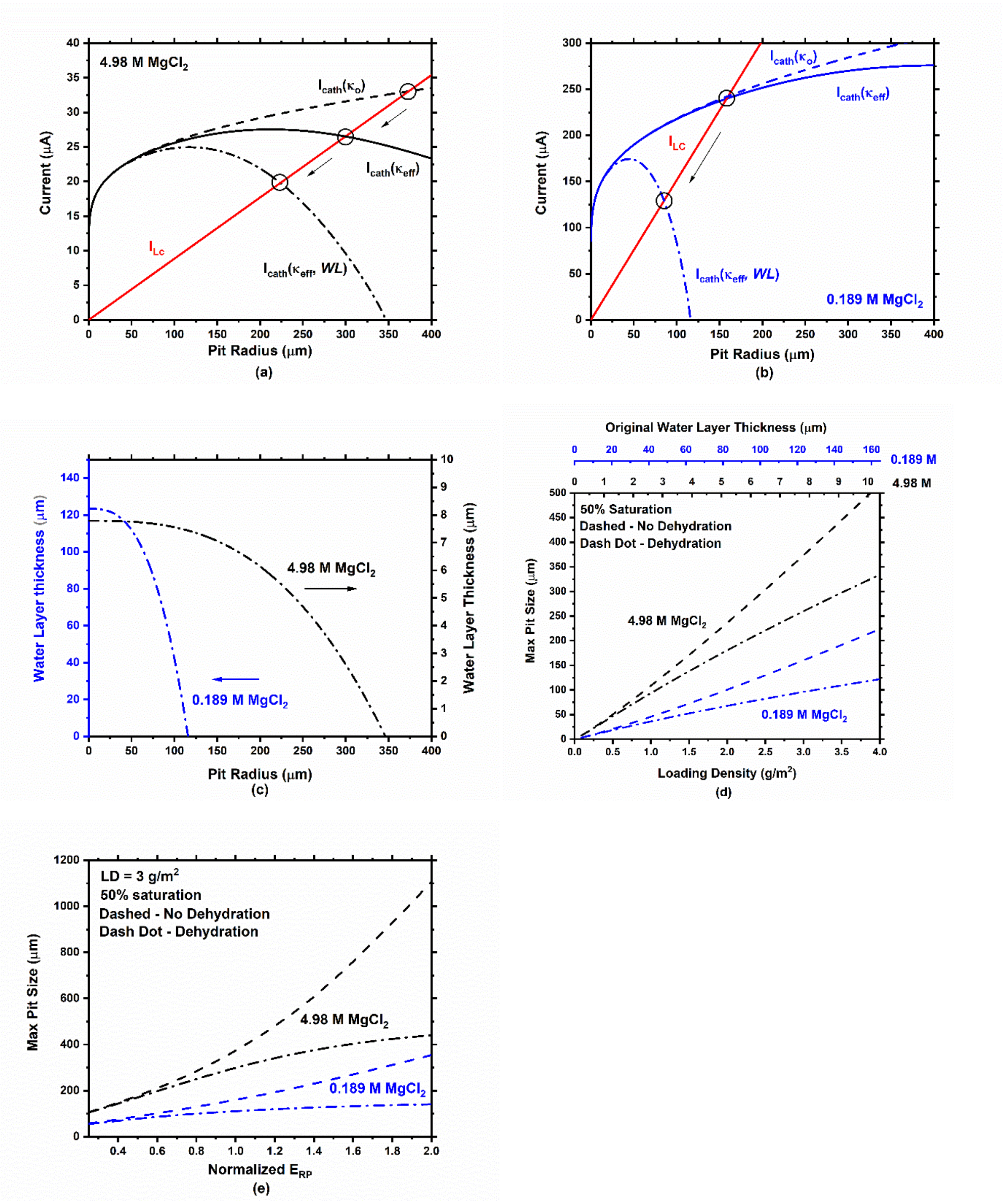

Figure 11: Effect of dehydration reactions on maximum pit sizes predictions for (a) 4.98 and (b) 0.189 M $MgCl_2$. A pit saturation level of 50% was used with LD = 3 g/m^2 for (a) and (b). (c) Effect of dehydration on water layer thickness. (d) Effect of variations in loading density (initial water layer thickness) on maximum pit sizes considering dehydration. (e) Effect of E_{RP} variations on maximum pit sizes considering dehydration.

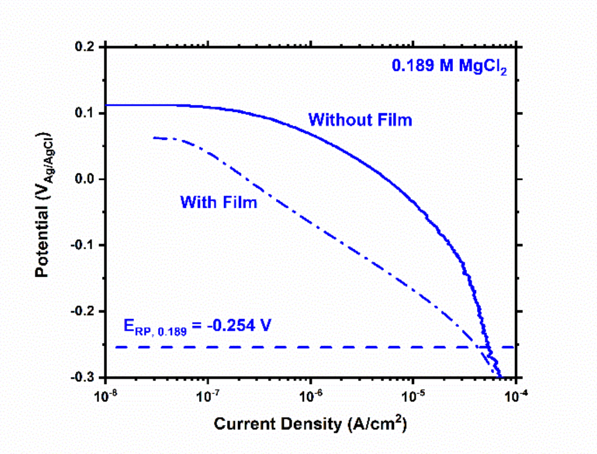

Figure 12: Effect of $Mg(OH)_2$ film on the cathodic polarization of SS304L in 0.189 M $MgCl_2$. The film was formed after polarization in 0.189 M $MgCl_2$ from OCP to -1.2 V and allowed to dry for roughly 24 hours before performing the subsequent polarization scan.

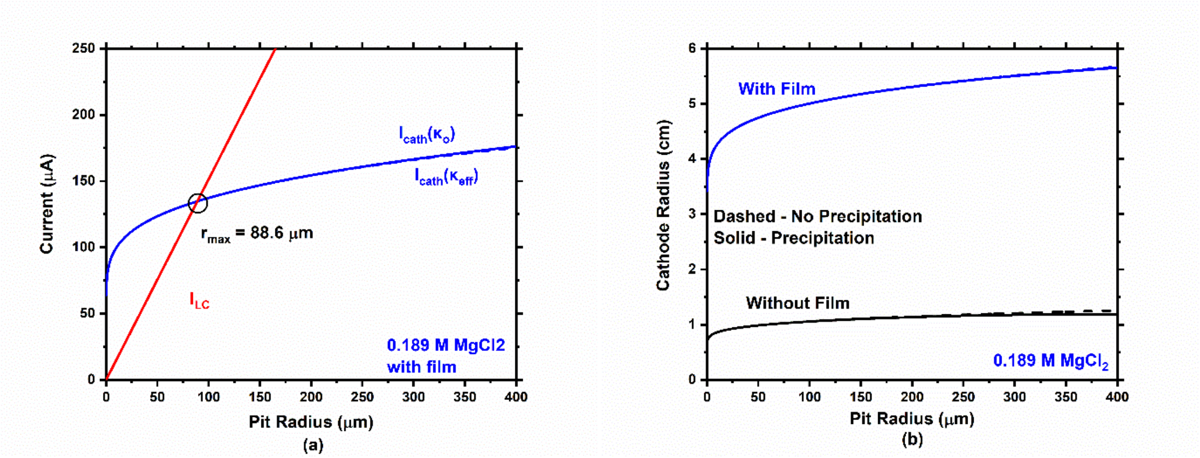

Figure 13: (a) Influence of $Mg(OH)_2$ film on the surface of SS304L on maximum pit size predictions for 0.189 M $MgCl_2$. (b) Influence of film on the cathodic radius calculations. It is noted that dehydration reactions are not shown as there is no significant change in predicted maximum pit size over the range of interest.

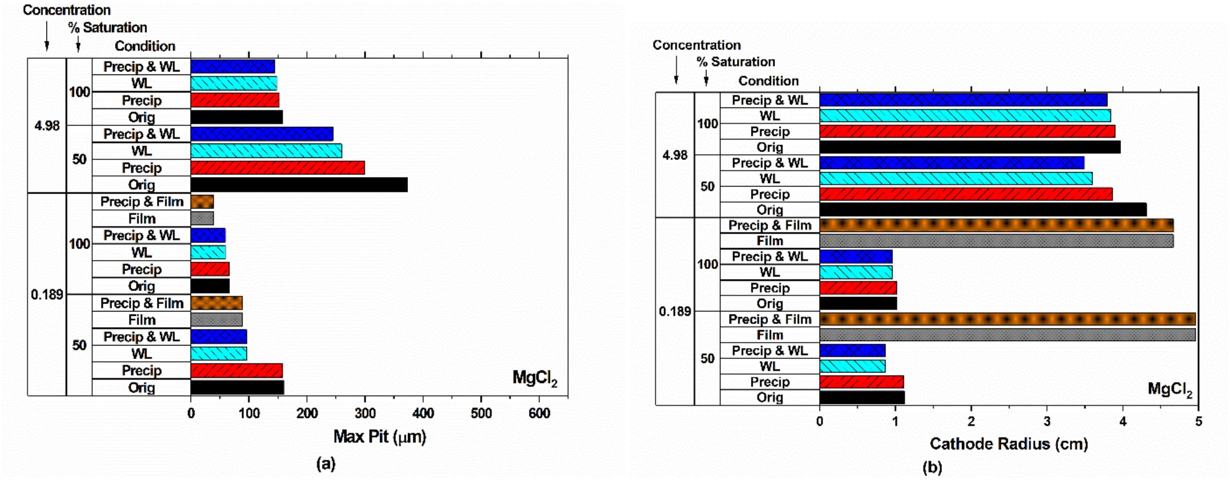

Figure 14: Influence of all cathode evolution scenarios explored for $MgCl_2$ electrolytes on (a) pit size and (b) current. LD = $3g/m^2$ in all scenarios. The labels correspond to the following scenarios: Orig – Original maximum pit formulation; Precip – Considering precipitation reactions and the influence on conductivity; WL – considering only dehydration reactions; Precip & WL – considering Precip. and WL together; Film – Original formulism with new cathodic polarization; Precip & Film – New cathodic polarization scan and precipitation reactions.

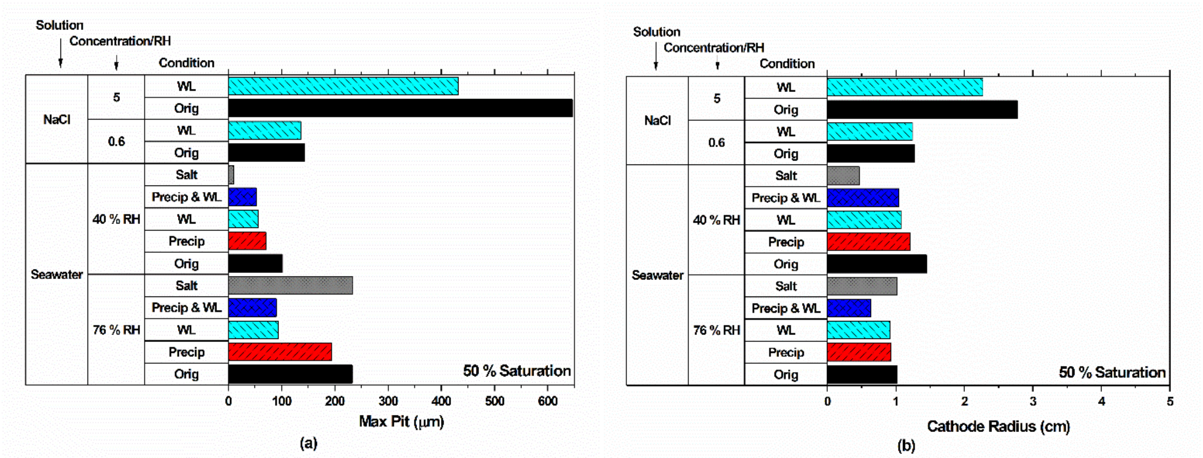

Figure 15: Influence of all scenarios explored for sea-salt and NaCl brines on (a) pit size and (b) current. LD = $3g/m^2$ and 50 % saturation is used in all scenarios. The labels correspond to the following scenarios: Orig – Original maximum pit formulation; Precip – considers precipitation reactions and the influence on conductivity; WL – considers only dehydration reactions; Precip & WL – considers precip and WL together; Salt – considerations from the fractional water content due to precipitated salt in solution.

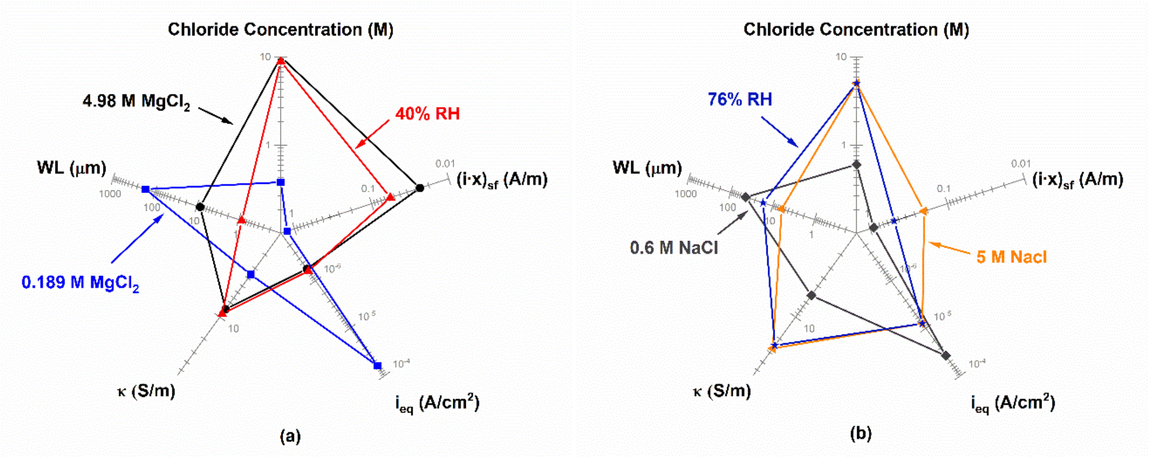

Figure 16: Radar plots comparing properties for (a) $MgCl_2$ solutions and sea-salt at 40 % RH and (b) NaCl solutions and sea-salt at 76 % RH. Examined in the plots are chloride concentration, water layer thickness, pit stability product under a salt film, equivalent current density, and conductivity of the solution.

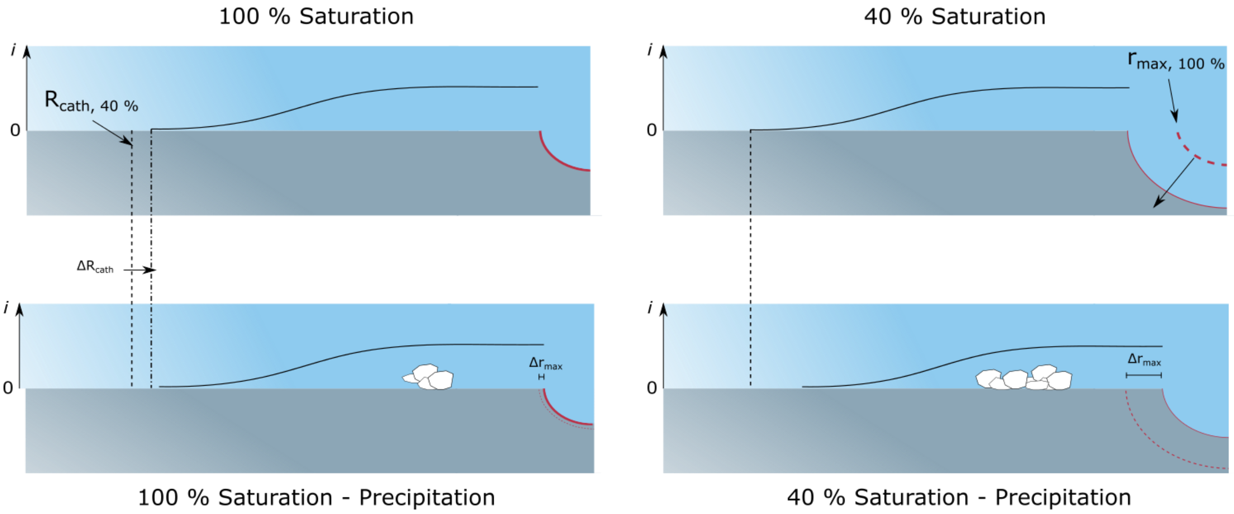

Figure 17: Governing factors for maximum pit size predictions when considering percent pit saturation and precipitation.

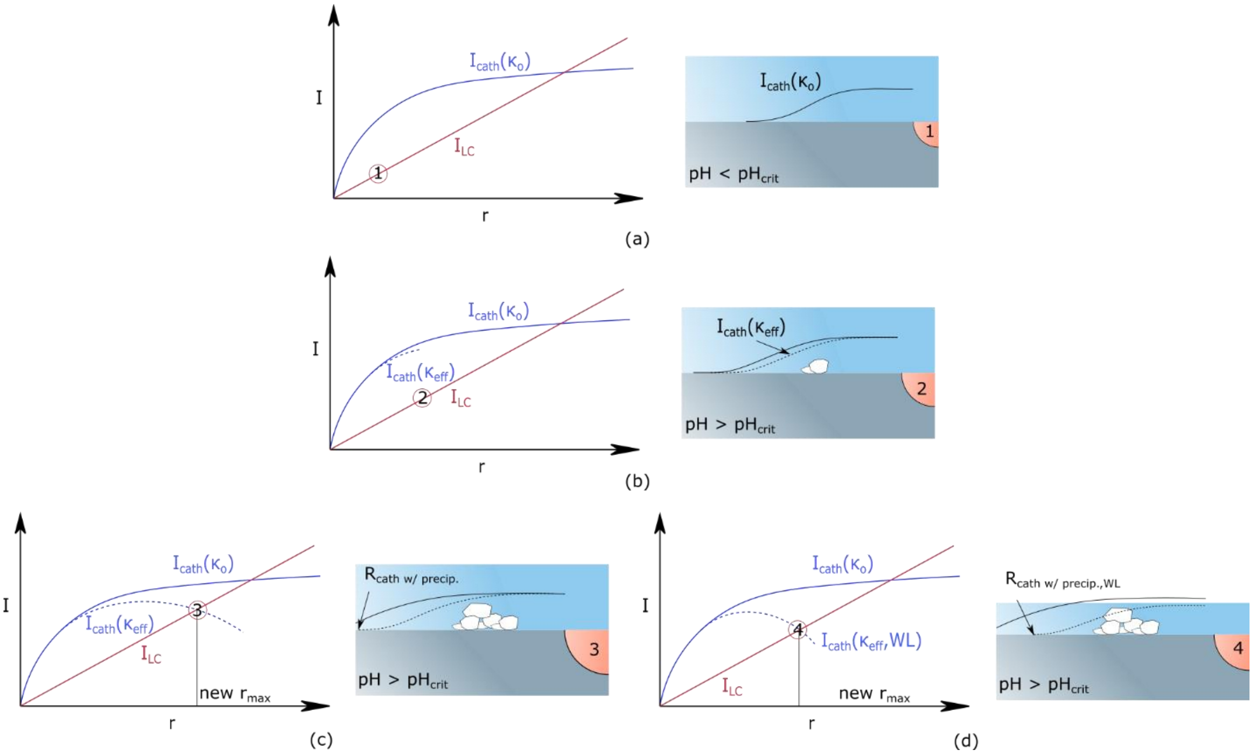

Figure 18: Qualitative representation of governing reactions for atmospheric corrosion and relative severity for solutions containing precipitates. (a) A small pit that has not reached the bounding cathodic current nor the critical pH for precipitation. (b) A medium sized pit that has not reached the bounding cathodic current however has reached a pH in which precipitation is thermodynamically possible. (c) Maximum pit size when only precipitation is considered in the cathode. (d) Maximum pit size when precipitation and dehydration are considered in the cathode.

Tables

Table 1: Precipitate Parameters

Solution	Precipitate	ρ_{precip} (g/cm^3)	MW_{precip} (g/mol)	n_{precip}
0.189 M $MgCl_2$ 76 % RH sea-salt	$Mg(OH)_2$	2.34	58.3	2
4.98 M $MgCl_2$ 40 % RH sea-salt	$Mg_2(OH)_3Cl \cdot 4H_2O$	1.79	182.6	3

G. Design, Construction, and Validation for in-situ Water Layer Thickness Determination during Accelerated Corrosion Testing

Design, Construction, and Validation for in-situ Water Layer Thickness Determination during Accelerated Corrosion Testing

R. M. Katona,[1,2] S.Tokuda,[3] J. Perry,[1] R. G. Kelly[1,*]

[1] Materials Science and Engineering, University of Virginia, Charlottesville, VA 22904 USA
[2] Sandia National Laboratories, Albuquerque, NM 87123 USA
[3] Department of Materials Science, Tohoku University, Aoba-ku, Sendai 980-8579, Japan
[*]corresponding author; rgk6y@virginia.edu

Abstract

A sensor to determine water layer (WL) thickness, ranging from 0-5 mm, in salt-spray testing is presented. WL thickness is based on electrical resistivity and sensor design was guided by finite element modeling with validation under known WL thicknesses. WLs were measured in continuous salt spray testing and angle of exposure played the largest role in thicknesses. At angles greater than 20˚ from vertical, semi-periodic run-off decreased WLs up to 80%. Finally, exposure angle determines if thin-film conditions are achieved, likely influencing corrosion rate and morphology. Allowances for sample angle in testing standards pose a potentially large source of variability.

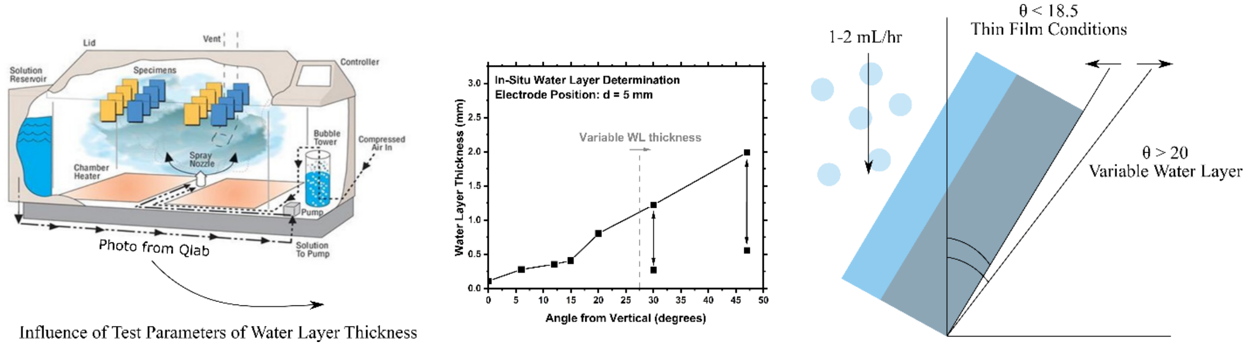

Key Words

atmospheric corrosion; electrochemical impedance spectroscopy (EIS); finite element modeling (FEM); salt spray testing; ASTM B117; water layer

Introduction

Salt spray is a common exposure condition for many metallic structures and is known to be particularly aggressive. In order to mimic service conditions, laboratory accelerated tests, using some form of salt spray, are very common. There are various forms of accelerated tests including continuous salt spray tests [1-3], cyclic testing [4], and constant relative humidity testing [5]. One of the most well-known and widely used laboratory accelerated tests is ASTM B117, characterized by a constant salt spray of 5 wt % sodium chloride (NaCl) at a temperature of 35˚C [1]. Another common test is ASTM G85, in which samples experience cyclic conditions consisting of a continuous salt fog, a dry period when a fan runs, and a dwell period. This cycle repeats for the duration of the test. The solution within ASTM G85 can also vary depending on what annex of the test is being used [4]. Other stipulations within all accelerated tests include the deposition rate of the salt (typically 1-2 mL/hr), the angle of sample exposure, and continuity of exposure to name a few. Although the tests are useful, they often do not directly simulate real world conditions and have shown large test-to-test and chamber-to-chamber variability [6-8]. One possible source of both the variability and the poor correlation with service performance is the lack of control and knowledge of the water layer (WL) thickness experienced in these tests.

An often-controlling characteristic of salt spray conditions, whether in testing or service, is the WL formed on the surface. The role of the WL thickness as a factor controlling for the rate of cathodic reactions has been studied and relates to the diffusion distance of oxygen in solution [9-13]. The corrosion dependence due to changes in WL thicknesses was initially described qualitatively by Tomashov [13]. For bulk, full immersion conditions, a constant corrosion rate is seen, and this rate persists for thick water layers. Decreasing the film thickness causes a transition to an increased corrosion rate which is governed by electrolyte thickness as described by the diffusion of oxygen across the WL. Reduced dissolution is seen by further decreasing the WL thickness given by anodic control before the final regime is reached and is characterized by a very low corrosion rate of dry chemical oxidation due to the lack of a continuous film [13]. Numerous studies have quantitatively explored this phenomenon in terms of finding the critical value of WL thickness where bulk, constant corrosion rate conditions are seen, however, that value has ranged in literature from 230 to 1000 µm (0.23 to 1 mm) [9-24]. More recently, Liu et al. determined the natural convection boundary layer to be 0.8 mm for a 0.6 M NaCl solution [9]. Another important factor in corrosion testing is the time of wetness a sample experiences during exposure [25,26]. Created sensors have been applied to accelerated tests [6], however do not give information regarding the WL present. As the WL thickness has been shown to have a such an impact on the corrosion rate, it is important to understand WL thicknesses in accelerated testing in to order to develop more accurate and consistent accelerated testing conditions.

The goal of this study was to create a sensor with which the WL thickness could be determined under salt spray testing conditions. There are methods currently in literature to determine WL thickness, ranging from capacitive methods [27-29] to laser/optical [30,31] and ultrasonic [32] based methods, that fall short of the present goal. Although these sensors have been proven to be successful in each application, there are various aspects of the sensors which limit the applicability to salt spray environments. Capacitance-based sensors are generally large (on the order of 2,500 mm^2 [28]), and concerns over forming a uniform water layer are present due to the general hydrophobicity of the materials of construction. Furthermore, capacitive sensors have a sensitivity range of ~10 pF/mm, where mm is WL thickness [28], and in a salt spray chamber, significant electrical noise from the machinery could cause for inaccuracies of WL measurement. Other capacitive sensors have also been coupled with an insulating cover, with the purpose of enhancing the resolution of the measurement [27,29]. As measuring WL thickness in a salt spray environment is of interest, there should be no hindrance of the salt spray to the surface. Finally, laser, optical and ultrasonic systems [30–32] are costly and implementation into a salt spray environment raises concerns about longevity. Thus, a small, cost-effective, impedance-based sensor will be created alleviating these concerns.

It has previously been proposed that the WL thickness on corroding samples in ASTM B117 is on the order of 3-4 mm [12,33,34] largely influenced by the formation of corrosion products, thus, creating a sensor which is sensitive in the range of 0-5 mm is the goal of this study. Using Finite Element Modeling (FEM), a solution resistance sensor was designed which was sensitive in this range, inert in order to avoid complications due to the formation of corrosion products, and able to form a continuous WL. Construction and testing of the sensor were completed and the sensor was applied to study the WL that forms during continuous salt spray testing. The effects of sample angle, deposition rate, and solution conductivity were assessed.

Modeling and Experimental Approach

Methodology

The resistance of a parallelepiped (R_s), shown schematically in Figure 1(a) is dependent upon the length (L), width (w), and WL thickness, as well as the ionic conductivity of the solution (κ) and can be expressed as:

$$R_s = \frac{L}{WL * w} * \frac{1}{\kappa} \qquad 1$$

Equation 1 is valid when the resistance is measured from the respective ends of a WL layer in a parallelepiped geometry, as shown by the red ends in Figure 1(a). Such a geometry is not ideal for a WL sensor in a salt spray system due to both the difficulty in defining the WL sensed as between the two surfaces on the ends as well as the effects of the menisci that would form on those surfaces on the measurements.

A more practical design approach is shown in Figure 1(b) and (c). The sensing electrodes are embedded into an insulating, wettable planar surface. Neither solution flow nor capillary effects would influence the measurement. However, the expression for the solution resistance is not as well defined as Equation 1. The equivalent expression for the resistance of the WL for the geometry of Figure 1(c) is given by:

$$R_s = \frac{\Delta V}{\int I} \qquad 2$$

where ΔV is the potential difference between two points in the electrolyte and $\int I$ is the total current passing between those two points. This expression is also dependent on the parameters in Equation 1, however, it cannot be solved analytically. Equation 2 can be numerically evaluated (in this case using FEM) for a potential difference applied across two points. This approach of measurement of the resistance between two embedded points on a surface covered by a WL will serve as the basis for calculating the resistance of various WL thicknesses as a function of sensor and experimental parameters. Optimization of the sensor parameters will create a sensor design suited for measurements under salt spray conditions.

Finite Element Modeling Analysis

The modeling framework is based on the Laplace Equation [35] utilizing COMSOL Multiphysics v5.5 (COMSOL, Inc., Burlington, MA) FEM software. A three-dimensional model of the WL on top of the sensor was created in COMSOL according to the representative diagram seen in Figure 1(c). The material in which the wires were mounted was assumed to be electrically insulating. A uniform solution layer was created on top of the sensor and was assumed to be rectangular in shape. Various conductivities, widths, and heights were assigned to the WL. A steady state, secondary current distribution model was used to calculate the total interfacial current when a potential difference was applied between two electrodes. The measured resistance of the WL was then calculated based on Equation 2. The effects of the width and length of the sensor as well as the radius and spacing of the sensing wires on the measured resistance and sensitivity to WL were explored. Resistances were calculated as a function of WL thickness for the various properties explored.

Sensor Materials and Preparation

Based upon the modeling results, a sensor was constructed using nickel (99.98%) wire, obtained from Goodfellow Metals, with a radius of 0.5 mm and then mounted in plexiglass (polymethyl methacrylate). The plexiglass had the following dimensions: w = 10 mm, L = 50 mm, and a variable d according to Figure 1(c). Prior to testing, the sensor was ground to 1200 grit silicon carbide paper and placed in a Henniker HPT100 Plasma Cleaner to remove hydrocarbon contaminants on the surface of the plexiglass. The plasma cleaner was applied for 1 hour, under 100 Watts in an oxygen-only environment. After cleaning, the sensor was immediately submerged in deionized water to limit the recontamination of hydrocarbons. Plasma cleaning allowed for a uniform WL to form [36], creating an experimental system geometry that is directly comparable to the modeled geometry. In the absence of plasma cleaning, the surface was hydrophobic and water droplets formed beads on the surface of the plexiglass. The effect of plasma cleaning is displayed in Figure 1(b) and (c).

High-frequency electrochemical impedance spectroscopy (EIS) was used to determine WL thicknesses. The frequency was scanned from 7 MHz to 1 kHz with six measurement points per decade of frequency. At high frequencies, the main contribution to the impedance measurements is the solution resistance as the interfacial resistance will be bypassed due to the interfacial capacitor's impedance being inversely proportional to the frequency. This condition is depicted in Figure 1(c). Sine waves with an amplitude of 10 mV were applied about opcorrosen circuit potential and each point was an average of 10 measures. The scan in frequency was repeated for the duration of the test (at least 24 h) with each scan taking roughly 2 min. For analysis, a frequency of $3 \cdot 10^5$ Hz was chosen to calculated WL thickness because the phase angle was relatively constant throughout at this frequency. This selection will be further elaborated in the Discussion section.

Sensor Calibration

Confirmation of WL resistances predicted by FEM was carried out by the use of two methods to create a known WL thickness: (i) the use of tape with known thicknesses and a hydrophobic membrane and (ii) placing known volumes of liquid on top of the sensor with a walled structure to contain the WL. To investigate the resistances of very thin WLs, a ceramic film, composed of anodic aluminum oxide (AAO), was treated with trimethoxy(octyl)silane to increase the hydrophobic behavior without affecting other properties of the membrane [37]. AAO is considered to be an electrical insulator and any current flow would be through the solution [38,39]. Tape of known thicknesses (ranging from 54 um to 137 um), obtained from McMaster-Carr, were placed around the edge of the sample and the AAO membrane was placed on top. This created a continuous thin WL on the surface, and EIS measurements were then taken as depicted in Figure 2(b). Investigating thicker WL's involved the creation of a walled structure around the sensor. A known volume of liquid was then placed on top of the sensor which created a thin film on the surface and is shown schematically in Figure 2(a). Through the known density of the liquid as well as the area of exposure, the WL thickness can be calculated. EIS measurements were taken and the resistance was evaluated. The resistance measured with EIS was compared to the modeled resistances with COMSOL to create a calibration curve.

In-situ Determination of Water Layer

In-situ measurements were made in a commercial salt spray chamber (Q-FOG cyclic corrosion chamber from Q-lab). A continuous salt spray was used in which the collection rate was determined by funnels placed at sample height with a horizontal collection area of 80 cm^2 in line with ASTM standards [1,4]. Solution deposition rates were between 1 - 2 mL/hr in accordance with ASTM G85 [4] and ASTM B117 [1]. The collection rates were determined by an average of four funnels which were placed around the sensor location and had a temporal sensitivity of ± 0.1 mL/hr. The chamber contained heating plates which were kept constant at 25˚C. The angle of the sensor was ranged from 0˚ to 47˚ from the vertical, however specific angles were targeted in the range of 6˚ to 40˚ from vertical in order to cover the range allowed by ASTM G85 (6˚ to 45˚) and ASTM B117 (15˚ to 30˚). This angle is depicted schematically in Figure 3. These collection rates, as well as angles, cover the range of many other accelerated corrosion standards [2,3,5]. NaCl solutions were made using both 0.03 M and 0.6 M having measured conductivities of $\kappa = 0.4$ S/m and $\kappa = 8$ S/m, respectively. Equilibrium WL thicknesses, measured at a frequency of $3 \cdot 10^5$ Hz, were achieved after roughly 12 hours as indicated by the measured resistance reaching steady state; therefore, all tests were conducted for at least 24 hours. The measured resistances were converted to WL thickness based on the calibration curves constructed from FEM results.

Results

Finite Element Modeling

Various geometric parameters were explored with COMSOL to assist in the design of the sensor. The key geometric parameters of interest were the length (L) and width (w) of the sensor as well as the radius (r) and spacing (d) of the wires. These aspects are displayed schematically in Figure 1(b). Modeled resistances as a function of WL thickness are seen in Figure 4 and Figure 5. First, the length of the sensor (between 50 mm and 100 mm) was shown to have little to no impact on the measured resistance at various WL thicknesses as shown in Figure 4(a) whereas the width of the sample, shown in Figure 4(b), has a large impact on the measured resistance. With increased sample width, the calculated resistance decreased in both electrode spacings (d = 5 and 40 mm). The next aspect of the sensor which was explored was the radius of the wire used in EIS measurements. With increased radius of the wire, the measured resistance was decreased as seen in Figure 5(a).

Based on COMSOL modeling and the desire to have a sensor be sensitive in a WL thickness range from 0-5 mm [12,33,34], a sensor was created which was 10 mm wide with a length of 50 mm. The wires had a radius of 0.5 mm and were made of nickel (conductivity of $1.4 \cdot 10^7$ S/m) to reduce the resistance when a current is passed through the wires. The wires were mounted in the configuration seen in Figure 1(b) with distances between the individual wires displayed in Figure 1(c). The calculated resistances based on this configuration are seen in Figure 5(b) across various solution conductivities ranging from dilute to saturated NaCl.

Sensor Calibration

Confirmation of the calculated resistances is seen in Figure 6 and Figure 7, and good agreement is seen in all scenarios explored. When measuring with a known volume of a dilute NaCl electrolyte ($\kappa = 0.4$ S/m), the resistances matched well with predictions with an average percent error of 6.5% (Figure 6(a)). In a more concentrated NaCl solution ($\kappa = 8$ S/m), the resistances matched well again with a lower percent error of 5.1%. The 6.5% error equates to an average difference in calculated WL thickness of 0.04 mm and will be taken as the error of the sensor. It is noted that all measured resistances in Figure 6 are slightly below the expected predictions from COMSOL. During the experimentation it was noticed that a small convex meniscus was seen on the top of known volume as shown in Figure 6(c). This would increase the WL slightly in the center of the width and, based on Equation 1, the resistance would decrease.

Further validation of the sensor was completed using a saturated NaCl ($\kappa = 23$ S/m) electrolyte, as seen in Figure 7, under both an AAO membrane and known volumes. Again, the measured resistances of the saturated solution matched well with the modeled predictions. The resistances measured under the AAO membrane, Figure 7(b), showed a smaller average error of 0.8%. All the data presented below from the *in-situ* tests were gathered with an electrode spacing of d = 5 mm as tests with a larger spacing of d = 40 mm were not as sensitive in the range of interest.

In-situ Water Layer Determination

Representative Bode magnitude and phase angle plots from *in-situ* measurement of WL thickness during salt spray are seen in Figure 8(a) and (b) respectively. The test used 0.6 M NaCl ($\kappa = 8$ S/m), a sample surface angle of exposure of 20˚ from vertical, and a solution deposition rate of 1.7 mL/hr. Resistances at a single frequency were then chosen from Bode plot, ensuring that the resistances were representative of solution resistances across all time periods as indicated by the phase angle in Figure 8(b). The resistances are plotted as function of time in Figure 8(c) and were converted to WL thicknesses based on the resistances in Figure 5(b). The thickness of the WL was further converted to salt loading density (LD) based on WL thickness, molarity (M), and molecular weight (MW) of the solution ($LD = \frac{(WL*w*L)*M*MW}{w*L} = WL * M * MW$). Resistances and WL thicknesses are also shown for the same solution and deposition rate however at an angle of 30˚ from vertical in Figure 8(d). At both angles, it is noted that the maximum WL thickness was achieved after roughly 12 hours (43,200 seconds), although all tests were run for at least 24 hours (86,400 seconds) in order to observe the behavior of the WL over a large range of time.

One major observation from Figure 8(c) and (d) is that at larger angles (i.e., closer to horizontal), the WL can have run-off events in which a portion of the WL slides off the plexiglass. This shedding was seen at angles >20˚, independent of κ or solution deposition rate. It is also noted that not all of the water would slide off of the surface of the plexiglass. The amount of water that was left on the surface was variable as denoted by the WL thicknesses after the slip event. These run-off events were quasi-periodic in nature.

In order to test the effect of halting a salt spray test, the spray was stopped after roughly 45 hours and measurements were continuously taken. After the spray was stopped, a fan continuously circulated the air in the chamber. The lid was not raised to avoid influence from the external environment. The results can be seen in Figure 9. Within 1 hour of the shut-off, the WL thickness decreased 0.15 mm (18.5% of the steady state value of 0.81 mm). Within 112 min of the shut-off, there was no detectable WL on the surface of the sensor, i.e., a continuous WL was no longer present at this time as given by resistance measurements.

In-situ tests were performed at various angles ranging from 0˚ to 47˚ all using a constant spacing of d = 5 mm, covering the range of angles allowed in various accelerated corrosion test standards. These tests showed an increasing WL thickness with increasing angle of exposure as seen in Figure 10. When exploring the rate of salt spray deposition, there was not a significant difference between 1.2 mL/hr (Figure 10(b)) and 1.7 mL/hr (Figure 10(a)) when 0.6 M NaCl ($\kappa = 8$ S/m) was used. There was a larger difference between the two at an angle of 30˚, however the discrepancy could have been due to run-off events occurring in the WL which are denoted by double arrow in Figure 10. Finally, when 0.03 M NaCl ($\kappa = 0.4$ S/m, Figure 10(b)) was used, there was a slight increase in the WL thickness. Replicates were conducted of various tests and the test-to-test variability was ~0.2 mm.

Discussion

Design and Characteristics of WL sensor

The primary function of the created sensor is to measure the resistance of a WL on an inclined surface and, using the resistance as measured with EIS, calculate WL thickness based on a calibration curve. The overall EIS behavior and sensitivities of the sensor will be discussed. When performing EIS, the total impedance of the system is measured through applying a sinusoidal potential at a given frequency and measuring the current response. The current response, in terms of magnitude and phase shift from the excitation signal, describes the overall impedance of the system. If one were to measure the impedance across a single resistor as a function of excitation frequency, a constant impedance would be measured at all frequencies (as one would expect from Ohm's law). The current response is in phase with the potential excitation. For impedance measurements of a single capacitor, the impedance decreases with increasing frequency and the current response is 90˚ out of phase with the potential excitation. Thus, at high frequencies, the current flows easily though a capacitor. When a capacitor and a resistor are in parallel with one another, the current will always flow through the path of least resistance. Therefore, at sufficiently high frequencies, the current will pass through the capacitor as the impedance is lower than the resistor.

A simplified equivalent circuit for the WL sensor is presented in Figure 1(c) and is characterized by two resistor/capacitor parallel combinations in series with a single resistor. The resistor in parallel with the capacitor represents the interfacial charge transfer resistance (R_{ct}) and the capacitor represents the double layer capacitance (C_{dl}). The single resistor is the solution resistance (R_s) as is defined in Equation 2 and can be used to characterize the WL thickness. In this study, the impedance and resistance were measured at a high frequency in which the current will flow through C_{dl}, R_s, and C_{dl} as depicted in Figure 1(c). Thus, the major contribution to the resistance at high frequencies is R_s. In order to ensure that the resistance being measured is the solution resistance, the phase shift was examined (Figure 8). At a frequency of $3 \cdot 10^5$ Hz the phase shift is closest to zero (~10˚) and is indicative of solely a resistor being measured throughout all exposure testing. The finite value of the phase angle is likely due to the presence of a stray capacitance (most easily observed in Figure 8(a) and (b) for times ≤ 10,000 s) due to the need for long electrical leads from the sensor to outside the salt spray chamber. In order to mitigate this, an electronic system could further be built below the sensor in to decrease the wire length to the potentiostat.

The sensitivity of the created sensor to various WL thicknesses is based on the overall dimensions of the sensor, distance between electrodes, and conductivity of the solution. In order to determine the sensitivity, the change in resistance over the change in WL thickness was evaluated (*i.e.*, the slope of the line in Figure 5(b) with units ohms/mm of WL thickness). First, the overall sensor dimensions will be discussed. As seen in Figure 4(a), the length of the sensor (ranging from 50 - 100 mm) does not change the measured resistance significantly and would not provide a change in sensitivity. However, the sensor wires cannot be close to the edge as a convex meniscus (Figure 6(c)) could influence resistance measurements, thus, a distance of 5 mm from any edge of the sensor was adopted. Next, the radius of the electrode (Figure (a)) does change the measured resistance, but the sensitivity does not change (*i.e.* the slope is similar for all radii). Although the length and radius do not play a large role in sensitivity, the width of the sensor increases sensitivity with a decreased width (Figure 11(a)). Furthermore, a decreased width increases the likelihood of forming a continuous film. However, as previously stated, the electrode should be 5 mm from each edge, so a minimum sensor width of 10 mm was chosen.

The sensor is most sensitive for an electrode spacing of 40 mm under thin WL thicknesses (< 0.5 mm), as displayed in Figure 11(b). Although one would want the highest sensitivity for WL measurements, forming a continuous WL < 0.5 mm across the 40 mm electrode spacing is not always possible and would provide large sources of potential error for WL determination. A thin, continuous WL is more likely over a small electrode spacing (*i.e.* d = 5 mm), and this arrangement still provides a high sensitivity. The desired range of sensitivity is above 100 ohm/mm and is denoted by a gray box in Figure 11. The sensitivity becomes orders of magnitude smaller when considering higher conductivity electrolytes as shown in Figure 11(c). For example, in thick WLs (4.5 mm) and d = 5 mm, the sensitivity of the electrode drops below 1 ohm/mm and would not provide sufficient sensitivity to determine WL thicknesses. Although it might seem ideal to have one electrode separation that would be used for all WL thicknesses and solutions, it would not provide the best sensitivity. Thus, for thin WL, in the range of 0 mm to 1 mm, it was determined that an electrode spacing of 5 mm is best. For intermediate WL, in the range of 1 mm to 2 mm, an electrode spacing of 25 mm provides sufficient resolution and for large WL, in the range of 2 to 5 mm, an electrode spacing of 40 mm is appropriate.

As currently constructed, the sensor can be used to measure differences in WL thicknesses when a constant conductivity is present. In various accelerated tests and in atmospheric conditions, cycles exist where the WL will thin, concentrating salt concentrations, and changing the solution conductivity. In order to increase the utility of the sensor, it could be paired with a device that is capable of measuring solution conductivity in transient WLs such as an interdigitated electrode [40,41]. Although the behavior if these electrodes is not known in thinner water layers, a dependence on solution conductivity has been seen [41]. This approach would allow for the determination of WL thicknesses through cyclic conditions. Finally, it is noted that the sensor has a higher error when measuring WL thicknesses from a known volume (Figure 6) when compared to the use of an AAO membrane (Figure 7). It is thought to be due to a convex meniscus forming when the water is placed on the surface when a known volume is used and no meniscus when the AAO membrane is present. The convex meniscus would cause a slightly higher WL in the center of sample, which would cause for a lower resistance to be measured as given in Equation 1. To mitigate this problem, a wider sensor could be created to flatten out a convex meniscus, however the issue of having a non-continuous WL and less sensitive sensor becomes more problematic as the width of the sensor increases.

Within the realms of ASTM B117 and G85, the angle of exposure plays the largest role in water layer thickness

Sample exposure angle variability not only exists in accelerated testing due to variations in sample geometry, but such variability is specifically allowed by various standards. This variability can lead to test-to-test inconsistencies due to changing WL thicknesses. ASTM B117/B368 specifies angles between 15 and 30˚ [1,2], while ASTM D2247 states an angle of 15˚ [5] and ISO9227/GWM14872 requires an angle between 15 and 25˚ [3]. Finally, ASTM G85 requires an angle between 6 and 45˚ [4]. The inherent assumption of these standards is that within the range of sample exposure quoted in the standard, the results will be the same. This discussion excludes cyclic testing in which salt accumulation can occur on the surface of the alloy with repeated sprayings. ASTM G85 states that “test severity increases as angle from the vertical increases.” [4]. Increasing the angle would equate to a thicker WL, and greater salt deposition with time throughout the wet/dry/dwell cycles, as pointed out by Parker and Kelly [6], leading to an increase in corrosion rate.

The boundaries of WL thicknesses in this study ranged from 0.11 to 1.99 mm from 0˚ to 47˚ from vertical respectively. More specifically, within the realm of ASTM B117 [1], the WL thickness varies from 0.66 to 1.21 mm corresponding to 15˚ to 30˚ respectively. The WL experienced during atmospheric and accelerated corrosion has been shown to play a critical role in the electrochemical conditions including the transportation rate of oxygen to the surface, the rate of corrosion product precipitation, and the ability for pits to grow. ASTM B117 tacitly assumes a steady state WL thickness to achieve a steady state corrosion rate. As shown in Figure 8(b) and Figure 10, at angles larger than 20˚ from vertical, there are quasi-periodic fluctuations in the WL thickness. Below an angle of 20˚ from vertical, the salt spray leads to a steady state WL as the water runs down the surface constantly. At angles above a critical angle of 20˚, the WL increases to a critical thickness at which the weight of the water leads to a run-off of a large portion of the WL. This cycle is then repeated. The larger the angle from vertical, the more frequent run-off occurs, likely due to the larger effective deposition rate. Specifically, the rate of WL thickness growth (slope of WL vs. time graph in Figure 8(c) and (d)) and, therefore deposition rate, is roughly 2.1 times faster for sample at 30˚ in comparison to 20˚. Thus, at greater angles from the vertical, the run-off of water is closer to a cyclic test than a steady state test. Solution run-off can play a large role in the exposure testing of weathering steels, as the run-off of corrosion products have been shown to be an important factor in controlling the corrosion rates [42].

Another stipulation in both ASTM B117 and other accelerated corrosion tests is that the tests may be interrupted on a daily basis [1,3,4] which will affect the WL drastically. Within ASTM B117, the tests states that interruptions to an exposure can be made for a maximum of 60 min. per 24 hour period [1]. During interruptions, evaporation and run-off can occur and will decrease the WL thickness. This effect was studied in the present work for an electrode at an angle of 20˚, an electrolyte conductivity of 8 S/m, and a deposition rate of 1.7 mL/min which had a maximum WL thickness of 0.81 mm. As displayed in Figure 9, the sensor experienced a decrease in WL thickness of 0.15 mm in one hour (decrease of 18.5% of the original thickness) and did not have a uniform detectable WL after 112 min. If the test is re-started after 112 min., roughly 12 hours will pass before the WL reached a steady state thickness severely impacting the corrosion rate of the sample and repeatability of the exposure. Although the created sensor did not detect a water layer thickness after 112 min., a time of wetness sensor containing significantly smaller lead spacing could give a better representation of this scenario [25,26]. In addition, during the drying, the diffusion limited current density for oxygen reduction will move from the natural convection regime into one controlled by WL. It might be expected that samples at a more severe angle (<20˚) would experience a quicker dry-out period due to a smaller overall WL thickness and could be completely dry within the 60 min time period allowed. Furthermore, if the sample is moved or bumped while performing analysis of the samples more WL run-off would occur. According to ASTM G85 [4] and ISO 9927 [3], it is permissible to move the samples around the test chamber in order to achieve a random distribution of the samples. Every time the sample is moved, the WL has a strong tendency to run-off the surface of the alloy and will required a re-build period of roughly 12 hours. This effect could have important implications on the amount of time that corrosion can occur during an accelerated test. All of these effects would lead to test-to-test and chamber-to-chamber variability.

ASTM B117 suggests materials of construction for sample racks , however, there are no guidelines or restriction on the slot width for the samples which will have an impact on the sample angle. Take for example two samples of different thicknesses as depicted in Figure 12. Placing the two samples of different thicknesses in the same sample holder depicted will result in different angles of exposure. These different angles of exposure would greatly influence the WL thickness on the alloy surface. It is very important that when comparing corrosion rates or corrosion damage between samples that the samples are at the sample angles. Thus, it may be required to make custom sample holders based on the sample thickness to reduce test-to-test variability.

The angle of sample exposure in salt film environments determines if thin film conditions are achieved, influencing the rate of corrosion

The importance of the WL in corrosion testing cannot be overstated. The role of the WL thickness in an area that can serve as a cathode has been studied and is related to the diffusion distance of oxygen in solution [9-12]. Natural convection boundary layer thicknesses (δ_{nc}) for oxygen reduction reactions in literature range from 0.23 µm to 1 mm[9,13,15–19,22]. Tomashov estimated thin film conditions would exist for WL measurements < 1 mm [13] whereas the work of Amatore et al.[19] determined δ_{nc} to be 0.23 mm through the use of a micro-convection approach. Liu et al. used rotating disk electrode experiments to determine natural boundary thicknesses in 0.6 M

NaCl electrolytes and found a δ_{nc} of 0.8 mm [9]. As 0.6 M NaCl is a direct comparison to the electrolyte used in this study, 0.8 mm will be used as δ_{nc} for the following discussion.

Liu et al. determined the cathodic current available from a surface to support a dissolution reaction at one end of the rectangular cathode was dependent upon the stagnant WL thickness and sample size [9] and, therefore, the cathodic current available to support localized corrosion will be dependent upon the angle of exposure. For large cathodes (≥92.5 mm in length), they showed that the cathodic current increases above a WL of 0.8 mm as ohmic resistance is the dominating factor. For shorter cathodes (<92.5 mm) a competition between ohmic drop and mass-transfer kinetics suppresses the cathodic current density below either limiting behavior [9,43]. The boundaries of WL thicknesses measured in constant salt spray testing ranged from 1.99 to 0.11 mm from 47˚ to 0˚ from vertical respectively. In order to surpass thin film conditions ($\delta_{nc} = 0.8$ mm) an angle of 18.5˚ must be exceeded. However, once the sample surpasses an angle of 20˚ it is possible that you get run-off on the sample. With the variability in WL observed, conditions on the surface of the alloy move the surface from thin film to bulk conditions repeatedly and will continuously impact the cathodic current available. Such variability in cathodic current will affect corrosion damage during the accelerated testing. Available cathodic current has also been shown to effect the rate of stress corrosion cracking in atmospheric conditions [44]. Although the full extent of WL thickness of crack growth rate is not known, changes in the cathodic current available could influence the rate of stress corrosion cracking.

Another challenge arises when there is a dynamic WL, such as during ASTM G85 [4], due to the wetting and drying cycles present. Although the WL thickness presented in this study are only valid for constant salt spray testing, there lies value in discussing cyclic testing. Various modeling efforts have been put forth in order to describe the current density under transient WL's [10,11]. Dolgikh et al. determined that for the dynamic WL's, the oxygen reduction current density was determined by a competition between the shorter diffusion path due to thinner electrolyte layer thickness and the lower oxygen solubility as a result of solution concentrating during evaporation. The cathodic current density first increased with reduced WL and then reached at peak value at ~ 0.025 mm [10,43]. The WL at which the peak current density occurs was later decreased to 0.01 mm by Simillion at al. [11] who considered changes in ion diffusivity with the solution concentration with evaporating layers. As the peak current density occurs under very thin WL thicknesses, the WL thickness under constant salt spray conditions (wet cycle) is not as important. An angle of exposure solely cannot achieve this WL thickness, as WL's under completely vertical conditions are stable at 0.11 mm and run-off does not occur below 0.21 mm as depicted in Figure 10. Thus, the most important factors in cyclic testing are the angle, to achieve an increased salt load, and the relative humidity during the dwell period creating an equilibrium WL thickness with the salt concentration on the surface of the sample to increase cathodic current available. Finally, the role of corrosion and corrosion products in the retention of electrolyte needs to be considered when dealing with an actively corroding surface. Corrosion will cause a surface that is no longer flat due to dissolution, and the effects on the WL thickness are unknown. This topic is currently under investigation and will be reported on in the future. The presence of a corrosion product will lead to an increased WL, leading to increased mass transport distance for oxygen particularly when the tortuosity of the diffusion path is considered. In addition, the effective conductivity of the wetted corrosion product layer will lower than a pristine WL. These effects are the source of the much larger WL proposed in recent work [12,33,34] which combined current distribution modeling with experimental measurements of damage distribution to estimate the effective WL. These corrosion products can thus have important effects that will be addressed quantitatively in future work.

Conclusions

We present the design, construction, validation, and application of a sensor to determine WL thickness in the range of 0 to 5 mm in salt spray testing using finite element and experimental methods. The sensitivity of the sensor is based upon the width of the sample, distance between the electrodes, and solution conductivity as shown by FEM. The utility of the sensor was shown by measuring WL thickness in a continuous salt spray test similar to ASTM B117 and the effects of the range of specifications allowed within the standard were explored. Within the realms of accelerated corrosion testing, the angle of exposure plays the largest role in WL thickness. Furthermore, it was found that above an angle of 20° from vertical the WL experiences semi-periodic run-off events causing a transient decrease in the WL by up to 80%. Finally, the angle of sample exposure in salt spray environments determines if thin film conditions are achieved, influencing the rate of corrosion. The large allowances for sample angle present in most standards for laboratory corrosion chamber testing pose a large source of test-to-test variability.

Acknowledgements

Sandia National Laboratories is a multi-mission laboratory managed and operated by National Technology and Engineering Solutions of Sandia, LLC., a wholly owned subsidiary of Honeywell International, Inc., for the U.S. Department of Energy's National Nuclear Security Administration under contract DE-NA0003525. Financial assistance from the U.S. Department of Energy's Nuclear Energy University Program under contract DE-NE0008901 is also gratefully acknowledged. This paper is Sandia publication SAND2020-4214 J. The second author (S. Tokuda) was supported by JSPS KAKENHI Grant Numbers JP19J11684 and Interdepartmental Doctoral Degree Program for Multi-dimensional Materials Science Leaders in Tohoku University.

Data Availability

The raw/processed data required to reproduce these findings cannot be shared at this time as the data also forms part of an ongoing study.

References

[1] ASTM-B117-16 - Standard Practice for Operating Salt Spray (Fog) Apparatus, ASTM Int. (2017) 1–12. https://doi.org/10.1520/B0117-16.2.

[2] ASTM B368-09 - Standard Test Method for Copper-Accelerated Acetic Acid-Salt Spray (Fog) Testing (CASS Test), ASTM Int. (2014) 1–4. https://doi.org/10.1520/B0368-09R14.

[3] Corrosion tests in artificial atmospheres - Salt spray tests (ISO 9227:2014), Int. Organ. Stand. (2006) 1–28.

[4] ASTM G85-11 - Standard Practice for Modified Salt Spray (Fog) Testing 1, ASTM Int. (2017) 1–14. https://doi.org/10.1520/G0085-11.2.

[5] ASTM D2247-15 - Standard Practice for Testing Water Resistance of Coatings in 100% Relative Humidity, ASTM Int. (2014) 1–7. https://doi.org/10.1520/D2247-15.

[6] M.E. Parker, R.G. Kelly, Improved Atmospheric Corrosion Testing for Aluminum Alloys, Part I: Deconstructing ASTM G85-A2, CORROSION. 76 (2020) 39–50. https://doi.org/10.5006/3334.

[7] M.E. Parker, R.G. Kelly, Improved Atmospheric Corrosion Testing for Aluminum Alloys, Part II: Developing Improved Testing Protocol, CORROSION. 76 (2020) 51–62. https://doi.org/10.5006/3335.

[8] F. Bovard, J. Tardiff, T. Jafolla, D. McCune, G. Courval, K.A. Smith, F. Lee, F.W. Lutze, J. Repp, Development of an improved cosmetic corrosion test for finished aluminum autobody panels, SAE Tech. Pap. (2005) 776–790. https://doi.org/10.4271/2005-01-0542.

[9] C. Liu, J. Srinivasan, R.G. Kelly, Electrolyte film thickness effects on the cathodic current availability in a galvanic couple, J. Electrochem. Soc. 164 (2017) C845–C855. https://doi.org/10.1149/2.1641713jes.

[10] O. Dolgikh, A.C. Bastos, A. Oliveira, C. Dan, J. Deconinck, Influence of the electrolyte film thickness and NaCl concentration on the oxygen reduction current on platinum, Corros. Sci. 102 (2016) 338–347. https://doi.org/10.1016/j.corsci.2015.10.025.

[11] H. Simillion, N. Van den Steen, H. Terryn, J. Deconinck, Geometry influence on corrosion in dynamic thin film electrolytes, Electrochim. Acta. 209 (2016) 149–158. https://doi.org/10.1016/j.electacta.2016.04.072.

[12] R. Marshall, R. Kelly, A. Goff, C. Sprinkle, Galvanic Corrosion Between Coated Al Alloy Plate and Stainless Steel Fasteners, Part 1: FEM Model Development and Validation, Corrosion. 75 (2019) 1461–1473. https://doi.org/10.5006/3308.

[13] N.D. TOMASHOV, Development of the Electrochemical Theory of Metallic Corrosion, CORROSION. 20 (1964) 7t-14t. https://doi.org/10.5006/0010-9312-20.1.7t.

[14] M. Stratmann, H. Streckel, On the atmospheric corrosion of metals which are covered with thin electrolyte layers-II. Experimental results, Corros. Sci. 30 (1990) 697–714. https://doi.org/10.1016/0010-938X(90)90033-2.

[15] G.S. Frankel, M. Stratmann, M. Rohwerder, A. Michalik, B. Maier, J. Dora, M. Wicinski, Potential control under thin aqueous layers using a Kelvin Probe, Corros. Sci. (2007). https://doi.org/10.1016/j.corsci.2006.10.017.

[16] O. Dolgikh, A. –S Demeter, S. V. Lamaka, M. Taryba, A.C. Bastos, M.C. Quevedo, J. Deconinck, Simulation of the role of vibration on Scanning Vibrating Electrode Technique

measurements close to a disc in plane, Electrochim. Acta. 203 (2016) 379–387. https://doi.org/10.1016/j.electacta.2016.01.188.

[17] Y.L. Cheng, Z. Zhang, F.H. Cao, J.F. Li, J.Q. Zhang, J.M. Wang, C.N. Cao, A study of the corrosion of aluminum alloy 2024-T3 under thin electrolyte layers, Corros. Sci. 46 (2004) 1649–1667. https://doi.org/10.1016/j.corsci.2003.10.005.

[18] S.H. Zhang, S.B. Lyon, The electrochemistry of iron, zinc and copper in thin layer electrolytes, Corros. Sci. 35 (1993) 713–718. https://doi.org/10.1016/0010-938X(93)90207-W.

[19] C. Amatore, S. Szunerits, L. Thouin, J.S. Warkocz, The real meaning of Nernst's steady diffusion layer concept under non-forced hydrodynamic conditions. A simple model based on Levich's seminal view of convection, J. Electroanal. Chem. 500 (2001) 62–70. https://doi.org/10.1016/S0022-0728(00)00378-8.

[20] A. Nishikata, Y. Yamashita, H. Katayama, T. Tsuru, A. Usami, K. Tanabe, H. Mabuchi, An electrochemical impedance study on atmospheric corrosion of steels in a cyclic wet-dry condition, Corros. Sci. 37 (1995) 2059–2069. https://doi.org/10.1016/0010-938X(95)00104-R.

[21] A. Nishikata, Y. Ichihara, T. Tsuru, An application of electrochemical impedance spectroscopy to atmospheric corrosion study, Corros. Sci. 37 (1995) 897–911. https://doi.org/10.1016/0010-938X(95)00002-2.

[22] A. Nishikata, Influence of Electrolyte Layer Thickness and pH on the Initial Stage of the Atmospheric Corrosion of Iron, J. Electrochem. Soc. 144 (1997) 1244. https://doi.org/10.1149/1.1837578.

[23] M. Stratmann, H. Streckel, K.T. Kim, S. Crockett, On the atmospheric corrosion of metals which are covered with thin electrolyte layers-iii. the measurement of polarisation curves on metal surfaces which are covered by thin electrolyte layers, Corros. Sci. 30 (1990) 715–734. https://doi.org/10.1016/0010-938X(90)90034-3.

[24] M. Stratmann, H. Streckel, On the atmospheric corrosion of metals which are covered with thin electrolyte layers—I. Verification of the experimental technique, Corros. Sci. 30 (1990) 681–696. https://doi.org/10.1016/0010-938X(90)90032-Z.

[25] E. Schindelholz, R.G. Kelly, I.S. Cole, W.D. Ganther, T.H. Muster, Comparability and accuracy of time of wetness sensing methods relevant for atmospheric corrosion, Corros. Sci. 67 (2013) 233–241. https://doi.org/10.1016/j.corsci.2012.10.026.

[26] E. Schindelholz, L.K. Tsui, R.G. Kelly, Hygroscopic particle behavior studied by interdigitated array microelectrode impedance sensors, J. Phys. Chem. A. 118 (2014) 167–177. https://doi.org/10.1021/jp4098149.

[27] N. Li, M. Cao, X. Yu, J. Jia, Y. Yang, High Sensitive Capacitive Sensing Method for Thickness Detection of the Water Film on an Insulation Surface, IEEE Access. 7 (2019) 96384–96391. https://doi.org/10.1109/ACCESS.2019.2929585.

[28] J. Doring, L. Tharmakularajah, K.-L. Krieger, Study of interdigital electode structures for the detection of water spray, in: GMA/ITG-Fachtagung Sensoren Und Messsyst. 2019, Routledge, 2019: pp. 700–707. https://doi.org/10.5162/sensoren2019/P2.7.

[29] Y. Yu, L. Ma, H. Ye, Y. Zheng, Y. Ma, Design of instantaneous liquid film thickness measurement system for conductive or non-conductive fluid with high viscosity, AIP Adv. 7 (2017). https://doi.org/10.1063/1.4985721.

[30] S. Henkel, F. Beyrau, Y. Hardalupas, A.M.K.P. Taylor, Novel method for the measurement of liquid film thickness during fuel spray impingement on surfaces, Opt. Express. 24 (2016) 2542. https://doi.org/10.1364/oe.24.002542.

[31] M. Lubnow, T. Dreier, C. Schulz, Water Film Thickness Imaging based on Time-Multiplexed Near-Infrared Absorption, Opt. Express. 26 (2018) 20902–20912. https://doi.org/10.1364/LACSEA.2018.LW2C.3.

[32] A. Serizawa, K. Nagane, T. Kamei, Z. Kawara, Dynamic measurement of liquid film thickness in stratified flow by using ultrasonic echo technique, in: 4th Int. Top. Meet. Nucl. Therm. Hydraul. Oper. Saf., Taipei, 1994: pp. 42–C.

[33] C. Liu, Assessment of the Utility of Laplace’s Equation for Modeling of Localized Corrosion, University of Virginia (PhD Dissertation), 2018.

[34] L. Blohm, Galvanic Coupling of AA5XXX-H116 and CDA 706 Utilizing Laboratory, Outdoor, and Accelerated Testing, University of Virginia (Masters Thesis), 2018.

[35] C. Wagner, Contribution to the Theory of Cathodic Protection, J. Electrochem. Soc. 99 (1952) 1–12. https://doi.org/10.1149/1.2779653.

[36] M.T. Woldemedhin, M.E. Shedd, R.G. Kelly, Evaluation of the Maximum Pit Size Model on Stainless Steels under Thin Film Electrolyte Conditions, J. Electrochem. Soc. 161 (2014) E3216–E3224. https://doi.org/10.1149/2.023408jes.

[37] V. SZCZEPANSKI, I. VLASSIOUK, S. SMIRNOV, Stability of silane modifiers on alumina nanoporous membranes, J. Memb. Sci. 281 (2006) 587–591. https://doi.org/10.1016/j.memsci.2006.04.027.

[38] P. Takmakov, I. Vlassiouk, S. Smirnov, Hydrothermally shrunk alumina nanopores and their application to DNA sensing, Analyst. 131 (2006) 1248–1253. https://doi.org/10.1039/b608084g.

[39] O. Ozdemir, S.I. Karakashev, A. V. Nguyen, J.D. Miller, Adsorption and surface tension analysis of concentrated alkali halide brine solutions, Miner. Eng. 22 (2009) 263–271. https://doi.org/10.1016/j.mineng.2008.08.001.

[40] A. Dizon, M.E. Orazem, On the impedance response of interdigitated electrodes, Electrochim. Acta. 327 (2019). https://doi.org/10.1016/j.electacta.2019.135000.

[41] A. Dizon, M.E. Orazem, On experimental determination of cell constants for interdigitated electrodes, Electrochim. Acta. 337 (2020). https://doi.org/10.1016/j.electacta.2020.135732.

[42] M. Morcillo, B. Chico, I. Díaz, H. Cano, D. de la Fuente, Atmospheric corrosion data of weathering steels. A review, Corros. Sci. 77 (2013) 6–24. https://doi.org/10.1016/j.corsci.2013.08.021.

[43] C. Liu, R.G. Kelly, A Review of the Application of Finite Element Method (FEM) to Localized Corrosion Modeling, Corrosion. 75 (2019) 1285–1299. https://doi.org/10.5006/3282.

[44] P.J. Steiner, J.T. Burns, Mechanistic Studies of Intergranular Stress Corrosion Cracking in Al-Mg Alloys under Atmospheric Exposure Conditions, CORROSION. 74 (2018) 1117–1131. https://doi.org/10.5006/2853.

Figures

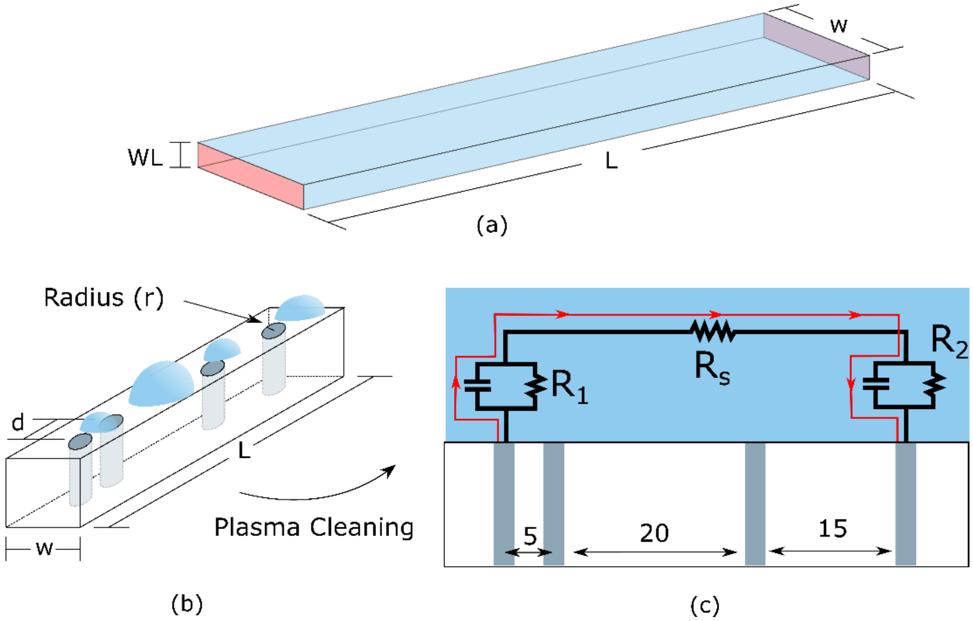

Figure 1: (a) Schematic to determine resistance of water layer thickness for a parallelepiped. The length (L), width (w), and water layer thickness (WL) are labeled. (b) Droplet formation on the surface of plexiglass surface before plasma cleaning. The radius (r) and distance between the electrodes (d) are labeled. (c) Water layer formation after plasma cleaning and current path measured under high frequency EIS. The distances between the wires are labeled in mm.

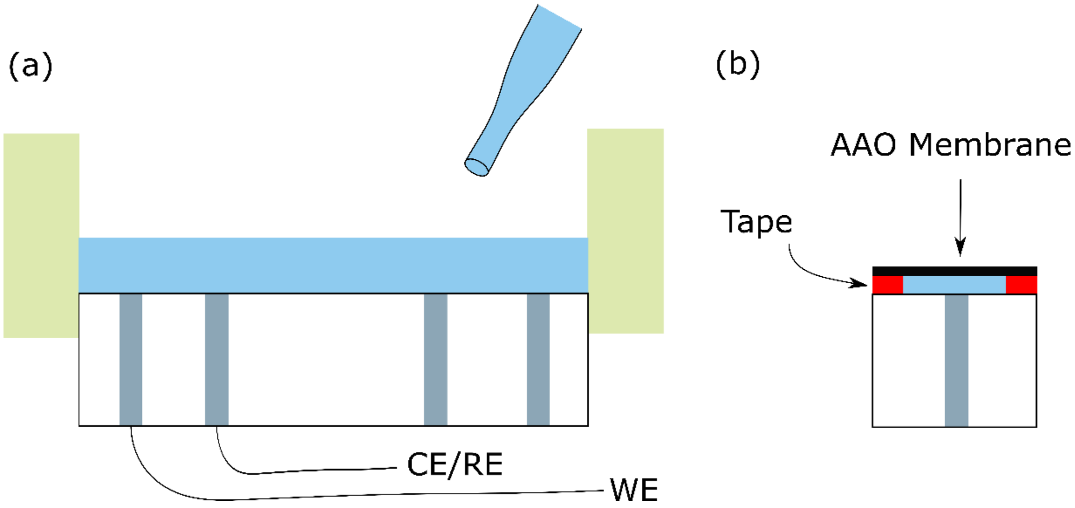

Figure 2: Calibration of the sensor through (a) the deposition of a known volume on the surface of the sensor and (b) known tape thicknesses and a hydrophobic AAO membrane.

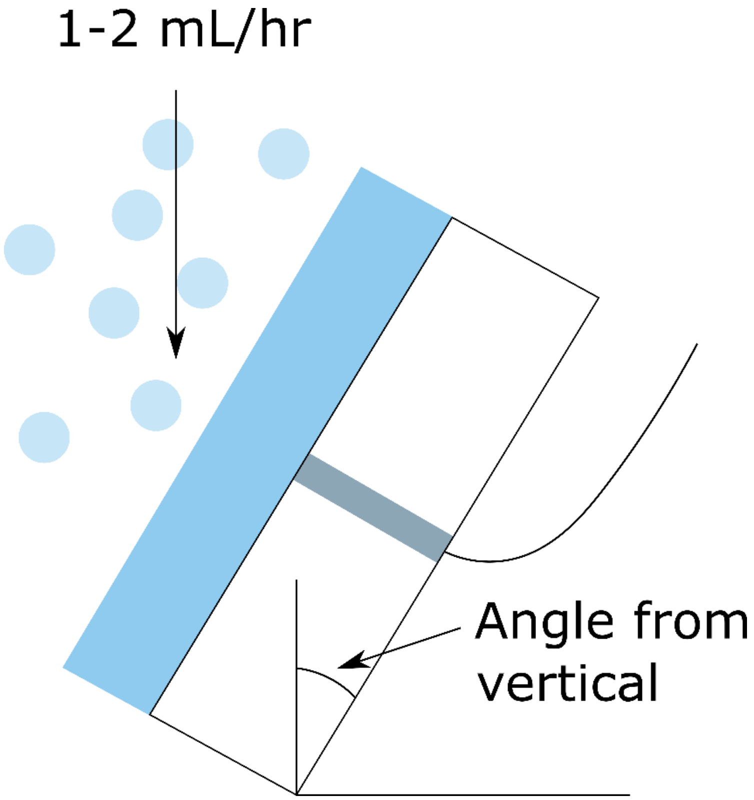

Figure 3: Set-up for determination of in-situ water layer thickness in a salt spray chamber.

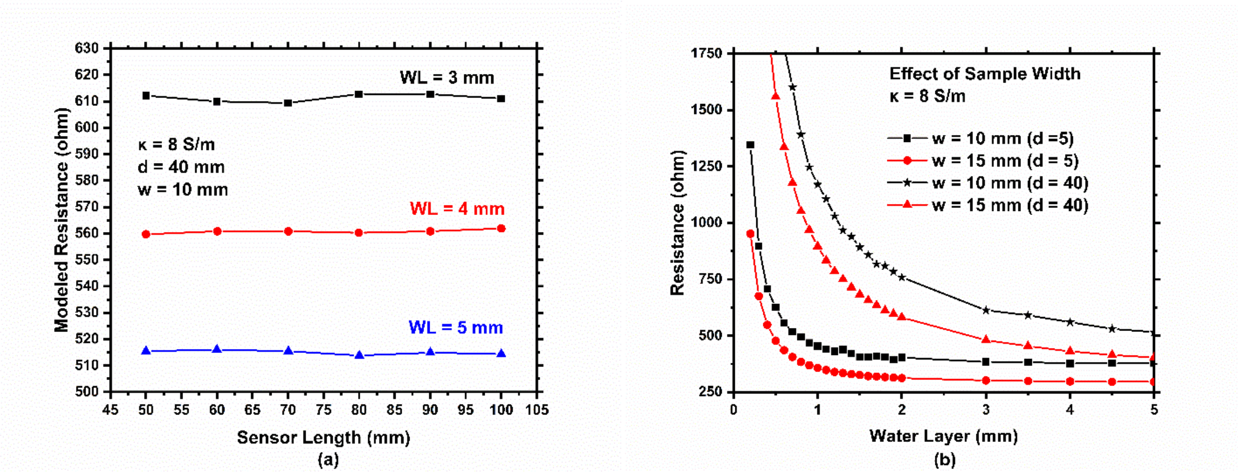

Figure 4: Effect of (a) depth and (b) width on the measured resistance as a function of water layer thickness.

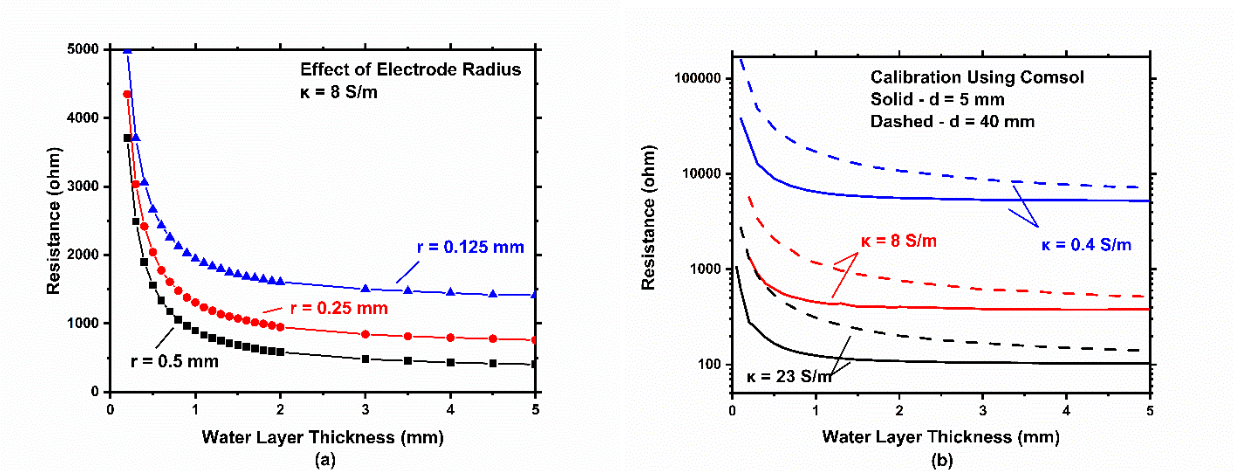

Figure 5: Effects of (a) electrode radius on resistance as a function of water layer thickness. (b) Effect of solution conductivity and electrode position on the calculated resistance as a function of water layer thickness. Note the resistance is a logarithmic scale in (b).

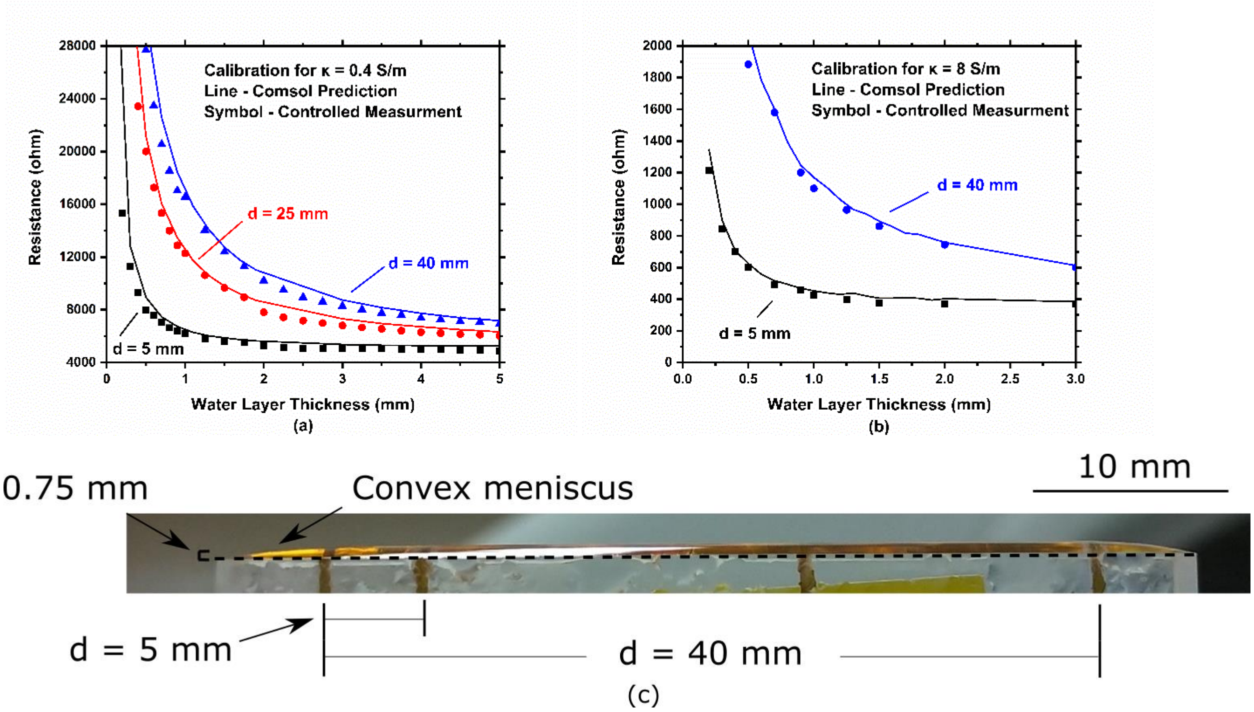

Figure 6: Calibration measurements of the sensor using a known volume of liquid in a controlled environment for an electrolyte with (a) $\kappa = 0.4$ S/m and (b) $\kappa = 8$ S/m. (c) Convex meniscus (gold-colored region) formed on the top of the plexiglass surface (highlighted by dotted line).

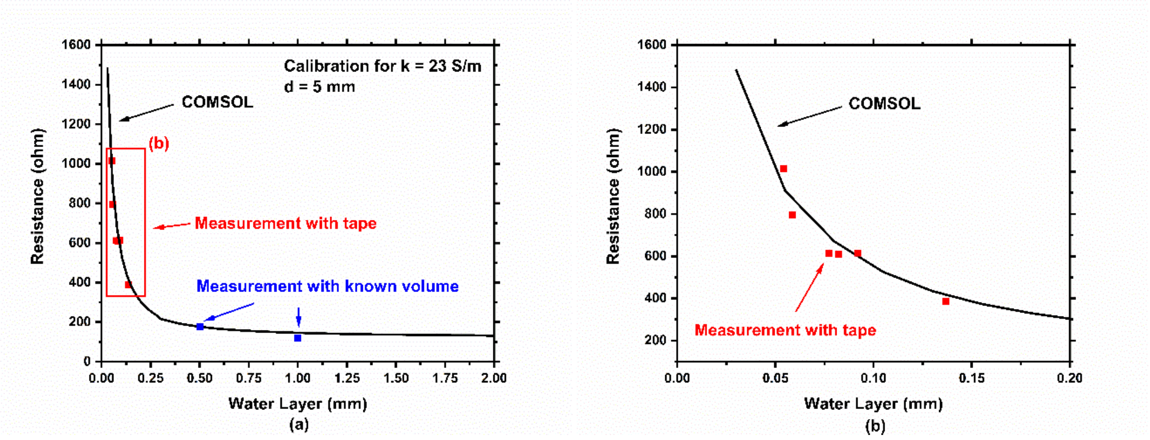

Figure 7: (a) Measured solution resistance at known thicknesses with of $\kappa = 23$ S/m. Two different methods were used including measurements under an AAO membrane and with a known volume of liquid. (b) Magnification of the denoted area in (a).

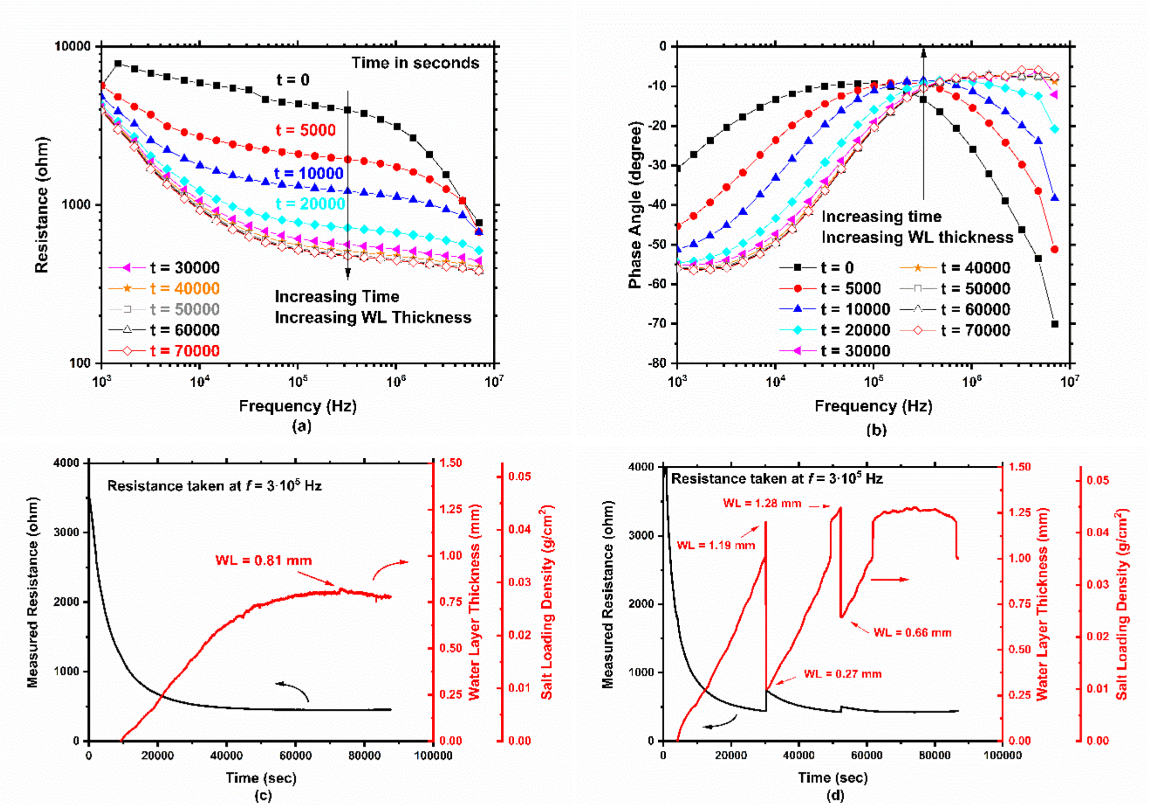

Figure 8: (a) In-situ EIS measurements as a function of time (in sec). Measurements were taken continuously, however, representative time steps are shown. (b) Phase angle for the test in (a). (c) Resistances at a frequency of $3 \cdot 10^5$ Hz from the continuous measurements in (a) and calculated water layer thicknesses. (a,) (b), (c) were for k = 8 and an angle of 20° and a deposition rate of 1.7 mL/hr. (d) Resistance measurements and calculated water layer thicknesses for k = 8, an angle of 30° and a deposition rate of 1.7 mL/hr.

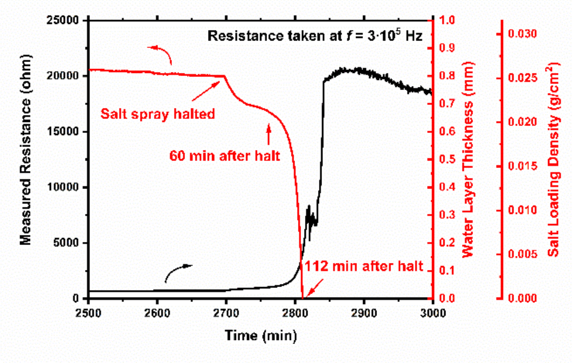

Figure 9: Effect of measured resistance and water layer thickness calculation at an angle of 20, k =8, and rate of 1.7 mL/hr after the salt spray test was halted. Salt spray testing ran for approximately 45 hours before the test was stopped. The lid was left in the closed position. A fan in the chamber was started after the salt spray was stopped.

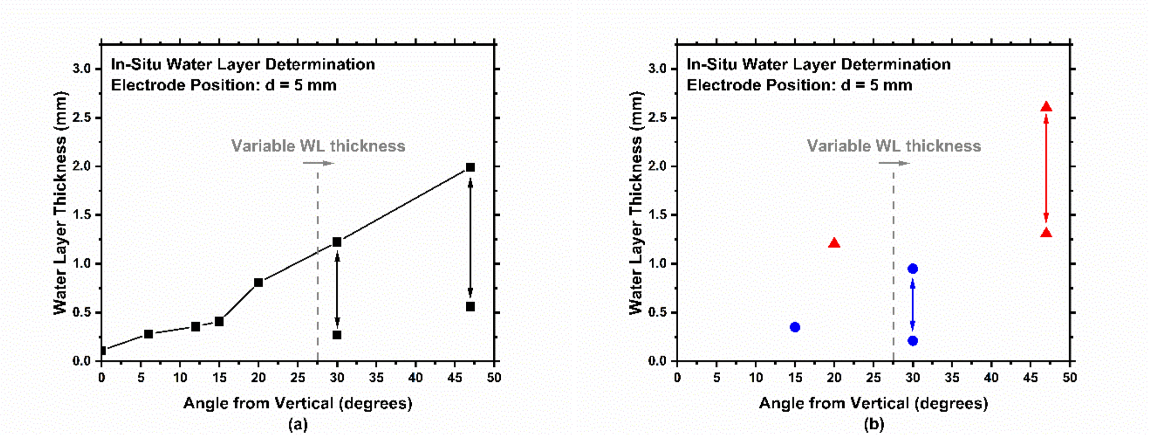

Figure 10: Maximum water layer thickness achieved during continuous salt spray testing as a function of angle, flow rate, and solution conductivity (solution concentration). (a) ■ *denotes a conductivity of 8 S/m and a collection rate of 1.7 mL/hr, (b)* ▲ *denotes a conductivity of 0.4 S/m and a collection rate of 1.7 mL/hr and* ● *denotes a conductivity of 8 S/m and a collection rate of 1.2 mL/hr, Having double arrows indicates the minimum water layer thickness reached after the water layer slips off as displayed in Figure 8(b).*

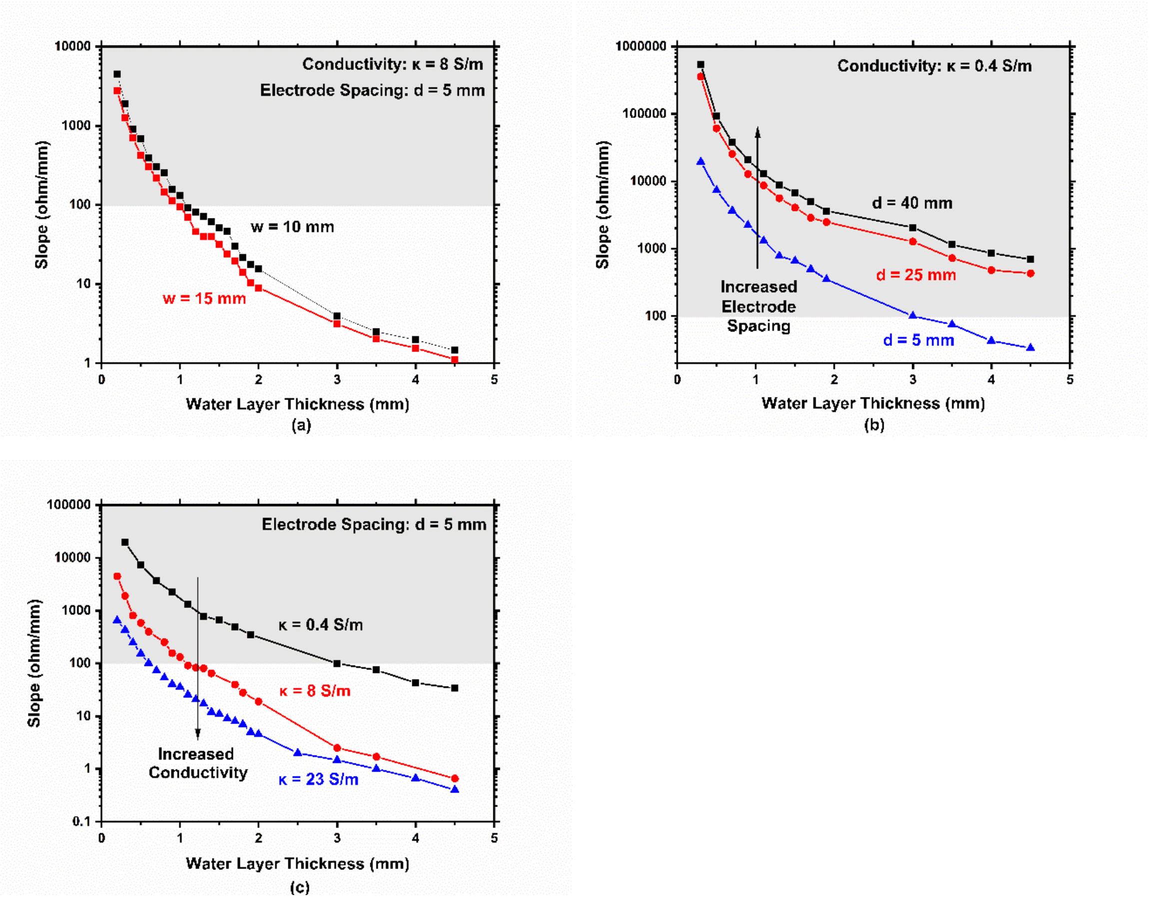

Figure 11: Sensitivities in resistance measurements as a function of (a) electrode width (b) electrode spacing and (c) solution conductivity. The ordinate axis is the slope of graphs such as Figure 5. The gray box is indicative of the desired range of sensitivity (>100 ohm/mm).

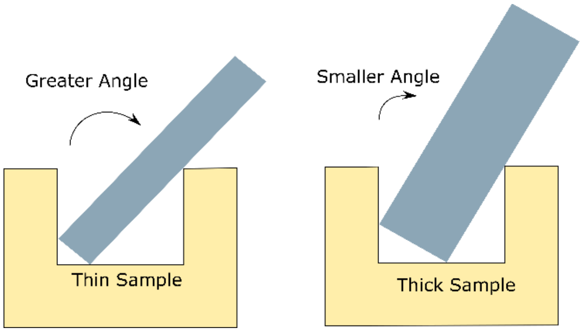

Figure 12: Effect of the sample thickness on the angle of exposure in a sample rack.